

Hydrogen Bonding between Water and Heterocyclic Compounds Explored by Microwave Spectroscopy

# **Charlotte Nicole Cummings**

Thesis submitted in partial fulfilment of the requirements for the award of

# **Doctor of Philosophy**

Chemistry- School of Natural and Environmental Sciences

# September 2024

Supervisors: Dr Nicholas R. Walker and Dr Benjamin R. Horrocks

#### **Abstract**

Microwave spectroscopy is a powerful spectroscopic technique used to study the rotational spectra of molecules and weakly-bound complexes in the gas phase. The assignment of the microwave spectrum allows the determination of rotational constants from which structural information of the molecular species under study can be derived. This technique has also been used extensively to study large amplitude motions and conformations of molecules, as well as to investigate non-covalent interactions when studying weakly-bound complexes.

Microwave spectroscopic studies of several alkyl-substituted heteroaromatic rings and their weakly-bound complexes with water are presented within this thesis. The studies have been performed using Chirped Pulse Fourier Transform Microwave spectroscopy, over the 2.0-18.5 GHz frequency region, in combination with either a heating reservoir or laser ablation for the study of volatile and non-volatile species respectively. The isolated molecules and hydrate complexes were generated and probed in a supersonic expansion comprised of low concentrations of the target molecule and water in an inert carrier gas. Quantum chemical calculations, Non-Covalent Interaction index and Natural Bond Orbital analyses have been performed alongside the experimental studies.

Structural parameters within the complexes of methylthiazole···H<sub>2</sub>O, 2-ethylfuran···H<sub>2</sub>O, 2-ethylthiazole···(H<sub>2</sub>O)<sub>n</sub> and ethylimidazole···(H<sub>2</sub>O)<sub>n</sub> have been precisely determined. It will be shown that each complex contains a comparatively strong O–H···X (X = N or O) hydrogen bond between water and a nitrogen or oxygen atom of the heteroaromatic ring. It will be further shown that weaker interactions between the oxygen atom of water and H, CH<sub>3</sub> or C<sub>2</sub>H<sub>5</sub> groups (C–H···O) located on the heteroaromatic ring have important effects. The results reveal a dynamic interplay between the formation of hydrogen bonds between the heterocycle and water, the amplitudes of  $V_3$  barriers to internal rotation (of CH<sub>3</sub> groups) and conformational preferences (of C<sub>2</sub>H<sub>5</sub> groups) across the series of complexes studied.

### Acknowledgements

"We know that doctorates aren't earned alone" – Alicia Thompson

As highlighted in the quote above, this thesis would not have been possible without the support I've received throughout my PhD journey. First and foremost, I would like to thank my supervisor, Nick Walker. Your continuous support, encouragement, and guidance over the past four years has been invaluable. From teaching me how to use PGOPHER for assigning spectra and how to perform experiments in the early stages of my PhD, to your optimism and encouragement during our meetings and for your support during the writing of this thesis, I am incredibly grateful.

I would also like to extend my thanks to everyone I've had the privilege of working with over the last few years. I would like to thank Surabhi Gupta, I consider myself incredibly fortunate to have collaborated on projects with you and appreciate your support and, most importantly, your friendship. Your visit to Newcastle and our trip to ISMS were some of the highlights of my PhD. A special thanks to Eva Gougoula for your guidance and assistance during the initial stages of my PhD. The projects we have both worked on significantly influenced the direction of my subsequent research, for which I am thankful. I am also grateful to the wider microwave spectroscopy community and feel incredibly lucky to be part of such a supportive and collaborative research community. In particular, I would like to thank Lam Nguyen and Isabelle Kleiner for their invaluable assistance with projects involving internal rotation.

I would also like to extend my thanks to everyone within the Chemistry Department at Newcastle University. Over the past eight years, both as an undergraduate and a PhD student, I have had a wonderful time in the department. My time at Newcastle has significantly shaped me both as a scientist and as an individual. In particular, I would like to thank Cristina Navarro Reguero for all your kindness and continuous support over these eight years. I am also extremely grateful to Morag Grierson, Marcello D'Avino, Lama Alharthi, Liam McGarry, and David Stokoe for your friendship over the past four years and I am grateful that we have had the opportunity to go through the PhD journey together.

Finally, I would like to thank Melissa, Dominic and my parents. I am incredibly grateful for your continuous support and belief in me, even during times when I doubted myself. Without your encouragement and support, this PhD and thesis would not have been possible.

## **Table of Contents**

Abstract	i
Acknowledgements	iii
Table of Contents	V
List of Tables	X
List of Figures	xvii
Publications	xxii
Oral Presentations	xxiii
Poster Presentations	XXV
Chapter 1. Introduction	1
1.1 Hydrogen bonding interactions	1
1.2 Microsolvation of heteroaromatic rings	6
1.2.1 Hydrate complexes formed with five-membered rings	7
1.2.2 Hydrate complexes formed with six-membered rings	12
1.3 Internal rotation	14
1.3.1 Methylated heteroaromatic rings	16
1.3.2 Effect of ring substituents	18
1.3.3 Effect of complex formation	19
1.4 Conformationally flexible aromatic derivatives	22
1.4.1 Alkyl-substituted aromatic rings	23
1.4.2 Other substituted aromatic rings	24
1.5 Thesis Overview	28
1.6 References	30
Chapter 2. Theory.	35
2.1 Introduction	35
2.2 Born-Oppenheimer approximation	37

2.3 Moments of inertia	38
2.4 Types of molecules	40
2.4.1 Linear tops	40
2.4.2 Symmetric tops	41
2.4.3 Asymmetric tops	43
2.5 Rotational transitions and selection rules	46
2.6 Centrifugal distortion and the Reduced Hamiltonian	49
2.7 Hyperfine structure and nuclear quadrupole coupling	52
2.8 Internal rotation	55
2.9 Quantum chemical calculations	60
2.10 Spectral assignment and fitting	63
2.11 Structure determination methods	64
2.11.1 Planar (second) moments and inertial defect	64
2.11.2 Substitution (r <sub>s</sub> ) geometry	65
2.11.3 Effective ground state (r <sub>0</sub> ) geometry	67
2.12 Non-Covalent Interactions (NCI) index	68
2.13 Natural Bond Orbital (NBO) analysis	70
2.14 References	71
Chapter 3. Experimental.	73
3.1 Introduction	73
3.2 Microwave circuitry: 7.0 – 18.5 GHz experiment	76
3.2.1 Excitation circuit	76
3.2.2 Sample polarisation and molecular emission	76
3.2.3 Detection circuit	76
3.3 Microwave circuitry: 2.0 – 8.0 GHz experiment	78
3.3.1 Excitation circuit	78
3.3.2 Detection circuit	78
3.4 Molecular sources	79

3.4.1 Heated reservoir	79
3.4.2 Laser ablation source	80
3.5 Vacuum Chamber and Pumps	84
3.6 Supersonic Expansion	86
3.7 Trigger sequence and timings	89
3.8 Spectral lines: Linewidth and intensity	91
3.9 References	93
Chapter 4. Non-Covalent Interactions in the Molecular Geometries of Complexes For between Structural Isomers of Methylthiazole and Water Revealed by Micro Spectroscopy	wave
4.1 Introduction	
4.2 Experimental Methods	97
4.3 Quantum Chemical Calculations	98
4.4 Spectral Analysis and Assignment	101
4.4.1 Effective (A- species only) fits	101
4.4.2 Internal rotation and global fits	108
4.5 Molecular Geometries	114
4.6 Non-Covalent Interactions	122
4.7 Discussion	126
4.8 2-MT···H <sub>2</sub> O: Interim global fits	133
4.9 Conclusions	135
4.10 References	136
Chapter 5. Characterisation of the Molecular Geometry of 2-Ethylfuran····H <sub>2</sub> O by Micro Spectroscopy.	
5.1 Introduction	139
5.2 Experimental Methods	142
5.3 Quantum Chemical Calculations	144
5.4 Spectral Analysis	146
5.4.1 Initial observations: 2-ethylfuran monomer	146

5.4.2 Assignment of the monohydrate complex of 2-ethylfuran	148
5.5 Molecular Geometry	151
5.6 Non-Covalent Interactions	
5.7 Discussion	158
5.8 Conclusions	164
5.9 References	
Chapter 6. The Conformational Preference of 2-Ethylthiazole and Complexes with Water Revealed by Microwave Spectroscopy	-
6.1 Introduction	167
6.2 Experimental Methods	170
6.3 Quantum Chemical Calculations	172
6.4 Spectral Analysis	177
6.4.1 Assignment of the 2-ethylthiazole monomer	177
6.4.2 Assignment of hydrate complexes	180
6.5 Molecular Geometry	185
6.5.1 2-ethylthiazole monomer	185
6.5.2 Hydrate complexes	187
6.6 Non-Covalent Interactions	192
6.7 Discussion	196
6.8 Conclusions	200
6.9 References	201
Chapter 7. Microwave spectra and molecular geometries of Ethylimidazo	le isomers and their
hydrate complexes	202
7.1 Introduction	202
7.2 Experimental Methods	204
7.3 Quantum Chemical Calculations	207
7.3.1 Ethylimidazole monomers	207
7.3.2 Hydrate complexes	211

7.4 Spectral analysis and assignment	214
7.4.1 Assignment of N-ethylimidazole and 2-ethylimidazole monomers	214
7.4.2 Assignment of hydrate complexes	220
7.5 Molecular geometry	227
7.5.1 Ethylimidazole monomers	227
7.5.2 Hydrate complexes	230
7.6 Nuclear Quadrupole Coupling Constants	235
7.7 Non-Covalent Interactions	238
7.8 Discussion	240
7.9 Conclusion	247
7.10 References	248
Chapter 8. Conclusions.	250
8.1 References	255
Appendix	256

## **List of Tables**

Table 2.1 Summary of selection rules for asymmetric top molecules
Table 4.1 Spectroscopic parameters of 2-MT···H <sub>2</sub> O, 4-MT···H <sub>2</sub> O and 5-MT···H <sub>2</sub> O calculated
at different levels of theory. <sup>a</sup>
Table 4.2 Spectroscopic constants determined for five isotopologues of 2-MT····H <sub>2</sub> O by A-
species only (effective) fits performed using PGOPHER
Table 4.3 Spectroscopic constants determined for five isotopologues of 4-MT···H <sub>2</sub> O by A-
species only (effective) fits performed using PGOPHER
Table 4.4 Spectroscopic constants determined for five isotopologues of 5-MT····H <sub>2</sub> O by A-
species only (effective) fits performed using PGOPHER
Table 4.5 Results of XIAM and BELGI-C <sub>s</sub> -hyperfine fits of spectroscopic parameters to the
frequencies of A- and E-species transitions of the main isotopologues110
Table 4.6 Spectroscopic parameters determined from global (XIAM) fits obtained by fitting to
the frequencies of A- and E- species transitions for five isotopologues of 4-MT···H <sub>2</sub> O112
Table 4.7 Spectroscopic parameters determined from global (XIAM) fits obtained by fitting to
the frequencies of A- and E- species transitions for five isotopologues of 5-MT···H <sub>2</sub> O113
Table 4.8 Comparison of DFT calculated (r <sub>e</sub> ) and experimentally-determined (r <sub>s</sub> ) atomic
coordinates of H <sub>2</sub> O in 2-MT···H <sub>2</sub> O, 4-MT···H <sub>2</sub> O and 5-MT···H <sub>2</sub> O116
Table 4.9 Comparison of the DFT calculated and experimentally-determined structural
parameters
Table 4.10 Comparison of experimentally-determined $(r_0)$ structural parameters for complexes
formed between 5-membered N-heterocyclic rings and H <sub>2</sub> O
Table 5.1 Spectroscopic parameters of 2-EF···H <sub>2</sub> O (C <sub>1</sub> conformer) calculated at different levels
of theory
Table 5.2 Spectroscopic parameters of 2-EF···H <sub>2</sub> O (C <sub>s</sub> conformer) calculated at different levels
of theory
Table 5.3 Experimentally determined spectroscopic parameters of five isotopologues of 2-
$EF \cdots H_2O.$ 150
Table 5.4 Comparison of experimentally determined ( $r_s$ ) and $r_e$ atomic coordinates of H <sub>2</sub> O in 2-
$EF\cdots H_2O.$ 151
Table 5.5 Comparison of DFT calculated $(r_e)$ and experimentally determined $(r_0)$ structural
parameters of 2-EF···H <sub>2</sub> O152
Table 5.6 Comparison of experimentally-determined $(r_0)$ structural parameters of complexes
formed between furan derivatives and H <sub>2</sub> O

Table 6.1 Spectroscopic parameters of the C <sub>1</sub> conformation of 2-ethylthiazole calculated at
different levels of theory
Table 6.2 Spectroscopic parameters of 2-ET $\cdots$ H <sub>2</sub> O calculated at different levels of theory. 174
Table 6.3 Spectroscopic parameters of 2-ET···(H <sub>2</sub> O) <sub>2</sub> calculated at different levels of theory
Table 6.4 Spectroscopic parameters determined for 2-ethylthiazole by fitting experimentally-
recorded transition frequencies to parameters in Watson's S-reduced Hamiltonian
Table 6.5 Spectroscopic constants determined for <sup>34</sup> S and <sup>13</sup> C isotopologues of 2-ethylthiazole.
Values of centrifugal distortion constants ( $D_J$ , $D_{JK}$ , $D_K$ , $d_1$ and $d_2$ ) and nuclear quadrupole
coupling constants ( $\chi_{aa}$ (N3) and [ $\chi_{bb}$ (N3) – $\chi_{cc}$ (N3)])) held fixed to those determined for the
parent isotopologue, displayed in Table 6.4, when fits were performed179
Table 6.6 Experimentally-determined spectroscopic parameters for six isotopologues of 2-
ET···H <sub>2</sub> O
Table 6.7 Experimentally-determined spectroscopic parameters for three isotopologues of 2-
$ET \cdots (H_2O)_2 \dots 184$
Table 6.8 Nuclear quadrupole coupling constants in the principle nuclear axis framework
determined using QDIAG
Table 6.9 Comparison of DFT calculated $(r_e)$ and experimentally determined $(r_s)$ atomic
coordinates of heavy atoms in 2-ethylthiazole
Table 6.10 Comparison of experimentally-determined $(r_{\rm s})$ and DFT-calculated $(r_{\rm e})$ atomic
coordinates of $H_2O$ and $S$ in $2\text{-ET}\cdots H_2O$ and $O$ atoms in $2\text{-ET}\cdots (H_2O)_2$
Table 6.11 Comparison of DFT-calculated ( $r_e$ ) and experimentally-determined ( $r_0$ ) structural
parameters for 2-ET···H <sub>2</sub> O
Table 6.12 Comparison of DFT-calculated ( $r_e$ ) and experimentally-determined ( $r_0$ ) structural
parameters of 2-ET···(H <sub>2</sub> O) <sub>2</sub> 190
Table 6.13 Comparison of experimentally-determined ( $r_0$ ) structural parameters for complexes
formed between 5-membered N-heterocyclic rings and H <sub>2</sub> O
Table 7.1 Spectroscopic parameters of N-ethylimidazole (C <sub>1</sub> conformer) calculated at different
levels of theory
Table 7.2 Spectroscopic parameters of possible C <sub>s</sub> conformations of 2-ethylimidazole
calculated at different levels of theory
Table 7.3 Spectroscopic parameters of the $C_1$ conformation of 2-ethylimidazole calculated at
different levels of theory

Table 7.4 Spectroscopic parameters determined for N-ethylimidazole and 2-ethylimidazole
generated by fitting experimentally obtained transition frequencies to Watson's S- reduced
Hamiltonian
Table 7.5 Spectroscopic parameters determined for <sup>13</sup> C isotopologues of N-ethylimidazole and
2-ethylimidazole. Values of centrifugal distortion constants $(D_J, D_{JK}, D_K, d_1 \text{ and } d_2)$ and nuclear
quadrupole coupling constants ( $\chi_{aa}$ (N1), [ $\chi_{bb}$ (N1) – $\chi_{cc}$ (N1)], $\chi_{aa}$ (N3) and [ $\chi_{bb}$ (N3) – $\chi_{cc}$ (N3)])
held fixed to those determined for the parent isotopologue of each molecule, displayed in Table
7.4, when fits were performed
Table 7.6 Experimentally-determined spectroscopic parameters determined for four
isotopologues of N-EI···H <sub>2</sub> O.
Table 7.7 Experimentally-determined spectroscopic parameters determined for five
isotopologues of 2-EI···H <sub>2</sub> O
Table 7.8 Experimentally determined spectroscopic parameters determined for three
isotopologues of N-EI···(H <sub>2</sub> O) <sub>2</sub> . 226
Table 7.9 Comparison of DFT calculated and experimentally determined atomic coordinates of
heavy atoms in N-ethylimidazole and 2-ethylimidazole
Table 7.10 Comparison of experimentally-determined ( $r_s$ ) and $r_e$ atomic coordinates of H <sub>2</sub> O in
N-EI···H <sub>2</sub> O, 2-EI···H <sub>2</sub> O and $N$ -EI···(H <sub>2</sub> O) <sub>2</sub>
Table 7.11 Comparison of DFT calculated $(r_e)$ and experimentally determined $(r_0)$ structural
parameters of N-EI···H <sub>2</sub> O and 2-EI···H <sub>2</sub> O.
Table 7.12 Comparison of DFT-calculated $(r_e)$ and experimentally-determined $(r_0)$ structural
parameters of $N$ -EI···(H <sub>2</sub> O) <sub>2</sub>
Table 7.13 Nuclear quadrupole coupling constants in the principal nuclear axis framework
determined using QDIAG. 236
Table 7.14 Comparison of interatomic distances ( $r_0$ and $r_e$ ) in imidazole-containing complexes.
Table 7.15 Comparison of intermolecular angles in imidazole-containing complexes 243
Table 7.16 Comparison of intermolecular parameters in dihydrate complexes formed with N-
containing heteroaromatic rings. 246
Table 8.1 Comparison of experimentally determined structural parameters within the
monohydrate complexes of five-membered heterocycles
Table 8.2 Comparison of experimentally determined structural parameters within dihydrate
complexes of five-membered heterocycles 253

A1 (Chapter 4) Atomic coordinates of the optimised geometry of 2-MT···H <sub>2</sub> O calculated at the
$\omega$ B97X-D/aug-cc-pVQZ level of theory.
A2 (Chapter 4) Atomic coordinates of the optimised geometry of 2-MT···H <sub>2</sub> O calculated at the
B3LYP(D3BJ)/aug-cc-pVTZ level of theory
A3 (Chapter 4) Atomic coordinates of the optimised geometry of 2-MT···H <sub>2</sub> O calculated at the
MP2/aug-cc-pVDZ level of theory
A4 (Chapter 4) Atomic coordinates of the optimised geometry of 4-MT···H <sub>2</sub> O calculated at the
$\omega$ B97X-D/aug-cc-pVQZ level of theory
A5 (Chapter 4) Atomic coordinates of the optimised geometry of 4-MT···H <sub>2</sub> O calculated at the
B3LYP(D3BJ)/aug-cc-pVTZ level of theory
A6 (Chapter 4) Atomic coordinates of the optimised geometry of 4-MT···H <sub>2</sub> O calculated at the
MP2/aug-cc-pVDZ level of theory
A7 (Chapter 4) Atomic coordinates of the optimised geometry of 5-MT···H <sub>2</sub> O calculated at the
$\omega$ B97X-D/aug-cc-pVQZ level of theory.
A8 (Chapter 4) Atomic coordinates of the optimised geometry of 5-MT···H <sub>2</sub> O calculated at the
B3LYP(D3BJ)/aug-cc-pVTZ level of theory
A9 (Chapter 4) Atomic coordinates of the optimised geometry of 5-MT···H <sub>2</sub> O calculated at the
MP2/aug-cc-pVDZ level of theory
A10 (Chapter 4) Nuclear quadrupole coupling constants in the principle nuclear axis framework
determined using QDIAG
A11 (Chapter 4) Molecular parameters of 4-MT···H <sub>2</sub> <sup>16</sup> O and 5-MT···H <sub>2</sub> <sup>16</sup> O in the rho axis
system (RAM) obtained using the BELGI-C <sub>s</sub> -hyperfine code
A12 (Chapter 4) Inertial defect and planar moments of 2-MT···H <sub>2</sub> O, 4-MT···H <sub>2</sub> O and 5-
MT···H <sub>2</sub> O calculated using rotational constants determined from global (XIAM) fits263
A13 (Chapter 4) Atomic coordinates of 2-MT···H <sub>2</sub> O and 5-MT···H <sub>2</sub> O determined by the $r_0$
method. 264
A14 (Chapter 4) Atomic coordinates of 4-MT···H <sub>2</sub> O determined by the $r_0$ method. Fit 1
assumes $\angle$ (O-H <sub>b</sub> ···N3-C2) = 0° and $\angle$ (H <sub>nb</sub> -O-H <sub>b</sub> ···N3) = 180°. Fit 2 assumes
$\angle$ (O-H <sub>b</sub> ···N3-C2) = 180 ° and $\angle$ (H <sub>nb</sub> -O-H <sub>b</sub> ···N3) = 180°
A15 (Chapter 4) Results of a new fit of structural parameters of thiazole···H <sub>2</sub> O (ref 24) using
STRFIT
A16 (Chapter 4) NBO stabilisation energy contributions (≥ 0.21 kJ mol <sup>-1</sup> ) of 2-MT···H <sub>2</sub> O, 4-
$MT\cdots H_2O \ and \ 5-MT\cdots H_2O \ calculated \ at \ the \ B3LYP(D3BJ)/aug\text{-}cc\text{-}pVTZ \ level \ of \ theory. 271$
A17 (Chapter 5) Atomic coordinates of the optimised geometry of 2-EF···H <sub>2</sub> O (C <sub>1</sub> conformer)
calculated at the $\omega$ B97X-D/aug-cc-pVQZ level of theory.
xiii

A18 (Chapter 5) Atomic coordinates of the optimised geometry of 2-EF···H <sub>2</sub> O (C <sub>1</sub> conformer)
calculated at the B3LYP(D3BJ)/aug-cc-pVTZ level of theory
A19 (Chapter 5) Atomic coordinates of the optimised geometry of 2-EF···H <sub>2</sub> O (C <sub>1</sub> conformer)
calculated at the B3LYP(D3BJ)/Def2-TZVP of theory
A20 (Chapter 5) Atomic coordinates of the optimised geometry of 2-EF···H <sub>2</sub> O (C <sub>1</sub> conformer)
calculated at the MP2/aug-cc-pVDZ of theory
A21 (Chapter 5) Atomic coordinates of the optimised geometry of 2-EF···H <sub>2</sub> O (C <sub>s</sub> conformer)
calculated at the $\omega$ B97X-D/aug-cc-pVQZ level of theory
A22 (Chapter 5) Atomic coordinates of the optimised geometry of 2-EF···H <sub>2</sub> O (C <sub>s</sub> conformer)
calculated at the B3LYP(D3BJ)/aug-cc-pVTZ level of theory
A23 (Chapter 5) Atomic coordinates of the optimised geometry of 2-EF···H <sub>2</sub> O (C <sub>s</sub> conformer)
calculated at the B3LYP(D3BJ)/Def2-TZVP of theory
A24 (Chapter 5) Atomic coordinates of the optimised geometry of 2-EF···H <sub>2</sub> O (C <sub>s</sub> conformer)
calculated at the MP2/aug-cc-pVDZ of theory. 275
A25 (Chapter 5) Atomic coordinates of 2-EF···H <sub>2</sub> O determined by the $r_0$ method
A26 (Chapter 5) NBO stabilisation energy contributions ( $\geq 0.21~kJ~mol^{-1}$ ) of 2-EF $\cdots$ H <sub>2</sub> O (C <sub>1</sub>
conformer) calculated at the B3LYP(D3BJ)/aug-cc-pVTZ level of theory
A27 (Chapter 5) NCI isosurfaces and plots of the RDG (a.u.) vs $sign(\lambda_2)\rho$ of the $C_s$ conformation
of 2-EF···H <sub>2</sub> O. Positive and negative values of $sign(\lambda_2)\rho$ respectively denote repulsive (red)
and attractive (blue) interactions. The isosurface s value is 0.5 au
A28 (Chapter 5) NBO stabilisation energy contributions ( $\geq 0.21~kJ~mol^{-1}$ ) of 2-EF $\cdots$ H <sub>2</sub> O (C <sub>s</sub>
conformer) calculated at the B3LYP(D3BJ)/aug-cc-pVTZ level of theory
A29 (Chapter 6) Atomic coordinates of the optimised geometry of 2-ethylthiazole calculated at
the $\omega$ B97X-D/aug-cc-pVQZ level of theory.
A30 (Chapter 6) Atomic coordinates of the optimised geometry of 2-ethylthiazole calculated at
the B3LYP(D3BJ)/aug-cc-pVTZ level of theory
A31 (Chapter 6) Atomic coordinates of the optimised geometry of 2-ethylthiazole calculated at
the B3LYP(D3BJ)/Def2-TZVP level of theory
A32 (Chapter 6) Atomic coordinates of the optimised geometry of 2-ethylthiazole calculated at
the MP2/aug-cc-pVDZ level of theory
A33 (Chapter 6) Atomic coordinates of the optimised geometry of 2-ET···H <sub>2</sub> O calculated at the
$\omega$ B97X-D/aug-cc-pVQZ level of theory
A34 (Chapter 6) Atomic coordinates of the optimised geometry of 2-ET···H <sub>2</sub> O calculated at the
B3LYP(D3BJ)/aug-cc-pVTZ level of theory. 282

A35 (Chapter 6) Atomic coordinates of the optimised geometry of 2-ET···H <sub>2</sub> O calculated at the
B3LYP(D3BJ)/Def2-TZVP level of theory
A36 (Chapter 6) Atomic coordinates of the optimised geometry of 2-ET···H <sub>2</sub> O calculated at the
MP2/aug-cc-pVDZ level of theory
A37 (Chapter 6) Atomic coordinates of the optimised geometry of 2-ET···(H <sub>2</sub> O) <sub>2</sub> calculated at
the $\omega$ B97X-D/aug-cc-pVQZ level of theory.
A38 (Chapter 6) Atomic coordinates of the optimised geometry of 2-ET···(H <sub>2</sub> O) <sub>2</sub> calculated at
the B3LYP(D3BJ)/aug-cc-pVTZ level of theory
A39 (Chapter 6) Atomic coordinates of the optimised geometry of 2-ET···(H <sub>2</sub> O) <sub>2</sub> calculated at
the B3LYP(D3BJ)/Def2-TZVP level of theory
A40 (Chapter 6) Atomic coordinates of the optimised geometry of 2-ET···(H <sub>2</sub> O) <sub>2</sub> calculated at
the MP2/aug-cc-pVDZ level of theory
A41 (Chapter 6) Experimental geometrical parameters of 2-ethylthiazole derived using EVAL.
A42 (Chapter 6) Atomic coordinates of 2-ET···H <sub>2</sub> O and 2-ET···(H <sub>2</sub> O) <sub>2</sub> determined by the $r_0$
method
A43 (Chapter 6) NBO stabilisation energy contributions (≥ 0.21 kJ mol <sup>-1</sup> ) of 2-ET···H <sub>2</sub> O
calculated at the B3LYP(D3BJ)/aug-cc-pVTZ level of theory
A44 (Chapter 6) NBO stabilisation energy contributions (≥ 0.21 kJ mol <sup>-1</sup> ) of 2-ET···(H <sub>2</sub> O) <sub>2</sub>
calculated at the B3LYP(D3BJ)/aug-cc-pVTZ level of theory
A45 (Chapter 7) Atomic coordinates of the optimised geometry of N-ethylimidazole and 2-
ethylimidazole calculated at the $\omega$ B97X-D/aug-cc-pVQZ level of theory
A46 (Chapter 7) Atomic coordinates of the optimised geometry of N-ethylimdazole and 2-
ethylimidazole calculated at the B3LYP(D3BJ)/aug-cc-pVTZ level of theory293
A47 (Chapter 7) Atomic coordinates of the optimised geometry of N-ethylimidazole and 2-
ethylimdazole calculated at the B3LYP(D3BJ)/Def2-TZVP level of theory294
A48 (Chapter 7) Atomic coordinates of the optimised geometry of N-ethylimidazole and 2-
ethylimidazole calculated at the MP2/aug-cc-pVDZ level of theory
A49 (Chapter 7) Spectroscopic parameters of N-EI···H <sub>2</sub> O and 2-EI···H <sub>2</sub> O calculated at
different levels of theory
A50 (Chapter 7) Spectroscopic parameters of N-EI···(H <sub>2</sub> O) <sub>2</sub> calculated at different levels of
theory
A51 (Chapter 7) Atomic coordinates of the optimised geometry of N-EI···H <sub>2</sub> O and 2-EI···H <sub>2</sub> O
calculated at the ωB97X-D/aug-cc-pVQZ level of theory

A32 (Chapter 7) Atomic coordinates of the optimised geometry of N-E1H2O and 2-E1H2O
calculated at the B3LYP(D3BJ)/aug-cc-pVTZ level of theory
A53 (Chapter 7) Atomic coordinates of the optimised geometry of N-EI···H <sub>2</sub> O and 2-EI···H <sub>2</sub> O
calculated at the B3LYP(D3BJ)/Def2-TZVP level of theory
A54 (Chapter 7) Atomic coordinates of the optimised geometry of N-EI···H <sub>2</sub> O and 2-EI···H <sub>2</sub> O
calculated at the MP2/aug-cc-pVDZ level of theory
A55 (Chapter 7) Atomic coordinates of the optimised geometry of N-EI···(H <sub>2</sub> O) <sub>2</sub> calculated at
the ωB97X-D/aug-cc-pVQZ level of theory
A56 (Chapter 7) Atomic coordinates of the optimised geometry of N-EI···(H <sub>2</sub> O) <sub>2</sub> calculated at
the B3LYP(D3BJ)/aug-cc-pVTZ level of theory
A57 (Chapter 7) Atomic coordinates of the optimised geometry of N-EI···(H <sub>2</sub> O) <sub>2</sub> calculated at
the B3LYP(D3BJ)/Def2-TZVP level of theory
A58 (Chapter 7) Atomic coordinates of the optimised geometry of N-EI···(H <sub>2</sub> O) <sub>2</sub> calculated at
the MP2/aug-cc-pVDZ level of theory
A59 Experimental geometrical parameters of N-ethylimidazole derived using EVAL 306
A60 Experimental geometrical parameters of 2-ethylimidazole derived using EVAL 307
A61 Atomic coordinates of $N$ -EI···H <sub>2</sub> O and 2-EI···H <sub>2</sub> O determined by the $r_0$ method 308
A62 (Chapter 7) Atomic coordinates of $N$ -EI···(H <sub>2</sub> O) <sub>2</sub> determined by the $r_0$ method 309
A63 (Chapter 7) NBO stabilisation energy contributions (≥ 0.21 kJ mol <sup>-1</sup> ) of N-EI···H <sub>2</sub> O and
2-EI···H <sub>2</sub> O calculated at the B3LYP(D3BJ)/aug-cc-pVTZ level of theory
A64 (Chapter 7) NBO stabilisation energy contributions ( $\geq 0.21 \text{ kJ mol}^{-1}$ ) of N-EI···(H <sub>2</sub> O) <sub>2</sub>
calculated at the B3LYP(D3BJ)/aug-cc-pVTZ level of theory311

# **List of Figures**

Figure 1.1 Structures of five- and six-membered heteroaromatic rings
Figure 1.2 The two observed isomers of a complex formed between imidazole and water
reported in reference 32. Isomer II is calculated to be 7.25 kJmol <sup>-1</sup> higher in energy than Isomer
I at the $\omega$ B97X-D/aug-cc-pVQZ level of theory9
Figure 1.3 The observed isomers of thiazole···(H <sub>2</sub> O) <sub>2</sub> reported in reference 21. Isomer II is
calculated to be 3.4 kJmol $^{-1}$ higher in energy than Isomer I at the $\omega$ B97X-D/aug-cc-pVQZ level
of theory11
Figure 1.4 Barriers to internal rotation of the methyl group in isomers of methylated five-
membered and larger heteroaromatic rings, in cm <sup>-1</sup> , avaliable in the current literature.
Conventional atom labels of five- and six-membered heteroaromatic rings are given on the left,
where X is a heteroatom and Y is a heteroatom or carbon.
Figure 1.5 Different possible conformations of ethyl-substituted rings owing to the rotation of
the ethyl group relative to the ring plane. When the ethyl group is co-planar with the ring, the
conformation has C <sub>s</sub> symmetry (upper panel). When the ethyl group is rotated out of the ring
plane, the conformation has C1 symmetry (lower panel). The experimentally observed
conformation of 2-ethylimidazole (pictured in figure) will be discussed in Chapter 722
Figure 2.1 Correlation diagram relating the energy levels of an asymmetric top molecule to
those of the limiting prolate and oblate symmetric top
Figure 2.2 Example of a three-fold potential energy curve of methyl internal rotation and
torsional sublevels. $V_3$ is the height of potential energy barrier to internal rotation. "A" and "E"
denote the two torsional sublevels
Figure 2.3 NCI isosurfaces and plot of RDG (a.u.) vs $sign(\lambda_2)\rho$ for 2-methylimidazole···H <sub>2</sub> O.
Positive and negative values of $sign(\lambda_2)\rho$ respectively denote repulsive (red) and attractive
(blue) interactions. Correlation between troughs observed on NCI plot and isosurfaces are
indicated. The isosurface s value is 0.5 au
Figure 3.1 The CP-FTMW spectrometer at Newcastle University
Figure 3.2 Microwave circuitry of the Newcastle CP-FTMW spectrometer configured for the
7.0 – 18.5 GHz experiment
Figure 3.3 Microwave circuitry of the Newcastle CP-FTMW spectrometer configured for the
2.0 – 8.0 GHz experiment
Figure 3.4 (1) Reservoir and modified faceplate used in the experiments studying volatile
molecules. (2) Reservoir mounted to general pulsed valve. (3) Glass wool in reservoir prior to
introduction of chemical sample79

Figure 3.5 The two ablation sources that can be used for the study of solid target molecules and
integrated into the Newcastle CP-FTMW spectrometer. (left) Design 1 of the ablation source.
(right) Design 2 of the ablation source
Figure 3.6 Experimental set up of the laser ablation source (Design 2) within the vacuum
chamber. (a) Motor. (b) Paddle. (c) Switch. (d) Rod holder and spacer. (e) Sample rod. (f)
Orifice. (g) Direction of laser beam. 82
Figure 3.7 Schematic of the Newcastle CP-FTMW spectrometer vacuum chamber 85
Figure 3.8 Schematic of a supersonic expansion propagating from the pulsed valve/heated
reservoir set up. The Mach number (M) at various stages is labelled, which is a measure of the
gas sample speed relative to the speed of sound $(M = 1)$ . Not to scale
Figure 4.1 The equilibrium (r <sub>e</sub> ) geometries of 2-MT···H <sub>2</sub> O (upper-left), 4-MT···H <sub>2</sub> O (upper-
right) and 5-MT···H <sub>2</sub> O (lower) calculated at the $\omega B97X$ -D/aug-cc-pVQZ level of theory 99
Figure 4.2 Small section of the rotational spectrum of 4-MT···H <sub>2</sub> O (upper panel) and 5-
MT···H <sub>2</sub> O (lower panel). Two rotational transitions of each complex are displayed. The
experimental spectrum (black) is shown above a simulation (red and green). The simulation for
the E-species (green) is generated by moving the A-species (red) simulation by an appropriate
amount of MHz
Figure 4.3 Two alternative geometries of 4-MT $\cdots$ H <sub>2</sub> O determined by $r_0$ fits performed 120
Figure 4.4 NCI isosurfaces and plots of the RDG (a.u.) vs $sign(\lambda_2)\rho$ of 2-MT···H <sub>2</sub> O (left), 4-
$MT\cdots H_2O$ (middle) and 5- $MT\cdots H_2O$ (right). Positive and negative values of $sign(\lambda_2)\rho$
respectively denote repulsive (red) and attractive (blue) interactions. The isosurface s value is
0.5 au
Figure 4.5 NBO plots associated with intermolecular interactions present within 2-MT $\cdots$ H <sub>2</sub> O
(left), 4-MT···H <sub>2</sub> O (middle) and 5-MT···H <sub>2</sub> O (right). $E^{(2)}$ represents the second order
perturbation energy of each interaction
Figure 4.6 Geometries of nine thiazole- and imidazole-containing monohydrate complexes. The
complexes are separated into two sub-sets for reasons given in text. (top) Monohydrate
complexes containing no CH3 group or a CH3 group located remote to H2O, which are the first
sub-set of Table 4.10. (bottom) Monohydrate complexes containing a CH3 group located
adjacent to H <sub>2</sub> O, which are the second sub-set of Table 4.10.
Figure 5.1 The two observed conformations of 2-ethylfuran reported in reference 3. The $C_{\text{s}}$
conformer is calculated to be $1.93~kJmol^{-1}$ higher in energy than the $C_1$ conformer at the MP2/6-
31G(d,p) level of theory
Figure 5.2 Potential energy scans obtained by rotating the ethyl group relative to the furan ring
in 2-ethylfuran. Calculations performed at the B3LYP(D3BJ)/aug-cc-pVTZ,

minimum structure. For 2-ethylimidazole, the C<sub>1</sub> conformer is also calculated to be the global minimum structure at the B3LYP(D3BJ)/aug-cc-pVTZ level of theory with the C<sub>s</sub> conformers  $\angle$ (C7–C6–C2–N3) = 0° and 180° calculated to be 0.3 and 2.9 kJmol<sup>-1</sup> higher in energy. .... 205 Figure 7.2 Potential energy scans obtained by rotating the ethyl group relative to the imidazole ring in N-ethylimidazole (top) and 2-ethylimidazole (bottom). Calculations performed at the B3LYP(D3BJ)/aug-cc-pVTZ, B3LYP(D3BJ)/Def2-TZVP and MP2/aug-cc-pVDZ levels of theory by scanning  $\angle$ (C7–C6–N1–C2) in N-ethylimidazole and  $\angle$ (C7–C6–C2–N3) in 2-Figure 7.3 Equilibrium (r<sub>e</sub>) geometries of N-EI···H<sub>2</sub>O (left) and 2-EI···H<sub>2</sub>O (right) calculated Figure 7.4 Equilibrium ( $r_e$ ) geometry of N-EI···(H<sub>2</sub>O)<sub>2</sub> calculated at the  $\omega$ B97X-D/aug-ccpVQZ level of theory. 212 Figure 7.5 (top) The microwave spectrum of N-ethylimidazole recorded in the 2.0 - 8.0 GHzregion averaged over 1.02 M FID's. (middle) and (bottom) Examples of transitions assigned to the N-ethylimidazole monomer, N-EI···H $_2^{16}$ O and N-EI···(H $_2^{16}$ O)<sub>2</sub>. Experimental spectrum Figure 7.6 (top) The microwave spectrum of 2-ethylimidazole, recorded in the 7.0 - 18.5 GHz region while probing a gaseous sample containing 2-ethylimidazole, H<sub>2</sub><sup>16</sup>O and argon, averaged over 510 k FID's. (bottom) Expanded portion of the experimental spectrum (black) above PGOPHER simulation (green and blue). (bottom-left)  $3_{13} \rightarrow 2_{02}$  rotational transition of the 2ethylimidazole monomer. (bottom-right)  $6_{06} \rightarrow 5_{05}$  rotational transition of 2-EI···H<sub>2</sub><sup>16</sup>O.... 216 Figure 7.7 NCI isosurfaces and plots of the RDG (a.u.) vs  $sign(\lambda_2)\rho$  of N-EI···H<sub>2</sub>O, N- $EI\cdots(H_2O)_2$  and 2- $EI\cdots H_2O$ . Positive and negative values of  $sign(\lambda_2)\rho$  respectively denote 



#### **Publications**

Revisiting the Microwave Spectrum and Molecular Structure of 1-Fluoronaphthalene, Surabhi Gupta, Charlotte N. Cummings, Nicholas R. Walker and Elangannan Arunan, Submitted for publication.

Quantum Method Benchmarking through Rotational Spectroscopy of Cysteamine Monohydrate Complex: Bridging Theory and Experiment, Wentao Song, Assimo Maris, Charlotte N. Cummings, Luca Evangelisti, Nicholas R. Walker and Sonia Melandri, Submitted for publication.

Microwave Spectroscopic and Computational Analyses of the Phenylacetylene···Methanol Complex: Insights into Intermolecular Interactions, Surabhi Gupta, Charlotte N. Cummings, Nicholas R. Walker and Elangannan Arunan, *Phys. Chem. Chem. Phys.*, 2024, 26, 19795-19811. DOI: 10.1039/d4cp01916d.

Hydrogen Bonding and Molecular Geometry in Isolated Hydrates of 2-Ethylthiazole Characterised by Microwave Spectroscopy, Charlotte N. Cummings and Nicholas R. Walker, *ChemPhysChem*, 2024, **25**, e202400011; DOI:10.1002/cphc.202400011.

Noncovalent Interactions in the Molecular Geometries of 4-Methylthiazole···H<sub>2</sub>O and 5-Methylthiazole···H<sub>2</sub>O Revealed by Microwave Spectroscopy, Charlotte N. Cummings, Isabelle Kleiner and Nicholas R. Walker, *J. Phys. Chem. A*, 2023, 127, **39**, 8133–8145; DOI:10.1021/acs.jpca.3c05360

Cooperative hydrogen bonding in thiazole···(H<sub>2</sub>O)<sub>2</sub> revealed by microwave spectroscopy, Eva Gougoula, <u>Charlotte N. Cummings</u>, Yugao Xu, Tao Lu, Gang Feng and Nicholas R. Walker, *J. Chem. Phys.*, 2023, **158**, 114307; DOI: 10.1063/5.0143024

Microwave spectra, molecular geometries, and internal rotation of CH<sub>3</sub> in *N*-methylimidazole···H<sub>2</sub>O and 2-methylimidazole···H<sub>2</sub>O Complexes, Eva Gougoula, <u>Charlotte N. Cummings</u>, Chris Medcraft, Juliane Heitkämper and Nicholas R. Walker, *Phys. Chem. Chem. Phys.*, 2022, **24**, 12354-12362; DOI: 10.1039/d1cp05526g

#### **Oral Presentations**

Conformational preferences of ethyl-substituted heteroaromatic rings and complexes with water, Charlotte N. Cummings and Nicholas R. Walker, Virtual International Microwave Seminar Series, online - Invited talk in early career researcher seminar, January 2024.

Barriers to internal rotation and molecular geometries of complexes formed between isomers of methylthiazole and water studied by microwave spectroscopy, Charlotte N. Cummings, Wentao Song, Ha Vinh Lam Nguyen and Nicholas R. Walker, International Symposium on Molecular Spectroscopy, Urbana-Champaign, USA, June 2023.

Characterisation of the molecular geometry of 2-ethylfuran····H<sub>2</sub>O by microwave spectroscopy, Charlotte N. Cummings and Nicholas R. Walker, International Symposium on Molecular Spectroscopy, Urbana-Champaign, USA, June 2023.

Characterisation of the molecular geometries of monohydrate complexes formed with heteroaromatic rings studied by microwave spectroscopy, Charlotte N. Cummings and Nicholas R. Walker, Newcastle University Chemistry and Alumni Research Symposium, Newcastle Upon Tyne, UK, March 2023.

Monohydrate complexes of ethyl-substituted heteroaromatic rings studied by microwave spectroscopy, Charlotte N. Cummings and Nicholas R. Walker, Spectroscopy and Dynamics Group Meeting, Durham, UK, Newcastle Upon Tyne, UK, January 2023.

Microwave Spectroscopy of N-methylimidazole···H<sub>2</sub>O and 2-methylimidazole···H<sub>2</sub>O Complexes and beyond, Charlotte N. Cummings, Eva Gougoula, Chris Medcraft, Julianne Heitkämper and Nicholas R. Walker, HBOND2022, Bilbao, Spain, September 2022.

Analysis of the Microwave Spectrum, Structure and Internal Rotation of the CH<sub>3</sub> group in *N*-methylimidazole···H<sub>2</sub>O and 2-methylimidazole···H<sub>2</sub>O complexes, Charlotte N. Cummings, Eva Gougoula, Chris Medcraft, Julianne Heitkämper and Nicholas R. Walker, Annual Northern Universities Meeting on Chemical Physics, Durham, UK, July 2022.

Characterisation of the Structure of the Hydrogen-Bonded complex, thiazole···(H<sub>2</sub>O)<sub>2</sub>, by Fourier-transform microwave spectroscopy, Charlotte N. Cummings, Eva Gougoula, Yugao Xu, Tao Lu, Gang Feng and Nicholas R. Walker, International Symposium on Molecular Spectroscopy, Online, June 2022.

Analysis of the Microwave Spectrum, Structure and Internal Rotation of the CH<sub>3</sub> group in *N*-methylimidazole···H<sub>2</sub>O and 2-methylimidazole···H<sub>2</sub>O complexes, Charlotte N. Cummings, Eva Gougoula, Chris Medcraft, Julianne Heitkämper and Nicholas R. Walker, International Symposium on Molecular Spectroscopy, Online, June 2022.

Characterisation of the Structure of the Hydrogen-Bonded complex, thiazole···(H<sub>2</sub>O)<sub>2</sub>, by Fourier-transform microwave spectroscopy, Charlotte N. Cummings, Eva Gougoula, Yugao Xu, Tao Lu, Gang Feng and Nicholas R. Walker, Spectroscopy and Dynamics Group Meeting, Online, April 2023.

Analysis of the Microwave Spectrum, Structure and Internal Rotation of the CH<sub>3</sub> group in *N*-methylimidazole···H<sub>2</sub>O and 2-methylimidazole···H<sub>2</sub>O complexes, Charlotte N. Cummings, Eva Gougoula, Chris Medcraft, Julianne Heitkämper and Nicholas R. Walker, UK-India Microwave Symposium, Online, December 2021.

#### **Poster Presentations**

The conformational preference of 2-Ethylthiazole and its weakly bound complexes with water revealed by Microwave Spectroscopy, Charlotte N. Cummings and Nicholas R. Walker, Faraday Community Poster Symposium, London, UK, November 2023.

The study of methyl internal in 2-methylthiazole···H<sub>2</sub>O using Microwave Spectroscopy, Charlotte N. Cummings, Wentao Song and Nicholas R. Walker, HBOND2022, Bilbao, Spain, September 2022.

Characterisation of thiazole… (H<sub>2</sub>O)<sub>2</sub> by rotational spectroscopy, Charlotte N. Cummings and Nicholas R. Walker, SAgE PGR Conference, Newcastle Upon Tyne, UK, July 2021.

Characterisation of thiazole… (H<sub>2</sub>O)<sub>2</sub> by rotational spectroscopy, Charlotte N. Cummings and Nicholas R. Walker, Institute of Physics: Planetary Atmospheres: from Earth and beyond, Online, June 2021.

The Chirped Pulse Fourier Transform Microwave (CP-FTMW) spectrometer at Newcastle University, Charlotte N. Cummings and Nicholas R. Walker, Spectroscopy and Dynamics Group Meeting, Online, January 2021.



## Chapter 1. Introduction.

### 1.1 Hydrogen bonding interactions

Through-space interactions which exist between molecules (intermolecular) or separate parts of the same molecule (intramolecular) are known as non-covalent interactions. There are many types of non-covalent interactions such as ionic, hydrogen bonds, van der Waals and  $\pi$  interactions, to name a few. Some of the aforementioned non-covalent interactions are weaker and can exist over longer distances than covalent bonds. A vast amount of research interest is concerned with furthering our understanding of these types of interactions owing to the important role non-covalent interactions play in many aspects of chemistry, physics and biology. For example, non-covalent interactions are present between the base pairs in DNA resulting in its double helix structure. Furthermore, molecular recognition processes such as those between odorants and olfactory receptors occur via non-covalent interactions.

The main focus of this thesis is investigating hydrogen bonding interactions, which is one of the most widely studied non-covalent interaction owing to the importance and countless examples of this type of interaction in nature. Typically, a hydrogen bonding interaction is written as follows: X–H···Y–Z, where X–H is the hydrogen bond donor and Y–Z is the hydrogen bond acceptor. Research has shown the existence of many different types of hydrogen bonding interactions and for this reason the hydrogen bond was re-defined by an IUPAC task group in 2011<sup>1,2</sup>:

"The hydrogen bond is an attractive interaction between a hydrogen atom from a molecule or a molecular fragment X—H in which X is more electronegative than H, and an atom or a group of atoms in the same or a different molecule, in which there is evidence of bond formation."

The updated definition is inclusive of hydrogen bond donors in which X is any atom which has an electronegativity greater than that of hydrogen. Therefore, in addition to the classic examples of hydrogen bond donors (F–H, O–H and N–H), the definition now includes weaker hydrogen bond donors such as C–H and S–H. Typically a hydrogen bond acceptor (Y) is an electronegative atom which has a lone pair or the  $\pi$ -system of a pair/group of atoms (Y–Z). A comprehensive list of criteria for an interaction to be categorised as a hydrogen bond is provided by E. Arunan *et al.*<sup>1</sup> It is known that strong hydrogen bonding interactions exist over a shorter

distance and are linear, whereas, those which are categorised as weak often exhibit a hydrogen bond angle which deviates significantly from linearity and typically exists over a longer distance. There has been a growing amount of research interest concerned with systems which exhibit weaker hydrogen bonding interactions, one such example being those which include C–H···O.

Research into non-covalent interactions and specifically hydrogen bonding spans across a wide range of research disciplines, including gas-phase spectroscopy which has proved a particularly effective means for studying these types of interactions. Studies on weakly-bound complexes generated in an isolated cold environment, such as those probed by microwave spectroscopy studies (see Chapter 3), provide an excellent insight into the hydrogen bonds and other non-covalent interactions present between the molecular sub-units of the complex, in an environment free of matrix or solvent effects. The study of species in the gas phase allows small molecular clusters to be probed, such that an understanding is gained about the position at which a small number of molecules, such as water, binds to an organic molecule. Additionally, the interactions which are present between the sub-units can be investigated. The first steps of microsolvation can be understood by studying complexes formed with an increasing number of water molecules in a step-wise manner. Studying hydrogen bonding interactions within the gas-phase can be used to further the understanding of these types of interactions which can be applied to hydrogen bonding interactions within the solution phase.

Molecules and complexes probed by microwave spectroscopy are neutral and this technique allows for the determination of precise structural information from the assignment of multiple isotopologues of a given species. This means that geometrical parameters such as the length of the hydrogen bond and the hydrogen bond angle can be experimentally-determined when studying weakly-bound complexes using microwave spectroscopy. Other spectroscopic techniques such as those which employ infrared radiation infer the formation of hydrogen bonding interactions from a redshift in the stretching frequency of the X–H bond. While hydrogen bonding interactions within charged species can be investigated by mass spectrometry. Spectroscopic techniques such as those employing infrared radiation and/or mass spectrometry cannot unambiguously determine molecular structure like microwave spectroscopy can. This was evidenced by a series of studies on the binary complex of phenylacetylene and methanol. This complex was first studied by IR-UV double resonance spectroscopy<sup>3</sup> and later using Fourier-transform infrared (FT-IR) spectroscopy. The studies reported different structures for this complex and recently microwave spectroscopy was

employed for an unambiguous assignment of this complex in favour of the structure proposed by the FT-IR study and for an investigation into the internal dynamics.<sup>a</sup>

Often multiple binding sites in which non-covalent interactions can form are present within a given molecule, such that competition between specific binding sites and types of intermolecular interactions which can form may exist. The binding preferences of molecules can be explored through the study of weakly-bound complexes in the gas phase. The aromatic ring derivative phenylacetylene can form interactions at the  $\pi$ -system of the acetylene group or phenyl ring, the acetylene C–H group or a C–H situated on the phenyl ring. Numerous studies have been performed investigating the structure of complexes formed between phenylacetylene and other small molecules, such as methanol as mentioned above, using a variety of spectroscopic techniques. Focussing only on a select few studied by microwave spectroscopy, phenylacetylene···H<sub>2</sub>O,<sup>5</sup> phenylacetylene···H<sub>2</sub>S<sup>6</sup> and phenylacetylene···CH<sub>3</sub>OH, the preferred binding site of each of these small molecules at phenylacetylene has been revealed. It has been observed that the complexes formed with water and methanol are structurally similar. Within the lowest energy geometry of the complexes, both water and methanol preferentially bind at the  $\pi$ -system of the acetylene group via a O–H $\cdots\pi$  hydrogen bonding interaction. Additionally, it has been revealed that both complexes are further stabilised by a weaker interaction between the O atom of water or methanol and a C-H on the phenyl ring (C-H···O). Whereas, in the case of phenylacetylene...H<sub>2</sub>S, hydrogen sulphide preferentially binds above the phenyl ring and interacts with the  $\pi$ -system via a S–H··· $\pi$  interaction.

Furthermore, the study of isolated weakly-bound complexes can also be used to model the non-covalent interactions present in larger or more complex systems. As mentioned earlier, non-covalent interactions are important in molecular recognition processes. It is believed that odorant molecules bind to amino acids within receptor molecules via non-covalent interactions, therefore, it is of interest to understand the binding preferences of these molecules and the intermolecular interactions which may form. Fenchone<sup>7</sup> is an example of an odorant molecule and its weakly-bound complexes formed with other small molecules including water<sup>8, 9</sup> have been the subject of several microwave spectroscopy studies. Complexes of fenchone with ethanol, benzene and phenol are of particular interest as these molecules can be used to mimic interactions with the side chains of the amino acids serine, phenylaniline and tyrosine respectively.<sup>10, 11</sup>

<sup>-</sup>

<sup>&</sup>lt;sup>a</sup> Unpublished work by S. Gupta *et al*. (in peer review)

Hydrogen bonded complexes comprised of water interacting with other molecules including itself, <sup>12-20</sup> organic molecules<sup>5, 8, 9, 21</sup> and inorganic species<sup>22-24</sup> have been extensively studied. Water is bifunctional, meaning that it has the capability of donating a hydrogen bond from one of its O-H bonds and accepting a hydrogen bond from another species through lone pairs located on its oxygen atom. The structures of clusters of pure water, (H<sub>2</sub>O)<sub>n</sub> (where n is the number of water molecules, n = 2 - 10) have been revealed using a variety of different gasphase spectroscopic techniques. Early studies on pure water probed the water dimer, (H<sub>2</sub>O)<sub>2</sub>. <sup>12</sup>, <sup>13</sup> The interatomic distance between the two oxygen atoms was experimentally determined to be 2.976(10) Å. The water trimer, 15 water tetramer 16 and water pentamer 17 were each first observed using far infrared vibration-rotational-tunnelling (FIR-VRT) spectroscopy. Each of these clusters are structurally similar and the water molecules preferentially bind in ring structures. For example, the water trimer effectively forms a six-membered ring via three hydrogen bonding interactions. In this arrangement each water sub-unit simultaneously donates and accepts one hydrogen bond. It was observed that the interatomic distance between the oxygen atoms in each of the trimer, tetramer and pentamer clusters are shorter than observed for the water dimer. Additionally, the interatomic separation decreases as the cluster size increases. This decrease can be attributed to cooperativity effects within the hydrogen bonding network owing to the interactions becoming shorter and stronger.

Isolated clusters of the water trimer, tetramer and pentamer are non-polar such that these clusters cannot be observed by microwave spectroscopy. Whereas microwave spectroscopy studies are possible for each of the water hexamer, heptamer, nonamers and decamers and decamers since each cluster possesses a dipole moment. The study on the water hexamer revealed the co-existence of three isomers (prism, cage and book) of this complex within the supersonic expansion while two isomers of the water heptamer (both in a prism arrangement) were observed. In each of the prism arrangements of the water hexamer and heptamer, each water sub-unit simultaneously donates two and accepts one hydrogen bonding interaction. In the cage arrangement of the water hexamer, four of the water sub-units form three hydrogen bonds, while the other two water molecules form two interactions, each having a non-bonding hydrogen atom. The book arrangement of the water hexamer is structurally similar to the water trimer, tetramer and pentamer since each water molecule simultaneously donates and accepts one hydrogen bond. The water nonamer and decamer also exhibit three dimensional structures whereby each water molecule forms two or three hydrogen bonding interactions. 20

This thesis is concerned with hydrogen bonded complexes formed between water and organic molecules, specifically those which contain an aromatic ring. A considerable amount of

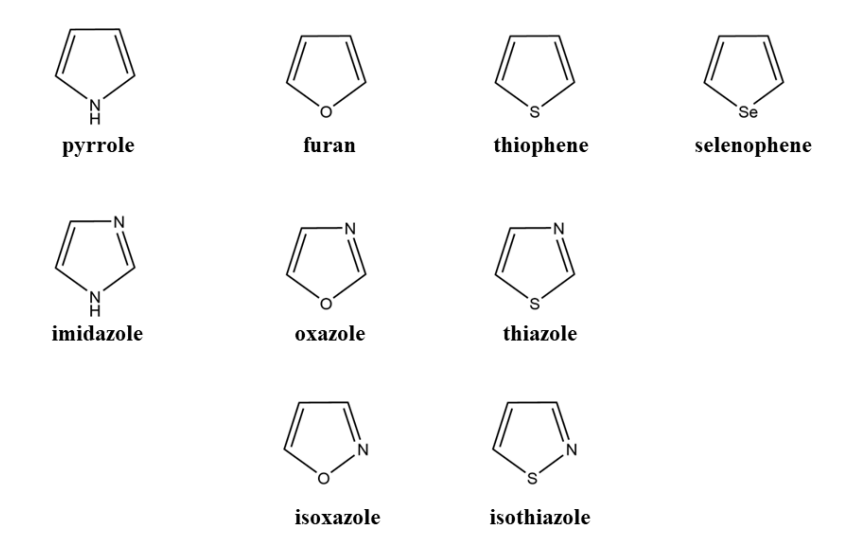
research on the monohydrate complexes formed with aromatic rings containing one or two heteroatoms has been performed and this will be summarised in the following section (Section 1.2). However, significantly fewer studies are available on complexes comprised of aromatic rings and two or more water molecules. The step-wise hydration of organic molecules can be revealed by probing complexes formed with an increasing number of water molecules. Therefore, the study of these complexes is of particular interest as this provides an insight into the first steps of microsolvation. Complexes comprised of a non-aromatic organic molecule and up to three waters can usually be probed by microwave spectroscopy. In complexes formed with two or three water molecules, typically water binds to the organic molecule in an arrangement such that a ring-like structure is formed between the sub-units via three hydrogen bonding interactions in the former and four hydrogen bonds in the latter. This arrangement maximises the number of hydrogen bonding interactions and is similar to the structures of the water trimer and tetramer. This arrangement was observed in the thiazole...(H<sub>2</sub>O)<sub>2</sub> complex, in which the water sub-units interact with thiazole via O-H···N and C-H···O interactions while a third hydrogen bonding interaction is present between the two water sub-units.<sup>21</sup> Cooperativity effects are also evident in clusters formed between water and organic molecules such that the interatomic distance between the oxygen atom is smaller than that of the isolated water dimer, see Table 6 of reference 21. An increasing number of studies are now becoming available on complexes formed between organic molecules (typically non-aromatic) and between four and seven water molecules, in which the water molecules typically bind to the organic sub-unit in arrangements similar to those reported for larger pure water clusters.

#### 1.2 Microsolvation of heteroaromatic rings

Aromatic rings, particularly those which contain one or more heteroatoms, have multiple distinct binding sites in which non-covalent interactions can form. These molecules are abundant in biology and are commonly the building blocks of larger biomolecules and macromolecules. Some notable examples include the nitrogen-containing heterocycles, imidazole and pyrimidine, being present in DNA and RNA nucleobases and several amino acids contain aromatic rings. Furthermore, nitrogen containing five-membered rings (known as azoles) are present within compounds which are anti-fungal agents. Since aromatic and heteroaromatic rings are abundant in nature and possess competing sites in which non-covalent interactions can form it is therefore of interest to understand the binding preferences of these molecules. This can be achieved by studying isolated weakly-bound complexes formed between (hetero)aromatic rings and other small molecules such as water, ammonia, hydrogen sulphide and methanol which interact via non-covalent interactions. Complexes formed with aromatic and heteroaromatic rings have been extensively studied by a variety of different spectroscopic techniques including microwave and infrared spectroscopy aided by quantum chemical calculations.

Numerous studies have been performed investigating complexes formed between five- and sixmembered heteroaromatic rings and water. Water is abundant in biology, therefore, the understanding of how biomolecules and water interact is of vital importance. By studying complexes formed between the building blocks of these biomolecules i.e. heteroaromatic rings and water the fundamental binding preferences of these molecules can be established. Additionally, complexes formed with multiple water molecules can provide an insight into the first steps of microsolvation. The structures of some heterocyclic rings are displayed in Figure 1.1. Hydrate complexes formed with each of the heteroaromatic rings have been studied, with the only exception being isothiazole. These weakly-bound complexes are usually formed via one or more hydrogen bonding interactions. Each of the heterocycles (displayed in Figure 1.1) and water are bifunctional. The heterocycles can accept a hydrogen bond from water either at the heteroatom or  $\pi$ -system such that complexes are stabilised by a  $O_w$ -H···X (where X is the heteroatom) or  $O_w$ -H··· $\pi$  interactions. Alternatively, these molecules can donate a hydrogen bond such that complexes contain a C/X-H···O<sub>w</sub> interaction. In this section, the hydrate complexes formed with heteroaromatic rings available within the current literature and the interactions which stabilise these weakly-bound complexes will be discussed.

#### 5-membered heteroaromatic rings:



#### 6-membered heteroaromatic rings:

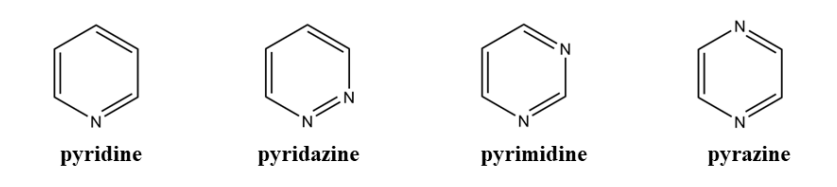


Figure 1.1 Structures of five- and six-membered heteroaromatic rings.

### 1.2.1 Hydrate complexes formed with five-membered rings

As mentioned earlier the hydrate complexes formed with five-membered rings containing one or two heteroatoms have been extensively studied. The monohydrate complexes formed with pyrrole, <sup>25</sup> furan, <sup>26</sup> thiophene <sup>27, 28</sup> and selenophene, <sup>29</sup> which each contain one heteroatom only, will be considered first. One isomer of the monohydrate complex of pyrrole was observed in a microwave spectroscopy study. <sup>25</sup> In this complex, a hydrogen bonding interaction forms between the pyrrolic nitrogen (N–H) of the ring and the O atom of the water molecule. In this complex pyrrole is the hydrogen bond donor while the water sub-unit is the hydrogen bond acceptor, such that the complex is denoted H<sub>2</sub>O···pyrrole following the standard labelling convention that the hydrogen bond acceptor (Lewis base) is listed first. Complexes in which the water molecule is the hydrogen bond donor (Lewis acid) are denoted as B···H<sub>2</sub>O (where B is the heteroaromatic ring). This convention will be followed throughout this thesis. Each of furan, thiophene and selenophene contain a group 16 atom located at the 1-position of the ring. The structure of furan···H<sub>2</sub>O<sup>26</sup> was established by matrix-isolation FT-IR spectroscopy. It was identified that water binds to the furan ring at the oxygen atom and unlike in the H<sub>2</sub>O···pyrrole

complex the water molecule acts as the hydrogen bond donor and the heteroaromatic ring is the hydrogen bond acceptor. The geometry identified is stabilised by a Ow-H···Oring interaction and this structure was predicted to be the global minimum by quantum chemical calculations. Studies on the monohydrate complexes formed with thiophene and selenophene have revealed that the presence of a larger, less electronegative heteroatom influences the binding site of water. The monohydrate complex of thiophene was first studied using matrix isolation FT-IR spectroscopy in 2019 and later studied using microwave spectroscopy in 2021.<sup>27, 28</sup> Each study identified one isomer of this complex only, however, the geometries identified in the studies differ. Quantum chemical calculations reported in both studies identify the geometry whereby the water molecule is located above the plane of the thiophene ring, which is stabilised by a  $O_w$ -H··· $\pi$  interaction, to be the global minimum structure. This structure of the thiophene...H<sub>2</sub>O complex was identified in the microwave spectroscopy study.<sup>28</sup> Whereas the IR study<sup>27</sup> observed an isomer of the complex which was predicted to be slightly higher in energy by quantum chemical calculations. This complex forms via a C-H···O<sub>w</sub> interaction in which the water molecule accepts a hydrogen bond from a C-H located adjacent to the sulphur atom of the ring. Two isomers of the monohydrate complex of selenophene were observed by matrix-isolation FT-IR spectroscopy.<sup>29</sup> In one isomer of the complex, water is located above the selenophene ring and contains a  $O_w$ -H $\cdots\pi$  interaction, while the second isomer is formed by a C-H···O<sub>w</sub> interaction, like what was observed in the case of the thiophene complexes. The studies on the monohydrate complexes of pyrrole, furan, thiophene and selenophene have revealed that the identity of the heteroatom within the ring has a significant influence on the position in which water binds, such that the binding preferences differ across the series of molecules. When an electronegative heteroatom is present within the ring, in the case of pyrrole and furan, the water molecule preferentially interacts with the heteroatom. Whereas, when a less electronegative heteroatom is present, in the case of thiophene and selenophene, the water molecule interacts with the  $\pi$ -system or accepts a hydrogen bond from a C–H of the ring, rather than forming an interaction with the heteroatom.



# Isomer II – $H_2O$ ···imidazole

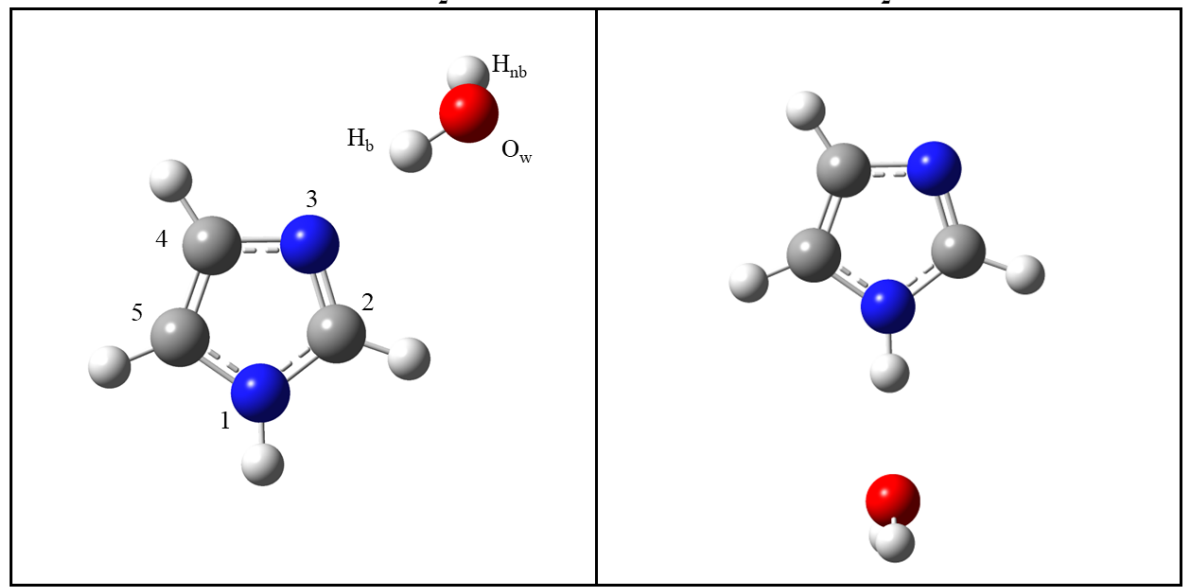


Figure 1.2 The two observed isomers of a complex formed between imidazole and water reported in reference 32. Isomer II is calculated to be 7.25 kJmol<sup>-1</sup> higher in energy than Isomer I at the  $\omega$ B97X-D/aug-cc-pVQZ level of theory.

The remaining five-membered heteroaromatic rings contain two heteroatoms. Each of imidazole, thiazole and oxazole have a pyridinic nitrogen atom located at the 3-position of the ring and differ only in the heteroatom located at the 1-position. While in the case of isoxazole, the pyridinic nitrogen atom is instead located at the 2-position of the ring. The monohydrate complexes of each have been studied revealing the position in which the first water molecule binds to each ring. Additionally, studies on the dihydrate complexes of thiazole, oxazole and isoxazole are available. The geometry of thiazole···(H<sub>2</sub>O)<sub>n</sub> complexes (where n defines the number of water molecules present within the complex) were identified using microwave spectroscopy, 21, 30 while the investigation of hydrate complexes formed with oxazole was performed using helium nanodroplet infrared spectroscopy.<sup>31</sup> One isomer of each of thiazole···H<sub>2</sub>O<sup>30</sup> and oxazole···D<sub>2</sub>O<sup>31</sup> were identified. In both monohydrate complexes, the water molecule preferentially binds to the pyridinic nitrogen atom of the ring in each case, such that the complexes form via a Ow-H/D···N interaction. In both cases, this geometry was identified to be the global minimum structure by quantum chemical calculations, with complexes in which water binds at the other heteroatom being predicted to be higher in energy. In the case of imidazole, two isomers of the monohydrate complex were identified by microwave spectroscopy,<sup>32</sup> while an earlier study employing FT-IR spectroscopy identified only one isomer of this complex.<sup>33</sup> Both studies identified the isomer (imidazole···H<sub>2</sub>O, Figure 1.2 left) in which the water molecule binds at the pyridinic nitrogen atom via a Ow-H···N

interaction, like what has been observed for the thiazole···H<sub>2</sub>O and oxazole···D<sub>2</sub>O complexes. A second slightly higher energy isomer (H<sub>2</sub>O···imidazole, Figure 1.2 right) was identified by microwave spectroscopy only, in which the water molecule interacts with the pyrrolic nitrogen atom instead, such that the complex is stabilised by a N–H···O<sub>w</sub> interaction, analogous to the structure identified for H<sub>2</sub>O···pyrrole. The water molecule binds to the pyridinic nitrogen atom in the case of isoxazole···H<sub>2</sub>O.<sup>34, 35</sup> In the microwave spectroscopy study, it was identified that the O atom of the water molecule is orientated towards the C3–H3 bond and away from the oxygen atom of the ring.<sup>34</sup> While in the recent helium nanodroplet infrared spectroscopy study, two structures of isoxazole···D<sub>2</sub>O were identified.<sup>35</sup> The authors suggested that the more abundant isomer forms via one hydrogen bonding interaction (O<sub>w</sub>–D···N) only. While in the other isomer, water binds to the isoxazole ring via two interactions, O<sub>w</sub>–D···N and C–H···O<sub>w</sub>.

In the case of imidazole, thiazole, oxazole and isoxazole, the site in which the water molecule binds is more consistent across this series of molecules compared to the heteroaromatic rings containing one heteroatom only. It is evident from the studies on the monohydrate complexes, that water typically binds at the pyridinic nitrogen atom of each ring. In the case of imidazole···H<sub>2</sub>O,<sup>32</sup> thiazole···H<sub>2</sub>O<sup>30</sup> and isoxazole···H<sub>2</sub>O,<sup>34</sup> structural information acquired from microwave spectroscopy studies identified that the primary hydrogen bond (O<sub>w</sub>-H···N) in each complex deviates from linearity, suggesting that an additional weaker C-H···O<sub>w</sub> interaction is present within each of the complexes. The O atom of water is orientated towards C2-H2 and away from C4-H4 in imidazole···H<sub>2</sub>O and thiazole···H<sub>2</sub>O, suggesting there is a preference for the C2-H2···O<sub>w</sub> over the C4-H4···O<sub>w</sub> interaction. In the case of the oxazole···D<sub>2</sub>O<sup>31</sup> complex, it could not be identified whether the structure contained one or two hydrogen bonding interactions. In the structure stabilised by one hydrogen bond, quantum chemical calculations predict that the angle of the primary hydrogen bond deviates slightly from linearity. However, in the possible structure in which an additional C2-H2···O<sub>w</sub> interaction is present, the primary hydrogen bond angle is predicted to deviate significantly from linearity, like what was observed experimentally for the aforementioned complexes.

# Thiazole $\cdots$ (H<sub>2</sub>O)<sub>2</sub>

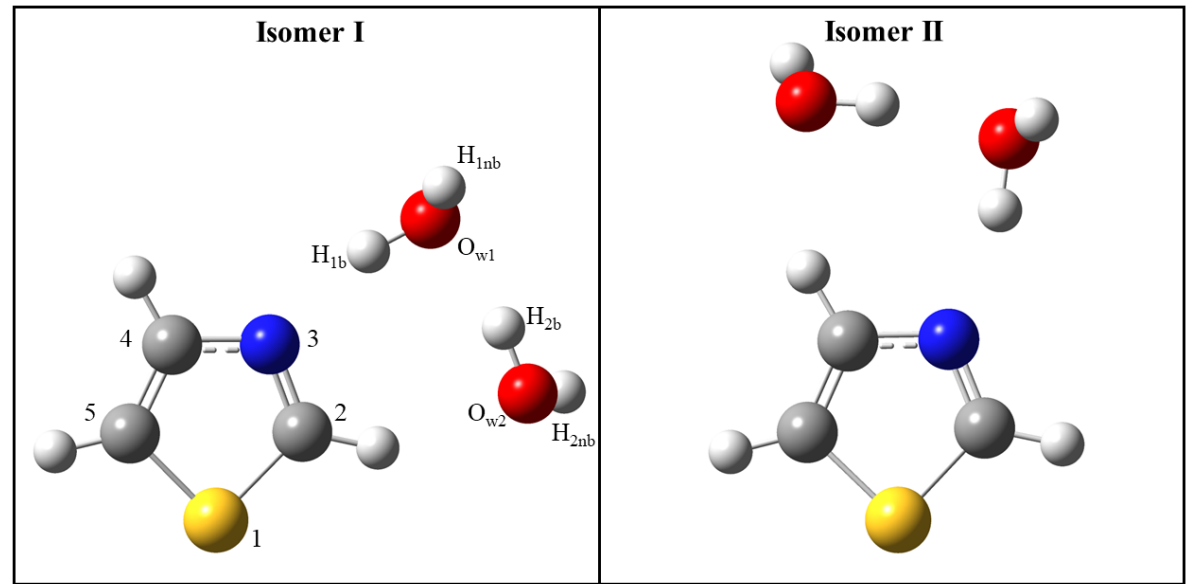


Figure 1.3 The observed isomers of thiazole···( $H_2O$ )<sub>2</sub> reported in reference 21. Isomer II is calculated to be 3.4 kJmol<sup>-1</sup> higher in energy than Isomer I at the  $\omega$ B97X-D/aug-cc-pVQZ level of theory.

Hydrate complexes comprised of a five-membered heteroaromatic ring and two water molecules have also been studied. Two isomers of the thiazole ··· (H<sub>2</sub>O)<sub>2</sub> complex were observed in a 2023 study (see Figure 1.3).<sup>21</sup> Each isomer of the complex is stabilised by three hydrogen bonding interactions, two comparatively strong Owl-H1b...N and Ow2-H2b...O1 interactions and a third weaker C-H···O<sub>w2</sub> interaction. The two isomers of the dihydrate complex differ in the third weaker interaction. In the global minimum structure (Isomer I), the second water molecule is positioned such that a weak interaction can form with C2–H2 whereas in the higher energy isomer (Isomer II) a weak interaction forms between the second water molecule and C4-H4. One isomer of each of oxazole···(D<sub>2</sub>O)<sub>2</sub> and isoxazole···(D<sub>2</sub>O)<sub>2</sub> have been observed by helium nanodroplet infrared spectroscopy. 31, 35 Both complexes are also stabilised by the same three hydrogen bonding interactions mentioned above. In the case of oxazole $\cdots$ (D<sub>2</sub>O)<sub>2</sub>, the second water molecule can also form an interaction with either C2–H2 or C4–H4, however, owing to the technique employed for the study, the geometry of this complex could not be unambiguously assigned.<sup>31</sup> However, the authors tentatively assigned the spectrum to the structure which contains the interaction C2-H2···O<sub>w2</sub>. Whereas in the case of isoxazole···(D<sub>2</sub>O)<sub>2</sub>, the spectrum was unambiguously assigned to the structure which contains a weaker hydrogen bonding interaction with C3-H3.35

# 1.2.2 Hydrate complexes formed with six-membered rings

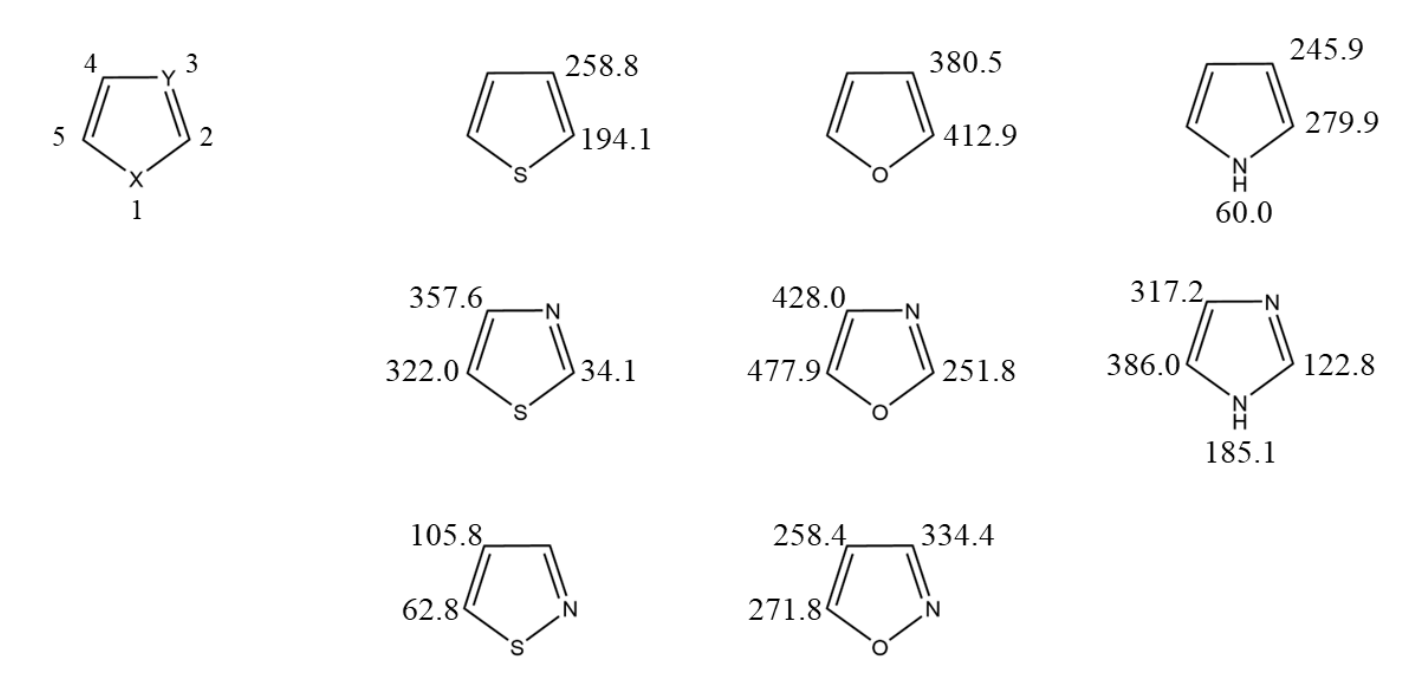
The structures of several six-membered heteroaromatic rings containing one or two nitrogen atoms are displayed in Figure 1.1. Each of pyridine, pyridazine, pyrimidine and pyrazine rings are structurally similar to benzene, however, it has been observed through the studies of the monohydrate complexes formed with each of these rings that the presence of the nitrogen atom has a significant influence on the binding site of water. The monohydrate complex formed with benzene was the first of these complexes to be studied.<sup>36, 37</sup> It was observed that the water molecule is located above the plane of the benzene ring and each of the hydrogen atoms interact with the  $\pi$ -system via O-H··· $\pi$  interactions. It was identified that in the case of pyridine...H<sub>2</sub>O,<sup>38</sup> that water preferentially binds at the nitrogen atom via a O–H···N interaction rather than interacting with the  $\pi$ -system. In each of the benzene···H<sub>2</sub>O and pyridine···H<sub>2</sub>O complexes, large amplitude motions associated with the water sub-unit were observed owing to the symmetry of the complexes. The water molecule was also found to bind at one of the nitrogen atoms in the case of the pyridazine...H<sub>2</sub>O<sup>39</sup> complex such that four inequivalent geometries are possible. The authors assigned the spectrum of pyridazine... H<sub>2</sub>O to the structure whereby the O atom is orientated away from the second nitrogen atom and towards the adjacent C-H bond. This complex was observed to be effectively planar, unlike pyridine... H<sub>2</sub>O, which has a large and positive inertial defect. The structure of pyrimidine...H<sub>2</sub>O<sup>40</sup> was found to be very similar to that of pyridazine...H<sub>2</sub>O, the water molecule also interacts with one of the nitrogen atoms in the ring, again resulting in four different possible structures of the complex. In the case of pyrimidine···H<sub>2</sub>O, two adjacent C–H bonds are available for the O atom of water to interact with, resulting in non-equivalent structures. The observed structure has the O atom orientated away from the C-H located between the two nitrogen atoms. The nitrogen atoms are located on opposite sides of the ring in the case of pyrazine such that the ring belongs to the D<sub>3h</sub> symmetry group. The pyrazine···H<sub>2</sub>O<sup>41</sup> complex is stabilised by a O–H···N interaction and the O atom of the water molecule interacts with either of the C-H bonds adjacent to the nitrogen atom. The water molecule tunnels between the two equivalent structures like what was observed in the pyridine···H<sub>2</sub>O complex. Studies on the pyridine···H<sub>2</sub>O, pyridazine···H<sub>2</sub>O, pyrimidine···H<sub>2</sub>O and pyrazine···H<sub>2</sub>O complexes have revealed that in each case the water molecule preferentially binds at the nitrogen atom of the ring and a secondary interaction is present with a neighbouring C-H bond. The presence of the additional interaction results in the primary hydrogen bond deviating from linearity in each case.<sup>38-41</sup> The structures of these complexes are significantly different to what was observed for benzene... H<sub>2</sub>O indicating that the presence of the electronegative heteroatom changes the binding preference of the water

molecule. This was also observed in the hydrate complexes formed with the fused rings phenanthrene and phenanthridine. The water molecule(s) bind above the plane of the ring and interact with the  $\pi$ -system via  $O-H\cdots\pi$  interaction in the phenanthrene  $(H_2O)_n$  (where n=1-3) complexes. Whereas in complexes formed with the nitrogen-containing phenanthridine, water preferentially binds to the ring via  $O-H\cdots N$  and  $C-H\cdots O$  interactions.

# 1.3 Internal rotation

Internal rotation is an example of a large amplitude motion in which part of a molecule rotates with respect to the rest of the molecule. Methyl groups are an example of an internal rotor which has been widely studied using microwave spectroscopy. Typically, the rotation of a methyl group is not free and is hindered by a three-fold potential energy barrier denoted  $V_3$ . When one methyl group is present, the molecules rotational states are split into two torsional sub-levels, denoted A and E, if multiple methyl internal rotors are present further splitting into additional sub-levels is observed. This manifests as a splitting of rotational transitions present within the microwave spectrum and the extent of this splitting is dependent on the magnitude of the  $V_3$ barrier. The magnitude of the  $V_3$  barrier can take a wide range of values, typically between 0 cm<sup>-1</sup> (free rotation) and 1000 cm<sup>-1</sup>. A larger frequency interval between torsional sub-levels is observed when the  $V_3$  barrier is low, while smaller frequency intervals are observed for higher magnitudes of  $V_3$ . Methylated heteroaromatic rings have been extensively studied using microwave spectroscopy and the  $V_3$  barrier to internal rotation of these molecules have been determined. In this section, the  $V_3$  barrier to internal rotation of methylated heteroaromatic rings will be discussed as well as observed effects on the  $V_3$  barrier of both aromatic and non-aromatic molecules which occur as a result of substitution or complexation. Further details regarding internal rotation and specialist programs used for the fitting of internal rotors is provided in Chapter 2.

# 5-membered heteroaromatic rings:



# Larger heteroaromatic rings:

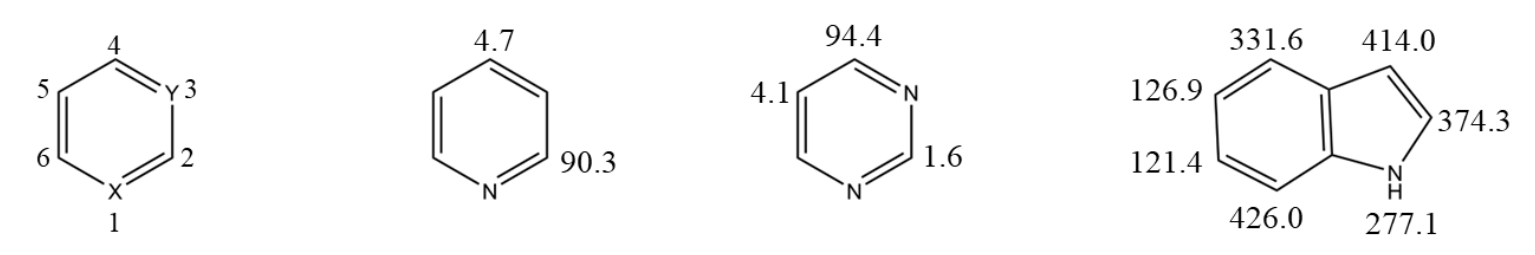


Figure 1.4 Barriers to internal rotation of the methyl group in isomers of methylated five-membered and larger heteroaromatic rings, in cm<sup>-1</sup>, avaliable in the current literature. Conventional atom labels of five- and six-membered heteroaromatic rings are given on the left, where X is a heteroatom and Y is a heteroatom or carbon.

# 1.3.1 Methylated heteroaromatic rings

Isomers of the methylated forms of five-membered aromatic rings containing one or more heteroatoms have been studied extensively using rotational spectroscopy. The  $V_3$  barriers of each isomer of methylthiophene, 43-45 methylfuran, 46-48 methylpyrrole, 49-51 methylthiazole, 52-55 methyloxazole,<sup>56, 57</sup> methylimidazole,<sup>58, 59</sup> methylisothiazole,<sup>b,60, 61</sup> and methylisoxazole<sup>62, 63</sup> have been determined, as shown in Figure 1.4. The  $V_3$  barrier height is known to vary across the series of molecules and additionally differs among isomers of a given heteroaromatic ring. Therefore, it is interesting to empirically review the magnitudes of the  $V_3$  barriers of these molecules and factors that may influence the barrier height. Isomers of methylthiophene, 43-45 methylfuran<sup>46-48</sup> and methylpyrrole<sup>49-51</sup> will be considered first and each contain one heteroatom, sulphur, oxygen and nitrogen respectively. Each of methylthiophene and methylfuran have two isomers, in which the methyl group is substituted onto the carbon located at the 2- or 3-position in the ring, whereas methylpyrrole has an additional third isomer whereby the methyl group is substituted onto the nitrogen atom (N-methylpyrrole<sup>49</sup>). Owing to the symmetry of the N-methylpyrrole ring, the methyl internal rotation is hindered by a six-fold potential barrier ( $V_6$ ) of 60 cm<sup>-1</sup> rather than  $V_3$ . When an internal rotor is substituted onto a frame that has  $C_{2V}$  symmetry, the  $V_3$  term in the Fourier series vanishes and the  $V_6$  term remains (more details provided in Chapter 2). Whereas each of 2-methylpyrrole<sup>50</sup> and 3-methylpyrrole<sup>51</sup> do not belong to the C<sub>2V</sub> symmetry group therefore the methyl internal rotation is instead hindered by a  $V_3$  barrier. It can be observed in the isomers of methylthiophene, methylfuran and methylpyrrole that the magnitude of the  $V_3$  barrier changes depending on the position the methyl group is located at and also varies with the identity of the heteroatom. No consistent trend is observed in the position in which the highest barrier is observed, for methylthiophene a higher barrier height is observed for the 3-isomer whereas for each of methylfuran and methylpyrrole a higher barrier is observed when the methyl group is substituted at the 2-position.

The remaining methylated derivatives of five-membered heterocycles contain two heteroatoms. Thiazole, imidazole and oxazole each have a nitrogen atom located at the 3-position and differ in the heteroatom located at the 1-position. A nitrogen atom is located at the 2-position of each of isothiazole and isoxazole with a sulphur atom located in the 1-position of the former and oxygen in the case of the latter. In each of methylthiazole,  $^{52-55}$  methyloxazole  $^{56, 57}$  and methylimidazole  $^{58, 59}$  a clear trend in the barrier height is observed. The lowest  $V_3$  barrier is obtained when the methyl group is located between the two heteroatoms (2-isomer), while

\_

<sup>&</sup>lt;sup>b</sup> No study available on 3-methylisothiazole

significantly higher barriers are observed for the 4- and 5-isomers of each. 2-methylthiazole has the lowest  $V_3$  barrier of 34.1 cm<sup>-1</sup>, while 2-methylimidazole and 2-methyloxazole have  $V_3$  barriers of 122.8 cm<sup>-1</sup> and 251.8 cm<sup>-1</sup> respectively. For the 4- and 5-isomers of methylisothiazole<sup>60, 61</sup> and methylisoxazole<sup>62, 63</sup> no consistent trend in the barrier heights is observed, like what was previously discussed in the case of the 2- and 3- isomers of methylthiophene and methyloxazole. A lower  $V_3$  barrier is obtained for the 5-isomer of methylisothiazole and for the 4-isomer of methylisoxazole. A notable observation is that in each of methylthiophene and methylisothiazole the lowest barrier is observed for the isomer in which the methyl group is situated adjacent to the sulphur atom. While the methyl group being situated adjacent to the oxygen atom in the case of methyloxazole and methylisoxazole results in a higher magnitude of  $V_3$ . The highest value of  $V_3$  is obtained when the methyl group is substituted at the 3-position in methylisoxazole.

It is evident from the varying magnitudes of  $V_3$  observed for the series of methylated fivemembered heteroaromatic rings presented in Figure 1.4 that the height of the hindering potential energy barrier is influenced by the position at which the methyl group is substituted on the ring and additionally the identity of the heteroatom(s) present within the ring. Steric effects cannot explain the variation in the  $V_3$  barrier height in these molecules. In the case of methylthiazole, methylimidazole and methyloxazole the lowest  $V_3$  barriers are obtained when the methyl group is substituted at the carbon atom located at the 2-position, which is more sterically hindered than the 4- and 5-isomers owing to being located between two heteroatoms. This therefore suggests that electronic effects have a significant influence on the barrier height of the methylated heteroaromatic rings. The contribution of electronic effects when  $\pi$  electrons are located adjacent to a methyl group was noted by Spangler.<sup>64</sup> More recently the role of electronic interactions on the barrier height was discussed using a theoretical approach by Wang *et al.*<sup>65</sup>

The internal rotation of methylated derivatives of several larger nitrogen-containing aromatic rings (shown in Figure 1.4) have also been studied allowing the barriers to internal rotation to be determined. The barrier heights of two isomers of methylpyridine<sup>66-68</sup> and three isomers of methylpyrimidine<sup>61, 69, 70</sup> have been reported. The  $V_3$  barriers determined for 2-methylpyridine<sup>66, 67</sup> and 4-methylpyrimidine<sup>61</sup> are similar, 90.3 cm<sup>-1</sup> in the former and 94.4 cm<sup>-1</sup> in the latter. This can likely be attributed to the local environment around the methyl group being essentially the same in both molecules. The  $V_6$  barriers of each of 4-methylpyridine,<sup>68</sup> 2-methylpyrimidine<sup>69</sup> and 5-methylpyrimidine<sup>70</sup> have been reported to be 4.7 cm<sup>-1</sup>, 1.6 cm<sup>-1</sup> and 4.1 cm<sup>-1</sup> respectively. The values obtained for each of 4-methylpyridine and 5-methylpyrimidine compare with the barrier reported for toluene ( $V_6 = 4.8 \text{ cm}^{-1}$ ).<sup>71-73</sup> Again, this is likely due to the fact that the local

environment surrounding the methyl group in each of 4-methylpyridine and 5-methylpyrimidine is very similar to that of toluene. The  $V_6$  barrier determined for 2-methylpyrimidine, where the methyl group is located between the two nitrogen atoms, is lower than for the other two isomers. This is consistent with the isomers of methylthiazole, methylimidazole and methyloxazole whereby the methyl group is situated between the heteroatoms each having a lower barrier than other isomers. Methylindole is the largest nitrogen-containing heteroaromatic ring to be studied with  $V_3$  barriers determined for each of the seven isomers of this molecule.<sup>74</sup> The lowest barriers were obtained for the isomers in which the methyl group is substituted at the 5- and 6- positions which are located on the benzene ring and are similar in magnitude. While significantly higher barriers were obtained when the methyl group is substituted at other positions.

# 1.3.2 Effect of ring substituents

Studies on aromatic molecules which possess a methyl group and other ring substituents have revealed the effect the position and identity of the substituent has on the barrier to internal rotation of the methyl group. Derivatives of toluene, such as (but not limited to) halotoluenes, have been widely studied with additional substituents located ortho, meta or para with respect to the position of the methyl group. As mentioned earlier the  $(V_6)$  barrier to internal rotation in toluene is 4.8 cm<sup>-1</sup> such that the rotation of the methyl group is essentially unhindered.<sup>71-73</sup> When a single substituent is located *ortho* or *meta* to the methyl group, the ring symmetry is broken such that the methyl rotation is hindered by a  $V_3$  barrier rather than  $V_6$ . A significantly higher  $V_3$  barrier is usually observed when an atom or group is located adjacent to the methyl group (in the ortho position) compared to the barrier height when the same substituent is instead located in the meta position. In the case of fluorotoluene, V<sub>3</sub> barriers of 227.3 cm<sup>-1</sup> and 16.9 cm<sup>-2</sup> were obtained when the fluorine atom is located *ortho* and *meta* to the methyl group respectively. 75-77 Whereas a  $V_6$  barrier identical to that of toluene was observed when the fluorine atom is substituted para to the methyl group. 78 Higher barriers of 469.2, 502.3 and 530.0 cm<sup>-1</sup> are reported when chlorine, bromine and iodine are located *ortho* to the methyl group, indicating that in this case steric hinderance is the dominant effect on the  $V_3$  barrier. <sup>79,80</sup> However, when a chlorine atom is located *meta* to the methyl group, a  $V_3$  barrier of 3.2 cm<sup>-1</sup> is observed which is lower than the magnitude of the barrier when a fluorine atom is located in that position.81

Significantly fewer studies on methylated five-membered heteroaromatic rings with additional substituents have been reported. When a vinyl group is located adjacent to a methyl group in the case of 4-methyl-5-vinylthiazole,  $^{82}$  it was noted that the  $V_3$  barrier of the methyl group (107.1 cm<sup>-1</sup>) is considerably lower than the barrier in 4-methylthiazole. This was also observed in the case of 4,5-dimethylthiazole<sup>83</sup> in which two methyl groups are located adjacent to each other. The  $V_3$  barrier of the methyl group located at the 4- and 5-positions are reported to be 126.5 cm<sup>-1</sup> and 61.7 cm<sup>-1</sup>, which are lower than what was previously reported for each of 4methylthiazole<sup>54</sup> and 5-methylthiazole<sup>55</sup> (357.6 and 322 cm<sup>-1</sup> respectively). In both cases, the methyl groups are more sterically hindered than in the case of 4-methylthiazole and 5methylthiazole such that an increase in the magnitude of  $V_3$  may be expected, as observed in the case of the *ortho*- substituted toluene derivatives. However, the decrease in  $V_3$  suggests electronic effects are the dominant influence. In both studies the authors suggested that the presence of additional substituents has an influence on the distribution of  $\pi$ -electrons in the aromatic ring, resulting in the reduction in the  $V_3$  barrier height. Several other studies on dimethylated five-membered heteroaromatic rings with either equivalent<sup>84-86</sup> or non-equivalent<sup>87</sup> methyl groups have been reported. The only other thiazole derivative to be studied is 2,4dimethylthiazole<sup>87</sup> which has two non-equivalent methyl groups located remote to each other. For each methyl group, the  $V_3$  barrier is changed to what was observed in the mono-methylated analogues, however, this change is minor compared to what was observed in the case of 4methyl-5-vinylthiazole and 4,5-dimethylthiazole.

# 1.3.3 Effect of complex formation

The investigation of complexes formed between molecules which possess internal rotors and other small molecules, such as water or argon, have revealed the influence that the formation of such complexes has on the methyl internal rotation. Only a limited number of studies have been conducted on complexes formed with derivatives of aromatic rings which possess internal rotors. Complexes of *N*-methylpyrrole, <sup>88</sup> *para*-fluorotoluene <sup>89</sup> and 2-methylpyridine <sup>67</sup> with argon have each been studied using microwave spectroscopy, while complexes formed between three isomers of methylindole and argon have been studied by rotationally resolved fluorescence excitation spectroscopy. <sup>90</sup> For each of *N*-methylpyrrole <sup>88</sup> and *para*-fluorotoluene, <sup>89</sup> owing to the symmetry of the environment surrounding the methyl group within the isolated monomers, the internal rotation is hindered by a *V*<sub>6</sub> barrier. Whereas, upon complexation the barrier height is changed such that a *V*<sub>3</sub> barrier is observed in each case. A small (2 %) increase in the *V*<sub>3</sub> barrier of the methyl group in 2-methylpyridine was observed

upon the formation of its weakly-bound complex with argon. <sup>67</sup> While varying degrees of change in  $V_3$  were reported upon the formation of argon complexes with isomers of methylindole <sup>90</sup> in both the ground and first excited states. In each case an increase in the barrier height was observed. Studies on monohydrate complexes formed with 2-methoxypyridine <sup>91</sup> and acetophenone <sup>92</sup> have noted a change in the barrier height upon complexation. In each of 2-methoxypyridine and acetophenone, the methyl group is not bound directly to the aromatic ring and high  $V_3$  barriers are obtained in the isolated monomers, 707 cm<sup>-1</sup> in the former and 627 cm<sup>-1</sup> in the latter. An increase in  $V_3$  compared to the isolated monomer was observed upon the formation of the monohydrate complex in the case of 2-methoxypyridine whereas a decrease in  $V_3$  was observed in the case of acetophenone. In each of 2-methoxypyridine····H<sub>2</sub>O and acetophenone····H<sub>2</sub>O, the water molecule binds adjacent to the methyl group and a weak hydrogen bonding interaction is present between the O atom of water and the methyl group  $(C-H···O_w)$ . It is therefore interesting that an increase in the barrier height is observed in the case of the former while the opposite is observed in the latter.

Studies on non-aromatic molecules have also noted the  $V_3$  barrier to internal rotation being changed upon the formation of a complex with water. A significant increase in  $V_3$  was observed for the methyl group that water interacts with in each of N-methylformamide...H<sub>2</sub>O,<sup>93</sup> trifluoroacetone···H<sub>2</sub>O,<sup>94</sup> diacetyl···H<sub>2</sub>O<sup>95</sup> and dimethoxymethane···H<sub>2</sub>O<sup>96</sup> compared to the unhydrated monomer or another methyl group within the molecule. In each case, the increase was attributed to the presence of a hydrogen bonding interaction between the water molecule and methyl group such that the rotation becomes more hindered. In the case of dimethoxymethane, a second methyl group is present which is also changed relative to the unhydrated form, however, in this case a decrease in V<sub>3</sub> is observed. <sup>96</sup> Recently, a study on hydrate complexes formed with methyl carbamate found that the  $V_3$  barrier height progressively increases with the degree of microsolvation.<sup>97</sup> Unlike the aforementioned studies, the water molecule(s) in methyl carbamate  $\cdots$  (H<sub>2</sub>O)<sub>n</sub> (n = 1 – 3) do not form an interaction with the methyl group, therefore, the presence of an interaction hindering the methyl rotation cannot be the reason  $V_3$  increases in this case. The authors suggested that the increase may be due to an extension of the resonance and  $\pi$ -cooperative effects to the other side of the molecule where the methyl group is situated. The formation of hydrate complexes is also known to result in a decrease in the  $V_3$  barrier to internal rotation. This has been observed in cases where the water molecule binds remote<sup>98, 99</sup> to and adjacent to the methyl group. <sup>92, 99</sup> The monohydrate and dihydrate complex formed with acetic acid was reported in 2008.98 The water molecule(s) coordinates with the carboxylic acid group, which is located on the opposite side of the

molecule to the methyl group and a decrease in the  $V_3$  barrier height is observed upon the hydration of this molecule. The decrease in  $V_3$  was attributed to a redistribution of electrons within the carboxyl group which occurs as a result of the formation of the hydrate complexes. A lowering of  $V_3$  was also observed in each isomer of methyl vinyl ketone···H<sub>2</sub>O<sup>99</sup> compared to the unhydrated monomers. In this case, a more significant decrease was observed in the isomers in which the water sub-unit is adjacent to the methyl group such that a weak C-H···O<sub>w</sub> interaction is present.

# 1.4 Conformationally flexible aromatic derivatives

When a substituent comprised of a chain of more than one heavy atom, connected by single bonds, is substituted onto an aromatic or heteroaromatic ring, these molecules have a degree of conformational flexibility. This results in these molecules having the capability to adopt different conformations owing to the substituent having several degrees of freedom, including the rotation of the group relative to the ring and rotations within the side chain. Microwave spectroscopy studies have explored the structures of numerous aromatic ring derivatives which have side chains containing two, three or four heavy atoms. Given that the distribution of mass differs across each conformation of the same molecule, microwave spectroscopy proves particularly useful in the study of conformationally flexible molecules since each have a distinct microwave spectrum. Therefore, different conformations of the same molecule are distinguishable by this technique. In this section the trends in observed conformations of aromatic ring derivatives will be discussed.

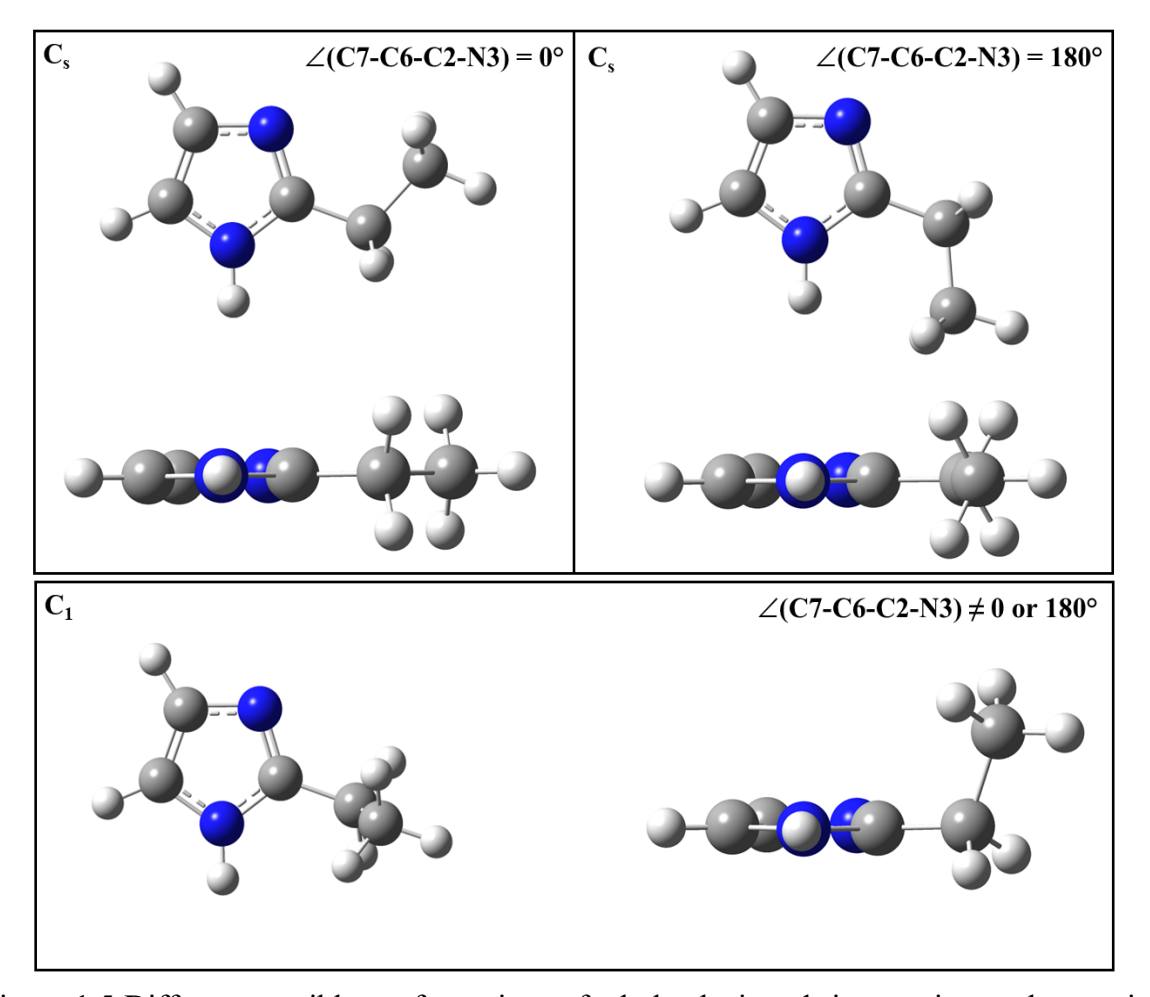


Figure 1.5 Different possible conformations of ethyl-substituted rings owing to the rotation of the ethyl group relative to the ring plane. When the ethyl group is co-planar with the ring, the conformation has  $C_s$  symmetry (upper panel). When the ethyl group is rotated out of the ring plane, the conformation has  $C_1$  symmetry (lower panel). The experimentally observed conformation of 2-ethylimidazole (pictured in figure) will be discussed in Chapter 7.

# 1.4.1 Alkyl-substituted aromatic rings

A limited number of microwave spectroscopy studies on alkyl-substituted rings are available in the current literature. When an ethyl group is substituted onto an aromatic ring, these molecules have the ability to adopt conformations which have  $C_s$  or  $C_1$  symmetry (see Figure 1.5) owing to the rotation of the ethyl group relative to the rigid aromatic frame. Conformations which have  $C_s$  symmetry (Figure 1.5, upper) have both carbon atoms of the ethyl group co-planar with the aromatic ring, such that the dihedral angle which defines the rotation of the ethyl group relative to the plane of the ring is  $\angle(C-C-X-X)=0^\circ$  or  $180^\circ$  (where "X" denotes atoms within the ring). Conformers which possess  $C_1$  symmetry (Figure 1.5, lower) have the ethyl group rotated out of the plane of the ring such that  $\angle(C-C-X-X)\neq 0^\circ$  or  $180^\circ$ . Additional conformations are available for molecules which have longer alkyl chains owing to the flexibility which exists within the side chain.

Studies on ethyl-substituted benzene, 100, 101 aniline 102 and furan 103 rings have revealed the lowest energy conformations that each molecule adopts in the gas phase. Ethylbenzene<sup>100, 101</sup> was found to adopt a C<sub>1</sub> conformation only. The local environment surrounding the ethyl group is highly symmetric resulting in the ethyl group being rotated 90° relative to the benzene ring. Three isomers of ethylaniline, 2-ethylaniline, 3-ethylaniline and 4-ethylaniline, have been studied whereby the ethyl group is located ortho, meta and para respectively to the exocyclic amine group. 102 In each of 3-ethylaniline and 4-ethylaniline, the ethyl group is remote to the amine group and was found to be rotated  $87.4^{\circ}$  and  $91.3^{\circ}$  relative to the ring plane in the  $r_{\rm s}$ geometry. The dihedral angles in each of these isomers are similar to what was observed for the equivalent angle in ethylbenzene owing to the local environment surrounding the ethyl group being essentially the same in each case. Slightly more of a deviation of the dihedral angle from 90° is observed in the case of 3-ethylaniline, which is likely due to the asymmetry of this ring being greater than in 4-ethylaniline. In the 2-ethylaniline isomer, the ethyl group is located adjacent to the amine group and the  $\angle$ (C8–C7–C2–C1) dihedral angle was determined to be 75.6°. The deviation from 90° is more significant in this case and the authors attributed this to the presence of a weak intramolecular hydrogen bonding interaction between the nitrogen atom of the amine group and the ethyl group. Unlike ethylbenzene and each isomer of ethylaniline, the ethyl-substituted five-membered ring, 2-ethylfuran, 103 was found to adopt two distinct conformations. This molecule adopts conformers which have C<sub>s</sub> and C<sub>1</sub> symmetry and the  $\angle$ (C7–C6–C2–O1) dihedral angle was determined to be 180° and 63.3° respectively, in the  $r_s$ geometries. Consistent with the observations of 2-ethylaniline, when the ethyl group is in a C<sub>1</sub> configuration in 2-ethylfuran, the dihedral angle which defines the rotation of the ethyl group

relative to the ring plane deviates from 90°. In both cases, the local environment surrounding the ethyl group has a higher degree of asymmetry compared to ethylbenzene and additionally it was observed that the ethyl group rotates towards the electronegative atom or group. It is therefore possible that a weak intramolecular interaction exists between the oxygen atom of the furan ring and the ethyl group in 2-ethylfuran.

The studies on ethyl-substituted rings have revealed that typically the ethyl group adopts a  $C_1$  configuration in the lowest-energy conformation of these molecules, with 2-ethylfuran being the only example whereby a conformer adopting a  $C_s$  configuration is observed. Additionally, some variation in the  $\angle$ (C-C-X-X) dihedral angle has been observed across the series of molecules. Studies on alkyl-substituted rings which contain 3 or 4 carbon atoms in the side chain have also been conducted revealing the low energy conformations available for longer carbon chains. Two conformers of propylbenzene have been observed, *trans* and *gauche*. Both conformations are calculated to be similar in energy and the propyl group is located out of the plane of the benzene ring in each. The conformers differ in the location of the third carbon atom in the chain relative to the benzene ring. The number of conformations is greater in the case of butylbenzene owing to the longer alkyl-chain. Four conformations of this molecule were observed. Similar to each of ethylbenzene and propylbenzene, the carbon chain in butylbenzene is located out of the plane of the ring in each experimentally observed structure.

# 1.4.2 Other substituted aromatic rings

Considerably more studies on aromatic ring derivatives with substituents containing a nitrogen, oxygen or sulphur heteroatom in the chain have been conducted. First the derivatives with substituents which have two heavy atoms in the chain, with the general formula,  $CH_2XH_n$  (where X = N, O or S) will be discussed. Furfuryl amine,  $^{104}$  furfuryl alcohol $^{105, 106}$  and furfuryl mercaptan $^{106, 107}$  are furan derivatives which are analogous to 2-ethylfuran, differing only in the group bound to C6. Furfuryl amine was found to adopt one conformation which has  $C_1$  symmetry and the  $\angle(N7-C6-C2-O1)$  angle was determined to be  $65.4^{\circ}$ . $^{104}$  Whereas additional conformations of each of furfuryl alcohol $^{105, 106}$  and furfuryl mercaptan $^{106, 107}$  are available, owing to the rotation of the terminal hydrogen atom of the alcohol and thiol group relative to the oxygen atom in the ring, resulting in non-equivalent structures. In the lowest energy structure of furfuryl alcohol and furfuryl mercaptan, a  $C_1$  configuration is adopted and the terminal hydrogen atom is orientated towards the oxygen atom of the furan ring. The  $\angle(O7/S7-C6-C2-O1)$  dihedral angle was determined to be  $66.5^{\circ}$  in the former and  $71.8^{\circ}$  in the latter

(derived from the  $r_0$  coordinates<sup>106</sup>) which are similar to the magnitude of the equivalent angle in each of 2-ethylfuran and furfuryl amine. The lowest energy conformation of each of furfuryl amine, furfuryl alcohol and furfuryl mercaptan contains a  $X-H\cdots O1$  (where X=N, O or S) intramolecular hydrogen bond which ultimately stabilises this configuration compared to other possible conformations. Unlike furfuryl amine, additional conformations of furfuryl alcohol and furfuryl mercaptan have been observed. For both molecules, the structure whereby the terminal hydrogen atom is orientated away from O1 was observed. Several transitions of a third conformation of furfuryl mercaptan were identified during a 2018 reinvestigation, <sup>106</sup> in this structure the carbon and sulphur atoms of the chain are co-planar with the furan ring, in a structure analogous to the C<sub>s</sub> conformation of 2-ethylfuran. Thenyl alcohol and thenyl mercaptan have also been studied. 108 The thenyl derivatives are analogous to furfuyl alcohol and furfuryl mercaptan, differing only in the heteroatom located within the aromatic ring (sulphur rather than oxygen). Only one conformation of each of thenyl alcohol and thenyl mercaptan was observed experimentally. In the lowest energy conformation of both molecules the terminal hydrogen atom of the alcohol and thiol group is orientated adjacent to the carboncarbon double bond and away from the ring sulphur atom. The lowest energy structures of furfuryl and thenyl derivatives differ, indicating that the identity of the heteroatom within the ring has an influence on the energy ordering of conformations.

Rotational spectroscopy studies on benzylamine, <sup>109</sup> benzyl alcohol <sup>110</sup> and benzyl mercaptan <sup>111</sup> have revealed the lowest energy conformations of each. As mentioned earlier, ethylbenzene adopts one conformation in which the ethyl group is orientated perpendicular to the plane of the benzene ring. Each of benzylamine, benzyl alcohol and benzyl mercaptan have been found to adopt conformations whereby the side chain is orientated out of the plane of the benzene ring. However, unlike the series of furan derivatives, more variation in the  $\angle$ (X8–C7–C1–C2) dihedral angle is observed across the benzene derivatives. The study on benzylamine 109 observed two low energy conformations of this molecule. The global minimum structure of benzylamine is analogous to the structure of ethylbenzene with the ∠(N8–C7–C1–C2) angle determined to be 89.1°. The second conformation which is slightly higher in energy contains a C-H···N intramolecular hydrogen bond, resulting in a significantly different value of ∠(N8– C7-C1-C2) of 39.9°. Gauche conformations were observed for each of benzyl alcohol110 and benzyl mercaptan, 111 with the ∠(X8–C7–C1–C2) dihedral angle being 54.5° in the former and 73.9° in the latter. In the case of both benzyl alcohol and benzyl mercaptan the gauche conformation has four equivalent configurations, and the tunnelling barrier was found to be similar in both the alcohol and thiol analogues. This was not observed in the case of the furfuryl

and thenyl derivatives owing to the asymmetry within the ring. Finally, the most recent in the series of aromatic ring derivatives containing a  $CH_2XH_n$  substituent to be studied by microwave spectroscopy is picolylamine.<sup>112</sup> Three isomers of this molecule were investigated in a 2024 study, which found that each of 3-picolylamine and 4-picolylamine contain a  $C-H\cdots N_{\text{(amine)}}$  intramolecular hydrogen bond resulting in the  $\angle (N8-C7-C-C)$  dihedral angles in these molecules to vary significantly from the equivalent angles observed in each of 3-ethylaniline and 4-ethylaniline. For 3-picolyamine, the  $\angle (N8-C7-C3-C4)$  dihedral angle was found to be 24.2° while the  $\angle (N8-C7-C4-C3)$  dihedral angle was determined to be 34.7° for 4-picolylamine, in the  $r_s$  geometries. Whereas the observed conformation of 2-picolyamine is stabilised by a  $N_{\text{(amine)}}-H\cdots N_{\text{(ring)}}$  intramolecular interaction and the  $\angle (N8-C7-C2-N1)$  dihedral angle was found to be 44.8°.

It is evident from the substituted aromatic rings containing CH<sub>2</sub>XH<sub>n</sub> discussed that the energy ordering of conformations is strongly influenced by intramolecular interactions present. Typically, the lowest energy forms of these molecules are stabilised by an intramolecular hydrogen bond between the terminal hydrogen of the amine, alcohol or thiol group of the side chain and the heteroatom or  $\pi$ -system of the aromatic ring. Benzene derivatives which have three heavy atoms in the side chain, namely 2-phenylethanol, 113, 114 2-phenylethanethiol 115 and 2-phenylamine<sup>116, 117</sup> have also been studied. In the case of 2-phenylethanol<sup>113, 114</sup> and 2phenylethanethiol, 115 the global minimum structure of both molecules is a gauche-gauche, folded conformation such that each contain a S/O-H $\cdots\pi$  intramolecular interaction. Interestingly, in the case of 2-phenylethanol and 2-phenylethanethiol, it appears that the identity of the heteroatom within the side chain has an influence on the energy ordering of the conformations (as shown in Figure 1 of reference 115). A second higher energy structure was observed for each of 2-phenylethanol and 2-phenylethanethiol, however, the structures of the observed higher energy form differ owing to the difference in the energy ordering. Both the higher energy forms of 2-phenylethanol and 2-phenylethanethiol adopt an anti, extended configuration but differ in the orientation of the terminal hydrogen of the alcohol or thiol group. Four conformations, two gauche and two anti, of 2-phenylethylamine have been experimentally observed. 116, 117 Both gauche conformations are lower in energy than the anti conformations owing to the presence of a N-H $\cdots\pi$  intramolecular hydrogen bonding interaction in each. For the majority of aromatic derivatives containing a CH<sub>2</sub>XH<sub>n</sub> or CH<sub>2</sub>CH<sub>2</sub>XH<sub>n</sub> side chain, the substituent is rotated out of the plane of the aromatic ring. In each of the aforementioned molecules, the heteroatom is located one or more carbon atoms away from the aromatic ring. However, for each of 2-methoxyfuran, anisole and phenetole, the oxygen atom is located first in the chain and adjacent to the aromatic ring. 2-methoxyfuran  $^{118}$  and anisole  $^{119}$  were each found to adopt a  $C_s$  conformation only, differing from the alkyl and hydroxymethyl analogues of each. The authors of the 2-methoxyfuran study suggested that this conformation is preferred owing to this structure allowing the extended delocalisation of  $\pi$  electrons onto the oxygen atom, stabilising this geometry. Whereas in the case of phenetole  $^{120}$  two conformations were observed. The lowest energy structure has  $C_s$  symmetry such that each of the heavy atoms within the ethoxy side chain are co-planar with the benzene ring. The ethyl group is rotated out of the plane of the benzene ring in the higher energy conformation by  $\sim 70^\circ$ .

#### 1.5 Thesis Overview

The studies discussed within this Chapter has highlighted the vast amount of research interest surrounding aromatic and heteroaromatic rings within the microwave spectroscopy community owing to the presence of these molecules in nature. Additionally, this research has provided an understanding of fundamental molecular physics and furthered understanding of non-covalent interactions. The investigation of isolated weakly-bound complexes formed with heteroaromatic rings have revealed the binding preferences of these molecules, with the first steps of microsolvation being of particular interest owing to the presence of these rings in biology. Derivatives of aromatic rings have also received a significant amount of attention, with numerous studies being performed on substituted rings. Microwave spectroscopy studies on methylated heteroaromatic rings have revealed that the magnitude of the  $(V_3)$  barrier to internal rotation of the methyl group varies quite significantly across this series of molecules. It has also been observed that the presence of additional ring substituents and the formation of weaklybound complexes can influence the barrier height, with a considerably greater number of studies being performed on the former compared to the latter. Finally, many aromatic ring derivatives have substituents which are conformationally flexible. The lowest energy conformations of these molecules have been revealed by microwave spectroscopy and it has been observed that typically the lowest energy forms are stabilised by intramolecular hydrogen bonding interactions. The work presented within this thesis combines these research themes by focussing on the investigation of the first steps of microsolvation of substituted heteroaromatic rings.

Microwave spectroscopy studies on several methyl- and ethyl-substituted heterocyclic rings and weakly-bound complexes formed with water will be presented. Each study was performed using the chirped pulse Fourier transform microwave (CP-FTMW) spectrometer at Newcastle University with spectra collected over the frequency range 2.0 – 18.5 GHz. The target molecules were transferred to the gas-phase by means of heating or laser ablation. Alongside experimental studies, quantum chemical calculations, Non-Covalent Interaction (NCI) index and Natural Bond Orbital (NBO) analyses have been performed. The molecular structure of each species under study has been precisely determined and this work has revealed the influence that weak interactions between the O atom of water and H, CH<sub>3</sub> and C<sub>2</sub>H<sub>5</sub> groups of the heterocyclic ring (C–H···O) has on the intermolecular parameters of the primary hydrogen bond, the V<sub>3</sub> barrier to internal rotation of the methyl group and the conformational preference of ethyl groups.

In Chapter 2 aspects of the fundamental theoretical basis of rotational spectroscopy which are relevant to this thesis will be discussed. Additionally, details of the programs and methods used within the studies will be provided. The components and operation of the Newcastle CP-FTMW

spectrometer<sup>121-123</sup> will be discussed in Chapter 3 which were used for all experimental measurements presented herein. Binary complexes formed between each isomer of methylthiazole and water are reported in Chapter 4. The assignment of the microwave spectra of these complexes has allowed the  $V_3$  barrier to internal rotation and molecular geometries to be determined. The results will be discussed alongside the methylimidazole···H<sub>2</sub>O complexes which have also been recently studied by our group, <sup>124</sup> providing an insight into the influence that the formation of the hydrate complex has on the methyl internal rotation and revealing the effect the presence of the methyl group has on intermolecular parameters associated with the primary hydrogen bonding interaction. In Chapter 5, the monohydrate complex formed with 2ethylfuran will be discussed. A recent study reported two conformations of the 2-ethylfuran monomer. 103 The experiments conducted and reported herein have provided additional information regarding the experimental energy ordering of the two conformations of the monomer, which was unable to be determined during the previous study. The monohydrate complex was probed during the same experiments and the molecular geometry of this complex has been determined. It will be shown that the experimentally observed lowest energy geometry of 2-ethylfuran changes depending on whether it is an isolated molecule or bound within a complex. The 2-ethylthiazole monomer and two of its weakly-bound complexes formed with water, 2-ethylthiazole···H<sub>2</sub>O and 2-ethylthiazole···(H<sub>2</sub>O)<sub>2</sub>, were probed and studied for the first time by microwave spectroscopy, with results presented in Chapter 6. This work identified that the ethyl group is rotated out of the plane of the thiazole ring in each of the monomer and hydrate complexes. The dihedral angle which defines the rotation of the ethyl group within the isolated monomer will be compared to the equivalent angle in other ethyl-substituted aromatic rings within the current literature. Within the hydrate complexes it was observed that weak interactions form between the water sub-unit and the ethyl group. It has been revealed that these weak interactions have a significant effect on the intermolecular parameters associated with the primary hydrogen bond through comparisons with the un-ethylated analogues of the complexes, thiazole···(H<sub>2</sub>O)<sub>n</sub>.<sup>21, 30</sup> Finally, in Chapter 7 the lowest energy geometries of two isomers of ethylimidazole, N-ethylimidazole and 2-ethylimidazole, have been determined using microwave spectroscopy. It will be shown that the substitution position of the ethyl group on the imidazole ring influences the observed conformation of the molecule. Additionally, hydrate complexes formed with the isomers of ethylimidazole, N-ethylimidazole... $(H_2O)_n$  (n = 1, 2) and 2-ethylimidazole···H<sub>2</sub>O have been observed and are presented herein. The molecular geometries and structural parameters determined will be compared with other imidazolecontaining complexes.<sup>32, 124</sup>

# 1.6 References

- 1. E. Arunan, G. R. Desiraju, R. A. Klein, J. Sadlej, S. Scheiner, I. Alkorta, D. C. Clary, R. H. Crabtree, J. J. Dannenberg, P. Hobza, H. G. Kjaergaard, A. C. Legon, B. Mennucci and D. J. Nesbitt, *Pure and Applied Chemistry*, 2011, **83**, 1637-1641.
- 2. E. Arunan, G. R. Desiraju, R. A. Klein, J. Sadlej, S. Scheiner, I. Alkorta, D. C. Clary, R. H. Crabtree, J. J. Dannenberg, P. Hobza, H. G. Kjaergaard, A. C. Legon, B. Mennucci and D. J. Nesbitt, *Pure and Applied Chemistry*, 2011, **83**, 1619-1636.
- 3. P. C. Singh and G. N. Patwari, *The Journal of Physical Chemistry A*, 2008, **112**, 5121-5125.
- 4. G. Karir, N. O. B. Lüttschwager and M. A. Suhm, *Physical Chemistry Chemical Physics*, 2019, **21**, 7831-7840.
- 5. M. Goswami and E. Arunan, *Physical Chemistry Chemical Physics*, 2011, **13**, 14153-14162
- 6. M. Goswami and E. Arunan, *Journal of Molecular Spectroscopy*, 2011, **268**, 147-156.
- 7. D. Loru, M. A. Bermúdez and M. E. Sanz, *The Journal of Chemical Physics*, 2016, **145**, 074311.
- 8. M. Chrayteh, E. Burevschi, D. Loru, T. R. Huet, P. Dréan and M. E. Sanz, *Physical Chemistry Chemical Physics*, 2021, **23**, 20686-20694.
- 9. E. Burevschi, M. Chrayteh, S. I. Murugachandran, D. Loru, P. Dréan and M. E. Sanz, *Journal of the American Chemical Society*, 2024, **146**, 10925-10933.
- 10. D. Loru, I. Peña and M. E. Sanz, *Physical Chemistry Chemical Physics*, 2019, **21**, 2938-2945.
- 11. E. Burevschi, E. R. Alonso and M. E. Sanz, *Chemistry A European Journal*, 2020, **26**, 11327-11333.
- 12. T. R. Dyke, K. M. Mack and J. S. Muenter, *The Journal of Chemical Physics*, 1977, **66**, 498-510.
- 13. J. A. Odutola and T. R. Dyke, *The Journal of Chemical Physics*, 1980, **72**, 5062-5070.
- 14. F. N. Keutsch, J. D. Cruzan and R. J. Saykally, *Chemical Reviews*, 2003, **103**, 2533-2578
- 15. N. Pugliano and R. J. Saykally, *Science*, 1992, **257**, 1937-1940.
- 16. J. D. Cruzan, L. B. Braly, K. Liu, M. G. Brown, J. G. Loeser and R. J. Saykally, *Science*, 1996, **271**, 59-62.
- 17. K. Liu, M. G. Brown, J. D. Cruzan and R. J. Saykally, *Science*, 1996, **271**, 62-64.
- 18. C. Pérez, M. T. Muckle, D. P. Zaleski, N. A. Seifert, B. Temelso, G. C. Shields, Z. Kisiel and B. H. Pate, *Science*, 2012, **336**, 897-901.
- 19. C. Pérez, S. Lobsiger, N. A. Seifert, D. P. Zaleski, B. Temelso, G. C. Shields, Z. Kisiel and B. H. Pate, *Chemical Physics Letters*, 2013, **571**, 1-15.
- 20. C. Pérez, D. P. Zaleski, N. A. Seifert, B. Temelso, G. C. Shields, Z. Kisiel and B. H. Pate, *Angewandte Chemie International Edition*, 2014, **53**, 14368-14372.
- 21. E. Gougoula, C. N. Cummings, Y. Xu, T. Lu, G. Feng and N. R. Walker, *The Journal of Chemical Physics*, 2023, **158**, 114307.
- 22. C. Medcraft, E. Gougoula, D. M. Bittner, J. C. Mullaney, S. Blanco, D. P. Tew, N. R. Walker and A. C. Legon, *The Journal of Chemical Physics*, 2017, **147**, 234308.
- 23. S. J. Harris, A. C. Legon, N. R. Walker and D. E. Wheatley, *Angewandte Chemie International Edition*, 2010, **49**, 181-183.
- 24. V. A. Mikhailov, F. J. Roberts, S. L. Stephens, S. J. Harris, D. P. Tew, J. N. Harvey, N. R. Walker and A. C. Legon, *The Journal of Chemical Physics*, 2011, **134**, 134305.
- 25. M. J. Tubergen, A. M. Andrews and R. L. Kuczkowski, *The Journal of Physical Chemistry*, 1993, **97**, 7451-7457.
- 26. S. P. Lockwood, T. G. Fuller and J. J. Newby, *The Journal of Physical Chemistry A*, 2018, **122**, 7160-7170.

- 27. J. G. Wasserman, K. J. Murphy and J. J. Newby, *The Journal of Physical Chemistry A*, 2019, **123**, 10406-10417.
- 28. W. G. D. P. Silva and J. van Wijngaarden, *The Journal of Physical Chemistry A*, 2021, **125**, 3425-3431.
- 29. J. J. Newby, T. Sivells and A. N. Carney, *Journal of Molecular Spectroscopy*, 2022, **389**, 111689.
- 30. W. Li, J. Chen, Y. Xu, T. Lu, Q. Gou and G. Feng, *Spectrochimica Acta Part A: Molecular and Biomolecular Spectroscopy*, 2020, **242**, 118720.
- 31. T. K. Roy, K. Chatterjee, J. Khatri, G. Schwaab and M. Havenith, *AIP Advances*, 2021, **11**, 115112.
- 32. E. Gougoula, D. J. Cole and N. R. Walker, *The Journal of Physical Chemistry A*, 2020, **124**, 2649-2659.
- 33. J. Zischang, J. J. Lee and M. A. Suhm, *The Journal of Chemical Physics*, 2011, **135**, 061102.
- 34. S. McGlone, P. Moreschini, T. K. Ha and A. Bauder, *Molecular Physics*, 2001, **99**, 1353-1364.
- 35. T. K. Roy, K. Chatterjee, J. Khatri, G. Schwaab and M. Havenith, *The Journal of Physical Chemistry A*, 2021, **125**, 4766-4774.
- 36. S. Suzuki, P. G. Green, R. E. Bumgarner, S. Dasgupta, W. A. Goddard and G. A. Blake, *Science*, 1992, **257**, 942-945.
- 37. H. S. Gutowsky, T. Emilsson and E. Arunan, *The Journal of Chemical Physics*, 1993, **99**, 4883-4893.
- 38. R. B. Mackenzie, C. T. Dewberry, R. D. Cornelius, C. J. Smith and K. R. Leopold, *The Journal of Physical Chemistry A*, 2017, **121**, 855-860.
- 39. W. Caminati, P. Moreschini and P. G. Favero, *The Journal of Physical Chemistry A*, 1998, **102**, 8097-8100.
- 40. S. Melandri, M. E. Sanz, W. Caminati, P. G. Favero and Z. Kisiel, *Journal of the American Chemical Society*, 1998, **120**, 11504-11509.
- 41. W. Caminati, L. B. Favero, P. G. Favero, A. Maris and S. Melandri, *Angewandte Chemie International Edition*, 1998, **37**, 792-795.
- 42. D. Loru, A. L. Steber, P. Pinacho, S. Gruet, B. Temelso, A. M. Rijs, C. Pérez and M. Schnell, *Physical Chemistry Chemical Physics*, 2021, **23**, 9721-9732.
- 43. N. M. Pozdeev, R. G. Latypova and L. N. Gunderova, *Journal of Structural Chemistry*, 1976, **17**, 313-314.
- 44. K. J. Koziol, H. El Hadki, A. Lüchow, N. Vogt, J. Demaison and H. V. Nguyen, *Spectroscopy Journal*, 2023, **1**, 49-64.
- 45. T. Ogata and K. Kozima, *Journal of Molecular Spectroscopy*, 1972, **42**, 38-46.
- 46. I. A. Finneran, S. T. Shipman and S. L. Widicus Weaver, *Journal of Molecular Spectroscopy*, 2012, **280**, 27-33.
- 47. W. G. Norris and L. C. Krisher, *The Journal of Chemical Physics*, 2003, **51**, 403-406.
- 48. T. Ogata and K. Kozima, Bulletin of the Chemical Society of Japan, 1971, 44, 2344-2346.
- 49. J. Makarewicz, S. Huber, B. Brupbacher-Gatehouse and A. Bauder, *Journal of Molecular Structure*, 2002, **612**, 117-123.
- 50. T. Nguyen, C. Dindic, W. Stahl, H. V. L. Nguyen and I. Kleiner, *Molecular Physics*, 2020, **118**, 1668572.
- 51. T. Nguyen, W. Stahl, H. V. L. Nguyen and I. Kleiner, *Journal of Molecular Spectroscopy*, 2020, **372**, 111351.
- 52. J. U. Grabow, H. Hartwig, N. Heineking, W. Jäger, H. Mäder, H. W. Nicolaisen and W. Stahl, *Journal of Molecular Structure*, 2002, **612**, 349-356.
- 53. T. Nguyen, V. Van, C. Gutlé, W. Stahl, M. Schwell, I. Kleiner and H. V. L. Nguyen, *The Journal of Chemical Physics*, 2020, **152**, 134306.

- 54. W. Jäger and H. Mäder, Zeitschrift für Naturforschung A, 1987, 42, 1405-1409.
- 55. W. Jäger and H. Mäder, Journal of Molecular Structure, 1988, 190, 295-305.
- 56. E. R. L. Fliege, Zeitschrift für Naturforschung A, 1990, 45, 911-922.
- 57. E. Fliege, H. Dreizler, M. Meyer, K. Iqbal and J. Sheridan, *Zeitschrift für Naturforschung A*, 1986, **41**, 623-636.
- 58. E. Gougoula, C. Medcraft, J. Heitkämper and N. R. Walker, *The Journal of Chemical Physics*, 2019, **151**, 144301.
- 59. E. Antonelli, E. Gougoula, N. R. Walker, M. Schwell, H. V. L. Nguyen and I. Kleiner, *The Journal of Chemical Physics*, 2024, **160**, 214309.
- 60. H. W. Nicolaisen, J. U. Grabow, N. Heineking and W. Stahl, *Zeitschrift für Naturforschung A*, 1991, **46**, 635-638.
- 61. H. V. Nguyen, W. Caminati and J.-U. Grabow, *Molecules*, 2022, 27.
- 62. E. Fliege, H. Dreizler, J. Sheridan and C. T. Walls, *Journal of Molecular Spectroscopy*, 1985, **113**, 362-372.
- 63. W. Jäger, H. Dreizler, H. Mäder, J. Sheridan and C. T. Walls, *Zeitschrift für Naturforschung A*, 1987, **42**, 501-506.
- 64. L. H. Spangler, Annual Review of Physical Chemistry, 1997, 48, 481-510.
- 65. K. Wang, X. He, C. Rong, A. Zhong, S. Liu and D. Zhao, *Theoretical Chemistry Accounts*, 2022, **141**, 68.
- 66. H. Dreizler, H. D. Rudolph and H. Mäder, *Zeitschrift für Naturforschung A*, 1970, **25**, 25-35.
- 67. S. Wörmke, K. Brendel, U. Andresen and H. Mäder, *Molecular Physics*, 2004, **102**, 1625-1639.
- 68. H. D. Rudolph, H. Dreizler and H. Seiler, *Zeitschrift für Naturforschung A*, 1967, **22**, 1738-1743.
- 69. W. Caminanti, G. Cazzoli and D. Trojano, *Chemical Physics Letters*, 1976, 43, 65-68.
- 70. W. Caminati, G. Cazzoli and A. M. Mirri, *Chemical Physics Letters*, 1975, **31**, 104-107.
- 71. H. D. Rudolph, H. Dreizler, A. Jaeschke and P. Wendung, *Zeitschrift für Naturforschung A*, 1967, **22**, 940-944.
- 72. W. A. Kreiner, H. D. Rudolph and B. T. Tan, *Journal of Molecular Spectroscopy*, 1973, **48**, 86-99.
- 73. V. Amir-Ebrahimi, A. Choplin, J. Demaison and G. Roussy, *Journal of Molecular Spectroscopy*, 1981, **89**, 42-52.
- 74. R. M. Gurusinghe and M. J. Tubergen, *The Journal of Physical Chemistry A*, 2016, **120**, 3491-3496.
- 75. S. Jacobsen, U. Andresen and H. Mäder, Structural Chemistry, 2003, 14, 217-225.
- 76. H. D. Rudolph and A. Trinkaus, *Zeitschrift für Naturforschung A*, 1968, **23**, 68-76.
- 77. K. P. R. Nair, S. Herbers, H. V. L. Nguyen and J.-U. Grabow, *Spectrochimica Acta Part A: Molecular and Biomolecular Spectroscopy*, 2020, **242**, 118709.
- 78. J. Rottstegge, H. Hartwig and H. Dreizler, *Journal of Molecular Structure*, 1999, **478**, 37-47.
- 79. D. Gerhard, A. Hellweg, I. Merke, W. Stahl, M. Baudelet, D. Petitprez and G. Wlodarczak, *Journal of Molecular Spectroscopy*, 2003, **220**, 234-241.
- 80. S. Herbers, P. Buschmann, J. Wang, K. G. Lengsfeld, K. P. R. Nair and J.-U. Grabow, *Physical Chemistry Chemical Physics*, 2020, **22**, 11490-11497.
- 81. K. P. R. Nair, S. Herbers, A. Lesarri and J.-U. Grabow, *Journal of Molecular Spectroscopy*, 2019, **361**, 1-7.
- 82. S. Khemissi, M. Schwell, I. Kleiner and H. V. L. Nguyen, *Molecular Physics*, 2022, **120**, e2052372.
- 83. V. Van, T. Nguyen, W. Stahl, H. V. L. Nguyen and I. Kleiner, *Journal of Molecular Structure*, 2020, **1207**, 127787.

- 84. V. Van, W. Stahl and H. V. L. Nguyen, *Physical Chemistry Chemical Physics*, 2015, **17**, 32111-32114.
- 85. V. Van, J. Bruckhuisen, W. Stahl, V. Ilyushin and H. V. L. Nguyen, *Journal of Molecular Spectroscopy*, 2018, **343**, 121-125.
- 86. T. Nguyen, W. Stahl, H. V. L. Nguyen and I. Kleiner, *The Journal of Chemical Physics*, 2021, **154**, 204304.
- 87. S. Khemissi, V. Van, M. Schwell, I. Kleiner and H. V. L. Nguyen, *The Journal of Physical Chemistry A*, 2023, **127**, 5779-5789.
- 88. S. Huber, J. Makarewicz and A. Bauder, *Molecular Physics*, 1998, **95**, 1021-1043.
- 89. J. Rottstegge, H. Hartwig and H. Dreizler, *Journal of Molecular Spectroscopy*, 1999, **195**, 1-10.
- 90. T. M. Korter and D. W. Pratt, *The Journal of Physical Chemistry B*, 2001, **105**, 4010-4017.
- 91. W. Cheng, Y. Zheng, G. Feng, J.-U. Grabow and Q. Gou, *Spectrochimica Acta Part A: Molecular and Biomolecular Spectroscopy*, 2020, **239**, 118434.
- 92. J. Lei, J. Zhang, G. Feng, J.-U. Grabow and Q. Gou, *Physical Chemistry Chemical Physics*, 2019, **21**, 22888-22894.
- 93. W. Caminati, J. C. López, S. Blanco, S. Mata and J. L. Alonso, *Physical Chemistry Chemical Physics*, 2010, **12**, 10230-10234.
- 94. L. B. Favero, L. Evangelisti, A. Maris, A. Vega-Toribio, A. Lesarri and W. Caminati, *The Journal of Physical Chemistry A*, 2011, **115**, 9493-9497.
- 95. L. B. Favero and W. Caminati, *The Journal of Physical Chemistry A*, 2009, **113**, 14308-14311.
- 96. L. B. Favero, B. M. Giuliano, S. Melandri, A. Maris and W. Caminati, *Chemistry A European Journal*, 2007, **13**, 5833-5837.
- 97. P. Pinacho, J. C. López, Z. Kisiel and S. Blanco, *The Journal of Chemical Physics*, 2024, **160**, 164315.
- 98. B. Ouyang and B. J. Howard, *Physical Chemistry Chemical Physics*, 2009, **11**, 366-373.
- 99. C. Cabezas, M. Juanes, R. T. Saragi, A. Lesarri and I. Peña, *Spectrochimica Acta Part A: Molecular and Biomolecular Spectroscopy*, 2022, **270**, 120846.
- 100. W. Caminati, D. Damiani, G. Corbelli, B. Velino and C. W. Bock, *Molecular Physics*, 1991, **74**, 885-895.
- 101. B. Maté, R. D. Suenram and C. Lugez, *The Journal of Chemical Physics*, 2000, **113**, 192-199.
- 102. J. Wang, S. Herbers, P. Buschmann, K. Lengsfeld, J.-U. Grabow, G. Feng and Q. Gou, *Chinese Journal of Chemical Physics*, 2020, **33**, 119-124.
- 103. H. V. L. Nguyen, *Journal of Molecular Structure*, 2020, **1208**, 127909.
- 104. I. Hedgecock, N. W. Larsen, L. Nygaard, T. Pedersen and G. O. Sørensen, *Journal of Molecular Structure*, 1990, **223**, 33-44.
- 105. K.-M. Marstokk and H. Møllendal, Acta Chemica Scandinavica, 1994, 48, 25-31.
- 106. M. Juanes, A. Lesarri, R. Pinacho, E. Charro, J. E. Rubio, L. Enríquez and M. Jaraíz, *Chemistry A European Journal*, 2018, **24**, 6564-6571.
- 107. K.-M. Marstokk and H. Møllendal, Acta Chemica Scandinavica, 1994, 48, 298-305.
- 108. M. Juanes, R. T. Saragi, R. Pinacho, J. E. Rubio and A. Lesarri, *Physical Chemistry Chemical Physics*, 2020, **22**, 12412-12421.
- 109. S. Melandri, A. Maris, P. G. Favero and W. Caminati, *ChemPhysChem*, 2001, **2**, 172-177.
- 110. K. A. Utzat, R. K. Bohn, J. A. Montgomery, Jr., H. H. Michels and W. Caminati, *The Journal of Physical Chemistry A*, 2010, **114**, 6913-6916.
- 111. R. T. Saragi, M. Juanes, W. Caminati, A. Lesarri, L. Enríquez and M. Jaraíz, *The Journal of Physical Chemistry A*, 2019, **123**, 8435-8440.

- 112. K. X. Shook, L. M. McDivitt, C. D. Shiery, J. R. Bailey, T. J. McMahon, R. A. Grimminger and R. G. Bird, *Journal of Molecular Spectroscopy*, 2024, **400**, 111874.
- 113. P. D. Godfrey, R. N. Jorissen and R. D. Brown, *The Journal of Physical Chemistry A*, 1999, **103**, 7621-7626.
- 114. R. D. Brown and P. D. Godfrey, *The Journal of Physical Chemistry A*, 2000, **104**, 5742-5746.
- 115. R. Tama Saragi, W. Li, M. Juanes, L. Enríquez, R. Pinacho, J. E. Rubio and A. Lesarri, *ChemPhysChem*, 2024, **25**, e202300799.
- 116. P. D. Godfrey, L. D. Hatherley and R. D. Brown, *Journal of the American Chemical Society*, 1995, **117**, 8204-8210.
- 117. J. C. López, V. Cortijo, S. Blanco and J. L. Alonso, *Physical Chemistry Chemical Physics*, 2007, **9**, 4521-4527.
- 118. J. A. Beukes, K. M. Marstokk and H. Møllendal, *Journal of Molecular Structure*, 2001, **567-568**, 19-27.
- 119. M. Onda, A. Toda, S. Mori and I. Yamaguchi, *Journal of Molecular Structure*, 1986, **144**, 47-51.
- 120. L. Ferres, W. Stahl and H. V. L. Nguyen, *Molecular Physics*, 2016, 114, 2788-2793.
- 121. S. L. Stephens and N. R. Walker, *Journal of Molecular Spectroscopy*, 2010, **263**, 27-33.
- 122. D. P. Zaleski, S. L. Stephens and N. R. Walker, *Physical Chemistry Chemical Physics*, 2014, **16**, 25221-25228.
- 123. G. A. Cooper, C. Medcraft, J. D. Littlefair, T. J. Penfold and N. R. Walker, *The Journal of Chemical Physics*, 2017, **147**, 214303.
- 124. E. Gougoula, C. N. Cummings, C. Medcraft, J. Heitkämper and N. R. Walker, *Physical Chemistry Chemical Physics*, 2022, **24**, 12354-12362.

# Chapter 2. Theory.

#### 2.1 Introduction

Spectroscopy is most simply described as the study of the absorption and emission of electromagnetic radiation by matter. Across the electromagnetic spectrum, light has different wavelengths which correspond to different frequencies and ultimately photons of radiation that have different energies. The energy of a photon is given by the following expression:

$$E = hv = \frac{hc}{\lambda} \tag{Eq 2.1}$$

where h is Planck's constant, v is the frequency of light, c is the speed of light in a vacuum and  $\lambda$  is the wavelength of light. When a molecule absorbs or emits light of a given energy, a transition between two discrete energy levels which match the energy of the photon occurs. The energy of a transition is given by:

$$E_1 - E_2 = \Delta E = hv \tag{Eq 2.2}$$

Rotational spectroscopy is concerned with rotational transitions of molecules or weakly-bound complexes within the gas phase, which occur when the electromagnetic radiation is of the frequency 1 - 300 GHz. When a molecule absorbs and subsequently emits a photon within this frequency range, a change in the rotational state of the molecule occurs, induced by a transition between two discrete rotational energy levels which match the energy of the photon. Within this thesis, microwave spectroscopic experiments have been performed, utilising radiation over the frequency range 2.0 – 18.5 GHz to probe changes in the rotational states of molecules and complexes to acquire their microwave spectrum. From the spectrum obtained, rotational constants and other spectroscopic constants can be determined from fitting of experimentally observed rotational transitions to a Hamiltonian. Information regarding the molecular geometry of the species under investigation can be derived from the rotational constants, owing to the inverse relationship with the moments of inertia, including atomic coordinates, bond lengths, bond angles and dihedral angles. In addition to determination of molecular structure, rotational spectroscopy has also been used to investigate changes in the electronic environment if a quadrupolar nucleus is present. This technique can also be used to determine the energetic barrier hindering an internal rotation, when an internal rotor such as CH<sub>3</sub> is present. When applied to the study of weakly-bound complexes, rotational spectroscopy can be used to establish the binding preferences of molecules and provide an insight into intermolecular interactions such as hydrogen bonding and van der Waals interactions. For this reason, rotational spectroscopy has been used extensively to study the structure, internal dynamics and non-covalent interactions of molecular species in the gas phase.

The aim of this chapter is to demonstrate and discuss the aspects of the fundamental theoretical basis of rotational spectroscopy which have been applied to the molecules and complexes studied within this thesis. The following texts have been used during the preparation of this chapter: Microwave Molecular Spectra<sup>1</sup> by Gordy and Cook, Modern Spectroscopy<sup>2</sup> by Hollas and Microwave Spectroscopy<sup>3</sup> by Townes and Schawlow.

# 2.2 Born-Oppenheimer approximation

The Born-Oppenheimer approximation is based upon the assumption that electronic and nuclear motions can be treated independently since each type of motion occurs on a different timescale. Under this approximation, nuclei are considered as fixed while electrons move around them, allowing the Schrödinger equation to be solved for electrons alone. This is assumed since nuclei are considerably heavier than electrons and therefore move relatively slowly in comparison. The total Hamiltonian for a molecular system is expressed as:

$$\widehat{H}_{total} = \widehat{H}_{el} + \widehat{H}_{vib} + \widehat{H}_{rot} + \widehat{H}_{trans}$$
 (Eq 2.3)

where  $\hat{H}_{el}$  is the electronic Hamiltonian,  $\hat{H}_{vib}$  is the vibrational Hamiltonian,  $\hat{H}_{rot}$  is the rotational Hamiltonian and  $\hat{H}_{trans}$  is the translational Hamiltonian.

The total energy is given by the following equation:

$$E_{total} = E_{el} + E_{vib} + E_{rot} + E_{trans}$$
 (Eq 2.4)

The total wavefunction is given by:

$$\psi_{total} = \psi_{el}\psi_n = \psi_{el}\psi_{vib}\psi_{rot}\psi_{trans}$$
 (Eq 2.5)

where  $\psi_{el}$  is the electronic wavefunction and  $\psi_n$  is the nuclear wavefunction. The nuclear wavefunction can be expressed as  $\psi_n = \psi_{vib}\psi_{rot}$ 

#### 2.3 Moments of inertia

In classical mechanics, the angular momentum (P) of a rigid rotating molecule can be calculated by the following equation:

$$P = I \times \omega \tag{Eq 2.6}$$

where I is the moment of inertia tensor and  $\omega$  is the angular velocity.

The moment of inertia about one of the principal axes is given by the following equation:

$$I = \sum_{i} m_i r_i^2 \tag{Eq 2.7}$$

where  $m_i$  and  $r_i$  are the mass and distance of an atom from a particular axis. The moment of inertia can be expressed as a matrix in the principal axis system:

$$I = \begin{pmatrix} I_{aa} & I_{ab} & I_{ac} \\ I_{ba} & I_{bb} & I_{bc} \\ I_{ca} & I_{cb} & I_{cc} \end{pmatrix}$$
(Eq 2.8)

The principal axes are denoted a, b and c and are mutually perpendicular to each other. The origin of the principal axes is located at the centre of mass. The location of the origin at the centre of mass results in the off-diagonal terms within the moment of inertia tensor being equal to zero such that they vanish, leaving only the diagonal terms.

$$I = \begin{pmatrix} I_{aa} & 0 & 0\\ 0 & I_{bb} & 0\\ 0 & 0 & I_{cc} \end{pmatrix}$$
 (Eq 2.9)

The diagonal terms are known as the principal moments of inertia,  $I_{aa}$ ,  $I_{bb}$  and  $I_{cc}$ , which are the moments of inertia about each of the a, b and c principal axes respectively. The principal moments of inertia can be expressed as:

$$I_{aa} = \sum_{i} m_i (b_i^2 + c_i^2)$$
 (Eq 2.10)

$$I_{bb} = \sum_{i} m_i (a_i^2 + c_i^2)$$
 (Eq 2.11)

$$I_{cc} = \sum_{i} m_i (a_i^2 + b_i^2)$$
 (Eq 2.12)

By convention, the moment of inertia about the c- inertial axis ( $I_{cc}$ ) is the largest since the mass distribution is the greatest about this axis, whereas the moment of inertia about the a- inertial axis ( $I_{aa}$ ) is the smallest. Such that:

$$I_{cc} \ge I_{bb} \ge I_{aa}$$
 (Eq 2.13)

# 2.4 Types of molecules

Molecules can be classified as either a linear top, symmetric top or asymmetric top depending on their shape and moments of inertia. Each of the molecules and hydrate complexes presented in Chapters 4-7 are asymmetric tops.

# 2.4.1 Linear tops

Diatomic and polyatomic molecules can be categorised as linear tops when all atoms within the molecule are located along the a-inertial axis such that the moment of inertia about the a- axis is approximately equal to zero. The following relationship holds between the moments of inertia about the a-, b- and c- axes of linear top molecules:

$$I_{cc} = I_{bb} > I_{aa} \cong 0 \tag{Eq 2.14}$$

The rigid rotor approximation can be used to describe the end over end rotation of diatomic and polyatomic molecules. The model assumes that nuclei are point masses joined by a bond which is a rigid, weightless rod such that the nuclei are at a fixed distance. The Hamiltonian of a diatomic or polyatomic linear molecule under the rigid rotor approximation is given by:

$$\widehat{H}_{rot} = \frac{\widehat{P}^2}{2I} \tag{Eq 2.15}$$

The total angular momentum,  $\hat{P}^2$ , is quantised and must have values equal to,  $\frac{h^2}{4\pi^2}J(J+1)$ . The allowed rotational energy levels of a rigid rotor  $(E_r)$  are given by the following equation:

$$E_r = \frac{h^2}{8\pi^2 I} J(J+1)$$
 (Eq 2.16)

where h is Planck's constant, J is the rotational quantum number and I is the moment of inertia,  $I = \mu r^2$  ( $\mu$  is the reduced mass, given by  $\mu = \frac{m_1 m_2}{m_1 + m_2}$ ). For a linear polyatomic molecule, I is given by the mass of the atom multiplied by the square of the distance between the atom and a particular axis (Equation 2.7).

Dividing the expression above by Planck's constant allows  $E_r$  to be expressed in units of frequency, which is more appropriate for microwave spectroscopy, which gives:

$$E(J) = \frac{E_r}{h} = \frac{h}{8\pi^2 I}J(J+1)$$
 (Eq 2.17)

Since  $B = \frac{h}{8\pi^2 I}$  the expression can be re-written as:

$$E(J) = BJ(J+1)$$
 (Eq 2.18)

where B is the rotational constant.

The transition between two energy levels can be calculated by substituting the appropriate values of J into the equation above and the difference between energy levels is found to be a multiple of two (2B, 4B, 6B...). Under the rigid rotor approximation, the spacing between two adjacent transitions is equal to 2B. However, in reality a small decrease in the transition spacing is observed with increasing values of J, which is due to the centrifugal force that the nuclei experience as they rotate. Therefore, additional terms are usually included known as the centrifugal distortion constants to account for this, which will be discussed in more detail later.

#### 2.4.2 Symmetric tops

For a molecule to be classified as a symmetric top it must possess a n-fold axis of symmetry,  $C_n$ , where n > 2. One of the principal axes of inertia will lie along the symmetry axis. Symmetric top molecules have two moments of inertia which are equal and a third which is unique and non-zero. These molecules can be classified as either "prolate" or "oblate".

For prolate symmetric tops:

$$I_{cc} = I_{hh} > I_{gg}$$
 (Eq 2.19)

For oblate symmetric tops:

$$I_{cc} > I_{bb} = I_{aa} \tag{Eq 2.20}$$

The terms "prolate" and "oblate" refer to the shape of the molecule along its symmetry axis. Prolate symmetric tops are elongated whereas oblate symmetric tops have a flattened shape. The a- inertial axis lies along the symmetry plane in a prolate symmetric top. Methyl iodide and trifluoromethyl iodide are examples of molecules which are prolate symmetric tops each possessing a  $C_3$  axis of symmetry. Whereas, in oblate symmetric tops the c- inertial axis lies along the symmetry plane. Benzene is an oblate symmetric top and has a  $C_6$  axis of symmetry.

The Hamiltonian for a non-linear molecule under the rigid rotor approximation is given by:

$$\widehat{H}_{rot} = \frac{1}{2} \left( \frac{\widehat{P}_a^2}{I_{aa}} + \frac{\widehat{P}_b^2}{I_{bb}} + \frac{\widehat{P}_c^2}{I_{cc}} \right)$$
 (Eq 2.21)

or

$$\widehat{H}_{rot} = A\widehat{P}_a^2 + B\widehat{P}_b^2 + C\widehat{P}_c^2 \tag{Eq 2.22}$$

The total angular momentum is given by:

$$\hat{P}^2 = \hat{P}_a^2 + \hat{P}_b^2 + \hat{P}_c^2 \tag{Eq 2.23}$$

The Hamiltonian of a prolate symmetric top can therefore be expressed as:

$$\widehat{H}_{rot} = \frac{\widehat{P}^2}{2I_{bb}} + \frac{1}{2} \left( \frac{1}{I_{aa}} - \frac{1}{I_{bb}} \right) \widehat{P}_a^2$$
 (Eq 2.24)

Since  $I_{bb} = I_{cc}$  for a prolate symmetric top and the total angular momentum equation can be re-arranged to  $\hat{P}^2 - \hat{P}_a^2 = \hat{P}_b^2 + \hat{P}_c^2$ .

Similarly, for an oblate symmetric top, the Hamiltonian can be expressed as:

$$\widehat{H}_{rot} = \frac{\widehat{P}^2}{2I_{hh}} + \frac{1}{2} \left( \frac{1}{I_{cc}} - \frac{1}{I_{hh}} \right) \widehat{P}_c^2$$
 (Eq 2.25)

Since  $I_{aa} = I_{bb}$  for an oblate symmetric top and the total angular momentum equation can be re-arranged to  $\hat{P}^2 - \hat{P}_c^2 = \hat{P}_a^2 + \hat{P}_b^2$ .

The energy levels of prolate and oblate symmetric tops are quantised and are given in the equations below. In each case the energy expression has been divided by Planck's constant such that the energy level equation is expressed in units of frequency:

Prolate symmetric top:

$$E_{rot} = \frac{h^2}{8\pi^2 I_{hh}} J(J+1) + \left(\frac{h^2}{8\pi^2 I_{aa}} - \frac{h^2}{8\pi^2 I_{hh}}\right) K^2$$
 (Eq 2.26)

$$E(J,K) = \frac{E_{rot}}{h} = BJ(J+1) + (A-B)K^2$$
 (Eq 2.27)

Oblate symmetric top:

$$E_{rot} = \frac{h^2}{8\pi^2 I_{bb}} J(J+1) + \left(\frac{h^2}{8\pi^2 I_{cc}} - \frac{h^2}{8\pi^2 I_{bb}}\right) K^2$$
 (Eq 2.28)

$$E(J,K) = \frac{E_{rot}}{h} = BJ(J+1) + (C-B)K^2$$
 (Eq 2.29)

The energy level expression for a symmetric top requires the inclusion of two quantum numbers. In addition to the rotational quantum number, J, also known as the total angular momentum quantum number, a second quantum number, K, is included. K represents a portion of the total angular momentum that lies along the unique axis. For prolate and oblate symmetric top molecules the angular momentum along the unique axis is,  $\hat{P}_a^2$  and  $\hat{P}_c^2$ , respectively, which can be expressed in terms of K,  $\hat{P}_a^2$  or  $\hat{P}_c^2 = \frac{h^2}{4\pi^2}K^2$ , resulting in the above equations. For a given value of J, the second quantum number K can take a number of values however each is always less than or equal to J. The K levels for a given value of J are doubly degenerate owing to the  $K^2$  term in the energy level expressions. With the exception being the K=0 levels. Since the above expressions of the energy levels are derived from the rigid rotor Hamiltonian, again, this fails to account for centrifugal force experienced by molecules upon rotation.

# 2.4.3 Asymmetric tops

The vast majority of molecules possess some degree of asymmetry and are therefore classified as asymmetric tops. The rotational constants and moments of inertia about each principal axis are unique in asymmetric top molecules, such that:

$$A > B > C \tag{Eq 2.30}$$

and

$$I_{aa} \neq I_{bb} \neq I_{cc} \tag{Eq 2.31}$$

Asymmetric tops can usually either be categorised as "near-prolate" or "near-oblate". The moment of inertia about the a- inertial axis is much lower than about the b- and c- axes in a near prolate asymmetric top. Whereas in a near oblate asymmetric top the moment of inertia about the c-inertial axis is much greater than that about the a- and b- axes.

For a near-prolate asymmetric top:

$$I_{cc} \approx I_{hh} > I_{gg}$$
 (Eq 2.32)

For a near-oblate asymmetric top:

$$I_{cc} > I_{bb} \approx I_{aa}$$
 (Eq 2.33)

Each of the molecules and hydrate complexes presented within this thesis are near-prolate asymmetric tops. Examples of near-oblate asymmetric tops include imidazole and pyrazine.

A quantitative measure of molecules asymmetry is given by Ray's asymmetry parameter,  $\kappa$ :

$$\kappa = \frac{2B - A - C}{A - C} \tag{Eq 2.34}$$

Where A, B and C are rotational constants (see equation 2.37 below) with respect to the a, b and c axes. The limiting values of  $\kappa$  are -1 and +1 which correspond to the prolate (B = C) and oblate (A = B) symmetric tops respectively. A molecule that yields a value of  $\kappa$  between the two limits is considered asymmetric, with the greatest degree of asymmetry being observed when  $\kappa = 0$ . When the value of  $\kappa$  approaches the prolate limit, these molecules are classified as near-prolate asymmetric tops. Whereas near-oblate asymmetric tops have a value of  $\kappa$  which approaches the oblate limit. For example,  $\kappa$  is determined to be -0.90 and -0.89 for N-ethylimidazole and 2-ethylimidazole (Chapter 7) respectively, each of these molecules are therefore classified as near-prolate asymmetric tops.

The rigid rotor Hamiltonian for a non-linear molecule is given by:

$$\hat{H}_{rot} = \frac{1}{2} \left( \frac{\hat{P}_a^2}{I_{aa}} + \frac{\hat{P}_b^2}{I_{bb}} + \frac{\hat{P}_c^2}{I_{cc}} \right)$$
 (Eq 2.35)

or

$$\widehat{H}_{rot} = A\widehat{P}_a^2 + B\widehat{P}_b^2 + C\widehat{P}_c^2$$
 (Eq 2.36)

where  $\hat{P}_a$ ,  $\hat{P}_b$  and  $\hat{P}_c$  are the components of angular momentum of rotation along the a, b and c axes respectively and A, B and C are rotational constants which have an inverse relationship with the moments of inertia,  $I_{aa}$ ,  $I_{bb}$  and  $I_{cc}$ . Rotational constants are defined as:

$$A = \frac{h}{8\pi^2 I_{aa}}, B = \frac{h}{8\pi^2 I_{bb}}, C = \frac{h}{8\pi^2 I_{cc}}$$
 (Eq 2.37)

The Hamiltonian for an asymmetric top molecule can be expressed in terms of Ray's asymmetry parameter,  $\kappa$ , which is given in the following equation:

$$\widehat{H}_{rot} = \frac{1}{2}(A+C)\widehat{P}^2 + \frac{1}{2}(A-C)\widehat{H}_{\kappa}$$
 (Eq 2.38)

where:

$$\hat{P}^2 = \hat{P}_a^2 + \hat{P}_b^2 + \hat{P}_c^2 \tag{Eq 2.39}$$

The reduced Hamiltonian is given by:

$$\widehat{H}_{\kappa} = \widehat{P}_a^2 + \kappa \widehat{P}_b^2 - \widehat{P}_c^2 \tag{Eq 2.40}$$

For a near-prolate asymmetric top, the energy level equation is:

$$E(J,K) \cong B_{har}J(J+1) + (A - B_{har})K^2$$
 (Eq 2.41)

Likewise, for a near-oblate asymmetric top, the energy level equation is:

$$E(J,K) \cong B_{har}J(J+1) + (C - B_{har})K^2$$
 (Eq 2.42)

where  $B_{bar} = \frac{1}{2}(B+C)$  for a near prolate asymmetric top and  $B_{bar} = \frac{1}{2}(A+B)$  for a near oblate asymmetric top.

## 2.5 Rotational transitions and selection rules

In order for a transition to occur between two discrete rotational energy levels, several selection rules must be obeyed. Firstly, the molecule under study must possess a dipole moment for a transition to be observed using rotational spectroscopy. This means that the electric dipole moment component along at least one of the molecules principal inertial axes must be non-zero  $(\mu \neq 0)$ . Transitions (absorption or emission) between two rotational energy levels are allowed if the following changes in J are obeyed:

$$\Delta J = 0, \pm 1 \tag{Eq 2.43}$$

The change in the rotational state of a molecule upon the emission of a photon is given by the following expression:

$$\Delta J = J'(upper state, higher energy)$$
 (Eq 2.44)  
-  $J''(lower state, lower energy)$ 

where J is the rotational quantum number, single prime "'" denotes the upper state of the transition whereas double prime "'" denotes the lower state of the transition.

Each of the allowed changes in J correspond to a different branch of the rotational spectrum. When  $\Delta J = +1$  the transitions are referred to as R-branch transitions,  $\Delta J = 0$  are Q-branch transitions and finally  $\Delta J = -1$  are P-branch transitions. The vast majority of transitions observed within the 2.0 - 18.5 GHz frequency region for the molecular species discussed within this thesis are R-branch transitions.

The following notation will be used to represent an emission transition between two rotational states for an asymmetric top molecule:

$$J'_{K'_{-1}K'_{+1}} \to J''_{K''_{-1}K''_{+1}}$$
 (Eq 2.45)

 $K_{-1}$  and  $K_{+1}$  are labels in the notation which link the energy levels of asymmetric tops to a K value in the prolate limit in the case of the former and to a K value in the oblate limit in the latter (see Figure 2.1). For symmetric top molecules, K is a quantum number which represent the portion of the total angular momentum that lies along the symmetry (unique) axis. Since the energy level expression (Equation 2.27 and 2.29) for a symmetric top molecules contains a  $K^2$  term each K level is doubly degenerate, except when K = 0. Asymmetric top molecules possess

no axis of symmetry, therefore, K is no longer a good quantum number and K levels are no longer degenerate.

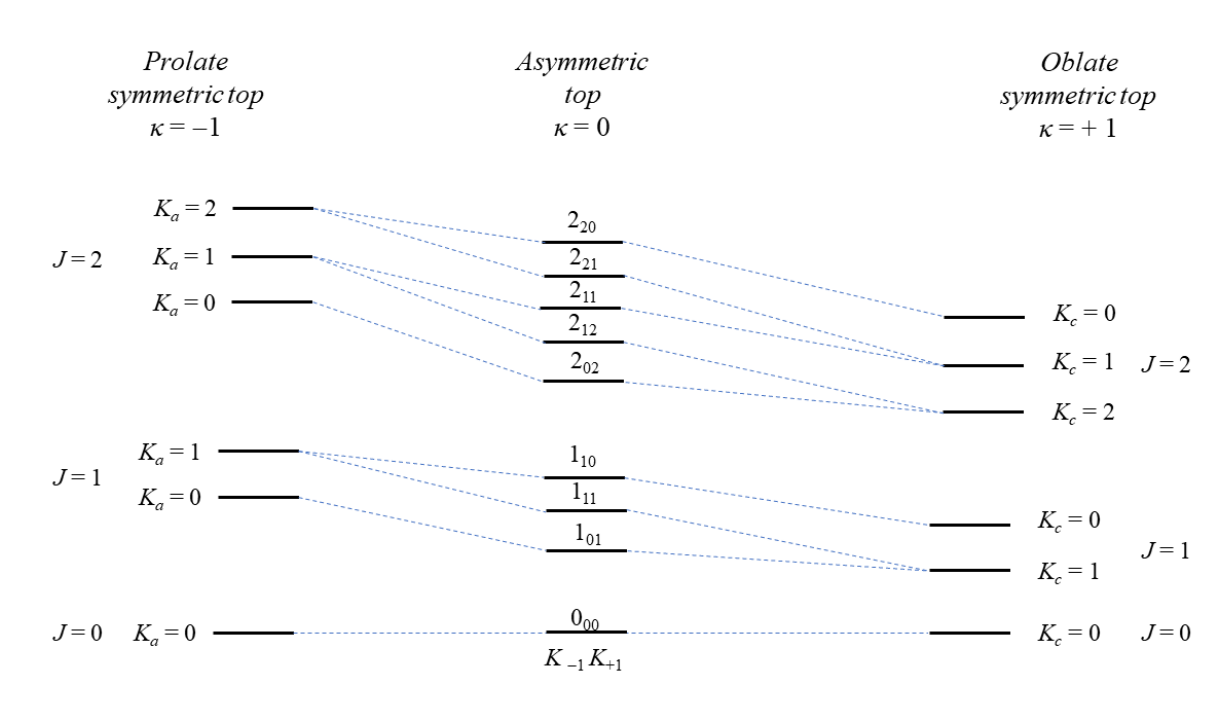


Figure 2.1 Correlation diagram relating the energy levels of an asymmetric top molecule to those of the limiting prolate and oblate symmetric top.

The type of transitions observed within the spectrum is governed by the dipole moment along each of the a, b and c axis, non-zero dipole moments along each axis yield a-, b- and c- type transitions respectively. For example, a- type transitions represent a rotation about the a-axis. Each type of transition is distinct in the allowed change in parity of the  $K_{-1}$  and  $K_{+1}$  labels. a-type transitions have a change in the parity of the  $K_{+1}$  label only, c-type transitions have a change in the parity of both  $K_{-1}$  and  $K_{+1}$  labels.

A summary of the types of rotational transitions and the governing selection rules is provided in Table 2.1 below. Cooke and Ohring provide a more comprehensive account of selection rules and spectral patterns of each type of transition of asymmetric top molecules.<sup>4</sup>

Table 2.1 Summary of selection rules for asymmetric top molecules.

Dipole moment	Type of transition	$\Delta J$	$\Delta K_{-1}$	$\Delta K_{+1}$
component				
$\mu_a \neq 0$	a-type	$0,\pm 1$	$0, \pm 2$	<u>±</u> 1, <u>±</u> 3
$\mu_b \neq 0$	<i>b</i> -type	$0,\pm 1$	$\pm 1, \pm 3 \dots$	$\pm 1, \pm 3 \dots$
$\mu_c \neq 0$	<i>c</i> -type	$0, \pm 1$	<u>±</u> 1, <u>±</u> 3	$0, \pm 2 \dots$

# 2.6 Centrifugal distortion and the Reduced Hamiltonian

Each equation of the Hamiltonian and energy levels presented so far within this Chapter is under the rigid rotor approximation, which assumes the nuclear framework of a molecule is rigid. This approximation neglects effects from centrifugal forces acting upon the molecule as it rotates which results in the distortion of bond lengths and angles. Under the rigid rotor approximation, the spacings between rotational transitions is constant, however, in reality shifts are observed as a result of the distortion experienced by molecules rotating. Additional terms known as centrifugal distortion constants are included in the Hamiltonian to account for this. The effect of the centrifugal distortion becomes greater as the molecular structure becomes more complex, such that the inclusion of centrifugal distortion terms is of greater importance in asymmetric top molecules compared to symmetric top or linear molecules. In the case of symmetric top molecules, small shifts in the rotational frequencies of a transition are observed as a result of centrifugal distortion. Considerably larger shifts are observed in the case of asymmetric tops, owing to the presence of more transitions between states of higher J values (larger angular momentum) which therefore have a larger rotational energy. For transitions between states of lower J values, only slight deviations from the rigid rotor approximation are observed since effects of centrifugal distortion are small.

The Hamiltonian of a semi-rigid rotor is given by:

$$\widehat{H} = \widehat{H}_{rot} + \widehat{H}_{dis} \tag{Eq 2.46}$$

where  $\widehat{H}_{rot}$  is the rotational Hamiltonian for a rigid rotor and  $\widehat{H}_{dis}$  accounts for centrifugal distortion effects.

Likewise, the energy of a semi-rigid asymmetric rotor is expressed as:

$$E = E_r + E_{dis} \tag{Eq 2.47}$$

where  $E_r$  is the energy of a rigid rotor and  $E_{dis}$  includes terms which account for centrifugal distortion.

For a semi-rigid diatomic molecule:

$$E(I) = BI(I+1) - DI^{2}(I+1)^{2}...$$
 (Eq 2.48)

where D is the quartic centrifugal distortion constant.

The expression of the energy levels of a semi-rigid prolate symmetric top accounting for centrifugal distortion effects is:

$$E(J,K) = BJ(J+1) + (A-B)K^2 - D_J J^2 (J+1)^2 -$$
 (Eq 2.49)  
$$D_{JK}J(J+1)K^2 - D_K K^4 \dots$$

Replacing the term (A - B) with (C - B) gives the energy level equation for a semi-rigid oblate symmetric top. For symmetric top molecules, three quartic centrifugal distortion constants are included in the energy expression:  $D_J$ ,  $D_{JK}$  and  $D_K$ .

For an asymmetric rotor:

$$E_{dis} = -\Delta_J J^2 (J+1)^2 - \Delta_{JK} J (J+1) \langle P_z^2 \rangle - \Delta_K \langle P_z^4 \rangle -$$
 (Eq 2.50)  
$$\delta_1 E_r J (J+1) - \delta_2 \langle P_z^2 \rangle \dots$$

Five quartic centrifugal distortion constants are required in the energy expression for an asymmetric top molecule,  $\Delta_J$ ,  $\Delta_{JK}$ ,  $\Delta_K$ ,  $\delta_1$  and  $\delta_2$ , to describe the rotational energy levels.

In each of these equations (2.48, 2.49 and 2.50), higher order distortion constants such as sextic (H), sectic (L) and octic (M) have been omitted. These higher order distortion constants are often required to be included in the Hamiltonian for fitting of the rotational spectrum when higher J transitions are observed. For the molecular species presented in this thesis, the inclusion of quartic distortion constants only, proved sufficient to achieve a satisfactory fit.

The reduced Hamiltonian is commonly used to assign the rotational spectrum of asymmetric top molecules since it reduces the number of centrifugal distortion constants required to characterise the system and removes any parameters which are determined poorly. Watson<sup>5, 6</sup> introduced an asymmetric (A) reduction and a symmetric (S) reduction, commonly referred to as Watson's A-reduced Hamiltonian and Watson's S-reduced Hamiltonian respectively. The choice of reduction used in the assignment is dependent on the degree of asymmetry of the molecule. For molecules approaching either the prolate or oblate limit, the S-reduction is more appropriate, whereas, for molecules which have higher degrees of asymmetry (do not have  $\kappa$  approaching the limits) the A-reduction is more appropriate.

Watson's A-reduced Hamiltonian:

$$H^{A} = \frac{1}{2} (B^{A} + C^{A}) P^{2} + \left[ A^{A} - \frac{1}{2} (B^{A} + C^{A}) \right] P_{Z}^{2} + \frac{1}{2} (B^{A} - (\text{Eq } 2.51))$$

$$C^{A}) (P_{X}^{2} - P_{Y}^{2}) - \Delta_{J} P^{4} - \Delta_{JK} P^{2} P_{Z}^{2} - \Delta_{K} P_{Z}^{4} - 2\delta_{J} P^{2} (P_{X}^{2} - P_{Y}^{2}) - \delta_{K} [P_{Z}^{2} (P_{X}^{2} - P_{Y}^{2}) + P_{Z}^{2} (P_{X}^{2} - P_{Y}^{2})] ...$$

$$(\text{Eq } 2.51)$$

Watson's S-reduced Hamiltonian:

$$H^{S} = \frac{1}{2} (B^{S} + C^{S}) P^{2} + \left[ A^{S} - \frac{1}{2} (B^{S} + C^{S}) \right] P_{Z}^{2} + \frac{1}{4} (B^{S} - (\text{Eq } 2.52))$$

$$C^{S} (P_{+}^{2} - P_{-}^{2}) - D_{J} P^{4} - D_{JK} P^{2} J_{Z}^{2} - D_{K} P_{Z}^{4} - 2d_{1} P^{2} (P_{+}^{2} - P_{-}^{2}) - d_{2} (P_{+}^{4} - P_{-}^{4}) \dots$$
(Eq 2.52)

# 2.7 Hyperfine structure and nuclear quadrupole coupling

Nuclear spin is the total angular momentum of an atomic nucleus and is a fundamental property which arises from the composition of protons and neutrons within the nucleus of an atom. The nuclear spin is expressed as the nuclear spin quantum number, which is denoted as I. Nuclei which possess an even number of protons and neutrons have a nuclear spin quantum number of 0. Whereas nuclei which have an odd number of either protons or neutrons possess a nuclear spin and  $I = \frac{1}{2}$ . A spherical and symmetric nuclear charge distribution is observed in nuclei with a nuclear spin quantum number of 0 or  $\frac{1}{2}$  and molecular species comprising only these types of nuclei, such as 2-ethylfuran in Chapter 5, have rotational transitions that do not exhibit a hyperfine structure. When a nucleus has an odd number of protons and neutrons, it also has a nuclear spin and  $I > \frac{1}{2}$ . These types of nuclei are known as quadrupolar nuclei and have a nonspherical distribution of nuclear charge. Molecular species which contain one or more quadrupolar nuclei, such as the thiazole and imidazole derivatives presented in Chapters 4, 6 and 7, have rotational transitions which exhibit hyperfine structure. It is possible for isotopes of the same elements to have different nuclear spins due to the differing numbers of neutrons, for example  $^{14}N$  is a quadrupolar nucleus (I = 1) whereas  $^{15}N$  is not a quadrupolar nucleus,  $I = \frac{1}{2}$ , therefore, <sup>15</sup>N-containing species do not exhibit hyperfine structure unlike <sup>14</sup>N containing species.

The non-spherical distribution of nuclear charge results in a nuclear electric quadrupole moment at the nucleus. The quadrupole moment gives rise to an electric field gradient (EFG) at the nucleus due to the non-spherical distribution of electric charge. Coupling between the quadrupole moment and EFG results in the splitting of rotational transitions (hyperfine structure). The hyperfine structure of a transition is dependent on the number of quadrupolar nuclei present within the molecular species, the nuclear spin quantum numbers of each nucleus and the J quantum number.

In order to model hyperfine structure of a semi-rigid molecule an additional term is required to be added to the Hamiltonian:

$$\widehat{H} = \widehat{H}_{rot} + \widehat{H}_{dis} + \widehat{H}_0$$
 (Eq 2.53)

where:

$$\widehat{H}_Q = -\frac{1}{6}Q(X): \nabla E(X)...$$
 (Eq 2.54)

This term models the interaction between the nuclear electric quadrupole moment of the nucleus, X, Q(X), and the EFG,  $\nabla E(X)$ . If a molecular species contains multiple quadrupolar nuclei, such as imidazole (two <sup>14</sup>N nuclei) additional terms are included in  $\hat{H}_Q$ .

The total angular momentum of a molecular species containing one or more quadrupolar nuclei is denoted F which is the sum of the nuclear spin (I) and the molecular angular rotational momentum (J). The total angular momentum quantum number (F) is therefore given by:

$$F = I + J \tag{Eq 2.55}$$

which can take values of:

$$F = I + J, I + J - 1, I + J - 2, ..., |J - I|$$
 (Eq 2.56)

Additional selection rules are required in order for a hyperfine rotational transition to be allowed:

$$\Delta J = 0, \pm 1, \qquad \Delta F = 0, \pm 1, \qquad \Delta I = 0$$
 (Eq 2.57)

Such that a rotational transition occurs between two energy levels of different J and F quantum numbers without changing the nuclear spin of the molecular species.

Modelling of hyperfine structure within a rotational spectrum results in the determination of nuclear quadrupole coupling constants, alongside other spectroscopic parameters, during the assignment process. Nuclear quadrupole coupling constants  $\chi_{aa}(X)$ ,  $\chi_{bb}(X)$  and  $\chi_{cc}(X)$  can be directly determined from the hyperfine structure of rotational transitions and describe the coupling between the nuclear spin of a quadrupolar nucleus (X) with the overall rotation of the molecule along each of the a, b and c inertial axes respectively. These nuclear quadrupole coupling constants are the diagonal terms of the following matrix:

$$\chi = \begin{pmatrix} \chi_{aa} & \chi_{ba} & \chi_{ca} \\ \chi_{ab} & \chi_{bb} & \chi_{cb} \\ \chi_{ac} & \chi_{bc} & \chi_{cc} \end{pmatrix}$$
(Eq 2.58)

During assignments of a rotational spectrum the nuclear quadrupole coupling constants  $\chi_{aa}(X)$  and  $[\chi_{bb}(X) - \chi_{cc}(X)]$  are commonly determined rather than each of  $\chi_{aa}(X)$ ,  $\chi_{bb}(X)$  and  $\chi_{cc}(X)$  individually. However, the individual diagonal nuclear quadrupole coupling constants

can be determined from the experimental values of  $\chi_{aa}(X)$  and  $[\chi_{bb}(X) - \chi_{cc}(X)]$  using Laplace's equation below:

$$\chi_{aa} + \chi_{bb} + \chi_{cc} = 0$$
 (Eq 2.59)

Both on- and off-diagonal terms of the nuclear quadrupole tensor are required for a complete understanding of the EFG about a quadrupolar nucleus. However, as mentioned earlier, usually only on diagonal terms are determined during spectral analysis. Off-diagonal elements in the matrix such as  $\chi_{ab}$  are typically not included nor determined during the assignment of microwave spectra in cases where the nuclei present have small nuclear quadrupole coupling (such as <sup>14</sup>N, I = 1) since the magnitudes of these constants are often smaller than the on-diagonal terms, therefore, are typically poorly determined.

Nuclear quadrupole coupling constants are sensitive to changes in the electronic environment about the quadrupolar nucleus, therefore, it is often useful to compare values of nuclear quadrupole coupling constants of different molecular species to understand any changes in the electronic environment which may occur. Since the nuclear quadrupole coupling constants determined during the analysis are in the principal inertial axis system, which is unique to each molecular species, they must be transformed into a common frame of reference to facilitate the comparison.  $\chi_{aa}$ ,  $\chi_{bb}$  and  $\chi_{cc}$  are transformed from the principal inertial axis system into the principal nuclear axis system by means of rotation of the principal inertial axes by an angle,  $\theta$ , into the principal nuclear axes (x, y and z) resulting in the generation of the diagonal terms  $\chi_{xx}$ ,  $\chi_{yy}$  and  $\chi_{zz}$ . The diagonalisation results in the off-diagonal terms becoming zero:

$$\chi = \begin{pmatrix} \chi_{xx} & 0 & 0 \\ 0 & \chi_{yy} & 0 \\ 0 & 0 & \chi_{zz} \end{pmatrix}$$
 (Eq 2.60)

This transformation is performed using Kisiel's QDIAG program available on the PROSPE website.<sup>7</sup> In addition to the three on-diagonal terms, one off-diagonal term such as  $\chi_{ab}$  is required for the transformation. As mentioned earlier, off-diagonal terms are typically not determined during the assignment for nitrogen containing species, therefore, the values of  $\chi_{ab}$  included in the analysis were the results of quantum chemical calculations.

## 2.8 Internal rotation

Internal rotation is a phenomenon where one part of a molecule rotates with respect to the rest of the molecule and is an example of a large amplitude motion. The group which rotates is commonly referred to as the internal rotor, which is bound by a single bond to the rest of the molecule which it rotates against, which is known as the frame. The rotation of the internal rotor with respect to the rest of the molecule is described by the angle  $\alpha$ , which is known as the torsional angle or angle of internal rotation. It is known that in many cases that this internal rotation is not free and is hindered by a potential energy barrier. The potential energy function for a barrier with N-fold symmetry is given by the Fourier series:

$$V(\alpha) = \frac{1}{2}V_N(1 - \cos N\alpha) + \frac{1}{2}V_{2N}(1 - \cos 2N\alpha) + \dots$$
 (Eq 2.61)

The most commonly studied internal rotors have  $C_{3V}$  symmetry. Examples of such internal rotors include methyl (CH<sub>3</sub>) and trifluoromethyl (CF<sub>3</sub>) groups. When a methyl group is present within a molecule its internal rotation is hindered by a three-fold potential barrier, since N is therefore equal to 3, equation 2.61 now becomes:

$$V(\alpha) = \frac{1}{2}V_3(1 - \cos 3\alpha) + \frac{1}{2}V_6(1 - \cos 6\alpha) + \dots$$
 (Eq 2.62)

Generally, higher terms in the expansion (when N > 3) have magnitudes which are significantly smaller than  $V_3$  therefore the expression is often simplified and only the first term is retained:

$$V(\alpha) = \frac{1}{2}V_3(1 - \cos 3\alpha)$$
 (Eq 2.63)

Where  $V_3$  is the height of the potential energy barrier and is commonly expressed in units of cm<sup>-1</sup>. A schematic representation of a three-fold potential barrier hindering methyl internal rotation is given in Figure 2.2. As mentioned earlier the rotation of a methyl group is usually not free, therefore, the value of  $V_3$  can vary quite significantly typically taking values between 0 and 1000 cm<sup>-1</sup>. A  $V_3$  barrier of 0 cm<sup>-1</sup> represents a case where the internal rotor rotates freely and low barriers to internal rotation are generally considered to be when  $V_3$  is lower than 200 cm<sup>-1</sup>. Barriers to internal rotation are considered high when  $V_3$  is greater than about 600 cm<sup>-1</sup> with intermediate cases having  $V_3$  between about 200 and 600 cm<sup>-1</sup>. The presence of a single internal rotor which has a three-fold potential barrier leads to the splitting of rotational energy levels into two torsional sublevels, denoted A ( $\sigma = 0$ ) and E ( $\sigma = \pm 1$ ) (Figure 2.2), which

consequently results in the splitting of rotational transitions into A- and E- species transitions due to quantum chemical tunnelling through the barrier. The observed frequency interval of the splitting between the A and E species transitions directly correlates with the magnitude of the potential energy barrier, such that the frequency interval between A and E is large when the hindering potential barrier is low whereas the observed splitting is small when the barrier is high.

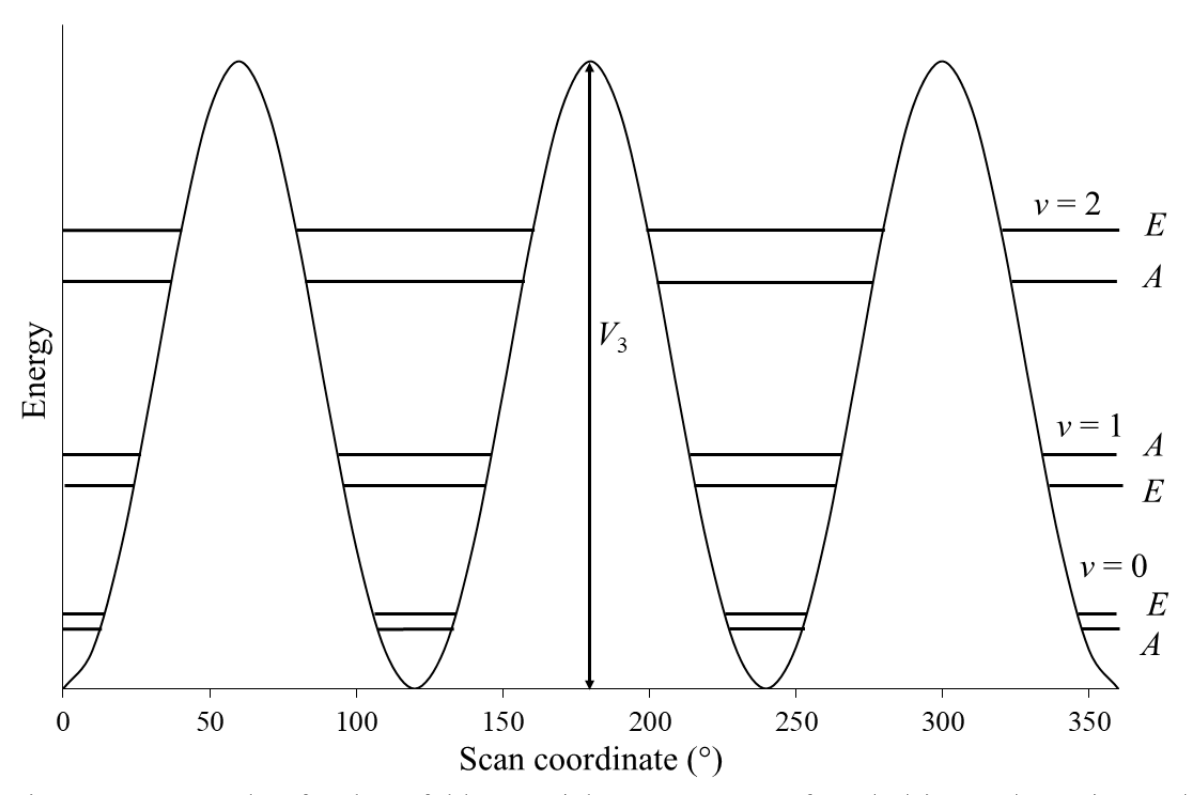


Figure 2.2 Example of a three-fold potential energy curve of methyl internal rotation and torsional sublevels.  $V_3$  is the height of potential energy barrier to internal rotation. "A" and "E" denote the two torsional sublevels.

The equation for the torsional energy levels in a molecular species which has a three-fold hindering potential barrier is:

$$-F\frac{d^2U(\alpha)}{d\alpha^2} + \left[\frac{V_3}{2}(1-\cos 3\alpha) - E\right]U(\alpha) = 0$$
 (Eq 2.64)

where:

 $V_3$  is the barrier height, F is the reduced rotational constant which is inversely proportional to the reduced moment of inertia,  $I_r$ ,  $F = \frac{h}{8\pi^2 I_r}$ , E is the total energy of the system and  $U(\alpha)$  is the periodic wavefunction for the internal rotation. Typically,  $F_0$  is in the range 157 – 162 GHz for a methyl top bound to a rigid frame owing to the value of  $I_r \approx 3.2 \ u \ \text{Å}^2$ .

Specialist fitting programs are often required for the total assignment of systems which include internal rotation problems, since additional terms are required to be included in the Hamiltonian, which will be described in more detail below.

Several different methods and programs can be used for the treatment of systems which include an internal rotor, which have been summarised in various review articles. 8-10 The different methods and programs differ in the axis system used for the Hamiltonian and the method ("local" or "global") used for the treatment of torsional ( $v_t$ ) states. Axis systems commonly used include the Principal Axis System (PAM) and the Rho Axis System (RAM). The "local" method treats each  $v_t$  state separately without accounting for interactions between the different torsional states. This approach separates the  $v_t$  states into groups by symmetry species and treats each with its own Hamiltonian. Whereas "global" methods use only one Hamiltonian to deal with the total set of  $v_t$  states associated with a given large amplitude motion. The programs XIAM<sup>11</sup> and BELGI-C<sub>8</sub>-hyperfine<sup>12, 13</sup> have been used within this thesis for the treatment of internal rotation in Chapter 4.

XIAM was developed by Hartwig and co-workers. This program uses a combined axis method (CAM)<sup>8, 14, 15</sup> historically known as the Internal Axis Method (IAM) and uses a "local" approach for the treatment of internal rotation. Fits performed using XIAM use a Hamiltonian constructed in the principal axis system such that the axis system employed depends on the coordinate system of the molecule of interest. However, the internal rotation operator within the Hamiltonian (for each internal rotor) is transformed into an individual rho axis system, in order to eliminate Coriolis coupling terms, which occur between the internal rotation and the overall rotational angular momenta. After diagonalisation, the resulting eigenvalues are transformed (rotated) back to the principal axis system. XIAM can be used to study molecular species which include up to three internal rotors and one quadrupolar nucleus and has commonly been employed for the study of methyl internal rotation. This program allows a global fit of *A*- and *E*- species transitions to be performed, however, problems can be encountered during the treatment of molecular systems with a low hindering barrier height, such as 2-methylthiazole, <sup>16</sup> owing to the "local" approach employed by the program and the limited number of higher order terms.

The Hamiltonian for an asymmetric rigid rotor molecule in the principal axis system is:

$$H = H_r + H_T \tag{Eq 2.65}$$

where  $H_r$  is the rigid rotor Hamiltonian and  $H_T$  is the torsional Hamiltonian. This can also be expressed as:

$$H = AP_a^2 + BP_b^2 + CP_c^2 + F(p_\alpha - \rho_a P_a - \rho_b P_b - \rho_c P_c)^2 + V(\alpha)$$
 (Eq 2.66)

where A, B and C are the rotational constants (given by Equation 2.37), F is the reduced rotational constant of the internal rotor  $F = \frac{\hbar^2}{2rI_\alpha}$ , with  $r = 1 - \sum_g \lambda_g^2 \frac{I_\alpha}{I_g}$  where  $\lambda_g$  are the direction cosines of the internal rotation axis, i, of the top in the principal axis system ( $\lambda_g = \cos \angle(i,g)$ ) and  $I_g$  are the components of the moments of inertia of the whole molecule in the g = a, b or c principal axis system.  $p_\alpha$  is the internal rotation angular momentum associated with the torsional angle  $\alpha$ .  $P_g$  are components of the total angular momentum and  $\rho_g$  are components of the  $\rho$  vector principal moments of inertia  $I_g$ ,  $\rho_g = \frac{\lambda_g I_\alpha}{I_g}$ .

BELGI-C<sub>s</sub> was developed by Kleiner et al. 12 The program was later extended to BELGI-C<sub>s</sub>hyperfine<sup>13</sup> allowing the treatment of internal rotation in molecular systems which possess one internal rotor and a single quadrupolar nucleus. Unlike XIAM, each BELGI code employs a "global" approach and uses a Hamiltonian written only in the rho axis system, allowing an improvement in the computation time compared to methods which employ the principal axis system and for Coriolis coupling terms to be eliminated. The rho axis system is related to the principal axis system by a rotation about the angle  $\theta_{RAM}$ . The axis system is rotated such that the new z-axis is parallel to the  $\rho$  vector. The program uses a two-step diagonalisation procedure of the Hamiltonian. The torsional Hamiltonian term is diagonalised first. The resulting eigenfunctions from this diagonalisation procedure are then used to generate the basis set which is used for the diagonalisation of the other terms in the RAM Hamiltonian. The program allows the inclusion of higher order terms between internal and global rotation. Global fits performed using BELGI provide spectroscopic parameters which are in the rho axis system, therefore, cannot be directly compared with constants determined in the principal axis system (e.g. determined using XIAM). It is possible to transform rotational constants from the rho axis system into the principal axis system to facilitate direct comparison.

The Hamiltonian in the rho axis system  $(H_{RAM})$  is written as:

$$H_{RAM} = H_r + H_{CD} + H_T + H_{int}$$
 (Eq 2.67)

where  $H_r$  is the rotational Hamiltonian,  $H_{CD}$  is the centrifugal distortion Hamiltonian,  $H_T$  is the torsional Hamiltonian and  $H_{int}$  contains higher order terms of torsional-rotational interactions.

 $H_r$  and  $H_T$  are given by the following equations:

$$H_r = A(\cos\theta_{RAM}P_a - \sin\theta_{RAM}P_b)^2 + B(\sin\theta_{RAM}P_a - \cos\theta_{RAM}P_b)^2$$
 (Eq 2.68)  
+  $CP_C^2$ 

$$H_r = A_{RAM} P_a^2 + B_{RAM} P_b^2 + C_{RAM} P_c^2 + D_{ab} (P_a P_b + P_b P_a)$$
 (Eq 2.69)

$$H_T = F(p_a - \rho P_a)^2 + V(\alpha)$$
 (Eq 2.70)

where A, B and C are the rotational constants in the principal axis system and  $A_{RAM}$ ,  $B_{RAM}$  and  $C_{RAM}$  are the rotational constants in the rho axis system.  $D_{ab}$  is an out-of-plane parameter arising from the use of a non-principal system.

## 2.9 Quantum chemical calculations

Quantum chemical calculations have a wide variety of diverse applications in science ranging from accelerating drug discovery to predicting structure and molecular properties and use in molecular spectroscopy. Spectra recorded using CP-FTMW spectroscopy typically contains hundreds or thousands of spectral transitions owing to the broadband nature of the technique. The experimental spectrum recorded consists of the spectra of each species present within the supersonic expansion as they are probed concurrently. Often multiple species (the target molecule, fragmentation products, weakly-bound complexes with the carrier gas or other small molecules) are present within the spectrum and their spectral patterns are likely to overlap, making it difficult to distinguish and assign the transitions to a molecular species, particularly in the case of asymmetric top molecules. Quantum chemical calculations are a vital tool which can aid the assignment of transitions present within a microwave spectrum. Some chemical intuition is required to predict any molecular species, other than the target molecule, which may be present within the supersonic expansion, allowing calculations to be performed for each possible species. The calculations provide a prediction for spectroscopic parameters of the molecular species being searched for in its equilibrium geometry. Even though the results of the calculation are for the molecular species in its equilibrium geometry, whereas the experiment probes the species in its vibrational ground state, the spectroscopic constants generated from the calculations usually prove a good starting point for the spectral assignment. Spectroscopic parameters generated from the calculations include rotational constants, centrifugal distortion and nuclear quadrupole coupling constants (if appropriate) and the calculation output also gives the dipole moment components in which the types of transition (a-, b- or c-type) expected to be observed within the spectrum can be inferred. This information can be gained from a simple geometry optimisation calculation in which the total energy of the structure of the molecule or complex is minimised by varying the position of the atoms in small increments until a minimum is found. An additional key word, freq=vibrot, is added to the Gaussian input file to perform a frequency calculation in tandem with the geometry optimisation, providing predictions for the centrifugal distortion constants and to indicate if the optimised structure is an energy minimum or a saddle point.

Potential energy scans are performed for molecular species which include large amplitude motions and are conformationally flexible. For molecules which include internal rotors such as the methylthiazole···H<sub>2</sub>O complexes presented in Chapter 4, potential energy scans are performed to predict the magnitude of the barrier hindering the internal rotation of the methyl group. For conformationally flexible molecules, such as the ethyl-substituted heteroaromatic

rings presented in Chapters 5 - 7, potential energy scans are used to investigate the conformational landscape of these molecules and to gain an understanding of which conformations are of the lowest energy. Relaxed potential energy scans were performed for the molecular species presented within this thesis, varying the dihedral angle associated with either the rotation of the methyl group in the case of the former or the rotation of the ethyl group relative to the ring in the latter at a specific interval, while all other geometrical parameters were allowed to relax. Calculations were also performed in order to investigate the intermolecular interactions present within weakly-bound complexes, however, this will be discussed in more detail in Sections 2.12 and 2.13. Other methods and programs are available and are commonly used to complement microwave spectroscopy studies. For example, the CREST<sup>17</sup> (Conformer– Rotamer Ensemble Sampling Tool) software can be particularly useful while studying conformationally flexible molecules and weakly-bound complexes as it can be used to investigate the potential energy surface and identify low-energy structures. However, this program was not employed for the studies presented herein, owing to the heteroaromatic ring in each case being rigid and only the conformation of the ethyl group can vary, such that the potential energy surface can be explored using a relaxed potential energy scan. Similarly, the binding sites and preferences of heteroaromatic rings are well-established. Symmetry-Adapted Perturbation Theory (SAPT)<sup>18</sup> analysis is also often used during the study of noncovalently bound molecular species and can be performed using the PSI4 software.<sup>19</sup> This analysis breaks down the total interaction energy of a complex into its component energies, electrostatic, induction, dispersion and exchange, providing an insight into the component energies which stabilise the complex.

Density functional theory (DFT) and *ab initio* calculations have been performed using the Gaussian09 package.<sup>20</sup> The DFT hybrid functional<sup>21-23</sup> of Becke, Lee, Yang and Parr (B3LYP) is used in conjunction with Grimme's dispersion correction<sup>24</sup> (D3) and the Becke-Johnson damping function<sup>25, 26</sup> (BJ), D3BJ. The *ab initio* method second order Møller-Plesset perturbation theory<sup>27</sup> (MP2) was also used for calculations. The MP2 method accounts for dispersion interactions therefore a correction and damping function is not required in conjunction with this functional. These methods were combined with different Dunning's augmented correlation consistent basis sets<sup>28, 29</sup> (aug-cc-pVnZ where n=2 or 3) or Ahlrichs' valence polarised basis set<sup>30, 31</sup> (Def2-TZVP). The B3LYP functional and MP2 method with appropriate basis sets were chosen for calculations since they provide a good ratio between accuracy, providing rotational constants which are in very good agreement with experimentally determined constants, and computational time. Calculations were also performed using the

long-range corrected hybrid functional,  $^{32}$   $\omega$ B97X-D, with Dunning's quadrupole- $\zeta$  aug-cc-pVQZ basis set.

# 2.10 Spectral assignment and fitting

The rotational spectrum of molecules and complexes presented within this thesis have been assigned using Colin Western's PGOPHER<sup>33</sup> program. Assignments were performed using PGOPHER owing to its graphical interface which proves particularly useful for visualising the broadband microwave spectrum which is acquired using the CP-FTMW spectroscopy technique. A simulation of the rotational spectrum is initially produced using the results of quantum chemical calculations, which provide a prediction for the rotational constants and other spectroscopic constants. This is usually a good initial starting point for the assignment. The types of transitions which are expected to be present within the spectrum can also be inferred from the results of the calculations. Experimentally observed rotational transitions are assigned using either Watson's A- or S- reduced Hamiltonian implemented within PGOPHER allowing the determination of experimental spectroscopic parameters and the assignment of quantum numbers. However, for each of the molecules and complexes presented herein, Watson's S- reduced Hamiltonian<sup>5, 6</sup> was employed since this is more appropriate for asymmetric top molecules approaching either the prolate or oblate limit. From the assignment, rotational constants, centrifugal distortion constants and nuclear quadrupole coupling constants can be determined for the species under study. As discussed earlier, the rotational spectrum becomes more complicated in cases where molecules undergo large amplitude motions such as internal rotation. For molecules or complexes which have internal rotors, PGOPHER cannot be used for the complete assignment. The Hamiltonian implemented within the program does not include a part which can handle internal rotation, therefore, simultaneous fitting of A- and Especies transitions cannot be performed using PGOPHER. For this reason, specialist programs, XIAM<sup>11</sup> and BELGI-C<sub>s</sub>-hyperfine<sup>12</sup> were employed in Chapter 4 to perform global fits of the monohydrate complexes of methylthiazole. Each of XIAM and BELGI-C<sub>s</sub>-hyperfine are ideal for the study of species which have one or more internal rotors and also possess one quadrupolar nucleus since they allow the inclusion of internal rotation parameters vital for the assignment. XIAM is available on the PROSPE website<sup>7</sup> whereas BELGI-C<sub>s</sub>-hyperfine fits were kindly performed by Isabelle Kleiner (Université de Paris and Université Paris Est Creteil) who developed the program. Neither XIAM nor BELGI have a graphical interface, therefore, PGOPHER was used in tandem with XIAM when performing global fits to aid the assignment. A- species only (effective) fits were performed using PGOPHER prior to the global fits being performed.

## 2.11 Structure determination methods

Microwave spectroscopy is one of the most precise techniques for determining molecular structure. Structural information can be derived from the moments of inertia which can be obtained from the experimentally determined rotational constants (A, B and C) due to the inverse relationship discussed earlier. A simple first insight into the structure can be gained from the calculation of planar (second) moments and the inertial defect which provides information regarding the mass distribution and degree of planarity of a molecular species. In order to gain a sufficient amount of data to evaluate the molecular structure of a given molecule or complex through the determination of structural parameters, it is necessary to assign the spectra of several isotopologues. Due to the high sensitivity of this technique this is often achieved in natural abundance. However, particularly during the study of weakly-bound complexes formed with water molecules, experiments are performed using isotopically enriched samples in order to achieve one or multiple substitutions at the water sub-unit. When an atom is replaced for an isotopic variant, its position can be precisely determined. Kraitchman's equations can be used to determine the substitution coordinates of the atoms where isotopic substitution is achieved without making any assumptions regarding the molecular structure of the species under study. The assignment of both singly and multiply substituted molecular species allow the ground state effective geometry to be derived. However, when sufficient numbers of isotopologues are unable to be studied assumptions about the molecular structure are therefore required. The structure methods mentioned above will be discussed in detail in the following sub-sections.

# 2.11.1 Planar (second) moments and inertial defect

Planar moments,  $P_{aa}$ ,  $P_{bb}$  and  $P_{cc}$ , also known as second moments provide a simple first insight into molecular structure.<sup>34</sup> Each planar moment is a measure of the mass distribution along a given axis. For example,  $P_{cc}$  is a measure of the extension of mass along the c- inertial axis and can be also thought of as a measure of the mass located outside the ab plane. The planar moments are derived from the structural information contained in rotational constants and moments of inertia. A conversion factor of  $h/8\pi^2$  is required when converting rotational constants (in MHz) to moments of inertia (in u Å<sup>2</sup>) before they can be used in the following equations to determine planar moments:

$$P_{aa} = \sum_{i} m_i a_i^2 = (I_{bb} + I_{cc} - I_{aa})/2$$
 (Eq 2.71)

$$P_{bb} = \sum_{i} m_i b_i^2 = (I_{aa} + I_{cc} - I_{bb})/2$$
 (Eq 2.72)

$$P_{cc} = \sum_{i} m_i c_i^2 = (I_{aa} + I_{bb} - I_{cc})/2$$
 (Eq 2.73)

Generally, for a near prolate asymmetric top it follows that A > B > C, therefore,  $P_{aa} > P_{bb} > P_{cc}$ . Planar moments can also be useful for determining if a molecule has a plane of symmetry. The value of  $P_{cc}$  will be used in Chapters 5-7 to identify if each molecule or complex possesses either  $C_s$  or  $C_1$  symmetry. It has been shown that molecules which belong to the  $C_s$  point group, that have two symmetry operations (the identity operation and one mirror plane) each have similar values of  $P_{cc}$ . For example, the  $C_s$  forms of ethyl formate and ethyl cyanoformate have  $P_{cc}$  values of 3.26 and 3.18 u Å<sup>2</sup> respectively. 35-37

The inertial defect,  $\Delta$ , is a measure of planarity. If a species is planar and at equilibrium, the inertial defect is expected to be zero, whereas, for a non-planar molecule the inertial defect is non-zero. The calculation of the difference in the principal moments of inertia gives the inertial defect, by the following expression:

$$\Delta = I_{cc} - I_{bb} - I_{aa} = -2P_{cc}$$
 (Eq 2.74)

The inertial defect can also be derived directly from  $P_{cc}$ . As mentioned above for a planar molecule or complex the inertial defect is expected to be zero when it is calculated from equilibrium rotational constants, however, deviations from zero are usually observed due to species experiencing zero-point vibrations. In-plane vibrations contribute positively to the inertial defect whereas out-of-plane vibrations contribute negatively, therefore, it is often observed that planar molecules have small positive values of the inertial defect. It will be shown that hydrate complexes generally have negative values of the inertial defect owing to out-of-plane vibrations from the water sub-unit.

## 2.11.2 Substitution (r<sub>s</sub>) geometry

The position of an atom within a given molecule can be determined from the changes in the moment of inertia which occur upon isotopic substitution of a single atom. This allows the coordinates of the atom which has undergone isotopic substitution to be determined with respect to the principal axes of the original molecule, relative to the centre of mass. This approach was

introduced by Kraitchman<sup>38</sup> and the following equations are implemented within the program KRA, available on the PROSPE website,<sup>7</sup> allowing the calculation of substitution  $(r_s)$  coordinates of a non-planar asymmetric top:

$$|a| = \left[\frac{\Delta P_a}{\mu} \left(1 + \frac{\Delta P_b}{I_a - I_b}\right) \left(1 + \frac{\Delta P_c}{I_a - I_c}\right)\right]^{1/2}$$
 (Eq 2.75)

$$|b| = \left[\frac{\Delta P_b}{\mu} \left(1 + \frac{\Delta P_c}{I_b - I_c}\right) \left(1 + \frac{\Delta P_a}{I_b - I_a}\right)\right]^{1/2}$$
 (Eq 2.76)

$$|c| = \left[\frac{\Delta P_c}{\mu} \left(1 + \frac{\Delta P_a}{I_c - I_a}\right) \left(1 + \frac{\Delta P_b}{I_c - I_b}\right)\right]^{1/2}$$
 (Eq 2.77)

where:

 $\Delta P_a$ ,  $\Delta P_b$  and  $\Delta P_c$  are the changes in the planar moments of inertia along the a-, b- and c- axis respectively,  $\Delta P_a = \frac{1}{2} \left( -\Delta I_a + \Delta I_b + \Delta I_c \right)$ ,  $\Delta P_b = \frac{1}{2} \left( -\Delta I_b + \Delta I_c + \Delta I_a \right)$  and  $\Delta P_c = \frac{1}{2} \left( -\Delta I_c + \Delta I_a \right)$ ,  $\Delta I_a + \Delta I_b$ ,

 $\Delta I_a$ ,  $\Delta I_b$  and  $\Delta I_c$  are the difference in the moment of inertia between the isotopically substituted and parent molecule along the a-, b- and c- axis respectively,  $\Delta I_a = I'_a - I_a$ ,  $\Delta I_b = I'_b - I_b$  and  $\Delta I_c = I'_c - I_c$ 

 $I_a$ ,  $I_b$  and  $I_c$  are the moments of inertia of the parent species and  $I'_a$ ,  $I'_b$  and  $I'_c$  are the moments of inertia of the isotopically substituted species.  $\mu$  is the mass difference between the parent and isotopically substituted molecule.

The uncertainty in the  $r_s$  coordinates obtained is known as the Costain error. <sup>39,40</sup> The uncertainty  $(\delta_Z)$  is inversely proportional to the magnitude of the coordinate (|z|) and can be calculated as  $\delta_Z = 0.0015/|z|$ . The Kraitchman method assumes the molecular structure is unaltered upon isotopic substitution. This is a reasonable assumption for the vast majority of cases; however, this is not true in the case of H/D substitution. Upon substitution of hydrogen with deuterium an increase in the bond length occurs. <sup>41</sup> Therefore, for this reason, the coordinates of hydrogen atoms are not as well determined using the  $r_s$  method as those of other heavy atoms. Kraitchman's equations only calculate the relative magnitudes of the coordinates and do not consider the sign of the substitution coordinates. Generally, the signs of the  $r_s$  coordinates are assigned from the equilibrium  $(r_s)$  coordinates calculated from quantum chemical calculations.

The vibration-rotation effects are not accounted for in this approach. Therefore, it is possible that a negative value can be obtained, leading to the generation of an imaginary result. The method also does not perform well when an atom lies close to one of the inertial axes or the centre of mass often resulting in imaginary values. The substitution geometry of a molecule can be determined if a sufficient number of single isotopic substitutions are achieved, therefore, the  $r_s$  coordinates of multiple atoms can be determined. The EVAL program is used to derive parameters internal to the molecule from the  $r_s$  coordinates.

# 2.11.3 Effective ground state (r<sub>0</sub>) geometry

Throughout this thesis, the effective ground state  $(r_0)$  geometry has been determined to evaluate structural parameters of the weakly-bound complexes studied. The  $r_0$  method<sup>42</sup> is employed in Kisiel's STRFIT program by a least-squares fit of the structural parameters to the moments of inertia of all available isotopologues. STRFIT uses a system of internal coordinates (a z-matrix) whereby the position of every atom is defined with reference to position of other atoms within the molecule or complex. The "origin" within the coordinate system is the first atom listed within the z-matrix and beyond this, the internal coordinate system is defined by the user. Accurate  $r_0$  structural parameters are generated by fitting the parameters defined in the z-matrix to the moments of inertia of a wide variety of isotopologues. Both singly and multiply substituted isotopologues can be used in the determination of the ground state geometry, unlike the  $r_s$  geometry. For various reasons, the parameter map defined within STRFIT can be quite different from the configuration of chemical bonds within the molecule or complex. The  $r_0$ method does not consider changes in the geometry which may be induced by isotopic substitution or large amplitude motions. As mentioned earlier, assumptions regarding the molecular structure of the species under study are required when insufficient amounts of isotopologues are available. Owing to the chirped pulse technique employed to study the hydrate complexes presented in this thesis, isotopic substitution was typically only achieved at the water sub-unit. Isotopic substitution at the heteroaromatic sub-unit was unable to be achieved in natural abundance. Therefore, initial assumptions regarding the geometry of these hydrate complexes were required, and the z-matrix was constructed using the equilibrium geometry from quantum chemical calculations. Further information about the construction of the z-matrix, assumptions made for each species studied and fitted structural parameters will be provided in Chapters 4 - 7.

# 2.12 Non-Covalent Interactions (NCI) index

The non-covalent interaction (NCI) index is a method of visualising weak intramolecular and intermolecular interactions developed in 2010 by Yang's group.<sup>43</sup> This method identifies and evaluates non-covalent interactions based on the electron density and its derivatives and only requires information regarding the molecular geometry for the analysis. The non-covalent interactions identified from the analysis are presented as 3D real space surfaces (isosurfaces) within the molecular geometry and as a plot of the reduced electron gradient against the sign of the second eigenvalue of the Hessian matrix ( $\lambda_2$ ) of the electron density ( $\rho$ ), sign( $\lambda_2$ ) $\rho$ . The reduced electron density (s) is given by the following equation:

$$s = \frac{1}{2(3\pi^2)^{1/3}} \frac{|\nabla \rho|}{\rho^{4/3}}$$
 (Eq 2.78)

Plots are generated using the program Multiwfn<sup>44</sup> and isosurfaces are visualised using the software VMD.<sup>45</sup> On the NCI plot produced by the analysis, troughs, the points on the scatter plot where s (or RDG (reduced density gradient) on the plots presented herein) exponentially decays to 0 indicate the presence of non-covalent interactions. RDG is plotted against  $sign(\lambda_2)\rho$  as this can be used to differentiate between different types of interactions e.g bonding or non-bonding interactions. When  $\lambda_2 < 0$ , this indicates that the interaction is bonding whereas if  $\lambda_2 > 0$  the interaction is non-bonding. Hydrogen bonding interactions will appear as a trough with negative values of  $sign(\lambda_2)\rho$  and a blue isosurface within the molecular geometry. Van der Waals and weak hydrogen bonding interactions have values of  $sign(\lambda_2)\rho$  which are negative and close to zero and are indicated by light green isosurfaces within the molecular geometry. An example NCI analysis performed for the 2-methylimidazole···H<sub>2</sub>O complex is presented in Figure 2.3.

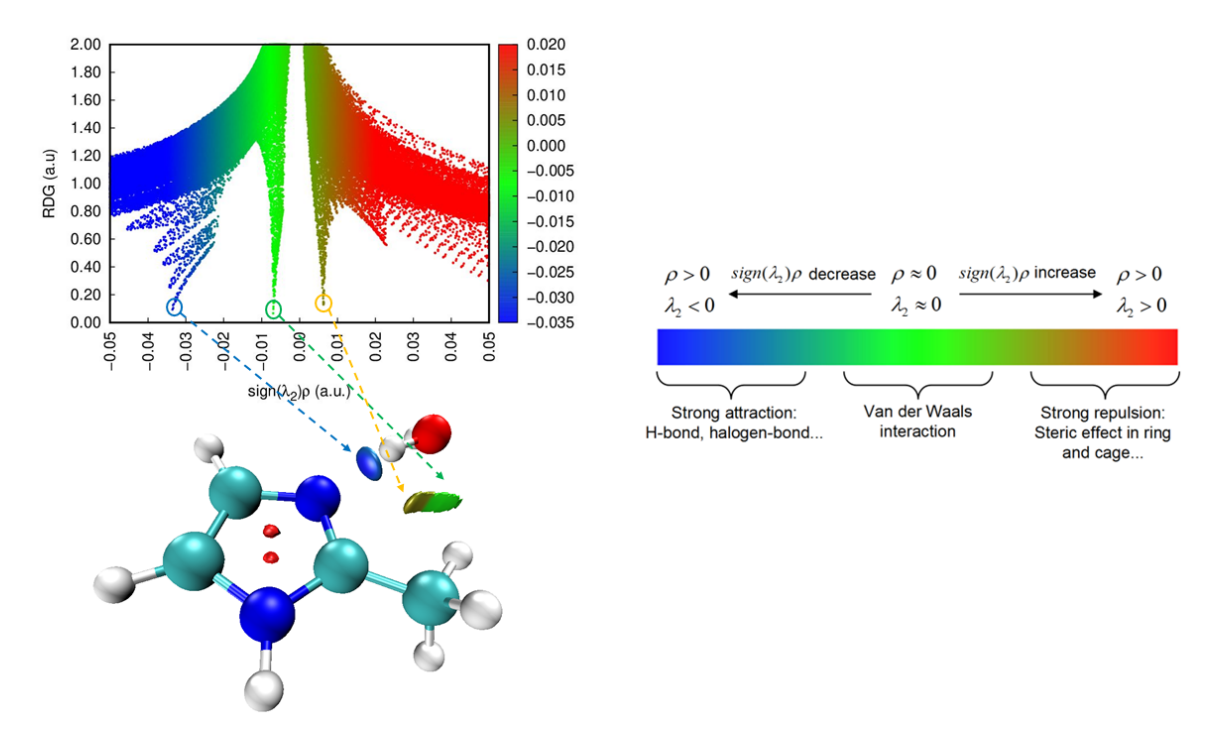


Figure 2.3 NCI isosurfaces and plot of RDG (a.u.) vs  $sign(\lambda_2)\rho$  for 2-methylimidazole···H<sub>2</sub>O. Positive and negative values of  $sign(\lambda_2)\rho$  respectively denote repulsive (red) and attractive (blue) interactions. Correlation between troughs observed on NCI plot and isosurfaces are indicated. The isosurface s value is 0.5 au.

# 2.13 Natural Bond Orbital (NBO) analysis

Natural bond orbital (NBO) analyses have been performed for each hydrate complex studied within this thesis to visualise the orbitals involved in the intermolecular interactions observed and to allow the comparison of the relative strength of each interaction. This method was developed by Frank Weinhold. Calculations have been performed using NBO 3.1 which is integrated into the Gaussian09 package. An additional key word "pop=(full,nboread)" was added into the command line to obtain the results. For the calculations performed herein, the optimised structures for each hydrate complex calculated at the  $\omega$ B97X-D/aug-cc-pVQZ were used and the NBO analysis was performed at the B3LYP(D3BJ)/aug-cc-pVTZ level. From the analysis the second order stabilisation energies ( $E^{(2)}$ ) of each interaction are calculated which have energies above the threshold of 0.21 kJ mol<sup>-1</sup>.

# 2.14 References

- 1. W. Gordy and R. I. Cook, *Microwave Molecular Spectra*, John Wiley & Sons, New York, 3rd edn., 1984.
- 2. J. M. Hollas, *Modern Spectroscopy*, John Wiley & Sons, Chichester, 4th edn., 2004.
- 3. C. H. Townes and A. L. Schawlow, *Microwave Spectroscopy*, Dover Publications, New York, 2nd edn.
- 4. S. A. Cooke and P. Ohring, *Journal of Spectroscopy*, 2013, **2013**, 698392.
- 5. J. K. G. Watson, *The Journal of Chemical Physics*, 1967, **46**, 1935-1949.
- 6. J. K. G. Watson, *The Journal of Chemical Physics*, 1968, **48**, 4517-4524.
- 7. Z. Kisiel, PROSPE Programs for ROtational SPEctroscopy, <a href="http://info.ifpan.edu.pl/~kisiel/prospe.htm">http://info.ifpan.edu.pl/~kisiel/prospe.htm</a>, (accessed 21/06/2024, 2024).
- 8. I. Kleiner, Journal of Molecular Spectroscopy, 2010, **260**, 1-18.
- 9. I. Kleiner, ACS Earth and Space Chemistry, 2019, **3**, 1812-1842.
- 10. H. V. L. Nguyen and I. Kleiner, *Physical Sciences Reviews*, 2022, 7, 679-726.
- 11. H. Hartwig and H. Dreizler, *Zeitschrift für Naturforschung A*, 1996, **51**, 923-932.
- 12. J. T. Hougen, I. Kleiner and M. Godefroid, *Journal of Molecular Spectroscopy*, 1994, **163**, 559-586.
- 13. R. Kannengießer, W. Stahl, H. V. L. Nguyen and I. Kleiner, *The Journal of Physical Chemistry A*, 2016, **120**, 3992-3997.
- 14. R. C. Woods, *Journal of Molecular Spectroscopy*, 1966, **21**, 4-24.
- 15. R. C. Woods, Journal of Molecular Spectroscopy, 1967, 22, 49-59.
- 16. T. Nguyen, V. Van, C. Gutlé, W. Stahl, M. Schwell, I. Kleiner and H. V. L. Nguyen, *The Journal of Chemical Physics*, 2020, **152**, 134306.
- 17. P. Pracht, F. Bohle and S. Grimme, *Physical Chemistry Chemical Physics*, 2020, **22**, 7169-7192.
- 18. T. M. Parker, L. A. Burns, R. M. Parrish, A. G. Ryno and C. D. Sherrill, *The Journal of Chemical Physics*, 2014, **140**, 094106.
- 19. R. M. Parrish, L. A. Burns, D. G. A. Smith, A. C. Simmonett, A. E. DePrince, III, E. G. Hohenstein, U. Bozkaya, A. Y. Sokolov, R. Di Remigio, R. M. Richard, J. F. Gonthier, A. M. James, H. R. McAlexander, A. Kumar, M. Saitow, X. Wang, B. P. Pritchard, P. Verma, H. F. Schaefer, III, K. Patkowski, R. A. King, E. F. Valeev, F. A. Evangelista, J. M. Turney, T. D. Crawford and C. D. Sherrill, *Journal of Chemical Theory and Computation*, 2017, 13, 3185-3197.
- Gaussian 09 (Revision D.01), M. J. Frisch, G. W. Trucks, H. B. Schlegel, G. E. Scuseria, M. A. Robb, J. R. Cheeseman, G. Scalmani, V. Barone, B. Mennucci, G. A. Petersson, H. Nakatsuji, M. Caricato, X. Li, H. P. Hratchian, A. F. Izmaylov, J. Bloino, G. Zheng, J. L. Sonnenberg, M. Hada, M. Ehara, K. Toyota, R. Fukuda, J. Hasegawa, M. Ishida, T. Nakajima, Y. Honda, O. Kitao, H. Nakai, T. Vreven, J. Montgomery, J. A., J. E. Peralta, F. Ogliaro, M. Bearpark, J. J. Heyd, E. Brothers, K. N. Kudin, V. N. Staroverov, T. Keith, R. Kobayashi, J. Normand, K. Raghavachari, A. Rendell, J. C. Burant, S. S. Iyengar, J. Tomasi, M. Cossi, N. Rega, J. M. Millam, M. Klene, J. E. Knox, J. B. Cross, V. Bakken, C. Adamo, J. Jaramillo, R. Gomperts, R. E. Stratmann, O. Yazyev, A. J. Austin, R. Cammi, C. Pomelli, J. W. Ochterski, R. L. Martin, K. Morokuma, V. G. Zakrzewski, G. A. Voth, P. Salvador, J. J. Dannenberg, S. Dapprich, A. D. Daniels, O. Farkas, J. B. Foresman, J. V. Ortiz, J. Cioslowski and D. J. Fox, Gaussian, Inc., Wallingford, CT, 2013.
- 21. B. Miehlich, A. Savin, H. Stoll and H. Preuss, *Chemical Physics Letters*, 1989, **157**, 200-206.
- 22. S. H. Vosko, L. Wilk and M. Nusair, *Canadian Journal of Physics*, 1980, **58**, 1200-1211.

- 23. A. D. Becke, *The Journal of Chemical Physics*, 1993, **98**, 5648-5652.
- 24. S. Grimme and M. Steinmetz, *Physical Chemistry Chemical Physics*, 2013, **15**, 16031-16042.
- 25. S. Grimme, S. Ehrlich and L. Goerigk, *Journal of Computational Chemistry*, 2011, **32**, 1456-1465.
- 26. A. D. Becke and E. R. Johnson, *The Journal of Chemical Physics*, 2005, **123**, 154101.
- 27. C. Møller and M. S. Plesset, *Physical Review*, 1934, **46**, 618-622.
- 28. R. A. Kendall, T. H. Dunning and R. J. Harrison, *The Journal of Chemical Physics*, 1992, **96**, 6796-6806.
- 29. T. H. Dunning, *The Journal of Chemical Physics*, 1989, **90**, 1007-1023.
- 30. F. Weigend, *Physical Chemistry Chemical Physics*, 2006, **8**, 1057-1065.
- 31. F. Weigend and R. Ahlrichs, *Physical Chemistry Chemical Physics*, 2005, 7, 3297-3305.
- 32. J.-D. Chai and M. Head-Gordon, *Physical Chemistry Chemical Physics*, 2008, **10**, 6615-6620.
- 33. C. M. Western, *Journal of Quantitative Spectroscopy and Radiative Transfer*, 2017, **186**, 221-242.
- 34. R. K. Bohn, J. A. Montgomery, H. H. Michels and J. A. Fournier, *Journal of Molecular Spectroscopy*, 2016, **325**, 42-49.
- 35. J. M. Riveros and E. B. Wilson, Jr., *The Journal of Chemical Physics*, 1967, **46**, 4605-4612.
- 36. D. P. Zaleski, J. L. Neill, M. T. Muckle, N. A. Seifert, P. Brandon Carroll, S. L. Widicus Weaver and B. H. Pate, *Journal of Molecular Spectroscopy*, 2012, **280**, 68-76.
- 37. R. D. Suenram, N. S. True and R. K. Bohn, *Journal of Molecular Spectroscopy*, 1978, **69**, 435-444.
- 38. J. Kraitchman, American Journal of Physics, 1953, 21, 17-24.
- 39. C. C. Costain, *The Journal of Chemical Physics*, 1958, **29**, 864-874.
- 40. C. C. Costain, *Trans.Am. Crystallogr. Assoc*, 1966, **2**, 157-164.
- 41. A. R. Ubbelohde and K. J. Gallagher, *Acta Crystallogr.*, 1955, **8**, 71-83.
- 42. Z. Kisiel, Journal of Molecular Spectroscopy, 2003, 218, 58-67.
- 43. E. R. Johnson, S. Keinan, P. Mori-Sánchez, J. Contreras-García, A. J. Cohen and W. Yang, *Journal of the American Chemical Society*, 2010, **132**, 6498-6506.
- 44. T. Lu and F. Chen, *Journal of Computational Chemistry*, 2012, **33**, 580-592.
- 45. W. Humphrey, A. Dalke and K. Schulten, *Journal of Molecular Graphics*, 1996, **14**, 33-38.
- 46. A. E. Reed, L. A. Curtiss and F. Weinhold, *Chemical Reviews*, 1988, **88**, 899-926.

# Chapter 3. Experimental.

### 3.1 Introduction

The first reported use of microwave spectroscopy, using microwave radiation to irradiate a molecule of interest, was in 1934. Cleeton and Williams<sup>1</sup> studied the absorption spectrum of ammonia using microwave radiation generated from a custom-made magnetron oscillator over the 1 – 4 cm region. During World War 2, many powerful sources of microwave radiation were developed for use in radio detection and ranging (RADAR) technologies. The availability of powerful sources of microwave radiation such as the klystron led to many more laboratory-based experiments being conducted post-war. Early experiments were performed utilising the microwave emission of a klyston source coupled with a waveguide cell allowing the measurement of the molecular absorption of microwave radiation by a target molecule to be investigated. Many of the initial studies were performed on ammonia, studies investigating the inversion vibration of this molecule resulted in the identification of the rotational structure and hyperfine structure of transitions.<sup>2, 3</sup> Later, in 1968 ammonia was the first stable polyatomic molecule to be identified in the interstellar medium (ISM).<sup>4</sup> Typically, the target molecules which were the subject of early microwave spectroscopy experiments consisted of small, gasphase molecules allowing their molecular structure to be determined.

The subsequent evolution of this technique, which was made possible by advances in technology, permitted the study of the structure of larger and more complex molecular species and the transfer of molecules which are solid or liquid into the gas phase. Organic molecules which exhibited large amplitude motions such as internal rotation became the subject of microwave spectroscopy studies and the use of high temperature ovens allowed the study of alkali and alkaline earth metal-containing gas-phase species. For A large turning point in the field of microwave spectroscopy came in the 1970s with the introduction of Fourier transform (FT) spectrometers, which was made possible by developments in vacuum technology, molecular beams, and electronics. The general mechanism of Fourier transform spectroscopy involves a pulse of radiation exciting the molecular species and the subsequent emission is collected in the time domain. Ekkers and Flygare were the first to construct a Fourier transform microwave (FTMW) spectrometer in 1975. This spectrometer used high powered pulses of microwave radiation of a selected frequency to probe molecular species. Molecular emissions were recorded and averaged in the time domain before being Fourier transformed into the frequency domain using a computer. The FTMW spectrometer has many advantages over the

spectrometers previously used including an improved spectral resolution and signal-to-noise. Shortly after in 1981, the next development within the field was made, Balle and Flygare developed a spectrometer which included a Fabry-Perot cavity. In this spectrometer, known as the Balle-Flygare Fourier transform microwave (BF-FTMW) spectrometer, both the polarising microwave radiation and supersonically expanding jet containing the molecular ensemble are pulsed. The introduction of supersonic expansion into the technique permitted the study of transient and short-lived species owing to the cold temperatures within the expansion, which would be unstable and dissociate at room temperature. The development of the BF-FTMW spectrometer was therefore crucial in the growth of the study of weakly-bound complexes. However, the main limitation of this technique is the low bandwidth, typically only up to 1 MHz can be scanned at once resulting in long data acquisition times.

The next major advancement in the field was in 2006, the chirped-pulse Fourier transform microwave (CP-FTMW) spectrometer was developed by Pate and co-workers. 11, 12 This spectrometer resulted in a greater than 1000-fold improvement of data acquisition time owing to the broadband nature of the technique. <sup>13</sup> A chirped pulse of microwave radiation is generated from an arbitrary waveform generator (AWG) allowing a significantly greater bandwidth, of up to 12 GHz, to be scanned in a single data acquisition. The inclusion of a travelling wave tube amplifier (TWTA) in the experimental set up ensures sufficient power for the polarisation across the entire bandwidth with minimal losses. The CP-FTMW spectrometer at Newcastle University<sup>14-16</sup> (Figure 3.1) has been used to perform experiments presented within this thesis. The spectrometer is based on the original design of Pate's CP-FTMW spectrometer with several modifications. The spectrometer operates over the frequency range 2.0 - 18.5 GHz. Separate experiments are performed to independently probe the 2.0 - 8.0 GHz and 7.0 - 18.5 GHz frequency bands which require the spectrometer to be slightly re-configured for each experiment involving changes to the microwave circuitry. Experiments performed in the 2.0 – 8.0 GHz and/or 7.0 – 18.5 GHz regions are presented herein. The CP-FTMW spectroscopy technique has been applied to the study of both volatile and non-volatile molecules. The Newcastle CP-FTMW spectrometer allows the study of both, owing to the inclusion of either a heating reservoir for the study of volatile molecules or a bespoke laser ablation source for the study of non-volatile molecules in the experimental set up. In this Chapter the components of the instrument and operation of the Newcastle CP-FTMW spectrometer will be discussed in detail.

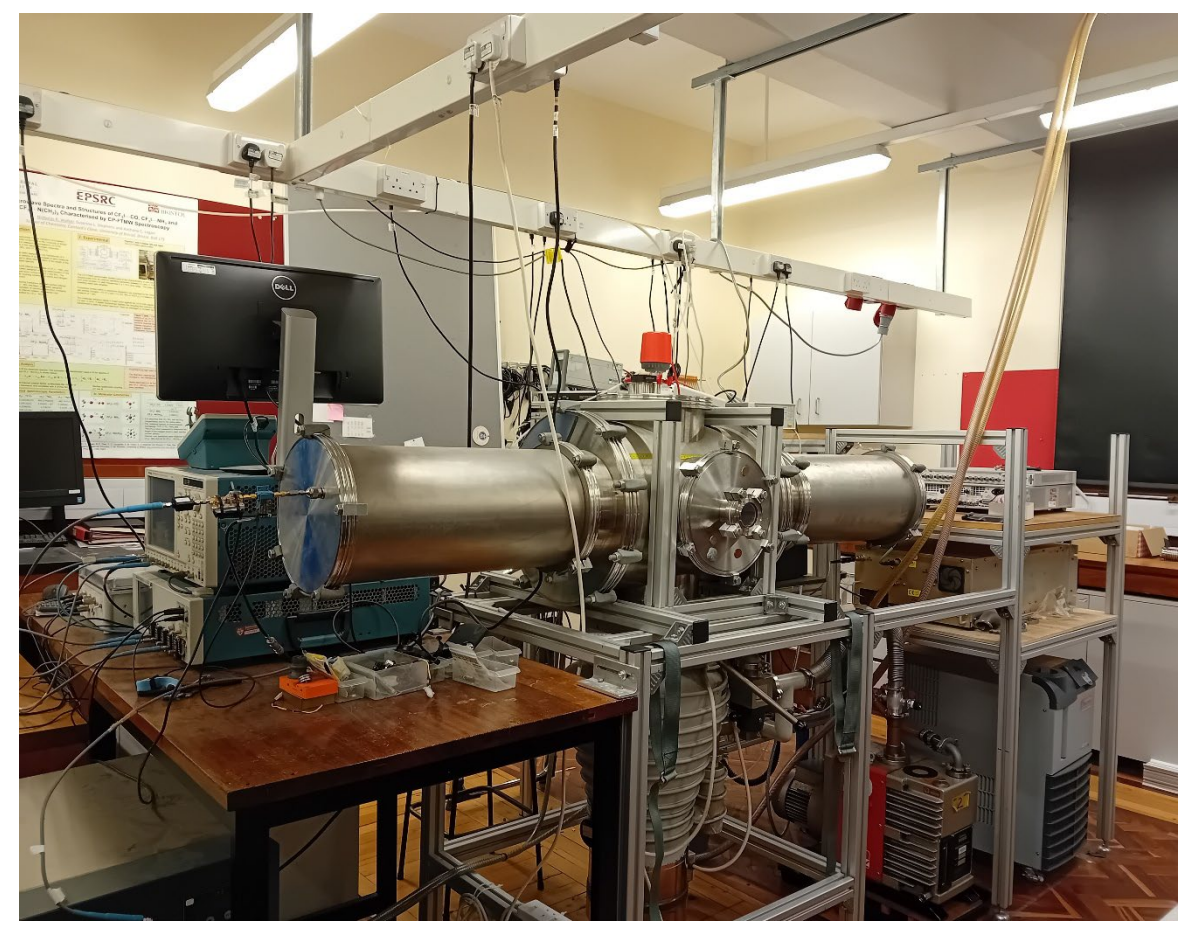


Figure 3.1 The CP-FTMW spectrometer at Newcastle University.

# 3.2 Microwave circuitry: 7.0 – 18.5 GHz experiment

### 3.2.1 Excitation circuit

A chirped pulse which sweeps over the frequency range 12.0 – 0.5 GHz with a duration of 1 μs is generated by a 20 GS/s Arbitrary Waveform Generator (AWG, Tektronix AWG 7102). The chirped pulse moves through a low pass filter (Lorch, 12.2 GHz) and a triple balance mixer (MITEQ, TBO 440LWI-R) before being mixed against a filtered 19 GHz reference supplied by a phase locked dielectric resonant oscillator (PDRO, Herley CTI, XPDRO-14373). The lower frequency sideband (7.0 – 18.5 GHz) is selected by a low pass filter (K&L Microwave, 3C60-19000/T100-O/O) while the higher frequency sideband (12.5 – 31.0 GHz) is filtered out. The lower frequency sideband passes through a pre-amplifier (MITEQ, AMF-5F-080018-14-10P-R) and is attenuated before being delivered to a 300 W Travelling Wave Tube Amplifier (TWTA, AR UK Ltd) for amplification. After amplification the chirped pulse is broadcast into the vacuum chamber via a horn antenna (ATM 750-442-C3) towards the supersonically expanding gas sample.

# 3.2.2 Sample polarisation and molecular emission

The target molecule is introduced into a carrier gas (e.g. argon or neon) from a molecular source by means of heating or laser vaporisation (Section 3.4.1 and 3.4.2). The gas sample undergoes supersonic expansion into the vacuum chamber (more detail will be provided in Section 3.6) such that the molecular species are probed by the microwave radiation while being in low vibrational and rotational states and in a collision-free environment. The polarising pulse of microwave radiation and expanding gas sample are mutually perpendicular and intersecting. The oscillating electric field of the microwave radiation couples with the electric field of rotating polar molecular species such that the dipole moments are aligned and transitions to higher rotational states are induced. The molecular ensemble is polarised for a duration of 1  $\mu$ s halfway between the horn antenna. After 1  $\mu$ s, the molecular species relax back to a lower rotational energy level resulting in the emission of a free induction decay (FID) in the time domain.

#### 3.2.3 Detection circuit

Eight FID's of the molecular emission are received per gas pulse at the second horn antenna located on the opposite side of the vacuum chamber. A pin diode limiter (ACLM-4539C6R1K) and pin diode switch (Arra H8753-8OD) protect the detection circuitry from the high-powered

radiation transmitted into the vacuum chamber and is open for the duration that the polarisation pulse is switched off. The FID's are amplified by a low noise amplifier (MITEQ, AMF-5F-08001800-14-10P-R) and subsequently mixed against a 19 GHz signal supplied by the PDLO at a triple balanced mixer (MITEQ, TBO 440LWI-R). The FID's then pass through a low pass filter, removing the higher frequency sideband (above 12 GHz), allowing only the 0.5-12 GHz FID's to be digitalised at the 100 GS/s oscilloscope (Tektronix DPO72304XS). The first 20  $\mu$ s of the FID's are digitally recorded (beyond 20  $\mu$ s the intensity is effectively zero) and co-added together in the time domain before a Fourier Transform of the data is performed using either a Kaiser-Bessel or High Resolution Window function.

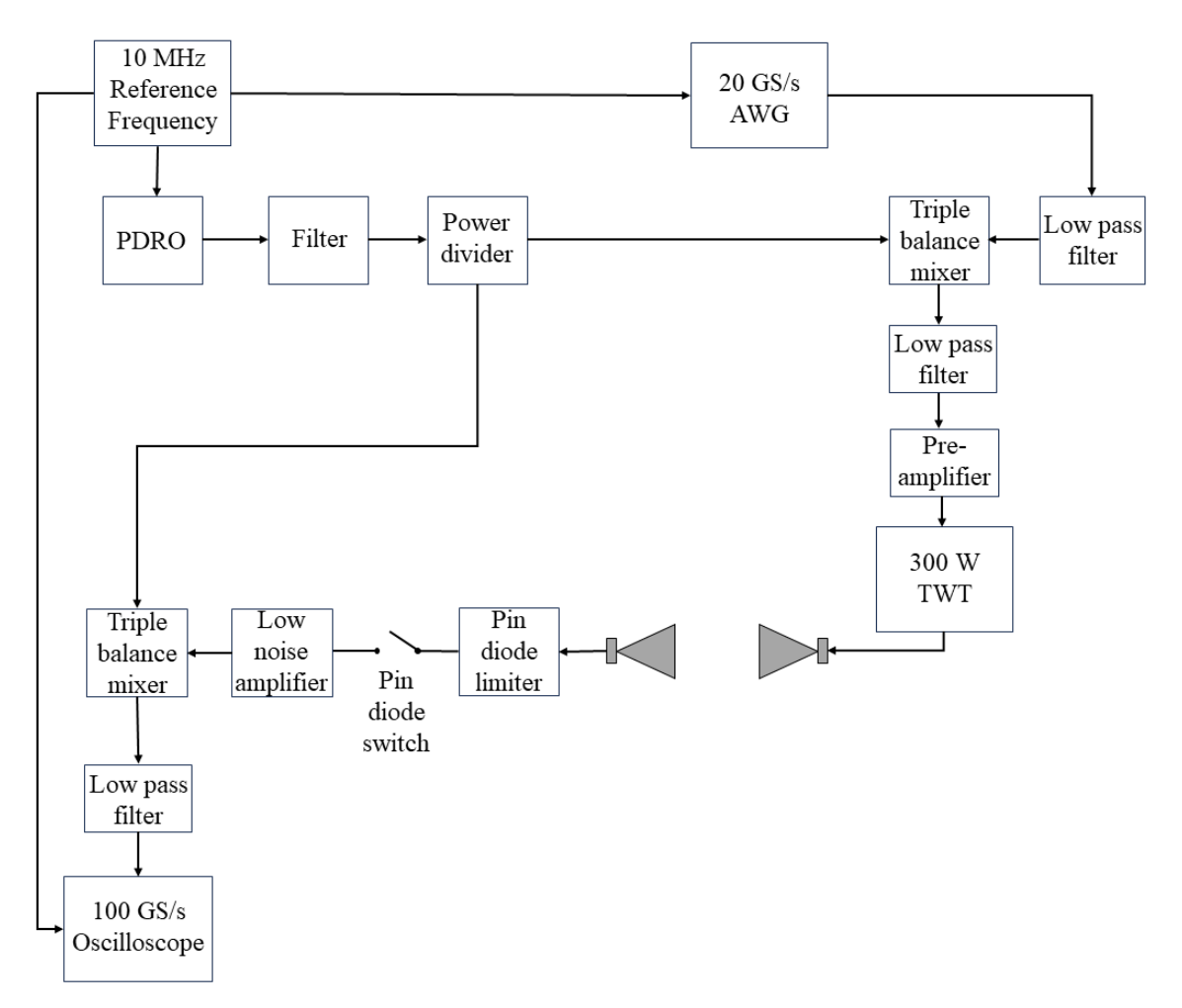


Figure 3.2 Microwave circuitry of the Newcastle CP-FTMW spectrometer configured for the 7.0 - 18.5 GHz experiment.

# 3.3 Microwave circuitry: 2.0 – 8.0 GHz experiment

### 3.3.1 Excitation circuit

In order to decrease the spectral range to the lower frequency experiment, various components of the excitation circuit are removed. The 20 GS/s AWG generates a chirped pulse of microwave radiation that sweeps over the frequency range 2.0 – 8.0 GHz and has a duration of 1 μs, which eliminates the need for any mixing to occur. The low pass filters, triple balance mixer and PDLO are removed from the excitation circuitry. The chirped pulse is sent directly from the AWG to a 450 W TWTA (Applied Systems Engineering, Model 167) for amplification, prior to entering the TWTA the chirped pulse is attenuated. After amplification the polarisation pulse is broadcast into the vacuum chamber via the transmission horn antenna.

## 3.3.2 Detection circuit

The detection circuitry is much the same as described in the 7.0 - 18.5 GHz experimental set up. The FID's spanning the 2.0 - 8.0 GHz range can be directly digitised at the 100 GS/s oscilloscope owing to its range, therefore, eliminating the need for mixing at the detection end of the circuit. The PDLO, triple balance mixer and low pass filter are therefore removed from the detection circuit.

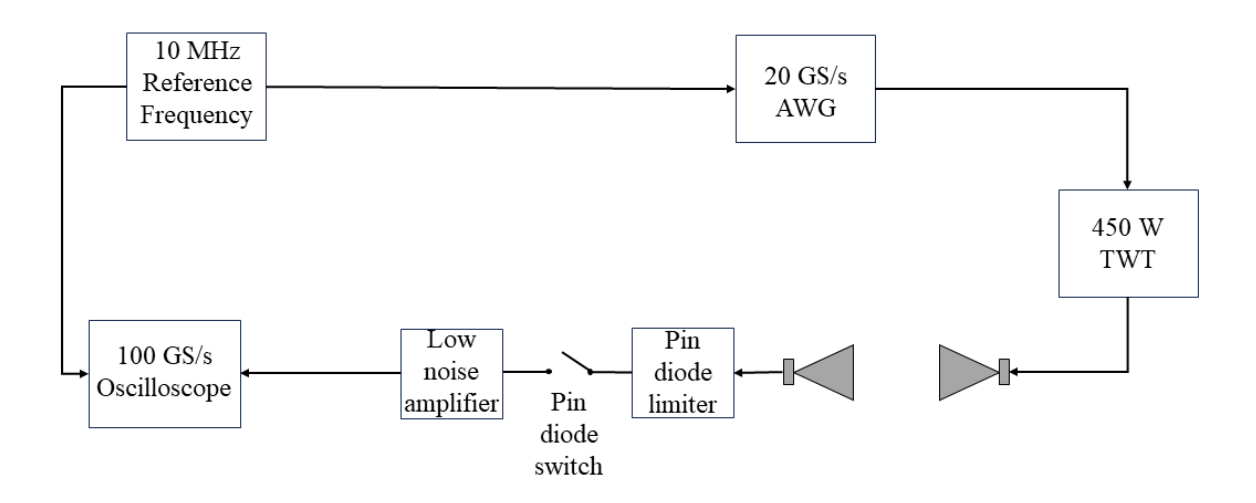


Figure 3.3 Microwave circuitry of the Newcastle CP-FTMW spectrometer configured for the 2.0 - 8.0 GHz experiment.

#### 3.4 Molecular sources

### 3.4.1 Heated reservoir

For the study of volatile molecules, reservoirs which have the capability to be heated are typically employed. The custom-made reservoir (Figure 3.4, (1)), which was used in the study of molecules which are liquid at room temperature presented herein, is based on the design of the Sanz group. 17 The reservoir contains the molecule of interest under study and is mounted to a faceplate of a pulsed valve (Figure 3.4, (2)) at the point directly prior to supersonic expansion. The faceplate is modified to contain four holes (each of  $\sim 0.05$  mm diameter) around the orifice. Two o-rings are placed on the faceplate, allowing the reservoir to be pressurised and to avoid chemical or gas leaks. A band heater (RS, 155 W, 230 V ac) is placed round the reservoir to heat the sample, allowing the microwave spectrum of molecules with low vapour pressures to be acquired. The temperature of the band heater can be varied and is regulated by a thermocouple and temperature controller (Lumel, RE70). The carrier gas passes over the sample located within the reservoir and the vapours of the target molecule are seeded into the carrier gas before the carrier gas/target molecule mixture undergoes supersonic expansion into the vacuum chamber. It was identified during previous studies<sup>18, 19</sup> employing the heated reservoir set up, that syringing the chemical sample onto glass wool within the reservoir (Figure 3.4, (3)) extended the lifetime of the sample which allowed for longer data acquisition times. The same methodology was employed for the studies presented herein. Typically, between 0.2 - 0.4 mL of chemical sample was required for a single experiment, in which data could be acquired for several days without the need to replace the sample.



Figure 3.4 (1) Reservoir and modified faceplate used in the experiments studying volatile molecules. (2) Reservoir mounted to general pulsed valve. (3) Glass wool in reservoir prior to introduction of chemical sample.

## 3.4.2 Laser ablation source

A laser ablation source can be included in the Newcastle CP-FTMW spectrometer to transfer solid target molecules into the gas phase for study. This technique is commonly employed for target molecules which are solid at room temperature, which either have high boiling points or that decompose at low temperatures. Laser vaporisation has been extensively used in the group to study metal-containing species<sup>20-22</sup> and has been employed elsewhere in conjunction with microwave spectroscopy for the study of biomolecules.<sup>23-27</sup> More recently, laser ablation has been used by our group to study weakly-bound complexes formed between high melting point biomolecules (such as imidazole) and other small molecules.<sup>18, 28-30</sup>

Laser vaporisation involves the removal of material from a solid sample rod by a short, intense laser pulse. This process allows the solid target molecule to be transferred into the gas phase without destroying the molecular structure. However, typically a small portion of the sample material undergoes fragmentation such that fragmentation products of the target molecule are also observed in the spectrum recorded. A nanosecond Nd:YAG laser (Photonics Solutions, Continuum, Minilite II) is focussed at a rotating and translating rod which contains the molecule of interest, transferring it into the gas phase. It is necessary to rotate and translate the sample rod to ensure a fresh surface is exposed to each laser pulse to obtain continuously intense molecular signals. This is achieved using a motor and the Laser Ablation Controller, which will be discussed in more detail below. The laser ablation source is fixed directly to the faceplate of a general pulsed valve such that the rotating rod is 2-3 mm from the orifice and the vapourised material enters the supersonically expanding gas sample. The direction of the laser beam, orientation of the sample rod and expanding gas sample are mutually perpendicular. Recent experiments have employed the fundamental harmonic of the Nd:YAG laser (1064 nm, 43 mJ/pulse, 10 ns) during the study of imidazole-containing species. Whereas many previous laser ablation studies by the group typically used the second harmonic of this laser (532 nm, 15 mJ/pulse, 10 ns). The change to the fundamental harmonic was necessary owing to the decreasing power of the second harmonic after much use. The fundamental harmonic was found to boost the molecular signal of both 4-methylimidazole and 5-methylimidazole during the study of the methylimidazole monomers<sup>31</sup> and provide suitable conditions for the generation of weakly-bound complexes allowing the study of imidazole···H<sub>2</sub>O,<sup>30</sup> isomers methylimidazole···H<sub>2</sub>O<sup>18</sup> and 2-ethylimidazole···H<sub>2</sub>O (Chapter 7).

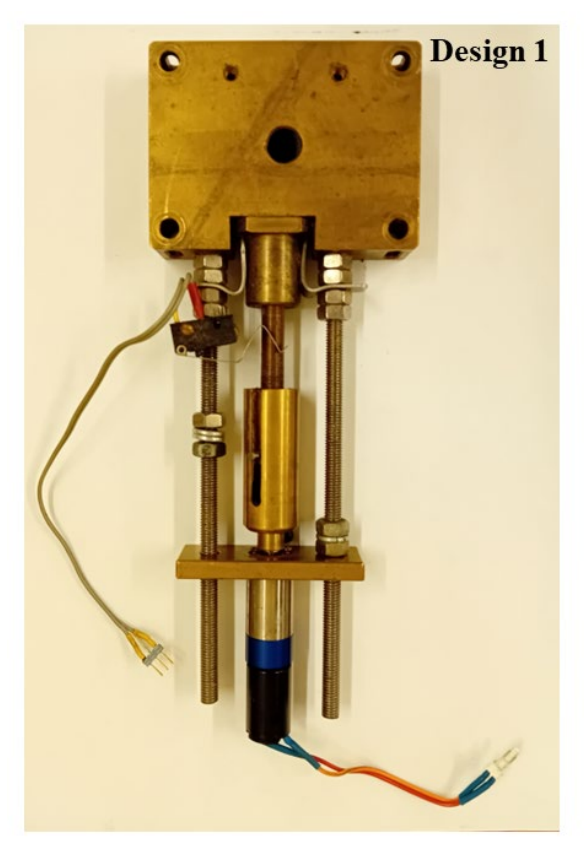




Figure 3.5 The two ablation sources that can be used for the study of solid target molecules and integrated into the Newcastle CP-FTMW spectrometer. (left) Design 1 of the ablation source. (right) Design 2 of the ablation source.

Two ablation sources (as shown in Figure 3.5) of differing designs can be integrated into the spectrometer for laser vaporisation experiments. Each ablation source has its own advantages. Design 1 ("large block") allows the laser beam to be focussed through a small hole onto a sample rod enclosed within a brass block. Whereas in design 2 ("open block") the ablation source has a more open design, and the motor is located above the sample rod. Each laser ablation source accommodates sample rods of differing size. The sample rods used in design 1 have a diameter of 5 mm and those used in design 2 have a larger diameter of 13 mm. Design 2 allows the inclusion of sample rods which are longer than those used in design 1. The amount of sample required during the preparation of the 13 mm rod is greater than that required for a 5 mm rod. Therefore, preparation of 5 mm sample rods and use of design 1 of the laser ablation source is advantageous when the target molecule is expensive or only small amounts of sample are available. Rods prepared for the use in design 2 of the laser ablation source require more chemical sample, however, typically result in longer data acquisition times. Design 2 of the laser ablation source was used during studies of imidazole, <sup>28, 30</sup> isomers of methylimidazole<sup>31</sup> and 2-ethylimidazole (Chapter 7) since each sample is inexpensive.

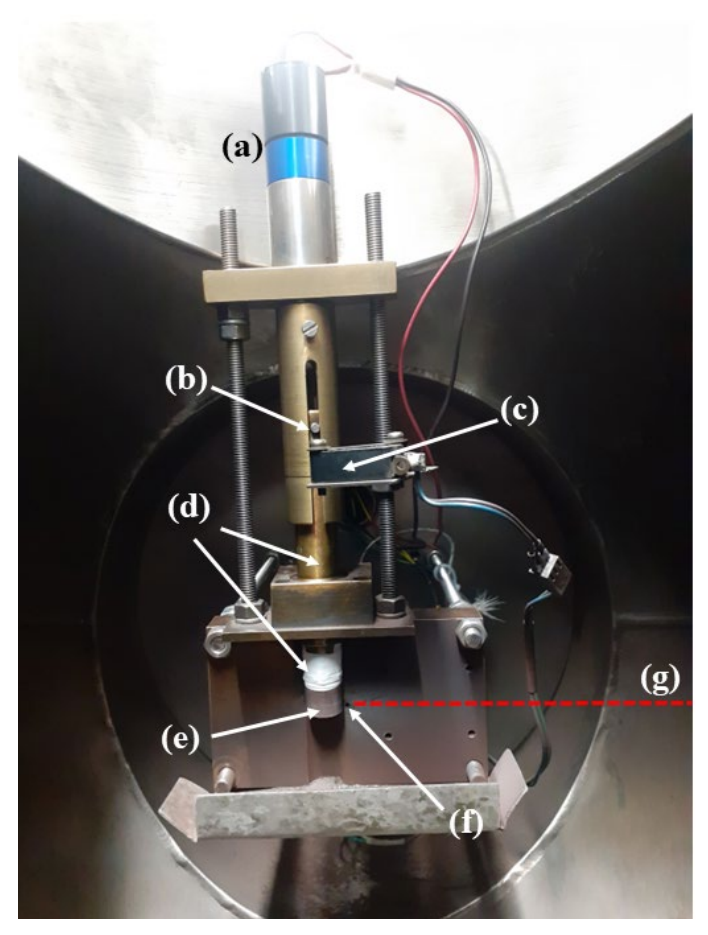


Figure 3.6 Experimental set up of the laser ablation source (Design 2) within the vacuum chamber. (a) Motor. (b) Paddle. (c) Switch. (d) Rod holder and spacer. (e) Sample rod. (f) Orifice. (g) Direction of laser beam.

Sample rods are usually prepared by grinding and mixing the target molecule with a metal-containing matrix such as Cu, Zn or AgI powder. A previous study observed a signal boost for the imidazole dimer<sup>28</sup> when sample rods composed of a 1:1 ratio of imidazole and copper were used in experiments, compared to sample rods which were prepared of imidazole alone. The use of a matrix material also results in a lower amount of target molecule sample being required for the preparation of the rods. The target molecule/matrix mixture is placed within a die (Specac) and pressurised using a hydraulic benchtop press. Typically, 5 or 6 tonnes of pressure was applied to prepare each sample rod. For experiments performed using 2-ethylimidazole (Chapter 7) a 1:1 mass ratio of 2-ethylimidazole and copper powder was used to prepare a sample rod which was 13 mm in diameter and  $\sim$  1.2 cm in length. Sample rods are attached to the spacer of the rod holder (Figure 3.6, (d)) in each design of the ablation source. As mentioned earlier, for the duration of the experiment sample rods are continuously rotated and translated to ensure a fresh surface of the rod is exposed to the laser pulse (Figure 3.6 (g)). The following sequence of events occur when design 2 of the ablation source is employed in experiments. A

motor (Faulhaber 22/7 989:1 K179, Figure 3.6 (a)) rotates the sample rod (Figure 3.6 (e)) and is initially translated in a downwards direction owing to the rod holder being threaded. The rod will rotate downwards until the paddle (Figure 3.6 (b)) hits a switch (Figure 3.6 (c)), which is set at the point to coincide with when the laser beam is hitting the top of the sample rod. The rod will rotate in the opposite direction and move in an upwards direction for a given time. Typically, the rod will be rotated quicker in the reverse direction. The reverse translation timings and rotation speed are controlled by the Laser Ablation Controller, which also has a setting for "short", "medium" and "long" sample rods. Typically, the medium setting is used for sample rods of 1-2 cm length. This process is repeated for the duration of the experiment.

# 3.5 Vacuum Chamber and Pumps

A schematic of the Newcastle CP-FTMW spectrometer vacuum chamber is displayed in Figure 3.7. The vacuum chamber consists of a six-way cross which has four ISO 250 and two ISO 400 ports. The transmission and detection horn antenna are located on opposite sides of the vacuum chamber. Mounted to each ISO 400 port is an adaptor reducing to an ISO 250 port to which each have a tube attached with a horn antenna encased within. The chamber is evacuated by a diffusion pump (Edwards, Diffstak 250), which is mounted to the bottom flange and is backed by a mechanical rotary pump (Edwards, E2M40). The diffusion pump is continuously water cooled. The pumping system allows a high vacuum to be achieved within the chamber, typically a pressure on the order of 10<sup>-6</sup> mbar is achieved prior to starting an experiment. The pressure of the rotary pump and chamber are monitored using a Pirani gauge (Edwards APG100) and a Penning gauge (Edwards, AIM-X-NW25) respectively. The location of the Penning gauge has recently been changed such that it is now mounted to the flange located on the top of the chamber. The gas line enters the chamber through the back flange, the pulsed valve (Parker, series 9) is located at the end of the gas line and is positioned halfway between the horn antenna. Either the heated reservoir or ablation source were attached to the pulsed valve for the experiments performed in this thesis. The necessary cables and power supplies for the pulsed valve, heated reservoir and ablation source are fed through the back flange. The front flange has a viewport window such that the inside of the chamber can be viewed while under vacuum and experiments can be monitored. The top, front and back flanges are removable allowing easy access into the chamber to set up experiments. The chamber's interior is lined with microwaveabsorbent polyurethane foam (Emerson and Cuming, HR-1).

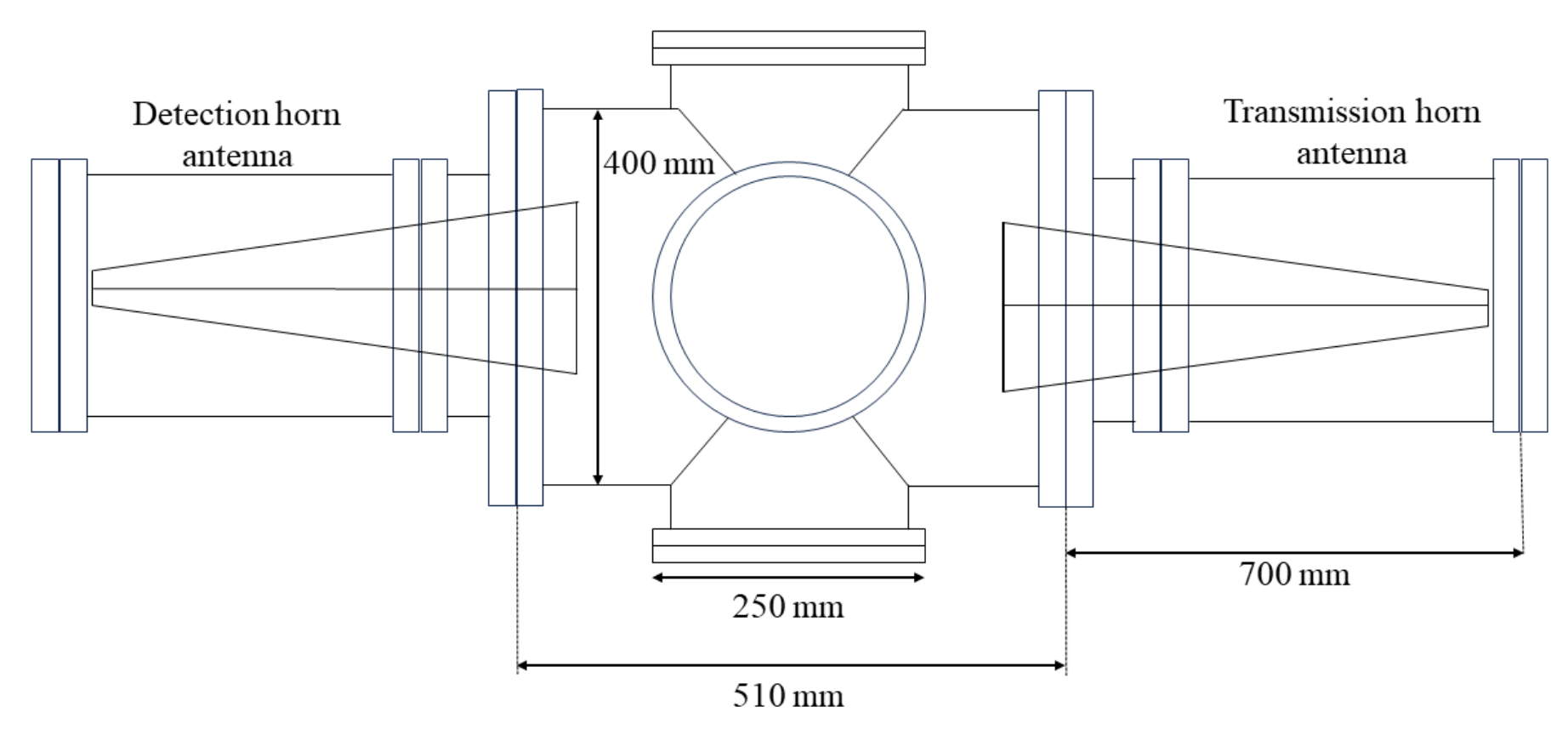


Figure 3.7 Schematic of the Newcastle CP-FTMW spectrometer vacuum chamber.

# 3.6 Supersonic Expansion

Supersonic expansion is a technique commonly employed in gas-phase spectroscopy that involves expanding a gas sample through an orifice from a region of high pressure into a region of low pressure, typically a vacuum chamber. Initially, as the gas expands, the species within the gas sample can undergo collisions. As the gas sample is accelerated away from the highpressure region, the velocities of the molecular species approach the same value which is greater than the local speed of sound (Mach number, M >> 1). The gas sample cools to a few Kelvin (~ 3 K) during this process as heat energy is converted into translational energy. As the gas expands and the molecular species accelerate at the same terminal velocity, the rate of collisions rapidly decreases until a point is reached in which collisions are effectively halted. This is known as the zone of silence and is the point at which the expanding gas sample is irradiated. Typically, supersonic expansions are generated using a gas sample comprised of a high concentration of a noble gas (known as the carrier gas or backing gas) such as helium, neon, argon and krypton and a low concentration of the target molecule under study. Vapours of the target molecule are seeded into the carrier gas before the gas sample undergoes expansion when volatile molecules are under study. Whereas during the study of solid target molecules by means of laser ablation the molecular species enter the expanding gas sample at the point immediately after the orifice. It is known that the choice of carrier gas influences the molecular species present within the supersonic expansion and this will be discussed in more detail below. This technique is advantageous for the study of molecules and weakly-bound complexes using microwave spectroscopy. The use of a supersonic expansion simplifies the microwave spectrum obtained owing to the molecular species being rotationally and vibrationally cooled such that typically only low energy states are populated. Additionally, the use of a supersonic expansion permits the study of weakly-bound complexes since the energy required for complex formation is absorbed by the carrier gas molecules and this environment allows the complexes to remain associated.

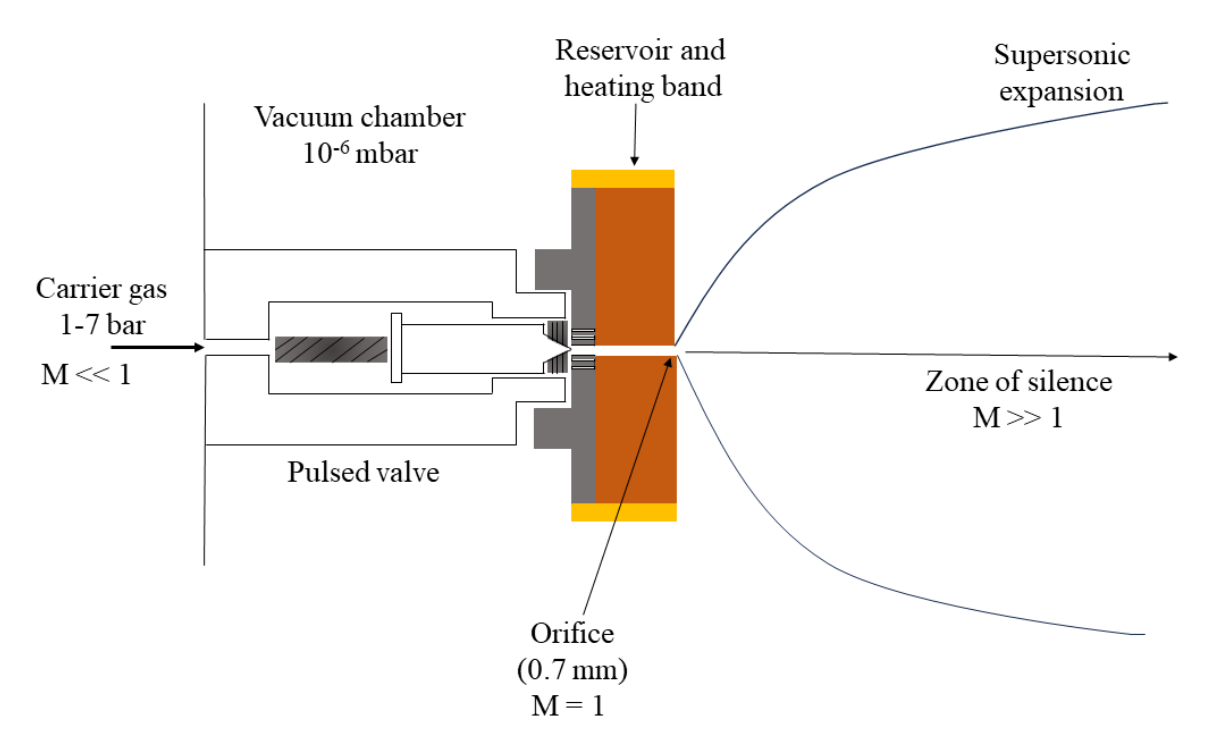


Figure 3.8 Schematic of a supersonic expansion propagating from the pulsed valve/heated reservoir set up. The Mach number (M) at various stages is labelled, which is a measure of the gas sample speed relative to the speed of sound (M = 1). Not to scale.

A gas sample comprised of the target molecule,  $H_2O$  (introduced upstream of the orifice) and an argon or neon carrier gas is expanded through a 0.7 mm orifice using a pulsed general valve (Parker, series 9) for the experiments performed herein. A backing pressure of 1-7 bar was selected for the carrier gas and the chamber typically had a pressure on the order of  $10^{-6}$  mbar. These conditions proved effective for the generation of weakly-bound complexes in their zero-point vibrational state within the supersonic expansion. A depiction of the supersonic expansion propagating from the general valve modified with a heating reservoir (described in Section 3.4.1) is presented in Figure 3.8.

The molecular species present within the supersonic expansion can be influenced by the choice of carrier gas. Particularly, this has an impact on the concentration of higher energy conformers or isomers present. Ruoff *et al.* noted that conformational relaxation is dependent on the carrier gas.<sup>32</sup> The relative transition intensities of both higher energy and more stable species were investigated while employing different noble gases as the carrier. They observed that when the barrier to interconversion between conformers was 350 cm<sup>-1</sup> (4.2 kJ mol<sup>-1</sup>) or less the transition intensity was influenced by the choice of carrier gas. Relaxation of higher energy to lower energy forms of a molecule or complex occur as a result of collisions with the atoms of the carrier gas. Heavier carrier gases (argon or krypton) are more efficient at relaxation, therefore,

usually the concentration of higher energy forms present within an argon or krypton expansion is less than if helium or neon was used. For this reason, rotational spectroscopy studies on molecules which exhibit conformational flexibility typically employ helium or neon carrier gases in experiments such that a greater amount of higher energy conformations are more likely to be probed by the experiment. Although, it is also possible to observe transitions of species other than the global minimum structure when using argon. A study<sup>33</sup> on the acyclic monoterpene, citronellal, observed 15 different conformations of this molecule while using neon as the carrier gas. However, when performing an experiment using argon, transitions from only 8 of the 15 conformers were observed in the spectrum acquired, indicating that several of the conformers have undergone relaxation in the argon expansion. Four conformers of transurocanic acid<sup>34</sup> were observed while probing the microwave spectrum of this molecule in a neon expansion. When performing an equivalent experiment using argon, transitions for each of the four conformations were present, suggesting that a high barrier to interconversion is present between the conformers such that higher energy forms cannot relax in the argon expansion. This has also been recently observed for isomers of the thiazole...(H<sub>2</sub>O)<sub>2</sub> complex, the higher energy form of the dihydrate complex was able to be observed while employing argon as the carrier gas.<sup>19</sup> For each of the studies on ethyl-substituted heterocycles presented in Chapters 5-7, which are conformationally flexible owing to the rotation of the ethyl group relative to the heteroaromatic ring, separate experiments were performed using argon and neon as the carrier gas. It will be discussed in Chapter 5 how the choice of carrier gas influences the conformations of the 2-ethylfuran monomer present within the expansion.

# 3.7 Trigger sequence and timings

The triggering sequence and timings are controlled by two delay generators and the AWG. The triggering sequence is of vital importance ensuring the experiment runs smoothly allowing spectra to be acquired while also safeguarding the instrument from damage. The timings associated with the trigger sequence have been selected to optimise the experiment and maximise the signal intensity achieved. The sequence and duration associated with each trigger will be described in detail below, this is the same regardless of what frequency band is being probed by the experiment, however, some differences arise depending on whether the experiment uses the heated reservoir or ablation source to study the target molecule. Additional triggers within the sequence of the experiment are required when the laser is in use. Each of the delay generators and AWG allow the triggering and timings to be controlled with high accuracy and ensure phase stability in the time domain. The first delay generator (Quantum Composers, 9520 series) has a phase jitter of less than 50 ps while the second delay generator (Quantum Composers, 9518+ series) has a phase jitter of less than 30 ps.

Four channels of the first delay generator are used to control various aspects of the experiment. Channel A is internally triggered and starts the triggering sequence of the experiment. This channel is used to trigger the IOTA one pulse driver for a duration of  $\sim 2 \mu s$  with respect to the starting point of the experiment  $(T_0)$ , triggering the gas pulse. The gas pulse usually has a duration of 900 μs. The AWG is triggered for a duration of ~ 51 μs by Channel B of the delay generator. This signifies the point in time that the chirped pulse is generated with respect to the gas pulse at T<sub>0</sub>. A series of eight chirped pulses is produced by the AWG which each have a duration of 1 µs and are separated by 25 µs. The delay of this trigger with respect to T<sub>0</sub> varies from experiment-to-experiment, since it is dependent on various factors such as the tension of the nozzle, target molecule under study and the type of experiment. Typically, a longer delay between the gas pulse and chirped pulse is selected for laser ablation experiments compared to experiments employing the heated reservoir set up. The delay is selected to maximise the intensity of the molecular signal and usually takes a value within the range 700 – 1700 μs after T<sub>0</sub>. For experiments employing the heated reservoir, triggers from Channel A and B are only required from the first delay generator. However, for experiments using the Nd:YAG laser, an additional two triggers are required in the triggering sequence, which are controlled by the first delay generator. The Q-switch of the laser is triggered by Channel C for a duration of 100 μs. Again, the timing of this trigger with respect to T<sub>0</sub> varies from experiment-to-experiment and is optimised to maximise signal intensity. The Q-switch is triggered typically no more than 500

 $\mu$ s before the chirped pulse. The flash lamp of the laser is triggered 162  $\mu$ s before the Q-switch for a duration of 100  $\mu$ s by Channel D.

The AWG is used to externally trigger the second delay generator and the oscilloscope. The second delay generator has two channels in use, both of which are required to safeguard the instrument from damage, triggering the pin diode switch and the TWT. Channel A of this delay generator sends a trigger pulse to the pin diode switch 750 ns after the AWG trigger (T<sub>0</sub> of the second delay generator). This pulse triggers the switch to open for 2 us allowing FID's of the molecular emission to be collected. Channel B of the second delay generator sends a pulse to trigger the TWT which has a duration of 1.5 µs and a delay of 1 µs with respect to T<sub>0</sub>. The timings of each trigger pulse protect the detection circuitry from the high-powered microwave radiation such that the switch is closed for the duration of the polarisation pulse. The second trigger that the AWG sends is to the oscilloscope after the pin diode switch closes (2.75 µs after T<sub>0</sub>). This triggers the oscilloscope to collect the 8 FID's which are in the time domain. The oscilloscope uses a fast frame mode which contains 9 frames. The first 8 frames contain each of the 8 FID's collected of the molecular emission per gas pulse while the 9th frame contains an average of the 8 FID's collected. A Fourier transform is performed using either a Kaiser-Bessel or High-Resolution Window function such that the frequency domain spectrum can be viewed in real-time on the oscilloscope allowing the experiment to be monitored. A python script is used to automate saving the data acquired at regular intervals, typically a data file is saved every 30,000 FID's collected which corresponds to approximately 30 minutes of real-time data collection. The script saves the data in the time domain and a Fourier transform is performed using another python script remote from the oscilloscope to acquire the frequency domain spectrum.

The repetition rate of the experiments performed in this thesis is 2 Hz such that the triggering sequence repeats every 0.5 s. The repetition rate of the experiment is controlled by the first delay generator, however, the maximum repetition rate is governed by the pumping speed and the sampling rate of the oscilloscope. The maximum repetition rate of the experiment is 4.5 Hz such that the triggering sequence would repeat every  $\sim 0.2$  s.

# 3.8 Spectral lines: Linewidth and intensity

The linewidth and intensity of spectral transitions are each dependent on several factors. At full width half maximum (FWHM) the linewidth of an isolated, unblended, transition measured by the Newcastle CP-FTMW spectrometer is ~ 100 kHz and line centre frequencies can be estimated with an accuracy of ~ 10 kHz. The linewidth is limited by and is inversely proportional to the duration of the FID recorded. The first 20 µs of the FID is recorded such that the minimal linewidth of spectral transitions is ~ 50 kHz. The linewidth is also influenced by the type of Fourier transform performed to acquire the frequency domain spectrum. Typically, the linewidth at FWHM is greater when employing a Kaiser-Bessel window function for the Fourier transform compared to when the High-Resolution window function is utilised. Sharper transitions are obtained when using the High-Resolution window for the Fourier transform whereas an improved baseline resolution is obtained while using the Kaiser-Bessel window. Better resolution at the baseline allows low intensity molecular signals to be more easily distinguished from noise. For this reason, both the High-Resolution and Kaiser-Bessel window functions have been employed to acquire the frequency domain spectrum during the studies presented within this thesis. Accuracy in transition frequencies and phase reproducibility in the time domain is provided by a Rubidium Frequency Standard (Stanford Research Systems, SRS FS725) or an Analog Signal Generator (Agilent MXG N5183 A) which supplies a 10 MHz reference signal which the AWG, PDRO and oscilloscope are phase-locked to. An Analog Signal Generator was used in combination with a distribution board in experiments to supply the reference frequency while the Rubidium Frequency Standard was sent away for calibration owing to loss of the frequency lock. Checks were performed to ensure the line centre frequencies had not drifted during this period ensuring reproducibility of assignments. The Rubidium Frequency Standard supplies the 10 MHz signal with an accuracy of  $\pm 5 \times 10^{-11}$ .

The intensity of a given spectral line (S) is dependent on several different factors which are summarised in the following relationship<sup>12, 35, 36</sup>:

$$S \propto \omega \cdot \mu^2 \cdot E_{pulse} \cdot \Delta N_0 \cdot \left(\frac{\pi}{\alpha}\right)^{1/2}$$
 (Eq 3.1)

where  $\omega$  is the frequency,  $\mu^2$  is the square of the transition dipole moment,  $E_{pulse}$  is the electric field strength of the polarising pulse,  $\Delta N_0$  is the population difference between states and  $\alpha$  is the linear sweep rate.

The intensity of a molecular transition measured using the Newcastle CP-FTMW spectrometer has units which are in millivolts (mV). Information can be inferred from the relative intensities of the transitions present within the spectrum, however, the exact concentration of molecular species within the supersonic expansion cannot be determined.

# 3.9 References

- 1. C. E. Cleeton and N. H. Williams, *Physical Review*, 1934, **45**, 234-237.
- 2. B. Bleaney and R. P. Penrose, *Nature*, 1946, **157**, 339-340.
- 3. W. E. Good, *Physical Review*, 1946, **70**, 213-218.
- 4. A. C. Cheung, D. M. Rank, C. H. Townes, D. D. Thornton and W. J. Welch, *Physical Review Letters*, 1968, **21**, 1701-1705.
- 5. M. L. Stitch, A. Honig and C. H. Townes, *Physical Review*, 1952, **86**, 813-814.
- 6. A. Honig, M. L. Stitch and M. Mandel, *Physical Review*, 1953, **92**, 901-902.
- 7. M. L. Stitch, A. Honig and C. H. Townes, *Review of Scientific Instruments*, 1954, **25**, 759-764.
- 8. J. Ekkers and W. H. Flygare, *Review of Scientific Instruments*, 1976, 47, 448-454.
- 9. T. J. Balle and W. H. Flygare, *Review of Scientific Instruments*, 1981, **52**, 33-45.
- 10. A. C. Legon, Annual Review of Physical Chemistry, 1983, 34, 275-300
- 11. G. G. Brown, B. C. Dian, K. O. Douglass, S. M. Geyer and B. H. Pate, *Journal of Molecular Spectroscopy*, 2006, **238**, 200-212.
- 12. G. G. Brown, B. C. Dian, K. O. Douglass, S. M. Geyer, S. T. Shipman and B. H. Pate, *Review of Scientific Instruments*, 2008, **79**, 053103.
- 13. G. B. Park and R. W. Field, The Journal of Chemical Physics, 2016, 144, 200901.
- 14. S. L. Stephens and N. R. Walker, *Journal of Molecular Spectroscopy*, 2010, **263**, 27-33.
- 15. D. P. Zaleski, S. L. Stephens and N. R. Walker, *Physical Chemistry Chemical Physics*, 2014, **16**, 25221-25228.
- 16. G. A. Cooper, C. Medcraft, J. D. Littlefair, T. J. Penfold and N. R. Walker, *The Journal of Chemical Physics*, 2017, **147**, 214303.
- 17. D. Loru, M. A. Bermúdez and M. E. Sanz, *The Journal of Chemical Physics*, 2016, **145**, 074311.
- 18. E. Gougoula, C. N. Cummings, C. Medcraft, J. Heitkämper and N. R. Walker, *Physical Chemistry Chemical Physics*, 2022, **24**, 12354-12362.
- 19. E. Gougoula, C. N. Cummings, Y. Xu, T. Lu, G. Feng and N. R. Walker, *The Journal of Chemical Physics*, 2023, **158**, 114307.
- 20. D. M. Bittner, S. L. Stephens, D. P. Zaleski, D. P. Tew, N. R. Walker and A. C. Legon, *Physical Chemistry Chemical Physics*, 2016, **18**, 13638-13645.
- 21. C. Medcraft, D. M. Bittner, D. P. Tew, N. R. Walker and A. C. Legon, *The Journal of Chemical Physics*, 2016, **145**, 194306.
- 22. C. Medcraft, E. Gougoula, D. M. Bittner, J. C. Mullaney, S. Blanco, D. P. Tew, N. R. Walker and A. C. Legon, *The Journal of Chemical Physics*, 2017, **147**, 234308.
- 23. S. Blanco, A. Lesarri, J. C. López and J. L. Alonso, *Journal of the American Chemical Society*, 2004, **126**, 11675-11683.
- 24. A. Lesarri, S. Mata, E. J. Cocinero, S. Blanco, J. C. López and J. L. Alonso, *Angewandte Chemie International Edition*, 2002, **41**, 4673-4676.
- 25. A. Lesarri, E. J. Cocinero, J. C. López and J. L. Alonso, *Angewandte Chemie International Edition*, 2004, **43**, 605-610.
- 26. S. Mata, I. Peña, C. Cabezas, J. C. López and J. L. Alonso, *Journal of Molecular Spectroscopy*, 2012, **280**, 91-96.
- 27. C. Bermúdez, S. Mata, C. Cabezas and J. L. Alonso, *Angewandte Chemie International Edition*, 2014, **53**, 11015-11018.
- 28. J. C. Mullaney, D. P. Zaleski, D. P. Tew, N. R. Walker and A. C. Legon, *ChemPhysChem*, 2016, **17**, 1154-1158.
- 29. J. C. Mullaney, C. Medcraft, D. P. Tew, L. Lewis-Borrell, B. T. Golding, N. R. Walker and A. C. Legon, *Physical Chemistry Chemical Physics*, 2017, **19**, 25080-25085.

- 30. E. Gougoula, D. J. Cole and N. R. Walker, *The Journal of Physical Chemistry A*, 2020, **124**, 2649-2659.
- 31. E. Gougoula, C. Medcraft, J. Heitkämper and N. R. Walker, *The Journal of Chemical Physics*, 2019, **151**, 144301.
- 32. R. S. Ruoff, T. D. Klots, T. Emilsson and H. S. Gutowsky, *The Journal of Chemical Physics*, 1990, **93**, 3142-3150.
- 33. S. R. Domingos, C. Pérez, C. Medcraft, P. Pinacho and M. Schnell, *Physical Chemistry Chemical Physics*, 2016, **18**, 16682-16689.
- 34. G. A. Cooper, C. Medcraft, E. Gougoula and N. R. Walker, *Physical Chemistry Chemical Physics*, 2019, **21**, 9495-9503.
- 35. J. C. McGurk, T. G. Schmalz and W. H. Flygare, *The Journal of Chemical Physics*, 1974, **60**, 4181-4188.
- 36. F. Wolf, Journal of Physics D: Applied Physics, 1994, 27, 1774.

# Chapter 4. Non-Covalent Interactions in the Molecular Geometries of Complexes Formed between Structural Isomers of Methylthiazole and Water Revealed by Microwave Spectroscopy.

Publication (4-Methylthiazole···H<sub>2</sub>O and 5-Methylthiazole···H<sub>2</sub>O):

<u>Charlotte N. Cummings</u>, Isabelle Kleiner and Nicholas R. Walker, *J. Phys. Chem. A*, 2023, 127, 39, 8133–8145

# 4.1 Introduction

As highlighted in Chapter 1, microwave spectroscopy has been used to study numerous fivemembered heteroaromatic rings and their derivatives. Thiazole is an example of a fivemembered ring which contains sulphur and nitrogen heteroatoms in the 1- and 3- positions respectively (the atom numbering is shown in Figure 4.1) and was first studied using this technique in 1962 by Bak et al. The molecular geometry of thiazole was determined in subsequent investigations which analysed the spectra of many isotopologues.<sup>2, 3</sup> The variation in the  $V_3$  barrier to internal rotation of a CH<sub>3</sub> group substituted at the 2-, 4- and 5- position of the thiazole ring has been studied. The magnitude of this barrier is reported to be 34.1 cm<sup>-1</sup> for 2-methylthiazole, <sup>4, 5</sup> 357.6 cm<sup>-1</sup> for 4-methylthiazole<sup>6</sup> and 332.0 cm<sup>-1</sup> for 5-methylthiazole.<sup>7</sup> Similar studies have been performed to explore the variation in the  $V_3$  barrier height for isomers methylimidazole,<sup>8, 9</sup> of other methylated five-membered heterocycles including 14 16 methylpyrrole, 10-12 methyloxazole, 13, methylisoxazole, 15, methylfuran, 17-19 methylisothiazole<sup>20</sup> and methylthiophene<sup>21-23</sup>, see Chapter 1 section 1.3. Generally, in fivemembered rings containing two heteroatoms, the lowest  $V_3$  barrier is observed for the isomer where the CH<sub>3</sub> group is substituted onto the 2-position whereas higher barriers are observed where CH<sub>3</sub> is substituted onto the 4- or 5- positions. This variation in  $V_3$  for isomers of the same molecule arises due to the overlap between the  $\pi$ -like orbital on the methyl group and the  $\pi$ orbitals of the heterocyclic ring differing with the substitution position of the methyl group. When methylation occurs at the 2- position, the identity of the heteroatoms is particularly important. For example, the  $(V_3)$  barrier is 122.8 cm<sup>-1</sup> for 2-methylimidazole whereas for 2methyloxazole it is 251.8 cm<sup>-1</sup>.

In 2020, the monohydrate complex of thiazole was reported by W. Li *et al* with a subsequent investigation into the isomers of the dihydrate complex of thiazole reported shortly after.<sup>24, 25</sup> In each hydrate complex, the primary hydrogen-bonding interaction is between the nitrogen

atom of the thiazole moiety which acts as the hydrogen bond acceptor and an O–H of the H<sub>2</sub>O sub-unit which acts as hydrogen bond donor. An additional two hydrogen bonding interactions were observed in the dihydrate complex, a comparatively strong interaction between the two H<sub>2</sub>O molecules and a third interaction in which the second H<sub>2</sub>O molecule accepts a weak hydrogen bond from the thiazole ring. The authors of the study on the thiazole···H<sub>2</sub>O complex did not invoke the presence of a weak hydrogen bond between the O atom of H<sub>2</sub>O and a hydrogen atom located on C2 of thiazole but such an interaction was proposed for the similar complex, imidazole···H<sub>2</sub>O.<sup>26</sup>

The internal rotation and molecular geometries of *N*-methylimidazole···H<sub>2</sub>O, 2-methylimidazole···H<sub>2</sub>O, 4-methylimidazole···H<sub>2</sub>O and 5-methylimidazole···H<sub>2</sub>O have recently been studied by our group.<sup>27,c</sup> A weak hydrogen bonding interaction between the O atom of H<sub>2</sub>O and the CH<sub>3</sub> group (attached to the 2- position) was found to cause a significant increase in *V*<sub>3</sub> in 2-methylimidazole···H<sub>2</sub>O relative to the result for the 2-methylimidazole monomer.<sup>8, 27</sup> Whereas, the *V*<sub>3</sub> barrier to internal rotation of the CH<sub>3</sub> group in 4-methylimidazole····H<sub>2</sub>O was found to be lower than what was previously observed for the isolated 4-methylimidazole monomer. No significant difference between *V*<sub>3</sub> for the CH<sub>3</sub> groups in *N*-methylimidazole and *N*-methylimidazole····H<sub>2</sub>O was found, which is consistent with the H<sub>2</sub>O sub-unit binding at a position that is remote from the CH<sub>3</sub> group.<sup>8, 27</sup> The *V*<sub>3</sub> barriers to internal rotation in each of 5-methylimidazole····H<sub>2</sub>O and 5-methylimidazole where also observed to be very similar.

In this Chapter, the non-covalent interactions that are present in each of 2-methylthiazole···H<sub>2</sub>O, 4-methylthiazole···H<sub>2</sub>O and 5-methylthiazole····H<sub>2</sub>O (hereafter denoted as 2-MT···H<sub>2</sub>O, 4-MT···H<sub>2</sub>O and 5-MT····H<sub>2</sub>O respectively) will be investigated. The implications of the non-covalent interactions on the molecular geometry and the  $V_3$  barriers to internal rotation of the CH<sub>3</sub> groups will be explored. It will be shown in the case of 2-MT····H<sub>2</sub>O and 4-MT····H<sub>2</sub>O that in addition to the primary hydrogen bond between the nitrogen of thiazole and an O–H of H<sub>2</sub>O, that an additional weaker hydrogen bond interaction is present between the O atom of H<sub>2</sub>O and the CH<sub>3</sub> group. The value of  $V_3$  for the 4-MT····H<sub>2</sub>O complex is slightly lower than that for the 4-methylthiazole monomer. It will be shown that the values of  $V_3$  for the 5-methylthiazole monomer and for 5-MT····H<sub>2</sub>O are not significantly different.

<sup>&</sup>lt;sup>c</sup> 4-methylimidazole···H<sub>2</sub>O and 5-methylimidazole···H<sub>2</sub>O unpublished work by E. Gougoula *et al.* 

# 4.2 Experimental Methods

The broadband rotational spectra of each of 2-MT···H<sub>2</sub>O, 4-MT···H<sub>2</sub>O and 5- MT···H<sub>2</sub>O were recorded over the frequency range 7.0 – 18.5 GHz. The spectra were acquired in separate experiments, while probing a gaseous sample containing a low concentration of the methylthiazole sample and water in an argon carrier gas. 2-Methylthiazole (TCI Chemicals, 98 %), 4-Methylthiazole (Sigma Aldrich, 99 %) and 5-Methylthiazole (TCI Chemicals, 98 %) are liquids under ambient conditions and were used in experiments without any further purification. A reservoir containing methylthiazole located within the vacuum chamber was heated to between 50 – 60 °C (depending on the isomer being studied) allowing the introduction of the target molecule into the flow of a carrier gas directly prior to supersonic expansion. Each experiment used argon (BOC, 99.998 %) as the carrier gas with a backing pressure of 1 bar. This was found to be sufficient to record the microwave spectra of the methylthiazole monomer and generate the monohydrate complex within the supersonic expansion. An additional reservoir located within the gas line was used to introduce water into the carrier gas flow. Experiments were performed using D<sub>2</sub>O (Sigma Aldrich, 99.9 % D atom) and H<sub>2</sub><sup>18</sup>O (Sigma Aldrich, 97 % <sup>18</sup>O atom) when performing experiments to study D- and <sup>18</sup>O-containing isotopologues.

#### 4.3 Quantum Chemical Calculations

The initial estimates for the geometries of each of 2-MT···H<sub>2</sub>O, 4-MT···H<sub>2</sub>O and 5-MT···H<sub>2</sub>O were guided by the geometry of the thiazole... H<sub>2</sub>O complex. A water molecule was positioned alongside the optimised geometry of the methylthiazole monomer anticipating an intermolecular hydrogen bonding interaction with the nitrogen of the heteroaromatic ring. Geometry optimisation calculations were performed at three different levels of theory. The functional and basis set combinations which were chosen have previously been used in studies of similar complexes formed between heteroaromatic rings and H<sub>2</sub>O, <sup>26, 27</sup> reliably predicting rotational constants that were highly consistent with experimentally-determined results. Initially the geometries were optimised at the B3LYP(D3BJ)/aug-cc-pVTZ level of theory, with subsequent calculations also being performed using the \omega B97X-D/aug-cc-pVQZ and MP2/augcc-pVDZ levels. The optimised geometries of each monohydrate complex calculated at the ωB97X-D/aug-cc-pVQZ level are shown in Figure 4.1, with the associated atomic coordinates calculated at each level of theory provided in the Appendix, Tables A1 - A9. The lowest energy geometry of each of 2-MT···H<sub>2</sub>O, 4-MT···H<sub>2</sub>O and 5-MT···H<sub>2</sub>O, is calculated to be a nearprolate asymmetric top. The projection of the dipole moment onto the a-inertial axis leads to  $\mu_a$ having a significantly greater magnitude than  $\mu_b$  or  $\mu_c$  in each case. One dimensional relaxed scans were performed by scanning the  $\angle$ (H6-C6-C2-N3), energy  $\angle$ (H6-C6-C4-N3) and  $\angle$ (H6-C6-C5-C4) dihedral angles in 2-MT···H<sub>2</sub>O, 4-MT···H<sub>2</sub>O and 5-MT···H<sub>2</sub>O respectively, allowing the  $V_3$  barrier to internal rotation to be calculated for each complex. Equilibrium rotational constants ( $A_e$ ,  $B_e$ ,  $C_e$ ), nuclear quadrupole coupling constants  $(\chi_{aa}(N3), [\chi_{bb}(N3) - \chi_{cc}(N3)])$ , electric dipole moment components  $(|\mu_a|, |\mu_b|, |\mu_c|)$  and  $V_3$  barriers are summarised in Table 4.1.

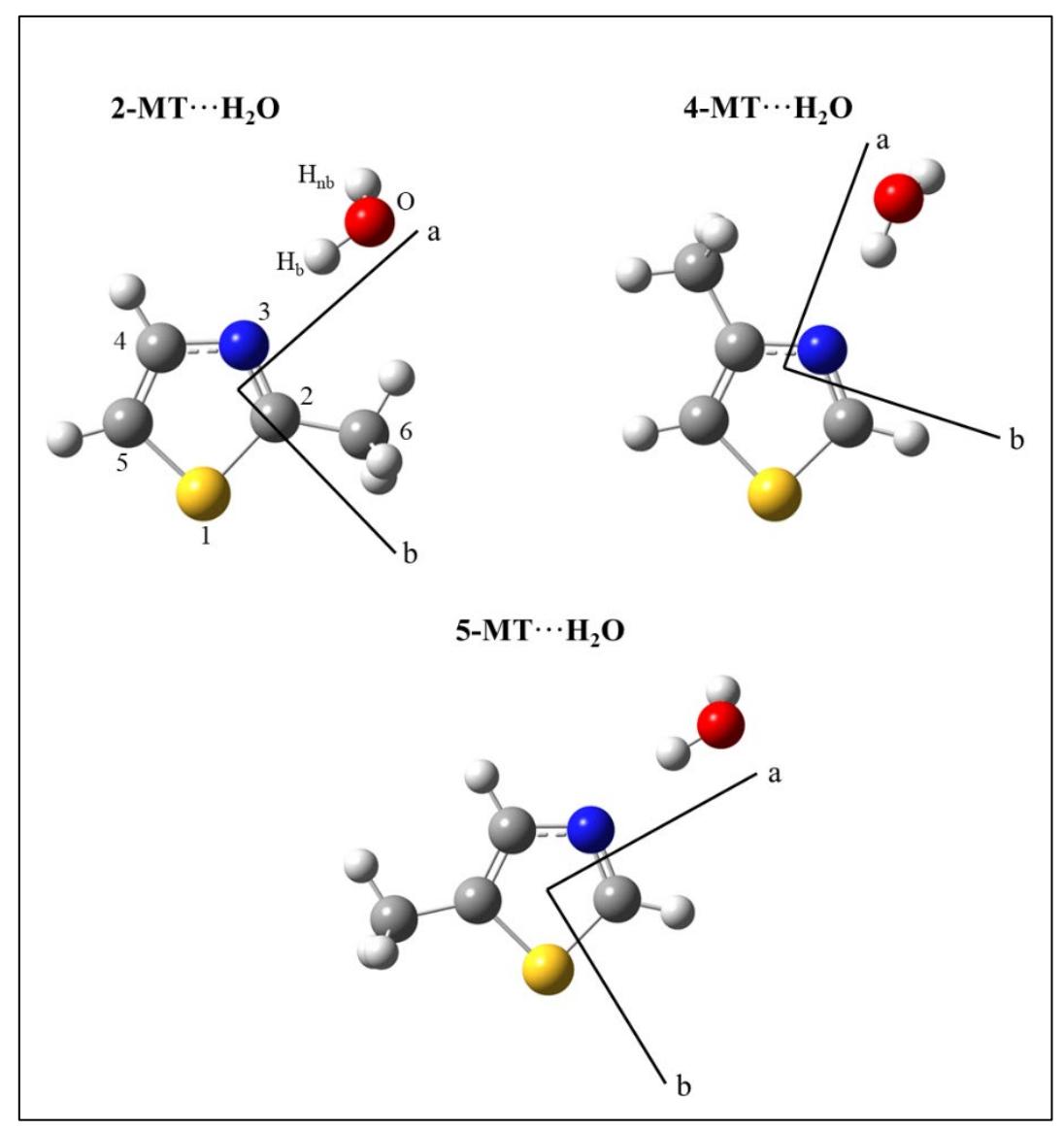


Figure 4.1 The equilibrium ( $r_e$ ) geometries of 2-MT···H<sub>2</sub>O (upper-left), 4-MT···H<sub>2</sub>O (upper-right) and 5-MT···H<sub>2</sub>O (lower) calculated at the  $\omega$ B97X-D/aug-cc-pVQZ level of theory.

Table 4.1 Spectroscopic parameters of 2-MT $\cdots$ H<sub>2</sub>O, 4-MT $\cdots$ H<sub>2</sub>O and 5-MT $\cdots$ H<sub>2</sub>O calculated at different levels of theory.<sup>a</sup>

2-MT···H₂O					
	ωB97X-D/aug-	B3LYP(D3BJ)	MP2/aug-cc-pVDZ		
	cc-pVQZ	/aug-cc-pVTZ			
$A_e$ (MHz)	3673.899	3659.982	3665.179		
$B_e$ (MHz)	1382.509	1387.510	1374.148		
$C_e  (\mathrm{MHz})$	1013.161	1014.177	1006.101		
$\chi_{aa}$ (N3) (MHz)	-3.9852	-3.8233	-3.0911		
$[\chi_{bb}(N3) - \chi_{cc}(N3)]$ (MHz)	-0.977	-0.7647	-0.6578		
$V_3 \text{ (cm}^{-1})^{6}$	-	95.370	23.204		
$ \mu_{\rm a} ,  \mu_{\rm b} ,  \mu_{\rm c}  ({\rm D})^{\rm c}$	2.91, 0.21, 1.15	2.74, 0.36, 1.05	2.64, 0.89, 0.01		
	4-MT···				
	ωB97X-D/aug-	B3LYP(D3BJ)	MP2/aug-cc-pVDZ		
	cc-pVQZ	/aug-cc-pVTZ	C		
$A_e$ (MHz)	3681.328	3753.020	4031.812		
$B_e$ (MHz)	1300.843	1291.582	1255.932		
$C_e(MHz)$	972.818	968.054	963.409		
$\chi_{aa}$ (N3) (MHz)	-3.7393	-3.5887	-2.4257		
$[\chi_{bb}(N3) - \chi_{cc}(N3)]$ (MHz)	-1.5097	-1.3805	-1.4242		
$V_3$ (cm <sup>-1</sup> )	287.173	288.398	309.154		
$ \mu_{\rm a} ,  \mu_{\rm b} ,  \mu_{\rm c}   ({\rm D})$	2.86, 0.75, 1.36	2.96, 0.17, 0.95	2.82, 0.19, 0.0		
	5-MT···				
	ωB97X-D/aug-	B3LYP(D3BJ)	MP2/aug-cc-pVDZ		
	cc-pVQZ	/aug-cc-pVTZ	0 1		
$A_e$ (MHz)	4532.340	4318.523	4740.083		
$B_e$ (MHz)	1091.668	1096.919	1085.845		
$C_e(\mathrm{MHz})$	887.458	882.231	890.486		
$\chi_{aa}$ (N3) (MHz)	-3.7701	-3.8673	-2.9369		
$[\chi_{bb}(N3) - \chi_{cc}(N3)]$ (MHz)	-1.8699	-1.3865	-1.0101		
$V_3$ (cm <sup>-1</sup> )	297.946	318.831	283.265		
$ \mu_{\rm a} ,  \mu_{\rm b} ,  \mu_{\rm c}   ({\rm D})$	4.13, 0.49, 1.30	4.30, 0.35, 1.37	3.85, 0.66, 1.17		

<sup>&</sup>lt;sup>a</sup> Calculated rotational constants are in the equilibrium geometry  $(A_e, B_e, C_e)$  whereas experimentally determined rotational constants are in the zero-point state  $(A_0, B_0, C_0)$ .

<sup>&</sup>lt;sup>b</sup> The  $V_3$  barrier was calculated by scanning ∠(H6–C6–C2–N3) for 2-MT···H<sub>2</sub>O, ∠(H6–C6–C4–N3) for 4-MT···H<sub>2</sub>O and ∠(H6–C6–C5–C4) for 5-MT···H<sub>2</sub>O.

<sup>&</sup>lt;sup>c</sup> Electric dipole moment components along the principal inertial axes.

# 4.4 Spectral Analysis and Assignment

Separate experiments were performed to obtain the rotational spectra, over the  $7.0 - 18.5 \, \mathrm{GHz}$ frequency region, for each of the target molecules (2-methylthiazole, 4-methylthiazole or 5methylthiazole) using the experimental procedures outlined in Section 4.2. The spectra acquired were averaged over 1.56 M, 1.62 M and 1.47 M FID's which correspond to approximately 26, 27, 24.5 hours of data collection respectively. The most intense transitions in each spectrum recorded were those of the methylthiazole monomer (2-methylthiazole, 4-methylthiazole or 5methylthiazole as appropriate to the experiment being performed). For each of the methylthiazole monomers, splitting of rotational transitions into A- and E- species transitions was observed owing to the presence of the CH<sub>3</sub> internal rotor. The  $V_3$  barrier to internal rotation of the CH<sub>3</sub> group in each of 4-methylthiazole and 5-methylthiazole are reported to be 357.6 and 332.0 cm<sup>-1</sup> respectively.<sup>6, 7</sup> Pairs of transitions for each of the 4-methylthiazole and 5methylthiazole monomers were readily identified in the spectrum since the magnitude of the  $V_3$ barrier in each case leads to a relatively small frequency interval between A- and E- species transitions of a given rotational transition. The V<sub>3</sub> barrier of the CH<sub>3</sub> group in the 2methylthiazole<sup>4, 5</sup> monomer is reported to be much lower (34.1 cm<sup>-1</sup>) than those of 4methylthiazole and 5-methylthiazole. Therefore, the frequency interval of the observed splitting is much greater. Transitions of the water dimer,  $(H_2^{16}O)_2^{28, 29}$  at 7354.864, 8344.588 and 12320.997 MHz were consistently observed during initial experiments, indicating that water was present within the supersonic expansion, therefore, hydrate complexes formed with the methylthiazole isomers were subsequently searched for.

# 4.4.1 Effective (A- species only) fits

The optimised geometry of each of 2-MT···H<sub>2</sub>O, 4-MT···H<sub>2</sub>O and 5-MT···H<sub>2</sub>O (Figure 4.1) was calculated to be a near-prolate asymmetric top with the strongest dipole moment component along the a-inertial axis. In each spectrum, transitions fitted to Watson's S-reduced Hamiltonian<sup>30, 31</sup> were tentatively assigned to the parent (H<sub>2</sub><sup>16</sup>O) isotopologue of the monohydrate complex of each isomer of methylthiazole. Initial fits were performed using PGOPHER<sup>32</sup> and considered A-species ( $\sigma = 0$ ) transitions only. The *effective* rotational constants, centrifugal distortion constants and nuclear quadrupole coupling constants determined for each of 2-MT···H<sub>2</sub><sup>16</sup>O, 4-MT···H<sub>2</sub><sup>16</sup>O and 5-MT···H<sub>2</sub><sup>16</sup>O are displayed in Tables 4.2 - 4.4. Good agreement between the experimentally determined *effective* rotational constants ( $A_0$ ',  $B_0$ ',  $C_0$ ') and equilibrium rotational constants ( $A_e$ ,  $B_e$ ,  $C_e$ ) predicted by theory were observed for each monohydrate complex. The assignment of each complex consisted of

a-type transitions only, no b- or c- type transitions were able to be observed within the spectrum. When calculated at the ωB97X-D/aug-cc-pVQZ level for 2-MT···H<sub>2</sub>O, 4-MT···H<sub>2</sub>O and 5-MT···H<sub>2</sub>O respectively, the values of  $\mu_a$  are 2.91 D, 2.86 D and 4.13 D, those for  $\mu_b$  are 0.21 D, 0.75 D and 0.49 D and those for  $\mu_c$  are 1.15 D, 1.36 D and 1.30 D. The rapid zero-point vibrational motion of the monohydrate complex (explained in more detail in Section 4.5) will mean that the average of  $\mu_c$  in the zero-point state is much lower than implied by the  $r_e$  result. The projection of the dipole moment onto the a-inertial axis leads to  $\mu_a$  having a considerably greater magnitude than either  $\mu_b$  or  $\mu_c$  in each complex. Transition intensities are proportional to the square of the dipole moment, therefore, it is unsurprising that b- and c-type transitions were not identified for each monohydrate complex. Rotational transitions for each monohydrate complex are split into A- and E-species transitions, like what was observed for the isolated monomers, due to the presence of the CH<sub>3</sub> internal rotor, which will be discussed in Section 4.4.2. In addition to splitting's due to internal rotation, transitions of each torsional sub-level exhibit hyperfine structure owing to the presence of one quadrupolar nucleus ( $^{14}$ N, I = 1). Nuclear quadrupole coupling constants were therefore included in the fit to model the hyperfine structure of each transition. Values obtained for  $\chi_{aa}(N3)$ ,  $\chi_{bb}(N3)$  and  $\chi_{cc}(N3)$  which are in the inertial axis system, were transformed into the principal axis system, to facilitate direct comparison of nuclear quadrupole coupling constants determined for the methylthiazole···H<sub>2</sub>O complexes with those of the respective methylthiazole monomer<sup>4-7</sup> and thiazole.<sup>2</sup> The transformation was performed using the program QDIAG<sup>33</sup> and utilised the off-diagonal term,  $\chi_{ab}$ , calculated at the  $\omega$ B97X-D/aug-cc-pVQZ level of theory to generate  $\chi_{xx}(N3)$ ,  $\chi_{yy}(N3)$  and  $\chi_{zz}(N3)$  for each complex. The diagonalised nuclear quadrupole coupling constants generated for each of 2-MT···H<sub>2</sub>O, 4-MT···H<sub>2</sub>O and 5-MT···H<sub>2</sub>O are displayed in the Appendix, A.10. It can be observed that the magnitudes of the nuclear quadrupole coupling constants of each monohydrate complex are lower than those previously observed for thiazole and the methylthiazole monomer. As discussed in Chapter 2, nuclear quadrupole coupling constants are sensitive to changes in the electronic environment around the nitrogen nucleus, therefore, a change in the diagonalised values upon the formation of each monohydrate complex implies that there is a slight change in the electric field gradient at N3 (relative to that of the isolated monomer) upon the attachment of H<sub>2</sub>O. However, particularly in 4-MT···H<sub>2</sub>O and 5-MT···H<sub>2</sub>O the uncertainties are large relative to the parameter values, so it is not possible to confirm this effect with certainty nor any consequences for the  $V_3$  barriers within the complexes.

Experiments were performed using H<sub>2</sub><sup>18</sup>O, D<sub>2</sub>O and HDO allowing the assignment of additional isotopologues where the isotopic substitution is achieved at the H<sub>2</sub>O sub-unit. For each of 2-

MT···H<sub>2</sub>O, 4-MT···H<sub>2</sub>O and 5-MT···H<sub>2</sub>O an additional three singly substituted isotopologues (H<sub>2</sub><sup>18</sup>O, DOH and HOD) and one multiply substituted isotopologue (D<sub>2</sub>O) was assigned. The assignment of additional isotopologues further confirmed that the molecular carrier of each spectrum had been correctly assigned. Spectroscopic parameters determined in the effective (Aspecies only) fits for each isotopologue are given in Tables 4.2 - 4.4. For each isotopologue  $\chi_{aa}(N3)$  was determined during the fit. However,  $[\chi_{bb}(N3) - \chi_{cc}(N3)]$  was determined only for the parent (H216O) isotopologue and was held fixed at this result when fits of other isotopologues were performed. Experiments performed herein exclusively used argon as the backing gas. Argon is known to encourage relaxation to conformers of low energy within the supersonically expanding gas jet.34 The spectra of higher-energy isomers of each methylthiazole···H<sub>2</sub>O complex were searched for, however, were unable to be assigned. The study of thiazole...H<sub>2</sub>O<sup>24</sup> identified the spectrum of only one isomer of this complex while using helium as the carrier gas. It is known that helium is less efficient at relaxation, therefore, is more likely to allow for the generation and study of higher-energy isomers. Spectral transitions assigned to each of 2-MT···H<sub>2</sub>O, 4-MT···H<sub>2</sub>O and 5-MT···H<sub>2</sub>O showed no evidence of any large amplitude motions associated with the H<sub>2</sub>O sub-unit, consistent with the observation of other similar complexes in which the H<sub>2</sub>O is the hydrogen bond donor.<sup>24, 26, 27</sup>

Table 4.2 Spectroscopic constants determined for five isotopologues of 2-MT···H<sub>2</sub>O by A- species only (effective) fits performed using PGOPHER.

		$2-MT\cdots H_2$	C		
	$H_2^{16}O$	$H_2^{18}O$	DOH	HOD	$D_2O$
$A_0'(\text{MHz})$	3710.790(20) <sup>a</sup>	3704.777(19)	3698.509(23)	3685.982(31)	3674.602(35)
$B_0'$ (MHz)	1370.92962(99)	1288.45381(87)	1348.9649(12)	1315.6152(12)	1295.7135(13)
$C_0'$ (MHz)	1004.3490(11)	958.96521(86)	991.6850(11)	972.8360(12)	961.2353(12)
$D_{J}(\mathrm{kHz})$	0.2234(44)	0.2266(30)	0.2199(49)	0.2132(54)	0.2169(64)
$D_{JK}$ (kHz)	5.681(25)	5.420(23)	5.573(42)	5.330(40)	5.271(85)
$d_1$ (kHz)	-0.0956(55)	-0.0827(37)	-0.0945(55)	-0.0676(50)	-0.0793(57)
$d_2$ (kHz)	-0.0591(33)	-0.0493(23)	-0.0462(55)	-0.0421(35)	-0.0414(36)
$\chi_{aa}$ (N3) (MHz)	-3.560(15)	-3.559(16)	-3.459(30)	-3.629(36)	-3.670(39)
$\left[\chi_{bb}\left(N3\right)-\chi_{cc}\left(N3\right)\right]$	-0.562(43)	$[-0.562]^{b}$	[-0.562]	[-0.562]	[-0.562]
$\sigma_{rms} (kHz)^{c}$	9.9	9.1	10.9	11.6	12.5
$N^{\mathrm{d}}$	74	82	59	58	52
$\Delta_0'$ (u Å <sup>2</sup> )	-1.6408(10)	-1.6451(9)	-1.6696(11)	-1.7569(14)	-1.8122(15)
$P'_{aa}(u \text{ Å}^2)$	367.8193(5)	391.4143(4)	373.8073(5)	383.2605(7)	389.1330(8)
$P_{bb}^{(u)}$ (u Å <sup>2</sup> )	135.3714(5)	135.5903(4)	135.8092(5)	136.2299(7)	136.6269(8)
$P_{cc}^{\prime}$ (u Å <sup>2</sup> )	0.8204(5)	0.8225(4)	0.8348(5)	0.8784(7)	0.9061(8)

<sup>&</sup>lt;sup>a</sup> Numbers in parentheses are one standard deviation in units of the last significant figure.

<sup>&</sup>lt;sup>b</sup> The value of  $[\chi_{bb}$  (N3) –  $\chi_{cc}$  (N3)] fixed to the value determined for 2-MT···H<sub>2</sub><sup>16</sup>O.

<sup>&</sup>lt;sup>c</sup> Root mean square (rms) deviation of the fit.

<sup>&</sup>lt;sup>d</sup> Number of hyperfine components included in the fit.

Table 4.3 Spectroscopic constants determined for five isotopologues of 4-MT···H<sub>2</sub>O by A- species only (effective) fits performed using PGOPHER.

-		4-MT···H₂O			
	H <sub>2</sub> <sup>16</sup> O	$\frac{4 \text{ W1} \text{ H}_2 \text{ S}}{\text{H}_2^{18} \text{O}}$	DOH	HOD	$D_2O$
$A_0'(MHz)$	3863.593(29) <sup>a</sup>	3829.970(45)	3838.701(58)	3810.250(59)	3787.508(75)
$B_0^{0}$ (MHz)	1262.9442(17)	1193.8902(16)	1245.9908(27)	1218.7228(33)	1203.1565(15)
$C_0'$ (MHz)	958.38922(100)	916.1630(13)	947.0710(22)	929.9074(25)	919.5068(18)
$D_J(kHz)$	0.2380(80)	0.2039(62)	0.231(14)	0.213(20)	0.213(13)
$D_{JK}$ (kHz)	2.309(64)	2.761(61)	2.32(22)	2.24(14)	2.08(28)
$d_1(\mathrm{kHz})$	-0.0421(61)	-0.0422(60)	-0.039(12)	-0.051(14)	-
$\chi_{aa}$ (N3) (MHz)	-3.247(46)	-3.344(34)	-3.28(14)	-3.27(11)	-3.31(13)
$[\chi_{bb} (N3) - \chi_{cc} (N3)] (MHz)$	-1.30(28)	$[-1.30]^{b}$	[-1.30]	[-1.30]	[-1.30]
$\sigma_{rms} (kHz)^c$	22.9	18.0	23.7	23.8	24.1
$N^{\mathrm{d}}$	82	77	48	44	38
$\Delta_0'$ (u Å <sup>2</sup> )	-3.6436(12)	-3.6326(17)	-3.6346(24)	-3.8435(27)	-3.8577(29)
$P'_{aa}$ (u Å <sup>2</sup> )	398.3376(6)	421.4882(9)	403.7868(12)	412.7574(14)	418.1154(15)
$P_{hh}^{\prime\prime}$ (u Å <sup>2</sup> )	128.9836(6)	130.1375(9)	129.8363(12)	130.7149(14)	131.5042(15)
$P_{cc}^{\prime}$ (u Å <sup>2</sup> )	1.8218(6)	1.8163(9)	1.8173(12)	1.9218(14)	1.9289(15)

<sup>&</sup>lt;sup>a</sup> Numbers in parentheses are one standard deviation in units of the last significant figure.

<sup>&</sup>lt;sup>b</sup> The value of  $[\chi_{bb}$  (N3) –  $\chi_{cc}$  (N3)] fixed to the value determined for 4-MT···H<sub>2</sub><sup>16</sup>O.

<sup>&</sup>lt;sup>c</sup> Root mean square (rms) deviation of the fit.

<sup>&</sup>lt;sup>d</sup> Number of hyperfine components included in the fit.

Table 4.4 Spectroscopic constants determined for five isotopologues of 5-MT···H<sub>2</sub>O by A- species only (effective) fits performed using PGOPHER.

		$5-MT\cdots H_2O$			
	$H_2^{16}O$	$H_2^{18}O$	DOH	HOD	$D_2O$
$A_0'(MHz)$	4859.032(66) <sup>a</sup>	4856.524(91)	4833.356(64)	4829.876(14)	4805.957(96)
$B_0'$ (MHz)	1085.71851(67)	1021.60625(67)	1066.47904(62)	1042.9804(12)	1025.58745(86)
$C_0'$ (MHz)	892.51934(75)	848.6413(11)	878.64582(81)	863.11291(93)	850.42008(100)
$D_{J}\left(\mathrm{kHz}\right)$	0.1808(42)	0.1887(36)	0.1793(38)	0.1401(69)	0.1678(59)
$D_{JK}\left(\mathrm{kHz}\right)$	12.089(24)	11.430(64)	11.682(67)	7.86(21)	10.85(11)
$\chi_{aa}$ (N3) (MHz)	-2.936(62)	-2.939(85)	-2.91(10)	-2.80(15)	-2.55(28)
$\left[\chi_{bb}\left(N3\right)-\chi_{cc}\left(N3\right)\right]\left(MHz\right)$	-1.17(39)	$[-1.17]^{b}$	$[-1.17]^{b}$	$[-1.17]^{b}$	$[-1.17]^{b}$
$\sigma_{rms} (kHz)^{c}$	16.7	16.5	16.9	20.9	18.9
$N^{\mathrm{d}}$	68	64	61	39	52
$\Delta_0'$ (u Å <sup>2</sup> )	-3.2483(15)	-3.2370(21)	-3.2574(15)	-3.6582(9)	-3.6572(23)
$P'_{aa}$ (u Å <sup>2</sup> )	463.8547(8)	493.0721(11)	472.2475(8)	482.7236(4)	490.9417(11)
$P'_{bb}$ (u Å <sup>2</sup> )	102.3840(8)	102.4434(11)	102.9320(8)	102.8069(4)	103.3282(11)
$P_{cc}^{\prime\prime}$ (u Å <sup>2</sup> )	1.6242(8)	1.6185(11)	1.6287(8)	1.8291(4)	1.8286(11)

<sup>&</sup>lt;sup>a</sup> Numbers in parentheses are one standard deviation in units of the last significant figure.

<sup>&</sup>lt;sup>b</sup> The value of  $[\chi_{bb}$  (N3) –  $\chi_{cc}$  (N3)] fixed to the value determined for 5-MT···H<sub>2</sub><sup>16</sup>O.

<sup>&</sup>lt;sup>c</sup> Root mean square (rms) deviation of the fit.

<sup>&</sup>lt;sup>d</sup> Number of hyperfine components included in the fit.

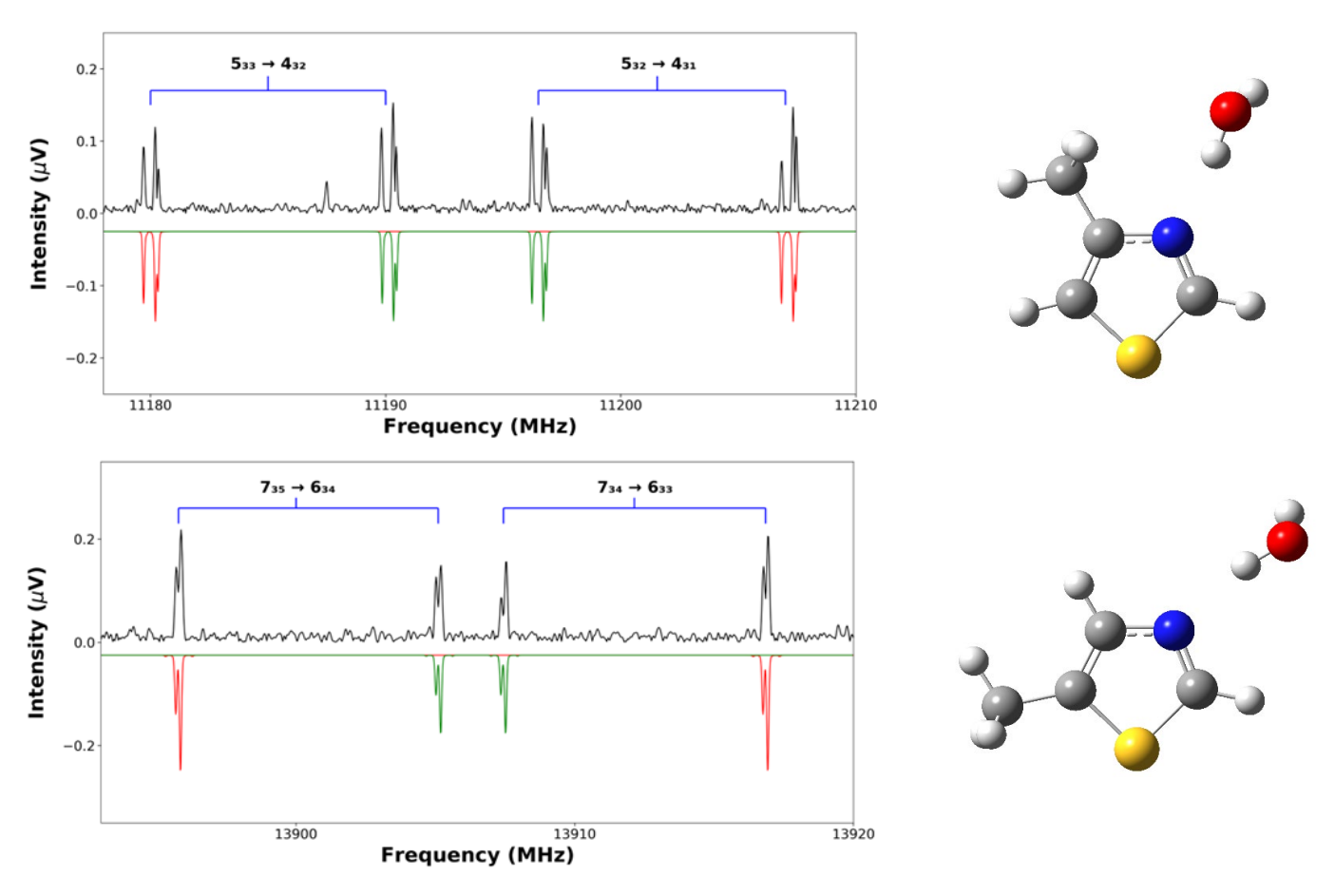


Figure 4.2 Small section of the rotational spectrum of  $4\text{-MT}\cdots H_2O$  (upper panel) and  $5\text{-MT}\cdots H_2O$  (lower panel). Two rotational transitions of each complex are displayed. The experimental spectrum (black) is shown above a simulation (red and green). The simulation for the *E*-species (green) is generated by moving the *A*-species (red) simulation by an appropriate amount of MHz.

# 4.4.2 Internal rotation and global fits

As mentioned earlier, the  $V_3$  barrier to internal rotation of the methyl group in each of the isomers of methylthiazole have been studied previously. 4-7 The published results for the 4- and 5-methylthiazole monomers as well as results of potential energy scans performed for each monohydrate complex, provide a sufficient prediction of  $V_3$  for 4-MT···H<sub>2</sub>O and 5-MT···H<sub>2</sub>O, such that E- species transitions were readily identified in the spectrum for each of these complexes. The A- and E- species transitions for a given rotational transition exhibit the same hyperfine structure, as shown in Figure 4.2, which aided the assignment. For 2-MT···H<sub>2</sub>O, the situation is different and is an example of a more challenging case. The  $V_3$  barrier determined for 2-methylthiazole (34.1 cm<sup>-1</sup>) is significantly lower than that observed for the other two structural isomers of methylthiazole. It will be shown in Sections 4.5 and 4.6 (Molecular geometries and Non-Covalent Interactions) that the molecular geometry of 2-MT···H<sub>2</sub>O is as shown in Figure 4.1 and that a weak hydrogen bond is present within this complex between the O atom of  $H_2O$  and the closest H atom on the  $CH_3$  group. It is probable that a change in the  $V_3$ barrier to internal rotation will occur upon the formation of the monohydrate complex based on the observation of other studies where H<sub>2</sub>O binds to a molecule adjacent to a CH<sub>3</sub> group. <sup>27, 35-38</sup> Quantum chemical calculations performed and discussed in Section 4.3 provide very different predictions for the  $V_3$  barrier height depending on the level of theory used, however, each predict the barrier height to be less than 100 cm<sup>-1</sup>. Although it is likely that the barrier height will change, it will remain much lower than the magnitude of the barriers determined for 4-MT···H<sub>2</sub>O and 5-MT···H<sub>2</sub>O. Analysis of the methyl internal rotation within 2-MT···H<sub>2</sub>O and preparation of global fits is still ongoing, for this reason, only the global fits of 4-MT···H<sub>2</sub>O and 5-MT···H<sub>2</sub>O will be discussed further in this section. Observations from interim global fits of 2-MT···H<sub>2</sub>O performed using XIAM will be discussed in Section 4.8.

Two alternative methods were used to perform global fits which simultaneously fitted both A- $(\sigma=0)$  and E- $(\sigma=\pm1)$  species transitions. Global fits of 4-MT···H<sub>2</sub><sup>16</sup>O and 5-MT···H<sub>2</sub><sup>16</sup>O were performed using the programs XIAM<sup>39</sup> and BELGI-C<sub>s</sub>-hyperfine<sup>40, 41</sup> which each employ a different frame of reference for the treatment of internal rotation. The XIAM code uses the combined axis method<sup>42</sup> (CAM) whereas the BELGI-C<sub>s</sub>-hyperfine program uses the rho axis method<sup>40</sup> (RAM). Each method and program were described in more detail in Section 2.8 of Chapter 2. Parameters were fitted using each program, allowing the dependencies of the results on the specific Hamiltonian model to be investigated. The experiments performed during the present work probe complexes in their torsional ground states ( $v_t = 0$ ) preventing the independent determination of the internal rotational constant,  $F_0$  and  $V_3$  (see equations in

Chapter 2, Section 2.8). Previous studies on 4-methylthiazole and 5-methylthiazole by Jäger and Mäder reported that the moments of inertia of the methyl top,  $I_a$ , to be 3.1743(10) and 3.1860(69) u Å<sup>2</sup> respectively which imply  $F_0$  of 159.21(5) GHz and 158.63(34) GHz respectively.<sup>6, 7</sup> However, in the global fits performed using XIAM for 4-MT···H<sub>2</sub><sup>16</sup>O and 5-MT···H<sub>2</sub><sup>16</sup>O the value of  $F_0$  was assumed to be 160 GHz in each case. This assumption was made due to an upcoming publication on the updated analysis of the 4-methylthiazole and 5-methylthiazole monomers<sup>d</sup> which will assume  $F_0 = 160$  GHz (*ab initio* value calculated at the MP2(ae)/6-311++G(d,p) level) in the global fits of each monomer. Each BELGI-C<sub>s</sub>-hyperfine fit uses a fixed value for the reduced internal rotation constant, F, which leads to assumed values of 161.84 GHz and 164.61 GHz for 4-MT···H<sub>2</sub>O and 5-MT···H<sub>2</sub>O complexes respectively.

Each fit performed assumed that the axis of the CH<sub>3</sub> rotor lies in the ab plane of each complex. Rotational constants  $(A_0, B_0 \text{ and } C_0)$ , centrifugal distortion constants  $(D_J, D_{JK})$  and the nuclear quadrupole coupling constant ( $\chi_{aa}(N3)$ ) were determined for 4-MT···H<sub>2</sub>O and 5-MT···H<sub>2</sub>O during the fits performed using XIAM. An additional centrifugal distortion constant,  $d_1$ , was included to achieve a satisfactory fit for isotopologues of 4-MT···H<sub>2</sub>O. In each XIAM fit performed, the value of  $[\chi_{bb}(N3) - \chi_{cc}(N3)]$  was held fixed to the value determined in the effective (A-species only) fit for the parent isotopologue. Internal rotation parameters,  $V_3$  and  $\angle(i, b)$  which denotes the angle between the CH<sub>3</sub> rotor axis and the b inertial axis were determined by fits performed using XIAM. The root mean square deviation of the fit performed for each of 4-MT···H<sub>2</sub><sup>16</sup>O and 5-MT···H<sub>2</sub><sup>16</sup>O was 21.9 kHz and 20.5 kHz respectively which is approximately two times the measurement accuracy expected for unblended lines. The  $V_3$ barrier and  $\angle(i, b)$  was also determined during fits performed using BELGI-C<sub>s</sub>-hyperfine<sup>e</sup> along with  $\rho$  and  $D_{AB}$  which are parameters in the vibration-rotation-torsion Hamiltonian used by the analysis. 40 The  $\rho$  parameter represents the coupling constant between internal and global rotation and  $D_{AB}$  is related to the angle between the RAM and the PAM axis framework. The rms deviations of the fits performed for 4-MT···H<sub>2</sub><sup>16</sup>O and 5-MT···H<sub>2</sub><sup>16</sup>O using BELGI-C<sub>s</sub>hyperfine was of 20.5 kHz and 17.7 kHz respectively.

-

<sup>&</sup>lt;sup>d</sup> Unpublished work by K. Koziol and H. V. L. Nguyen. Reported in Microwave Spectroscopy Information Letter, Vol. LXVI

<sup>&</sup>lt;sup>e</sup> BELGI-C<sub>s</sub>-hyperfine fits for 4-MT···H<sub>2</sub><sup>16</sup>O and 5-MT···H<sub>2</sub><sup>16</sup>O performed by Isabelle Kleiner (Université de Paris and Université Paris Est Creteil)

Table 4.5 Results of XIAM and BELGI-C<sub>s</sub>-hyperfine fits of spectroscopic parameters to the frequencies of A- and E-species transitions of the main isotopologues.

	$4-MT\cdots H_2^{16}O$		5-MT···]	$H_2^{16}O$
	XIAM <sup>a</sup>	BELGI <sup>b</sup>	XIAM <sup>a</sup>	BELGI <sup>b</sup>
$A_0$ (MHz)	3863.381(53) <sup>c</sup>	3863(21)	4857.887(94) <sup>c</sup>	4857.9(16)
$B_0$ (MHz)	1262.9188(25)	1263(21)	1085.7196(10)	1085.7(16)
$C_0$ (MHz)	958.3805(22)	958.37546(84)	892.5126(11)	892.5059(11)
$D_{J}\left( \mathrm{kHz}\right)$	0.2430(97)	-	0.1835(57)	-
$D_{JK}$ (kHz)	2.123(84)	-	12.051(37)	-
$d_1(\text{kHz})$	-0.0604(97)	-	-	-
$\chi_{aa}$ (N3) (MHz)	-3.252(19)	-3.248(42)	-2.949(37)	-2.959(53)
$\left[\chi_{bb}\left(N3\right)-\chi_{cc}\left(N3\right)\right]$	$[-1.30]^{d}$	-1.165(97)	$[-1.17]^{d}$	-1.18(15)
(MHz)		, ,		
$F_0$ (GHz)	$[160.0]^{e}$	[160.0]	[160.0]	[160.0]
$V_3 \text{ (cm}^{-1})$	340.05(56)	329(5)	325.16(38)	329(4)
$\angle (i, b) (^{\circ})$	45.38(39)	43.6(10)	71.66(71)	72.10(51)
$\Delta_0$ (u Å <sup>2</sup> )	-3.6540(23)	-3.670(41)	-3.2681(22)	-3.2612(16)
$\sigma_{\rm RMS}$ (kHz)	21.9	20.5	20.5	17.7
$N_{ m A}$ / $N_{ m E}$ $^{ m f}$	82/54	82/54	68/53	68/53

<sup>&</sup>lt;sup>a</sup> Values in the principal axis system.

<sup>&</sup>lt;sup>b</sup> Values after transformation into the principal axis system. Detailed results of BELGI-C<sub>s</sub>-hyperfine fits in the Rho Axis System (including centrifugal distortion constants) are provided in Table A.11. Centrifugal distortion constants determined by BELGI-C<sub>s</sub>-hyperfine cannot be directly compared with those determined by XIAM because of the different models employed.

<sup>°</sup> The results of the  $\omega$ B97X-D/aug-cc-pVQZ calculation are  $A_e$  = 3681.328 MHz ,  $B_e$  = 1300.843 MHz and  $C_e$  = 972.818 MHz for 4-MT···H<sub>2</sub>O and  $A_e$  = 4532.340 MHz,  $B_e$  = 1091.668 MHz and  $C_e$  = 887.458 MHz for 5-MT···H<sub>2</sub>O.

<sup>&</sup>lt;sup>d</sup> [ $\chi_{bb}(N3) - \chi_{cc}(N3)$ ] held fixed to the value determined by the *A*-species only (*effective*) fit for 4-MT···H<sub>2</sub><sup>16</sup>O or 5-MT···H<sub>2</sub><sup>16</sup>O as appropriate (see Tables 4.3, 4.4).

<sup>&</sup>lt;sup>e</sup> The values of  $F_0$  are fixed to 160 GHz (see text for justification).

 $<sup>^{\</sup>rm f}$   $N_{\rm A}$  and  $N_{\rm E}$  denote the number of A-species and E- species transitions respectively included in the fit.

The results of the global fits for 4-MT···H<sub>2</sub><sup>16</sup>O and 5-MT···H<sub>2</sub><sup>16</sup>O are displayed in Table 4.5 while the results of the XIAM fits for additional isotopologues are presented in Tables 4.6 and 4.7. For 4-MT···H<sub>2</sub><sup>16</sup>O, the  $V_3$  barrier was determined to be 340.05(56) cm<sup>-1</sup> and 329(5) cm<sup>-1</sup> when fits were performed using XIAM and BELGI-C<sub>s</sub>-hyperfine respectively. Whereas for 5- $MT \cdots H_2^{16}O$ ,  $V_3$  was determined to be 325.16(38) cm<sup>-1</sup> and 329(4) cm<sup>-1</sup>. These results compare with the published results for the 4-methylthiazole<sup>6</sup> and 5-methylthiazole<sup>7</sup> monomers of 357.6(1) cm<sup>-1</sup> and 332.0(8) cm<sup>-1</sup> respectively (determined using the internal axis method). The values of  $V_3$  are sensitive to changes in the assumed values of F and  $F_0$ . For example, if the value of  $F_0$  was assumed to be consistent with the  $F_0$  result generated from  $I_\alpha$  reported by Jäger and Mäder (159.21 GHz rather than 160.0 GHz),  $V_3$  is determined to be 338.53(56) cm<sup>-1</sup> using XIAM, which is slightly lower than the value reported in Table 4.5. The parameter  $\angle(i, b)$  was determined to be 45.38(39) and 43.6(10)° for 4-MT···H<sub>2</sub><sup>16</sup>O and to be 71.66(71)° and 72.10(51)° for 5-MT···H<sub>2</sub><sup>16</sup>O when fits were performed using XIAM and BELGI-C<sub>s</sub>-hyperfine respectively. In the  $r_0$  geometries of 4-MT···H<sub>2</sub>O and 5-MT···H<sub>2</sub>O (which will be discussed in detail in Section 4.5)  $\angle(i, b)$  is 46.7(33)° and 70.9(18)° respectively, which are similar to the values obtained in the global fits. It can be observed that across the range of isotopologues the values of  $V_3$  and  $\angle(i, b)$  determined during the global fits vary slightly. Slight variations are to be expected owing to statistical variance, changes in zero-point effects on isotopic substitution and slight changes in the orientation of inertial axes upon isotopic substitution.

Table 4.6 Spectroscopic parameters determined from global (XIAM) fits obtained by fitting to the frequencies of A- and E- species transitions for five isotopologues of 4-MT···H<sub>2</sub>O.

	$H_2^{16}O$	$H_2^{18}O$	DOHa	HODa	D <sub>2</sub> O
$A_{\theta}$ (MHz)	3863.381(53) <sup>b</sup>	3829.702(62)	3838.532(84)	3809.98(10)	3787.428(93)
$B_{\theta}\left(\mathrm{MHz}\right)$	1262.9188(25)	1193.8656(25)	1245.9618(17)	1218.7017(42)	1203.1367(30)
$C_{\theta}\left(\mathrm{MHz}\right)$	958.3805(22)	916.1610(22)	947.0629(22)	929.9048(39)	919.4958(33)
$D_J(\mathrm{kHz})$	0.2430(97)	0.2141(94)	0.198(17)	0.255(19)	0.214(17)
$D_{J\!K}\left(\mathrm{kHz}\right)$	2.123(84)	2.937(86)	2.08(29)	2.23(28)	1.82(38)
$d_1$ (kHz)	-0.0604(97)	-0.0421(98)	[-0.039]	-0.061(19)	-0.069(16)
$\chi_{aa}$ (N3) (MHz)	-3.252(19)	-3.335(22)	-3.198(84)	-3.275(63)	-3.344(63)
$[\chi_{bb}(N3) - \chi_{cc}(N3)] \text{ (MHz)}$	[-1.30]	[-1.30]	[-1.30]	[-1.30]	[-1.30]
$F_0$ (GHz)	$[160.0]^{c}$	[160.0]	[160.0]	[160.0]	[160.0]
$V_3$ (cm <sup>-1</sup> )	340.05(56)	339.43(70)	339.50(97)	344.2(12)	342.21(11)
$\angle (i, b)$ (°)	45.38(39)	44.17(46)	45.68(71)	44.72(85)	44.12(74)
$\Delta_0$ (u Å)	-3.6540(23)	-3.6493(27)	-3.6453(32)	-3.859(4)	-3.861(4)
$\sigma_{RMS}$ (kHz)	21.9	22.9	28.6	28.7	21.9
$N_{ m A}/N_{ m E}^{ m d}$	82/54	77/44	48/29	44/17	38/20

<sup>&</sup>lt;sup>a</sup> The ordering of atoms is  $H_bOH_{nb}$  such that  $H_b$  is deuterium for the isotopologue denoted as "DOH".

<sup>&</sup>lt;sup>b</sup> Numbers in parentheses are one standard deviation in units of the last significant figure.

<sup>&</sup>lt;sup>c</sup> The value of  $F_0$  is fixed to 160 GHz.

 $<sup>^{\</sup>rm d}N_{\rm A}$  and  $N_{\rm E}$  denote the number of A- species and E- species transitions respectively included in the fit.

Table 4.7 Spectroscopic parameters determined from global (XIAM) fits obtained by fitting to the frequencies of A- and E- species transitions for five isotopologues of 5-MT···H<sub>2</sub>O.

	$H_2^{16}O$	$H_2^{18}O$	DOH <sup>a</sup>	HODa	D <sub>2</sub> O
$A_{\theta}$ (MHz)	4857.887(94) <sup>b</sup>	4855.47(11)	4832.393(93)	4829.07(27)	4804.82(18)
$B_{\theta}$ (MHz)	1085.7196(10)	1021.60693(83)	1066.48040(90)	1042.9847(25)	1025.5885(16)
$C_{\theta}\left(\mathrm{MHz} ight)$	892.5126(11)	848.6339(14)	878.6371(12)	863.1044(23)	850.4142(18)
$D_J(\mathrm{kHz})$	0.1835(57)	0.1873(46)	0.1753(55)	0.145(11)	0.172(10)
$D_{JK}$ (kHz)	12.051(37)	11.359(78)	11.707(98)	8.10(35)	10.98(20)
$\chi_{aa}(N3)$ (MHz)	-2.949(37)	-2.915(39)	-2.907(49)	-2.74(12)	-2.86(10)
$[\chi_{bb}(N3) - \chi_{cc}(N3)] \text{ (MHz)}$	[-1.17]	[-1.17]	[-1.17]	[-1.17]	[-1.17]
$F_0$ (GHz)	[160.0] <sup>c</sup>	[160.0]	[160.0]	[160.0]	[160.0]
$V_3$ (cm <sup>-1</sup> )	325.16(38)	324.86(36)	324.44(40)	324.82(80)	324.52(72)
$\angle (i, b)$ (°)	71.66(71)	70.90(66)	70.42(71)	70.8(15)	70.1(12)
$\Delta_0$ (u Å)	-3.2681(22)	-3.2541(26)	-3.2719(22)	-3.668(6)	-3.677(4)
$\sigma_{\rm RMS}$ (kHz)	20.5	17.4	19.1	23.6	25.1
$N_{ m A}/N_{ m E}^{ m d}$	68/53	64/61	61/49	39/20	52/39

<sup>&</sup>lt;sup>a</sup> The ordering of atoms is  $H_bOH_{nb}$  such that  $H_b$  is deuterium for the isotopologue denoted as "DOH".

<sup>&</sup>lt;sup>b</sup> Numbers in parentheses are one standard deviation in units of the last significant figure.

<sup>&</sup>lt;sup>c</sup> The value of  $F_0$  is fixed to 160 GHz.

 $<sup>^{\</sup>rm d}N_{\rm A}$  and  $N_{\rm E}$  denote the number of A-species and E- species transitions respectively included in the fit.

#### 4.5 Molecular Geometries

It will be shown that each of 2-MT···H<sub>2</sub>O, 4-MT···H<sub>2</sub>O and 5-MT···H<sub>2</sub>O adopt the connectivities shown in Figure 4.1 as calculated at the  $\omega$ B97X-D/aug-cc-pVQZ level of theory. The hydrogen atom which participates in the hydrogen bonding interaction is denoted as "H<sub>b</sub>" and the non-bonding hydrogen atom is denoted as "H<sub>nb</sub>". In the discussion that follows, comparison of the  $r_s$  coordinates derived from experimental results and  $r_e$  coordinates will allow the assignment of each singly substituted deuterium isotopologues to the correct spectrum. The isotopologue labelled "DOH" has the isotopic substitution in the H<sub>b</sub> position, while the "HOD" isotopologue has the isotopic substitution in the H<sub>nb</sub> position. This labelling convention will also be implemented in Chapters 5 – 7 during the discussion of other hydrate complexes. Throughout this section, analysis of the molecular geometry has utilised rotational constants determined from global fits performed in XIAM for 4-MT···H<sub>2</sub>O and 5-MT···H<sub>2</sub>O, whereas analysis of the molecular geometry of 2-MT···H<sub>2</sub>O was performed using rotational constants determined from PGOPHER fits, for reasons discussed earlier.

Planar moments ( $P_{aa}$ ,  $P_{bb}$  and  $P_{cc}$ ) were calculated (using Equations 2.71 – 2.73) for each isotopologue of 2-MT···H<sub>2</sub>O, 4-MT···H<sub>2</sub>O and 5-MT···H<sub>2</sub>O. The results are shown in Table A.12. Consistently across each complex it can be observed that for the isotopologues that contain  $H_2^{18}O$  or DOH the value obtained for  $P_{cc}$  are very similar to those of the parent isotopologues (H<sub>2</sub><sup>16</sup>O) confirming that both H<sub>b</sub> and the oxygen atom lie within (or very close to) the ab plane. The magnitude of  $P_{cc}$  was found to be slightly greater than that of the parent isotopologue for HOD or  $D_2O$  containing isotopologues. The inertial defect,  $\Delta_0$ , is calculated from the moments of inertia about the a, b and c inertial axes using Equation 2.74. In the vibrational ground state, the inertial defect is expected to be non-zero and a small positive result is expected where a species is planar. In-plane vibrations make positive contributions to  $\Delta_0$ whereas negative contributions are expected from out-of-plane vibrations. The inertial defects of thiazole,<sup>2</sup> 2-methylthiazole,<sup>4, 5</sup> 4-methylthiazole<sup>6</sup> and 5-methylthiazole<sup>7</sup> monomers were calculated to be 0.0744(4), -3.0828(12), -3.091994(33) and -3.0769(7) u Å<sup>2</sup> respectively. The presence of the methyl group results in out-of-plane vibrations leading to the negative values of  $\Delta_0$  for each of the methylthiazole monomers. The values of  $\Delta_0$  for 4-MT···H<sub>2</sub><sup>16</sup>O and 5-MT···H<sub>2</sub><sup>16</sup>O are calculated to be -3.6540(23) and -3.2681(22) u Å<sup>2</sup>, respectively.  $\Delta_0$  becomes more negative upon the attachment of H<sub>2</sub>O to each of 4-methylthiazole and 5-methylthiazole owing to the addition of out-of-(ab)-plane mass. The value of  $\Delta_0$  becomes even more negative on substitution of a deuterium atom into the H<sub>nb</sub> position of each complex. It can be concluded from the variation in the values of the planar moments and inertial defects obtained that H<sub>b</sub> and O lie within (or close) to the *ab* plane of the complex while  $H_{nb}$  contributes mass outside this plane. Previous studies<sup>26, 27</sup> have identified that the  $H_{nb}$  atom undergoes rapid zero-point vibrational motion in complexes formed between a heteroaromatic ring and  $H_2O$ . These motions rapidly interchange  $H_{nb}$  between equivalent positions on either side of the plane of the ring. Hence, in the zero-point state,  $H_{nb}$  contributes additional out-of-plane mass even while the complex has an average geometry in which  $H_{nb}$  lies in the plane of the heavy atoms of the thiazole ring.

For 2-MT···H<sub>2</sub>O, the situation is different. The  $\Delta_0$  of 2-MT···H<sub>2</sub><sup>16</sup>O was calculated to be -1.6408(10) u Å<sup>2</sup> whereas the  $\Delta_0$  of the 2-methylthiazole monomer was previously reported to be -3.0828(12) u Å<sup>2</sup>. It appears that the attachment of H<sub>2</sub>O to 2-methylthiazole induces additional in-plane vibrations which contribute positively to the inertial defect such that  $\Delta_0$ increases by 1.4422 u Å<sup>2</sup>. The vast majority of studies have observed negative contributions to the inertial defect upon monohydration of aromatic rings, however, it was reported upon the attachment of H<sub>2</sub>O to pyridine<sup>43</sup> and isoxazole<sup>44</sup> that an increase in the inertial defect was observed compared to the un-hydrated monomer. For each of pyridine...H2O and isoxazole···H<sub>2</sub>O, tunnelling states (0<sup>+</sup> and 0<sup>-</sup>) were observed as a result of H<sub>2</sub>O undergoing large amplitude motions, which resulted in positive (in-plane) contributions to the inertial defect. Tunnelling states were also reported for pyrazine... H<sub>2</sub>O, 45 however, the value of the inertial defect was determined to be negative and close to zero ( $\Delta_0 = -0.23$  u Å<sup>2</sup>). For 2-MT···H<sub>2</sub>O, tunnelling states have not been assigned for this complex, nevertheless, it is likely that H<sub>2</sub>O is undergoing some motion within the complex contributing positively to the  $\Delta_0$ . Similar to the observations for 4-MT···H<sub>2</sub>O and 5-MT···H<sub>2</sub>O,  $\Delta_0$  becomes more negative when a deuterium atom is substituted at the H<sub>nb</sub> position in the case of the HOD and D<sub>2</sub>O isotopologues, while  $P_{cc}$  becomes larger, suggesting  $H_{nb}$  lies outside of the ab plane. Negative contributions due to the H<sub>nb</sub> atom and out-of-plane hydrogen atoms of the methyl group also contribute to the inertial defect, which may explain why the  $\Delta_0$  value still remains negative unlike the positive values observed in pyridine $\cdots$ H<sub>2</sub>O and isoxazole $\cdots$ H<sub>2</sub>O.

Table 4.8 Comparison of DFT calculated ( $r_e$ ) and experimentally-determined ( $r_s$ ) atomic coordinates of H<sub>2</sub>O in 2-MT···H<sub>2</sub>O, 4-MT···H<sub>2</sub>O and 5-MT···H<sub>2</sub>O.

		$2-MT\cdots H_2O^a$		
	Method	a / Å	b / Å	c / Å
$H_b$	$r_{\rm e}$ (calc.) <sup>b</sup>	2.5142	-0.5766	0.0228
	$r_{\rm s}$ (exp.)	2.44751(63) <sup>c</sup>	-0.6709(23)	0.121(13)
O	r <sub>e</sub> (calc.)	3.4603	-0.3613	0.0312
	$r_{\rm s}$ (exp.)	3.45873(44)	-0.3498(43)	$[0]^d$
$H_{nb}$	r <sub>e</sub> (calc.)	3.8259	-0.7932	-0.7380
	$r_{\rm s}$ (exp.)	3.92648(40)	-0.9578(16)	-0.2470(63)
		4-MT···H₂O		
	Method	a / Å	<i>b</i> / Å	c / Å
$H_b$	r <sub>e</sub> (calc.)	2.4267	0.82547	-0.0070
	$r_{\rm s}$ (exp.)	2.33263(77)	0.9330(19)	[0]
O	$r_{\rm e}$ (calc.)	3.3820	0.8789	-0.1626
	$r_{\rm s}$ (exp.)	3.42010(46)	0.7971(20)	[0]
$H_{nb}$	$r_{\rm e}$ (calc.)	3.7542	1.1917	0.6593
	$r_{\rm s}$ (exp.)	3.78858(51)	1.3515(15)	0.3282(61)
		$5-MT\cdots H_2O$		
	Method	a / Å	<i>b</i> / Å	c / Å
$H_b$	$r_{\rm e}$ (calc.)	2.9450	0.43150	0.0290
	$r_{\rm s}$ (exp.)	2.89860(58)	0.7489(23)	0.046(38)
O	r <sub>e</sub> (calc.)	3.9031	0.3160	0.1152
	$r_{\rm s}$ (exp.)	3.85045(41)	0.1796(87)	[0]
$H_{nb}$	r <sub>e</sub> (calc.)	4.2699	0.6475	-0.7016
	$r_{\rm s}$ (exp.)	4.34578(51)	0.6656(34)	-0.4576(50)

<sup>&</sup>lt;sup>a</sup> Results for  $r_s$  coordinates of 2-MT···H<sub>2</sub>O obtained using results of A-species only (effective) fits.

 $<sup>^{\</sup>rm b}$   $r_{\rm e}$  geometries calculated at the  $\omega$ B97X-D/aug-cc-pVQZ level of theory.

<sup>&</sup>lt;sup>c</sup> Numbers in parentheses are Costain errors for  $r_s$  results and one standard deviation in units of the last significant figure for  $r_0$  results.

 $<sup>^{\</sup>rm d}$  Imaginary values obtained for  $r_{\rm s}$  coordinates are indicated in square brackets and assumed to be zero.

Measured shifts in rotational constants upon isotopic substitution at the H and O atoms of the  $H_2O$  sub-unit allowed the determination of the substitution  $(r_s)$  coordinates using the Kraitchman method<sup>46</sup> implemented in the program, KRA.<sup>33</sup> The coordinates (and their Costain errors<sup>47, 48</sup>) displayed in Table 4.8 were calculated from the results of the fits presented in Tables 4.2, 4.6 and 4.7 for 2-MT···H<sub>2</sub>O, 4-MT···H<sub>2</sub>O and 5-MT···H<sub>2</sub>O, respectively. Signs of the coordinates were chosen to be consistent with the results of the ωB97X-D/aug-cc-pVQZ calculations. For each of 4-MT···H<sub>2</sub>O and 5-MT···H<sub>2</sub>O, imaginary or very small coordinates were obtained for the c-coordinates of the H<sub>b</sub> and O atoms, reaffirming both of these atoms lie within (or very near to) the ab plane in each complex. For 2-MT···H<sub>2</sub>O, the  $r_s$  coordinates also suggest that the O atom lies within the ab plane, however, unlike 4-MT···H<sub>2</sub>O and 5-MT···H<sub>2</sub>O, the c-coordinate of H<sub>b</sub> was calculated to be non-zero suggesting it lies slightly outside of the ab plane. Generally, good agreement is observed between the  $r_s$  and  $r_e$  coordinates displayed in Table 4.8. However, some differences between the coordinates calculated using each method for  $H_{nb}$  can be observed (particularly in the case of the c-coordinate). This difference is unsurprising and arises since the results of the  $\omega$ B97X-D/aug-cc-pVQZ are in the equilibrium  $(r_e)$  geometry whereas the experiment probes the complexes in the zero-point vibrational ground state. Therefore, precise agreement between  $r_e$  and  $r_s$  results are not expected. Nevertheless, the results confirm the geometries of the complexes are consistent with those presented in Figure 4.1.

The  $r_0$  method<sup>49</sup> was used to determine intermolecular bond lengths and angles using the program STRFIT available on the PROSPE website.<sup>33</sup> Since isotopic substitution within the methylthiazole sub-unit is unavailable for each monohydrate complex, the *z*-matrix was constructed by assuming the geometrical parameters which are internal to the methylthiazole monomer are equal to their values in the  $r_e$  calculated geometry of the complex. It was chosen to fix the values of the dihedral angles ( $\angle$ (C2–N3···H<sub>b</sub>–O) and  $\angle$ (H<sub>nb</sub>–O–H<sub>b</sub>···N3)) such that the H<sub>b</sub> and O lie within the plane of the ring (and therefore the *ab* plane). As mentioned earlier, the H<sub>nb</sub> atom within each complex is expected to undergo rapid zero-point vibrations between equivalent positions on either side of the plane of the ring. Therefore, different assumptions for the values of the  $\angle$ (C2–N3···H<sub>b</sub>–O) and  $\angle$ (H<sub>nb</sub>–O–H<sub>b</sub>···N3) dihedral angles were tested as described below. For each complex, three geometrical parameters, r(H<sub>b</sub>···N3),  $\angle$ (H<sub>b</sub>···N3–C2) and  $\angle$ (O–H<sub>b</sub>···N3), were determined during the  $r_0$  fit, to provide an insight into the position and orientation of the H<sub>2</sub>O molecule. From the analysis definitive results for the geometries of 2-MT···H<sub>2</sub>O and 5-MT···H<sub>2</sub>O can be obtained but some ambiguity is observed with regards to the geometry of 4-MT···H<sub>2</sub>O. Fitted  $r_0$  parameters for each complex are displayed below in

Table 4.9 while atomic coordinates determined from each fit are given in the Appendix, Tables A.13 and A.14.

Table 4.9 Comparison of the DFT calculated and experimentally-determined structural parameters.

	2-MT···H <sub>2</sub> O <sup>a</sup>	
Parameter	Method	Value
<i>r</i> (H <sub>b</sub> ···N3) / Å	r <sub>e</sub> (calc.)	1.948 <sup>b</sup>
	$r_0$ (exp.)	1.9884(53) <sup>c</sup>
$\angle$ (H <sub>b</sub> ···N3–C2) /°	r <sub>e</sub> (calc.)	115.2
	$r_0$ (exp.)	112.6(16)
$\angle$ (O-H <sub>b</sub> ···N3) /°	r <sub>e</sub> (calc.)	167.4
,	$r_0$ (exp.)	170.2(50)
	$4-MT\cdots H_2O$	
Parameter	Method	Value
$r(H_b \cdots N3) / Å$	r <sub>e</sub> (calc.)	1.957
	$r_0$ : fit 1 (exp.) <sup>d</sup>	2.0265(87)
	$r_0$ : fit 2 (exp.) <sup>d</sup>	2.0296(68)
∠(H <sub>b</sub> ···N3–C2) /°	r <sub>e</sub> (calc.)	130.9
	$r_0$ : fit 1 (exp.)	139.2(22)
	$r_0$ : fit 2 (exp.)	134.7(14)
$\angle$ (O-H <sub>b</sub> ···N3) /°	r <sub>e</sub> (calc.)	170.9
	$r_0$ : fit 1 (exp.)	169.3(71)
	$r_0$ : fit 2 (exp.)	167.4(43)
	$5-MT\cdots H_2O$	
Parameter	Method	Value
$r(H_b \cdots N3) / Å$	r <sub>e</sub> (calc.)	1.960
	$r_0$ (exp.)	2.0037(42)
∠(H <sub>b</sub> ···N3–C2) /°	r <sub>e</sub> (calc.)	112.0
	$r_0$ (exp.)	99.40(78)
∠(O–H <sub>b</sub> ···N3) /°	r <sub>e</sub> (calc.)	168.4
	$r_0$ (exp.)	166.0(23)

<sup>&</sup>lt;sup>a</sup> Results for  $r_0$  structural parameters of 2-MT···H<sub>2</sub>O obtained using results of A-species only (*effective*) fits.

<sup>&</sup>lt;sup>b</sup>  $r_e$  geometries calculated at the  $\omega$ B97X-D/aug-cc-pVQZ level of theory.

<sup>&</sup>lt;sup>c</sup> Numbers in parentheses are one standard deviation in units of the final significant figure.

 $<sup>^</sup>d$  Fit 1 assumes  $\angle(O-H_b\cdots N3-C2)=0^\circ$  and  $\angle(H_{nb}-O-H_b\cdots N3)=180^\circ.$  Fit 2 assumes  $\angle(O-H_b\cdots N3-C2)=180^\circ$  and  $\angle(H_{nb}-O-H_b\cdots N3)=180^\circ.$ 

Within the 2-MT···H<sub>2</sub>O complex, as shown by quantum chemical calculations and confirmed by the values of the  $r_s$  coordinates, the H<sub>2</sub>O molecule binds to the methylthiazole ring at the nitrogen atom, adjacent to the methyl group situated at C2. Under the assumption,  $\angle$ (C2-N3···H<sub>b</sub>-O) = 0° and  $\angle$ (H<sub>nb</sub>-O-H<sub>b</sub>···N3) = 180°, the intermolecular bond distance,  $r(H_b \cdots N3)$ , and two intermolecular angles,  $\angle(H_b \cdots N3 - C2)$  and  $\angle(O - H_b \cdots N3)$  were determined to be 1.9884(53) Å, 112.6(16)° and 170.2(50)° when using the rotational constants of the effective (A- species only) fits which are similar to the  $r_e$  results of 1.948 Å, 115.2° and 167.4°. When performing a fit under the alternate assumption,  $\angle$ (O–H<sub>b</sub>···N3–C2) = 180° and  $\angle(H_{nb}-O-H_b\cdots N3)=180^\circ$ , the fit did not converge. The local environment surrounding the H<sub>2</sub>O binding site in 5-MT···H<sub>2</sub>O is essentially the same as each of thiazole···H<sub>2</sub>O, imidazole···H<sub>2</sub>O and N-methylimidazole···H<sub>2</sub>O.<sup>24, 26, 27</sup> Under the assumption that  $\angle$ (O-H<sub>b</sub>···N3-C2) = 0° and  $\angle$ (H<sub>nb</sub>-O-H<sub>b</sub>···N3) = 180° the results of the  $r_0$  fit are r(H<sub>b</sub>···N3) = 2.0037(42) Å,  $\angle(H_b \cdot \cdot \cdot N3 - C2)$  =  $99.40(78)^\circ$  and  $\angle(O - H_b \cdot \cdot \cdot N3)$  =  $166.0(23)^\circ$ . The  $r_0$ parameters obtained for each of  $r(H_b \cdots N3)$  and  $\angle(O-H_b \cdots N3)$  are in very good agreement with the  $r_e$  calculated results. However, a ~13° difference between the  $r_e$  and  $r_0$  results is observed for the  $\angle$ (H<sub>b</sub>···N3–C2) intermolecular angle. A similar deviation between the  $r_e$  and  $r_0$  results of this angle was also reported in the studies of imidazole...H2O26 and Nmethylimidazole···H<sub>2</sub>O.<sup>27</sup> Under the alternative assumption, where  $\angle$ (O–H<sub>b</sub>···N3–C2) = 180°, the parameters cannot be fitted, consistent with the findings of previous studies. An equivalent analysis of the  $r_0$  geometry was performed for 5-MT···H<sub>2</sub>O using *effective* rotational constants  $(A_0', B_0')$  and  $(A_0')$  displayed in Table 4.4, which leads to  $r(H_b \cdots N3)$ ,  $\angle(H_b \cdots N3 - C2)$  and  $\angle$ (O-H<sub>b</sub>···N3) being 2.0035(42) Å, 99.41(79)° and 166.1(23)°. Each of the  $r_0$  parameters determined using the *effective* ground state rotational constants are in very good agreement with the parameters determined using the results of the XIAM global fits. This indicates that for 2-MT···H<sub>2</sub>O, using results of *effective* fits during the  $r_0$  structure determination provides an excellent insight into the intermolecular distances and angles of this complex, even though global fits are yet to be finalised.

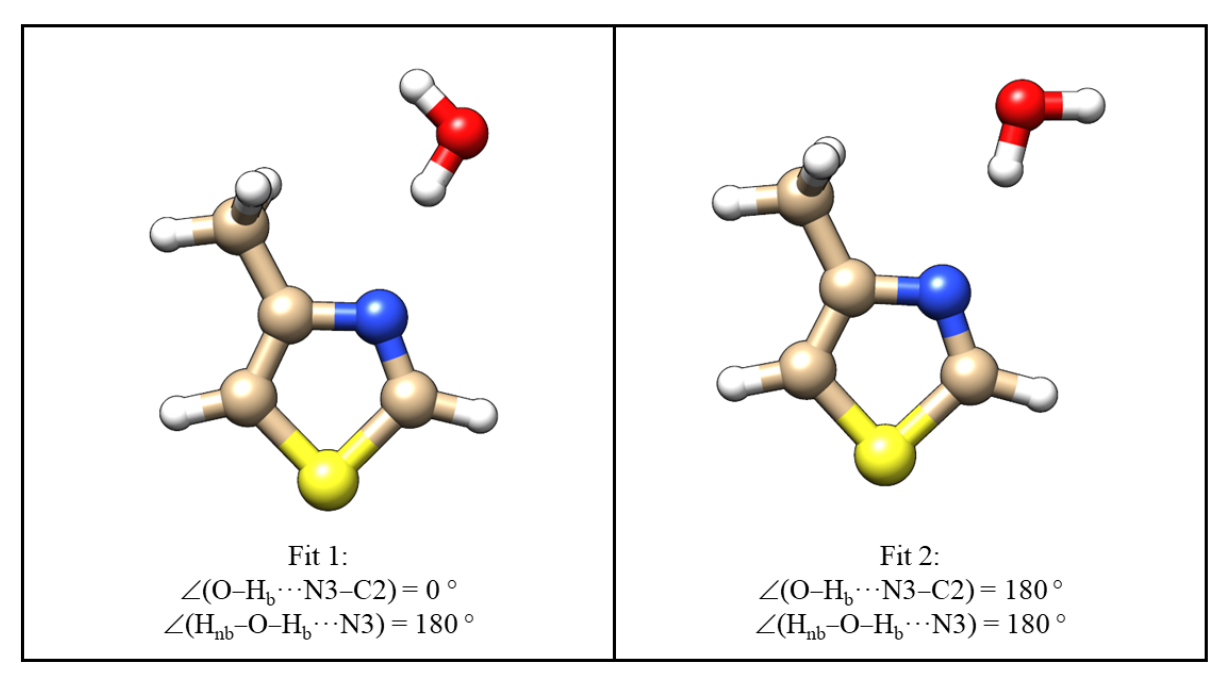


Figure 4.3 Two alternative geometries of 4-MT $\cdots$ H<sub>2</sub>O determined by  $r_0$  fits performed.

It was found that while fitting  $r(H_b \cdots N3)$ ,  $\angle(H_b \cdots N3 - C2)$  and  $\angle(O - H_b \cdots N3)$  under the two alternative assumptions,  $\angle(O-H_b\cdots N3-C2) = 0$  or  $180^{\circ}$ , that each fit converged for 4-MT···H<sub>2</sub>O. The geometrical parameters obtained under each assumption are very similar, with low uncertainties associated with each. The results generated from each fit are displayed in Table 4.9, fit 1 assumes  $\angle(O-H_b\cdots N3-C2)=0^\circ$  and  $\angle(H_{nb}-O-H_b\cdots N3)=180^\circ$  while fit 2 assumes  $\angle(O-H_b\cdots N3-C2) = 180^{\circ}$  and  $\angle(H_{nb}-O-H_b\cdots N3) = 180^{\circ}$ . The structures of the possible geometries are presented in Figure 4.3, which were generated using the atomic coordinates determined from each fit (given in Table A.14). Previous studies such as isoxazole···H<sub>2</sub>O<sup>44</sup> have used the values of nuclear quadrupole coupling constants to distinguish between several possible alternative geometries. The values of nuclear quadrupole coupling constants represent projections of the nuclear quadrupole coupling tensor onto the inertial axes within the complex. For 4-MT···H<sub>2</sub>O, each of the two alternative geometries have a very similar orientation of the inertial axis framework, consequently, nuclear quadrupole coupling constants cannot be used to distinguish between the two alternative geometries. Therefore, each of fit 1 and fit 2 are equally acceptable solutions for the molecular geometry of 4-MT···H<sub>2</sub>O from the perspective of the experimental data of the present work alone. However, it will be shown, in Section 4.7, that the ambiguity in the molecular geometry of 4-MT···H<sub>2</sub>O can be resolved by considering this complex in the broader, emerging trend in the molecular geometries of methylthiazole···H<sub>2</sub>O and methylimidazole···H<sub>2</sub>O complexes.

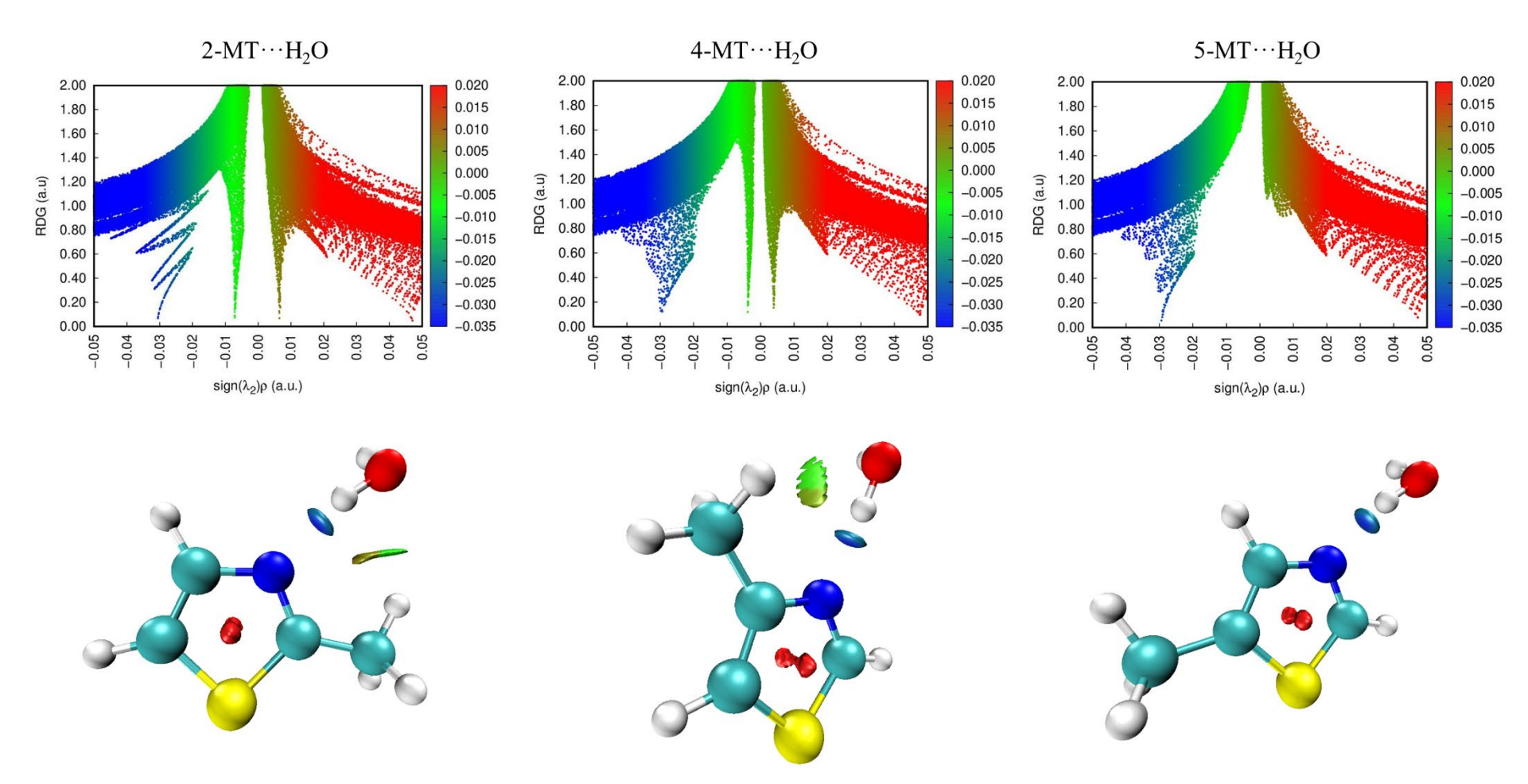


Figure 4.4 NCI isosurfaces and plots of the RDG (a.u.) vs  $sign(\lambda_2)\rho$  of 2-MT···H<sub>2</sub>O (left), 4-MT···H<sub>2</sub>O (middle) and 5-MT···H<sub>2</sub>O (right). Positive and negative values of  $sign(\lambda_2)\rho$  respectively denote repulsive (red) and attractive (blue) interactions. The isosurface s value is 0.5 au.

### **4.6 Non-Covalent Interactions**

In the previous section, analysis of the molecular geometry of each methylthiazole···H<sub>2</sub>O complex showed that H<sub>2</sub>O attaches to each methylthiazole ring at the nitrogen atom. A nonlinear primary hydrogen bonding interaction is present within each complex suggesting that the monohydrate complexes are further stabilised by a secondary interaction involving the O atom of H<sub>2</sub>O. Non-covalent interaction (NCI)<sup>50</sup> and natural bond orbital (NBO)<sup>51</sup> analyses were conducted for each monohydrate complex to visualise the intermolecular interactions present. NCI index plots (displayed in Figure 4.4) of the reduced density gradient, RDG, versus the sign of the second eigenvalue of the Hessian matrix  $(\lambda_2)$  of the electronic density  $(\rho)$ , sign $(\lambda_2)\rho$ , were generated using the programme Multiwfn.<sup>52</sup> The analysis was performed on the geometries of each complex calculated at the ωB97X-D/aug-cc-pVQZ level of theory. A strong attractive (hydrogen bonding) interaction is present within each complex indicated by a trough in each NCI plot at sign( $\lambda_2$ ) $\rho \approx -0.03$  and the presence of a dark blue isosurface located between the nitrogen atom of the thiazole ring and one of the hydrogen atoms of the H<sub>2</sub>O sub-unit. In each of 2-MT···H<sub>2</sub>O and 4-MT···H<sub>2</sub>O, additional troughs were also observed in the NCI plot and a second isosurface is also present. The isosurface has an area of weak attraction (light green, negative sign $(\lambda_2)\rho$  value) and an area of weak repulsion (dark green, positive sign $(\lambda_2)\rho$  value). Whereas for 5-MT···H<sub>2</sub>O, the analysis does not indicate the presence of any additional isosurfaces within this complex. This is inconsistent with the experimental results since the primary hydrogen bond  $\angle$ (O-H<sub>b</sub>···N3) was determined to be non-linear in the  $r_0$  geometry  $(\angle(O-H_b\cdots N3) = 166.0(23)^\circ)$  indicating the presence of a secondary interaction within this complex. This inconsistency likely arises since the interaction between O of H<sub>2</sub>O and H bound to C2 is present but too weak to be identified by the analysis. The absence of a second isosurface was also observed in the NCI analysis performed in the study of thiazole... H<sub>2</sub>O.<sup>24</sup> During the work presented herein, the molecular geometry of thiazole... H<sub>2</sub>O was re-analysed using the results presented within the original study. Further details of the re-analysis and why this was performed is given in the Appendix (A.15). During the re-analysis the primary hydrogen bond of thiazole···H<sub>2</sub>O was determined to be  $\angle$ (O–H<sub>b</sub>···N3) = 168.9(1)° in the  $r_0$  geometry. The implication is that the geometry of the non-covalent interactions present within 5-MT···H<sub>2</sub>O is very similar to that within thiazole...H<sub>2</sub>O as expected.

NBO analysis (displayed in Figure 4.5 and Table A.16) was performed at the B3LYP(D3BJ)/aug-cc-pVTZ level of theory using the geometries of each monohydrate complex calculated at the  $\omega$ B97X-D/aug-cc-pVQZ level. The analysis was performed to evaluate the intermolecular orbital interactions present and to determine the second-order

stabilisation energies ( $E^{(2)}$ ) associated with each interaction. The largest  $E^{(2)}$  contribution in each of the methylthiazole···H<sub>2</sub>O complexes corresponds to the interaction between the lone pair of the nitrogen atom and the antibonding  $\sigma^*(O-H_b)$  orbital. The  $E^{(2)}$  values obtained for this interaction are 39.46, 37.74 and 35.90 kJ mol<sup>-1</sup> in each of 2-MT···H<sub>2</sub>O, 4-MT···H<sub>2</sub>O and 5-MT···H<sub>2</sub>O respectively, which are consistent with the result reported for thiazole···H<sub>2</sub>O<sup>24</sup> ( $E^{(2)}$  = 35.60 kJ mol<sup>-1</sup>). For 2-MT···H<sub>2</sub>O and 4-MT···H<sub>2</sub>O, the NCI analysis revealed an additional weak interaction between the O atom of H<sub>2</sub>O and the hydrogen atoms of the methyl group. This interaction was also identified in the NBO analysis. The lone pair of the O atom of H<sub>2</sub>O forms an interaction with C6–H6, with a second-order stabilisation energy of 2.97 kJ mol<sup>-1</sup> within 2-MT···H<sub>2</sub>O and 0.42 kJ mol<sup>-1</sup> within 4-MT···H<sub>2</sub>O. It can therefore be inferred that the relative strength of this interaction is greater in 2-MT···H<sub>2</sub>O compared to 4-MT···H<sub>2</sub>O. In each case, the strength of the interaction is apparently strong enough to cause the primary hydrogen bond to deviate from linearity.

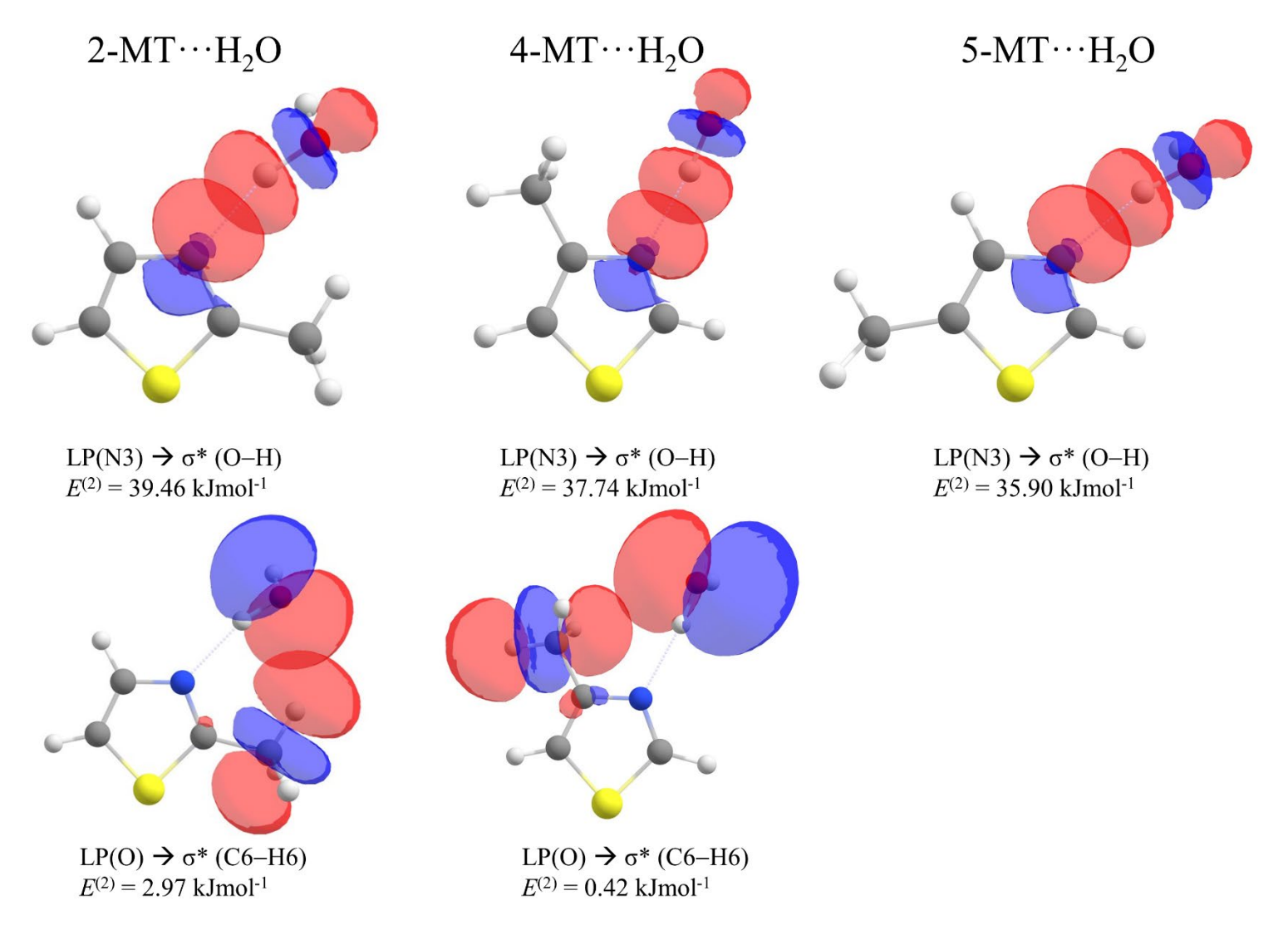


Figure 4.5 NBO plots associated with intermolecular interactions present within 2-MT···H<sub>2</sub>O (left), 4-MT···H<sub>2</sub>O (middle) and 5-MT···H<sub>2</sub>O (right).  $E^{(2)}$  represents the second order perturbation energy of each interaction.

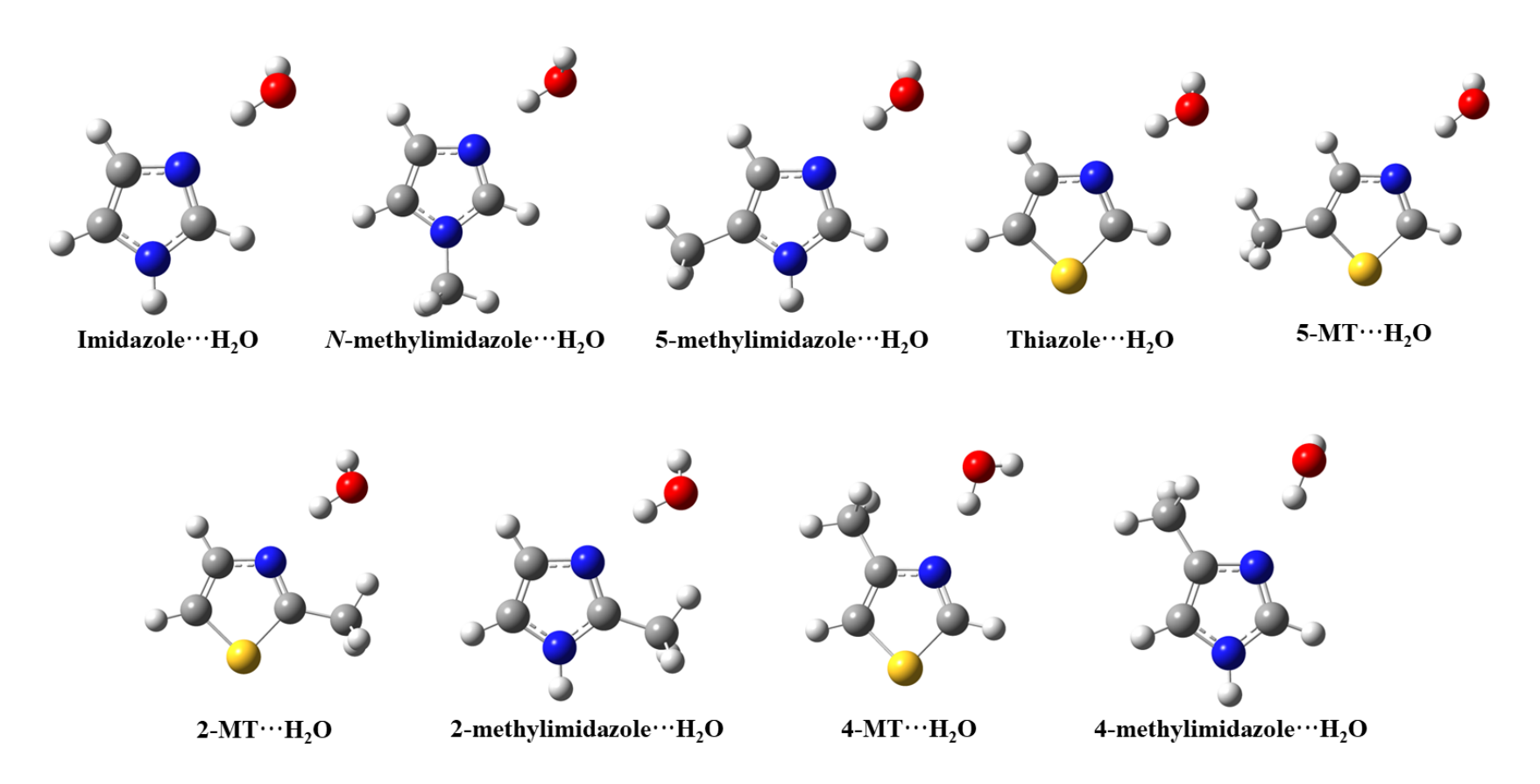


Figure 4.6 Geometries of nine thiazole- and imidazole-containing monohydrate complexes. The complexes are separated into two subsets for reasons given in text. (top) Monohydrate complexes containing no CH<sub>3</sub> group or a CH<sub>3</sub> group located remote to H<sub>2</sub>O, which are the first sub-set of Table 4.10. (bottom) Monohydrate complexes containing a CH<sub>3</sub> group located adjacent to H<sub>2</sub>O, which are the second sub-set of Table 4.10.

### 4.7 Discussion

The structures of nine monohydrate complexes of heteroaromatic rings containing thiazole and imidazole are presented in Figure 4.6. In each of the hydrate complexes, H<sub>2</sub>O acts as the hydrogen bond donor while the pyridinic nitrogen of the thiazole or imidazole ring acts as the hydrogen bond acceptor. Intermolecular parameters associated with the primary hydrogen bonding interaction in each complex are given in Table 4.10. A general trend can be observed in the length of the primary hydrogen bonds, in imidazole-containing complexes this distance is typically slightly shorter than thiazole containing complexes. The monohydrate complexes presented in Table 4.10 are separated into two sub-sets. The first sub-set of complexes is comprised of imidazole···H<sub>2</sub>O,<sup>26</sup> thiazole···H<sub>2</sub>O,<sup>24</sup> N-methylimidazole···H<sub>2</sub>O,<sup>27</sup> 5methylimidazole···H<sub>2</sub>O<sup>f</sup> and 5-MT···H<sub>2</sub>O. In each of these complexes, H<sub>2</sub>O binds at the nitrogen (N3) atom, via a strong hydrogen bond, and an additional weaker hydrogen-bonding interaction is present between the O atom of H<sub>2</sub>O and a hydrogen attached to C2 of the heteroaromatic ring, C2-H2···O. For 5-MT···H<sub>2</sub>O, the length of the weaker hydrogen bond is 2.953(4) Å in the  $r_0$  geometry. As shown in Figure 4.6, the CH<sub>3</sub> group in each of Nmethylimidazole···H<sub>2</sub>O, 5-methylimidazole···H<sub>2</sub>O and 5-MT···H<sub>2</sub>O is remote (on the opposite side of the ring) from the H<sub>2</sub>O sub-unit, therefore, is not positioned to interact with it through hydrogen bonding. The intermolecular angles  $\angle(H_b \cdots N3 - C2)$  and  $\angle(O - H_b \cdots N3)$  are very similar across the series of complexes within the first sub-set. This is unsurprising considering the local environment surrounding the H<sub>2</sub>O binding site is essentially the same in each of the aforementioned complexes. The second sub-set of complexes consists of 2-MT···H<sub>2</sub>O, 2methylimidazole···H<sub>2</sub>O,<sup>27</sup> 4-MT···H<sub>2</sub>O and 4-methylimidazole···H<sub>2</sub>O (Figure 4.6 and Table 4.10). The  $\angle$ (H<sub>b</sub>···N3–C2) angle in each of these complexes is somewhat greater than those observed for the complexes within the first sub-set. For 2-MT···H<sub>2</sub>O, the value of  $\angle$ (H<sub>b</sub>···N3–C2) was determined to be 112.6(16)° in the  $r_0$  geometry, which is ~17° greater than the same angle within thiazole...H2O (and other monohydrate complexes within the first subset) and very similar to what was previously identified for the same parameter in 2methylimidazole···H<sub>2</sub>O.<sup>27</sup> The difference in this angle is a consequence of the position of the CH<sub>3</sub> group on C2 of the thiazole or imidazole ring, which allows for a weak hydrogen bond between O of H<sub>2</sub>O and the CH<sub>3</sub> group (rather than a hydrogen atom). Thus, the value of ∠(H<sub>b</sub>···N3−C2) is significantly greater in each of 2-MT···H<sub>2</sub>O and 2-methylimidazole···H<sub>2</sub>O relative to thiazole···H<sub>2</sub>O and imidazole···H<sub>2</sub>O, respectively. For each of the complexes mentioned above, the values of the geometrical parameters can be rationalised by the non-

-

f Unpublished work by E. Gougoula et al.

covalent interactions present within the complex. It was discussed in Section 4.5 (Molecular geometries) that it is not possible to distinguish between the two alternative geometries of 4-MT···H<sub>2</sub>O from the experimental data alone. The possible geometries of 4-MT···H<sub>2</sub>O will be now re-examined considering the non-covalent interactions present and the trends in the intermolecular parameters discussed above.

Table 4.10 Comparison of experimentally-determined ( $r_0$ ) structural parameters for complexes formed between 5-membered N-heterocyclic rings and  $H_2O$ .

Complex	[H-bond donor on het. ring] <sup>a</sup>	<i>r</i> (H <sub>b</sub> ···N3) / Å	∠(H <sub>b</sub> ···N3–C2)	∠(O–H <sub>b</sub> ···N3)
Imidazole…H <sub>2</sub> O <sup>b</sup>	C-H on C2	1.927(27) <sup>e</sup>	99.9(41)	172.1(26)
N-methylimidazole···H <sub>2</sub> O <sup>b</sup>	C-H on C2	1.922(4)	101.0(16)	177(5)
5-methylimidazole···H <sub>2</sub> O <sup>c</sup>	C-H on C2	1.9605(32)	104.53(90)	168.8(25)
$ ext{Thiazole} \cdots  ext{H}_2 ext{O}^ ext{b}$	C-H on C2	1.977(7)	95.6(4)	168.9(1)
$5-MT\cdots H_2O$	C-H on C2	2.0037(42)	99.40(78)	166.0(23)
2-MT···H₂O <sup>d</sup>	CH <sub>3</sub> on C2	1.9884(53)	112.6(16)	170.2(50)
2-methylimidazole···H <sub>2</sub> O <sup>b</sup>	CH <sub>3</sub> on C2	1.923(5)	116.9(9)	166.3(28)
$4-MT\cdots H_2O^f$	CH <sub>3</sub> on C4	2.0296(68)	134.7(14)	167.4(44)
4-methylimidazole···H <sub>2</sub> O <sup>c</sup>	CH <sub>3</sub> on C4	1.9750(17)	138.7(12)	173.6(37)

<sup>&</sup>lt;sup>a</sup> Indicates the atom or group of the heteroaromatic sub-unit which acts as the hydrogen bond donor in the secondary (weaker) hydrogen bond within the complex.

The results of the  $r_0$  fits for each of the alternative geometries of 4-MT···H<sub>2</sub>O (presented in Table 4.9) imply a value of  $\angle$ (H<sub>b</sub>···N3–C2) which is significantly greater than the equivalent angles in each of the other thiazole or imidazole-containing complexes. Since the values of  $\angle$ (H<sub>b</sub>···N3–C2) in each of the other complexes were rationalised by the secondary weaker hydrogen bonding interaction present, the simplest physical rationalisation of the results for 4-MT···H<sub>2</sub>O, is to invoke the presence of a weak interaction between O of H<sub>2</sub>O and the CH<sub>3</sub> group bound to C4. This would therefore imply that  $\angle$ (O–H<sub>b</sub>···N3–C2) should be assumed

<sup>&</sup>lt;sup>b</sup> Results for imidazole···H<sub>2</sub>O, *N*- and 2-methylimidazole···H<sub>2</sub>O complexes from reference 26 and 27 respectively. Results for thiazole···H<sub>2</sub>O following re-analysis of results presented in reference 24 (see Table A.15).

<sup>&</sup>lt;sup>c</sup> Unpublished results by E. Gougoula et al.

<sup>&</sup>lt;sup>d</sup> Results for  $r_0$  structural parameters of 2-MT···H<sub>2</sub>O obtained using results of A-species only fits.

<sup>&</sup>lt;sup>e</sup> Uncertainties in parentheses are those quoted in the primary source.

f Results of fit 2 for 4-MT···H<sub>2</sub>O (see Table 4.9).

equal to 180°, in the zero-point geometry, with the lone pair on the oxygen oriented towards the CH<sub>3</sub> group. The ambiguity in the molecular geometry of 4-MT···H<sub>2</sub>O can therefore be resolved in favour of the  $r_0$  geometry of fit 2. The results of fit 2 imply that the values of each of  $r(H_b \cdots N3)$ ,  $\angle (H_b \cdots N3 - C2)$  and  $\angle (O - H_b \cdots N3)$  in 4-MT···H<sub>2</sub>O are 2.0296(68) Å, 134.7(14)° and  $167.4(44)^{\circ}$ , respectively, which compare to the  $r_{\rm e}$  results of 1.957 Å,  $130.9^{\circ}$  and  $170.9^{\circ}$ . The values of the angles  $\angle$ (O–H<sub>b</sub>···N3–C2) and  $\angle$ (H<sub>nb</sub>–O–H<sub>b</sub>···N3) are 141.7° and 140.1° in the  $r_e$  geometry of 4-MT···H<sub>2</sub>O. The former of these angles is significantly closer to 180° than to 0°, supporting the conclusion that fit 2 leads to the more accurate description of the experimentally-determined geometry. For 5-MT···H<sub>2</sub>O, the DFT-calculated geometry has  $\angle$ (O-H<sub>b</sub>···N3-C2) = -6.9° and  $\angle$ (H<sub>nb</sub>-O-H<sub>b</sub>···N3) = 122.7°. Again, this is consistent with the assumptions made when performing fits to determine  $r_0$  parameters of this complex  $(\angle(O-H_b\cdots N3-C2)=0^\circ$  and  $\angle(H_{nb}-O-H_b\cdots N3)=180^\circ$ ). In the  $r_0$  geometry of 4-MT···H<sub>2</sub>O, two of the hydrogen atoms are orientated such that  $\angle (H6-C6-C4-N3) = \pm 60^{\circ}$  and the distance between O of H<sub>2</sub>O and each of these hydrogens is 3.118(4) Å. By rotating the CH<sub>3</sub> group such that a single hydrogen atom of CH<sub>3</sub> is located in the ab plane, the intermolecular distance is reduced and is now 2.500(4) Å, which is a suitable distance for a hydrogen bonding interaction to form.

For 4-methylimidazole···H<sub>2</sub>O<sup>g</sup>, the geometrical parameters displayed in Table 4.10 were determined while assuming the angles  $\angle$ (O–H<sub>b</sub>···N3–C2) and  $\angle$ (H<sub>nb</sub>–O–H<sub>b</sub>···N3) are equal to 180°. Unlike what has been observed presently in the case of 4-MT···H<sub>2</sub>O, it was only possible to fit the geometrical parameters when  $\angle$ (O–H<sub>b</sub>···N3–C2) = 180°, when assuming  $\angle$ (O–H<sub>b</sub>···N3–C2) = 0° the fit did not converge. The value of  $\angle$ (H<sub>b</sub>···N3–C2) within the  $r_0$  geometry of 4-methylimidazole···H<sub>2</sub>O is determined to be 138.7(12)° which is very similar to the value of the same parameter within 4-MT···H<sub>2</sub>O. Again, implying that a weak interaction is present within the 4-methylimidazole···H<sub>2</sub>O complex between O of H<sub>2</sub>O and the CH<sub>3</sub> group bound to C4. The results for the angle  $\angle$ (O–H<sub>b</sub>···N3) are very similar across the entire series of complexes in Table 4.10, suggesting that this parameter is less sensitive to the balance of electrostatic forces present compared to  $\angle$ (H<sub>b</sub>···N3–C2). In each complex, the primary hydrogen bond consistently deviates from linearity owing to the presence of a secondary weaker interaction in each complex.

<sup>&</sup>lt;sup>g</sup> Unpublished work by E. Gougoula *et al*.

The  $V_3$  barriers to internal rotation of the CH<sub>3</sub> group in structural isomers of methylimidazole and their monohydrate complexes have been studied previously.<sup>8, 27</sup> It should be noted that within the following discussion the  $V_3$  barriers of each imidazole derivative were determined using XIAM, during the analysis it was necessary to neglect hyperfine splittings of the A- and E-species transitions. For each of N-methylimidazole···H<sub>2</sub>O and 5-methylimidazole···H<sub>2</sub>O, the  $V_3$  barrier to internal rotation determined for each monohydrate complex is similar to the  $V_3$ determined for N-methylimidazole and 5-methylimidazole monomers respectively. The Nmethylimidazole···H<sub>2</sub>O and 5-methylimidazole···H<sub>2</sub>O complexes have V<sub>3</sub> barriers of 182.21(12) and 382.200(24) cm<sup>-1</sup> respectively, while the  $V_3$  barriers determined for the unhydrated monomers are 185.104(11) cm<sup>-1</sup> for N-methylimidazole and 386.001(19) cm<sup>-1</sup> for 5-methylimidazole, respectively. This is consistent with the CH<sub>3</sub> group being remote from and not interacting with the H<sub>2</sub>O molecule within each of N-methylimidazole···H<sub>2</sub>O and 5methylimidazole···H<sub>2</sub>O. The V<sub>3</sub> barrier to internal rotation in the 2-methylimidazole···H<sub>2</sub>O complex was found to be 154.99(8) cm<sup>-1</sup>, this is significantly greater than the  $V_3$  barrier determined for the 2-methylimidazole monomer (122.7529(38) cm<sup>-1</sup>). The difference between the  $V_3$  determined for 2-methylimidazole and for 2-methylimidazole... $H_2O$  was attributed to the presence of a weak hydrogen-bonding interaction between H<sub>2</sub>O and the CH<sub>3</sub> group within the monohydrate complex. Whereas the  $V_3$  barrier was determined to be 280.77(30) cm<sup>-1</sup> in the 4-methylimidazole···H<sub>2</sub>O complex which is lower than what was previously determined for the 4-methylimidazole monomer (317.20(14))cm<sup>-1</sup>). As discussed above. methylimidazole···H<sub>2</sub>O complex adopts a geometry in which a weak interaction is present between H<sub>2</sub>O and CH<sub>3</sub>, however, in this case results in a decrease in the barrier height.

The  $V_3$  barrier to internal rotation of the 5-methylthiazole monomer was determined to be 332.0(8) cm<sup>-1</sup> when analysed by an internal axis method<sup>7</sup> which compares with 325.16(38) cm<sup>-1</sup> and 329(4) cm<sup>-1</sup> for 5-MT···H<sub>2</sub>O when fitted during the present work using XIAM and BELGI-C<sub>s</sub>-hyperfine respectively. The observed differences between the two results indicate that the choice of Hamiltonian used for the analysis affects the value of  $V_3$ . The range of spectroscopic transitions measured and the value assumed for  $F_0$  (which could not be directly fitted and was assumed to be equal to the value for the 5-methylthiazole monomer) will also have some influence on the value of  $V_3$  obtained by the analysis. Hence, the minor differences between the values of  $V_3$  determined for 5-methylthiazole and 5-MT···H<sub>2</sub>O likely arise because of limitations of the models employed and the narrow range of rotational transitions measured (with data obtained for A and E torsional levels of the  $v_t = 0$  state only) rather than due to a physical factor. For 4-MT···H<sub>2</sub>O, the  $V_3$  barrier to internal rotation was determined to be

340.05(56) cm<sup>-1</sup> and 329(5) cm<sup>-1</sup> for 4-MT···H<sub>2</sub>O when fits were performed using XIAM and BELGI respectively. This parameter was reported to be 357.6(1) cm<sup>-1</sup> for the 4-methylthiazole monomer during a previous study.<sup>6</sup> The  $V_3$  barriers determined for 4-MT···H<sub>2</sub>O and 4-methylthiazole indicate that the energetic barrier hindering the internal rotation lowers upon the formation of the monohydrate complex, which is consistent with what was observed in the methylimidazole analogue. For 4-methylimidazole···H<sub>2</sub>O the  $V_3$  barrier determined by XIAM is 280.77(30) cm<sup>-1</sup> which is significantly lower than the  $V_3$  determined for the 4-methylimidazole monomer (317.20(14) cm<sup>-1</sup>). In each of 4-MT···H<sub>2</sub>O and 4-methylimidazole···H<sub>2</sub>O the analysis of the molecular geometries implies that a weak hydrogen bond is present within each complex between the O atom of H<sub>2</sub>O and the CH<sub>3</sub> group at C4. A weak hydrogen bond with the CH<sub>3</sub> group was also noted in the case of 2-methylimidazole···H<sub>2</sub>O, however, within this complex, the presence of this interaction resulted in an increase in the  $V_3$  barrier.

A lowering in the  $V_3$  barrier to internal rotation of a CH<sub>3</sub> group upon the formation of complexes with H<sub>2</sub>O and other small molecules has been observed in a number of other studies. The rotational spectra and  $V_3$  barriers of the monohydrate and dihydrate complex of acetic acid were reported in 2008.<sup>53</sup> In each of these complexes, the H<sub>2</sub>O molecule(s) coordinate to the carboxyl acid group on the opposite side of the molecule to the CH<sub>3</sub> group. In the monohydrate complex, CH<sub>3</sub>COOH···H<sub>2</sub>O, the H<sub>2</sub>O molecule simultaneously acts as both hydrogen bond donor (to the carboxyl oxygen atom) and hydrogen bond acceptor (from the carboxyl O-H). The coordination of H<sub>2</sub>O results in a redistribution of electrons within the carboxyl group, resulting in a significantly reduced V<sub>3</sub> barrier to internal rotation of the CH<sub>3</sub> group relative to that in the acetic acid monomer. Three hydrogen bonds are present within the dihydrate complex, CH<sub>3</sub>COOH···(H<sub>2</sub>O)<sub>2</sub>, which cooperatively reinforce each other such that there is a further decrease in the V<sub>3</sub> barrier of CH<sub>3</sub> relative to that for the acetic acid monomer and the monohydrate complex. The V<sub>3</sub> barriers of CH<sub>3</sub>COOH, CH<sub>3</sub>COOH···H<sub>2</sub>O CH<sub>3</sub>COOH···(H<sub>2</sub>O)<sub>2</sub> are reported to be 168.16(10), 138.396(5) and 118.482(2) cm<sup>-1</sup> respectively and the lowering of the  $V_3$  barrier upon successive hydration was attributed to changes in electronic charge distribution within the acetic acid sub-unit. This study and other works<sup>54, 55</sup> show that the  $V_3$  barrier at a CH<sub>3</sub> group can be significantly reduced by charge redistribution within a molecule, and that such re-distribution might be caused by a hydrogen bonding interaction with H<sub>2</sub>O. Many studies of complexes formed between methanol and other small molecules such as CO,<sup>56</sup> CO<sub>2</sub>,<sup>57</sup> formaldehyde,<sup>57</sup> formamide<sup>58</sup> and acrylonitrile<sup>59</sup> have also noted a significant reduction in the  $V_3$  barrier of the CH<sub>3</sub> group in methanol upon complexation. A reduction in  $V_3$  has also been noted upon the formation of a homochalcogen bond rather than a hydrogen bond. Obenchain *et al.* reported that the  $V_3$  barrier in the dimethylsulfide monomer is 735.784(44) cm<sup>-1</sup> whereas it is 656.1(14) cm<sup>-1</sup> in the dimethylsulfide···SO<sub>2</sub> complex.<sup>60</sup>

The observed reduction in  $V_3$  implies that charge re-distribution occurs within the 4methylthiazole and 4-methylimidazole monomers upon the attachment of H<sub>2</sub>O. However, as noted earlier the geometries of each of 4-MT···H<sub>2</sub>O and 4-methylimidazole···H<sub>2</sub>O implies that a weak hydrogen bond is present between the H<sub>2</sub>O sub-unit and CH<sub>3</sub>. Previous studies on 2methylimidazole···H<sub>2</sub>O,<sup>27</sup> 2-methoxypyridine····H<sub>2</sub>O<sup>35</sup> and monohydrate complexes of nonaromatic molecules,  $^{36-38}$  each noted an increase in the value of  $V_3$  (relative to  $V_3$  for the isolated molecule), owing to the presence of a weak interaction with the CH<sub>3</sub> group. It is therefore evident that the magnitude of the  $V_3$  barrier is influenced by a balance of through-space (hydrogen bonding and other electrostatic) interactions and through-bond contributions (which arise because of charge re-distribution within a molecular sub-unit). For each of 4-MT···H<sub>2</sub>O and 4-methylimidazole···H<sub>2</sub>O, the balance of through-space and through-bond contributions to  $V_3$  cannot be independently distinguished through analysis of the experimental data alone. The value of  $V_3$  for 2-methylimidazole···H<sub>2</sub>O<sup>27</sup> is significantly higher than that for the 2methylimidazole monomer<sup>8</sup> which was attributed to the presence of a weak hydrogen bonding interaction. However, it is possible that a through-bond contribution to  $V_3$  of 2methylimidazole···H<sub>2</sub>O might act to reduce V<sub>3</sub>, relative to the value for the isolated 2methylimidazole molecule, even while the effect of the hydrogen bond between the O atom of H<sub>2</sub>O and the CH<sub>3</sub> group of 2-methylimidazole dominates and leads to the observed increase in  $V_3$ .

A comparison of the relative strength of the secondary interactions within 2-methylimidazole···H<sub>2</sub>O, 4-MT···H<sub>2</sub>O and 4-methylimidazole···H<sub>2</sub>O can provide some insight into the observed values of  $V_3$  in each of these complexes. The second order stabilisation energy of the interaction between the lone pair of the oxygen atom and the  $\sigma^*(C6-H6)$  antibonding orbital on the CH<sub>3</sub> group is calculated to be 0.42 kJ mol<sup>-1</sup> in 4-MT···H<sub>2</sub>O at the B3LYP/aug-cc-pVTZ level of theory. The same interaction within 4-methylimidazole····H<sub>2</sub>O was calculated to be 0.38 kJ mol<sup>-1</sup> (at the same level of theory). Whereas a considerably larger  $E^{(2)}$  was observed for the secondary interaction in the 2-methylimidazole····H<sub>2</sub>O complex (2.72 kJ mol<sup>-1</sup>). Evidently, the secondary hydrogen bond within 2-methylimidazole····H<sub>2</sub>O is stronger than that present within 4-MT····H<sub>2</sub>O and 4-methylimidazole····H<sub>2</sub>O, therefore, has a more significant effect on  $V_3$ . Since the hydrogen bond is weaker in each of 4-MT····H<sub>2</sub>O and 4-

methylimidazole···H<sub>2</sub>O it is likely that the through-bond charge re-distribution is the dominant effect, explaining why the  $V_3$  barrier is reduced compared to the unhydrated monomer in each of these complexes. As discussed earlier, the  $E^{(2)}$  value associated with the C6–H6···O interaction in 2-MT···H<sub>2</sub>O was calculated to be 2.97 kJ mol<sup>-1</sup>. The value obtained is very similar to that observed in 2-methylimidazole···H<sub>2</sub>O suggesting that it is probable that through-space interactions will be the dominant effect on  $V_3$  within 2-MT···H<sub>2</sub>O. The  $V_3$  of each of N-methylimidazole···H<sub>2</sub>O, 5-methylimidazole···H<sub>2</sub>O and 5-MT···H<sub>2</sub>O have been found to be similar to those of the respective monomers. It is likely in each of these complexes that both through-space and through-bond contributions to  $V_3$  are negligible in each case owing to the position of the coordinating H<sub>2</sub>O molecule relative to the CH<sub>3</sub> group.

### 4.8 2-MT···H<sub>2</sub>O: Interim global fits

The 2-methylthiazole monomer was first studied in 2002 by J. U. Grabow et al.4 In their analysis a global fit was performed using the combined axis method while neglecting hyperfine splittings. The  $V_3$  barrier to internal rotation of the methyl group was determined to be 34.938(20) cm<sup>-1</sup> and the standard deviation of the fit was 443 kHz. This molecule was the subject of a re-analysis in 2020,<sup>5</sup> using the programs XIAM and BELGI-C<sub>s</sub>-hyperfine for the treatment of the internal rotation problem. While fitting a significant number of experimentally observed A- and E-species transitions in XIAM, the  $V_3$  barrier was determined to be 34.79675(18) cm<sup>-1</sup>. However, the standard deviation of the fit was again more than 400 kHz which is much greater than the experimental accuracy. BELGI-C<sub>s</sub>-hyperfine was used to achieve a satisfactory fit, reducing the standard deviation of the fit to 3.2 kHz and determining  $V_3$  to be 34.2535(12) cm<sup>-1</sup>. Additional parameters were able to be included in the BELGI fit which are unavailable in the XIAM program allowing an improvement in the standard deviation of the fit to be achieved. In the XIAM and BELGI fits the  $V_3$  barriers are determined to be very similar even though different Hamiltonians are employed during the analysis and the rotational constants are very consistent when those determined using BELGI are transformed into the principal axis system.

As mentioned earlier the global fit for the 2-MT···H<sub>2</sub>O complex is proving more challenging than those of 4-MT···H<sub>2</sub>O and 5-MT···H<sub>2</sub>O and the analysis of the internal rotation within this complex is still in progress. Interim global fits have been performed using XIAM such that Aand E-species transitions can be fitted simultaneously. E- species transitions have been identified within the spectrum and quantum numbers assigned on the basis that E- species transitions have a similar hyperfine structure to their A- species counterpart. Global fits were first performed using the same procedure as used for 4-MT···H<sub>2</sub>O, 5-MT···H<sub>2</sub>O and isomers of methylimidazole··· $H_2O^{27}$  to determine  $V_3$  while holding  $F_0$  fixed at a value determined for the unhydrated monomer. While fixing  $F_0$  at a value between 157 – 160 GHz the standard deviation of each global fit of 2-MT···H<sub>2</sub><sup>16</sup>O was significantly higher than those obtained in each of the 4-MT···H<sub>2</sub>O and 5-MT···H<sub>2</sub>O XIAM fits and the experimental accuracy. For example, a standard deviation of over 1000 kHz was obtained while using the approximation that  $F_0 = 160$ GHz, which yielded a value of  $V_3$  of 48.721(14) cm<sup>-1</sup> and a reduced dimensionless barrier height, s, of 4.00. However, it was observed that a global fit of the parent isotopologue with a significantly reduced standard deviation of 97 kHz was obtained while floating the value of  $F_0$ such that it is determined to be 122.11(20) GHz. From this fit the derived value of  $V_3$  is 37.481(60) cm<sup>-1</sup> and s = 4.02. The value of  $F_0$  determined while floating this parameter is

significantly different to the typical value expected for a sp<sup>3</sup> hybridised methyl top bound to a rigid frame (157 – 162 GHz). Global fits for three additional isotopologues of 2-MT···H<sub>2</sub>O were also able to be performed each obtaining a value of  $V_3$  and  $F_0$  consistent with that of the parent H<sub>2</sub><sup>16</sup>O isotopologue and a similar standard deviation of the fit. It is possible that additional parameters which are not available in XIAM may be required to be included to achieve a global fit for this complex with a lower standard deviation like what was observed for the 2-methylthiazole monomer.

Analysis of the molecular geometry of the 2-MT $\cdots$ H<sub>2</sub>O complex has identified the presence of a hydrogen bonding interaction between the O atom of H<sub>2</sub>O and the CH<sub>3</sub> situated at C2. The NBO analysis implied that this interaction was of comparable strength to that observed in the 2-methylimidazole $\cdots$ H<sub>2</sub>O complex. In addition, it was observed that the inertial defect  $\Delta_0$  changes from -3.0828(12) u Å<sup>2</sup> (unhydrated 2-methylthiazole monomer) to -1.6408(10) u Å<sup>2</sup> upon the attachment of H<sub>2</sub>O. As discussed earlier typically  $\Delta_0$  becomes more negative upon the attachment of H<sub>2</sub>O to heteroaromatic rings. This suggests that the H<sub>2</sub>O molecule is undergoing some motion within the 2-MT $\cdots$ H<sub>2</sub>O complex which contributes positively to the inertial defect. It is likely that global fits of this complex are more complicated than for other molecular systems owing to aspects of the molecular geometry mentioned above resulting in the Hamiltonian models employed in internal rotation fitting programs being less appropriate and accurate.

Nevertheless, the results obtained for preliminary fits of 2-MT···H<sub>2</sub>O suggest the  $V_3$  barrier is changed compared to the isolated 2-methylthiazole monomer, consistent with results of 2-methylimidazole···H<sub>2</sub>O,<sup>27</sup> 4-MT···H<sub>2</sub>O and 4-methylimidazole···H<sub>2</sub>O. However, more work is required in order to finalise the global fits of this monohydrate complex.

### 4.9 Conclusions

Broadband microwave spectra of five isotopologues of each complex formed between the structural isomers of methylthiazole and H<sub>2</sub>O have been recorded over the 7.0 – 18.5 GHz frequency region. The molecular geometries and V<sub>3</sub> barriers to internal rotation of the CH<sub>3</sub> group within each complex have been investigated. Each monohydrate complex contains a strong primary hydrogen bond between the nitrogen atom of the thiazole ring and a hydrogen of H<sub>2</sub>O. The primary hydrogen bond within each complex was determined to be non-linear because of a secondary, weaker hydrogen bonding interaction between O and either the CH<sub>3</sub> group attached to C2/C4 in 2-MT···H<sub>2</sub>O and 4-MT···H<sub>2</sub>O or the hydrogen atom attached to C2 in 5-MT···H<sub>2</sub>O. The geometrical parameters determined for 2-MT···H<sub>2</sub>O and 4-MT···H<sub>2</sub>O indicate that the presence of a weak interaction with the CH<sub>3</sub> group has a large influence on the  $\angle$ (H<sub>b</sub>···N3-C2) angle, while the value obtained for this parameter in 5-MT···H<sub>2</sub>O is very similar to that of thiazole...H2O. Global fits were performed using XIAM and BELGI-Cshyperfine to determine the V<sub>3</sub> barrier to internal rotation of the CH<sub>3</sub> group in each of 4- $MT \cdots H_2O$  and 5- $MT \cdots H_2O$ . The  $V_3$  barrier obtained for 4- $MT \cdots H_2O$  is slightly lower than the result for the 4-methylthiazole monomer, which may be a result of charge re-distribution within the 4-methylthiazole sub-unit following the attachment of H<sub>2</sub>O. While the result for 5- $MT \cdots H_2O$  is essentially unchanged from the  $V_3$  determined previously for the 5-methylthiazole monomer. It was discussed that determining  $V_3$  for 2-MT···H<sub>2</sub>O is a more challenging case and further work is required to complete a global fit for this complex. Trends in the  $V_3$  barriers to internal rotation and intermolecular parameters have been found to be very consistent across the whole series of methylthiazole···H<sub>2</sub>O and methylimidazole···H<sub>2</sub>O complexes.

### 4.10 References

- 1. B. Bak, D. Christensen, L. Hansen-Nygaard and J. Rastrup-Andersen, *Journal of Molecular Spectroscopy*, 1962, **9**, 222-224.
- 2. L. Nygaard, E. Asmussen, J. H. Høg, R. C. Maheshwari, C. H. Nielsen, I. B. Petersen, J. Rastrup-Andersen and G. O. Sørensen, *Journal of Molecular Structure*, 1971, **8**, 225-233.
- 3. U. Kretschmer and H. Dreizler, *Zeitschrift für Naturforschung A*, 1993, **48**, 1219-1222.
- 4. J. U. Grabow, H. Hartwig, N. Heineking, W. Jäger, H. Mäder, H. W. Nicolaisen and W. Stahl, *Journal of Molecular Structure*, 2002, **612**, 349-356.
- 5. T. Nguyen, V. Van, C. Gutlé, W. Stahl, M. Schwell, I. Kleiner and H. V. L. Nguyen, *The Journal of Chemical Physics*, 2020, **152**, 134306.
- 6. W. Jäger and H. Mäder, Zeitschrift für Naturforschung A, 1987, 42, 1405-1409.
- 7. W. Jäger and H. Mäder, Journal of Molecular Structure, 1988, 190, 295-305.
- 8. E. Gougoula, C. Medcraft, J. Heitkämper and N. R. Walker, *The Journal of Chemical Physics*, 2019, **151**, 144301.
- 9. E. Antonelli, E. Gougoula, N. R. Walker, M. Schwell, H. V. L. Nguyen and I. Kleiner, *The Journal of Chemical Physics*, 2024, **160**, 214309.
- 10. J. Makarewicz, S. Huber, B. Brupbacher-Gatehouse and A. Bauder, *Journal of Molecular Structure*, 2002, **612**, 117-123.
- 11. T. Nguyen, W. Stahl, H. V. L. Nguyen and I. Kleiner, *Journal of Molecular Spectroscopy*, 2020, **372**, 111351.
- 12. T. Nguyen, C. Dindic, W. Stahl, H. V. L. Nguyen and I. Kleiner, *Molecular Physics*, 2020, **118**, 1668572.
- 13. E. Fliege, H. Dreizler, M. Meyer, K. Iqbal and J. Sheridan, *Zeitschrift für Naturforschung A*, 1986, **41**, 623-636.
- 14. E. R. L. Fliege, Zeitschrift für Naturforschung A, 1990, 45, 911-922.
- 15. E. Fliege, H. Dreizler, J. Sheridan and C. T. Walls, *Journal of Molecular Spectroscopy*, 1985, **113**, 362-372.
- 16. W. Jäger, H. Dreizler, H. Mäder, J. Sheridan and C. T. Walls, *Zeitschrift für Naturforschung A*, 1987, **42**, 501-506.
- 17. W. G. Norris and L. C. Krisher, *The Journal of Chemical Physics*, 2003, **51**, 403-406.
- 18. I. A. Finneran, S. T. Shipman and S. L. Widicus Weaver, *Journal of Molecular Spectroscopy*, 2012, **280**, 27-33.
- 19. T. Ogata and K. Kozima, Bulletin of the Chemical Society of Japan, 1971, 44, 2344-2346.
- 20. H. W. Nicolaisen, J. U. Grabow, N. Heineking and W. Stahl, *Zeitschrift für Naturforschung A*, 1991, **46**, 635-638.
- 21. N. M. Pozdeev, R. G. Latypova and L. N. Gunderova, *Journal of Structural Chemistry*, 1976, **17**, 313-314.
- 22. K. J. Koziol, H. El Hadki, A. Lüchow, N. Vogt, J. Demaison and H. V. Nguyen, *Spectroscopy Journal*, 2023, **1**, 49-64.
- 23. T. Ogata and K. Kozima, *Journal of Molecular Spectroscopy*, 1972, **42**, 38-46.
- 24. W. Li, J. Chen, Y. Xu, T. Lu, Q. Gou and G. Feng, *Spectrochimica Acta Part A: Molecular and Biomolecular Spectroscopy*, 2020, **242**, 118720.
- 25. E. Gougoula, C. N. Cummings, Y. Xu, T. Lu, G. Feng and N. R. Walker, *The Journal of Chemical Physics*, 2023, **158**, 114307.
- 26. E. Gougoula, D. J. Cole and N. R. Walker, *The Journal of Physical Chemistry A*, 2020, **124**, 2649-2659.
- 27. E. Gougoula, C. N. Cummings, C. Medcraft, J. Heitkämper and N. R. Walker, *Physical Chemistry Chemical Physics*, 2022, **24**, 12354-12362.
- 28. T. R. Dyke and J. S. Muenter, *The Journal of Chemical Physics*, 2003, **60**, 2929-2930.

- 29. L. H. Coudert, F. J. Lovas, R. D. Suenram and J. T. Hougen, *The Journal of Chemical Physics*, 1987, **87**, 6290-6299.
- 30. J. K. G. Watson, *The Journal of Chemical Physics*, 1967, **46**, 1935-1949.
- 31. J. K. G. Watson, The Journal of Chemical Physics, 1968, 48, 4517-4524.
- 32. C. M. Western, *Journal of Quantitative Spectroscopy and Radiative Transfer*, 2017, **186**, 221-242.
- 33. Z. Kisiel, PROSPE Programs for ROtational SPEctroscopy, <a href="http://info.ifpan.edu.pl/~kisiel/prospe.htm">http://info.ifpan.edu.pl/~kisiel/prospe.htm</a>, (accessed 21/06/2024, 2024).
- 34. R. S. Ruoff, T. D. Klots, T. Emilsson and H. S. Gutowsky, *The Journal of Chemical Physics*, 1990, **93**, 3142-3150.
- 35. W. Cheng, Y. Zheng, G. Feng, J.-U. Grabow and Q. Gou, *Spectrochimica Acta Part A: Molecular and Biomolecular Spectroscopy*, 2020, **239**, 118434.
- 36. L. B. Favero and W. Caminati, *The Journal of Physical Chemistry A*, 2009, **113**, 14308-14311.
- 37. L. B. Favero, L. Evangelisti, A. Maris, A. Vega-Toribio, A. Lesarri and W. Caminati, *The Journal of Physical Chemistry A*, 2011, **115**, 9493-9497.
- 38. W. Caminati, J. C. López, S. Blanco, S. Mata and J. L. Alonso, *Physical Chemistry Chemical Physics*, 2010, **12**, 10230-10234.
- 39. H. Hartwig and H. Dreizler, Zeitschrift für Naturforschung A, 1996, **51**, 923-932.
- 40. J. T. Hougen, I. Kleiner and M. Godefroid, *Journal of Molecular Spectroscopy*, 1994, **163**, 559-586.
- 41. R. Kannengießer, W. Stahl, H. V. L. Nguyen and I. Kleiner, *The Journal of Physical Chemistry A*, 2016, **120**, 3992-3997.
- 42. I. Kleiner, Journal of Molecular Spectroscopy, 2010, 260, 1-18.
- 43. R. B. Mackenzie, C. T. Dewberry, R. D. Cornelius, C. J. Smith and K. R. Leopold, *The Journal of Physical Chemistry A*, 2017, **121**, 855-860.
- 44. S. McGlone, P. Moreschini, T. K. Ha and A. Bauder, *Molecular Physics*, 2001, **99**, 1353-1364.
- 45. W. Caminati, L. B. Favero, P. G. Favero, A. Maris and S. Melandri, *Angewandte Chemie International Edition*, 1998, **37**, 792-795.
- 46. J. Kraitchman, American Journal of Physics, 1953, 21, 17-24.
- 47. C. C. Costain, *The Journal of Chemical Physics*, 1958, **29**, 864-874.
- 48. C. C. Costain, *Trans.Am. Crystallogr. Assoc*, 1966, **2**, 157-164.
- 49. Z. Kisiel, Journal of Molecular Spectroscopy, 2003, 218, 58-67.
- 50. E. R. Johnson, S. Keinan, P. Mori-Sánchez, J. Contreras-García, A. J. Cohen and W. Yang, *Journal of the American Chemical Society*, 2010, **132**, 6498-6506.
- 51. A. E. Reed, L. A. Curtiss and F. Weinhold, *Chemical Reviews*, 1988, 88, 899-926.
- 52. T. Lu and F. Chen, *Journal of Computational Chemistry*, 2012, **33**, 580-592.
- 53. B. Ouyang and B. J. Howard, *Physical Chemistry Chemical Physics*, 2009, **11**, 366-373.
- 54. J. Lei, J. Zhang, G. Feng, J.-U. Grabow and Q. Gou, *Physical Chemistry Chemical Physics*, 2019, **21**, 22888-22894.
- 55. C. Cabezas, M. Juanes, R. T. Saragi, A. Lesarri and I. Peña, *Spectrochimica Acta Part A: Molecular and Biomolecular Spectroscopy*, 2022, **270**, 120846.
- 56. F. J. Lovas, S. P. Belov, M. Y. Tretyakov, J. Ortigoso and R. D. Suenram, *Journal of Molecular Spectroscopy*, 1994, **167**, 191-204.
- 57. V. V. Ilyushin, F. J. Lovas and D. F. Plusquellic, *Journal of Molecular Spectroscopy*, 2006, **239**, 94-100.
- 58. F. J. Lovas, R. D. Suenram, G. T. Fraser, C. W. Gillies and J. Zozom, *The Journal of Chemical Physics*, 1988, **88**, 722-729.
- 59. C. Calabrese, A. Maris, A. Vigorito, S. Mariotti, P. Fathi, W. D. Geppert and S. Melandri, *The Journal of Physical Chemistry A*, 2020, **124**, 3601-3608.

60. D. A. Obenchain, L. Spada, S. Alessandrini, S. Rampino, S. Herbers, N. Tasinato, M. Mendolicchio, P. Kraus, J. Gauss, C. Puzzarini, J.-U. Grabow and V. Barone, *Angewandte Chemie International Edition*, 2018, **57**, 15822-15826.

# Chapter 5. Characterisation of the Molecular Geometry of 2-Ethylfuran···H<sub>2</sub>O by Microwave Spectroscopy.

### 5.1 Introduction

It was discussed in previous Chapters that when a methyl group is substituted onto a heteroaromatic ring it undergoes internal rotation and that the magnitude of the barrier is influenced by two factors: the substitution position of the methyl group and the identity of the heteroatom(s) present within the ring. The next smallest alkyl group that can be substituted onto a heteroaromatic ring is an ethyl group. The rotation of the ethyl group relative to the rigid (heterocyclic) frame results in ethylated heteroaromatic rings having some degree of conformational flexibility. Therefore, ethyl-substituted molecules have the potential to adopt different conformations. Conformers which have C<sub>s</sub> symmetry have both carbon atoms of the ethyl group co-planar with the aromatic ring, such that the dihedral angle which defines the rotation of the ethyl group relative to the ring is  $\angle(C-C-X-X) = 0^{\circ}$  or  $180^{\circ}$  (where "X" denotes atoms within the ring). In conformers which possess C<sub>1</sub> symmetry, the methyl group of the ethyl substituent is orientated out of the plane of the ring such that the dihedral angle is  $\angle$ (C–C–X– X)  $\neq$  0° or 180°. A limited number of microwave spectroscopy studies on ethyl-substituted rings are available in the current literature. <sup>1-3</sup> An example of an ethyl-substituted heteroaromatic ring is 2-ethylfuran, which is a derivative of furan where the ethyl group is substituted at the 2position (atom labelling shown in Figure 5.1). A recent study<sup>3</sup> on 2-ethylfuran identified that two conformations of this molecule are present within a helium supersonic expansion, which differ in the ∠(C7–C6–C2–O1) dihedral angle. The observed conformers of 2-ethylfuran are shown in Figure 5.1. Within the C<sub>s</sub> conformer, the heavy atoms of the ethyl group are co-planar with the furan ring such that the  $\angle$ (C7–C6–C2–O1) dihedral angle is equal to 180°. In the C<sub>1</sub> configuration, the ethyl group is rotated  $63.31(64)^{\circ}$  out of the plane of the furan ring, in the  $r_s$ geometry.

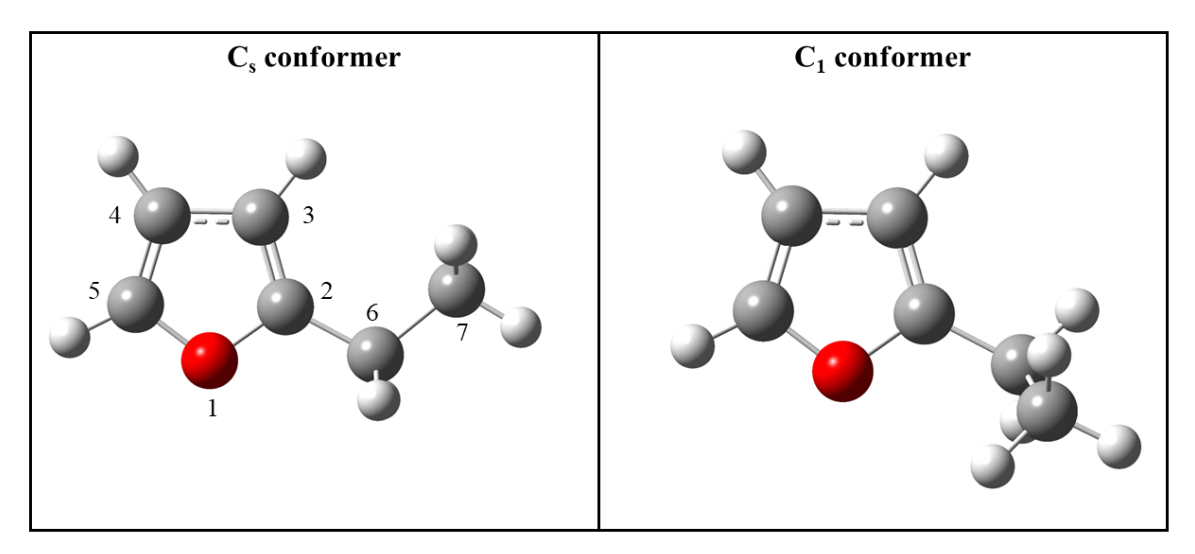


Figure 5.1 The two observed conformations of 2-ethylfuran reported in reference 3. The  $C_s$  conformer is calculated to be 1.93 kJmol<sup>-1</sup> higher in energy than the  $C_1$  conformer at the MP2/6-31G(d,p) level of theory.

Several other similar furan derivatives have been studied by microwave spectroscopy, including furfuryl alcohol,<sup>4, 5</sup> furfuryl mercaptan<sup>5, 6</sup> and furfuryl amine.<sup>7</sup> The three aforementioned molecules are analogous to 2-ethylfuran, only differing in the functional group bound to C6. Each molecule is reported to adopt conformations with C<sub>1</sub> symmetry only, unlike what has been observed for 2-ethylfuran. Within each of furfuryl alcohol, furfuryl mercaptan and furfuryl amine the lowest energy structure of each molecule contains an intramolecular interaction between the terminal hydrogen atom in each of the alcohol, thiol and amine functional groups and the oxygen atom within the furan ring. The presence of the  $X-H\cdots O1$  (where X=O, S or N) intramolecular hydrogen bond stabilises the structure of each molecule compared to other higher energy configurations. The dihedral angle analogous to ∠(C7–C6–C2–O1) within the lowest energy structure of furfuryl alcohol, furfuryl mercaptan and furfuryl amine have been determined to be 66.47(43)°, 71.81(38)° and 65.37(23)° respectively.<sup>5, 7</sup> It can be observed that the magnitude of the  $\angle$ (X7–C6–C2–O1) is similar in each of the furan derivatives which adopt conformations with C<sub>1</sub> symmetry. However, the situation is different for 2-methoxyfuran. <sup>8</sup> The substitution of a methoxy group yields only one conformation of this molecule, in which the methoxy group lies within the plane defined by the furan ring and therefore has C<sub>s</sub> symmetry. The ∠(C7–O6–C2–O1) dihedral angle is equal to 180° (denoted "syn" conformer within the study) the same as what was observed in the C<sub>s</sub> conformer of 2-ethylfuran. The authors suggested that the syn conformer is the lowest in energy and the preferred conformer due to this structure allowing the extended delocalisation of  $\pi$  electrons onto the oxygen atom, which ultimately stabilises this geometrical arrangement.

In Chapter 4, it was discussed that changes in the barrier to internal rotation of the methyl group in mono-methylated heteroaromatic rings occurs when the methyl group is situated adjacent to the position at which the H<sub>2</sub>O molecule binds, indicating that the formation of a hydrate complex can influence the internal dynamics of a molecule. A number of gas phase studies have identified a change in the lowest energy form of a molecule which occurs as a result of hydration or complexation with other small molecules. This typically occurs in order to facilitate the formation of additional intermolecular interactions within the complex. Such that the relative energy of conformations can differ between the isolated form of the molecule and when bound within a complex. Several studies have observed a torsional change<sup>9-11</sup> upon the formation of hydrate complexes while others have identified a change in the lowest energy conformation<sup>12</sup>, or a shift in the tautomeric equilibrium.<sup>14, 15</sup>

The microwave spectrum of one isomer of the monohydrate complex of 2-ethylfuran (hereafter denoted as 2-EF···H<sub>2</sub>O) has been assigned with the aid of quantum chemical calculations. In this Chapter, the molecular geometry and non-covalent interactions present within this binary complex will be discussed. It will be shown that the molecular geometry of 2-EF···H<sub>2</sub>O is similar to the lowest energy geometries of furfuryl alcohol···H<sub>2</sub>O<sup>5</sup> and furfuryl mercaptan···H<sub>2</sub>O,<sup>5</sup> however, the relative strength of the interaction(s) between H<sub>2</sub>O and the group located at the 2- position result in differences in the structural parameters obtained. A brief re-investigation of the 2-ethylfuran monomer will also be presented, additional information regarding the experimental energy ordering of the two conformers has been acquired by performing experiments utilising argon and neon as carrier gases, building upon the results of the previous study.<sup>3</sup> It will be shown that the experimentally observed lowest energy geometry of 2-ethylfuran changes depending on whether it is an isolated molecule or bound within a complex.

## **5.2 Experimental Methods**

The broadband microwave spectrum of 2-EF···H<sub>2</sub>O was recorded while probing a gaseous sample comprised of low concentrations of 2-ethylfuran and water in an inert carrier gas. The spectrum was recorded over the frequency range 7.0 – 18.5 GHz, using chirped pulse Fourier transform microwave (CP-FTMW) spectroscopy. 2-ethylfuran (Alfa Aesar, 98%) was seeded directly into the flow of a carrier gas from a bespoke reservoir prior to supersonic expansion. The vapour pressure (54 mmHg @ 25 °C) was sufficiently high to acquire the spectra of 2ethylfuran and its monohydrate complex without applying any heat to the reservoir. The gas sample undergoes supersonic expansion into a vacuum chamber via a pulse nozzle (Parker, Series 9) before irradiation by a microwave pulse. Species within the supersonic expansion are rotationally cold, with a temperature of approximately 3 K. A second reservoir located upstream (of the supersonic expansion) contained water, enabling desorption of water into the carrier gas to facilitate the formation of hydrate complexes. Separate experiments using argon (BOC, 99.998 %) and neon (BOC, CP grade) as carrier gases were performed probing the spectra of 2-ethylfuran and 2-ethylfuran···H<sub>2</sub><sup>16</sup>O. Subsequent experiments were performed using D<sub>2</sub>O (Sigma Aldrich, 99.9 % D atom) and  $\rm H_2^{18}O$  (Sigma Aldrich, 97 %  $^{18}O$  atom) to obtain the spectra of isotopologues of the complex. Isotopically enriched experiments which yielded spectra of D and <sup>18</sup>O permutations were performed using neon only.

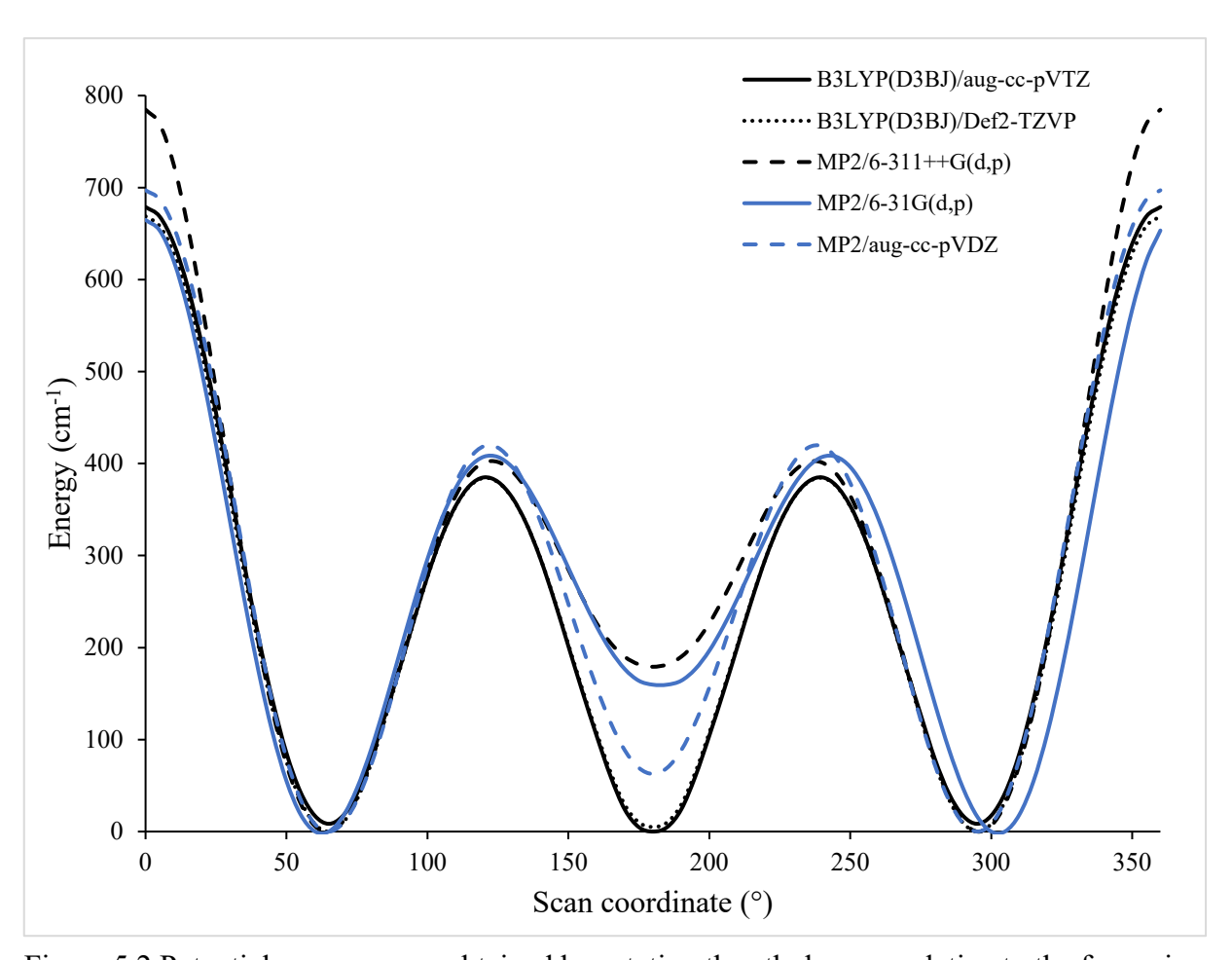


Figure 5.2 Potential energy scans obtained by rotating the ethyl group relative to the furan ring in 2-ethylfuran. Calculations performed at the B3LYP(D3BJ)/aug-cc-pVTZ, B3LYP(D3BJ)/Def2-TZVP, MP2/6-311++G(d,p), MP2/6-31G(d,p) and MP2/aug-cc-pVDZ levels of theory by scanning the  $\angle$ (C7–C6–C2–O1) dihedral angle.

### 5.3 Quantum Chemical Calculations

Potential energy scans (PES) were performed by scanning the ∠(C7–C6–C2–O1) dihedral angle (atom labelling given in Figure 5.1) at an interval of 5°. Scan calculations were performed at B3LYP(D3BJ)/aug-cc-pVTZ, B3LYP(D3BJ)/Def2-TZVP and MP2/aug-cc-pVDZ levels of theory. Each calculation predicts three minima (as shown in Figure 5.2), two of which are mirror images of each other and are therefore equivalent. The minima correspond to the C<sub>s</sub> and C<sub>1</sub> conformations of 2-ethylfuran identified in the previous study.<sup>3</sup> The geometries of both monomers were subsequently optimised at the B3LYP(D3BJ)/aug-cc-pVTZ and ωB97X-D/aug-cc-pVQZ level of theory. To calculate the optimised geometries of the monohydrate complexes, H<sub>2</sub>O was placed in close proximity to the O1 atom of each geometry of 2-ethylfuran. The geometries of the two conformations of 2-EF···H<sub>2</sub>O were optimised at the B3LYP(D3BJ)/aug-cc-pVTZ level of theory. The monohydrate complex formed with the C<sub>s</sub> conformer is calculated to be 1.01 kJ mol<sup>-1</sup> higher in energy than the complex formed with the C<sub>1</sub> conformer. Subsequent geometry optimisations were performed at the ωB97X-D/aug-ccpVQZ, B3LYP(D3BJ)/Def2-TZVP and MP2/aug-cc-pVDZ levels of theory. The optimised geometries of 2-EF···H<sub>2</sub>O, calculated at the ωB97X-D/aug-cc-pVQZ level of theory, are presented in Figure 5.3. Rotational constants ( $A_e$ ,  $B_e$  and  $C_e$ ) and dipole moment components  $(\mu_a, \mu_b, \mu_c)$  for each conformation of the monohydrate complex are given in Table 5.1 and 5.2. Atomic coordinates calculated at each level of theory are provided in Tables A.17 – A.24.

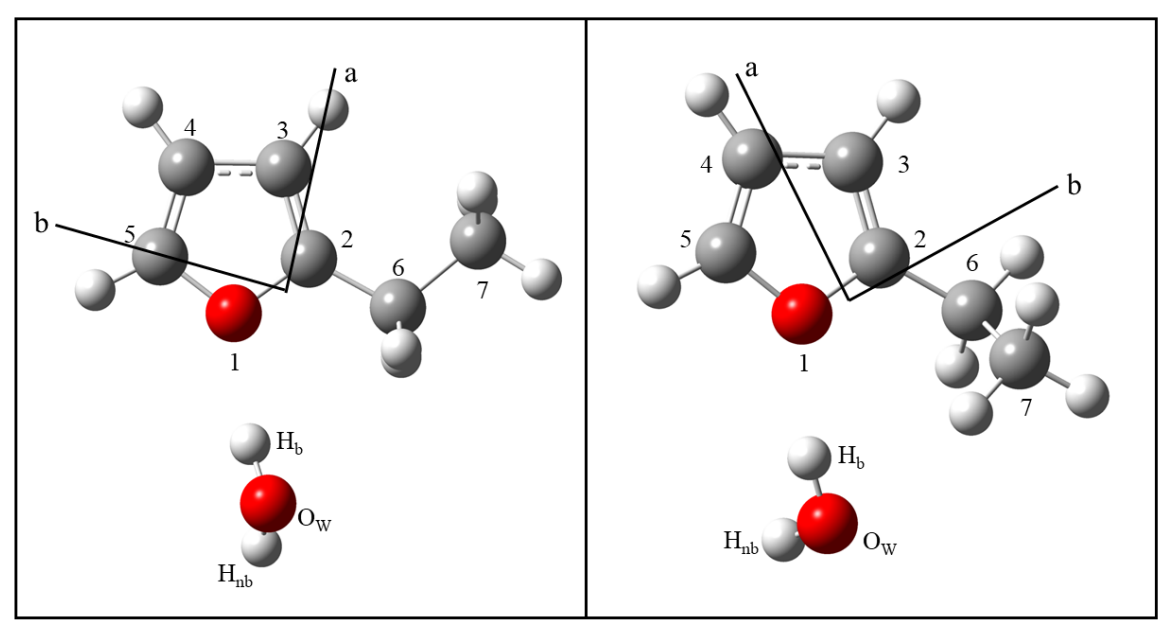


Figure 5.3 Equilibrium ( $r_e$ ) geometries of hydrate complexes formed with the  $C_s$  (left) and  $C_1$  (right) conformations of 2-ethylfuran calculated at the  $\omega$ B97X-D/aug-cc-pVQZ level of theory. The  $C_s$  conformer of the monohydrate complex is calculated to be 0.25 kJmol<sup>-1</sup> higher in energy.

Table 5.1 Spectroscopic parameters of 2-EF $\cdots$ H<sub>2</sub>O (C<sub>1</sub> conformer) calculated at different levels of theory.

$2-EF\cdots H_2O$ (C <sub>1</sub> conformer)				
	$\omega$ B97X-D/a	ug-cc-pVQZ	B3LYP(D3BJ)	/aug-cc-pVTZ
$A_e$ (MHz)	2520.742	$-0.4\%^{a}$	2539.834	+ 0.4 %
$B_e$ (MHz)	1483.172	+ 2.1 %	1480.461	+ 2.0 %
$C_e(\mathrm{MHz})$	1027.281	+ 1.7 %	1016.473	+ 0.6 %
$ \mu_{\rm a} ,  \mu_{\rm b} ,  \mu_{\rm c}  ({\rm D})^{\rm b}$	1.8, 0	.1, 0.9	1.8, 0.0, 0.7	
	B3LYP(D3B	J)/Def2-TZVP	MP2/aug-	cc-pVDZ
$A_e$ (MHz)	2507.921	- 0.9 %	2616.067	+ 3.4 %
$B_e$ (MHz)	1482.404	+ 2.1 %	1442.375	- 0.7 %
$C_e$ (MHz)	1025.619	+ 1.5 %	1030.142	+ 1.9 %
$[\mu_{\rm a}],  \mu_{\rm b} ,  \mu_{\rm c}   ({\rm D})$	2.0, 0	.3, 0.7	1.6, 0.	5, 0.3

<sup>&</sup>lt;sup>a</sup> Calculated by  $[(A_e - A_0)/A_0] \times 100$  % where  $A_e$  are the results of computational calculations presented above and  $A_0$  are the experimental rotational constants.

Table 5.2 Spectroscopic parameters of 2-EF $\cdots$ H<sub>2</sub>O (C<sub>s</sub> conformer) calculated at different levels of theory.

	2 EE	EH.O (C. confor	mar)	
2-EF···H <sub>2</sub> O ( $C_s$ conformer)				
	$\omega$ B97X-D/a	nug-cc-pVQZ	B3LYP(D3BJ)/aug-cc-pVTZ	
$A_e$ (MHz)	1926.004	$-24\%^{a}$	1894.604	− 25 %
$B_e$ (MHz)	1703.675	+ 17 %	1711.304	+ 18 %
$C_e  (\mathrm{MHz})$	922.305	- 8.7 %	923.990	<b>-8.5 %</b>
$ \mu_a ,  \mu_b ,  \mu_c  (D)^b$	1.7, 0	).1, 1.5	1.5, 0.3, 1.5	
	B3LYP(D3B	J)/Def2-TZVP	MP2/aug-	cc-pVDZ
$A_e$ (MHz)	1879.715	<b>− 26 %</b>	1909.812	<b>- 25 %</b>
$B_e$ (MHz)	1743.009	+ 20 %	1744.699	+ 20 %
$C_e(\mathrm{MHz})$	937.908	- 7.2 %	968.208	<b>-4.2 %</b>
$ \mu_{a} ,  \mu_{b} ,  \mu_{c} $ (D)	1.7, 0	0.5, 1.6	1.5, 0.	3, 0.1

<sup>&</sup>lt;sup>a</sup> Calculated by  $[(A_e - A_0)/A_0] \times 100$  % where  $A_e$  are the results of computational calculations presented above and  $A_0$  are the experimental rotational constants.

<sup>&</sup>lt;sup>b</sup> Electric dipole moment components along the principal inertial axes.

<sup>&</sup>lt;sup>b</sup> Electric dipole moment components along the principal inertial axes.

### **5.4 Spectral Analysis**

### 5.4.1 Initial observations: 2-ethylfuran monomer

It was discussed in the introduction that a previous microwave spectroscopy study identified two conformers of 2-ethylfuran (as shown in Figure 5.1) were present within a helium supersonic expansion.<sup>3</sup> In the present work, separate experiments were conducted using argon and neon as the carrier gas, as described in Section 5.2 (Experimental Methods). It was evident from the inspection of each spectrum recorded, that the spectrum obtained using neon as the carrier gas contained a series of rather strong transitions that were absent from the spectrum acquired with argon as the buffer gas. Figure 5.4 displays the 14650 – 15250 MHz region of the microwave spectra recorded using different carrier gases. It can be observed that in the spectrum recorded using neon (Figure 5.4, top) as a carrier gas transitions assigned to both the C<sub>s</sub> and C<sub>1</sub> conformations of this molecule are present, consistent with the findings of the previous study. Whereas, in the spectrum recorded in argon, the C<sub>s</sub> conformer transitions remained present and strong, whereas transitions of the C1 conformer are absent from the spectrum (as illustrated in Figure 5.4, bottom) or in a few cases were present but very weak. This observation is significant, as it provides information about the experimental energy ordering of the two conformers, which was unable to be determined during the previous study, this will be discussed in more detail in Section 5.7 (Discussion).

Within the spectra recorded, a- and b- type transitions were observed for both conformers, several c- type transitions were also present for the  $C_1$  conformer. Transitions from the  $^{13}$ C isotopologues of each conformer were also present in natural abundance, however, unlike the previous study transitions from the  $^{18}$ O isotopologue were unable to be identified, probably owing to its low natural abundance (0.2 %) and the S/N of the spectrum achieved during each experiment. In both spectra acquired during argon and neon experiments, transitions were present which were not assigned to either conformation of the monomer but were subsequently assigned to the monohydrate complex of 2-ethylfuran, which will be discussed in the following sections.

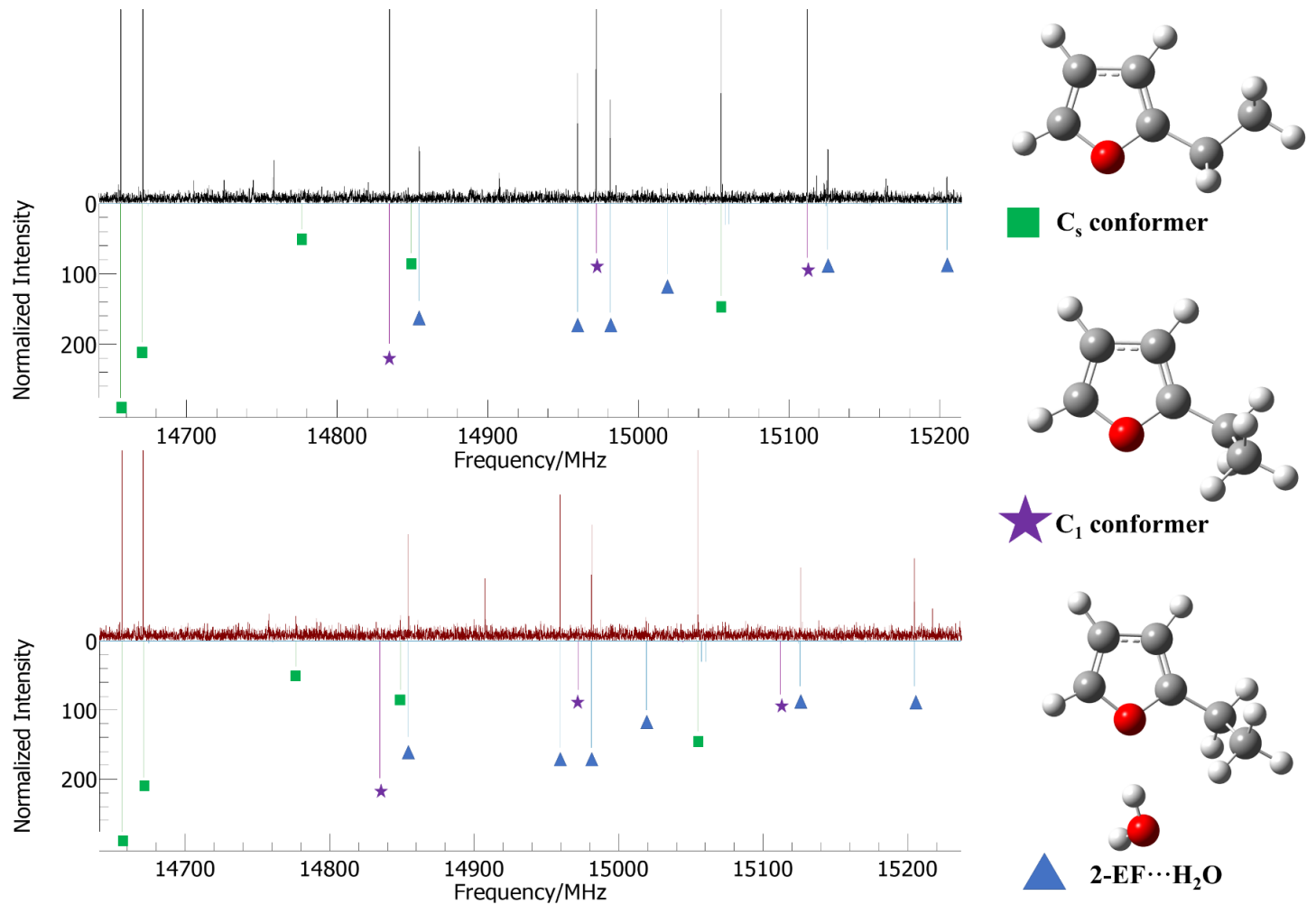


Figure 5.4 Small section of the broadband microwave spectrum recorded while using different carrier gases. (top) Experimental spectrum (black) recorded while using neon as the carrier gas above simulations prepared using PGOPHER of the C<sub>s</sub> conformer of 2-ethylfuran (green, square), C<sub>1</sub> conformer of 2-ethylfuran (purple, star) and 2-EF···H<sub>2</sub>O (blue, triangle). (bottom) Experimental spectrum (maroon) recorded while using argon as the carrier gas above simulations prepared using PGOPHER.

### 5.4.2 Assignment of the monohydrate complex of 2-ethylfuran

Many previous studies of complexes formed between heteroaromatic rings and H<sub>2</sub>O have identified that the H<sub>2</sub>O molecule generally binds at the more electronegative heteroatom present within the ring. This was observed in the monohydrate complexes of the isomers of methylthiazole (Chapter 4) and in the furan···H<sub>2</sub>O complex. <sup>16</sup> The monohydrate complex of furan was studied using matrix-isolation FTIR spectroscopy and it was identified that the H<sub>2</sub>O molecule preferentially binds to the oxygen atom of the furan ring, acting as a hydrogen bond donor. Several other studies on binary complexes formed between furan and its derivatives and small molecules have also reported the same binding motif.<sup>5, 17-20</sup> The initial predictions of the structure of the 2-EF···H<sub>2</sub>O complex were guided by the previous studies of furan containing complexes. Quantum chemical calculations (Section 5.3) predicted that the two possible conformations of the monohydrate complex are close in energy, therefore, both complexes were initially searched for. The structures of the possible monohydrate complexes are calculated to be near-prolate asymmetric tops, which have a dipole moment component that is strongest along the a-inertial axis. The results of quantum chemical calculations were used as the starting point for the assignment process. A series of transitions which were present in spectra recorded during both initial experiments when employing argon and neon as carrier gases was assigned to the monohydrate complex of 2-ethylfuran. In total, 32 rotational transitions across the frequency range 7.0 – 18.5 GHz were fitted to Watson's S-reduced Hamiltonian<sup>21</sup> implemented within PGOPHER.<sup>22</sup> The ground state rotational constants determined from the assignment are as follows:  $A_0 = 2530.5118(32)$  MHz,  $B_0 = 1451.9822(11)$  MHz and  $C_0 = 1010.60117(71)$  MHz. The experimental rotational constants are in significantly better agreement with the rotational constants predicted by theory calculated for the monohydrate complex formed with the C<sub>1</sub> conformation of 2-ethylfuran ( $A_e = 2521$  MHz,  $B_e = 1483$  MHz and  $C_e = 1027$  MHz) compared to the rotational constants predicted for the complex formed with the  $C_s$  conformation ( $A_e$  = 1926 MHz,  $B_e = 1704$  MHz and  $C_e = 922$  MHz). The spectrum was therefore tentatively assigned to the monohydrate complex formed with the C<sub>1</sub> conformation of 2-ethylfuran. Spectroscopic constants determined for this complex are displayed in Table 5.3. The assigned transitions consisted of R- branch a- type transitions only (J = 3 - 8) since no b- and c- type transitions of this complex were identified within the spectrum. Quantum chemical calculations predicted that the projection of the dipole moment onto the a- inertial axis is significantly greater than onto the b- and c- inertial axes. Each transition is unsplit (as shown in Figure 5.4), consistent with expectations, as no quadrupolar nuclei are present within the complex. The barrier to internal rotation of methyl groups within an ethyl substituent are often greater than

1000 cm<sup>-1</sup>, therefore, unlike what was observed for complexes presented in Chapter 4 splitting due to internal rotation are not observed in this case. Efforts were made to search for the other conformation of this binary complex which is formed with the  $C_s$  conformation of 2-ethylfuran. However, this could not be assigned during the present work. To verify the molecular carrier of the spectrum obtained, experiments were performed using isotopically enriched samples of  $D_2O$  and  $H_2^{18}O$  to yield the spectra of isotopologues containing HDO,  $D_2O$  and  $H_2^{18}O$ . This unambiguously confirmed the identity of the molecular carrier of the spectrum to be the monohydrate complex formed with the  $C_1$  conformation of 2-ethylfuran. Spectroscopic constants were determined for four additional isotopologues: 2-EF···H<sub>2</sub><sup>18</sup>O, 2-EF···DOH, 2-EF···HOD and 2-EF···D<sub>2</sub>O, which are displayed in Table 5.3. For each of the additional isotopologues the centrifugal distortion constants  $D_J$  and  $D_{JK}$  were determined in the fit, while the value of  $d_1$  was held fixed to the value determined previously for the parent isotopologue (2-EF···H<sub>2</sub><sup>16</sup>O).

Table 5.3 Experimentally determined spectroscopic parameters of five isotopologues of 2-EF···H<sub>2</sub>O.

	$2\text{-EF}\cdots\text{H}_2 ext{O}$				
	$H_2^{16}O$	$H_2^{18}O$	DOH	HOD	$D_2O$
$A_0$ (MHz)	2530.5118(32) <sup>a</sup>	2473.8961(56)	2502.7183(79)	2470.1215(98)	2445.5277(65)
$B_0$ (MHz)	1451.9822(11)	1395.45246(56)	1443.35048(91)	1416.6218(10)	1408.16994(72)
$C_0$ (MHz)	1010.60117(71)	974.62308(63)	1001.07474(90)	984.5466(11)	975.76183(83)
$D_J(\mathrm{kHz})$	0.673(11)	0.6394(56)	0.6381(85)	0.641(13)	0.6218(76)
$D_{JK}(\mathrm{kHz})$	-0.933(53)	-0.514(41)	-0.32(11)	-0.74(13)	-0.630(76)
$d_1$ (kHz)	-0.1334(68)	$[-0.1334]^{b}$	[-0.1334]	[-0.1334]	[-0.1334]
$\sigma_{rms} (kHz)^{c}$	10.2	7.9	10.9	10.9	9.7
$N^{\mathrm{d}}$	32	31	26	20	28
$P_{cc}$ (u Å <sup>2</sup> )	23.84899(25)	23.95407(29)	23.6193(4)	24.0174(5)	23.8061(4)

<sup>&</sup>lt;sup>a</sup> Numbers in parentheses are one standard deviation in units of the last significant figure.

 $<sup>^{\</sup>rm b}$  Values in square brackets held fixed at the result for the parent isotopologue, 2-EF···H $_2$ <sup>16</sup>O.

<sup>&</sup>lt;sup>c</sup> Root mean square (rms) deviation of the fit.

<sup>&</sup>lt;sup>d</sup> Number of rotational transitions included in the fit.

### **5.5 Molecular Geometry**

The planar moment,  $P_{cc}$ , was calculated for both possible conformations of the monohydrate complex using the equilibrium rotational constants calculated at the  $\omega$ B97X-D/aug-cc-pVQZ level of theory. For the  $C_s$  and  $C_1$  conformations of 2-EF···H<sub>2</sub>O,  $P_{cc}$  was calculated to be 24.6 and 5.5 u Å<sup>2</sup> respectively. The large difference in the values of  $P_{cc}$  is a result of more out of ab plane mass within the  $C_1$  conformer owing to the methyl group of the ethyl substituent being located out of the plane. In the  $C_1$  conformer of the monohydrate complex the ab plane and plane of the furan ring are separated by an angle of 20.7° in the  $\omega$ B97X-D/aug-cc-pVQZ calculated geometry whereas in the  $C_s$  configuration the planes are coincident. The  $P_{cc}$  value determined using the experimental rotational constants of 2-EF···H<sub>2</sub><sup>16</sup>O is 23.84899(25) u Å<sup>2</sup>. The experimentally determined value of  $P_{cc}$  is significantly closer to the value of  $P_{cc}$  determined using the calculated rotational constants of the  $C_1$  configuration of the monohydrate complex compared to the  $C_s$ . Therefore, reaffirming that the spectrum assigned belongs to the monohydrate complex formed with the  $C_1$  configuration of 2-ethylfuran.

Table 5.4 Comparison of experimentally determined ( $r_s$ ) and  $r_e$  atomic coordinates of H<sub>2</sub>O in 2-EF···H<sub>2</sub>O.

	Method	a / Å	b / Å	c / Å
$H_b$	r <sub>e</sub> (calc.) <sup>a</sup>	1.6377	1.4729	0.0505
	$r_{\rm s}$ (exp.)	$1.5102(10)^{b}$	1.57981(96)	[0] <sup>c</sup>
$O_{ m w}$	r <sub>e</sub> (calc.)	2.5712	1.6222	0.1961
	$r_{\rm s}$ (exp.)	2.62469(57)	1.57458(96)	0.2397(63)
$H_{nb}$	r <sub>e</sub> (calc.)	2.6603	2.4281	0.7115
	$r_{\rm s}$ (exp.)	2.87490(53)	2.23429(68)	0.4231(36)

<sup>&</sup>lt;sup>a</sup>  $r_e$  geometry calculated at the  $\omega$ B97X-D/aug-cc-pVQZ level of theory.

The substitution coordinates ( $r_s$ ) of the two hydrogen atoms ( $H_b$  and  $H_{nb}$ ) and oxygen atom ( $O_w$ ) of the  $H_2O$  sub-unit (atom labelling as presented in Figure 5.3) were calculated using Kraitchman's equations<sup>23</sup> implemented within the program KRA.<sup>24</sup> The  $r_s$  coordinates and their Costain errors determined are presented in Table 5.4 along with the  $\omega$ B97X-D/aug-cc-pVQZ calculated  $r_e$  coordinates. Generally, a good agreement between the  $r_s$  and  $r_e$  coordinates can be observed. The c-coordinate of the hydrogen atom of the  $H_2O$  sub-unit involved in the hydrogen

<sup>&</sup>lt;sup>b</sup> Numbers in parentheses after  $r_s$  results are Costain errors calculated as  $\delta a = 0.015/|a|$ .

<sup>&</sup>lt;sup>c</sup> Imaginary  $r_s$  coordinate obtained, therefore, value of coordinate assumed equal to zero.

bond ( $H_b$ ) was calculated to be imaginary, therefore, was assumed equal to zero suggesting that the  $H_b$  atom lies within the ab plane of the complex. A non-zero coordinate was obtained for the c-coordinate of the  $O_w$  atom. The  $r_s$  coordinate obtained suggests that this atom is displaced from the ab plane by 0.2397(63) Å. It was observed in many previous studies of monohydrated heteroaromatic rings, including those presented in Chapter 4, that the O atom of  $H_2O$  is coplanar with the ab plane of the complex. The result obtained for 2-EF··· $H_2O$  differs to what was observed previously suggesting the presence of the ethyl group adopting a  $C_1$  configuration has an effect on the position of the  $O_w$  atom. Weak intermolecular interactions exist within this complex between the  $O_w$  atom of the  $H_2O$  molecule and the closest H atom on  $C_0$  and  $C_0$  of the ethyl group, which will be demonstrated and discussed further in Section 5.6 (Non-Covalent Interactions). The presence of the  $C_0$ - $H_0$ - $O_w$  interaction may be the reason that the  $O_w$  atom is displaced out of the ab plane. Some variation between the  $r_s$  and  $r_c$  coordinates of the  $H_{nb}$  atom is observed. This variation is to be expected since the  $H_{nb}$  atom is not bound within a hydrogen bond, therefore, experiences rapid zero-point motions in the vibrational ground state resulting in the observed differences.

Table 5.5 Comparison of DFT calculated ( $r_e$ ) and experimentally determined ( $r_0$ ) structural parameters of 2-EF···H<sub>2</sub>O.

Parameter	Method	Value
<i>r</i> (O <sub>w</sub> ···O1) / Å	r <sub>e</sub> (calc.) <sup>a</sup>	2.960
	$r_0$ (exp.)	$3.0410(34)^{b}$
∠(O <sub>w</sub> ···O1–C2) /°	r <sub>e</sub> (calc.)	112.2
,	$r_0$ (exp.)	111.50(16)
<i>r</i> (H <sub>b</sub> ···O1) / Å	$r_{\rm e}$ (calc.)	2.014
	$r_0$ (exp., derived) <sup>c</sup>	2.0950(42)
$\angle$ (H <sub>b</sub> ···O1–C2) /°	r <sub>e</sub> (calc.)	116.1
	$r_0$ (exp., derived)	115.30(11)
$\angle (O_w-H_b\cdots O_1)/^\circ$	r <sub>e</sub> (calc.)	167.5
,	$r_0$ (exp., derived)	167.69(16)

<sup>&</sup>lt;sup>a</sup>  $r_e$  geometry calculated at the  $\omega$ B97X-D/aug-cc-pVQZ level of theory.

The effective ground state geometry of the complex was calculated using the  $r_0$  method<sup>25</sup> within STRFIT<sup>24</sup> to provide further insight into the molecular geometry of 2-EF···H<sub>2</sub>O and to evaluate the intermolecular distances and angles within this complex. It was discussed in Chapter 4 that for the methylthiazole···H<sub>2</sub>O complexes the  $r_0$  geometry was obtained while assuming that each

<sup>&</sup>lt;sup>b</sup> Numbers in parentheses are one standard deviation in units of the last significant figure.

<sup>&</sup>lt;sup>c</sup> Parameters derived using EVAL from  $r_0$  coordinates obtained.

atom of the H<sub>2</sub>O sub-unit lies within the plane defined by the thiazole ring. When employing the same approach and an equivalent connectivity for 2-EF···H<sub>2</sub>O, a large  $\chi^2$  value and deviation of the fit were obtained. Comparing the planar moment  $P_{cc}$  for the isolated  $C_1$ monomer<sup>3</sup> and 2-EF···H<sub>2</sub>O it is evident that within the complex more mass lies outside the ab plane. For the C<sub>1</sub> monomer, P<sub>cc</sub> is determined to be 14.925714(4) u Å<sup>2</sup> whereas for the monohydrate complex this is calculated to be 23.84899(25) u Å<sup>2</sup>. An increase in the value of  $P_{cc}$  upon the formation of the monohydrate complex and the observation that  $O_{w}$  has a non-zero c-coordinate suggests a larger fraction of the H<sub>2</sub>O mass lies outside the ab plane in 2-EF···H<sub>2</sub>O compared to the methylthiazole···H<sub>2</sub>O complexes. A different approach was therefore required when setting up the z-matrix for 2-EF···H<sub>2</sub>O. The  $r_0$  parameters displayed in Table 5.5 were determined under the following assumptions. Geometrical parameters internal to both the 2ethylfuran and H<sub>2</sub>O sub-units were assumed equal to the  $r_e$  parameters calculated at the  $\omega$ B97X-D/aug-cc-pVQZ level of theory. As mentioned in Chapter 2, the internal coordinate system defined within the z-matrix can be quite different from the configuration of chemical bonds within the complex. The z-matrix of 2-EF···H<sub>2</sub>O was constructed in such a way to allow for interatomic distances and angles containing only heavy atoms to be fitted. A lowering of the  $\chi^2$ value and standard deviation of the fit was observed under these assumptions. From the least squares fit of structural parameters to the rotational constants of all isotopologues (displayed in Table 5.3), one intermolecular distance,  $r(O_w \cdots O1)$  and one angle,  $\angle(O_w \cdots O1 - C2)$  was determined while keeping all other structural parameters fixed to the ωB97X-D/aug-cc-pVQZ calculated result. The interatomic distance between the O<sub>w</sub> atom of the H<sub>2</sub>O sub-unit and the O1 atom within the furan ring was calculated to be 3.0410(34) Å in the  $r_0$  geometry which compares with the  $r_e$  calculated result of 2.960 Å. The  $\angle$ (O<sub>w</sub>···O1–C2) angle was determined to be 111.50(16)° in the  $r_0$  geometry which is very similar to the  $r_e$  calculated result of 112.2°. Three additional geometrical parameters were derived from the  $r_0$  coordinates (Table A.25) after the fit was performed using the program EVAL. The hydrogen bond distance,  $r(H_b \cdots O1)$  and the angles  $\angle(H_b \cdots O1-C2)$  and  $\angle(O_w - H_b \cdots O1)$  were determined to be 2.0950(42) Å, 115.30(11)° and 167.69(16)° respectively. Consistent with expectations, the value obtained for the hydrogen bond angle,  $\angle(O_w-H_b\cdots O_1)$ , indicates that the primary hydrogen bond present within this complex is non-linear in a manner similar to that observed in many other complexes formed between heteroaromatic rings and H<sub>2</sub>O molecules.

#### **5.6 Non-Covalent Interactions**

It was discussed in the previous section that within the conformer of 2-EF···H<sub>2</sub>O observed experimentally that the H<sub>2</sub>O molecule binds to the furan ring at the O<sub>1</sub> position. In this interaction the H<sub>2</sub>O molecule acts as the hydrogen bond donor and the furan ring is the hydrogen bond acceptor. It was observed that the primary hydrogen bond is non-linear which can likely be attributed to additional weaker hydrogen bonding interactions within this complex, similar to what was previously observed and discussed in Chapter 4 for the methylthiazole...H2O complexes. Non-Covalent Interactions (NCI)<sup>26</sup> and Natural Bond Orbital (NBO)<sup>27</sup> analyses have been performed using the optimised geometry of 2-EF···H<sub>2</sub>O calculated at the  $\omega$ B97X-D/aug-cc-pVQZ level of theory to visualise the intermolecular interactions present within this complex. Figure 5.5 displays the NCI plot of the reduced density gradient (RDG) against the sign of the second eigenvalue of the Hessian matrix  $(\lambda_2)$  of the electronic density  $(\rho)$ ,  $(\text{sign}(\lambda_2)\rho)$ . A blue isosurface is visible located between H<sub>b</sub> of the H<sub>2</sub>O sub-unit and O1 of the furan ring, indicative of a relatively strong attractive hydrogen bonding interaction. A larger and more diffuse isosurface is located between the O<sub>w</sub> atom of the H<sub>2</sub>O molecule and the ethyl substituent. This isosurface has areas of weakly attractive and weakly repulsive interactions, providing evidence that additional weaker interactions are present within the complex. The light green areas of the isosurface represents attractive interactions which have a negative sign  $(\lambda_2)\rho$  value and the dark green areas represent slightly repulsive interactions which have a positive sign  $(\lambda_2)\rho$  value, as represented in the NCI plot. The areas of the isosurface indicating weakly attractive interactions are located between O<sub>w</sub> and the nearest H atoms located on C6 and C7. Each of the 2-ethylfuran and H<sub>2</sub>O sub-units therefore simultaneously act as a hydrogen bond donor and acceptor within this complex.

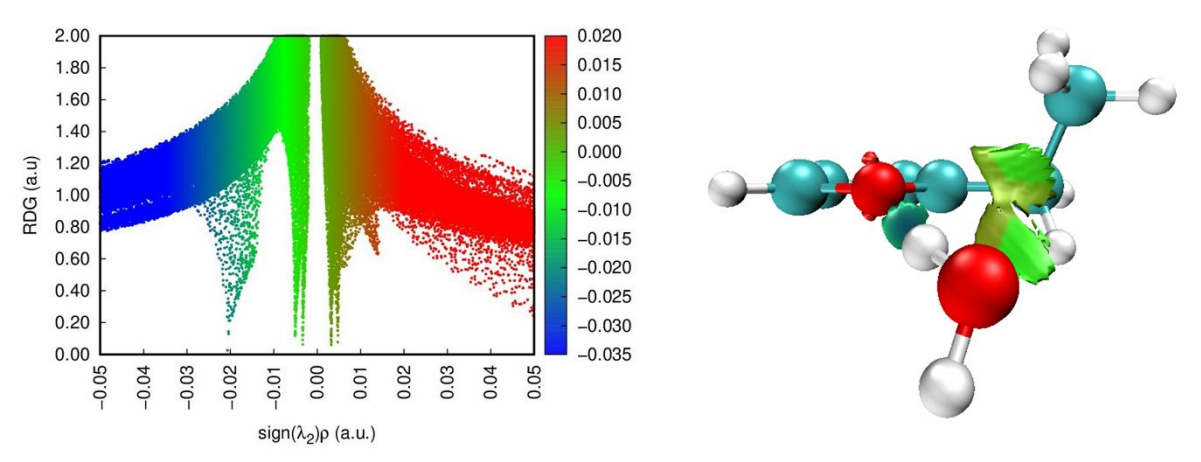


Figure 5.5 NCI isosurfaces and plots of the RDG (a.u.) vs  $sign(\lambda_2)\rho$  of the experimentally observed conformation of 2-EF···H<sub>2</sub>O (C<sub>1</sub> conformer). Positive and negative values of  $sign(\lambda_2)\rho$  respectively denote repulsive (red) and attractive (blue) interactions. The isosurface s value is 0.5 au.

NBO analysis was performed at the B3LYP(D3BJ)/aug-cc-pVTZ level of theory, using the same optimised geometry of 2-EF···H<sub>2</sub>O as what was used for the NCI analysis, to calculate second order stabilisation energies ( $E^{(2)}$ ) (Table A.26) associated with interactions present within the complex. The results of the analysis are shown graphically in Figure 5.6. The largest  $E^{(2)}$  contribution corresponds to the primary hydrogen bonding interaction between one of the lone pairs of the O1 atom and the antibonding  $\sigma^*(H_b-O)$  orbital of the H<sub>2</sub>O molecule. This interaction was calculated to have a second order stabilisation energy of 11.92 kJ mol<sup>-1</sup>. It has been reported within a different study that the equivalent interaction within furan...H2O was calculated to have a  $E^{(2)}$  contribution of 30.42 kJ mol<sup>-1</sup> (when calculated at the MP2/6-31+G\* level of theory).<sup>28</sup> However, when the structure was re-optimised at the ωB97X-D/aug-ccpVQZ level of theory and NBO analysis was subsequently performed (at the B3LYP(D3BJ)/aug-cc-pVTZ level) the  $E^{(2)}$  of the primary hydrogen bond was calculated to be 8.5 kJ mol<sup>-1</sup>, which is considerably closer to the value obtained for 2-EF···H<sub>2</sub>O. The analysis also identified that there is an additional interaction present within 2-EF···H<sub>2</sub>O between the second lone pair on the O1 atom and the  $\sigma^*(H_b-O_w)$  orbital of the H<sub>2</sub>O molecule. The second order stabilisation energy was calculated to be 0.96 kJ mol<sup>-1</sup>, which is considerably weaker than the interaction formed with the other lone pair. This is likely due to the orientation of this lone pair not being as favourable for overlap with the antibonding orbital of the H<sub>2</sub>O molecule. It was discussed earlier that the  $r_0$  geometrical parameters obtained implied that the  $O_w$  of the  $H_2O$ molecule interacts with the ethyl group and that an isosurface implying weak attractive interactions was identified within the NCI analysis. The NBO analysis revealed that two interactions are present between the lone pairs on O<sub>w</sub> and each H attached to C6. The second order stabilisation energies are calculated to be 0.88 and 0.33 kJ mol<sup>-1</sup>. Within the NCI analysis a light green area of the isosurface was present located between Ow and the nearest H7 atom, however, this interaction was not identified in the NBO analysis when using the optimised geometry calculated at the ωB97X-D/aug-cc-pVQZ level. The H7···O<sub>w</sub> interatomic distance is calculated to be 2.97 Å within the  $\omega$ B97X-D geometry and determined to be 2.8268(30) Å in the  $r_0$  geometry. The result is different when performing the analysis using the optimised geometry calculated at the B3LYP(D3BJ)/aug-cc-pVTZ level, the C7–H7···O<sub>w</sub> interaction was identified and  $E^{(2)}$  was calculated to be 0.33 kJ mol<sup>-1</sup>. This inconsistency between the NCI and NBO analysis likely arises due to the interaction being present however very weak. This was also observed in the case of thiazole...H2O and 5-methylthiazole...H2O, the value of the hydrogen bond angle obtained in each study implied that a secondary weaker hydrogen bonding interaction (C2–H2···O) was present within both complexes, yet the NCI and NBO analyses

did not identify these interactions within the complexes. The magnitudes of the C6–H6···O<sub>w</sub> interaction energies when using the B3LYP(D3BJ)/aug-cc-pVTZ geometry were calculated to have second order stabilisation energies of 0.46 and 0.25 kJ mol<sup>-1</sup>.

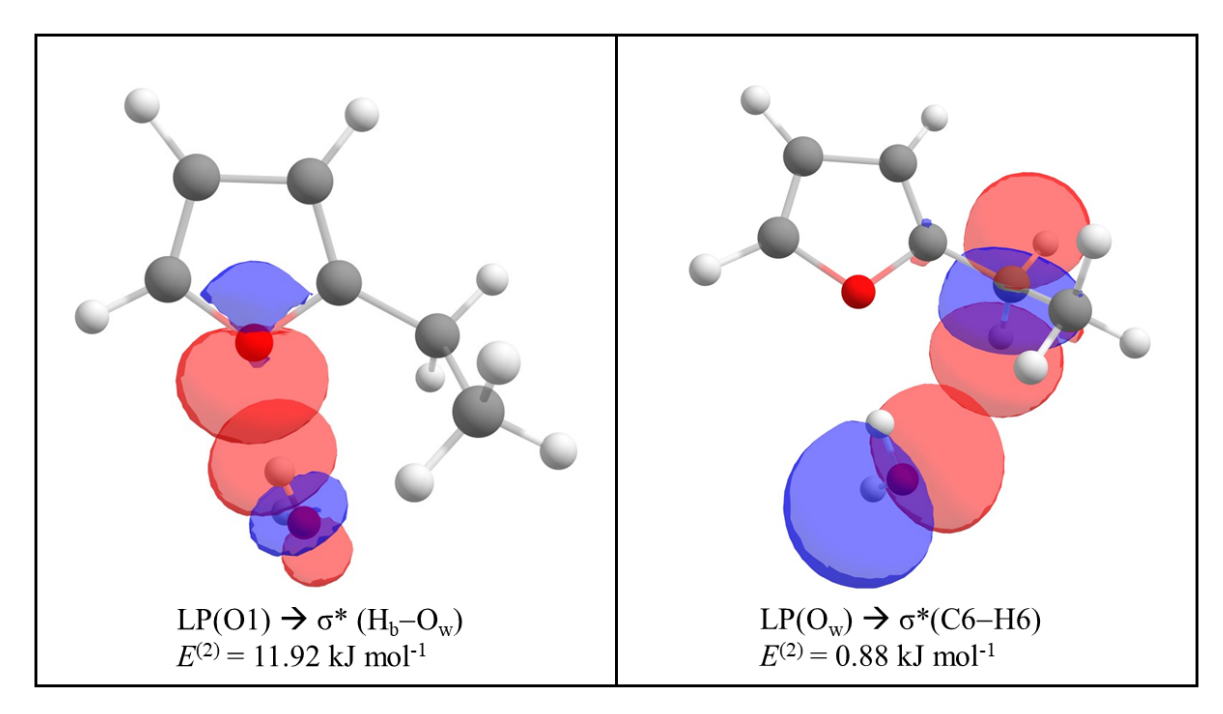


Figure 5.6 NBO plots associated with intermolecular interactions in 2-EF···H<sub>2</sub>O ( $C_1$  conformer).  $E^{(2)}$  represents the second order perturbation energy of each interaction.

An equivalent analysis was also performed for the higher energy isomer of 2-EF···H<sub>2</sub>O formed with the  $C_s$  conformation of 2-ethylfuran. This analysis was performed to provide an insight into the intermolecular interactions present within this conformation of the monohydrate complex which can provide an insight into why this is calculated to be higher in energy. The NCI analysis (see Appendix A.27) revealed the presence of three isosurfaces within this complex. A blue isosurface is present between O1 of the furan ring and  $H_b$  of the  $H_2O$  molecule indicating the presence of a hydrogen bonding interaction as previously observed in the case of the  $C_1$  conformer. Additional intermolecular interactions are also present within this complex. A weakly attractive interaction is present between  $O_w$  of  $H_2O$  and one of the H atoms located on C6 which is indicated by the light green isosurface located between. Since the heavy atoms within the ethyl group are coincident with the ab plane such that the  $\angle(C7-C6-C2-O1)$  dihedral angle is 180°, it is therefore not possible for the  $H_2O$  molecule to interact with one of the H atoms bound to C7. A third isosurface is located between C3-H3 and the methyl group of the ethyl substituent which has areas of weakly attractive and repulsive interactions. The area of repulsive interaction is likely a result of this arrangement being more sterically hindered than

the  $C_1$  configuration. Unsurprisingly, the largest  $E^{(2)}$  contribution identified by the NBO analysis (Table A.28) was from the primary hydrogen bond interaction,  $O_w$ – $H_b$ ···O1, with a second order stabilisation energy of 12.26 kJ mol<sup>-1</sup>. The magnitude of this interaction is ~1 kJ mol<sup>-1</sup> greater than for the same interaction within the complex formed with the  $C_1$  conformer. However, the opposite is observed when comparing the magnitudes of the second order stabilisation energies of the interaction between one of the lone pairs on  $O_w$  and  $\sigma^*(C6$ –H6). Within the complex formed with the  $C_s$  conformer this is calculated to be 0.25 kJ mol<sup>-1</sup> which is somewhat weaker than observed for the same interaction in the monohydrate complex formed with the  $C_1$  conformer (0.88 kJ mol<sup>-1</sup>). Comparing parameters associated with the primary hydrogen bond in the  $r_e$  geometries of each complex, it can be observed that the hydrogen bond distance is essentially the same, however, the hydrogen bond angle differs by ~3°. The hydrogen bond within the  $C_s$  conformer of 2-EF···H<sub>2</sub>O is closer to linearity than the  $C_1$  conformer which likely results in the different magnitudes of the interaction energies.

#### 5.7 Discussion

In this study and a previous work,<sup>3</sup> two conformations of 2-ethylfuran (C<sub>s</sub> and C<sub>1</sub>) were observed simultaneously within a supersonically expanding jet when either neon or helium was used as the carrier gas. However, when argon was employed, only transitions from the C<sub>s</sub> conformation of this molecule were visible within the spectrum. This observation indicates that for 2-ethylfuran the choice of carrier gas influences the conformers present within the expansion and can provide information about the experimental energy ordering of the observed conformers. It is known that the choice of carrier gas influences the relative concentration of conformers and isomers within a supersonic expansion, this phenomenon was first described by Ruoff et al. in 1990.<sup>29</sup> Relaxation from higher energy forms of a molecule to lower energy forms occurs as a result of collisions with the inert carrier gas within the supersonically expanding jet. When heavier carrier gases are employed, relaxation to low energy conformers progresses more efficiently compared to lighter carrier gases which results in higher energy conformers being populated within helium and neon expansions.<sup>30</sup> Since transitions of the C<sub>1</sub> conformer of 2-ethylfuran were absent from the spectrum recorded in argon, it suggests that this form of the molecule is higher in energy and that it is likely undergone relaxation into the lower energy C<sub>s</sub> form. Ruoff et al. suggested that if the barrier to interconversion is less than 350 cm<sup>-1</sup> (4.2 kJ mol<sup>-1</sup>) that higher energy conformers are likely to undergo relaxation when heavier carrier gases such as argon are employed. This observation suggests that the barrier to interconversion between the C1 and Cs configurations of 2-ethylfuran is sufficiently low to allow for relaxation. It was reported in the previous study<sup>3</sup> that calculations performed at the MP2/6-311++G(d,p) and MP2/6-31G(d,p) level of theory predicted that the global minimum would be the C<sub>1</sub> conformer and is calculated to be ~2 kJ mol<sup>-1</sup> lower in energy than the C<sub>s</sub>. Calculations performed herein at the MP2/aug-cc-pVDZ and B3LYP(D3BJ)/Def2-TZVP level also predicted that the C<sub>1</sub> conformer is lower in energy than the C<sub>s</sub> conformer by 0.75 and 0.06 kJ mol<sup>-1</sup> respectively. Only the calculation performed at the B3LYP(D3BJ)/aug-cc-pVTZ level predicts the C<sub>s</sub> conformer to be the global minimum, however, the difference in energy between the two conformers is calculated to be very small (0.1 kJ mol<sup>-1</sup>). Potential energy scans performed at each level of theory are displayed in Figure 5.2. It can therefore be concluded that generally quantum chemical calculations predict the C<sub>1</sub> to be the global minimum structure of this molecule which differs from what can be inferred from the experimental data which suggests the C<sub>s</sub> form is lower in energy.

Analysis of the microwave spectrum recorded allowed the assignment of one isomer of the monohydrate complex. Within the molecular geometry of the experimentally observed 2-

EF···H<sub>2</sub>O, the 2-ethylfuran sub-unit adopts a C<sub>1</sub> configuration, which was predicted to be the lowest energy geometry of this complex by quantum chemical calculations. Within the argon experiment in addition to transitions belonging to the monohydrate complex, only transitions from the C<sub>s</sub> conformer of the monomer was observed. It can therefore be inferred that the relative energies of the conformers change depending on whether 2-ethylfuran is an isolated molecule or bound within the hydrate complex.

Studies such as the microsolvation of glycidol, <sup>9</sup> 2-aminoethanol, <sup>10</sup> sulfanilamide, <sup>12</sup> mevalonolactone, 11 formanilide 13 and 2-hydroxypyridine/2-pyridone 14, 15 have observed changes in the lowest energy structure of the molecule upon the formation of complexes with H<sub>2</sub>O. Within the isolated molecules of glycidol,<sup>31, 32</sup> and 2-aminoethanol<sup>33</sup> an intramolecular hydrogen bond is present within each of the lowest energy geometries of the isolated monomers. Upon formation of the monohydrate complex it has been reported that in each case the intramolecular hydrogen bond is replaced by an intermolecular hydrogen bonding network and that a structural change occurs in order to accommodate this change. A significant torsional change of 9° and 18° within the backbone of each of glycidol and 2-aminoethanol respectively was reported to occur upon the formation of the monohydrate complex.<sup>9, 10</sup> Within the isolated monomer of sulfanilamide, <sup>12</sup> the hydrogen atoms within the sulfonyl amine (SO<sub>2</sub>NH<sub>2</sub>) group are positioned such that the functional group adopts an eclipsed arrangement, allowing the presence of an intramolecular hydrogen bond. Upon the formation of the monohydrate complex, the functional group adopts the higher energy staggered configuration allowing the H<sub>2</sub>O molecule to insert between and simultaneously interact with the -NH2 and -SO2 functional groups. 12 The hydration of mevalonolactone results in the simultaneous re-orientation of the hydroxy group and a change in the torsional angle within the molecules backbone upon the formation of the monohydrate complex.<sup>11</sup>

In each of the studies of the microsolvation of formanilide<sup>13</sup> and 2-hydroxypyridine/2-pyridone,<sup>14, 15</sup> it has been observed that the hydration of these molecules results in a shift in the conformational or tautomeric equilibria resulting in a change in the lowest energy form of the molecule. The isolated molecules of both formanilide<sup>34</sup> and the pyridine derivative<sup>35</sup> exist in two forms. Formanilide<sup>34</sup> contains an amide functional group which can adopt either a cis or trans configuration, with the trans conformer being lower in energy than the cis. Whereas a keto/enol tautomeric equilibrium is present within 2-pyridone/2-hydroxypyridine, with the hydroxy form being reported to be lower in energy.<sup>35</sup> Three isomers of the monohydrate complex and one isomer of the dihydrate complex formed with formanilide have been observed.<sup>13</sup> The isomer of the monohydrate complex formed with the cis configuration was

found to be lower in energy than the two isomers formed with the trans configuration. The hydrated form of the cis conformer allows the H<sub>2</sub>O molecule to simultaneously interact with both C=O and N-H, resulting in the stabilisation of the cis form of this molecule, whereas in each of the trans complexes only one intermolecular interaction can form between the sub-units. For 2-hydroxypyridine/2-pyridone, a monohydrate complex formed with each tautomer and the dihydrate complex formed with only 2-pyridone have been observed.<sup>14, 15</sup> It was reported that the species formed with the 2-pyridone form was more abundant within the supersonic jet suggesting that this is the lower energy form, and that hydration has shifted the tautomeric equilibrium towards the ketone.

In each of the aforementioned studies where a change in the lowest energy form of a molecule occurs upon microsolvation, the driving force for the change is the intermolecular interactions present within the hydrate complexes. The change occurs in order to maximise the number of hydrogen bonding interactions with  $H_2O$ . Therefore, it is likely that this is also the reason for the change in the lowest energy conformation of 2-ethylfuran upon the formation of the monohydrate complex. The NCI and NBO analysis discussed in Section 5.6 identified that in addition to the primary hydrogen bond, additional intermolecular interactions between the oxygen atom of the  $H_2O$  molecule and the ethyl substituent are also present within the monohydrate complex formed with the  $C_1$  conformation. Within the monohydrate complex formed with the  $C_8$  conformer, the  $O_w$  atom cannot form an interaction with  $C_7$ – $H_7$  and it can be observed that an isosurface was present within the NCI analysis showing weakly repulsive interactions. The intermolecular interactions present within 2-EF···H<sub>2</sub>O formed with the  $C_1$  conformer likely stabilises this complex, resulting in it being lower in energy than when formed with the  $C_8$  configuration.

Weakly-bound complexes comprised of furan or a furan derivative and another small molecule such as  $H_2O$ , 5, 16, 17, 36, 37 methanol, 17, 20, 38 formic acid, 18, 19 acetylene<sup>39</sup> and sulphur dioxide<sup>40</sup> have been widely studied using both microwave and FTIR spectroscopy techniques. For  $H_2O$  containing complexes, the vast majority are formed via the primary hydrogen bonding,  $O_w-H_b\cdots O1$ , interaction. However, some notable exceptions include the microsolvation of maleic anhydride<sup>36</sup> and isomers of furonitrile.<sup>37</sup> In the observed isomers of the hydrated forms the  $H_2O$  molecule(s) interact with the carbonyl or nitrile group rather than with the O1 atom situated within the ring. In each of maleic acid···( $H_2O$ )<sub>n</sub> (where n = 1-3) and furonitrile··· $H_2O$  isomers, the furan derivatives and  $H_2O$  molecules simultaneously act as hydrogen bond donor and acceptor, similar to what has been observed presently in the case of 2-EF··· $H_2O$ . The only exception being isomer 2-II of 2-furonitrile··· $H_2O$ .<sup>37</sup> In this complex only one hydrogen bond

is present between the two sub-units, such that the hydrogen bond angle is significantly closer to linearity compared to the 2-I isomer of the complex, owing to no additional intermolecular interactions being present.

Table 5.6 Comparison of experimentally-determined ( $r_0$ ) structural parameters of complexes formed between furan derivatives and  $H_2O$ .

Parameter	$2$ -EF····H $_2$ O	furfuryl	furfuryl
		alcohol····H <sub>2</sub> O	mercaptan···H <sub>2</sub> O
<i>r</i> (O <sub>W</sub> ···O1) / Å	3.0410(34) <sup>a</sup>	2.931(1) <sup>b</sup>	2.926(3) <sup>b</sup>
$\angle (O_W \cdots O1 - C2) / ^{\circ}$	111.50(16)	105.466(19) <sup>c</sup>	110.69(25) <sup>c</sup>
$r(H_b \cdots O1) / \mathring{A}$	2.0950(42)	2.155(6)	1.988(24)
$\angle(H_b\cdots O1-C2)/^\circ$	115.30(11)	117.433(60)	115.47(42)
$\angle (O_w - H_b \cdots O_1) / \circ$	167.69(16)	136.060(86)	162.37(79)

<sup>&</sup>lt;sup>a</sup> Numbers in parentheses are one standard deviation in units of the last significant figure.

The closest known comparators to 2-EF···H<sub>2</sub>O within the current literature are monohydrate complexes of furfuryl alcohol and furfuryl mercaptan.<sup>5</sup> As mentioned earlier the furan derivatives are analogous, only differing in the group bound to C6 (CH<sub>3</sub>, OH and SH) and it is known that the  $\angle$ (X7–C6–C2–O1) dihedral angle, which defines the rotation of the substituent relative to the plane of the furan ring, in each of the monomers are of a similar magnitude.<sup>3-6</sup> The study of furfuryl alcohol···H<sub>2</sub>O and furfuryl mercaptan····H<sub>2</sub>O found one isomer of the former and two isomers of the latter were present within a neon expansion. The structural parameters displayed in Table 5.6 have been derived from the  $r_0$  coordinates reported for the isomers which form through the same binding motif as 2-EF···H<sub>2</sub>O, denoted as GG'-W<sub>da</sub> in the study.<sup>5</sup> Within the lowest energy isomers of furfuryl alcohol···H<sub>2</sub>O and furfuryl mercaptan···H<sub>2</sub>O, the H<sub>2</sub>O molecule simultaneously acts as a hydrogen bond donor and acceptor, therefore, in addition to the Ow-Hb···O1 hydrogen bond an additional interaction forms with the terminal hydrogen atom of the alcohol or thiol group (O7/S7-H7···O<sub>w</sub>) acting as a hydrogen bond donor. This is similar to what has been observed in the case of 2-EF···H<sub>2</sub>O, although within this complex the O<sub>w</sub> atom simultaneously forms an interaction with the closest H atom bound to C7 and C6. Within the original study of furfuryl alcohol···H<sub>2</sub>O and furfuryl mercaptan···H<sub>2</sub>O, there was no indication given whether the O<sub>w</sub> atom of the H<sub>2</sub>O molecule interacts with the closest H atom of C6. From the  $r_0$  coordinates,  $O_w$  and the closest H atom

<sup>&</sup>lt;sup>b</sup> Results for interatomic distances within furfuryl alcohol···H<sub>2</sub>O and furfuryl mercaptan···H<sub>2</sub>O reported in reference 5.

<sup>&</sup>lt;sup>c</sup> Results for angles derived using EVAL from  $r_0$  coordinates given in reference 5.

located on C6 are separated by 3.0861(11) Å in the former and 2.845(16) Å in the latter. NCI analysis performed herein for furfuryl alcohol···H<sub>2</sub>O and furfuryl mercaptan···H<sub>2</sub>O do not indicate the presence of a weakly attractive interaction between O<sub>w</sub> and C6–H6. The hydrogen bond angle (∠(O<sub>w</sub>-H<sub>b</sub>···O1)) within each monohydrate complex is non-linear, consistent with expectations, owing to the presence of the hydrogen bonding interaction(s) whereby the furan derivative acts as the hydrogen bond donor. A notable observation is that the  $\angle(O_w-H_b\cdots O1)$ hydrogen bond angle within furfuryl alcohol···H<sub>2</sub>O deviates significantly further from linearity compared to the same parameter in 2-EF···H<sub>2</sub>O and furfuryl mercaptan···H<sub>2</sub>O, which are calculated to be of a similar magnitude. This can be attributed to the relative strength of the C7/O7/S7-H···O<sub>w</sub> interaction as this varies across the series of complexes. It is known that O-H is a stronger hydrogen bond donor compared to S-H and C-H which are typically categorised as weak hydrogen bond donors due to the relative polarisation of the bond being lower. The furfuryl alcohol···H<sub>2</sub>O study reported that the  $r(H7\cdots O_w)$  and  $r(H_b\cdots O1)$ intermolecular distances were determined to be 1.956(3) and 2.16(1) Å respectively. The hydrogen bond interaction with the alcohol group is shorter than the interaction formed with the O1 atom of the furan ring, indicating that in fact the O7–H7···O<sub>w</sub> interaction is the stronger hydrogen bond within this complex. Which may explain why the intermolecular distance  $r(H_b \cdots O1)$  is longer in furfuryl alcohol···H<sub>2</sub>O compared to 2-EF···H<sub>2</sub>O and furfuryl mercaptan···H<sub>2</sub>O. It can be observed that the magnitude of the  $\angle$ (H<sub>b</sub>···O1–C2) angle is similar in each of the complexes. It was discussed in Chapter 4 (methylthiazole···H<sub>2</sub>O) that one of the consequences of a methyl group being positioned adjacent to the location at which the H<sub>2</sub>O molecule binds was that the  $\angle(H_b \cdots N3-C2)$  angle obtained was significantly greater than its unmethylated analogue. For each of 2-EF···H<sub>2</sub>O, furfuryl alcohol···H<sub>2</sub>O and furfuryl mercaptan···H<sub>2</sub>O the group substituted on the ring is at the 2-position, adjacent to the H<sub>2</sub>O binding site. It is therefore possible that the same effect could be present within the monohydrated furan derivatives. However, owing to the lack of structural information about the furan···H<sub>2</sub>O complex available within the current literature this is unable to be experimentally verified. Comparing the  $r_{\rm e}$  parameters calculated at the  $\omega B97X$ -D/aug-ccpVQZ level of theory it can be observed that within the equilibrium geometry that the angle ∠(H<sub>b</sub>···O1–C2) is somewhat greater within 2-EF···H<sub>2</sub>O (116.1°) compared to furan···H<sub>2</sub>O (106.3°). It is also interesting to note that the magnitude of this  $r_0$  parameter within each of the furan derivatives is similar to what was observed in 2-methylthiazole···H<sub>2</sub>O (112.6(16)°) and 2-methylimidazole···H<sub>2</sub>O<sup>41</sup> (116.9(9)°) suggesting that the identity of the substituent adjacent

to the $\rm H_2O$ molecule and hydrogen bond acceptor have minimal effect on the magnitude of this angle.	1

#### 5.8 Conclusions

To conclude the broadband microwave spectrum of two conformations of the isolated 2ethylfuran monomer and one isomer of the 2-EF···H<sub>2</sub>O have been observed over the frequency range 7.0 – 18.5 GHz in separate experiments using argon and neon as carrier gases. The experiments performed herein provided information about the experimental energy ordering of the observed conformers of the 2-ethylfuran monomer, which was unable to be determined during the previous study. Rotational transitions belonging to the C<sub>s</sub> conformer were present in spectra acquired using argon and neon as carrier gases, whereas transitions of the conformer with C<sub>1</sub> symmetry were only present within the spectrum acquired using neon. Since transitions of the C<sub>1</sub> conformer were absent from the spectrum recorded in argon, it suggests that this form of the molecule is higher in energy and the barrier to interconversion between the two conformers is sufficiently low to allow for relaxation into the C<sub>s</sub> form within the argon expansion. The microwave spectra of five isotopologues of 2-EF···H<sub>2</sub>O were recorded which allowed the unambiguous assignment to the monohydrate complex formed with the C<sub>1</sub> configuration of 2-ethylfuran. This conformation of the monohydrate complex was predicted to be the lowest in energy by quantum chemical calculations. A change in the relative energy ordering of the conformations of 2-ethylfuran occurs upon the formation of the monohydrate complex and the driving force for this change is the intermolecular interactions present within the complex. The 2-EF···H<sub>2</sub>O complex contains a primary hydrogen bonding interaction between the H<sub>2</sub>O molecule and oxygen atom of the furan ring, with the former acting as the hydrogen bond donor and the latter being the hydrogen bond acceptor. Analysis of the molecular geometry identified that additional weaker hydrogen bonds are present within the complex between the oxygen atom of the H<sub>2</sub>O molecule and nearest hydrogen atoms on the ethyl group.

## **5.9 References**

- 1. W. Caminati, D. Damiani, G. Corbelli, B. Velino and C. W. Bock, *Molecular Physics*, 1991, **74**, 885-895.
- 2. J. Wang, S. Herbers, P. Buschmann, K. Lengsfeld, J.-U. Grabow, G. Feng and Q. Gou, *Chinese Journal of Chemical Physics*, 2020, **33**, 119-124.
- 3. H. V. L. Nguyen, *Journal of Molecular Structure*, 2020, **1208**, 127909.
- 4. K.-M. Marstokk and H. Møllendal, *Acta Chemica Scandinavica*, 1994, **48**, 25-31.
- 5. M. Juanes, A. Lesarri, R. Pinacho, E. Charro, J. E. Rubio, L. Enríquez and M. Jaraíz, *Chemistry A European Journal*, 2018, **24**, 6564-6571.
- 6. K.-M. Marstokk and H. Møllendal, *Acta Chemica Scandinavica*, 1994, **48**, 298-305.
- 7. I. Hedgecock, N. W. Larsen, L. Nygaard, T. Pedersen and G. O. Sørensen, *Journal of Molecular Structure*, 1990, **223**, 33-44.
- 8. J. A. Beukes, K. M. Marstokk and H. Møllendal, *Journal of Molecular Structure*, 2001, **567-568**, 19-27.
- 9. A. R. Conrad, N. H. Teumelsan, P. E. Wang and M. J. Tubergen, *The Journal of Physical Chemistry A*, 2010, **114**, 336-342.
- 10. M. J. Tubergen, C. R. Torok and R. J. Lavrich, *The Journal of Chemical Physics*, 2003, **119**, 8397-8403.
- 11. S. R. Domingos, C. Pérez and M. Schnell, *The Journal of Chemical Physics*, 2017, **147**, 124310.
- 12. S. Mato, R. Aguado, S. Mata, J. L. Alonso and I. León, *Physical Chemistry Chemical Physics*, 2022, **24**, 24032-24038.
- 13. P. Pinacho, S. Blanco and J. C. López, *Physical Chemistry Chemical Physics*, 2019, **21**, 2177-2185.
- 14. A. Maris, P. Ottaviani and W. Caminati, *Chemical Physics Letters*, 2002, **360**, 155-160.
- 15. S. Mata, V. Cortijo, W. Caminati, J. L. Alonso, M. E. Sanz, J. C. López and S. Blanco, *The Journal of Physical Chemistry A*, 2010, **114**, 11393-11398.
- 16. S. P. Lockwood, T. G. Fuller and J. J. Newby, *The Journal of Physical Chemistry A*, 2018, **122**, 7160-7170.
- 17. D. Bernhard, M. Fatima, A. Poblotzki, A. L. Steber, C. Pérez, M. A. Suhm, M. Schnell and M. Gerhards, *Physical Chemistry Chemical Physics*, 2019, **21**, 16032-16046.
- 18. T. Yang, L. Wang, Z. Wang, Y. Xu and G. Feng, *The Journal of Physical Chemistry A*, 2022, **126**, 4608-4616.
- 19. E. Sánchez-García, A. Mardyukov, M. Studentkowski, L. A. Montero and W. Sander, *The Journal of Physical Chemistry A*, 2006, **110**, 13775-13785.
- 20. H. C. Gottschalk, A. Poblotzki, M. Fatima, D. A. Obenchain, C. Pérez, J. Antony, A. A. Auer, L. Baptista, D. M. Benoit, G. Bistoni, F. Bohle, R. Dahmani, D. Firaha, S. Grimme, A. Hansen, M. E. Harding, M. Hochlaf, C. Holzer, G. Jansen, W. Klopper, W. A. Kopp, M. Krasowska, L. C. Kröger, K. Leonhard, M. Mogren Al-Mogren, H. Mouhib, F. Neese, M. N. Pereira, M. Prakash, I. S. Ulusoy, R. A. Mata, M. A. Suhm and M. Schnell, *The Journal of Chemical Physics*, 2020, 152, 164303.
- 21. J. K. G. Watson, *The Journal of Chemical Physics*, 1968, **48**, 4517-4524.
- 22. C. M. Western, *Journal of Quantitative Spectroscopy and Radiative Transfer*, 2017, **186**, 221-242.
- 23. J. Kraitchman, American Journal of Physics, 1953, 21, 17-24.
- 24. Z. Kisiel, PROSPE Programs for ROtational SPEctroscopy, <a href="http://info.ifpan.edu.pl/~kisiel/prospe.htm">http://info.ifpan.edu.pl/~kisiel/prospe.htm</a>, (accessed 21/06/2024, 2024).
- 25. Z. Kisiel, Journal of Molecular Spectroscopy, 2003, 218, 58-67.
- 26. E. R. Johnson, S. Keinan, P. Mori-Sánchez, J. Contreras-García, A. J. Cohen and W. Yang, *Journal of the American Chemical Society*, 2010, **132**, 6498-6506.

- 27. A. E. Reed, L. A. Curtiss and F. Weinhold, *Chemical Reviews*, 1988, 88, 899-926.
- 28. D. Kaur and S. Khanna, Computational and Theoretical Chemistry, 2011, 963, 71-75.
- 29. R. S. Ruoff, T. D. Klots, T. Emilsson and H. S. Gutowsky, *The Journal of Chemical Physics*, 1990, **93**, 3142-3150.
- 30. S. R. Domingos, C. Pérez, C. Medcraft, P. Pinacho and M. Schnell, *Physical Chemistry Chemical Physics*, 2016, **18**, 16682-16689.
- 31. W. V. F. Brooks and K. V. L. N. Sastry, *Canadian Journal of Chemistry*, 1975, **53**, 2247-2251.
- 32. K.-M. Marstokk, H. Møllendal and Y. Stenstrøm, *Acta Chemica Scandinavica*, 1992, **46**, 432-441.
- 33. R. E. Penn and R. F. Curl, Jr., *The Journal of Chemical Physics*, 1971, **55**, 651-658.
- 34. S. Blanco, J. C. López, A. Lesarri, W. Caminati and J. L. Alonso \*, *Molecular Physics*, 2005, **103**, 1473-1479.
- 35. L. D. Hatherley, R. D. Brown, P. D. Godfrey, A. P. Pierlot, W. Caminati, D. Damiani, S. Melandri and L. B. Favero, *The Journal of Physical Chemistry*, 1993, **97**, 46-51.
- 36. J. Li, X. Wang, X. Zhang, J. Chen, H. Wang, X. Tian, X. Xu and Q. Gou, *Physical Chemistry Chemical Physics*, 2023, **25**, 4611-4616.
- 37. M. Melosso, S. Alessandrini, L. Spada, A. Melli, X. Wang, Y. Zheng, C. Duan, J. Li, W. Du, Q. Gou, L. Bizzocchi, L. Dore, V. Barone and C. Puzzarini, *Physical Chemistry Chemical Physics*, 2023, **25**, 31281-31291.
- 38. X. Jiang, S. Liu, N. T. Tsona, S. Tang, L. Ding, H. Zhao and L. Du, *RSC Advances*, 2017, 7, 2503-2512.
- 39. E. Sánchez-García, A. Mardyukov, A. Tekin, R. Crespo-Otero, L. A. Montero, W. Sander and G. Jansen, *Chemical Physics*, 2008, **343**, 168-185.
- 40. J. J. Oh, L.-W. Xu, A. Taleb-Bendiab, K. W. Hillig and R. L. Kuczkowski, *Journal of Molecular Spectroscopy*, 1992, **153**, 497-510.
- 41. E. Gougoula, C. N. Cummings, C. Medcraft, J. Heitkämper and N. R. Walker, *Physical Chemistry Chemical Physics*, 2022, **24**, 12354-12362.

# Chapter 6. The Conformational Preference of 2-Ethylthiazole and its Weakly-Bound Complexes with Water Revealed by Microwave Spectroscopy.

Publication:

Charlotte N. Cummings and Nicholas R. Walker, ChemPhysChem, 2024, 25, e202400011

## 6.1 Introduction

Five- and six-membered nitrogen containing heterocycles are important building blocks of biomolecules and typically have multiple binding sites for non-covalent interactions. Weaklybound complexes formed between heterocycles such as thiazole, imidazole and their derivatives with small molecules such as H<sub>2</sub>O provide an insight into the binding preferences of these molecules. The study of these complexes can be achieved using microwave spectroscopy, which can distinguish fine details of structure of molecular species in an isolated environment free of solvent or matrix effects. Each of thiazole and imidazole has a pyridinic nitrogen, located at the 3-position of the ring, which can accept hydrogen bonding interactions. Microwave spectroscopy has recently been employed for the study of B···H<sub>2</sub>O complexes (where B is thiazole, imidazole, methylthiazole or methylimidazole<sup>3</sup>). The lowest-energy isomer of each monohydrate complex was formed via a pair of hydrogen bonding interactions such that each of the heterocycle and H<sub>2</sub>O simultaneously act as hydrogen bond donor and acceptor. A comparatively strong hydrogen bond forms between a O-H of H<sub>2</sub>O and the pyridinic nitrogen on the heteroaromatic ring, while a weaker hydrogen bond forms between the O of H<sub>2</sub>O and a hydrogen atom or CH<sub>3</sub> group located at the 2- or 4-position of the ring. In this Chapter, investigations into the 2-ethylthiazole molecule and two of its weakly-bound complexes formed with H<sub>2</sub>O, 2-ethylthiazole···H<sub>2</sub>O and 2-ethylthiazole···(H<sub>2</sub>O)<sub>2</sub> (hereafter referred to as 2-ET···H<sub>2</sub>O and 2-ET···(H<sub>2</sub>O)<sub>2</sub> respectively) using microwave spectroscopy will be presented. This work explores how the presence of the alkyl group located at the 2-position of the ring influences the configuration of hydrogen bonds within the complex and how the attachment of H<sub>2</sub>O influences the conformational preferences of the ethyl group.

<sup>h</sup> Presented in Chapter 4

Rotational spectroscopy studies have revealed the lowest-energy conformations of ethylated derivatives of benzene,<sup>4</sup> aniline,<sup>5</sup> and furan.<sup>6</sup> As discussed in earlier chapters, the conformers of these molecules which have  $C_s$  symmetry have the carbon atoms of the ethyl group co-planar with the ring, whereas conformers which have  $C_1$  symmetry have the ethyl group rotated out of the plane of the ring. The dihedral angle which defines the rotation of the ethyl group relative to the ring plane was found to be close to  $90^\circ$  in the lowest-energy conformations of ethylbenzene, 3-ethylaniline and 4-ethylaniline. The equivalent angle in the  $C_1$  conformations of each of 2-ethylaniline and 2-ethylfuran was found to be  $75.6(8)^\circ$  in the former and  $63.31(64)^\circ$  in the latter. Two conformations of 2-ethylfuran were observed during a microwave spectroscopy study, which entrained this molecule in a helium supersonic expansion with the second conformation having  $C_s$  symmetry. The deviation in the  $\angle(C8-C7-C2-C1)$  dihedral angle in 2-ethylaniline from  $90^\circ$  was rationalised by the presence of a weak hydrogen bonding interaction between the nitrogen atom of the amine group and the ethyl group. It will be shown that  $\angle(C7-C6-C2-N3)$  for 2-ethylthiazole also deviates from  $90^\circ$  in similarity with the results obtained for 2-ethylaniline and 2-ethylfuran.

A series of recent works have investigated the binding of H<sub>2</sub>O to thiazole and imidazole, with recent interest focussing on the effects of the weak hydrogen bond formed between the O atom of H<sub>2</sub>O and a neighbouring atom or group located at the 2- or 4- position of the ring. As mentioned in Chapter 4, recent work by our group has shown that the  $(V_3)$  barriers to internal rotation of the CH<sub>3</sub> group within each of N-methylimidazole···H<sub>2</sub>O, 5-methylimidazole···H<sub>2</sub>O<sup>i</sup> and 5-methylthiazole···H<sub>2</sub>O are very similar to those within the respective N-methylimidazole,<sup>7</sup> 5-methylimidazole<sup>7</sup> and 5-methylthiazole<sup>8</sup> monomers. A significant increase in  $V_3$  was observed upon the attachment of H<sub>2</sub>O to 2-methylimidazole, which was attributed to the presence of a weak hydrogen bonding interaction between O of H<sub>2</sub>O and the CH<sub>3</sub> group located at the 2position of the ring.<sup>3</sup> Whereas it was observed that  $V_3$  decreases somewhat upon the attachment of H<sub>2</sub>O to each of 4-methylthiazole<sup>9</sup> and 4-methylimidazole,<sup>7</sup> which may arise due to changes in the electronic structure within the ring upon the formation of the monohydrate complex. The present work extends the range of complexes characterised to include a monohydrate and dihydrate complex of a heteroaromatic that contains an ethyl group at the 2-position which can interact with the coordinating H<sub>2</sub>O molecule. The geometries of each of 2-ET···H<sub>2</sub>O and 2- $ET\cdots(H_2O)_2$  will be shown to be similar to those of thiazole··· $H_2O$ , <sup>1</sup> 2-methylthiazole··· $H_2O$ , 2-methylimidazole··· $H_2O^3$  and thiazole··· $(H_2O)_2$  (isomer I). The broad picture is that  $H_2O$ molecules which hydrate imidazole and thiazole significantly affect the conformational and

-

<sup>&</sup>lt;sup>i</sup> Unpublished work by E. Gougoula et al.

internal dynamics of substituents in the 2- and 4-positions of these heterocycles through weak hydrogen-bonding interactions.

## **6.2 Experimental Methods**

The broadband rotational spectrum of 2-ethylthiazole was recorded over the frequency range 2.0 – 18.5 GHz in two separate experiments, covering the 2.0 – 8.0 GHz and 7.0 – 18.5 GHz region. 2-ethylthiazole was obtained from TCI Chemicals and used in experiments without any further purification. This molecule is a liquid at room temperature and has a vapour pressure of 6.0 mmHg @ 25 °C. 2-ethylthiazole was vapourised from a reservoir at 70 °C seeding the vapours into the flow of an inert carrier gas at the point directly prior to supersonic expansion. Experiments were performed using either argon (BOC, 99.998 %) at a backing pressure of 3 bar or neon (BOC, CP grade) at 4 bar as the carrier gas. Deliberate efforts were made to introduce water into the supersonic expansion to facilitate the formation of hydrate complexes with 2-ethylthiazole. A second reservoir positioned upstream of the nozzle was used to introduce a low concentration of water (or an isotopic variant) into the flow of the carrier gas. Experiments to probe the spectra of D- and <sup>18</sup>O-containing isotopologues of the hydrate complexes were performed by introducing a small amount of D<sub>2</sub>O (Sigma Aldrich, 99.9 % D atom) and H<sub>2</sub><sup>18</sup>O (Sigma Aldrich, 97 % <sup>18</sup>O atom) into the second reservoir.

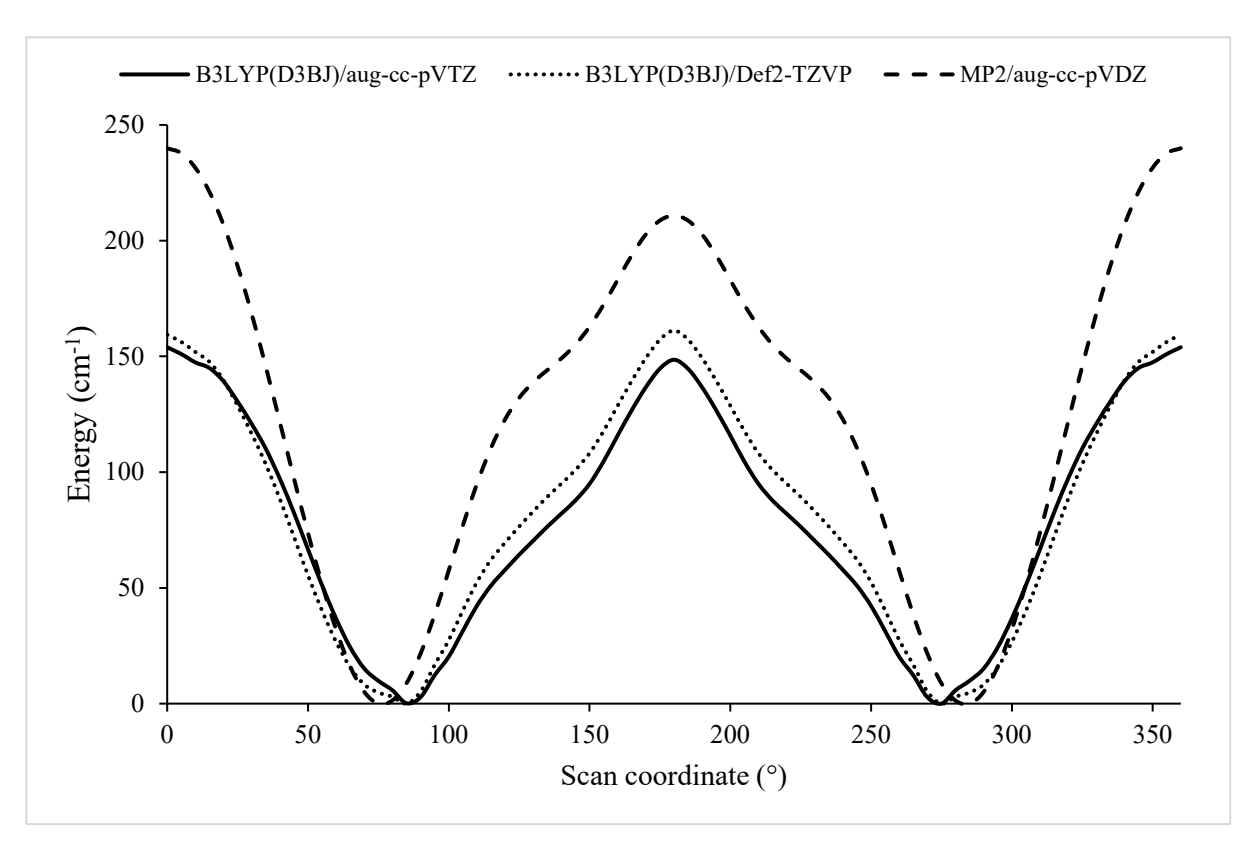


Figure 6.1 Potential energy scans obtained by rotating the ethyl group relative to the thiazole ring in 2-ethylthiazole. Calculations performed at the B3LYP(D3BJ)/aug-cc-pVTZ, B3LYP(D3BJ)/Def2-TZVP and MP2/aug-cc-pVDZ levels of theory by scanning the  $\angle$ (C7-C6-C2-N3) dihedral angle.

## **6.3 Quantum Chemical Calculations**

As discussed for 2-ethylfuran<sup>6</sup> in Chapter 5, 2-ethylthiazole also possesses a degree of conformational flexibility owing to the rotation of the ethyl group relative to the plane of the thiazole ring. One dimensional relaxed potential energy scans (PES) were performed by scanning the  $\angle$ (C7–C6–C2–N3) dihedral angle at an interval of 5° to explore the conformational landscape of this molecule. The results of the PES calculations are displayed in Figure 6.1. Scan calculations performed at the B3LYP(D3BJ)/aug-cc-pVTZ, B3LYP(D3BJ)/Def2-TZVP and MP2/aug-cc-pVDZ levels of theory, predict that the global minimum structure of 2-ethylthiazole has C<sub>1</sub> symmetry. At the B3LYP(D3BJ)/aug-cc-pVTZ level of theory the observed minima in the PES are located at  $\angle$  (C7–C6–C2–N3) =  $\pm$  85° (atom labelling provided in Figure 6.2). The global minimum structure of 2-ethylthiazole was optimised at the three levels of theory listed above. An additional calculation was also performed at the \omegaB97X-D/aug-cc-pVQZ level of theory. When calculating the optimised geometries of 2-ET···H<sub>2</sub>O and 2-ET···(H<sub>2</sub>O)<sub>2</sub>, it was first assumed that the 2-ethylthiazole subunit adopts the global minimum C<sub>1</sub> geometry identified above. To calculate the optimised geometry of 2-ET···H<sub>2</sub>O, a water molecule was placed in close proximity to the nitrogen atom of the thiazole ring and orientated such that the oxygen atom of H<sub>2</sub>O is positioned towards the ethyl group located at C2. For 2-ET···(H<sub>2</sub>O)<sub>2</sub>, an additional water molecule was positioned and orientated to allow for a O-H···O interaction to form between the two H<sub>2</sub>O molecules and the structure was optimised again. Geometry optimisation calculations of each of the hydrate complexes were performed at the same levels of theory listed above for the 2-ethylthiazole monomer. 2-ET···H<sub>2</sub>O and 2-ET···(H<sub>2</sub>O)<sub>2</sub> were each calculated to be a near-prolate asymmetric top, with a dipole moment component strongest along the a-inertial axis. The optimised geometries of 2-ethylthiazole, 2-ET···H<sub>2</sub>O and 2-ET···(H<sub>2</sub>O)<sub>2</sub> calculated at the ωB97X-D/augcc-pVQZ level of theory, are presented in Figure 6.2. Calculated rotational constants ( $A_e$ ,  $B_e$ ,  $C_e$ ), nuclear quadrupole coupling constants ( $\chi_{aa}(N3)$ , [ $\chi_{bb}(N3) - \chi_{cc}(N3)$ ]) and electric dipole moment components ( $\mu_a$ ,  $\mu_b$ ,  $\mu_c$ ) are given in Table 6.1 – 6.3. Calculated atomic coordinates for each species are provided in the Appendix, A.29 – A.40.

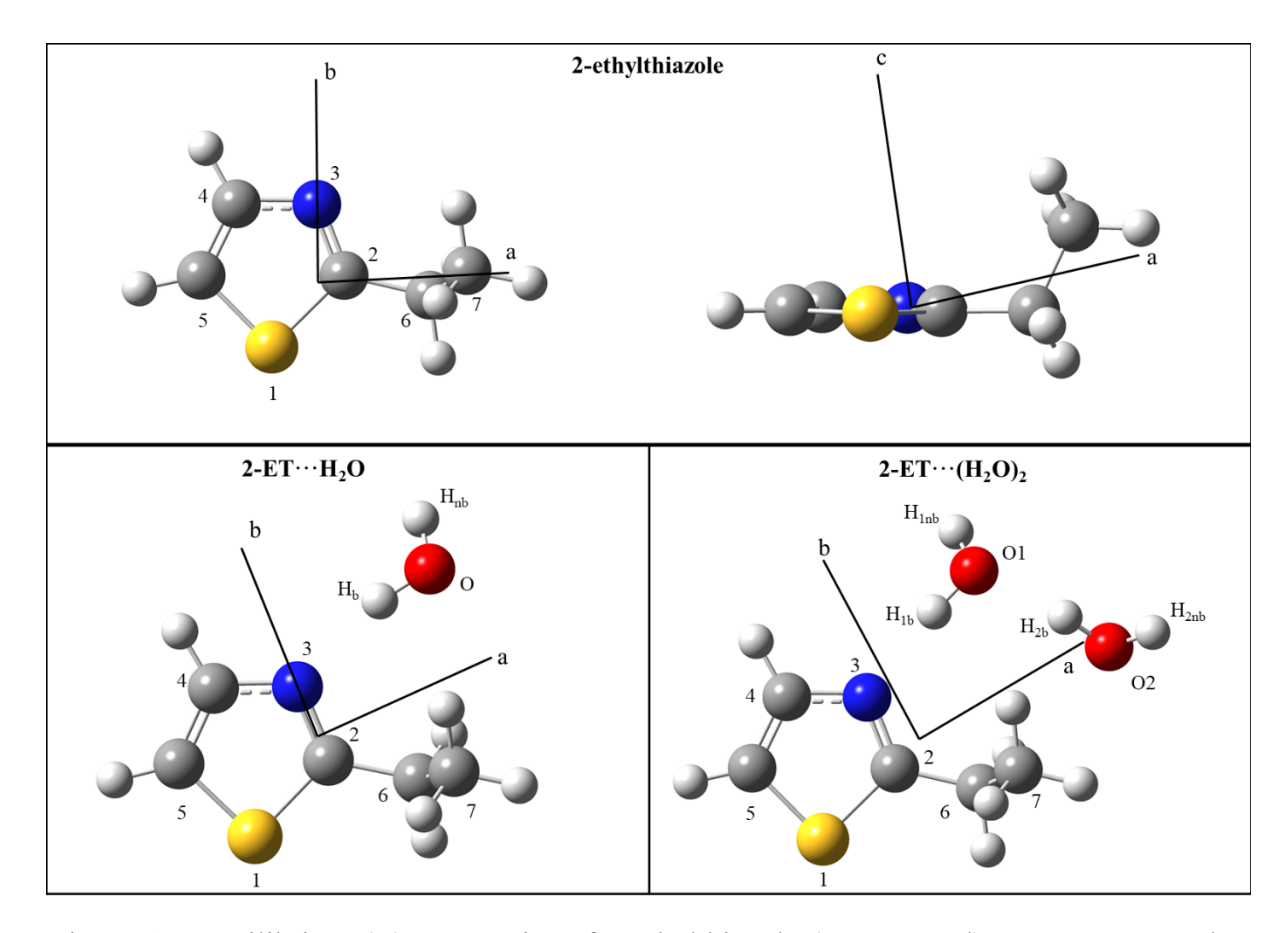


Figure 6.2 Equilibrium ( $r_e$ ) geometries of 2-ethylthiazole (upper panel), 2-ET···H<sub>2</sub>O and 2-ET···(H<sub>2</sub>O)<sub>2</sub> (lower panel) calculated at the  $\omega$ B97X-D/aug-cc-pVQZ level of theory.

Table 6.1 Spectroscopic parameters of the  $C_1$  conformation of 2-ethylthiazole calculated at different levels of theory.

		2-ethylthiazole		
	$\omega$ B97X-D	/aug-cc-pVQZ	B3LYP(D3BJ)	/aug-cc-pVTZ
$A_e$ (MHz)	4552.157	+ 2.1 % <sup>a</sup>	4432.894	- 0.5 %
$B_e$ (MHz)	1753.969	- 0.2 %	1755.656	- 0.1 %
$C_e(\mathrm{MHz})$	1379.700	- 0.5 %	1390.529	+0.2 %
$\chi_{aa}$ (N3) (MHz)	-0.033	+1000 %	0.505	+ 35 %
$\left[\chi_{\rm bb}(\rm N3) - \chi_{\rm cc}\left(\rm N3\right)\right]$	-5.163	+7.6 %	-5.486	+13.0
(MHz)				
$ \mu_{\rm a} ,  \mu_{\rm b} ,  \mu_{\rm c}  ({\rm D})^{\rm b}$	0.2,	1.1, 0.2	0.0, 1.	.1, 0.2
	B3LYP(D3)	BJ)/Def2-TZVP	MP2/aug-	·cc-pVDZ
$A_e$ (MHz)	4460.635	+ 0.1 %	4342.279	- 2.6%
$B_e$ (MHz)	1753.841	- 0.2 %	1748.648	-0.5%
$C_e(\mathrm{MHz})$	1388.361	+ 0.1%	1377.164	-0.7%
$\chi_{aa}$ (N3) (MHz)	0.329	+ 0.2 %	0.185	<i>−</i> 77.5 %
$[\chi_{bb}(N3) - \chi_{cc}(N3)]$	-5.390	+ 11.5 %	-3.673	<b>-29.7 %</b>
(MHz)				
$ \mu_{\rm a} ,  \mu_{\rm b} ,  \mu_{\rm c}   ({\rm D})$	0.1,	1.1, 0.8	0.3, 1.	.3, 0.3
0 0 1 1 11 5// /	1// 7 4000/	. 1 / .1	1. 0	

<sup>&</sup>lt;sup>a</sup> Calculated by  $[(A_e - A_0)/A_0] \times 100$  % where  $A_e$  are the results of computational calculations presented above and  $A_0$  are the experimental rotational constants.

Table 6.2 Spectroscopic parameters of 2-ET···H<sub>2</sub>O calculated at different levels of theory.

		$2-ET\cdots H_2O$		
	$\omega$ B97X-D/	aug-cc-pVQZ	B3LYP(D3BJ)	/aug-cc-pVTZ
$A_e$ (MHz)	2361.978	+ 1.2 % <sup>a</sup>	2331.420	- 0.1 %
$B_e$ (MHz)	1206.669	+ 0.9 %	1214.063	+ 1.5 %
$C_e(\mathrm{MHz})$	852.409	+ 0.8 %	852.008	+ 0.8 %
$\chi_{aa}$ (N3) (MHz)	-3.160	+ 9.7%	-2.992	+ 4.5 %
$[\chi_{bb}(N3) - \chi_{cc}(N3)]$	-1.597	+ 23 %	-1.394	+ 12 %
(MHz)				
$ \mu_{\rm a} ,  \mu_{\rm b} ,  \mu_{\rm c}  ({\rm D})^{\rm b}$	2.6,	0.1, 0.5	2.6, 0.	.1, 0.4
	B3LYP(D3F	B3LYP(D3BJ)/Def2-TZVP		·cc-pVDZ
$A_e$ (MHz)	2352.655	+ 0.8 %	2378.124	+ 1.8 %
$B_e$ (MHz)	1212.012	+ 1.3%	1194.493	- 0.1 %
$C_e(\mathrm{MHz})$	855.194	+ 1.1 %	852.213	-0.8~%
$\chi_{aa}$ (N3) (MHz)	-2.968	+ 3.8 %	-2.299	<b>- 24%</b>
$[\chi_{bb}(N3) - \chi_{cc}(N3)]$	-1.517	+ 19 %	-1.373	+ 10 %
(MHz)				
$\mu_a$ , $\mu_b$ , $\mu_c$ (D)	2.7,	0.0, 0.8	2.6, 0	.3, 0.2

<sup>&</sup>lt;sup>a</sup> Calculated by  $[(A_e - A_0)/A_0] \times 100$  % where  $A_e$  are the results of computational calculations presented above and  $A_0$  are the experimental rotational constants.

<sup>&</sup>lt;sup>b</sup> Electric dipole moment components along the principal inertial axes.

<sup>&</sup>lt;sup>b</sup> Electric dipole moment components along the principal inertial axes.

Table 6.3 Spectroscopic parameters of 2-ET $\cdots$ (H<sub>2</sub>O)<sub>2</sub> calculated at different levels of theory.

		$2-ET\cdots(H_2O)_2$			
	ωB97X-D/	aug-cc-pVQZ	B3LYP(D3BJ)	/aug-cc-pVTZ	
$A_e$ (MHz)	1957.108	+ 2.3 % <sup>a</sup>	1877.716	+ 1.8 %	
$B_e$ (MHz)	719.758	<b>- 1.8 %</b>	728.153	+ 2.5 %	
$C_e$ (MHz)	575.700	<b>- 1.3 %</b>	579.073	+ 2.2 %	
$\chi_{aa}$ (N3) (MHz)	-2.843	+ 9.6 %	-2.813	+ 8.7 %	
$[\chi_{bb}(N3) - \chi_{cc}(N3)]$	-1.493	+ 15 %	-1.098	− 14 %	
(MHz)					
$\mu_{a}$ , $\mu_{b}$ , $\mu_{c}$ (D)	2.8,	0.6, 0.6	2.6, 0.	7, 0.5	
	B3LYP(D3E	B3LYP(D3BJ)/Def2-TZVP		MP2/aug-cc-pVDZ	
$A_e$ (MHz)	1887.126	- 1.3 %	1989.942	+ 3.9 %	
$B_e$ (MHz)	731.593	+ 3.0 %	709.895	+ 0.0 %	
$C_e  (\mathrm{MHz})$	590.102	+ 4.0 %	567.073	+ 0.1 %	
$\chi_{aa}$ (N3) (MHz)	-2.769	+ 7.2 %	-2.294	− 11 <b>%</b>	
$[\chi_{bb}(N3) - \chi_{cc}(N3)]$	-1.159	- 8.8 %	-1.153	<b>-9.3 %</b>	
(MHz)					
$ \mu_{\rm a} ,  \mu_{\rm b} ,  \mu_{\rm c}   ({\rm D})$	2.8,	0.7, 0.9	2.5, 1.	1, 0.1	

<sup>&</sup>lt;sup>a</sup> Calculated by  $[(A_e - A_0)/A_0] \times 100$  % where  $A_e$  are the results of computational calculations presented above and  $A_0$  are the experimental rotational constants.

<sup>&</sup>lt;sup>b</sup> Electric dipole moment components along the principal inertial axes.

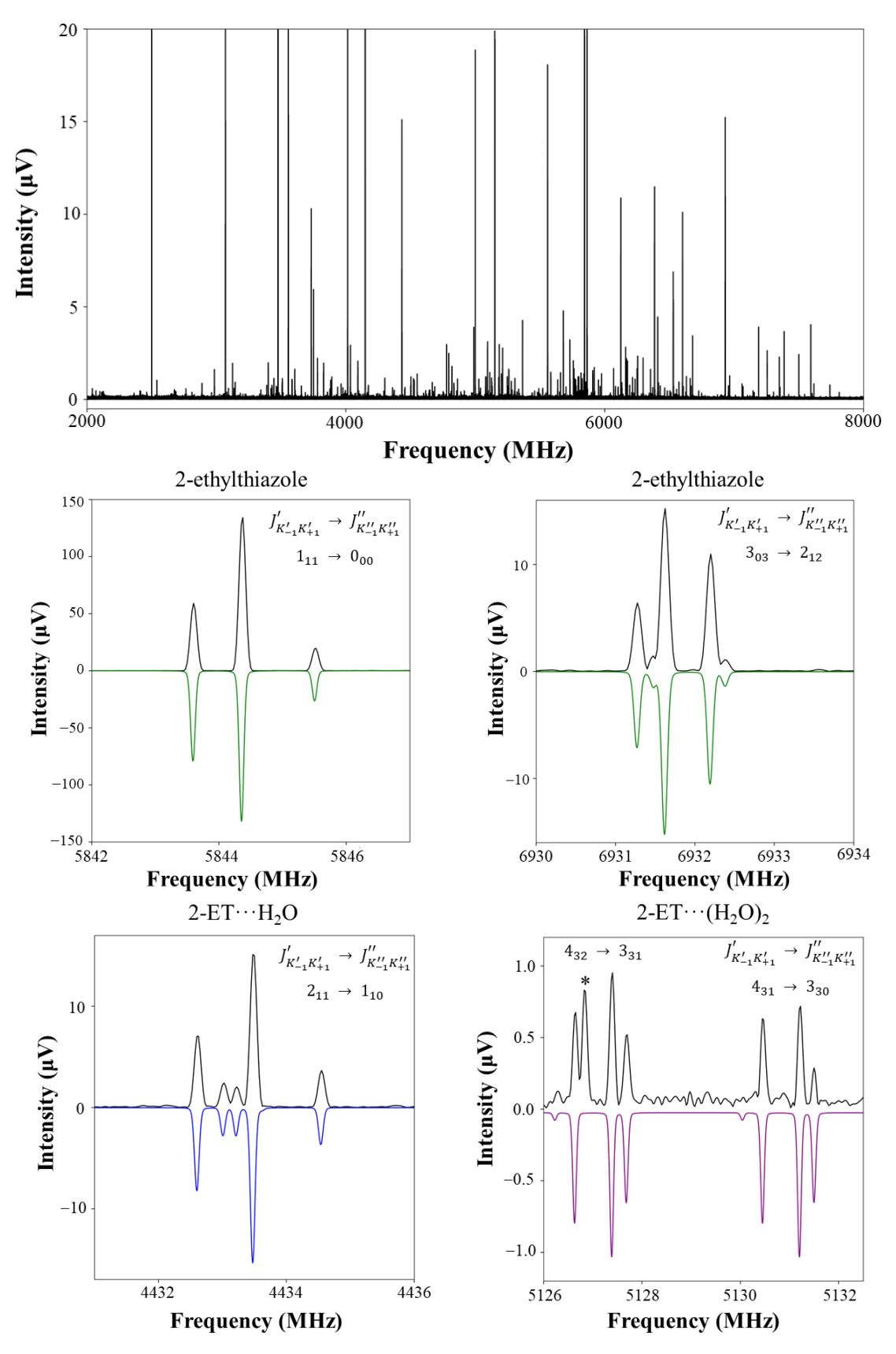


Figure 6.3 (top) The microwave spectrum of 2-ethylthiazole recorded in the 2.0-8.0 GHz region averaged over 1.08 M FID's. (middle) and (bottom) Examples of transitions assigned to the 2-ethylthiazole monomer,  $2-\text{ET}\cdots \text{H}_2^{16}\text{O}$  and  $2-\text{ET}\cdots (\text{H}_2^{16}\text{O})_2$ . Experimental spectrum (black) is located above PGOPHER simulation. The transition labelled with an asterisk is assigned to the <sup>34</sup>S isotopologue of 2-ethylthiazole.

## 6.4 Spectral Analysis

# 6.4.1 Assignment of the 2-ethylthiazole monomer

As outlined in Section 6.2 (Experimental Methods) separate experiments were performed in the 2.0 - 8.0 and 7.0 - 18.5 GHz frequency regions while using argon or neon as the carrier gas. The spectrum recorded over the 2.0 - 8.0 GHz region, collected over 1.08 M FID's, using neon as the carrier gas is displayed in Figure 6.3 (top). It was discussed in previous chapters that relaxation to lower energy conformers is more efficient when employing argon as a carrier gas compared with neon, so for this reason experiments were performed using both argon and neon as carrier gases. Transitions of the  $C_1$  conformer of the 2-ethylthiazole monomer were initially identified within a spectrum recorded over the 7.0 - 18.5 GHz frequency region while using argon as the carrier gas. The transitions were then observed again during a subsequent experiment performed using neon. No transitions of other conformers of 2-ethylthiazole were identified while performing experiments using argon or neon carrier gases, unlike what was observed in the case of 2-ethylfuran (Chapter 5).

The spectrum of the 2-ethylthiazole monomer was assigned by fitting experimentally observed transitions to Watson's S-reduced Hamiltonian<sup>11</sup> implemented within the program PGOPHER. <sup>12</sup> Rotational constants ( $A_0$ ,  $B_0$  and  $C_0$ ), centrifugal distortion constants ( $D_J$ ,  $D_{JK}$ ,  $D_K$ ,  $d_1$  and  $d_2$ ) and nuclear quadrupole coupling constants ( $\chi_{aa}(N3)$  and [ $\chi_{bb}(N3) - \chi_{cc}(N3)$ ]) were determined for this molecule, as shown in Table 6.4. Each transition exhibited hyperfine structure owing to the presence of a nitrogen nucleus (as shown in Figure 6.3 (middle)). In total, 180 hyperfine components were assigned across the 2.0 - 18.5 GHz frequency region. Within the spectrum, a-, b- and c- type transitions were observed for 2-ethylthiazole, as expected, since the results of calculations performed at several different levels of theory predict a non-zero dipole moment component in each direction. The observation of c-type transitions within the spectrum is significant as this indicates that mass lies outside of the ab plane, providing further evidence that this molecule is non-planar and possesses  $C_1$  symmetry. The spectrum was initially assigned to the global minimum structure identified by quantum chemical calculations (pictured in Figure 6.2) based on good agreement between the experimentally determined spectroscopic constants and equilibrium rotational constants presented in Table 6.1.

Table 6.4 Spectroscopic parameters determined for 2-ethylthiazole by fitting experimentally-recorded transition frequencies to parameters in Watson's S-reduced Hamiltonian.

Parameter	2-ethylthiazole
$A_0$ (MHz)	4457.00890(69) <sup>a</sup>
$B_0$ (MHz)	1758.06359(34)
$C_0(\mathrm{MHz})$	1387.24304(30)
$D_{J}\left(\mathrm{kHz} ight)$	0.5075(52)
$D_{JK}(\mathrm{kHz})$	19.280(16)
$D_K$ (kHz)	-16.603(77)
$d_1$ (kHz)	0.0038(15)
$d_2(kHz)$	0.05038(62)
$\chi_{aa}$ (N3) (MHz)	0.3284(45)
$[\chi_{bb}(N3) - \chi_{cc}(N3)]$ (MHz)	-4.7707(65)
$\sigma_{\rm rms}  ({\rm kHz})^{\rm b}$	9.0
$N^{c}$	180
$a/b/c^{-d}$	y/y/y
$\kappa^{\;e}$	-0.75
$P_{cc}$ (u Å <sup>2</sup> )	18.27429(5)

<sup>&</sup>lt;sup>a</sup> Numbers in parentheses are one standard deviation in units of the last significant figure.

To further confirm the assignment of this spectrum to the correct molecular carrier, singly substituted isotopologues were searched for within each spectrum recorded. The spectrum of one  $^{34}$ S and five  $^{13}$ C isotopologues were observed in natural abundance (with relative intensities of 4.25 % and 1.07 % respectively). The spectrum of each singly substituted isotopologue was assigned, only rotational constants ( $A_0$ ,  $B_0$  and  $C_0$ ) were determined during each fit, while centrifugal distortion and nuclear quadrupole coupling constants were held fixed at values determined for the parent isotopologue. The results of each fit are displayed in Table 6.5. For each of the singly substituted isotopologues only b- type transitions were observed, and hence fewer transitions could be assigned. Calculations performed at each level of theory anticipated that the projection onto the b- inertial axis is significantly greater than the projection onto the a- and c- inertial axes. Therefore, it is unsurprising that only b- type transitions were observed for the spectra of the lower abundance isotopologues. The spectrum of the  $^{15}$ N isotopologue was searched for within each spectrum recorded, however, was unable to be assigned owing to both its low natural abundance (0.4 %) and the sensitivity of the current experimental set up.

<sup>&</sup>lt;sup>b</sup> Root mean square (rms) deviation of the fit.

<sup>&</sup>lt;sup>c</sup> Number of hyperfine components included in the fit.

<sup>&</sup>lt;sup>d</sup> "y" indicates that this type of transition was observed.

<sup>&</sup>lt;sup>e</sup> Ray's asymmetry parameter.

Table 6.5 Spectroscopic constants determined for <sup>34</sup>S and <sup>13</sup>C isotopologues of 2-ethylthiazole. Values of centrifugal distortion constants ( $D_J$ ,  $D_{JK}$ ,  $D_K$ ,  $d_1$  and  $d_2$ ) and nuclear quadrupole coupling constants ( $\chi_{aa}$  (N3) and [ $\chi_{bb}$ (N3) –  $\chi_{cc}$  (N3)])) held fixed to those determined for the parent isotopologue, displayed in Table 6.4, when fits were performed.

	<sup>34</sup> S1 <sup>a</sup>	<sup>13</sup> C2	<sup>13</sup> C4
$A_0$ (MHz)	4357.86588(81) <sup>b</sup>	4452.8341(14)	4396.4858(11)
$B_0$ (MHz)	1751.57265(51)	1756.74396(74)	1744.74810(63)
$C_0  (\mathrm{MHz})$	1373.41575(41)	1386.73064(46)	1373.14018(59)
$\sigma_{rms} (kHz)^{c}$	14.0	11.6	13.4
$N^{ m d}$	65	29	33
$P_{cc}$ (u Å <sup>2</sup> )	18.26288(7)	18.36810(9)	18.28089(10)
	<sup>13</sup> C5	<sup>13</sup> C6	<sup>13</sup> C7
$A_0$ (MHz)	4454.3538(15)	4442.8581(21)	4440.9293(13)
$B_0$ (MHz)	1734.09199(73)	1735.91051(80)	1712.27425(74)
$C_0(\mathrm{MHz})$	1372.56000(57)	1374.68306(58)	1359.98662(57)
$\sigma_{rms}$ (kHz)	13.3	13.0	13.4
N	31	24	32
$P_{cc}$ (u Å <sup>2</sup> )	18.34640(10)	18.62486(11)	18.67258(10)

<sup>&</sup>lt;sup>a</sup> Atom numbering as defined in Figure 6.2.

<sup>&</sup>lt;sup>b</sup> Numbers in parentheses are one standard deviation in units of the last significant figure.

<sup>&</sup>lt;sup>c</sup> Root mean square (rms) deviation of the fit.

<sup>&</sup>lt;sup>d</sup> Number of hyperfine components included in the fit.

# 6.4.2 Assignment of hydrate complexes

After the assignment of the parent and lower abundant isotopologues of 2-ethylthiazole, many transitions within the spectrum recorded remained unassigned. It was anticipated that the transitions may assign to hydrate complexes formed with 2-ethylthiazole owing to previous studies identifying hydrate complexes forming with thiazole<sup>1, 10</sup> and its derivatives (Chapter 4) and due to the experimental conditions employed (as described in Section 6.2). Quantum chemical calculations predicted that the 2-ethylthiazole sub-unit would adopt the global minimum C<sub>1</sub> configuration when forming complexes with H<sub>2</sub>O. Each of 2-ET···H<sub>2</sub>O and 2-ET···(H<sub>2</sub>O)<sub>2</sub> were calculated to be near-prolate asymmetric tops with a dipole moment component strongest along the a- inertial axis of each complex. The binary complex formed between 2-ethylthiazole and one H<sub>2</sub>O molecule was sought after first. Transitions across the frequency range 2.0 - 18.5 GHz were fitted to Watson's S-reduced Hamiltonian<sup>11</sup> and tentatively assigned to 2-ET···H<sub>2</sub><sup>16</sup>O on the basis of good agreement between the experimentally determined ground state rotational constants and those predicted by theory. In total, 158 hyperfine components were assigned to the parent isotopologue with the standard deviation of the fit being 11.7 kHz. An example of a transition assigned to 2-ET···H<sub>2</sub><sup>16</sup>O is given in Figure 6.3 (bottom-left). The spectrum of the monohydrate complex was sufficiently intense to allow for the observation and assignment of the <sup>34</sup>S isotopologue of 2-ET···H<sub>2</sub>O in natural abundance. The assignment of this isotopologue further confirmed that the structure presented in Figure 6.2 is the molecular carrier of the observed spectrum. For each of the <sup>32</sup>Sand  $^{34}$ S-containing isotopologues of 2-ET···H<sub>2</sub>O, only a- type transitions were assigned, b- and c- type transitions were not present in the spectrum recorded. Consistent with expectations, transitions of only a single isomer of 2-ET···H<sub>2</sub>O were observed in the spectrum recorded using the experimental conditions employed herein. Previous studies on thiazole···H<sub>2</sub>O<sup>1</sup> and methylthiazole···H<sub>2</sub>O (Chapter 4) identified only one isomer of each monohydrate complex.

Two isomers of the dihydrate complex formed with thiazole, thiazole···(H<sub>2</sub>O)<sub>2</sub>, were identified in a recent microwave spectroscopy study.<sup>10</sup> It was observed that the (H<sub>2</sub>O)<sub>2</sub> sub-unit interacts with thiazole via a O–H···N and C–H···O interaction, while a third hydrogen bonding interaction is present between the two H<sub>2</sub>O molecules. The isomers differ in the C–H of the thiazole ring in which the O atom of the second H<sub>2</sub>O molecule forms an interaction with. In the global minimum structure, denoted isomer I in the study, the weaker hydrogen bonding interaction forms with C2–H2, whereas, in the higher energy isomer, isomer II, the interaction instead forms with C4–H4. Following the assignment of the 2-ET···H<sub>2</sub>O complex, the dihydrate complex formed with 2-ethylthiazole was subsequently searched for. Quantum chemical

calculations were performed to optimised the geometry of two isomers of 2-ET···(H<sub>2</sub>O)<sub>2</sub> equivalent to those observed for thiazole···(H<sub>2</sub>O)<sub>2</sub>. The lowest energy geometry of the dihydrate complex is shown in Figure 6.2. The second isomer in which the C4–H4···O interaction is present was calculated to be 1.8 kJ mol<sup>-1</sup> higher in energy. A series of transitions were fitted to Watson's *S*-reduced Hamiltonian<sup>11</sup> and tentatively assigned to the 2-ET···(H<sub>2</sub><sup>16</sup>O)<sub>2</sub> complex. Across the 2.0 – 18.5 GHz frequency region, 182 transitions were assigned to this complex with the most intense features being *a*- type transitions. Unlike what was previously observed for 2-ET···(H<sub>2</sub><sup>16</sup>O)<sub>2</sub>, several weaker *b*- type transitions were also assigned during the fitting of 2-ET···(H<sub>2</sub><sup>16</sup>O)<sub>2</sub>. The ground state rotational constants determined from the assignment are as follows:  $A_0 = 1911.5874(23)$  MHz,  $B_0 = 709.82247(45)$  MHz and  $C_0 = 566.38146(36)$  MHz, which are in better agreement with the equilibrium constants presented in Table 6.3 compared to those predicted for the higher energy isomer ( $A_e = 1494$  MHz,  $B_e = 779$  MHz and  $C_e = 536$  MHz). Therefore, the molecular carrier of the spectrum was assigned to the structure of 2-ET···(H<sub>2</sub>O)<sub>2</sub> shown in Figure 6.2. Transitions of the higher energy isomer of 2-ET···(H<sub>2</sub>O)<sub>2</sub> was searched for in the spectrum recorded, however, this was unable to be assigned.

Subsequent experiments were performed using isotopically enriched samples of H<sub>2</sub><sup>18</sup>O and D<sub>2</sub>O to probe the spectrum of additional isotopologues of the monohydrate and dihydrate complex, in which isotopic substitution was achieved at the H<sub>2</sub>O sub-unit(s). In addition to the <sup>32</sup>S and <sup>34</sup>S containing isotopologues of 2-ET···H<sub>2</sub><sup>16</sup>O discussed earlier, an additional four isotopologues of this complex (2-ET···H<sub>2</sub><sup>18</sup>O, 2-ET···DOH, 2-ET···HOD and 2-ET···D<sub>2</sub>O) were able to be assigned. Spectroscopic parameters determined for each isotopologue are displayed in Table 6.6. Rotational constants ( $A_0$ ,  $B_0$  and  $C_0$ ), centrifugal distortion constants ( $D_J$ ,  $D_{JK}$  and  $d_1$ ) were determined for each isotopologue, however, for 2-ET···HOD it was necessary to hold  $d_1$  fixed to the value determined for the parent isotopologue to achieve a satisfactory fit. The nuclear quadrupole coupling constants,  $\chi_{aa}(N3)$  and  $[\chi_{bb}(N3) - \chi_{cc}(N3)]$ , were both determined for the  $H_2^{16}O$  isotopologue. During the fits of other isotopologues,  $\chi_{aa}$  (N3) was determined for each species while  $[\chi_{bb}(N3) - \chi_{cc}(N3)]$  was held fixed to the value determined for the parent isotopologue. For the dihydrate complex, the spectrum of two singly substituted <sup>18</sup>O isotopologues were observed during an experiment employing H<sub>2</sub><sup>18</sup>O. Spectroscopic parameters determined during fits of each isotopologue of the dihydrate complex, 2- $ET\cdots(H_2^{16}O)_2$ , 2- $ET\cdots(H_2^{18}O)(H_2^{16}O)$  and 2- $ET\cdots(H_2^{16}O)(H_2^{18}O)$ , are displayed in Table 6.7. Transitions of the 2-ET···(H<sub>2</sub><sup>16</sup>O)<sub>2</sub> complex were fitted to determine ground state rotational constants ( $A_0$ ,  $B_0$  and  $C_0$ ), centrifugal distortion constants ( $D_J$ ,  $D_{JK}$ ,  $d_1$  and  $d_2$ ) and nuclear quadrupole coupling constants ( $\chi_{aa}(N3)$  and [ $\chi_{bb}(N3) - \chi_{cc}(N3)$ ]). For the singly substituted <sup>18</sup>O isotopologues, significantly fewer transitions were able to be assigned compared to the parent isotopologue. This is due to isotopic "scrambling" which occurs upon the introduction of the  $H_2^{18}O$  sample, resulting in the relative abundance of  $^{18}O$  containing isotopologues being lower. Additionally, the transitions assigned for each  $^{18}O$  isotopologue were observed in the 2.0-8.0 GHz region only, owing to an improved S/N of the spectrum obtained during that experiment. Therefore, for this reason, during fits performed for each  $^{18}O$  isotopologue the values of  $D_{JK}$ ,  $d_1$ ,  $d_2$  and  $[\chi_{bb}(N3) - \chi_{cc}(N3)]$  were held fixed to the values determined for the parent isotopologue.

Diagonalised values of the nuclear quadrupole coupling constants determined for 2-ethylthiazole, 2-ET···H<sub>2</sub>O and 2-ET···(H<sub>2</sub>O)<sub>2</sub> determined during fits performed using PGOPHER generally agree with those predicted by quantum chemical calculations. However, to facilitate broader comparisons, the nuclear quadrupole coupling constants of the parent isotopologue of each species (displayed in Tables 6.4, 6.6 and 6.7) were each diagonalised and transformed into the principal nuclear axis framework, using the QDIAG program available on the PROSPE<sup>13</sup> website. The values of  $\chi_{xx}$ ,  $\chi_{yy}$  and  $\chi_{zz}$  were generated using the off-diagonal term,  $\chi_{ab}$ , calculated at the B3LYP(D3BJ)/aug-cc-pVTZ level in each case. The values obtained for each of 2-ethylthiazole, 2-ET···H<sub>2</sub>O and 2-ET···(H<sub>2</sub>O)<sub>2</sub> (displayed in Table 6.8) are lower than those reported for the thiazole monomer, like what was observed previously for the methylthiazole···H<sub>2</sub>O complexes (Chapter 4).

Table 6.6 Experimentally-determined spectroscopic parameters for six isotopologues of 2-ET···H<sub>2</sub>O.

	$H_2^{16}O$	<sup>34</sup> S1	$H_2^{18}O$	DOH	HOD	D <sub>2</sub> O
$A_0  (\mathrm{MHz})$	2334.3770(12) <sup>a</sup>	2324.477(15)	2303.7980(68)	2314.9159(69)	2295.6969(83)	2278.7560(70)
$B_0  (\mathrm{MHz})$	1195.92729(35)	1178.9223(14)	1143.55402(69)	1184.02980(74)	1162.20114(53)	1150.80772(83)
$C_0(\mathrm{MHz})$	845.54396(28)	835.8513(12)	815.32658(70)	837.04353(65)	823.88092(65)	815.97858(72)
$D_{J}(\mathrm{kHz})$	0.2274(21)	0.2424(91)	0.2120(26)	0.2097(69)	0.2302(43)	0.1911(44)
$D_{JK}(\mathrm{kHz})$	0.446(13)	0.39(15)	0.740(26)	0.632(89)	0.432(57)	0.631(41)
$d_1$ (kHz)	-0.0704(13)	-0.0770(65)	-0.0474(23)	-0.0646(39)	$[-0.0704]^{b}$	-0.0520(32)
$\chi_{aa}$ (N3) (MHz)	-2.8552(82)	-2.899(22)	-2.9841(87)	-2.888(13)	-2.962(11)	-3.038(14)
$[\chi_{bb}(N3) - \chi_{cc}(N3)] \text{ (MHz)}$	-1.225(19)	[-1.225]	[-1.225]	[-1.225]	[-1.225]	[-1.225]
$\sigma_{\rm rms}({\rm kHz})^{\rm c}$	11.7	16.0	11.9	15.2	13.7	12.0
$N^{ m d}$	158	68	125	88	84	97
$P_{cc}$ (u Å <sup>2</sup> )	20.69033(13)	20.7336(9)	20.7282(4)	20.6886(4)	20.7878(5)	20.7884(5)

<sup>&</sup>lt;sup>a</sup> Numbers in parentheses are one standard deviation in units of the last significant figure.

<sup>&</sup>lt;sup>b</sup> Values in square brackets held fixed at the result for the parent isotopologue, 2-ET $\cdots$ H<sub>2</sub><sup>16</sup>O.

<sup>&</sup>lt;sup>c</sup> Root mean square (rms) deviation of the fit.

<sup>&</sup>lt;sup>d</sup> Number of hyperfine components included in the fit.

Table 6.7 Experimentally-determined spectroscopic parameters for three isotopologues of 2- $ET\cdots(H_2O)_2$ 

	$(H_2^{16}O)_2$	$(H_2^{18}O)(H_2^{16}O)$	$(H_2^{16}O)(H_2^{18}O)$
$A_0$ (MHz)	1911.5874(23) <sup>a</sup>	1864.280(55)	1901.6656(82)
$B_0  (\mathrm{MHz})$	709.82247(45)	698.6077(16)	682.2168(14)
$C_0(\mathrm{MHz})$	566.38146(36)	555.2502(13)	549.0672(15)
$D_{J}(\mathrm{kHz})$	0.20916(90)	0.211(18)	0.159(27)
$D_{JK}(\mathrm{kHz})$	-0.9039(65)	$[-0.9039]^{b}$	[-0.9039]
$d_1$ (kHz)	-0.0211(10)	[-0.0211]	[-0.0211]
$d_2(\mathrm{kHz})$	-0.00400(56)	[-0.004]	[-0.004]
$\chi_{aa}$ (N3) (MHz)	-2.5687(93)	-2.668(23)	-2.533(27)
$[\chi_{bb}(N3) - \chi_{cc}(N3)]$ (MHz)	-1.261(44)	[-1.261]	[-1.261]
$\sigma_{\rm rms}  ({ m kHz})^{ m c}$	11.0	15.4	14.6
$N^{ m d}$	182	38	30
$P_{cc}$ (u Å <sup>2</sup> )	42.0308(4)	42.156(4)	43.0567(16)

<sup>&</sup>lt;sup>a</sup> Numbers in parentheses are one standard deviation in units of the last significant figure.

Table 6.8 Nuclear quadrupole coupling constants in the principle nuclear axis framework determined using QDIAG

	2-ethylthiazole <sup>a</sup>	Thiazole <sup>b</sup>
$\chi_{xx}$ (N3) (MHz)	1.70(42)	1.83(18)
$\chi_{yy}$ (N3) (MHz)	2.2212(40)	2.585(11)
$\chi_{zz}$ (N3) (MHz)	-3.92(42)	-4.41(18)
	2-ET···H <sub>2</sub> O <sup>a</sup>	$2-ET\cdots(H_2O)_2^a$
$\chi_{xx}$ (N3) (MHz)	1.789(54)	1.63(18)
$\chi_{yy}$ (N3) (MHz)	2.040(10)	1.915(22)
$\chi_{zz}$ (N3) (MHz)	-3.829(51)	-3.55(18)

<sup>&</sup>lt;sup>a</sup> Calculated from experimentally determined values of nuclear quadrupole coupling constants,  $\chi_{aa}$ ,  $\chi_{bb}$  and  $\chi_{cc}$  (displayed in Tables 6.4, 6.6 and 6.7) and the off-diagonal term  $\chi_{ab}$  calculated at the B3LYP(D3BJ)/aug-cc-pVTZ level of theory.

<sup>&</sup>lt;sup>b</sup> Values in square brackets held fixed at the result for the parent isotopologue, 2-ET···(H<sub>2</sub><sup>16</sup>O)<sub>2</sub>.

<sup>&</sup>lt;sup>c</sup> Root mean square (rms) deviation of the fit.

<sup>&</sup>lt;sup>d</sup> Number of hyperfine components included in the fit.

<sup>&</sup>lt;sup>b</sup> Results for thiazole provided in reference 14.

#### 6.5 Molecular Geometry

## 6.5.1 2-ethylthiazole monomer

It was discussed earlier that one conformation of the 2-ethylthiazole monomer was observed experimentally. It was confirmed that the conformer was non-planar owing to the observation of a-, b- and c-type transitions within the spectrum, therefore, the conformation has C<sub>1</sub> symmetry. The inertial defect and planar moments of 2-ethylthiazole have been determined using equations presented in Chapter 2 (Equations 2.71 - 2.74) and the ground state rotational constants determined from the fits performed. Both the inertial defect ( $\Delta_0$ ) and the planar moment  $(P_{cc})$  provide a measure of planarity of a molecule. Considering the inertial defect first, previous studies identified that  $\Delta_0$  was 0.0744(4) u Å<sup>2</sup> and -3.083(12) u Å<sup>2</sup> for thiazole<sup>15</sup> and 2-methylthiazole, <sup>16, 17</sup> respectively. The small and positive result for thiazole is consistent with a planar geometry, whereas the result for 2-methylthiazole indicates the presence of a small amount of out-of-plane mass owing to the hydrogen atoms of the methyl group. Whereas for 2ethylthiazole,  $\Delta_0$  was determined to be large and negative, -36.54857(10) u Å<sup>2</sup>. The planar moment,  $P_{cc}$ , can be calculated directly from the inertial defect (Chapter 2, Equation 2.74) and was determined to be 18.27429(5) u  $Å^2$  for 2-ethylthiazole. The  $P_{cc}$  value obtained for 2ethylthiazole is similar to that reported for the  $C_1$  configuration of 2-ethylfuran<sup>6</sup> (14.925714(4) u  $Å^2$ ). The significant difference in the  $\Delta_0$  of 2-ethylthiazole compared with thiazole and 2methylthiazole and the large  $P_{cc}$  value is a consequence of the ethyl group being rotated out of the plane of the thiazole ring. Therefore, reaffirming, that this molecule possesses C<sub>1</sub> symmetry (as pictured in Figure 6.2).

Heavy atom substitution was achieved at each of the sulphur and carbon atoms of 2-ethylthiazole therefore allowing the determination of the substitution ( $r_s$ ) coordinates of each of these atoms. The experimentally determined  $r_s$  coordinates were generated using Kraitchman's equations<sup>18</sup> implemented within the program KRA (available on the PROSPE website<sup>13</sup>). The coordinates of each carbon and sulphur atom and the associated Costain errors<sup>19</sup> are displayed in Table 6.9, alongside  $r_c$  coordinates calculated at the  $\omega$ B97X-D/aug-cc-pVQZ level of theory. This method determines only the magnitude of each coordinate, therefore, signs were chosen to be consistent with the  $r_c$  coordinates. The c-coordinate for each carbon atom was determined to be non-zero indicating that each of these atoms lie outside the ab plane, in agreement with the  $r_c$  coordinates. Whereas an imaginary result was obtained for the c-coordinate of the sulphur atom, therefore, was assumed equal to zero. Using the  $r_s$  coordinates determined, the values of some bond lengths, bond angles and dihedral angles have been derived using EVAL, which are given in the Appendix, Table A.41. It was not possible to

generate all internal coordinates owing to the lack of information regarding the position of the nitrogen atom, however, it is interesting to consider the angle which defines the rotation of the ethyl group relative to the thiazole ring. This angle is represented by either the  $\angle$ (C7–C6–C2–S1) or  $\angle$ (C7–C6–C2–N3) dihedral angle. Within the present work only the  $\angle$ (C7–C6–C2–S1) angle can be determined from the experimental results alone, therefore, only this angle will be discussed further. In the  $r_s$  geometry,  $\angle$ (C7–C6–C2–S1) was determined to be –98.6(10)°. Quantum chemical calculations performed herein imply some variation in the magnitude of this dihedral angle across the different levels of theory tested, for example at the  $\omega$ B97X-D/aug-cc-pVQZ level this angle was calculated to be –110.3°, whereas better agreement with the experimental result is observed when using the B3LYP(D3BJ)/Def2-TZVP level (–97.9°). In the C<sub>1</sub> configuration of the molecule, the *ab* plane and the plane of the thiazole ring are not coincident and have been calculated to be separated by 12.6° in the  $\omega$ B97X-D/aug-cc-pVQZ geometry.

Table 6.9 Comparison of DFT calculated  $(r_e)$  and experimentally determined  $(r_s)$  atomic coordinates of heavy atoms in 2-ethylthiazole.

	Method	a / Å	<i>b</i> / Å	<i>c</i> / Å
S1	r <sub>e</sub> (calc.) <sup>a</sup>	-0.8060	-1.1343	0.0316
	$r_{\rm s}$ (exp.)	$-0.7346(20)^{b}$	-1.1517(13)	[0] <sup>c</sup>
C2	r <sub>e</sub> (calc.)	0.3888	0.0772	-0.2791
	$r_{\rm s}$ (exp.)	0.3501(43)	0.112(13)	-0.3071(49)
C4	r <sub>e</sub> (calc.)	-1.4040	1.3012	0.0678
	$r_{\rm s}$ (exp.)	-1.4755(10)	1.2572(12)	0.083(18)
C5	r <sub>e</sub> (calc.)	-1.9838	0.0889	0.2435
	$r_{\rm s}$ (exp.)	-1.97924(76)	[0]	0.2712(55)
C6	r <sub>e</sub> (calc.)	1.8216	-0.2626	-0.5475
	$r_{\rm s}$ (exp.)	1.82409(82)	-0.104(14)	-0.5973(25)
C7	r <sub>e</sub> (calc.)	2.7344	0.1609	0.6026
	$r_{\rm s}$ (exp.)	2.70335(56)	0.113(13)	0.6416(23)

<sup>&</sup>lt;sup>a</sup>  $r_e$  geometry calculated at the  $\omega$ B97X-D/aug-cc-pVQZ level of theory.

<sup>&</sup>lt;sup>b</sup> Numbers in parentheses after  $r_s$  results are Costain errors calculated as  $\delta a = 0.015/|a|$ .

<sup>&</sup>lt;sup>c</sup> Imaginary  $r_s$  coordinate obtained, therefore, value of coordinate assumed equal to zero.

## 6.5.2 Hydrate complexes

As discussed above for the 2-ethylthiazole monomer, the ab plane and the plane of the thiazole ring are also not coincident in each of 2-ET···H<sub>2</sub>O and 2-ET···(H<sub>2</sub>O)<sub>2</sub>. In the ωB97X-D/augcc-pVQZ calculated geometry, the planes are separated by 13.3° in the former and 9.1° in the latter. The planar moment,  $P_{cc}$ , will therefore provide the best initial insight into the geometry of each hydrate complex. For 2-ET···H<sub>2</sub><sup>16</sup>O, the P<sub>cc</sub> value determined is 20.69033(13) u Å. Evidently the addition of the H<sub>2</sub>O molecule contributes more out-of-(ab)plane mass since the value for  $P_{cc}$  is greater than observed for the isolated 2-ethylthiazole monomer (18.27429(5) u Å<sup>2</sup>). Previous studies on thiazole-containing monohydrate complexes have reported that the  $H_2O$  sub-unit contributes ~0.5 u Å<sup>2</sup> and ~0.2 u Å<sup>2</sup> to the  $P_{cc}$  of 4-methylthiazole··· $H_2O$  and 5methylthiazole···H<sub>2</sub>O (Chapter 4), respectively. In each case the contribution was attributed to zero-point vibrational motion affecting the non-bonding hydrogen atom, H<sub>nb</sub>, in each complex. Whereas in the case of 2-ethylthiazole, the value of  $P_{cc}$  obtained for 2-ET···H<sub>2</sub><sup>16</sup>O is approximately 2.4 u  $Å^2$  greater than that of the isolated monomer. This change in  $P_{cc}$  is somewhat too large to be attributed to zero-point vibrational motions alone and this will be discussed in more detail later. In the case of 2-ET···( $H_2^{16}O$ )<sub>2</sub>,  $P_{cc}$  was found to be 42.0308(4) u Å<sup>2</sup> which is significantly greater than values determined for 2-ethylthiazole and 2-ET···H<sub>2</sub>O. This suggests that a much larger fraction of the mass of the H<sub>2</sub>O molecules is located outside of the ab plane in 2-ET···( $H_2O$ )<sub>2</sub>. The values of  $P_{cc}$  were also calculated for each of the other isotopologues of 2-ET···H<sub>2</sub>O and 2-ET···(H<sub>2</sub>O)<sub>2</sub> and are reported in Tables 6.6 and 6.7. Only a small variation in the value of  $P_{cc}$  was observed across the range of isotopologues for each complex.

Table 6.10 Comparison of experimentally-determined ( $r_s$ ) and DFT-calculated ( $r_e$ ) atomic coordinates of H<sub>2</sub>O and S in 2-ET···H<sub>2</sub>O and O atoms in 2-ET···(H<sub>2</sub>O)<sub>2</sub>.

		2 ET 11 O		
		$2-\text{ET}\cdots\text{H}_2\text{O}$	7 / 0	, 0
	Method	a / Å	<i>b</i> / Å	c / Å
$H_b$	r <sub>e</sub> (calc.) <sup>a</sup>	2.1026	1.3232	-0.0913
	$r_{\rm s}$ (exp.)	2.05337(74) <sup>b</sup>	1.3645(11)	[0] <sup>c</sup>
О	r <sub>e</sub> (calc.)	3.0720	1.2903	-0.1282
	$r_{\rm s}$ (exp.)	3.10633(48)	1.2533(12)	-0.143(11)
$H_{nb}$	r <sub>e</sub> (calc.)	3.3434	2.1123	-0.5309
	$r_{\rm s}$ (exp.)	3.45971(44)	1.93983(78)	-0.3206(48)
S	$r_{\rm e}$ (calc.)	-1.7584	-0.6770	-0.1293
	$r_{\rm s}$ (exp.)	-1.75076(87)	-0.6783(22)	-0.150(10)
		2-ET···(H <sub>2</sub> O) <sub>2</sub>		
	Method	a / Å	<i>b</i> / Å	c / Å
O1	$r_{\rm e}$ (calc.) <sup>a</sup>	2.3485	1.8052	0.3492
	$r_{\rm s}$ (exp.)	2.37294(77)	1.8468(10)	0.2583(72)
O2	r <sub>e</sub> (calc.)	3.7194	-0.3532	-0.8088
	$r_{\rm s}$ (exp.)	3.74366(42)	-0.4345(36)	-0.7367(21)

<sup>&</sup>lt;sup>a</sup>  $r_e$  geometry calculated at the  $\omega$ B97X-D/aug-cc-pVQZ level of theory.

The assignment of several isotopologues in which the isotopic substitution occurs at the water sub-unit(s) was achieved for each of 2-ET···H<sub>2</sub>O and 2-ET···(H<sub>2</sub>O)<sub>2</sub> allowing the molecular carrier of each spectrum to be verified. Additionally, this allows for the determination of  $r_s$  coordinates and structural parameters for each complex. The  $r_s$  coordinates of each of the bonding hydrogen atom, H<sub>b</sub>, the oxygen atom, O, and the non-bonding hydrogen, H<sub>nb</sub> of 2-ET···H<sub>2</sub>O are presented in Table 6.10. Generally, a good level of agreement is observed between the experimentally determined  $r_s$  and  $\omega$ B97X-D/aug-cc-pVQZ calculated  $r_c$  coordinates. Minor differences are observed in the  $r_s$  and  $r_c$  coordinates of the H<sub>nb</sub> atom. Differences in the  $r_c$ ,  $r_s$  and  $r_c$  coordinates are expected owing to the results of quantum chemical calculations being in the equilibrium geometry whereas the experiment probes complexes in the vibrational ground state. The rapid zero-point motions of the H<sub>nb</sub> atom results in larger uncertainties associated with the coordinates and a greater deviation between results, as discussed in earlier Chapters. A notable observation is the small but non-zero c-coordinate determined for the O atom. This coordinate confirms that the O atom within 2-ET···H<sub>2</sub>O lies outside of the ab plane such that it

<sup>&</sup>lt;sup>b</sup> Numbers in parentheses after  $r_s$  results are Costain errors calculated as  $\delta a = 0.015/|a|$ .

<sup>&</sup>lt;sup>c</sup> Imaginary  $r_s$  coordinate was obtained therefore its value is assumed equal to zero.

would contribute to  $P_{cc}$ . Previous studies identified that the O atom of the H<sub>2</sub>O molecule lies within the *ab* plane in thiazole···H<sub>2</sub>O<sup>1</sup> and each of the methylthiazole···H<sub>2</sub>O complexes discussed in Chapter 4. Whereas in the case of the 2-ethylfuran···H<sub>2</sub>O complex (Chapter 5), the *c*-coordinate of the O atom was determined to be non-zero. The assignment of the <sup>34</sup>S-containing isotopologue of 2-ET···H<sub>2</sub><sup>16</sup>O allowed for the determination of the  $r_s$  coordinates of the sulphur atom within the thiazole ring. The  $r_s$  coordinates were determined to be -1.75076(87), -0.6783(22) and -0.150(10) Å which compare with the  $\omega$ B97X-D/aug-cc-pVQZ calculated  $r_s$  coordinates of -1.758, -0.677 and -0.129 Å.

Table 6.11 Comparison of DFT-calculated ( $r_e$ ) and experimentally-determined ( $r_0$ ) structural parameters for 2-ET···H<sub>2</sub>O.

	2-ET···H₂O	
Parameter	Method	Value
<i>r</i> (O⋯N3) / Å	r <sub>e</sub> (calc.) <sup>a</sup>	2.893
	$r_0$ (exp.)	$2.9257(48)^{b}$
∠(O…N3–C2) / °	r <sub>e</sub> (calc.)	109.1
	$r_0$ (exp.)	109.726(91)
$\angle$ (H <sub>b</sub> -O···N3) / °	r <sub>e</sub> (calc.)	9.1
,	$r_0$ (exp.)	11.3(36)
$r(H_b \cdots N3) / Å$	$r_{\rm e}$ (calc.)	1.940
	$r_0$ (exp., derived) <sup>c</sup>	1.983(13)
$\angle$ (H <sub>b</sub> ···N3–C2) / °	$r_{\rm e}$ (calc.)	113.6
,	$r_0$ (exp., derived)	115.1(17)
$\angle$ (O-H <sub>b</sub> ···N3) / °	$r_{\rm e}$ (calc.)	166.3
	$r_0$ (exp., derived)	163.3(52)

<sup>&</sup>lt;sup>a</sup>  $r_e$  geometry calculated at the  $\omega$ B97X-D/aug-cc-pVQZ level of theory.

The ground state ( $r_0$ ) structural parameters of the 2-ET···H<sub>2</sub>O complex were determined using Kisiel's STRFIT<sup>20</sup> program to provide an insight into the intermolecular interactions present. It was discussed in Chapter 5, that a different approach was employed during the  $r_0$  fit of 2-ethylfuran···H<sub>2</sub>O compared to what was described in Chapter 4 for the methylthiazole····H<sub>2</sub>O complexes. Given that a significant difference in  $P_{cc}$  was observed between the isolated 2-ethylthiazole monomer and the 2-ET····H<sub>2</sub>O complex, and the O atom being slightly displaced from the ab plane, the same approach as employed for 2-ethylfuran····H<sub>2</sub>O was applied to the

<sup>&</sup>lt;sup>b</sup> Numbers in parentheses are one standard deviation in units of the last significant figure.

 $<sup>^{</sup>c}$   $r(O\cdots N3)$ ,  $\angle(O\cdots N3-C2)$  and  $\angle(H_{b}-O\cdots N3)$  determined by fitting to the experimentally-determined rotational constants. Results for other parameters derived from the atomic coordinates using the EVAL program.

2-ET···H<sub>2</sub>O complex. The coordinates internal to each of the 2-ethylthiazole and H<sub>2</sub>O sub-units were initially assumed equal to the  $r_e$  calculated results and the z-matrix was constructed in a manner to allow for the fitting of interatomic distances and intermolecular angles which contain mostly heavy atoms. The described assumptions resulted in the  $r_0$  fitted parameters of  $r(O \cdots N3)$ ,  $\angle(O \cdots N3 - C2)$  and  $\angle(H_b - O \cdots N3)$  being in good agreement with the  $\omega B97X$ -D/aug-cc-pVQZ calculated parameters (displayed in Table 6.11). The  $r(O \cdot \cdot \cdot N3)$  distance was calculated to be 2.9257(48) Å and ∠(O···N3–C2) was determined to be 109.726(91)° which compare to the  $r_e$  calculated results of 2.893 Å and 109.1°. An additional three parameters, one intermolecular distance and two angles, were derived from the  $r_0$  coordinates (Appendix, A.42) obtained after the fit was performed. The 2-ET···H<sub>2</sub>O complex is formed via a hydrogen bonding interaction between a O-H bond of H<sub>2</sub>O and the nitrogen atom of the thiazole ring. The primary hydrogen bond angle is non-linear within this complex,  $\angle(H_b-O\cdots N3) =$ 163.3(52)°, implying the presence of additional weaker hydrogen bonding interactions between the O atom of H<sub>2</sub>O and the ethyl moiety located at the 2-position of the ring. The intermolecular interactions present within the complex will be discussed further in the following sections. The ∠(O–H<sub>b</sub>···N3) determined for 2-ET···H<sub>2</sub>O is similar to the same angle within the thiazole···H<sub>2</sub>O complex<sup>1</sup> (168.9(1)°) whereas the  $\angle$ (H<sub>b</sub>···N3–C2) angles determined for each of the complexes differ considerably. This angle was determined to be 115.1(17)° in 2-ET···H<sub>2</sub>O which is  $\sim 20^{\circ}$  greater than the value reported for thiazole···H<sub>2</sub>O (95.6(4)°).

Table 6.12 Comparison of DFT-calculated ( $r_e$ ) and experimentally-determined ( $r_0$ ) structural parameters of 2-ET···(H<sub>2</sub>O)<sub>2</sub>.

	2-ET···(H <sub>2</sub> O) <sub>2</sub>	
Parameter	Method	Value
<i>r</i> (O1⋯N3) / Å	r <sub>e</sub> (calc.) <sup>a</sup>	2.827
	$r_0$ (exp.)	2.8235(72) <sup>b</sup>
<i>r</i> (O1···O2) / Å	r <sub>e</sub> (calc.)	2.807
	$r_0$ (exp.)	2.894(21)
∠(O1···N3–C2) /°	r <sub>e</sub> (calc.)	118.4
,	$r_0$ (exp.)	120.55(15)

 $r_e$  geometry calculated at the  $\omega$ B97X-D/aug-cc-pVQZ level of theory.

The spectrum of three isotopologues of 2-ET···(H<sub>2</sub>O)<sub>2</sub> were assigned, 2-ET···(H<sub>2</sub><sup>16</sup>O)<sub>2</sub>, 2-ET···(H<sub>2</sub><sup>18</sup>O)(H<sub>2</sub><sup>16</sup>O) and 2-ET···(H<sub>2</sub><sup>16</sup>O)(H<sub>2</sub><sup>18</sup>O), allowing for the determination of the  $r_s$  coordinates of each oxygen atom. The  $r_s$  coordinates obtained are in good agreement with those

<sup>&</sup>lt;sup>b</sup> Numbers in parentheses are one standard deviation in units of the last significant figure.

determined by quantum chemical calculations. The c-coordinate of both oxygen atoms were determined to be non-zero, which is consistent with the  $P_{cc}$  result obtained for this complex being significantly greater than that of 2-ET···H<sub>2</sub>O. The  $r_s$  coordinates displayed in Table 6.10 imply an interatomic distance between the oxygen atoms,  $r(O1\cdots O2)$ , of 2.8413(40) Å. Dcontaining isotopologues of 2-ET···(H<sub>2</sub>O)<sub>2</sub> were searched for in the spectrum acquired during the experiment utilising D<sub>2</sub>O. The spectra of singly or multiply substituted deuterium isotopologues were unable to be assigned, probably owing to the lower abundance of these species within the supersonic expansion, precluding the determination of  $r_s$  coordinates of the hydrogen atoms and hydrogen-containing intermolecular parameters. A high standard deviation was obtained for the  $r_0$  fit when assuming all atoms of the  $H_2O$  sub-units lie within the plane of the thiazole ring. This is unsurprising given that the value of  $P_{cc}$  and coordinates of the oxygen atoms indicate a significant fraction of mass lies outside of the ab plane of the complex. A fit performed under the assumption that all internal coordinates of the H<sub>2</sub>O sub-units are equal to those calculated at the  $\omega$ B97X-D/aug-cc-pVQZ level yielded a lower standard deviation. Two interatomic distances,  $r(O1\cdots N3)$  and  $r(O1\cdots O2)$  and the  $\angle(O1\cdots N3-C2)$  angle were determined during the fit. The  $r_0$  parameters determined are displayed in Table 6.12 and are very consistent with the  $r_e$  calculated values. The value obtained for  $r(O1\cdots O2)$  during the  $r_0$ fit is 2.894(21) Å which is in good agreement with both the  $r_e$  calculated value of 2.807 Å and the  $r_s$  result mentioned earlier. It is interesting to compare the values of  $r(O1\cdots N3)$  and  $\angle$ (O1···N3–C2) obtained for the 2-ET···H<sub>2</sub>O and 2-ET···(H<sub>2</sub>O)<sub>2</sub> complexes. The r(O1···N3) distance is determined to be  $\sim 0.1$  Å shorter in 2-ET···(H<sub>2</sub>O)<sub>2</sub> compared to 2-ET···H<sub>2</sub>O. The ∠(O1···N3–C2) angle was found to differ significantly between the hydrate complexes, this angle was determined to be 120.55(15)° in the dihydrate and 109.726(91)° in the monohydrate complex. Atomic coordinates determined from the  $r_0$  fit of both 2-ET···H<sub>2</sub>O and 2-ET···(H<sub>2</sub>O)<sub>2</sub> are given in the Appendix, A.42.

#### **6.6 Non-Covalent Interactions**

To provide further insight into the intermolecular interactions present within each of 2-ET···H<sub>2</sub>O and 2-ET···(H<sub>2</sub>O)<sub>2</sub>, Non-Covalent Interaction (NCI) index<sup>21</sup> and Natural Bond Orbital (NBO)<sup>22</sup> analyses were performed for each complex. In each case the geometries of the hydrate complexes calculated at the \omegaB97X-D/aug-cc-pVQZ level of theory were used for the analysis. NCI plots of the reduced density gradient (RDG) versus the sign of the second eigenvalue of the Hessian matrix  $(\lambda_2)$  of the electronic density  $(\rho)$ , sign $(\lambda_2)\rho$ , are presented in Figure 6.4 and were generated using the Multiwfn program.<sup>23</sup> A dark blue isosurface is located between one of the O-H of H<sub>2</sub>O and the nitrogen atom of the thiazole ring, indicating the presence of a comparatively strong attractive hydrogen bonding interaction within the 2-ET···H<sub>2</sub>O complex. It was described above that the primary hydrogen bonding interaction (indicated by the blue isosurface) is non-linear, suggesting the presence of additional interactions within the complex. The NCI analysis also revealed the presence of a second larger isosurface located between the O atom of H<sub>2</sub>O and the ethyl group. This isosurface shows the presence of weakly attractive (light green, negative sign( $\lambda_2$ ) $\rho$ ) and weakly repulsive interactions (dark green, positive sign( $\lambda_2$ ) $\rho$ ) interactions. The weakly attractive interactions are between the O atom of H<sub>2</sub>O and the nearest H atoms located on C6 and C7. In the ωB97X-D/aug-cc-pVQZ geometry the O atom of H<sub>2</sub>O and the closest H6 atom are separated by 2.882 Å whereas the O atom and H7 are separated by 2.729 Å. Two dark blue isosurfaces were identified in the NCI analysis of 2-ET···(H<sub>2</sub>O)<sub>2</sub>. In addition to the interaction present between the nitrogen atom of the thiazole ring and the hydrogen atom (H<sub>1b</sub>) of the first H<sub>2</sub>O molecule, another relatively strong interaction is present between O1 of the first H<sub>2</sub>O molecule and one of the H atoms (H<sub>2b</sub>) on the second H<sub>2</sub>O molecule. The NCI analysis performed on 2-ET···(H<sub>2</sub>O)<sub>2</sub> also indicates that weakly attractive interactions are present between the O atoms of both H<sub>2</sub>O molecules and the hydrogen atoms located on the ethyl group, as what was previously observed in the monohydrate complex. The results of the NCI analysis indicate that each of 2-ethylthiazole and H<sub>2</sub>O sub-unit(s) within each of 2-ET···H<sub>2</sub>O and 2-ET···(H<sub>2</sub>O)<sub>2</sub> simultaneously act as a hydrogen bond donor and acceptor.

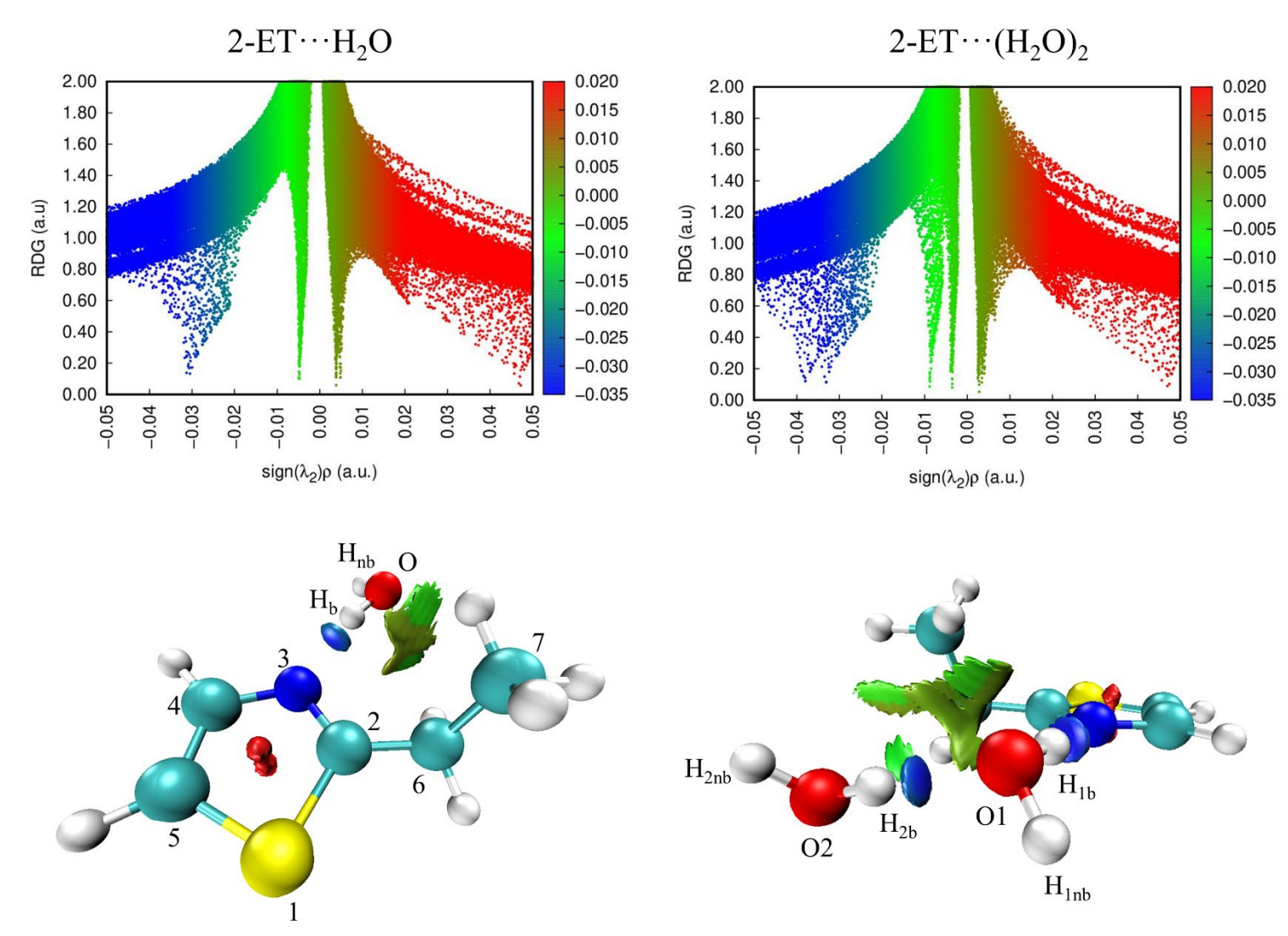


Figure 6.4 NCI isosurfaces and plots of the RDG (a.u.) vs  $sign(\lambda_2)\rho$  of 2-ET···H<sub>2</sub>O and 2-ET···(H<sub>2</sub>O)<sub>2</sub>. Positive and negative values of  $sign(\lambda_2)\rho$  respectively denote repulsive (red) and attractive (blue) interactions. The isosurface *s* value is 0.5 au.

NBO analysis was performed to calculate the second order stabilisation energies  $(E^{(2)})$  of each interaction present. The analysis was performed at the B3LYP(D3BJ)/aug-cc-pVTZ level of theory, using the ωB97X-D/aug-cc-pVQZ calculated geometries. The results of the NBO analysis are given in the Appendix, Tables A.43 and A.44. The largest  $E^{(2)}$  contribution within 2-ET···H<sub>2</sub>O corresponds to the interaction between the lone pair of the nitrogen atom and the anti-bonding  $\sigma^*(H_b-O)$  orbital of the H<sub>2</sub>O molecule. The  $E^{(2)}$  of this interaction was calculated to be 40.67 kJ mol<sup>-1</sup>, which is very similar to the values obtained for the equivalent interactions in the thiazole···H<sub>2</sub>O and methylthiazole···H<sub>2</sub>O (Chapter 4) complexes. The analysis also identified additional weaker interactions between the lone pairs of the O atom and the hydrogen atoms located on the ethyl group. The  $E^{(2)}$  of the C6–H6···O interaction was calculated to be 0.63 kJ mol<sup>-1</sup> and was determined to be slightly stronger than the interaction C7-H7···O (0.54 kJ mol<sup>-1</sup>). This is interesting given that the interatomic separation between the O atom and nearest H6 atom is calculated to be greater than the distance between O and the nearest H7 atom in the  $\omega B97X$ -D/aug-cc-pVQZ geometry. In the  $r_0$  geometry, the  $r(H6\cdots O)$  and  $r(H7\cdots O)$ distances were derived to be 2.926(3) Å and 2.765(3) Å, respectively. The natural bond orbitals (as shown in A.43) imply that the orientation of the interaction between the O lone pair and C6–H6 is more favourable than that between the O lone pair and C7–H7. The weak interactions between the O atom of H<sub>2</sub>O and the hydrogen atoms on the ethyl group, described above, are strong enough to cause the primary hydrogen bond to deviate from linearity.

The NBO analysis of 2-ET···(H<sub>2</sub>O)<sub>2</sub> identified that the largest  $E^{(2)}$  contribution corresponds to the interaction between the lone pair on the nitrogen atom and antibonding  $\sigma^*(H_{1b}-O1)$  orbital of the first H<sub>2</sub>O molecule. The second order stabilisation energy of this interaction was calculated to be 64.39 kJ mol<sup>-1</sup> within the dihydrate complex, which is considerably larger than the same interaction in the 2-ET···H<sub>2</sub>O complex. The NCI analysis identified the presence of another relatively strong hydrogen bonding interaction between the two H<sub>2</sub>O molecules within the 2-ET···(H<sub>2</sub>O)<sub>2</sub> complex. The interaction between a lone pair on O1 and the antibonding  $\sigma^*(O2-H_{2b})$  orbital is calculated to have a second order stabilisation energy of 51.04 kJ mol<sup>-1</sup>. Comparing the relative magnitudes of  $E^{(2)}$  calculated for each of the O1-H<sub>1b</sub>···N3 and O2-H<sub>2b</sub>···O1 interactions it is evident that the hydrogen bonding interaction is stronger in the former, consistent with the findings of the thiazole···(H<sub>2</sub>O)<sub>2</sub> study. The NBO analysis also calculated the second order stabilisation energies of the interactions between the O atoms of the H<sub>2</sub>O sub-units and the hydrogen atoms located on the ethyl group. The largest contribution of each of these interactions is due to the lone pair on O2 interacting with the antibonding  $\sigma^*(C6-H6)$ , with  $E^{(2)}$  calculated to be 3.39 kJ mol<sup>-1</sup> for this interaction. A weaker interaction

forms between the lone pair of O2 and the nearest H7 atom ( $E^{(2)} = 0.92 \text{ kJ mol}^{-1}$ ). An additional weak contribution of 0.21 kJ mol<sup>-1</sup> was identified by the analysis from an interaction between a lone pair on O1 and the  $\sigma^*(C7-H7)$  orbital. The derived interatomic distance between O2 and the nearest H6 atom is 2.608(9) Å in the  $r_0$  geometry whereas O1 is 2.963(15) Å from the nearest H7 and 3.355(12) Å from the nearest H6. The higher relative strength of the O1-H<sub>1b</sub>···N3 interaction in the 2-ET···(H<sub>2</sub>O)<sub>2</sub> complex compared with the equivalent interaction within 2-ET···H<sub>2</sub>O, and also the fact that the weaker interactions (involving the ethyl group) are stronger within 2-ET···(H<sub>2</sub>O)<sub>2</sub> than within 2-ET···H<sub>2</sub>O, confirms that cooperative hydrogen bonding effects are significant in the dihydrate complex.

#### 6.7 Discussion

The assignment of seven isotopologues of the 2-ethylthiazole molecule has allowed the lowest-energy conformer to be identified as having  $C_1$  symmetry. The dihedral angle which defines the rotation of the ethyl group relative to the plane of the thiazole ring,  $\angle$ (S1–C2–C6–C7), was determined to be –98.6(10)° in the  $r_s$  geometry whereas this dihedral angle was calculated to be –110° in the  $r_e$  geometry at the  $\omega$ B97X-D/aug-cc-pVQZ level of theory. It is interesting to empirically review the factors that influence the value of this angle with reference to results obtained for comparator molecules studied by rotational spectroscopy.

The lowest-energy conformation of ethylbenzene<sup>4</sup> was reported by W. Caminati et al. in 1991. This study identified that ethylbenzene adopts a C<sub>1</sub> configuration with the ethyl group rotated 90° relative to the benzene ring. This is unsurprising given the high symmetry of benzene and that this configuration minimises steric hindrance by orienting the ethyl group away from hydrogen atoms attached to the ring. Thiazole and furan rings are significantly less symmetric than benzene. Two distinct conformations of 2-ethylfuran (C<sub>s</sub> and C<sub>1</sub>) were characterised in a recent study<sup>6</sup> and the experimental energy ordering of the conformers was revealed by experiments discussed in Chapter 5. The ethyl group was found to be rotated 63.31(64)° (in the  $r_s$  geometry) out of the plane of the furan ring in the  $C_1$  conformation of this molecule. The difference between  $\angle$ (O1–C2–C6–C7) = 63.31(64)° for 2-ethylfuran and  $\angle$ (S1–C2–C6–C7)  $=-98.6(10)^{\circ}$  for 2-ethylthiazole indicates that the identities of the heteroatoms present within the ring has a significant effect on the molecular geometries of these molecules. In 2-ethylfuran, the ethyl group is rotated towards the O atom and away from C3. Whereas in 2-ethylthiazole, the ethyl group is rotated slightly towards N3 and away from S1. It is apparent that in both of 2-ethylfuran and 2-ethylthiazole that the direction that the ethyl group rotates moves the CH<sub>3</sub> group closer to the more electronegative heteroatom within the ring. The symmetry of interactions between electronic orbitals on the ring and on the ethyl group will also influence the rotation of the ethyl group. Therefore, it is not possible to say whether through-space or through-bond electronic effects have a more significant effect based on the empirical observations made above.

Further insight has been provided by a study on the isomers of ethylaniline.<sup>5</sup> Three isomers of this molecule were studied, 2-ethylaniline, 3-ethylaniline and 4-ethylaniline, in which the ethyl group is positioned *ortho*, *meta* and *para* respectively to the amine group. Each of 3-ethylaniline and 4-ethylaniline adopts a  $C_1$  configuration, where the ethyl group is rotated  $87.37(93)^{\circ}$  relative to the ring in the former and  $91.3(17)^{\circ}$  in the latter. In both of these molecules the ethyl

group is located remote from the amine group. In 2-ethylaniline, the ethyl group is located adjacent to the exocyclic amine group and the  $\angle$ (C8–C7–C2–C1) dihedral angle was identified to be 75.59(82)° (from the  $r_s$  coordinates). The authors suggested that the deviation of  $\angle$ (C8–C7–C2–C1) from 90° can be attributed to the presence of a weak interaction between the ethyl group and the nitrogen atom of the amine group. From the aforementioned molecules, the overall picture is that the molecular geometries observed for the  $C_1$  conformations of ethylated aromatic and heteroaromatic rings depend on the relative symmetries of the ethyl group and ring to each other. Each of 2-ethylthiazole, 2-ethylfuran and 2-ethylaniline are observed to deviate from the perpendicular geometry of the ethyl group observed in ethylbenzene. In each of these molecules, the ethyl group is bound to an asymmetric ring. On the other hand, the rotation of the ethyl group in each of 3-ethylaniline and 4-ethylaniline was found to be very close to that observed for ethylbenzene. This is consistent with the symmetry of the local environment surrounding the ethyl group being similar in each of these molecules.

Table 6.13 Comparison of experimentally-determined ( $r_0$ ) structural parameters for complexes formed between 5-membered N-heterocyclic rings and  $H_2O$ .

Complex	[H-bond donor on het. ring] <sup>d</sup>	<i>r</i> (H <sub>b</sub> ···N) / Å	∠(H <sub>b</sub> ····N−C2)	∠(O–H <sub>b</sub> ···N)
Imidazole…H <sub>2</sub> O <sup>a</sup>	C–H on C2	1.927(27) <sup>e</sup>	99.9(41)	172.1(26)
N-methylimidazole···H <sub>2</sub> O <sup>a</sup>	C-H on C2	1.922(4)	101.0(16)	177(5)
5-methylimidazole ···H <sub>2</sub> O <sup>b</sup>	C-H on C5	1.9605(32)	104.53(90)	168.8(25)
Thiazole…H <sub>2</sub> O <sup>a</sup>	C-H on C2	1.977(7)	95.6(4)	168.9(1)
5-methylthiazole···H <sub>2</sub> O <sup>c</sup>	C-H on C2	2.0037(42)	99.40(78)	166.0(23)
2-methylimidazole···H <sub>2</sub> O <sup>a</sup>	C-CH <sub>3</sub> on C2	1.923(5)	116.9(9)	166.3(28)
2-methylthiazole···H <sub>2</sub> O <sup>c</sup>	C-CH <sub>3</sub> on C2	1.9884(53)	112.6(16)	170.2(50)
$2\text{-ET}\cdots H_2O$	CH <sub>2</sub> CH <sub>3</sub> on	1.983(13)	115.1(17)	163.3(52)
	C2			
4-methylimidazole ···H <sub>2</sub> O <sup>b</sup>	C-CH <sub>3</sub> on C4	1.9750(17)	138.7(12)	173.6(37)
4-methylthiazole···H <sub>2</sub> O <sup>c</sup>	C-CH <sub>3</sub> on C4	2.0296(68)	$134.7(14)^{d}$	167.4(44)

<sup>&</sup>lt;sup>a</sup> Results from imidazole···H<sub>2</sub>O, *N*-methylimidazole···H<sub>2</sub>O and 2-methylimidazole···H<sub>2</sub>O from references 2 and 3. Results for thiazole···H<sub>2</sub>O following re-analysis presented in A.15 using data provided in reference 1.

<sup>&</sup>lt;sup>b</sup> Unpublished results by E. Gougoula et al.

<sup>&</sup>lt;sup>c</sup> Results for isomers of methylthiazole...H<sub>2</sub>O presented in Chapter 4.

<sup>&</sup>lt;sup>d</sup> Indicates the atom or group of the heteroaromatic sub-unit which acts as the hydrogen bond donor in the secondary (weaker) hydrogen bond within the complex.

<sup>&</sup>lt;sup>e</sup> Uncertainties in parentheses are those quoted in the primary source.

A good starting point for discussion of the geometry of  $2\text{-}\text{ET}\cdots\text{H}_2\text{O}$  is provided by a series of recent works that have investigated the monohydrate complexes of thiazole, imidazole, methylthiazole (Chapter 4) and methylimidazole. In each of the aforementioned complexes, the H<sub>2</sub>O molecule binds to the heterocycle via a comparatively strong hydrogen bond at the pyridinic nitrogen atom and forms a weaker interaction with a hydrogen atom or methyl group on a neighbouring ring position. The complexes can be separated into two groups (as shown in Table 6.13) according to their geometrical parameters. The geometrical parameters associated with the primary hydrogen bonding interaction are very similar in each of thiazole···H<sub>2</sub>O, imidazole···H<sub>2</sub>O<sup>2</sup> as well as in each of *N*-methylimidazole···H<sub>2</sub>O, 5-methylimidazole···H<sub>2</sub>O and 5-methylthiazole···H<sub>2</sub>O (where the methyl group is remote to the H<sub>2</sub>O molecule). The  $\angle(H_b \cdots N_3 - C_2)$  and  $\angle(O - H_b \cdots N_3)$  angles are found to be very similar across this group of complexes, with the value of  $\angle(H_b \cdots N_3 - C_2)$  ranging from 95.6(4)° to 104.53(90)° while values of  $\angle(O - H_b \cdots N_3)$  ranges from 166.0(23)° to 177(5)°. The value of  $\angle(H_b \cdots N_3 - C_2)$  obtained for 2-ET···H<sub>2</sub>O is considerably different, ~15° greater, than the range of angles identified in this series of complexes while the  $\angle(O - H_b \cdots N_3)$  angle is found to be similar.

The second sub-set of complexes is comprised of 2-methylimidazole···H<sub>2</sub>O,<sup>3</sup> 2methylthiazole···H<sub>2</sub>O, 4-methylimidazole···H<sub>2</sub>O<sup>j</sup> and 4-methylthiazole···H<sub>2</sub>O. As shown in Table 6.13, the value of the  $\angle$ (H<sub>b</sub>···N3–C2) angle obtained for each of these complexes is significantly different to what was observed for those within the first sub-set, owing to differences in the molecular geometries. In the second group of complexes, a methyl group is substituted at either the 2- or 4- position of the ring such that the H<sub>2</sub>O molecule forms an interaction with the methyl group rather than a neighbouring hydrogen atom. It was discussed earlier that interactions between the O atom of H<sub>2</sub>O and the ethyl group have been observed in 2-ET···H<sub>2</sub>O and that the ethyl group adopts a C<sub>1</sub> conformation within this complex. The NBO analysis indicated that interactions between the lone pairs on oxygen and each of  $\sigma^*(C6-H6)$ and  $\sigma^*(C7-H7)$  have similar contributions to the overall stabilisation energy of the complex. The weak hydrogen bonding interactions present within the 2-ET···H<sub>2</sub>O complex result in the values of the geometrical parameters associated with the primary hydrogen bond to be very similar to those of 2-methylimidazole···H<sub>2</sub>O and 2-methylthiazole···H<sub>2</sub>O. The hydrogen bond angle,  $\angle$ (O–H<sub>b</sub>···N3), in 2-methylimidazole···H<sub>2</sub>O, 2-methylthiazole···H<sub>2</sub>O and 2-ET···H<sub>2</sub>O is non-linear in each case, with the largest deviation from linearity observed for 2-ET···H<sub>2</sub>O. The value of  $\angle$  (H<sub>b</sub>···N3–C2) is somewhat greater in each of 4-methylimidazole···H<sub>2</sub>O and 4-

\_

<sup>&</sup>lt;sup>j</sup> Unpublished work by E. Gougoula *et al*.

methylthiazole···H<sub>2</sub>O (138.7(12)° in the former and 134.7(14)° in the latter) than the rest of the monohydrate complexes within this group. This is because the geometries of these complexes are somewhat different since the H<sub>2</sub>O molecule forms an interaction with the methyl group located at the 4-position.

The geometry of the 2-ET···( $H_2O$ )<sub>2</sub> complex is similar to those reported for thiazole···( $H_2O$ )<sub>2</sub> and phenanthridine...(H<sub>2</sub>O)<sub>2</sub>, <sup>10, 24</sup> which have each been shown to contain two strong and one weak hydrogen bonds. The (H2O)2 sub-unit donates a hydrogen bond to the nitrogen while accepting a weak hydrogen bond from one or more C-H bonds in each complex. The interatomic separation between the oxygen atoms within the  $H_2O$  dimer sub-unit,  $r(O1\cdots O2)$ in the three complexes is 2.894(21) Å, 2.826(33) Å and 2.85(1) Å respectively which compares with 2.976(10) Å for the isolated water dimer.<sup>25</sup> Cooperative effects within the hydrogen bonding network result in the shortening of this distance within the dihydrate complexes relative to the isolated water dimer. The (H<sub>2</sub>O)<sub>2</sub> is able to more effectively bridge the distance between the nitrogen and C-H bonds on the ethyl group than the single H<sub>2</sub>O molecule in 2-ET···H<sub>2</sub>O. Therefore this results in differences in the primary hydrogen bond angle within 2-ET···H<sub>2</sub>O and 2-ET···(H<sub>2</sub>O)<sub>2</sub>. In the ωB97X-D/aug-cc-pVQZ calculated geometry of 2-ET···(H<sub>2</sub>O)<sub>2</sub> the  $\angle$ (O1-H<sub>1b</sub>···N3) angle is 174° which is greater than the experimentallyobtained angle of 163.3(52)° within 2-ET···H<sub>2</sub>O and hence is closer to a linear configuration as expected for a stronger interaction. This is consistent with the results of the NBO analysis which identified that the second order stabilisation energy associated with this interaction within the dihydrate complex ( $E^{(2)} = 64.4 \text{ kJ mol}^{-1}$ ) is higher than in the monohydrate complex  $(E^{(2)} = 40.7 \text{ kJ mol}^{-1})$ . As discussed earlier the  $\angle (O1 \cdots N3 - C2)$  angle was observed to differ between the monohydrate and dihydrate complex of 2-ethylthiazole. The  $\angle$ (O1···N3–C2) angle is determined to be  $109.726(91)^{\circ}$  and  $120.55(15)^{\circ}$ , in the  $r_0$  geometries of 2-ET···H<sub>2</sub>O and 2-ET···(H<sub>2</sub>O)<sub>2</sub> respectively, while the same parameter is 91.98(10)° in thiazole···H<sub>2</sub>O<sup>1</sup> and 106.5(49)° in thiazole···(H<sub>2</sub>O)<sub>2</sub>.<sup>10</sup> This series of complexes illustrates that the presence of a group located at the 2- position has a clear and predictable effect on the position of the H<sub>2</sub>O sub-unit(s) and furthermore that the addition of a second H<sub>2</sub>O molecule to each of 2-ET···H<sub>2</sub>O and thiazole···H<sub>2</sub>O is similar. Interestingly, the  $\angle$ (O1···N3–C2) angle obtained for 2-ET···H<sub>2</sub>O is very consistent with the equivalent angle within 2-methylthiazole···H<sub>2</sub>O (Chapter 4),  $\angle$ (O1···N3-C2) = 109.36(22)°, indicating that the effect is the same independent of whether a methyl group or an ethyl group is located at the 2- position.

#### **6.8 Conclusions**

The molecular geometries of 2-ethylthiazole, 2-ET···H<sub>2</sub>O and 2-ET···(H<sub>2</sub>O)<sub>2</sub>, have been characterised using microwave spectroscopy. For each of the isolated monomer and hydrate complexes, one conformer was observed only during experiments performed using argon and neon carrier gases, consistent with the predictions of quantum chemical calculations. Analysis of the molecular geometry revealed that the angle which defines the rotation of the ethyl group relative to the thiazole ring,  $\angle$ (S1-C2-C6-C7), was determined to be -98.6(10)° (in the  $r_s$ geometry) in the 2-ethylthiazole monomer, which is consistent with a C<sub>1</sub> conformation. Each of 2-ET···H<sub>2</sub>O and 2-ET···(H<sub>2</sub>O)<sub>2</sub> contains a strong hydrogen bond between the nitrogen atom of the thiazole ring and a hydrogen atom of H<sub>2</sub>O and additional weaker interactions between the O atom of  $H_2O$  and C-H bonds of the ethyl group. The  $\angle(O\cdots N3-C2)$  and  $\angle(H_b\cdots N3-C2)$ angles are significantly greater for each of 2-ET···H<sub>2</sub>O and 2-ET···(H<sub>2</sub>O)<sub>2</sub> compared to its thiazole-containing analogue, owing to the presence of the alkyl group influencing the position of the coordinating H<sub>2</sub>O molecule(s). Cooperativity within the hydrogen bonding network is evident within 2-ET···(H<sub>2</sub>O)<sub>2</sub>, resulting in a shorter and stronger primary hydrogen bond compared to 2-ET···H<sub>2</sub>O and a reduction in the  $r(O1\cdots O2)$  distance with respect to that of the isolated water dimer.

#### **6.9 References**

- 1. W. Li, J. Chen, Y. Xu, T. Lu, Q. Gou and G. Feng, *Spectrochimica Acta Part A: Molecular and Biomolecular Spectroscopy*, 2020, **242**, 118720.
- 2. E. Gougoula, D. J. Cole and N. R. Walker, *The Journal of Physical Chemistry A*, 2020, **124**, 2649-2659.
- 3. E. Gougoula, C. N. Cummings, C. Medcraft, J. Heitkämper and N. R. Walker, *Physical Chemistry Chemical Physics*, 2022, **24**, 12354-12362.
- 4. W. Caminati, D. Damiani, G. Corbelli, B. Velino and C. W. Bock, *Molecular Physics*, 1991, **74**, 885-895.
- 5. J. Wang, S. Herbers, P. Buschmann, K. Lengsfeld, J.-U. Grabow, G. Feng and Q. Gou, *Chinese Journal of Chemical Physics*, 2020, **33**, 119-124.
- 6. H. V. L. Nguyen, *Journal of Molecular Structure*, 2020, **1208**, 127909.
- 7. E. Gougoula, C. Medcraft, J. Heitkämper and N. R. Walker, *The Journal of Chemical Physics*, 2019, **151**, 144301.
- 8. W. Jäger and H. Mäder, Journal of Molecular Structure, 1988, 190, 295-305.
- 9. W. Jäger and H. Mäder, Zeitschrift für Naturforschung A, 1987, 42, 1405-1409.
- 10. E. Gougoula, C. N. Cummings, Y. Xu, T. Lu, G. Feng and N. R. Walker, *The Journal of Chemical Physics*, 2023, **158**, 114307.
- 11. J. K. G. Watson, *The Journal of Chemical Physics*, 1968, **48**, 4517-4524.
- 12. C. M. Western, *Journal of Quantitative Spectroscopy and Radiative Transfer*, 2017, **186**, 221-242.
- 13. Z. Kisiel, PROSPE Programs for ROtational SPEctroscopy, <a href="http://info.ifpan.edu.pl/~kisiel/prospe.htm">http://info.ifpan.edu.pl/~kisiel/prospe.htm</a>, (accessed 21/06/2024, 2024).
- L. Nygaard, E. Asmussen, J. H. Høg, R. C. Maheshwari, C. H. Nielsen, I. B. Petersen, J. Rastrup-Andersen and G. O. Sørensen, *Journal of Molecular Structure*, 1971, 8, 225-233.
- 15. B. Bak, D. Christensen, L. Hansen-Nygaard and J. Rastrup-Andersen, *Journal of Molecular Spectroscopy*, 1962, **9**, 222-224.
- 16. J. U. Grabow, H. Hartwig, N. Heineking, W. Jäger, H. Mäder, H. W. Nicolaisen and W. Stahl, *Journal of Molecular Structure*, 2002, **612**, 349-356.
- 17. T. Nguyen, V. Van, C. Gutlé, W. Stahl, M. Schwell, I. Kleiner and H. V. L. Nguyen, *The Journal of Chemical Physics*, 2020, **152**, 134306.
- 18. J. Kraitchman, American Journal of Physics, 1953, 21, 17-24.
- 19. C. C. Costain, *The Journal of Chemical Physics*, 1958, **29**, 864-874.
- 20. Z. Kisiel, Journal of Molecular Spectroscopy, 2003, 218, 58-67.
- 21. E. R. Johnson, S. Keinan, P. Mori-Sánchez, J. Contreras-García, A. J. Cohen and W. Yang, *Journal of the American Chemical Society*, 2010, **132**, 6498-6506.
- 22. A. E. Reed, L. A. Curtiss and F. Weinhold, *Chemical Reviews*, 1988, **88**, 899-926.
- 23. T. Lu and F. Chen, *Journal of Computational Chemistry*, 2012, **33**, 580-592.
- 24. D. Loru, A. L. Steber, P. Pinacho, S. Gruet, B. Temelso, A. M. Rijs, C. Pérez and M. Schnell, *Physical Chemistry Chemical Physics*, 2021, **23**, 9721-9732.
- 25. J. A. Odutola and T. R. Dyke, *The Journal of Chemical Physics*, 1980, **72**, 5062-5070.

# Chapter 7. Microwave spectra and molecular geometries of Ethylimidazole isomers and their hydrate complexes.

#### 7.1 Introduction

Imidazole<sup>1</sup> is a five membered heteroaromatic ring which is an essential building block of a variety of biomolecules including the amino acid histidine, the neurotransmitter histamine and the DNA nucleobases adenine and guanine. It has been observed in nature that generally substitutions onto the imidazole ring are favoured at the 4- position (atom labels equivalent to those presented in Figure 7.1). Each of histidine<sup>2</sup> and histamine<sup>3</sup> have side chains which are located at the 4- position of the imidazole ring. Imidazole, like thiazole, is an example of a heterocycle which contains two heteroatoms located at the 1- and 3- positions, in the case of imidazole both heteroatoms are nitrogen. The microwave spectrum of imidazole was first studied by Christen et al. in 1981. Several substituted derivatives of imidazole have also been studied by rotational spectroscopy where substitutions onto the heteroaromatic ring are not limited to the 4- position. Vinyl substituted imidazole rings, 1-vinylimidazole and 4vinylimidazole, have been studied. The isomers differ in the substitution position on the ring and the atom located at the ring/vinyl junction, N in the former and C in the latter. The study on 1-vinylimidazole revealed that the target molecule adopts two conformations in the gas phase.<sup>4</sup> The lowest energy conformation was found to have a planar configuration consistent with expectations owing to the conjugation of  $\pi$  electrons on the imidazole and vinyl moieties which can be achieved in a planar configuration. A second conformation which is 5.5(7) kJ mol<sup>-1</sup> higher in energy was also observed. The higher energy conformer adopts a non-planar geometry, such that the vinyl group is rotated slightly out of the plane of the imidazole ring by 15(4)°. 4-vinylimidazole exists as a tautomeric pair with 5-vinylimidazole and were studied concurrently.<sup>5</sup> Two conformers of each tautomer have been experimentally observed differing in the orientation of the vinyl group relative to the imidazole ring. Three of the four observed conformers possess a planar geometry. The higher energy conformer of 5-vinylimidazole adopts a non-planar configuration, with the vinyl group predicted to rotate 8° out of the plane of the imidazole ring by quantum chemical calculations, similar to what was observed in the case of 1-vinylimidazole. 4-vinylimidazole is the breakdown product of another imidazole derivative, trans-urocanic acid, which has been the subject of a separate study. Trans-urocanic acid was transferred to the gas phase for study by means of laser ablation such that the decarboxylation of all the sample into 4-vinylimidazole could be avoided.<sup>6</sup> Four conformers of trans-urocanic acid have been observed, which differ in arrangement of atoms about the 4- position of the

imidazole ring and the carbonyl carbon located on the of the propenoic acid side chain. In the case of *trans*-urocanic acid each conformer observed is effectively planar with low frequency out-of-plane vibrations resulting in a slightly negative inertial defect.

Isomers of methylimidazole<sup>7</sup> such that the methyl group is substituted at each of the 1-, 2-, 4and 5- positions have been investigated to explore the variation in the  $V_3$  barrier to internal rotation of the methyl group with the substitution position. The variation in the  $V_3$  barrier height when the methyl group is substituted at different positions on the imidazole ring arises from the symmetry of the overlap between the  $\pi$ -like orbital on the methyl group and the  $\pi$ -orbitals of the imidazole ring. Subsequent investigations<sup>8</sup> revealed the effect monohydration has on the  $V_3$ barrier height for each of the isomers of methylimidazole, which was discussed alongside the monohydrate complexes of methylthiazole in Chapter 4. Building upon this work and other studies of ethyl-substituted aromatic rings, the microwave spectra of isomers of ethylimidazole and their hydrate complexes were recorded. In this Chapter, the results of studies on two isomers of ethylimidazole, N-ethylimidazole and 2-ethylimidazole will be presented. It will be shown that the conformation that the ethyl group adopts differs depending upon the position at which the ethyl group is substituted. The monohydrate complexes of each of N-ethylimidazole and 2ethylimidazole as well as the dihydrate of N-ethylimidazole have been studied for the first time (hereafter denoted as N-EI···H<sub>2</sub>O, 2-EI···H<sub>2</sub>O and N-EI···(H<sub>2</sub>O)<sub>2</sub> respectively). It will be shown that the experimentally observed lowest-energy geometry of 2-ethylimidazole changes depending on whether this molecule is isolated or bound within the monohydrate complex. Cooperativity effects are apparent within the hydrogen bond network upon the successive hydration of N-ethylimidazole. Intermolecular parameters determined for each of the hydrate complexes will be compared to other imidazole-containing monohydrate complexes and other complexes presented within this thesis.

#### 7.2 Experimental Methods

The broadband microwave spectra of N-ethylimidazole and 2-ethylimidazole have been recorded over the frequency ranges 2.0 - 18.5 and 7.0 - 18.5 GHz respectively. Nethylimidazole (Sigma Aldrich, 99 %) and 2-ethylimidazole (Sigma Aldrich, 98 %) were both obtained commercially and used in experiments without any further purification. Nethylimidazole is a liquid at ambient conditions with a vapour pressure reported to be 0.3 mmHg @ 25 °C. Similar to what was reported previously in Chapters 4 – 6, N-ethylimidazole was introduced into the flow of a carrier gas from a modified general valve heated to 80 °C. 2ethylimidazole is a white crystalline solid with a high boiling point, therefore, laser ablation was employed to transfer the target molecule into the gas phase. A cylindrical sample rod with a diameter of 13 mm was prepared by mixing and pressing a 1:1 mass ratio of 2-ethylimidazole and copper powder which was subsequently vapourised using the fundamental harmonic of a Nd:YAG laser as described in Chapter 3. Separate experiments to study each isomer of ethylimidazole were performed using argon (BOC, 99.998 %) and neon (BOC, CP grade) as carrier gases with a constant backing pressure of 4 bar for N-ethylimidazole and 7 bar for 2ethylimidazole. To facilitate the formation of hydrate complexes an additional reservoir containing water was positioned upstream of the modified general valve to introduce water into the flow of the carrier gas. Subsequent experiments to study D- and <sup>18</sup>O containing isotopologues were performed by using D<sub>2</sub>O (Sigma Aldrich, 99.9 % D atom) or H<sub>2</sub><sup>18</sup>O (Sigma Aldrich, 97 % <sup>18</sup>O atom).

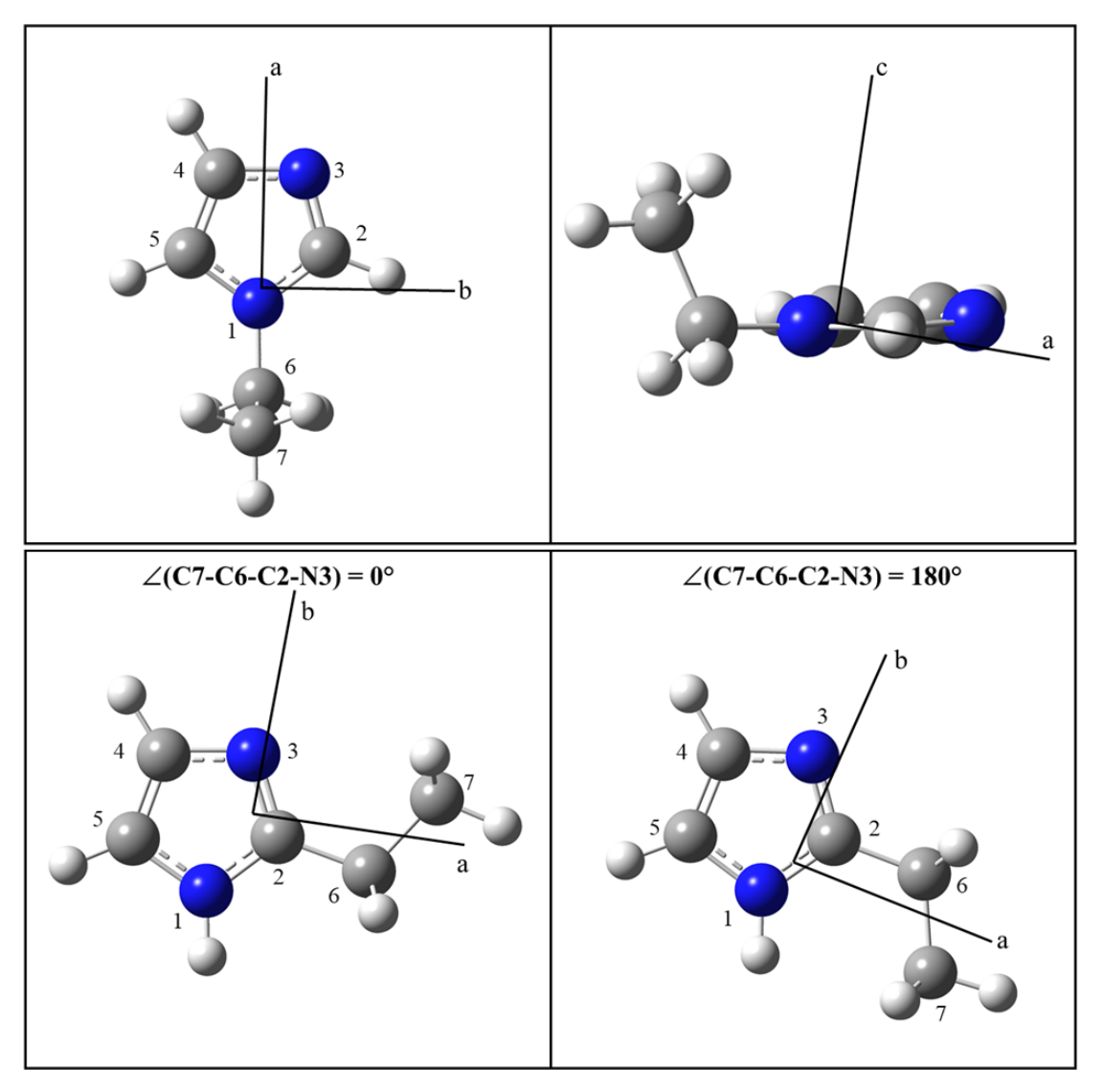


Figure 7.1 Equilibrium ( $r_e$ ) geometries of N-ethylimidazole (upper panel), two possible  $C_s$  conformations of 2-ethylimidazole (lower panel) calculated at the  $\omega$ B97X-D/aug-cc-pVQZ level of theory. The  $C_1$  conformation of N-ethylimidazole is calculated to be the global minimum structure. For 2-ethylimidazole, the  $C_1$  conformer is also calculated to be the global minimum structure at the B3LYP(D3BJ)/aug-cc-pVTZ level of theory with the  $C_s$  conformers  $\angle$ (C7–C6–C2–N3) = 0° and 180° calculated to be 0.3 and 2.9 kJmol<sup>-1</sup> higher in energy.

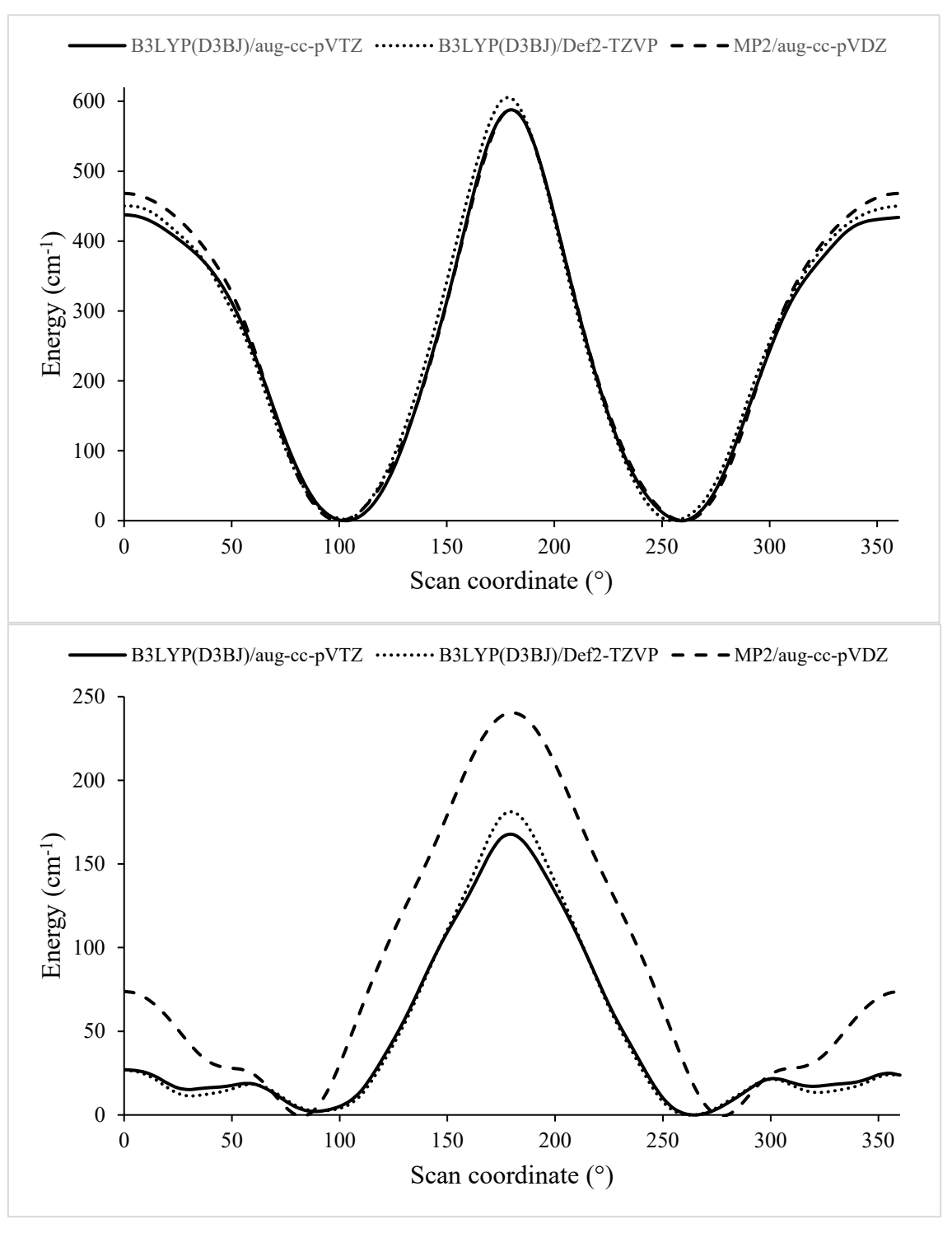


Figure 7.2 Potential energy scans obtained by rotating the ethyl group relative to the imidazole ring in N-ethylimidazole (top) and 2-ethylimidazole (bottom). Calculations performed at the B3LYP(D3BJ)/aug-cc-pVTZ, B3LYP(D3BJ)/Def2-TZVP and MP2/aug-cc-pVDZ levels of theory by scanning  $\angle$ (C7-C6-N1-C2) in N-ethylimidazole and  $\angle$ (C7-C6-C2-N3) in 2-ethylimidazole (atom labelling provided in Figure 7.1)

## 7.3 Quantum Chemical Calculations

## 7.3.1 Ethylimidazole monomers

One dimensional relaxed potential energy scans (PES) were performed for each of Nethylimidazole and 2-ethylimidazole providing an insight into the conformational landscape of both isomers. As described in Chapters 5 and 6 the ethyl group was rotated relative to the imidazole ring, rotating the dihedral angle  $\angle$  (C7–C6–N1–C2) in N-ethylimidazole and  $\angle$  (C7– C6-C2-N3) in 2-ethylimidazole (atom labelling provided in Figure 7.1) in increments of 5°. Scan calculations were performed at three different levels of theory: B3LYP(D3BJ)/aug-ccpVTZ, B3LYP(D3BJ)/Def2-TZVP and MP2/aug-cc-pVDZ as shown in Figure 7.2. Quantum chemical calculations predict that the global minimum has C<sub>1</sub> symmetry for N-ethylimidazole such that  $\angle$  (C7–C6–N1–C2) =  $\pm 105^{\circ}$  as shown as two minima located at  $105^{\circ}$  and  $260^{\circ}$  on the potential energy curve (Figure 7.2, top). Conformations of N-ethylimidazole which has C<sub>s</sub> symmetry such that  $\angle$ (C7–C6–N1–C2) = 0° or 180° are predicted to be 5.3 kJ mol<sup>-1</sup> (437 cm<sup>-1</sup> 1) and 7.0 kJ mol<sup>-1</sup> (588 cm<sup>-1</sup>) higher in energy than the global minimum structure. For 2ethylimidazole scan calculations presented in Figure 7.2 (bottom) revealed two global minima located about 90° and 265° with an additional two local minima at 30° and 320° in the B3LYP(D3BJ)/aug-cc-pVTZ calculation. Each minimum geometry possesses C<sub>1</sub> symmetry. The difference in energy between each of the C<sub>s</sub> conformations of 2-ethylimidazole and the global minimum structure is 0.3 kJ mol<sup>-1</sup> (27 cm<sup>-1</sup>) and 2.9 kJ mol<sup>-1</sup> (240 cm<sup>-1</sup>). The energy difference separating the possible conformations is significantly less in 2-ethylimidazole compared to N-ethylimidazole. The global minima and C<sub>s</sub> conformers of both isomers of ethylimidazole were optimised at the levels of theory identified above, with an additional optimisation calculation also performed at the  $\omega$ B97X-D/aug-cc-pVQZ level of theory. Figure 7.1 displays the optimised geometry of N-ethylimidazole and two possible forms of 2ethylimidazole calculated at the  $\omega$ B97X-D/aug-cc-pVQZ level of theory. Rotational constants  $(A_e, B_e \text{ and } C_e)$ , nuclear quadrupole coupling constants  $(\chi_{aa} \text{ (N1)}, [\chi_{bb} \text{ (N1)} - \chi_{cc} \text{ (N1)}], \chi_{aa} \text{ (N3)},$  $[\chi_{bb}(N3) - \chi_{cc}(N3)]$ ) and dipole moment components  $(\mu_a, \mu_b, \mu_c)$  calculated at different levels of theory mentioned above are given in Table 7.1 - 7.3, alongside percentage deviations between calculated and experimentally obtained results. Atomic coordinates are given in Tables A.45 - A.48.

Table 7.1 Spectroscopic parameters of N-ethylimidazole ( $C_1$  conformer) calculated at different levels of theory.

	λ7 -411:				
		midazole			
	ωB97X-D/aug-cc-pVQZ		B3LYP(D3BJ)/aug-cc-pVT		
$A_e$ (MHz)	6909.505	$+0.9\%^{a}$	6893.213	+0.7%	
$B_e  (\mathrm{MHz})$	1975.445	+0.8%	1960.887	+0.1%	
$C_e(\mathrm{MHz})$	1731.800	+1.4%	1709.196	+0.1%	
$\chi_{aa}$ (N1) (MHz)	1.386	+1.7%	1.387	+1.7%	
$[\chi_{bb}(N1) - \chi_{cc}(N1)]$ (MHz)	3.251	-3.1%	3.403	+1.4%	
$\chi_{aa}$ (N3) (MHz)	-2.294	+4.9%	-2.408	+10%	
$[\chi_{bb}(N3) - \chi_{cc}(N3)]$ (MHz)	-2.191	+57%	-1.744	+25%	
$ \mu_{\rm a} ,  \mu_{\rm b} ,  \mu_{\rm c}  ({\rm D})^{\rm b}$	4.1, 0.9, 0.8		4.1, 0.8, 0.8		
	B3LYP(D3BJ)/Def2-TZVP		MP2/aug-cc-pVDZ		
$A_e$ (MHz)	6894.620	+0.7%	6731.155	-1.7%	
$B_e$ (MHz)	1960.996	+0.1%	1948.273	-0.5%	
$C_e(\mathrm{MHz})$	1709.351	+0.1%	1700.843	-0.4%	
$\chi_{aa}$ (N1) (MHz)	1.371	+0.6%	1.129	-17%	
$[\chi_{bb}(N1) - \chi_{cc}(N1)]$ (MHz)	3.352	-0.1%	2.615	-22%	
$\chi_{aa}$ (N3) (MHz)	-2.443	+12%	-1.796	-18%	
$[\chi_{bb}(N3) - \chi_{cc}(N3)] (MHz)$	-1.842	+32%	-1.224	-12%	
$[\mu_{\rm a}], [\mu_{\rm b}], [\mu_{\rm c}] ({\rm D})^{\rm b}$	4.1, 0.8	3, 0.8	4.3, 0.9, 0	.9	

<sup>&</sup>lt;sup>a</sup> Calculated by  $[(A_e - A_0)/A_0] \times 100$  % where  $A_e$  are the results of computational calculations presented above and  $A_0$  are the experimental rotational constants.

<sup>&</sup>lt;sup>b</sup> Electric dipole moment components along the principal inertial axes.

Table 7.2 Spectroscopic parameters of possible C<sub>s</sub> conformations of 2-ethylimidazole calculated at different levels of theory.

			∠(C7–C6–C2–	$-N3) = 0^{\circ}$				
	ωB97X-D/au	ıg-cc-pVQZ	B3LYP(D3BJ)/a	aug-cc-pVTZ	B3LYP(D3BJ)	/Def2-TZVP	MP2/aug-	-cc-pVDZ
$A_e$ (MHz)	7267.322	+ 1.9 %a	7222.172	+ 1.2 %	7220.565	+ 1.2 %	6645.880	<b>-6.9 %</b>
$B_e$ (MHz)	1993.831	+ 0.6 %	1982.026	+ 0.0 %	1982.899	+ 0.0 %	1947.072	<b>- 1.8 %</b>
$C_{e}\left(\mathrm{MHz}\right)$	1596.365	+ 0.5 %	1585.359	- 0.2 %	1585.902	- 0.2 %	1684.544	+ 6.0 %
χ <sub>aa</sub> (N1) (MHz)	1.202	<b>- 8.9 %</b>	1.281	+ 2.4 %	1.242	- 0.7 %	0.896	<b>−28 %</b>
$[\chi_{bb}(N1) - \chi_{cc}(N1)]$ (MHz)	4.390	+ 4.3 %	4.453	+ 5.8 %	4.590	+ 9.0 %	3.762	- 11%
$\chi_{aa}$ (N3) (MHz)	0.113	<b>-51 %</b>	0.133	<b>- 42 %</b>	0.107	− 53 %	1.146	+ 400 %
$[\chi_{bb}(N3) - \chi_{cc}(N3)]$ (MHz)	-4.923	+ 17 %	-4.685	+ 12 %	-4.769	+ 12 %	-4.672	+ 11 %
$ \mu_{\rm a} ,  \mu_{\rm b} ,  \mu_{\rm c}  ({\rm D})^{\rm b}$	0.4, 3.	5, 0.1	0.4, 3.4	, 0.0	0.4, 3.4	+, 0.0	0.2, 3	.7, 0.3
			∠(C7–C6–C2–N	$\sqrt{3}$ ) = 180°				
	ωB97X-D/aι	ıg-cc-pVQZ	B3LYP(D3BJ)/a	aug-cc-pVTZ	B3LYP(D3BJ)	/Def2-TZVP	MP2/aug-	-cc-pVDZ
$A_e$ (MHz)	7184.231	+ 0.7 %	7143.403	+ 0.1 %	7140.688	+ 0.1 %	6952.623	- 2.6 %
$B_e$ (MHz)	2018.950	+ 1.9 %	2004.612	+ 1.2 %	2005.068	+ 1.2 %	1993.540	+ 0.5 %
$C_e(\mathrm{MHz})$	1607.211	+ 1.1 %	1596.053	+ 0.5 %	1596.271	+ 0.5 %	1580.194	- 0.6 %
$\chi_{aa}$ (N1) (MHz)	1.311	+ 4.8 %	1.332	+ 6.5 %	1.339	+ 7.1 %	1.101	<b>- 12 %</b>
$[\chi_{bb}(N1) - \chi_{cc}(N1)]$ (MHz)	3.926	− 6.7 %	4.020	<b>-4.5 %</b>	4.102	<b>-2.6 %</b>	3.359	<b>− 20 %</b>
χ <sub>aa</sub> (N3) (MHz)	1.954	+ 753 %	2.027	+ 785 %	2.006	+ 775 %	1.744	+661 %
$[\chi_{bb}(N3) - \chi_{cc}(N3)]$ (MHz)	-6.506	+ 55 %	-6.299	+ 50 %	-6.409	+ 53 %	-5.085	+ 21 %
$[\mu_{\rm a}], [\mu_{\rm b}], [\mu_{\rm c}] ({ m D})^{ m b}$	1.8, 3.	2, 0.0	1.8, 3.2	, 0.0	1.8, 3.1	, 0.0	1.8, 3	.3, 0.0

<sup>&</sup>lt;sup>a</sup> Calculated by  $[(A_e - A_0)/A_0] \times 100$  % where  $A_e$  are the results of computational calculations presented above and  $A_0$  are the experimental rotational constants.

<sup>&</sup>lt;sup>b</sup> Electric dipole moment components along the principal inertial axes.

Table 7.3 Spectroscopic parameters of the  $C_1$  conformation of 2-ethylimidazole calculated at different levels of theory.

	2-ethylimi	dazole (C1)		
	$\omega$ B97X-D/aug-cc-pVQZ		B3LYP(D3BJ)/aug-cc-pV	
$A_{e}\left(\mathrm{MHz}\right)$	6778.935	- 5.0 %	6744.551	- 5.5 %
$B_e  (\mathrm{MHz})$	1950.586	<b>- 1.5 %</b>	1934.778	<b>-2.3 %</b>
$C_e\left(\mathrm{MHz}\right)$	1703.448	+ 7.2 %	1688.980	+ 6.3 %
$\chi_{aa}$ (N1) (MHz)	1.003	<b>-20 %</b>	1.049	<b>- 16 %</b>
$[\chi_{bb}(N1) - \chi_{cc}(N1)]$ (MHz)	3.938	− 6.5 %	4.013	<b>-4.7 %</b>
χ <sub>aa</sub> (N3) (MHz)	1.509	+ 560 %	1.571	+ 586 %
$[\chi_{bb}(N3) - \chi_{cc}(N3)]$ (MHz)	-6.222	+ 49 %	-6.035	+ 44 %
$ \mu_{\rm a} ,  \mu_{\rm b} ,  \mu_{\rm c}   ({ m D})^{ m b}$	0.8, 3.5, 0.2		0.7, 3.4, 0.2	
	B3LYP(D3BJ)/Def2-TZVP		MP2/aug-cc-pVDZ	
$A_e$ (MHz)	6740.515	- 5.5 %	6645.823	- 6.9 %
$B_e  (\mathrm{MHz})$	1936.116	- 2.3 %	1947.095	<b>- 1.8 %</b>
$C_e  ({ m MHz})$	1689.921	+ 6.4 %	1684.603	+ 6.0 %
$\chi_{aa}$ (N1) (MHz)	1.023	<b>- 18 %</b>	0.896	− 28 %
$[\chi_{bb}(N1) - \chi_{cc}(N1)]$ (MHz)	4.118	<b>-2.2 %</b>	3.762	<b>-11%</b>
$\chi_{aa}$ (N3) (MHz)	1.554	+ 578 %	1.146	+ 400 %
$[\chi_{bb}(N3) - \chi_{cc}(N3)]$ (MHz)	-6.136	+ 47 %	-4.673	+ 11 %
$ \mu_a ,  \mu_b ,  \mu_c  (D)^b$	0.7, 3.4	l, 0.2	0.2, 3	.7, 0.4

<sup>&</sup>lt;sup>a</sup> Calculated by  $[(A_e - A_0)/A_0] \times 100$  % where  $A_e$  are the results of computational calculations presented above and  $A_0$  are the experimental rotational constants.

<sup>&</sup>lt;sup>b</sup> Electric dipole moment components along the principal inertial axes.

#### 7.3.2 Hydrate complexes

The study of the monohydration of imidazole<sup>9</sup> identified two isomers of this complex, one isomer where the water molecule binds at the pyridinic (N3) nitrogen and a second higherenergy form in which the water molecule binds at the pyrrolic (N1) nitrogen. Only one isomer was observed when water binds to each isomer of methylimidazole (methylimidazole···H<sub>2</sub>O).<sup>8</sup> In each isomer of methylimidazole···H<sub>2</sub>O, the H<sub>2</sub>O molecule binds at N3 of the methylimidazole ring such that H<sub>2</sub>O acts as the hydrogen bond donor and the nitrogen atom is the hydrogen bond acceptor. To calculate the optimised geometries of the monohydrate complexes of N-ethylimidazole and 2-ethylimidazole, a H<sub>2</sub>O molecule was placed in close proximity to the pyridinic nitrogen atom and orientated such that the O atom of H<sub>2</sub>O can form an interaction with the H atom or ethyl group located at C2. Optimisation calculations were performed using the same functionals and basis sets as described above. For 2-EI···H<sub>2</sub>O calculations converged to the same result, as shown in Figure 7.3, for each starting geometry of the 2-ethylimidazole sub-unit ( $\angle$ (C7–C6–C2–N3) = 0°, 90° or 180°). The geometry of a second isomer whereby the water molecule accepts a hydrogen bond from N-H of the imidazole ring was calculated to be approximately 15 kJ mol<sup>-1</sup> higher in energy at the B3LYP(D3BJ)/aug-ccpVTZ level of theory. For N-ethylimidazole, monohydrate complexes formed with the Cs  $(\angle(C7-C6-N1-C2) = 0^\circ)$  and  $C_1$  configurations were optimised. However, the monohydrate complex formed with the C<sub>s</sub> geometry was calculated to be significantly higher in energy (308 kJ mol<sup>-1</sup>), therefore, successive calculations for the geometry optimisations of higher order hydrates were calculated with the C<sub>1</sub> conformation only. The optimised geometries of N- $EI\cdots H_2O$  and N- $EI\cdots (H_2O)_2$  calculated at the  $\omega B97X$ -D/aug-cc-pVQZ level of theory are displayed in Figure 7.3 and 7.4. Rotational constants, nuclear quadrupole coupling constants and dipole moment components calculated for each hydrate complex of N-ethylimidazole and 2-ethylimidazole are given in the Appendix, Tables A.49 and A.50. Calculated atomic coordinates for each hydrate complex are displayed in Tables A.51 - A.58.

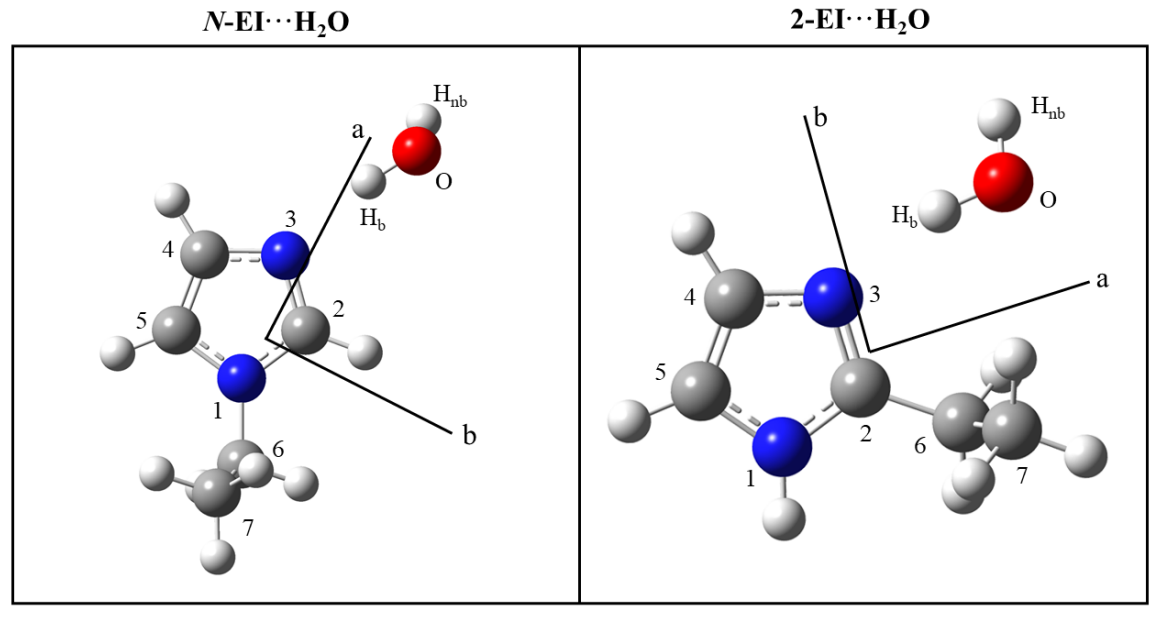


Figure 7.3 Equilibrium ( $r_e$ ) geometries of N-EI···H<sub>2</sub>O (left) and 2-EI···H<sub>2</sub>O (right) calculated at the  $\omega$ B97X-D/aug-cc-pVQZ level of theory.

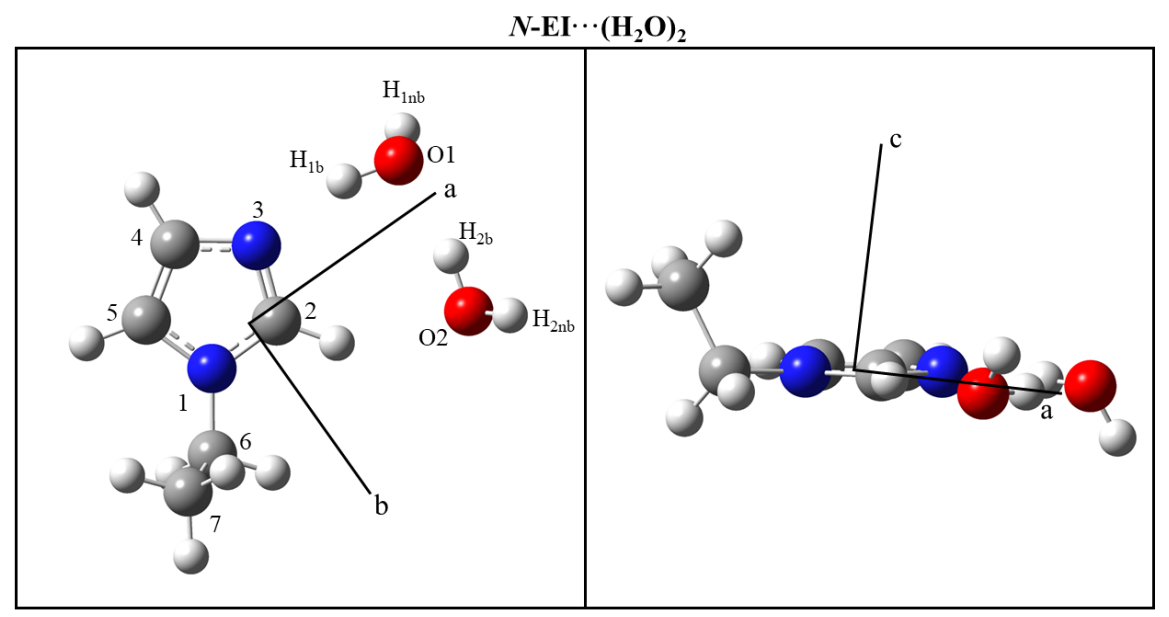


Figure 7.4 Equilibrium ( $r_e$ ) geometry of N-EI···(H<sub>2</sub>O)<sub>2</sub> calculated at the  $\omega$ B97X-D/aug-cc-pVQZ level of theory.

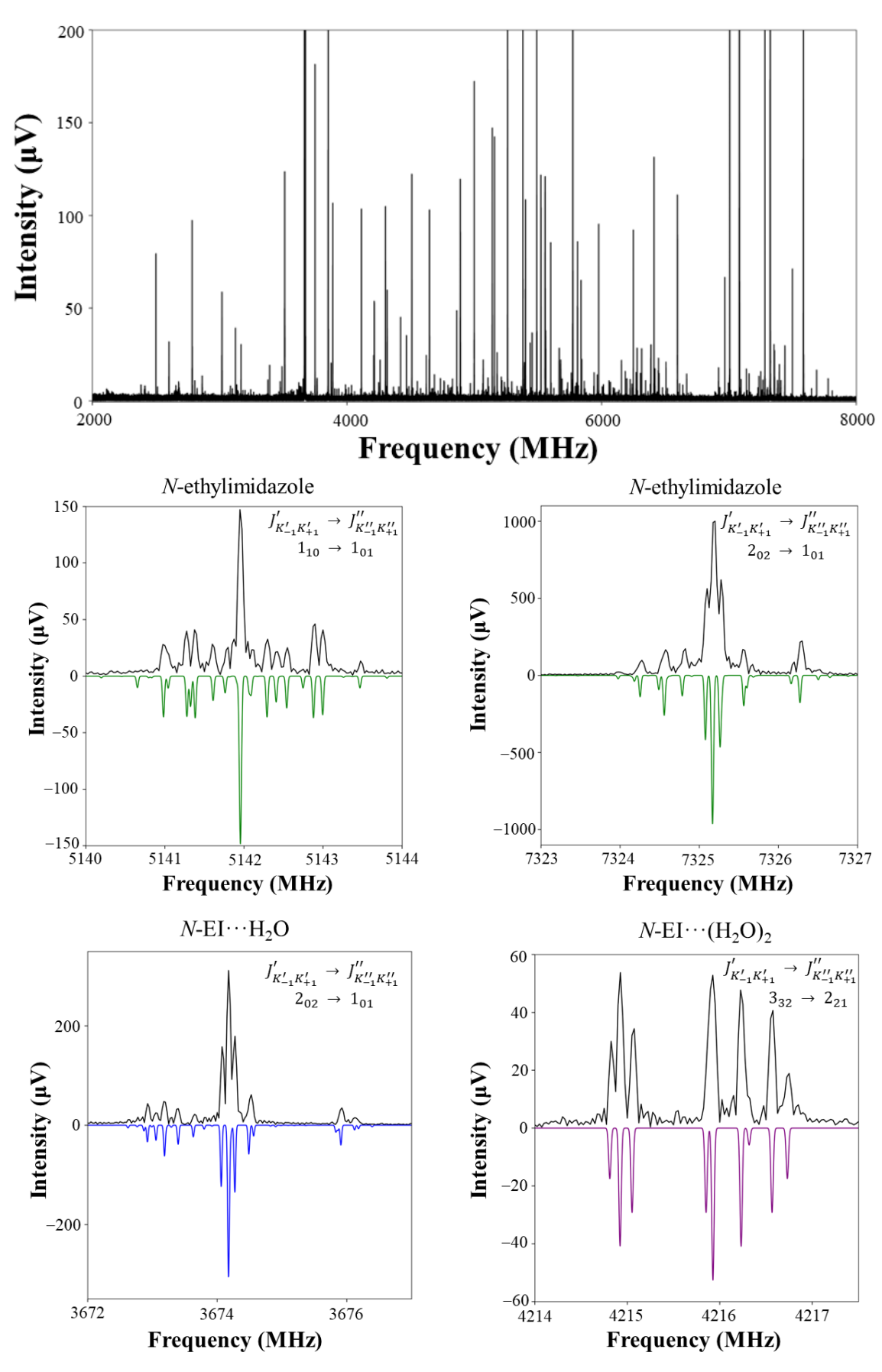


Figure 7.5 (top) The microwave spectrum of N-ethylimidazole recorded in the 2.0-8.0 GHz region averaged over 1.02 M FID's. (middle) and (bottom) Examples of transitions assigned to the N-ethylimidazole monomer, N-EI $\cdots$ H<sub>2</sub><sup>16</sup>O and N-EI $\cdots$ (H<sub>2</sub><sup>16</sup>O)<sub>2</sub>. Experimental spectrum (black) is located above PGOPHER simulation.

#### 7.4 Spectral analysis and assignment

## 7.4.1 Assignment of N-ethylimidazole and 2-ethylimidazole monomers

Separate experiments were performed to obtain the microwave spectra of each of the target molecules (N-ethylimidazole and 2-ethylimidazole) using the experimental procedures outlined in Section 7.2. For N-ethylimidazole experiments were performed in both the 2.0 - 8.0 and 7.0-18.5 GHz frequency bands. The spectrum recorded over the 2.0 - 8.0 GHz region, collected over 1.02 M FID's, using neon as the carrier gas is displayed in Figure 7.5 (top). Guided by the results of quantum chemical calculations the N-ethylimidazole monomer was searched for. As discussed in Section 7.3, calculations predicted the global minimum structure of this molecule to have C<sub>1</sub> symmetry, with the C<sub>s</sub> forms being significantly higher in energy, therefore, the initial search focussed on the assignment of the C<sub>1</sub> conformation. The C<sub>1</sub> conformer of Nethylimidazole was calculated to be a near-prolate asymmetric top with non-zero dipole moment components predicted along each inertial axis, with the projection onto the a-inertial axis being significantly greater than onto the b- and c- axes. Experimentally observed rotational transitions were fit to Watson's S-reduced Hamiltonian<sup>10</sup> within PGOPHER.<sup>11</sup> Spectroscopic parameters determined during the fit are presented in Table 7.4. A total of 193 hyperfine components were assigned to the N-ethylimidazole monomer across the whole frequency range with the standard deviation of the fit being 9.4 kHz. The tentative assignment to the C<sub>1</sub> configuration of this molecule was made on the basis of good agreement between the experimentally obtained rotational constants and those predicted by theory (displayed in Table 7.1). Each rotational transition displays hyperfine structure due to the presence of the two <sup>14</sup>N nuclei as shown in Figure 7.5 (middle). No splittings due to internal rotation were observed owing to the high  $V_3$  barrier to internal rotation of the methyl group. Within the spectrum a-, band c-type transitions were assigned, with the a-type transitions being the most intense features in the spectrum. The observation of numerous c-type transitions is notable as this confirms that N-ethylimidazole is non-planar and therefore has C<sub>1</sub> symmetry analogous to what was observed for the 2-ethylthiazole monomer in Chapter 6. Higher energy conformers were searched for within the spectra acquired, however, were not assigned.

Table 7.4 Spectroscopic parameters determined for *N*-ethylimidazole and 2-ethylimidazole generated by fitting experimentally obtained transition frequencies to Watson's *S*- reduced Hamiltonian.

Parameter	<i>N</i> -ethylimidazole	2-ethylimidazole
A <sub>0</sub> (MHz)	6849.8938(12) <sup>a</sup>	7134.96952(97)
` ,	· /	· /
$B_0$ (MHz)	1959.38843(38)	1981.99556(39)
$C_0$ (MHz)	1707.92229(39)	1588.95563(33)
$D_{J}(\mathrm{kHz})$	0.04593(96)	0.1766(70)
$D_{JK}(\mathrm{kHz})$	0.3862(41)	0.983(25)
$D_{K}\left( \mathrm{kHz}\right)$	-	1.753(99)
$d_1$ (kHz)	-	-0.03201(68)
$d_2(\mathrm{kHz})$	-	0.02587(31)
$\chi_{aa}$ (N1) (MHz)	1.3633(59)	1.2506(70)
$[\chi_{bb}(N1) - \chi_{cc}(N1)]$ (MHz)	3.3564(97)	4.2101(95)
$\chi_{aa}$ (N3) (MHz)	-2.1870(49)	0.2290(91)
$[\chi_{bb}(N3) - \chi_{cc}(N3)] (MHz)$	-1.398(14)	-4.1942(97)
$\sigma_{rms} (kHz)^b$	9.4	10.5
$N^{\mathrm{c}}$	193	267
$a/b/c^{d}$	y/y/y	y/y/n
$\kappa^{e}$	-0.90	-0.86
$P_{cc}$ (u Å <sup>2</sup> )	17.90160(4)	3.87943(4)

<sup>&</sup>lt;sup>a</sup> Numbers in parentheses are one standard deviation in units of the last significant figure.

<sup>&</sup>lt;sup>b</sup> Root mean square (rms) deviation of the fit.

<sup>&</sup>lt;sup>c</sup> Number of hyperfine components included in the fit.

<sup>&</sup>lt;sup>d</sup> a-, b- and c- type transitions. "y" indicates that this type of transition was observed.

<sup>&</sup>lt;sup>e</sup> Ray's asymmetry parameter.

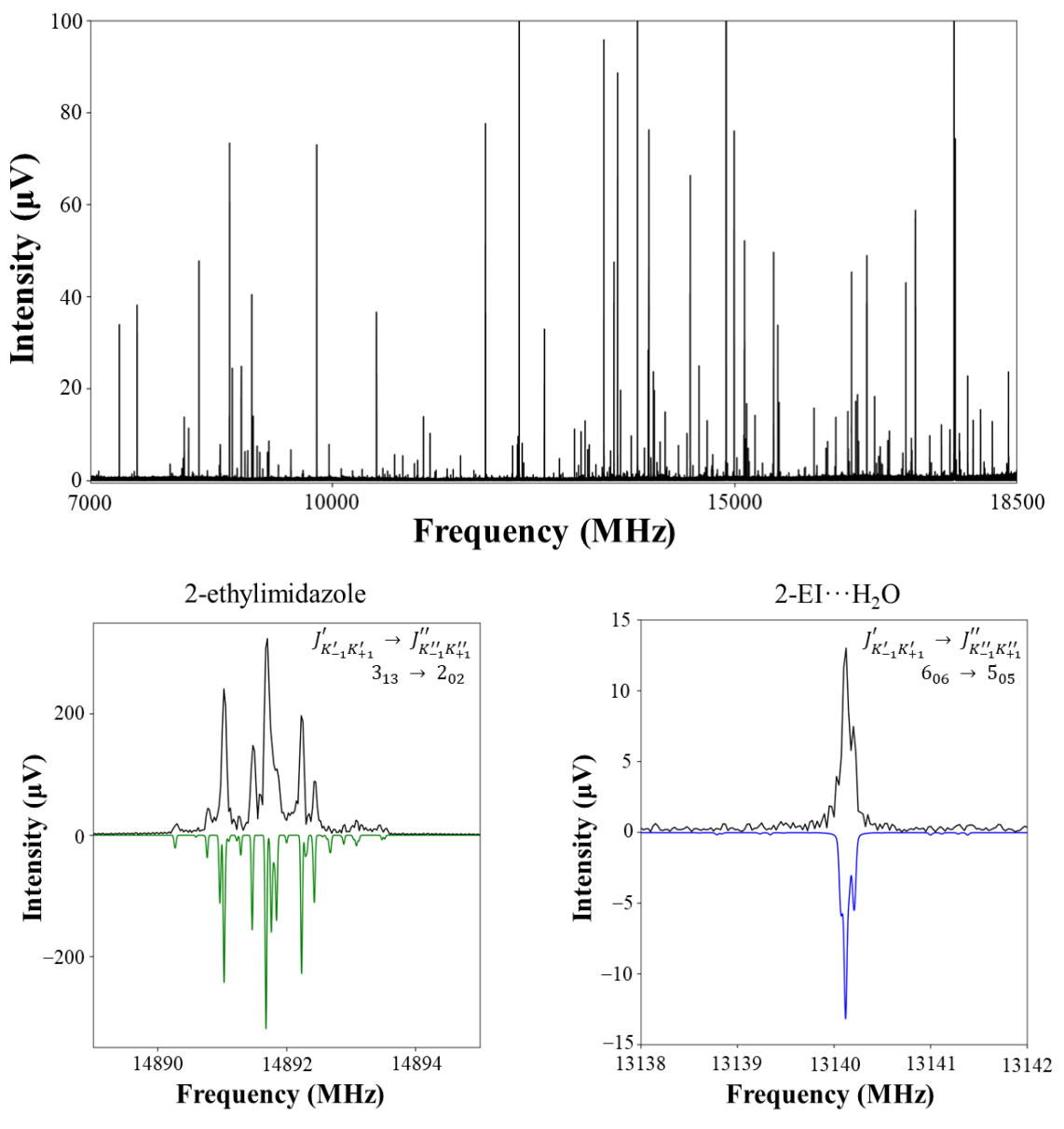


Figure 7.6 (top) The microwave spectrum of 2-ethylimidazole, recorded in the 7.0-18.5 GHz region while probing a gaseous sample containing 2-ethylimidazole,  $H_2^{16}O$  and argon, averaged over 510 k FID's. (bottom) Expanded portion of the experimental spectrum (black) above PGOPHER simulation (green and blue). (bottom-left)  $3_{13} \rightarrow 2_{02}$  rotational transition of the 2-ethylimidazole monomer. (bottom-right)  $6_{06} \rightarrow 5_{05}$  rotational transition of 2-EI···H<sub>2</sub><sup>16</sup>O.

The microwave spectrum of 2-ethylimidazole was recorded over the frequency range 7.0 - 18.5GHz using the experimental procedure detailed earlier. The initial experiment utilised argon as the carrier gas with a subsequent experiment performed using neon. The spectrum displayed in Figure 7.6 (top) was acquired while using argon as the carrier gas and is averaged over 510 k FID's, which corresponds to approximately 17 hours of data collection. Upon inspection the vast majority of intense transitions were present in both spectra acquired and each spectrum also contained many weaker transitions. A small amount of 2-ethylimidazole undergoes fragmentation into smaller molecules owing to the use of laser ablation in the experimental set up. Several of the weaker transitions were readily identified as fragmentation products of 2ethylimidazole, such as (but not limited to) imidazole, 1 CH<sub>3</sub>CN, 12, 13 C<sub>3</sub>HN, 14 C<sub>3</sub>H<sub>3</sub>N<sup>15</sup> etc. which were also identified in other studies of imidazole-containing species.<sup>6, 7, 9, 16</sup> The 2ethylimidazole monomer was initially searched for. A series of rotational transitions present within both spectra acquired were fitted using Watson's S-reduced Hamiltonian<sup>10</sup> implemented within PGOPHER.<sup>11</sup> In total, 267 hyperfine components were assigned consisting of *R*-branch a- and b- type transitions. Rotational constants determined from the assignment are as follows:  $A_0 = 7134.96952(97)$  MHz,  $B_0 = 1981.99556(39)$  MHz and  $C_0 = 1588.95563(33)$  MHz. Centrifugal distortion and nuclear quadrupole coupling constants determined from the assignment are displayed in Table 7.4. Quantum chemical calculations predicted the C<sub>1</sub> configuration to be the global minimum structure of 2-ethylimidazole with both C<sub>s</sub> conformations being higher in energy. Comparing the ground state rotational constants with those calculated by theory for the C<sub>1</sub> conformation (Table 7.3) it is evident that they are inconsistent, and the percentage deviations obtained are high (up to 7 % deviation). Which implies that the experimentally observed structure of 2-ethylimidazole does not possess C<sub>1</sub> symmetry. This can also be inferred from the observation of only a- and b- type transitions within the spectrum recorded, therefore, indicating no heavy atoms are located outside of the ab plane of this molecule. Subsequent comparisons with rotational constants calculated for the two possible  $C_s$  conformations of 2-ethylimidazole ( $\angle$ (C7–C6–C2–N3) = 0° or 180°) with the experimental results found significantly better agreement (Table 7.2). The  $B_0$  and  $C_0$  rotational constants are very consistent with  $B_e$  and  $C_e$  of the  $\angle$ (C7–C6–C2–N3) = 0° conformation calculated at DFT levels, with slightly higher deviations observed for the  $A_0$  rotational constant. Whereas the  $A_0$  constant is in very good agreement with the  $A_e$  constant of the  $\angle$ (C7–C6–C2– N3) = 180° conformation calculated at DFT levels, with slightly higher deviations observed for  $B_{\rm e}$  and  $C_{\rm e}$  for this conformer. Since the measured rotational constants agree equally well with the equilibrium rotational constants generated for both C<sub>s</sub> geometries, an assignment to either

geometry cannot be made through comparison of rotational constants alone. The ambiguity in the geometry of 2-ethylimidazole will be discussed in greater detail in the following sections.

To confirm the assignment of N-ethylimidazole and 2-ethylimidazole monomers to the correct molecular carriers, the spectra of the singly substituted isotopologues of each molecule were searched for. The rotational spectra of five singly substituted <sup>13</sup>C isotopologues of each isomer of ethylimidazole were identified within the spectra recorded. The spectrum of each isotopologue was assigned, allowing the determination of rotational constants  $(A_0, B_0 \text{ and } C_0)$ while centrifugal distortion and nuclear quadrupole coupling constants were held fixed at the values determined for the respective parent isotopologue. Rotational constants determined for each singly substituted isotopologue are given in Table 7.5. The number of transitions assigned for each rare isotopologue is significantly less than previously assigned to each parent species owing to <sup>13</sup>C having a lower natural abundance (1.07 %). For <sup>13</sup>C-containing isotopologues of N-ethylimidazole the vast majority of transitions assigned were a-type with several b- and ctype transitions also identified in the spectrum. Whereas, for 2-ethylimidazole only b-type transitions were observed for each <sup>13</sup>C isotopologue. This is consistent with the predictions of quantum chemical calculations that the projection of the dipole moment onto the b- inertial axis in 2-ethylimidazole is significantly greater than the projection onto the a- or c- axes. The spectrum of the <sup>15</sup>N isotopologues was searched for within each spectrum recorded, however, were unable to be assigned. The natural abundance of <sup>15</sup>N is significantly lower than <sup>13</sup>C, therefore, it is likely that the sensitivity of the current experimental set up is too low to allow for the detection of <sup>15</sup>N transitions since this isotopologue was also not assigned for 2ethylthiazole.

Table 7.5 Spectroscopic parameters determined for  $^{13}$ C isotopologues of N-ethylimidazole and 2-ethylimidazole. Values of centrifugal distortion constants ( $D_J$ ,  $D_{JK}$ ,  $D_K$ ,  $d_1$  and  $d_2$ ) and nuclear quadrupole coupling constants ( $\chi_{aa}$  (N1), [ $\chi_{bb}$ (N1) –  $\chi_{cc}$  (N1)],  $\chi_{aa}$  (N3) and [ $\chi_{bb}$ (N3) –  $\chi_{cc}$  (N3)]) held fixed to those determined for the parent isotopologue of each molecule, displayed in Table 7.4, when fits were performed.

	<i>N</i> -ethylin	nidazole	
	<sup>13</sup> C2 <sup>a</sup>	<sup>13</sup> C4	<sup>13</sup> C5
$A_0$ (MHz)	6744.094(16) <sup>b</sup>	6800.674(27)	6735.525(16)
$B_0$ (MHz)	1956.1465(38)	1935.7660(22)	1957.3723(32)
$C_0  (\mathrm{MHz})$	1698.8202(15)	1686.9833(16)	1699.5818(16)
$\sigma_{rms} (kHz)^{c}$	13.8	16.4	13.5
$N^{ m d}$	32	25	26
$P_{cc}$ (u Å <sup>2</sup> )	17.90134(30)	17.90596(25)	17.93476(27)
	<sup>13</sup> C6	<sup>13</sup> C7	
$A_0$ (MHz)	6817.90(63)	6811.678(16)	
$B_0$ (MHz)	1937.1373(52)	1910.6338(13)	
$C_0(\mathrm{MHz})$	1692.5868(37)	1672.73551(93)	
$\sigma_{rms}$ (kHz)	14.0	13.9	
N	28	37	
$P_{cc}$ (u Å <sup>2</sup> )	18.2156(35)	18.28716(15)	
	2-ethylin		
	<sup>13</sup> C2	<sup>13</sup> CX	<sup>13</sup> CY
$A_0$ (MHz)	7130.34900(96)	7043.0828(11)	7124.42250(86)
$B_0$ (MHz)	1981.83146(86)	1962.23759(41)	1950.73444(37)
$C_0(\mathrm{MHz})$	1588.63936(47)	1571.70025(36)	1568.29909(36)
$\sigma_{rms}$ (kHz)	8.9	12.4	12.7
N	33	54	69
$P_{cc}$ (u Å <sup>2</sup> )	3.88128(7)	3.87927(5)	3.88035(4)
	<sup>13</sup> C6	<sup>13</sup> C7	
$A_0$ (MHz)	7087.4707(11)	7114.9934(15)	
$B_0$ (MHz)	1962.18651(56)	1930.88048(72)	
$C_0(\mathrm{MHz})$	1574.00646(40)	1555.01871(56)	
$\sigma_{rms}$ (kHz)	12.8	10.4	
N	44	34	
$P_{cc}$ (u Å <sup>2</sup> )	3.89349(5)	3.88324(8)	

<sup>&</sup>lt;sup>a</sup> Atom numbering as defined in Figure 7.1.

<sup>&</sup>lt;sup>b</sup> Numbers in parentheses are one standard deviation in units of the last significant figure.

<sup>&</sup>lt;sup>c</sup> Root mean square (rms) deviation of the fit.

<sup>&</sup>lt;sup>d</sup> Number of hyperfine components included in the fit.

#### 7.4.2 Assignment of hydrate complexes

Many unassigned transitions remained within the spectra after the assignment of each ethylimidazole monomer and fragmentation products (within the 2-ethylimidazole spectrum). The monohydrate complexes of N-methylimidazole and 2-methylimidazole have been studied<sup>8</sup> previously, therefore, hydrate complexes formed with each isomer of ethylimidazole were subsequently searched for. The hydrate complexes were searched for in the spectra recorded using the rotational constants determined from DFT calculations as an initial starting point. Each of N-EI···H<sub>2</sub>O and 2-EI···H<sub>2</sub>O are calculated to be near-prolate asymmetric tops with the projection onto the dipole moment strongest along the a-inertial axis of each complex. In each spectrum, transitions fitted to Watson's S-reduced Hamiltonian were tentatively assigned to the parent (H<sub>2</sub><sup>16</sup>O) isotopologue of the monohydrate complex of each isomer of ethylimidazole. For  $N-EI\cdots H_2^{16}O$ , the assignment was made across the 2.0 – 18.5 GHz frequency range. A total of 220 hyperfine components were assigned with the standard deviation of the fit being 12.1 kHz. For this complex, the assignment consisted of a- type transitions only, no b- or c- type transitions were able to be identified within the spectrum. Whereas for 2-EI···H<sub>2</sub><sup>16</sup>O, 276 hyperfine components were assigned across the 7.0 - 18.5 GHz frequency region. The series of transitions assigned were present in both spectra recorded while using argon and neon as a carrier gas and consisted of a- and b- type transitions. The standard deviation of the fit performed was 11.5 kHz. The molecular carrier of this spectrum was tentatively assigned to 2-EI···H<sub>2</sub><sup>16</sup>O on the basis of very good agreement between experimentally-determined rotational constants and those predicted by theory. However, in the case of N-EI···H<sub>2</sub><sup>16</sup>O, the ground state rotational constants and those predicted by theory are not in satisfactory agreement. The deviation between experimentally determined rotational constants and calculated equilibrium rotational constants is considerably higher than any other species assigned within this thesis. This is unusual considering the functionals and basis sets chosen for the calculations performed have consistently predicted rotational constants which are in very good agreement with experimentally determined constants for other similar complexes formed between heterocycles and H<sub>2</sub>O. As shown in Table A.49, the deviation from experimentally determined constants is greater for calculations performed at the higher levels of theory,  $\omega B97X$ -D/aug-cc-pVQZ and B3LYP(D3BJ)/aug-cc-pVTZ, compared to those calculated for lower levels of theory, B3LYP(D3BJ)/Def2-TZVP and MP2/aug-cc-pVDZ. N-Interestingly, methylimidazole···H<sub>2</sub>O<sup>8</sup> calculations performed at the ωB97X-D/aug-cc-pVQZ B3LYP(D3BJ)/aug-cc-pVTZ level of theory also failed to accurately predict rotational constants with the deviation between experimental and theoretical results being high. It will be shown by the assignment of additional isotopologues that the molecular carrier of the spectrum

has been correctly assigned to  $N\text{-EI}\cdots\text{H}_2^{16}\text{O}$  which will be discussed later. Rotational constants, centrifugal distortion constants and nuclear quadrupole coupling constants determined for each of  $N\text{-EI}\cdots\text{H}_2^{16}\text{O}$  and  $2\text{-EI}\cdots\text{H}_2^{16}\text{O}$  are displayed in Tables 7.6 and 7.7 respectively. For  $N\text{-EI}\cdots\text{H}_2^{16}\text{O}$  the centrifugal distortion constants  $D_J$ ,  $D_{JK}$ ,  $d_1$  and  $d_2$  were included to achieve a satisfactory fit, whereas for  $2\text{-EI}\cdots\text{H}_2^{16}\text{O}$ ,  $D_K$  was determined during the fit rather than  $d_2$ . Examples of transitions assigned to each monohydrate complex are presented in Figure 7.5 and 7.6. The hyperfine structure is somewhat more blended for transitions of the hydrate complexes compared to each isolated monomer and nuclear quadrupole coupling constants were determined during the fits performed. For  $2\text{-EI}\cdots\text{H}_2^{16}\text{O}$ , each of  $\chi_{aa}$  (N1),  $[\chi_{bb}(\text{N1}) - \chi_{cc}(\text{N1})]$ ,  $\chi_{aa}$  (N3),  $[\chi_{bb}(\text{N3}) - \chi_{cc}(\text{N3})]$  were determined during the fit. Whereas for  $N\text{-EI}\cdots\text{H}_2^{16}\text{O}$ ,  $\chi_{aa}$  (N1),  $[\chi_{bb}(\text{N1}) - \chi_{cc}(\text{N1})]$ ,  $\chi_{aa}$  (N3) were determined while keeping  $[\chi_{bb}(\text{N3}) - \chi_{cc}(\text{N3})]$  fixed at the  $\omega$ B97X-D/aug-cc-pVQZ result. A lower deviation of the fit was obtained while holding this constant fixed at the  $\omega$ B97X-D/aug-cc-pVQZ result compared to other DFT calculated results.

After the assignment of each monohydrate complex, the spectrum was examined further for additional complexes formed with N-ethylimidazole and 2-ethylimidazole which may be present within the supersonic expansion including complexes formed with multiple water molecules or the carrier gas. A complex formed between N-ethylimidazole and two H<sub>2</sub>O molecules, N-EI···(H<sub>2</sub><sup>16</sup>O)<sub>2</sub> was tentatively assigned. In total, 393 hyperfine components were assigned to this complex, with transitions from both spectra recorded in the 2.0 - 8.0 GHz and 7.0 - 18.5 GHz regions included in the fit. The rotational constants determined from the assignment are as follows:  $A_0 = 1939.9230(32)$  MHz,  $B_0 = 806.47890(30)$  MHz and  $C_0 =$ 598.77701(22) MHz. Unlike what was previously observed for the monohydrate complex, the experimentally determined rotational constants are very consistent with those predicted by theory, for example,  $A_e = 2004.752$  MHz,  $B_e = 805.031$  MHz and  $C_e = 601.334$  MHz calculated at the  $\omega$ B97X-D/aug-cc-pVQZ level of theory. Therefore, a tentative assignment of the molecular carrier to N-EI···(H<sub>2</sub><sup>16</sup>O)<sub>2</sub> was made on the basis of good agreement. Spectroscopic constants determined in the fit are presented in Table 7.8. In the spectrum only a-type transitions were observed, consistent with the prediction that  $\mu_a$  is significantly greater than  $\mu_b$  and  $\mu_c$ , therefore, the projection onto the a-inertial axis is significantly greater than onto the b- or caxes. For thiazole···(H<sub>2</sub>O)<sub>2</sub>, two isomers of this complex were observed.<sup>17</sup> The lower energy isomer (isomer I) has a geometry equivalent to N-EI···(H<sub>2</sub>O)<sub>2</sub> presented in Figure 7.4, in which the second H<sub>2</sub>O molecule forms an interaction with the H atom bound to C2. A second, higher energy isomer of thiazole...(H<sub>2</sub>O)<sub>2</sub> (isomer II) was also identified within the spectrum whereby the second H<sub>2</sub>O molecule forms an interaction with the H atom bound to C4 instead. An additional calculation was performed for  $N\text{-EI}\cdots(H_2O)_2$  in which the second  $H_2O$  molecule is interacting with the H atom bound to C4 rather than C2. This geometry was calculated to be 6.5 kJ mol<sup>-1</sup> higher in energy at the B3LYP(D3BJ)/aug-cc-pVTZ level of theory. The energy difference between the two isomers of  $N\text{-EI}\cdots(H_2O)_2$  is greater than reported for thiazole···( $H_2O)_2$ . The spectrum was searched for the higher energy isomer, however, this was not assigned. Transitions of  $N\text{-EI}\cdots(H_2^{16}O)_3$  were also identified within the spectrum recorded and a tentative assignment made. Complexes formed with 2-ethylimidazole which contain multiple water molecules were also searched for in the spectra recorded, however, were not assigned during the present work.

Experiments were performed using H<sub>2</sub><sup>18</sup>O, D<sub>2</sub>O and HDO allowing the assignment of additional isotopologues where the isotopic substitution is on the H<sub>2</sub>O sub-unit. For N-EI···H<sub>2</sub>O, an additional three singly-substituted isotopologues (N-EI···H<sub>2</sub><sup>18</sup>O, N-EI···DOH and N-EI···HOD) were observed in two separate experiments performed using H<sub>2</sub><sup>18</sup>O and D<sub>2</sub>O. Spectroscopic parameters determined for each species are given in Table 7.6. The experiment performed which utilised D<sub>2</sub>O yielded the spectra of each singly substituted deuterium isotopologue, with the deuterium atom being involved in the hydrogen bonding interaction (DOH) or substituted at the non-bonding position (HOD). The use of H<sub>2</sub><sup>18</sup>O allowed the observation of three <sup>18</sup>O containing isotopologues, in addition to N-EI···H<sub>2</sub><sup>18</sup>O, the spectra of two singly substituted <sup>18</sup>O isotopologues of the dihydrate complex were also identified. The rotational constants determined for each of  $N-EI\cdots(H_2^{18}O)(H_2^{16}O)$  and  $N-EI\cdots(H_2^{16}O)(H_2^{18}O)$ are presented in Table 7.8. Only  $D_J$  and  $D_{JK}$  were determined in the fit of each <sup>18</sup>O isotopologue while all other spectroscopic parameters were held fixed at the value obtained for the parent isotopologue. Experiments performed yielding the spectra of singly substituted isotopologues of N-EI···H<sub>2</sub>O and N-EI···(H<sub>2</sub>O)<sub>2</sub> were performed in the 2.0 - 8.0 GHz region only, resulting in a significantly lower number of rotational transitions assigned for these species compared to the respective parent isotopologue. Experiments performed yielding an additional four isotopologues of 2-EI···H<sub>2</sub>O were performed in the 7.0 – 18.5 GHz frequency band. The spectroscopic constants determined for the H<sub>2</sub><sup>18</sup>O, DOH, HOD and D<sub>2</sub>O containing isotopologues of 2-EI···H<sub>2</sub>O are displayed in Table 7.7. The greater number of rotational transitions observed for each isotopologue allowed for the determination of centrifugal distortion and nuclear quadrupole coupling constants in each case, with only  $d_1$  held fixed at the value obtained for 2-EI···H<sub>2</sub><sup>16</sup>O for each of the singly substituted isotopologues. For the doubly deuterated isotopologue, 2-EI···D<sub>2</sub>O, fewer transitions were assigned compared to other D-containing isotopologues. H<sub>2</sub><sup>16</sup>O is usually present as a contaminant (typically within the gas line and on the walls of the vacuum chamber) during the experiment performed using  $D_2O$ . It is possible that more HDO was present within the supersonic expansion compared to  $D_2O$  during the experiments performed with the isomers of ethylimidazole. It was chosen to only float  $D_J$  and  $D_{JK}$  in the assignment of 2-EI···D<sub>2</sub>O while all other constants included in the fit were held fixed to the value determined for the parent isotopologue in order to achieve a satisfactory fit. Each spectrum acquired had a sufficient S/N allowing for the observation of both a- and b- type transitions of each isotopologue of 2-EI···H<sub>2</sub>O.

Table 7.6 Experimentally-determined spectroscopic parameters determined for four isotopologues of N-EI···H<sub>2</sub>O.

$N ext{-EI}\cdots ext{H}_2 ext{O}$					
	$H_2^{16}O$	$H_2^{18}O$	DOH	HOD	
$A_0$ (MHz)	3572.2584(94) <sup>a</sup>	3518.19(33)	3585.92(30)	3531.78(78)	
$B_0$ (MHz)	1006.11465(58)	956.0890(25)	986.2113(23)	972.4206(13)	
$C_0(\mathrm{MHz})$	835.10840(51)	797.5601(23)	822.1334(22)	810.3349(22)	
$D_{J}\left(\mathrm{kHz} ight)$	1.6005(17)	1.579(39)	1.743(34)	1.424(65)	
$D_{JK}(\mathrm{kHz})$	-22.021(20)	-21.30(30)	-22.01(26)	-17.5(18)	
$d_1$ (kHz)	-0.5324(21)	-0.632(42)	-0.703(41)	-0.182(26)	
$d_2$ (kHz)	0.0300(18)	$[0.0300]^{b}$	[0.0300]	[0.0300]	
$\chi_{aa}$ (N1) (MHz)	1.202(15)	1.168(17)	1.199(16)	1.236(26)	
$[\chi_{bb}(N1) - \chi_{cc}(N1)] (MHz)$	3.256(41)	[3.256]	[3.256]	[3.256]	
$\chi_{aa}$ (N3) (MHz)	-3.5941(88)	-3.623(14)	-3.608(11)	-3.640(19)	
$[\chi_{bb}(N3) - \chi_{cc}(N3)]$ (MHz)	$[-0.4071]^{c}$	[-0.4071]	[-0.4071]	[-0.4071]	
$\sigma_{rms} (kHz)^d$	12.1	11.4	11.5	12.6	
$N^{\rm e}$	220	55	58	46	
$P_{cc}$ (u Å <sup>2</sup> )	19.30753(30)	19.291(7)	19.331(6)	19.570(16)	

<sup>&</sup>lt;sup>a</sup> Numbers in parentheses are one standard deviation in units of the last significant figure.

<sup>&</sup>lt;sup>b</sup> Values in square brackets held fixed at the result for the parent isotopologue, *N*-EI···H<sub>2</sub><sup>16</sup>O.

<sup>° [</sup> $\chi_{bb}(N3) - \chi_{cc}(N3)$ ] fixed at result obtained at the  $\omega B97X$ -D/aug-cc-pVQZ level of theory.

<sup>&</sup>lt;sup>d</sup> Root mean square (rms) deviation of the fit.

<sup>&</sup>lt;sup>e</sup> Number of hyperfine components included in the fit.

Table 7.7 Experimentally-determined spectroscopic parameters determined for five isotopologues of 2-EI···H<sub>2</sub>O.

$2\text{-EI}\cdots ext{H}_2 ext{O}$					
	$H_2^{16}O$	$H_2^{18}O$	DOH	HOD	D <sub>2</sub> O
$A_0  (\mathrm{MHz})$	2590.5824(16) <sup>a</sup>	2533.9533(25)	2560.1978(45)	2526.0107(43)	2500.0347(85)
$B_0$ (MHz)	1493.05278(44)	1435.51609(44)	1482.34225(50)	1456.58441(53)	1445.87001(63)
$C_0(\mathrm{MHz})$	1020.78041(32)	985.11161(39)	1011.06555(41)	994.02511(40)	985.03928(49)
$D_{J}(\mathrm{kHz})$	0.04161(31)	0.04070(36)	0.04217(39)	0.04042(39)	0.04123(50)
$D_{JK}(\mathrm{kHz})$	-0.0363(15)	-0.0146(45)	-0.0351(35)	-0.0177(43)	-0.036(10)
$D_K(\mathrm{kHz})$	0.886(12)	0.853(20)	0.733(34)	0.799(32)	$[0.886]^{b}$
$d_1$ (kHz)	-0.01260(20)	[-0.01260]	[-0.01260]	[-0.01260]	[-0.01260]
$\chi_{aa}$ (N1) (MHz)	1.074(13)	1.148(26)	1.113(23)	1.084(31)	[1.074]
$\left[\chi_{bb}(N1) - \chi_{cc}(N1)\right] (MHz)$	3.508(24)	3.527(45)	3.445(54)	3.545(57)	[3.508]
$\chi_{aa}$ (N3) (MHz)	-1.640(11)	-1.624(28)	-1.552(25)	-1.687(35)	[-1.640]
$[\chi_{bb}(N3) - \chi_{cc}(N3)] (MHz)$	-1.589(27)	-1.518(49)	-1.574(49)	-1.474(58)	[-1.589]
$\sigma_{rms} (kHz)^{c}$	11.5	12.1	12.4	12.9	12.1
$N^{ m d}$	276	174	195	188	98
$P_{cc}$ (u Å <sup>2</sup> )	19.23969(11)	19.23989(15)	19.24162(21)	19.30749(21)	19.3135(4)

<sup>&</sup>lt;sup>a</sup> Numbers in parentheses are one standard deviation in units of the last significant figure.

<sup>&</sup>lt;sup>b</sup> Values in square brackets held fixed at the result for the parent isotopologue, 2-EI···H<sub>2</sub><sup>16</sup>O.

<sup>&</sup>lt;sup>c</sup> Root mean square (rms) deviation of the fit.

<sup>&</sup>lt;sup>d</sup> Number of hyperfine components included in the fit.

Table 7.8 Experimentally determined spectroscopic parameters determined for three isotopologues of N-EI $\cdots$ (H<sub>2</sub>O)<sub>2</sub>.

$N$ -EI $\cdots$ (H <sub>2</sub> O) <sub>2</sub>					
	$(H_2^{16}O)_2$	$(H_2^{18}O)(H_2^{16}O)$	$(H_2^{16}O)(H_2^{18}O)$		
$A_0  (\mathrm{MHz})$	1939.9230(32) <sup>a</sup>	1934.452(45)	1879.673(46)		
$B_0  (\mathrm{MHz})$	806.47890(30)	777.8903(16)	789.3989(12)		
$C_0(\mathrm{MHz})$	598.77701(22)	582.5727(14)	583.6746(11)		
$D_{J}(\mathrm{kHz})$	0.36150(83)	0.280(40)	0.351(22)		
$D_{JK}(\mathrm{kHz})$	-1.771(11)	-1.35(23)	-1.92(29)		
$d_1$ (kHz)	-0.13283(64)	$[-0.13283]^{b}$	[-0.13283]		
$\chi_{aa}$ (N1) (MHz)	1.033(10)	[1.033]	[1.033]		
$[\chi_{bb}(N1) - \chi_{cc}(N1)]$ (MHz)	3.574(25)	[3.574]	[3.574]		
$\chi_{aa}$ (N3) (MHz)	-3.2182(82)	[-3.2182]	[-3.2182]		
$[\chi_{bb}(N3) - \chi_{cc}(N3)]$ (MHz)	[-0.0228]	[-0.0228]	[-0.0228]		
$\sigma_{rms} (kHz)^c$	10.8	12.2	13.0		
$N^{ m d}$	393	45	44		
$P_{cc}$ (u Å <sup>2</sup> )	21.57251(29)	21.7178(33)	21.6077(34)		

<sup>&</sup>lt;sup>a</sup> Numbers in parentheses are one standard deviation in units of the last significant figure.

<sup>&</sup>lt;sup>b</sup> Values in square brackets held fixed at the result for the parent isotopologue, N-EI  $\cdots$  (H<sub>2</sub><sup>16</sup>O)<sub>2</sub>.

<sup>&</sup>lt;sup>c</sup> Root mean square (rms) deviation of the fit.

<sup>&</sup>lt;sup>d</sup> Number of hyperfine components included in the fit.

### 7.5 Molecular geometry

# 7.5.1 Ethylimidazole monomers

The comparison between ground state (experimentally-determined) rotational constants and rotational constants predicted by theory allowed the rotational spectrum of each isomer of ethylimidazole to be assigned. The molecular carrier of the *N*-ethylimidazole spectrum was assigned to the C<sub>1</sub> conformation whereas the molecular carrier of the 2-ethylimidazole spectrum was determined to have a geometry with C<sub>s</sub> symmetry. In this section, the molecular geometry of each ethylimidazole monomer will be presented and it will be discussed why the unambiguous assignment of the 2-ethylimidazole monomer to either C<sub>s</sub> geometry is not possible with the data presented in this chapter alone.

The inertial defect and planar moments of each ethylimidazole monomer have been determined using the equations presented in Chapter 2 (Equations 2.71 - 2.74) to provide a first insight into the geometries of these molecules. For both N-ethylimidazole and 2-ethylimidazole,  $\Delta_0$ determined from the experimental moments of inertia are negative, however, the magnitude of this value is significantly different. For N-ethylimidazole,  $\Delta_0$  was determined to be -35.80320(9) u  $Å^2$  whereas this was calculated to be -7.75887(8) u  $Å^2$  for 2-ethylimidazole. The imidazole monomer<sup>1</sup> has an  $\Delta_0$  of 0.02864(28) u Å<sup>2</sup> which is small and positive, typical of a planar molecule, the substitution of a methyl group results in additional out-of-plane vibrations resulting in a negative  $\Delta_0$  for N-methylimidazole and 2-methylimidazole (-3.2070(1) u Å<sup>2</sup> and -3.1497(7) u Å<sup>2</sup>).<sup>7</sup> In each of 2-ethylimidazole, N-methylimidazole and 2methylimidazole, all heavy atoms lie within the plane of the imidazole ring, therefore, only hydrogen atoms of the methyl or ethyl group contribute out-of-plane mass. Whereas Nethylimidazole adopts a conformation with C<sub>1</sub> symmetry, resulting in a significantly greater number of out-of-plane atoms. The planar moment,  $P_{cc}$ , evaluates the amount of mass located outside the ab plane of the molecule. The value of  $P_{cc}$  was determined to be 17.90160(4) and 3.87943(4) u  $Å^2$  for N-ethylimidazole and 2-ethylimidazole respectively. The  $P_{cc}$  values obtained are similar to the C<sub>1</sub> and C<sub>s</sub> conformations of 2-ethylfuran<sup>18</sup> which were determined to be 14.925714(4) and 3.241613(6) u  $Å^2$ . The value of  $P_{cc}$  is considerably greater for Nethylimidazole and the C1 conformer of 2-ethylfuran compared to 2-ethylimidazole and the Cs conformer of 2-ethylfuran as a result of the methyl group being located out of the ab plane. The ab plane and plane of the imidazole ring are coincident in 2-ethylimidazole. However, for Nethylimidazole the ab plane and the plane of the imidazole ring are separated by  $14.7^{\circ}$  in the ωB97X-D/aug-cc-pVQZ geometry.

Table 7.9 Comparison of DFT calculated and experimentally determined atomic coordinates of heavy atoms in *N*-ethylimidazole and 2-ethylimidazole.

		<i>N</i> -ethylimidazole		
	Method	a / Å	<i>b</i> / Å	c / Å
C2	r <sub>e</sub> (calc.) <sup>a</sup>	-0.6329	-1.0653	0.0468
	$r_{\rm s}$ (exp.)	$-0.6543(23)^{b}$	-1.0810(14)	$[0]^{c}$
C4	r <sub>e</sub> (calc.)	-1.7828	0.7053	-0.1776
	$r_{\rm s}$ (exp.)	-1.77657(85)	0.7365(20)	-0.067(22)
C5	r <sub>e</sub> (calc.)	-0.5253	1.1115	0.1592
	$r_{\rm s}$ (exp.)	-0.4823(31)	1.1085(14)	0.1858(81)
C6	r <sub>e</sub> (calc.)	1.6273	-0.1281	0.5882
	$r_{\rm s}$ (exp.)	1.6319(14)	-0.181(13)	0.5659(41)
C7	r <sub>e</sub> (calc.)	2.4843	0.0858	-0.6500
	$r_{\rm s}$ (exp.)	2.49561(60)	0.1710(88)	-0.6320(24)
		2-ethylimidazole		
	Method	a / Å	<i>b</i> / Å	c / Å
C2	$r_{\rm e}({\rm calc.})^{ m d}$	-0.1833	-0.2174	-0.0211
	$r_{\rm e}$ (calc.) <sup>e</sup>	-0.1597	-0.3179	0.0002
	$r_{\rm s}$ (exp.)	0.139(11)	0.2106(71)	0.043(34)
CX	r <sub>e</sub> (calc.)	1.5986	0.9682	-0.0028
	r <sub>e</sub> (calc.)	1.9785	-0.3746	-0.0005
	$r_{\rm s}$ (exp.)	1.60399(94)	0.9715(15)	[0]
CY	r <sub>e</sub> (calc.)	2.0211	-0.3231	0.0283
	r <sub>e</sub> (calc.)	1.6494	0.9451	0.0001
	$r_{\rm s}$ (exp.)	2.02776(74)	0.3271(46)	0.031(48)
C6	r <sub>e</sub> (calc.)	-1.6005	-0.6914	-0.0495
	r <sub>e</sub> (calc.)	-1.6033	-0.7078	0.0005
	$r_{\rm s}$ (exp.)	1.60362(94)	0.6857(22)	0.120(13)
C7	$r_{\rm e}$ (calc.)	-2.6077	0.4441	0.0539
	$r_{\rm e}$ (calc.)	-2.5766	0.4640	-0.0006
	$r_{\rm s}$ (exp.)	2.60512(58)	0.4513(33)	0.063(24)

<sup>&</sup>lt;sup>a</sup>  $r_e$  geometry calculated at the  $\omega$ B97X-D/aug-cc-pVQZ level of theory.

<sup>&</sup>lt;sup>b</sup> Numbers in parentheses after  $r_s$  results are Costain errors calculated as  $\delta a = 0.015/|a|$ .

 $<sup>^{\</sup>rm c}$  Imaginary  $r_s$  coordinate obtained, therefore, value of coordinate assumed equal to zero.

<sup>&</sup>lt;sup>d</sup>  $r_e$  geometry of 2-ethylimidazole conformation,  $\angle$ (C7–C6–C2–N3) = 0°, calculated at the ωB97X-D/aug-cc-pVQZ level of theory.

<sup>&</sup>lt;sup>e</sup>  $r_e$  geometry of 2-ethylimidazole conformation,  $\angle$ (C7–C6–C2–N3) = 180°, calculated at the ωB97X-D/aug-cc-pVQZ level of theory.

The assignment of spectra of five singly substituted <sup>13</sup>C isotopologues of N-ethylimidazole and 2-ethylimidazole permits the determination of  $r_s$  coordinates for each carbon atom. The experimentally determined coordinates were obtained using Kraitchman's equations<sup>19</sup> implemented within KRA.<sup>20</sup> The  $r_s$  coordinates determined for the carbon atoms within Nethylimidazole are given in Table 7.9 alongside their Costain errors.<sup>21, 22</sup> The coordinates obtained agree well with the  $r_e$  coordinates calculated at the  $\omega$ B97X-D/aug-cc-pVQZ level of theory. Signs of the  $r_s$  coordinates were chosen to be consistent with the  $r_e$  coordinates. Coordinates of N1 and N3 were not determined due to the <sup>15</sup>N isotopologues not being able to be assigned. The absence of experimental coordinates for N1 and N3 means that a full heavy atom structure determination is not possible. However, several bond lengths, angles and dihedral angles have been derived from the C coordinates which are displayed in Table A.59. Unfortunately, the lack of experimental information regarding the position of N1 therefore means that both the dihedral angles  $\angle(C7-C6-N1-C2)$  and  $\angle(C7-C6-N1-C5)$  cannot be experimentally determined. In the  $\omega B97X$ -D/aug-cc-pVQZ geometry, the former was calculated to be 95.4° with the latter being −79.4°. The dihedral angles ∠(C7–C6–C2–C4) and ∠(C7–C6–C5–C4) also describe the rotation of the ethyl group relative to the ring plane and these dihedral angles were able to be experimentally-determined. The former was found to be  $-106.59(86)^{\circ}$  and the latter was determined to be 99.1(18)° in the  $r_s$  geometry. For 2ethylimidazole, the  $r_s$  coordinates were also obtained for each carbon atom which are presented in Table 7.9. The  $r_{\rm e}$  coordinates of each C<sub>s</sub> form of 2-ethylimidazole calculated at the  $\omega$ B97X-D/aug-cc-pVQZ level of theory are given in Table A.45. It can be observed that the magnitude of the coordinates for the C2 atom are essentially the same in both geometries, likewise for C6 and C7. The experimentally obtained  $r_s$  coordinates of C2, C6 and C7 are in good agreement with the  $r_e$  calculated results. The c-coordinate of C7 is small and close to zero implying that this atom lies on (or very close to) the ab plane providing further confirmation that 2ethylimidazole adopts a geometry with C<sub>s</sub> symmetry.

The imidazole ring is very nearly symmetrical either side of the a-inertial axis only differing in the H atom bound to N1. This symmetry results in the  $r_e$  coordinates of C4 in the 0° C<sub>s</sub> form being essentially the same as the coordinates of C5 in the 180° C<sub>s</sub> form and vice versa. Likewise, for N1 and N3. The coordinates of atoms located in the 4- and 5- position therefore cannot be assigned from comparison between experiment and theory alone and are consequently indistinguishable from the data presented herein. For this reason, the coordinates have been assigned "CX" and "CY" labels in Table 7.9. Several bond lengths, angles and dihedral angles have been derived for 2-ethylimidazole which are displayed in Table A.60.

## 7.5.2 Hydrate complexes

The assignment of the parent and additional isotopologues allow for the investigation of the molecular geometries of each of N-EI···H<sub>2</sub>O, 2-EI···H<sub>2</sub>O and N-EI···(H<sub>2</sub>O)<sub>2</sub>. It will be shown that the geometries of 2-EI···H<sub>2</sub>O and N-EI···(H<sub>2</sub>O)<sub>2</sub> are as presented in Figure 7.3 and 7.4. For N-EI···H<sub>2</sub>O, it was discussed earlier that theory does not accurately predict rotational constants for this hydrate complex. It will be shown in the remainder of this Chapter that the experimental geometry of N-EI···H<sub>2</sub>O is consistent with expectations and with the wider emerging trend in the intermolecular parameters observed in this thesis and other recent work.

In each of the hydrate complexes, the ab plane and plane of the imidazole ring are not coincident. In the equilibrium geometries the planes are calculated to be separated by 12.8°, 14.0° and 10.4° in N-EI···H<sub>2</sub>O, 2-EI···H<sub>2</sub>O and N-EI···(H<sub>2</sub>O)<sub>2</sub> respectively. Therefore, the planar moment  $P_{cc}$  provides the best initial insight into the geometry.  $P_{cc}$  was calculated for each of N-EI···H<sub>2</sub><sup>16</sup>O and 2-EI···H<sub>2</sub><sup>16</sup>O using the ground state rotational constants presented earlier. The value obtained for  $P_{cc}$  was found to be very similar for each of the monohydrate complexes, 19.30753(30) u Å<sup>2</sup> and 19.23969(11) u Å<sup>2</sup> for N-EI···H<sub>2</sub><sup>16</sup>O and 2-EI···H<sub>2</sub><sup>16</sup>O respectively. Comparing the values obtained for each monohydrate complex with the respective isolated molecule, it can be observed that the value determined for N-EI···H<sub>2</sub><sup>16</sup>O is slightly greater than the  $P_{cc}$  of the N-ethylimidazole monomer (17.90160(4) u Å<sup>2</sup>). This change is consistent with what was observed for the monohydration of 2-ethylthiazole (Chapter 6). Whereas the  $P_{cc}$  of 2-EI···H<sub>2</sub><sup>16</sup>O is considerably larger than the value obtained for the 2ethylimidazole monomer (3.87943(4) u Å<sup>2</sup>). Since the  $P_{cc}$  value obtained for 2-EI···H<sub>2</sub>O is similar to the values determined for N-EI···H<sub>2</sub>O, 2-EF···H<sub>2</sub>O (Chapter 5) and 2-ET···H<sub>2</sub>O (Chapter 6), this further implies the 2-ethylimidazole sub-unit adopts a C<sub>1</sub> conformation within the experimental geometry of the monohydrate complex, like what was observed previously for the other complexes. Most of the difference in the  $P_{cc}$  value between the monomer and 2-EI···H<sub>2</sub><sup>16</sup>O can be attributed to the change in the conformation of the 2-ethylimidazole sub-unit. For N-EI···(H<sub>2</sub>O)<sub>2</sub>,  $P_{cc}$  was determined to be 21.57251(29) u Å<sup>2</sup> which is slightly greater than the values observed for N-EI···H<sub>2</sub>O and the N-ethylimidazole monomer. Implying the addition of the second water molecule somewhat increases the mass located outside of the ab plane of this complex. A notable observation is the  $P_{cc}$  value obtained for N-EI···(H<sub>2</sub>O)<sub>2</sub> is significantly lower than observed for 2-ET···( $H_2O$ )<sub>2</sub> (42.0308(4) u Å<sup>2</sup>). This difference probably arises from the variation in the group located at C2 which the H<sub>2</sub>O molecules form an interaction with. In the case of N-EI···(H<sub>2</sub>O)<sub>2</sub>, it will be shown that the O atom of the H<sub>2</sub>O water molecule forms

an interaction with the H atom bound to C2 whereas in  $2\text{-ET}\cdots(H_2O)_2$  several weak interactions were observed between each of the  $H_2O$  molecules and the ethyl group.

Table 7.10 Comparison of experimentally-determined ( $r_s$ ) and  $r_e$  atomic coordinates of H<sub>2</sub>O in N-EI···H<sub>2</sub>O, 2-EI···H<sub>2</sub>O and N-EI···(H<sub>2</sub>O)<sub>2</sub>.

		<i>N</i> -EI···H₂O		
	Method	a / Å	b / Å	c / Å
$H_b$	r <sub>e</sub> (calc.) <sup>a</sup>	-3.0255	-0.3763	-0.1635
	$r_{\rm s}$ (exp.)	-3.1866(11) <sup>b</sup>	[0] <sup>c</sup>	-0.156(17)
O	r <sub>e</sub> (calc.)	-3.8460	-0.8967	-0.1921
	$r_{\rm s}$ (exp.)	-3.64304(63)	-1.0926(22)	[0] <sup>c</sup>
$H_{nb}$	r <sub>e</sub> (calc.)	-4.373364	-0.566500	0.532094
	$r_{\rm s}$ (exp.)	-4.1366(20)	-1.1931(71)	0.526(16)
		$2-EI\cdots H_2O$		
	Method	a / Å	<i>b</i> / Å	c / Å
$H_b$	r <sub>e</sub> (calc.)	-1.5788	1.5069	0.0358
	$r_{\rm s}$ (exp.)	-1.55255(97)	1.53580(98)	0.045(34)
O	r <sub>e</sub> (calc.)	-2.5493	1.5868	0.0466
	$r_{\rm s}$ (exp.)	-2.58427(58)	1.55652(96)	[0]
$H_{nb}$	r <sub>e</sub> (calc.)	-2.7318	2.4418	0.4298
	$r_{\rm s}$ (exp.)	-2.85257(53)	2.28437(66)	0.2685(56)
		N-EI···(H <sub>2</sub> O) <sub>2</sub>		
	Method	a / Å	b / Å	c / Å
O1	r <sub>e</sub> (calc.)	3.3928	0.5699	0.2661
	$r_{\rm s}$ (exp.)	3.40145(50)	0.5640(31)	0.2769(63)
O2	re (calc.)	2.6126	-2.0796	-0.1480
	$r_{\rm s}$ (exp.)	2.58724(67)	-2.08965(84)	-0.138(13)

<sup>&</sup>lt;sup>a</sup>  $r_e$  geometry calculated at the  $\omega$ B97X-D/aug-cc-pVQZ level of theory.

<sup>&</sup>lt;sup>b</sup> Numbers in parentheses after  $r_s$  results are Costain errors calculated as  $\delta a = 0.015/|a|$ .

<sup>&</sup>lt;sup>c</sup> Imaginary  $r_s$  coordinate obtained, therefore, value of coordinate assumed equal to zero.

r<sub>s</sub> coordinates for each of the bonding hydrogen, H<sub>b</sub>, oxygen atom, O and non-bonding hydrogen, H<sub>nb</sub>, in each of N-EI···H<sub>2</sub>O and 2-EI···H<sub>2</sub>O have been determined. The assignment of the two singly substituted  $^{18}$ O isotopologues of N-EI···(H<sub>2</sub>O)<sub>2</sub> permits only the coordinates of each O atom to be determined. The  $r_s$  coordinates are presented in Table 7.10. In each of N-EI···H<sub>2</sub>O and 2-EI···H<sub>2</sub>O the c- coordinate of the O atom was calculated to be imaginary, therefore, assumed equal to zero, implying that in each complex the O atom lies within the ab plane. The  $r_s$  coordinates determined for 2-EI···H<sub>2</sub>O generally agree well with  $r_e$  coordinates calculated at the  $\omega$ B97X-D/aug-cc-pVQZ level of theory. Deviations between  $r_s$  and  $r_e$ coordinates of H<sub>nb</sub> are to be expected due to rapid zero-point motions which were discussed in more detail in previous Chapters. The  $r_s$  coordinates for N-EI···H<sub>2</sub>O are not in as good agreement with theory compared to the results obtained for 2-EI···H<sub>2</sub>O. Again, this likely arises due to issues regarding the equilibrium geometry generated from the quantum chemical calculations performed. For H<sub>b</sub> and O the experimental and theoretical results vary by up to  $\sim 0.2$  Å with higher deviations observed for H<sub>nb</sub>. Similar deviations between  $r_s$  and  $r_e$  coordinates calculated for N-methylimidazole··· $H_2O^8$  were also observed. The  $r_s$  coordinates determined for each O atom within N-EI···(H<sub>2</sub>O)<sub>2</sub> agree very well with the theoretical results calculated at the  $\omega$ B97X-D/aug-cc-pVQZ level (presented in Table 7.10). Non-zero c- coordinates were obtained for each O atom indicating that both are located outside the ab plane, which correlates with the larger value of  $P_{cc}$  obtained for N-EI···(H<sub>2</sub>O)<sub>2</sub>. From the  $r_{\rm s}$  coordinates the interatomic distance  $r(O1\cdots O2)$  was derived to be 2.8065(37) Å.

Intermolecular parameters vital to the understanding of the position and relative orientation of the water molecule(s) with respect to the imidazole ring were determined from the effective ground state geometry of each hydrate complex. It was described in Chapters 5 and 6 how the *z*-matrix was constructed for each  $r_0$  fit performed using STRFIT<sup>20</sup> and the initial assumptions regarding the starting geometry of the complexes. The same approach was employed herein for the hydrate complexes formed with isomers of ethylimidazole to determine O containing interatomic distances and angles. For 2-EI···H<sub>2</sub>O, one interatomic distance,  $r(O \cdot \cdot \cdot N3)$ , and two angles,  $\angle(O \cdot \cdot \cdot N3 - C2)$  and  $\angle(H_b - O \cdot \cdot \cdot N3)$  were determined from the  $r_0$  fit performed (Table 7.11). Whereas for  $N \cdot EI \cdot \cdot \cdot H_2O$ , two separate fits were performed which determined  $r(O \cdot \cdot \cdot N3)$  and  $\angle(O \cdot \cdot \cdot N3 - C2)$ , the first fit also determined the angle  $\angle(H_b - O \cdot \cdot \cdot N3)$ , while the second fit held this angle fixed at the DFT calculated result (6.8°). In each fit performed the values obtained for each of  $r(O \cdot \cdot \cdot N3)$  and  $\angle(O \cdot \cdot \cdot N3 - C2)$  are very similar and consistent with expectations. The angle  $\angle(H_b - O \cdot \cdot \cdot N3)$  is determined to be 28.4(34)° when included in the fit. The value obtained is considerably different from the  $r_c$  calculated result and the values obtained

for the same parameter in the  $r_0$  geometry of imidazole... $H_2O$  and N-methylimidazole... $H_2O$ . Therefore, for this reason the  $r_0$  parameters presented in Table 7.11 were determined while holding ∠(H<sub>b</sub>–O···N3) fixed to the ωB97X-D/aug-cc-pVQZ result. A difference of ~14° is observed in the  $\angle$ (O···N3–C2) angle in the  $r_0$  and  $r_e$  geometries of N-EI···H<sub>2</sub>O. The  $r_0$  result is very similar to the same parameter within imidazole···H<sub>2</sub>O (97.3(25)°) and Nmethylimidazole···H<sub>2</sub>O (100.14(18)°).<sup>8, 9</sup> After the fit was performed an additional three parameters  $r(H_b \cdots N3)$ ,  $\angle(H_b \cdots N3-C2)$  and  $\angle(O-H_b \cdots N3)$  were obtained from the  $r_0$ coordinates for each monohydrate complex. The values obtained for each of the angles  $\angle$ (O···N3–C2) and  $\angle$ (H<sub>b</sub>···N3–C2) are greater in 2-EI···H<sub>2</sub>O compared to N-EI···H<sub>2</sub>O by  $\sim$ 10° and  $\sim 13^{\circ}$  respectively. The primary hydrogen bond angle  $\angle (O-H_b\cdots N3)$  is non-linear in each monohydrate complex implying the presence of additional intermolecular interactions which result in this angle deviating from linearity. This will be discussed further in the following sections. Two interatomic distances,  $r(O1 \cdots N3)$  and  $r(O1 \cdots O2)$  and one angle  $\angle(O1 \cdots N3 - C2)$ were determined for  $N\text{-EI}\cdots(H_2O)_2$  in the  $r_0$  fit performed. The results obtained are presented in Table 7.12 alongside the  $r_e$  calculated results. The  $r_0$  values are in good agreement with the results calculated at the  $\omega$ B97X-D/aug-cc-pVQZ level of theory. The interatomic distance between the two O atoms,  $r(O1\cdots O2)$ , was determined to be 2.90(11) Å in the  $r_0$  geometry with the same parameter determined to be 2.8065(37) Å from the  $r_s$  coordinates. Atomic coordinates generated during the  $r_0$  fit of each hydrate complex are provided in Tables A.61 and A.62.

Table 7.11 Comparison of DFT calculated ( $r_e$ ) and experimentally determined ( $r_0$ ) structural parameters of N-EI···H<sub>2</sub>O and 2-EI···H<sub>2</sub>O.

	<i>N</i> -EI····H <sub>2</sub> O	
Parameter	Method	Value
<i>r</i> (O⋯N3) / Å	r <sub>e</sub> (calc.) <sup>a</sup>	2.883
,	$r_0$ (exp.)	2.9294(39) <sup>b</sup>
∠(O…N3–C2) /°	r <sub>e</sub> (calc.)	111.1
,	$r_0$ (exp.)	97.40(15)
$r(H_b \cdots N3) / Å$	$r_{\rm e}$ (calc.)	1.921
,	$r_0$ (exp.) derived <sup>c</sup>	1.9677(24)
$\angle$ (H <sub>b</sub> ···N3–C2) /°	r <sub>e</sub> (calc.)	114.6
,	$r_0$ (exp.) derived	100.77(18)
∠(O–H <sub>b</sub> …N3) /°	r <sub>e</sub> (calc.)	169.7
( ,	$r_0$ (exp.) derived	169.79(11)
	$2-\text{EI}\cdots\text{H}_2\text{O}$	
Parameter	Method	Value
<i>r</i> (O⋯N3) / Å	r <sub>e</sub> (calc.)	2.854
` ,	$r_0$ (exp.)	2.8967(42)
∠(O···N3–C2) /°	r <sub>e</sub> (calc.)	107.8
,	$r_0$ (exp.)	108.021(64)
∠(H <sub>b</sub> –O…N3) /°	r <sub>e</sub> (calc.)	9.6
-	$r_0$ (exp.)	11.5(31)
$r(H_b \cdots N3) / Å$	$r_{\rm e}$ (calc.)	1.901
,	$r_0$ (exp.) derived	1.952(18)
$\angle$ (H <sub>b</sub> ···N3–C2) /°	r <sub>e</sub> (calc.)	112.7
\	$r_0$ (exp.) derived	113.7(13)
∠(O–H <sub>b</sub> ···N3) /°	r <sub>e</sub> (calc.)	165.5
,	$r_0$ (exp.) derived	162.7(44)

 $r_e$  geometry calculated at the  $\omega$ B97X-D/aug-cc-pVQZ level of theory.

Table 7.12 Comparison of DFT-calculated ( $r_e$ ) and experimentally-determined ( $r_0$ ) structural parameters of N-EI···(H<sub>2</sub>O)<sub>2</sub>.

	N-EI···(H <sub>2</sub> O) <sub>2</sub>	
Parameter	Method	Value
<i>r</i> (O1⋯N3) / Å	r <sub>e</sub> (calc.) <sup>a</sup>	2.784
	$r_0$ (exp.)	$2.78(13)^{b}$
<i>r</i> (O1···O2) / Å	r <sub>e</sub> (calc.)	2.793
	$r_0$ (exp.)	2.90(11)
∠(O1···N3–C2) /°	r <sub>e</sub> (calc.)	105.9
	$r_0$ (exp.)	106.1(48)

<sup>&</sup>lt;sup>a</sup>  $r_e$  geometry calculated at the  $\omega$ B97X-D/aug-cc-pVQZ level of theory.

<sup>&</sup>lt;sup>b</sup> Numbers in parentheses are one standard deviation in units of the last significant figure.

<sup>&</sup>lt;sup>c</sup> Derived parameters have the values shown after a fit has been performed and were calculated using EVAL.

<sup>&</sup>lt;sup>b</sup> Numbers in parentheses are one standard deviation in units of the last significant figure.

# 7.6 Nuclear Quadrupole Coupling Constants

Diagonalised values of the nuclear quadrupole coupling tensor determined during fits of experimentally observed transitions to Watson's S-reduced Hamiltonian are given in Tables 7.4. The presence of two nitrogen nuclei, pyrrolic (N1) and pyridinic (N3), results in the hyperfine structure of rotational transitions being somewhat more blended, compared to other species containing one nitrogen nucleus presented in this thesis. However, for each of the ethylimidazole monomers, the values of nuclear quadrupole coupling constants could be determined during the fits performed. Values of  $\chi_{aa}(N1)$ ,  $[\chi_{bb}(N1) - \chi_{cc}(N1)]$  and  $\chi_{aa}(N3)$ determined for N-ethylimidazole are in very good agreement with the DFT-calculated results (as shown in Table 7.1). A greater amount of variation between the experimentally obtained and theoretically predicted values was observed for  $[\chi_{bb}(N3) - \chi_{cc}(N3)]$ . For 2-ethylimidazole, the experimentally obtained values of the nuclear quadrupole coupling constants differ sufficiently to allow the confident assignment to each of the pyrrolic and pyridinic nitrogen atoms. The values determined are compared to the computationally calculated values for each of the possible C<sub>s</sub> geometries. The calculated values presented in Table 7.2 vary between the two conformations, particularly in the case of N3. The percentage deviations between experimental and DFT-calculated results are on average much greater than those observed for Nethylimidazole. Focusing only on the comparison between experimental B3LYP(D3BJ)/aug-cc-pVTZ calculated results for each C<sub>s</sub> conformer, the largest percentage deviations in each case are observed for  $\chi_{aa}(N3)$ . In general, the experimental values are in better agreement with nuclear quadrupole coupling constants predicted for the  $\angle$ (C7–C6–C2–N3) = 0° conformation.

Values obtained for  $\chi_{aa}$ ,  $\chi_{bb}$  and  $\chi_{cc}$  were diagonalised and transformed into the principal axis system to determine  $\chi_{xx}$ ,  $\chi_{yy}$  and  $\chi_{zz}$  using the QDIAG program,<sup>20</sup> to provide a direct comparison between the nuclear quadrupole coupling constants determined for the isomers of ethylimidazole to those of imidazole and methylated derivatives. The results are presented in Table 7.13 alongside those reported previously for each of imidazole, *N*-methylimidazole and 2-methylimidazole.<sup>1, 7</sup> The values presented for *N*-ethylimidazole and 2-ethylimidazole were generated using the off-diagonal term,  $\chi_{ab}$ , calculated at the B3LYP(D3BJ)/aug-cc-pVTZ level of theory in each case. The values obtained for *N*-ethylimidazole are similar to those of imidazole and *N*-methylimidazole however are slightly lower in each case. The results for 2-ethylimidazole are more interesting in the context of the ambiguity in the geometry of this molecule. The experimental values of the nuclear quadrupole coupling constants were diagonalised using the  $\chi_{ab}$  values calculated for each  $C_s$  conformer. The results obtained when

using the  $\chi_{ab}$  values calculated for the  $\angle$ (C7–C6–C2–N3) = 0° conformer are presented in column 2 of Table 7.13 whereas the results in column 3 utilised the  $\chi_{ab}$  values of the  $\angle$ (C7–C6–C2–N3) = 180° conformer. The values obtained for  $\chi_{xx}(N1)$ ,  $\chi_{yy}(N1)$  and  $\chi_{zz}(N1)$  are very similar when generated using the different  $\chi_{ab}$  values and are very consistent with those of 2-methylimidazole.  $\chi_{xx}(N3)$ ,  $\chi_{yy}(N3)$  and  $\chi_{zz}(N3)$  are considerably different when calculated using the different  $\chi_{ab}$  values. The nuclear quadrupole coupling constants obtained using  $\chi_{ab}$  of the  $\angle$ (C7–C6–C2–N3) = 0° geometry are in significantly better agreement with those of imidazole and 2-methylimidazole.

Table 7.13 Nuclear quadrupole coupling constants in the principal nuclear axis framework determined using QDIAG.

	N-ethylimidazole <sup>a</sup>	2-ethylimidazole <sup>b</sup>	2-ethylimidazole <sup>b</sup>
$\chi_{xx}$ (N1) (MHz)	0.9075(95)	1.2371(68)	1.2057(64)
$\chi_{yy}$ (N1) (MHz)	1.4524(56)	1.493(10)	1.52470
$\chi_{zz}$ (N1) (MHz)	-2.3599(57)	-2.7304(59)	-2.7304(59)
$\chi_{xx}$ (N3) (MHz)	1.7925(74)	1.9826(67)	0.2322(96)
$\chi_{yy}$ (N3) (MHz)	2.01(13)	2.12(45)	1.9826(67)
$\chi_{zz}$ (N3) (MHz)	-3.81(16)	-4.11(45)	-2.215(12)
	Imidazole <sup>c</sup>	<i>N</i> -methylimdazole <sup>c</sup>	2-methylimdazole <sup>c</sup>
$\chi_{xx}$ (N1) (MHz)	0.890(52)	0.943(10)	1.225(28)
$\chi_{yy}$ (N1) (MHz)	1.633(58)	1.7427(64)	1.514(29)
$\chi_{zz}$ (N1) (MHz)	-2.524(12)	-2.6860(49)	-2.7395(58)
$\chi_{xx}$ (N3) (MHz)	1.835(24)	2.04(69)	1.97(26)
$\chi_{yy}$ (N3) (MHz)	2.278(24)	2.1419(27)	2.0124(59)
$\chi_{zz}$ (N3) (MHz)	-4.113(34)	-4.18(69)	-3.98(27)

<sup>&</sup>lt;sup>a</sup> Calculated from experimentally determined values of nuclear quadrupole coupling constants,  $\chi_{aa}$ ,  $\chi_{bb}$  and  $\chi_{cc}$  (displayed in Tables 7.4) and the off-diagonal term  $\chi_{ab}$  calculated at the B3LYP(D3BJ)/aug-cc-pVTZ level of theory.

<sup>&</sup>lt;sup>b</sup> Calculated from experimentally determined values of nuclear quadrupole coupling constants,  $\chi_{aa}$ ,  $\chi_{bb}$  and  $\chi_{cc}$  (displayed in Tables 7.4) and the off-diagonal term  $\chi_{ab}$  calculated at the B3LYP(D3BJ)/aug-cc-pVTZ level of theory when  $\angle$ (C7–C6–C2–N3) = 0° (column 2) and  $\angle$ (C7–C6–C2–N3) = 180° (column 3).

<sup>&</sup>lt;sup>c</sup> Results for imidazole, *N*-methylimidazole and 2-methylimidazole are provided in references 1 and 7.

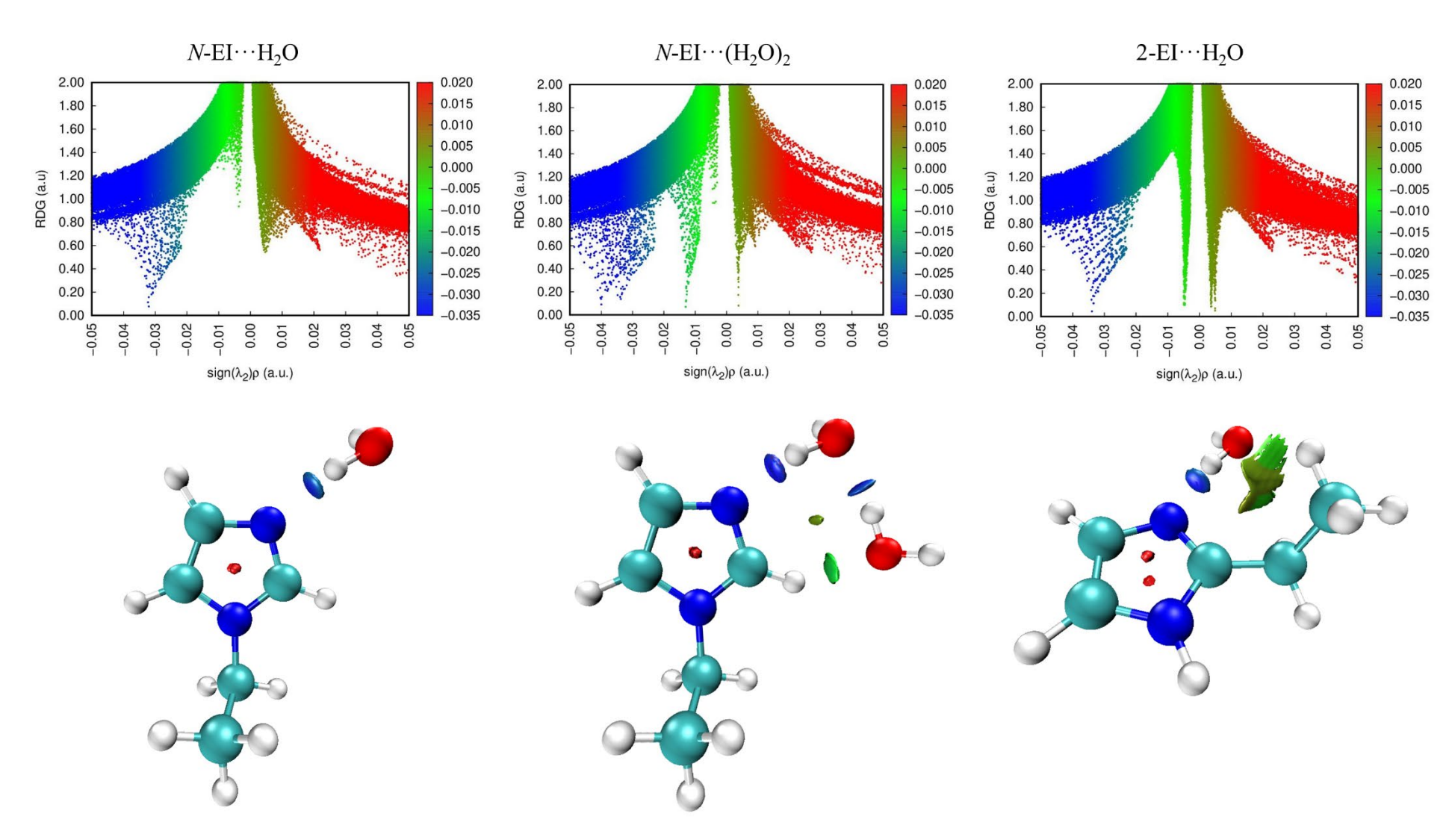


Figure 7.7 NCI isosurfaces and plots of the RDG (a.u.) vs  $sign(\lambda_2)\rho$  of N-EI···H<sub>2</sub>O, N-EI···(H<sub>2</sub>O)<sub>2</sub> and 2-EI···H<sub>2</sub>O. Positive and negative values of  $sign(\lambda_2)\rho$  respectively denote repulsive (red) and attractive (blue) interactions. The isosurface s value is 0.5 au.

#### 7.7 Non-Covalent Interactions

Non-Covalent Interaction (NCI)<sup>23</sup> and Natural Bond Orbital (NBO)<sup>24</sup> analyses have been performed for each hydrate complex assigned, N-EI···H<sub>2</sub>O, N-EI···(H<sub>2</sub>O)<sub>2</sub> and 2-EI···H<sub>2</sub>O using the optimised geometries calculated at the  $\omega B97X$ -D/aug-cc-pVQZ level of theory to visualise the intermolecular interactions present within each complex. Quantum chemical calculations and analysis of the molecular geometries (described in Section 7.5.2) of each complex revealed that the water molecule binds at the pyridinic nitrogen atom (N3) of the ethylimidazole ring. NCI plots of the reduced density gradient (RDG) against the sign of the second eigenvalue of the Hessian matrix  $(\lambda_2)$  of the electronic density  $(\rho)$ ,  $(\operatorname{sign}(\lambda_2)\rho)$  are displayed in Figure 7.7. The NCI analysis of each monohydrate complex shows the presence of a dark blue isosurface indicating the presence of a strong attractive interaction between the pyridinic nitrogen atom of the ethylimidazole ring and one of the H atoms of the H<sub>2</sub>O molecule. This interaction is the primary hydrogen bond (O-H<sub>b</sub>···N3) and as described in Section 7.5.2 was found to be non-linear in each monohydrate complex, suggesting the presence of additional intermolecular interactions within each complex. The NCI analysis of 2-EI···H<sub>2</sub>O reveals the presence of a large green isosurface positioned between the O atom of the water molecule and ethyl group similar to what was previously observed in 2-ethylfuran···H<sub>2</sub>O (Chapter 5) and 2ethylthiazole···H<sub>2</sub>O (Chapter 6). Again, the isosurface shows areas of weakly attractive interactions, signifying the presence of weak hydrogen bonding interactions between the O atom of H<sub>2</sub>O and the nearest H atom bound to C6 and C7, within this complex. Whereas, for N-EI···H<sub>2</sub>O, the analysis does not indicate the presence of any additional isosurfaces within this hydrate complex even though the primary hydrogen bond was determined to be non-linear  $(\angle(O-H_b\cdots N3) = 169.79(16)^\circ)$ . Within this complex the ethyl group is located remote (on the opposite side of the ring) to the H<sub>2</sub>O molecule, therefore, the water molecule forms an interaction with the H atom located at C2 rather than the ethyl moiety. It has been observed previously for other similar complexes including 5-methylthiazole···H<sub>2</sub>O in Chapter 4, that interactions between the O atom of H<sub>2</sub>O and an adjacent H atom located on the heterocycle are often present but too weak to be identified by the analysis. The NCI analysis of  $N-EI\cdots(H_2O)_2$ indicates the presence of three isosurfaces within this hydrate complex. Two dark blue isosurfaces are present indicating two strong attractive (hydrogen bonding) interactions, O1-H<sub>1b</sub>···N3 and O2-H<sub>2b</sub>···O1. A third light green isosurface is located between the O atom of the second H<sub>2</sub>O molecule and H bound to C2 of the imidazole ring, indicating the presence of an additional weaker hydrogen bond within the dihydrate.

NBO analysis (displayed in the Appendix, Table A.63 and A.64) was performed at the B3LYP(D3BJ)/aug-cc-pVTZ level of theory using the geometries of each hydrate complex calculated at the ωB97X-D/aug-cc-pVQZ level. For each of N-EI···H<sub>2</sub>O and 2-EI···H<sub>2</sub>O, the largest contribution corresponds to the interaction between the lone pair of the nitrogen atom (at position 3) of the ethylimidazole ring and the antibonding  $\sigma^*(H_b-O)$  orbital of the water molecule. The second order stabilisation energy of this interaction within N-EI···H<sub>2</sub>O and 2-EI···H<sub>2</sub>O is 45.86 and 50.88 kJ mol<sup>-1</sup> respectively. The  $E^{(2)}$  values obtained for this interaction are very similar to those calculated for imidazole...H2O, N-methylimidazole...H2O and 2methylimidazole···H<sub>2</sub>O (45.19, 46.44 and 49.83 kJ mol<sup>-1</sup>) at the same level of theory. The  $E^{(2)}$ of the O-H<sub>b</sub>···N3 interaction within each imidazole-containing complex is greater than the  $E^{(2)}$ calculated for the equivalent interaction in thiazole- and furan-containing complexes reported in Chapters 4-6 indicating that the relative strength of this interaction is greater in imidazolecontaining complexes. Within the NCI analysis of 2-EI···H<sub>2</sub>O, additional interactions were observed between the O atom of H<sub>2</sub>O and the ethyl group. The same interactions were identified in the NBO analysis. Each lone pair on the O atom forms an interaction with C6–H6 and C7–H7 with the second order stabilisation energy of each interaction calculated to be 0.63 and 0.54 kJ mol<sup>-1</sup> respectively. The relative strength of these interactions are consistent with the values obtained for the same interactions within the monohydrate complex of 2-ethylthiazole. As observed previously for other complexes the largest contribution within N-EI···(H<sub>2</sub>O)<sub>2</sub> corresponds to the primary hydrogen bonding interaction O1–H<sub>1b</sub>···N3 (72.34 kJ mol<sup>-1</sup>). The relative strength of this interaction is significantly greater than the equivalent interaction within the monohydrate complex. This was also observed for the hydrate complexes of 2-ethylthiazole (Chapter 6). The second largest contribution corresponds to the interaction between the two  $H_2O$  molecules bound to N-EI (O2- $H_{2b}$ ···O1).  $E^{(2)}$  was calculated to be 54.06 kJ mol<sup>-1</sup> for this interaction. The analysis identified two interactions between O2 of the second water molecule and the H atom bound to C2, one interaction forming with each lone pair of the oxygen atom. However, the interaction formed with lone pair 2 (see Table A.64) has a significantly greater second order stabilization energy of 12.09 kJ mol<sup>-1</sup>. The  $E^{(2)}$  of this interaction is of a similar magnitude to the equivalent interaction within thiazole... $(H_2O)_2$  (isomer I). 17

\_

<sup>&</sup>lt;sup>k</sup> Calculations performed during the present work.

#### 7.8 Discussion

In Section 6.7 of Chapter 6, several factors that influence the angle that describe the rotation of the ethyl group relative to the aromatic ring was discussed. These factors include the local environment surrounding the ethyl group, symmetry of the (hetero)aromatic ring and the identity of the heteroatoms present within the ring. It is interesting to consider the ethylimidazole isomers in the context of other ethyl-substituted rings. As mentioned earlier, the lack of experimental information regarding the position of N1 and N3 means that a full r<sub>s</sub> structure determination is not possible for each ethylimidazole monomer and consequently Ncontaining dihedral angles associated with the rotation of the ethyl group cannot be experimentally determined for each molecule. In the following discussion the dihedral angle in the equilibrium geometry of N-ethylimidazole will be used instead. The angles  $\angle$  (C7–C6–N1– C2) and  $\angle$ (C7–C6–N1–C5) where calculated to be 95° and -79.4° in the  $\omega$ B97X-D/aug-ccpVQZ geometry and calculated to be 101.6° and -74.2° in the B3LYP(D3BJ)/aug-cc-pVTZ geometry. In each geometry of N-ethylimidazole the rotation of the ethyl group relative to the ring deviates from 90°. This is unsurprising considering that N-ethylimidazole, like 2ethylfuran<sup>18</sup> and 2-ethylthiazole (Chapter 6), is less symmetric than that of ethylbenzene<sup>25</sup> and 4-ethylaniline<sup>26</sup> where the ethyl group is perpendicular to the ring plane in each case. A notable difference between N-ethylimidazole and other ethyl-substituted rings discussed here and in previous Chapters is the atom located at the ethyl/ring junction. In N-ethylimidazole the atom located at the ethyl/ring junction is nitrogen whereas in each of ethylbenzene, 25 2-/3-/4ethylaniline,<sup>26</sup> 2-ethylfuran,<sup>18</sup> 2-ethylthiazole and 2-ethylimidazole the ethyl group is bound at a carbon atom of the ring. Within the current literature, there have been more studies on nonaromatic molecules which contain an ethyl group bound to a heteroatom of a rigid frame, an example of such a group of molecules is ethyl-substituted amides. The ethyl groups bound to the nitrogen atom in each of N-ethylacetamide, 27, 28 N-ethylformamide 29, 30 and N,N-diethylpropionamide<sup>31</sup> have been found to adopt  $C_1$  configurations. A partial  $r_s$  structure determination is available for the two conformers of N-ethylformamide only. The structure of the trans-ac conformer was reported in 2005, the ethyl group was found to be rotated 82.17(19)° out of the plane of the amide group.<sup>29</sup> This molecule was revisited in a 2023 study, in which the higher energy cis-ac conformer was able to be assigned. In this conformation, the  $\angle$ (C2–C1– N-C) dihedral angle was determined to be  $-108.5(35)^{\circ}$ .

The work presented herein identified that 2-ethylimidazole adopts a C<sub>s</sub> conformation, therefore, the carbon atoms of the ethyl group are co-planar with the plane of the imidazole ring. This was concluded from comparisons made between experimentally-determined and equilibrium

rotational constants, the c-coordinate obtained for C7 in the substitution geometry and values obtained for each of  $\Delta_0$  and  $P_{cc}$ . However, from these observations alone the geometry of 2ethylimidazole could not be unambiguously assigned to either C<sub>s</sub> form (∠(C7–C6–C2–N3) =  $0^{\circ}$  or  $\angle$ (C7–C6–C2–N3) = 180°), presented in Figure 7.1. The conformational forms of the isolated molecules of each of N-ethylimidazole and 2-ethylimidazole differ suggesting that the substitution position of the ethyl group on the imidazole ring influences the conformation. In the case of ethylaniline, each isomer was found to adopt a geometry with C<sub>1</sub> symmetry, however, the dihedral angle associated with the rotation of the ethyl group varied across the isomers.<sup>26</sup> It is interesting to consider 2-ethylimidazole alongside other ethylated heteroaromatics where the ethyl group is located on the 2- position of the ring. The study on 2ethylfuran identified that this molecule adopts both a C<sub>s</sub> and C<sub>1</sub> configuration. Whereas for 2ethylthiazole (reported in Chapter 6) only one conformation of this molecule was observed, which was identified to have C<sub>1</sub> symmetry. Each of furan, thiazole and imidazole differ in the atoms located at the 1- and 3- position of the ring, it is therefore apparent that the identity of the heteroatoms has an influence on the conformation(s) of the ethyl group observed. Thus far 2-ethylfuran and 2-ethylimidazole are the only ethyl-substituted aromatic rings which have been found to adopt a C<sub>s</sub> conformation, however, many non-aromatic molecules have been identified to contain an ethyl group in a C<sub>s</sub> conformation.

2-ethylimidazole has been the subject of other studies. The FT-IR and FT-Raman spectra of 2ethylimidazole was reported in 2015 alongside investigations into the molecule using Hartree-Fock and DFT calculations.<sup>32</sup> This study briefly mentioned that 2-ethylimidazole belongs to the C<sub>s</sub> point group, however, the molecular geometry was not the main focus of this study and spectroscopic measurements were performed at ambient conditions suggesting multiple conformations could co-exist (since it is likely that the barrier to interconversion between the geometries can be overcome), therefore, the authors did not provide any insight into the lowest energy geometry of this molecule. The crystal structure of 2-ethylimidazole was determined using single crystal X-ray diffraction (XRD) and was reported in a 2019 study.<sup>33</sup> In the crystal structure of 2-ethylimidazole the ethyl group is rotated towards the pyrrolic nitrogen such that  $\angle$ (C7–C6–C2–N3) = 180°. Therefore, the crystal structure is equivalent to the highest energy geometry predicted by quantum chemical calculations. Nuclear quadrupole coupling constants have been used in studies to distinguish between several alternative geometries.<sup>34</sup> It was discussed earlier (Section 7.6) that in general better agreement was observed between experimentally-determined values of nuclear quadrupole coupling constants and those predicted for  $\angle$ (C7–C6–C2–N3) = 0° geometry. This was also reflected in comparison of the values obtained after the diagonalisation into the principle nuclear axes to those of imidazole and 2-methylimidazole. Each of  $\chi_{xx}$ ,  $\chi_{yy}$  and  $\chi_{zz}$  acquired when using the calculated  $\chi_{ab}$  of the  $\angle$ (C7–C6–C2–N3) = 0° geometry are considerably closer to the values determined previously for imidazole and 2-methylimidazole compared to the values obtained when using  $\chi_{ab}$  of the  $\angle$ (C7–C6–C2–N3) = 180° geometry. If nuclear quadrupole coupling constants are taken into consideration, the ambiguity in the geometry can be resolved to favour the  $\angle$ (C7–C6–C2–N3)  $=0^{\circ}$  form. However, this therefore suggests that the conformation of 2-ethylimidazole is different in the gas phase to that observed in the crystal structure. Further study is required in order to unambiguously assign the gas phase structure of 2-ethylimidazole. Several studies of imidazole-containing species<sup>6, 16, 35</sup> have studied deuterated isotopologues where the H/D exchange readily occurs at the pyrrolic nitrogen atom. Acquiring and assigning the spectrum of 2-ethylimidazole-D may resolve the ambiguity in the structure since the rotational constants predicted and scaled accordingly for each C<sub>s</sub> configuration are sufficiently different to allow for the assignment to either conformer. For the  $\angle$ (C7–C6–C2–N3) = 0° form the rotational constants are predicted to be A = 6722 MHz, B = 1977 MHz and C = 1564 MHz whereas for the  $\angle$ (C7–C6–C2–N3) = 180° form the rotational constants are predicted to be A = 6826 MHz, B = 1981 MHz and C = 1572 MHz.

Table 7.14 Comparison of interatomic distances ( $r_0$  and  $r_e$ ) in imidazole-containing complexes.

Complex	$r(H_b \cdots N)$	3) / Å	<i>r</i> (O···N3	s) / Å
	$r_0$	$r_e$	$r_0$	$r_e$
N-EI····H <sub>2</sub> O	1.9677(24)°	1.921 <sup>d</sup>	2.9294(39)	2.883
$2-EI\cdots H_2O$	1.952(18)	1.901	2.8967(42)	2.854
imidazole···H₂O <sup>a</sup>	1.927(27)	1.931	2.886(21)	2.887
N-methylimidazole···H <sub>2</sub> O <sup>a</sup>	1.922(4)	1.897	2.8802(48)	2.892
2-methylimidazole···H <sub>2</sub> O <sup>a</sup>	1.923(5)	1.881	2.8636(28)	2.864
4-methylimidazole···H <sub>2</sub> O <sup>b</sup>	1.9750(17)	1.925	2.9298(36)	2.891
5-methylimidazole···H <sub>2</sub> O <sup>b</sup>	1.9605(32)	1.924	2.9070(25)	2.890

<sup>&</sup>lt;sup>a</sup> Results from imidazole···H<sub>2</sub>O, *N*-methylimidazole···H<sub>2</sub>O and 2-methylimidazole···H<sub>2</sub>O from references 8 and 9.

<sup>&</sup>lt;sup>b</sup> Unpublished results by E. Gougoula *et al*.

<sup>&</sup>lt;sup>c</sup> Uncertainties in parentheses are those quoted in the primary source.

 $<sup>^{\</sup>rm d}$   $r_{\rm e}$  geometries calculated at the  $\omega$ B97X-D/aug-cc-pVQZ level of theory.

Table 7.15 Comparison of intermolecular angles in imidazole-containing complexes.

	∠(O…N3–C2)	$\angle(H_b\cdots N3-C2)$	$\angle$ (O-H <sub>b</sub> ···N3)
	/0	/0	/0
$N$ -EI $\cdots$ H <sub>2</sub> O	97.40(15)	100.77(18)	169.79(16)
$imidazole\cdots H_2O^a$	$97.3(25)^{\circ}$	99.9(41)	172.1(26)
<i>N</i> -methylimidazole···H <sub>2</sub> O <sup>a</sup>	100.14(18)	101.0(16)	177(5)
5-methylimidazole···H <sub>2</sub> O <sup>b</sup>	100.85(19)	104.53(90)	168.8(25)
$2\text{-EI}\cdots\text{H}_2\text{O}$	108.021(64)	113.7(13)	162.7(44)
2-methylimidazole···H <sub>2</sub> O <sup>a</sup>	112.398(78)	116.9(9)	166.3(28)
4-methylimidazole···H <sub>2</sub> O <sup>b</sup>	140.74(14)	138.7(12)	173.6(37)

<sup>&</sup>lt;sup>a</sup> Results from imidazole···H<sub>2</sub>O, *N*-methylimidazole···H<sub>2</sub>O and 2-methylimidazole···H<sub>2</sub>O from references 8 and 9.

Monohydrate complexes of imidazole and methylimidazole have been studied previously by our group.<sup>8, 9</sup> Interatomic distances and intermolecular angles determined in the ground state geometries of each of the aforementioned complexes as well as for N-EI···H<sub>2</sub>O and 2-EI···H<sub>2</sub>O are displayed in Tables 7.14 and 7.15. It should be noted, the  $r_0$  parameters determined for the monohydrates of imidazole and isomers of methylimidazole were obtained in a slightly different manner to those presented for N-EI···H<sub>2</sub>O and 2-EI···H<sub>2</sub>O. In the case of imidazole···H<sub>2</sub>O and methylimidazole···H<sub>2</sub>O, the parameters  $r(H_b \cdot \cdot \cdot N3)$ ,  $\angle(H_b \cdot \cdot \cdot N3 - C2)$  and  $\angle$ (O-H<sub>b</sub>···N3) were determined during the  $r_0$  fit with r(O···N3) and  $\angle$ (O···N3-C2) derived from the  $r_0$  coordinates after each fit was performed. For each monohydrate complex the  $H_2O$ molecule binds at N3 and the O atom forms an interaction with either the H atom or alkyl group (in the case of 2-EI···H<sub>2</sub>O and 2-methylimidazole···H<sub>2</sub>O<sup>8</sup>) bound to C2. The only exception is 4-methylimidazole···H<sub>2</sub>O, the water molecule orientates such that the secondary interaction forms with the methyl group bound to C4 rather than the H bound to C2. As shown in Table 7.14, the r(O cdots N3) distances were determined to be 2.9294(39) and 2.8967(42) Å in the  $r_0$ geometries of N-EI···H<sub>2</sub>O and 2-EI···H<sub>2</sub>O respectively which are very similar to the same parameter obtained for imidazole···H<sub>2</sub>O, 2.886(21) Å. The distances obtained are also within the range observed for the methylimidazole···H<sub>2</sub>O complexes. The values for  $r(H_b \cdots N3)$ determined for the isomers of ethylimidazole...H2O are slightly longer than observed for imidazole···H<sub>2</sub>O, N-methylimidazole···H<sub>2</sub>O and 2-methylimidazole···H<sub>2</sub>O. A clear trend in the intermolecular angles can be observed in the imidazole-containing monohydrate complexes

-

<sup>&</sup>lt;sup>b</sup> Unpublished results by E. Gougoula et al.

<sup>&</sup>lt;sup>c</sup> Uncertainties in parentheses are those quoted in the primary source.

<sup>&</sup>lt;sup>1</sup> Unpublished work by E. Gougoula *et al*.

presented in Table 7.15. For N-EI···H<sub>2</sub>O the angles  $\angle$ (O···N3–C2) and  $\angle$ (H<sub>b</sub>···N3–C2) were determined to be 97.40(15)° and 100.77(18)° respectively. The values obtained for N-EI···H<sub>2</sub>O are very similar to those of the monohydrates of imidazole, N-methylimidazole and 5methylimidazole. The local environment around the H<sub>2</sub>O molecule is essentially the same as that of imidazole···H<sub>2</sub>O in each of N-EI···H<sub>2</sub>O, N-methylimidazole···H<sub>2</sub>O and 5methylimidazole···H<sub>2</sub>O since the alkyl group is located remote to the H<sub>2</sub>O molecule in each complex. Therefore, it is unsurprising that the values of the intermolecular angles are very similar across the four monohydrate complexes of the first sub-set within Table 7.15. The values obtained for ∠(O–H<sub>b</sub>···N3) in each of the hydrate complexes in the first sub-set suggest the primary hydrogen bond is non-linear since the angle deviates from 180°. This implies that in each of the monohydrate complexes that a weak hydrogen bond forms with the H atom located at C2. It was discussed in the previous section that the NCI and NBO analyses performed for N-EI···H<sub>2</sub>O did not identify the C2-H2···O interaction. This was also the case in 5methylthiazole···H<sub>2</sub>O (Chapter 4) and for each of imidazole···H<sub>2</sub>O, N-methylimidazole···H<sub>2</sub>O and 5-methylimidazole···H<sub>2</sub>O. Indicating that the interaction is present but very weak such that the interaction energy is below the threshold for the analysis. It is also possible that theory underpredicts the strength of the C2–H2···O interaction energy since consistently the analysis hasn't identified this interaction, yet in each monohydrate complex studied the experimental value of  $\angle$ (O–H<sub>b</sub>···N3) deviates from 180° suggesting the interaction is present.

The second sub-set within Table 7.15 consists of 2-EI···H<sub>2</sub>O, 2-methylimidazole···H<sub>2</sub>O and 4-methylimidazole···H<sub>2</sub>O. In each complex the alkyl group is located adjacent to the H<sub>2</sub>O molecule such that additional weaker hydrogen bonding interactions form between O of H<sub>2</sub>O and the alkyl group. Therefore, the values obtained for  $\angle$ (O–H<sub>b</sub>···N3) suggest a non-linear primary hydrogen bond like what was observed for each complex within the first sub-set. For 2-EI···H<sub>2</sub>O, the angles  $\angle$ (O···N3–C2) and  $\angle$ (H<sub>b</sub>···N3–C2) are in excellent agreement with the values obtained for 2-ethylthiazole···H<sub>2</sub>O presented in Chapter 6 and are significantly different (~10° and ~14° larger) than the values obtained for the same parameters within imidazole···H<sub>2</sub>O and N-EI···H<sub>2</sub>O. The difference arises from the change in the local environment within the imidazole sub-unit close to the H<sub>2</sub>O molecule in 2-EI···H<sub>2</sub>O compared to the monohydrate complexes within the first sub-set. This was also observed in the case of 2-methylimidazole···H<sub>2</sub>O, although the angles determined vary slightly between 2-EI···H<sub>2</sub>O and 2-methylimidazole···H<sub>2</sub>O. This variation may arise from slight differences employed when determining the  $r_0$  geometry of each of the complexes or could possibly result from differences in the relative strength of the C–H···O interactions present within each complex. For 2-

methylimidazole···H<sub>2</sub>O, a secondary interaction forms between the O atom of H<sub>2</sub>O and the closest H atom located on the methyl group. NBO analysis calculated that the second order stabilisation energy of the C6–H6···O interaction to be 2.83 kJ mol<sup>-1</sup> (at the B3LYP/aug-cc-pVTZ level). Whereas within 2-EI···H<sub>2</sub>O two weaker interactions form between the O atom of H<sub>2</sub>O and the ethyl group such that the hydrogen bond is bifurcated. The NBO analysis calculated  $E^{(2)}$  was 0.63 kJ mol<sup>-1</sup> for C6–H6···O and 0.54 kJ mol<sup>-1</sup> for C7–H7···O. The lowest energy conformation of 2-ethylimidazole changes depending on whether it is an isolated molecule (C<sub>s</sub>) or within a weakly-bound complex (C<sub>1</sub>). This was also observed in the case of the monohydration of 2-ethylfuran and it was discussed in Chapter 5 that this change occurs in order to maximise the number of intermolecular interactions present within the complex.

Cooperativity within the hydrogen bonding network has been observed in many weakly-bound complexes in which more than one water molecule is present, this typically results in shorter and stronger hydrogen bonds within these complexes. The primary hydrogen bond, H<sub>b</sub>···N3, was determined to be 1.9677(24) Å within N-EI···H<sub>2</sub>O. However due to a lack of D-containing isotopologues the same distance within  $N-EI\cdots(H_2O)_2$  was unable to be experimentally verified. The H<sub>b</sub>···N3 distance was calculated to be 1.826 Å in the ωB97X-D/aug-cc-pVQZ calculated geometry of N-EI···(H<sub>2</sub>O)<sub>2</sub> which is shorter than the same distance calculated in the  $r_e$  geometry of N-EI···H<sub>2</sub>O (1.921 Å). A shortening in the primary hydrogen bond distance is implied in the experimental results. The O1···N3 distance was determined to be 2.78(13) Å in the  $r_0$  geometry of N-EI···(H<sub>2</sub>O)<sub>2</sub> which is shorter than the equivalent distance in N-EI···H<sub>2</sub>O (2.9294(39) Å). The relative strength of the primary hydrogen bond was calculated to be greater within N-EI···(H<sub>2</sub>O)<sub>2</sub> compared to N-EI···H<sub>2</sub>O. The NBO analysis revealed that the second order stabilisation energy of the O1– $H_{1b}$ ···N3 interaction was calculated to be 72.34 kJ mol<sup>-1</sup> for N-EI···(H<sub>2</sub>O)<sub>2</sub> whereas the equivalent interaction within N-EI···H<sub>2</sub>O was determined to be 45.86 kJ mol<sup>-1</sup>. Cooperativity within the hydrogen bond network is also apparent by the O1···O2 distance in the dihydrate complex. This distance was experimentally determined using the substitution coordinates of the O atoms and during the  $r_0$  fit of the complex. The values obtained using each method vary slightly, 2.8065(37) Å from the  $r_s$  coordinates and 2.90(11) Å in the ground state geometry. However, the values obtained using each method are shorter than observed for the isolated water dimer, 2.976(10) Å. <sup>36</sup> A shortening in the O···O distance has also been observed in each of thiazole...(H<sub>2</sub>O)<sub>2</sub>, <sup>17</sup> phenanthridine...(H<sub>2</sub>O)<sub>2</sub><sup>37</sup> and 2ethylthiazole···(H<sub>2</sub>O)<sub>2</sub> (Chapter 6) as displayed in Table 7.16 as well as many dihydrate complexes formed with other molecules.  $^{38-45}$  The  $\angle$ (O1···N3–C2) angle was determined to be  $106.1(48)^{\circ}$  for N-EI···(H<sub>2</sub>O)<sub>2</sub> which is ~ 9° greater than the same angle within the monohydrate complexes of imidazole and *N*-ethylimidazole. A change in the  $\angle$ (O···N3–C2) angle was also observed upon the successive hydration of thiazole and 2-ethylthiazole. For example, in thiazole···H<sub>2</sub>O,  $\angle$ (O···N3–C2) was determined to be 91.98(10)° whereas in thiazole···(H<sub>2</sub>O)<sub>2</sub> this was determined to be 106.5(49)°. It was discussed in Chapter 6 and earlier that the presence of an alkyl group located at the 2-position has a clear and predictable effect on the coordinating water molecules. It is therefore unsurprising that the  $\angle$ (O1···N3–C2) angles obtained for each of *N*-EI···(H<sub>2</sub>O)<sub>2</sub> and thiazole···(H<sub>2</sub>O)<sub>2</sub> are very similar due to an H atom being located at C2 in each case.

Table 7.16 Comparison of intermolecular parameters in dihydrate complexes formed with *N*-containing heteroaromatic rings.

	r(O1···O2) / Å	∠(O1···N3–C2) /°	ref
$(H_2O)_2$	2.976(10) <sup>a</sup>	-	36
N-EI···(H <sub>2</sub> O) <sub>2</sub>	2.90(11)	106.1(48)	This work
thiazole $\cdots$ (H <sub>2</sub> O) <sub>2</sub>	2.826(33)	106.5(49)	17
2-ethylthiazole $\cdots$ (H <sub>2</sub> O) <sub>2</sub>	2.894(21)	120.55(15)	Chapter 6
phenanthridine···H <sub>2</sub> O	2.85(1)	-	37

<sup>&</sup>lt;sup>a</sup> Uncertainties in parentheses are those quoted in the primary source.

#### 7.9 Conclusion

The broadband microwave spectra of N-ethylimidazole, 2-ethylimidazole and several of their hydrate complexes have been assigned and their molecular geometries analysed. Each of Nethylimidazole and 2-ethylimidazole adopt one confirmation only, however, the conformations observed differ with the position at which the ethyl group is substituted on the ring. Nethylimidazole adopts a geometry which has C<sub>1</sub> symmetry whereas 2-ethylimidazole was found have C<sub>s</sub> symmetry. Ambiguity surrounding the orientation of the ethyl group relative to the imidazole ring was resolved in favour of the  $\angle$ (C7–C6–C2–N3) = 0° geometry when nuclear quadrupole coupling constants were taken into consideration. Weakly-bound complexes formed between each isomer of ethylimidazole and H<sub>2</sub>O have been studied. Each of N-EI···H<sub>2</sub>O and 2-EI···H<sub>2</sub>O contains a strong primary hydrogen bond between the pyridinic nitrogen and one of the hydrogen atoms of H<sub>2</sub>O such that the imidazole ring is accepting the hydrogen bond. In both monohydrate complexes, H<sub>2</sub>O is orientated such that a weaker hydrogen bonding interaction forms between O of H<sub>2</sub>O and the group (H or C<sub>2</sub>H<sub>5</sub>) bound to C2. In N-EI···(H<sub>2</sub>O)<sub>2</sub>, a second strong hydrogen bond is present between the two water molecules, with the second water molecule forming an interaction with H bound to C2. For each of N-EI···H<sub>2</sub>O and N- $EI\cdots(H_2O)_2$ , the N-ethylimidazole sub-unit adopts a  $C_1$  conformation like what was observed for the isolated monomer. Whereas for 2-EI···H<sub>2</sub>O, the 2-ethylimidazole sub-unit adopts a C<sub>1</sub> geometry within the monohydrate complex differing to what was previously observed for the isolated molecule. Intermolecular parameters in the  $r_0$  geometry of each hydrate complex were determined and compared to other imidazole-containing complexes. The ∠(O···N3–C2) and ∠(H<sub>b</sub>···N3–C2) angles are significantly greater in 2-EI···H<sub>2</sub>O compared to N-EI···H<sub>2</sub>O and imidazole···H<sub>2</sub>O since the presence of the alkyl group in the 2- position has an effect on the coordinating  $H_2O$  molecule. The  $O1\cdots O2$  distance is shorter when  $(H_2O)_2$  is bound to Nethylimidazole compared to the isolated (H<sub>2</sub>O)<sub>2</sub> dimer due to cooperativity effects within the hydrogen bonding network.

#### 7.10 References

- 1. D. Christen, J. H. Griffiths and J. Sheridan, *Zeitschrift für Naturforschung A*, 1981, **36**, 1378-1385.
- 2. C. Bermúdez, S. Mata, C. Cabezas and J. L. Alonso, *Angewandte Chemie International Edition*, 2014, **53**, 11015-11018.
- 3. B. Vogelsanger, P. D. Godfrey and R. D. Brown, *Journal of the American Chemical Society*, 1991, **113**, 7864-7869.
- 4. S. Samdal and H. Møllendal, *The Journal of Physical Chemistry A*, 2011, **115**, 7559-7565.
- 5. P. D. Godfrey and E. G. Robertson, *The Journal of Chemical Physics*, 2012, **137**, 064306.
- 6. G. A. Cooper, C. Medcraft, E. Gougoula and N. R. Walker, *Physical Chemistry Chemical Physics*, 2019, **21**, 9495-9503.
- 7. E. Gougoula, C. Medcraft, J. Heitkämper and N. R. Walker, *The Journal of Chemical Physics*, 2019, **151**, 144301.
- 8. E. Gougoula, C. N. Cummings, C. Medcraft, J. Heitkämper and N. R. Walker, *Physical Chemistry Chemical Physics*, 2022, **24**, 12354-12362.
- 9. E. Gougoula, D. J. Cole and N. R. Walker, *The Journal of Physical Chemistry A*, 2020, **124**, 2649-2659.
- 10. J. K. G. Watson, *The Journal of Chemical Physics*, 1968, **48**, 4517-4524.
- 11. C. M. Western, *Journal of Quantitative Spectroscopy and Radiative Transfer*, 2017, **186**, 221-242.
- 12. M. Kessler, H. Ring, R. Trambarulo and W. Gordy, *Physical Review*, 1950, **79**, 54-56.
- 13. A. Bauer, Journal of Molecular Spectroscopy, 1971, 40, 183-206.
- 14. S. Thorwirth, H. S. P. Müller and G. Winnewisser, *Journal of Molecular Spectroscopy*, 2000, **204**, 133-144.
- 15. M. C. L. Gerry and G. Winnewisser, *Journal of Molecular Spectroscopy*, 1973, **48**, 1-16.
- 16. J. C. Mullaney, D. P. Zaleski, D. P. Tew, N. R. Walker and A. C. Legon, *ChemPhysChem*, 2016, **17**, 1154-1158.
- 17. E. Gougoula, C. N. Cummings, Y. Xu, T. Lu, G. Feng and N. R. Walker, *The Journal of Chemical Physics*, 2023, **158**, 114307.
- 18. H. V. L. Nguyen, *Journal of Molecular Structure*, 2020, **1208**, 127909.
- 19. J. Kraitchman, American Journal of Physics, 1953, 21, 17-24.
- 20. Z. Kisiel, PROSPE Programs for ROtational SPEctroscopy, <a href="http://info.ifpan.edu.pl/~kisiel/prospe.htm">http://info.ifpan.edu.pl/~kisiel/prospe.htm</a>, (accessed 21/06/2024, 2024).
- 21. C. C. Costain, *The Journal of Chemical Physics*, 1958, **29**, 864-874.
- 22. C. C. Costain, *Trans.Am. Crystallogr. Assoc*, 1966, **2**, 157-164.
- 23. E. R. Johnson, S. Keinan, P. Mori-Sánchez, J. Contreras-García, A. J. Cohen and W. Yang, *Journal of the American Chemical Society*, 2010, **132**, 6498-6506.
- 24. A. E. Reed, L. A. Curtiss and F. Weinhold, *Chemical Reviews*, 1988, 88, 899-926.
- 25. W. Caminati, D. Damiani, G. Corbelli, B. Velino and C. W. Bock, *Molecular Physics*, 1991, 74, 885-895.
- 26. J. Wang, S. Herbers, P. Buschmann, K. Lengsfeld, J.-U. Grabow, G. Feng and Q. Gou, *Chinese Journal of Chemical Physics*, 2020, **33**, 119-124.
- 27. R. Kannengießer, M. J. Lach, W. Stahl and H. V. L. Nguyen, *ChemPhysChem*, 2015, **16**, 1906-1911.
- 28. Y. Kawashima, N. Kuze, K. M. T. Yamada and E. Hirota, *Journal of Molecular Spectroscopy*, 2024, **400**, 111871.

- 29. K. Ohba, T. Usami, Y. Kawashima and E. Hirota, *Journal of Molecular Structure*, 2005, 744-747, 815-819.
- 30. C. Cabezas, Y. Kawashima, C. Bermúdez, T. Usami, E. Hirota and J. Cernicharo, *Spectrochimica Acta Part A: Molecular and Biomolecular Spectroscopy*, 2023, **291**, 122353.
- 31. R. Kannengießer, W. Stahl and H. V. L. Nguyen, *The Journal of Physical Chemistry A*, 2016, **120**, 5979-5984.
- 32. M. Arivazhagan, S. Manivel, S. Jeyavijayan and R. Meenakshi, *Spectrochimica Acta Part A: Molecular and Biomolecular Spectroscopy*, 2015, **134**, 493-501.
- 33. J. J. Calvin, P. F. Rosen, S. J. Smith and B. F. Woodfield, *The Journal of Chemical Thermodynamics*, 2019, **132**, 129-141.
- 34. S. McGlone, P. Moreschini, T. K. Ha and A. Bauder, *Molecular Physics*, 2001, **99**, 1353-1364.
- 35. G. A. Cooper, C. J. Anderson, C. Medcraft and N. R. Walker, *Journal of Molecular Spectroscopy*, 2018, **354**, 15-23.
- 36. J. A. Odutola and T. R. Dyke, *The Journal of Chemical Physics*, 1980, **72**, 5062-5070.
- 37. D. Loru, A. L. Steber, P. Pinacho, S. Gruet, B. Temelso, A. M. Rijs, C. Pérez and M. Schnell, *Physical Chemistry Chemical Physics*, 2021, **23**, 9721-9732.
- 38. S. Blanco, J. C. López, A. Lesarri and J. L. Alonso, *Journal of the American Chemical Society*, 2006, **128**, 12111-12121.
- 39. P. Pinacho, S. Blanco and J. C. López, *Physical Chemistry Chemical Physics*, 2019, **21**, 2177-2185.
- 40. S. Gruet, C. Pérez, A. L. Steber and M. Schnell, *Physical Chemistry Chemical Physics*, 2018, **20**, 5545-5552.
- 41. M. Chrayteh, E. Burevschi, D. Loru, T. R. Huet, P. Dréan and M. E. Sanz, *Physical Chemistry Chemical Physics*, 2021, **23**, 20686-20694.
- 42. C. Pérez, A. Krin, A. L. Steber, J. C. López, Z. Kisiel and M. Schnell, *The Journal of Physical Chemistry Letters*, 2016, 7, 154-160.
- 43. C. Pérez, J. L. Neill, M. T. Muckle, D. P. Zaleski, I. Peña, J. C. Lopez, J. L. Alonso and B. H. Pate, *Angewandte Chemie International Edition*, 2015, **54**, 979-982.
- 44. S. R. Domingos, C. Pérez and M. Schnell, *The Journal of Chemical Physics*, 2016, **145**, 161103.
- 45. A. L. Steber, C. Pérez, B. Temelso, G. C. Shields, A. M. Rijs, B. H. Pate, Z. Kisiel and M. Schnell, *The Journal of Physical Chemistry Letters*, 2017, **8**, 5744-5750.

# **Chapter 8. Conclusions**

Studies on weakly-bound complexes formed between water and various alkyl-substituted heterocyclic rings have been presented within this thesis. The broadband rotational spectrum of each species was probed using the CP-FTMW spectrometer at Newcastle University, over the 2.0 - 18.5 GHz region and the target molecule was transferred into the gas phase by means of heating or laser ablation. This work has focussed on revealing the influence that weak hydrogen bonding interactions can have on the internal dynamics and conformational preferences of methyl- and ethyl-substituted heteroaromatic rings. Specifically, this work has explored hydrate complexes of the following heteroaromatic ring derivatives: isomers of methylthiazole (Chapter 4), 2-ethylfuran (Chapter 5), 2-ethylthiazole (Chapter 6) and isomers of ethylimidazole (Chapter 7). The precise determination of the molecular geometries has revealed that each complex is stabilised by a comparatively strong primary hydrogen bonding interaction between the pyridinic nitrogen or oxygen atom within the heterocyclic ring and an O–H of H<sub>2</sub>O. Each complex was shown to contain one or more weaker hydrogen bonding interactions between O of H<sub>2</sub>O and a neighbouring group (H, CH<sub>3</sub> or C<sub>2</sub>H<sub>5</sub>).

In Chapter 4, the molecular geometries of the monohydrate complexes formed with each isomer of methylthiazole (MT···H<sub>2</sub>O) were revealed through the assignment of the rotational spectrum of several isotopologues of each complex. The  $V_3$  barriers to internal rotation of the CH<sub>3</sub> group in each of 4-MT···H<sub>2</sub>O and 5-MT···H<sub>2</sub>O were determined through global fits of each complex.<sup>1</sup> A small decrease in the  $V_3$  barrier was observed upon the attachment of water to 4-methylthiazole.<sup>2</sup> The lowering of  $V_3$  such that rotation becomes more unhindered is likely due to a charge redistribution within the 4-methylthiazole sub-unit which occurs upon the formation of the monohydrate complex. While the  $V_3$  of 5-MT···H<sub>2</sub>O was found to be essentially unchanged to that reported previously for the 5-methylthiazole monomer.<sup>3</sup> It was discussed that the global fit of 2-MT···H<sub>2</sub>O is proving more challenging, and the analysis is still in progress.

A binary complex formed between 2-ethylfuran and water (2-EF···H<sub>2</sub>O) was reported in Chapter 5. It was shown that this complex forms with 2-ethylfuran in a  $C_1$  conformation through a strong hydrogen bonding interaction between the sub-units ( $O_w$ –H···O1) while weaker interactions exist between the O of H<sub>2</sub>O and C–H of the ethyl moiety. The same work reported the experimental energy ordering of the 2-ethylfuran monomer which was unable to be determined from the previous microwave spectroscopy study of this molecule.<sup>4</sup> Both the  $C_s$  and

 $C_1$  conformers were observed in an experiment performed using a neon carrier gas. However, when argon backing gas was employed, only transitions from the  $C_s$  conformer were present in the spectrum recorded indicating that this is the global minimum structure. This work showed that the energy ordering of conformers changed between the isolated 2-ethylfuran monomer and its monohydrate complex.

In Chapter 6, the lowest-energy conformation of 2-ethylthiazole and two of its hydrate complexes, 2-ET···H<sub>2</sub>O and 2-ET···(H<sub>2</sub>O)<sub>2</sub> were discussed.<sup>5</sup> Transitions from only one conformer of 2-ethylthiazole were observed in experiments employing either argon or neon as the carrier gas. The experimentally observed lowest-energy conformation has C<sub>1</sub> symmetry and the  $\angle$ (C7–C6–C2–S1) angle, which defines the rotation of the ethyl group, was found to be – 98.6(10)°. The angle deviates somewhat from 90° owing to the asymmetry which exists in the thiazole ring, consistent with the empirical observations made through comparisons with other ethyl-substituted rings within the current literature. The H<sub>2</sub>O and (H<sub>2</sub>O)<sub>2</sub> sub-unit within the monohydrate and dihydrate complex respectively was found to act as a hydrogen bond donor to the ring at the pyridinic nitrogen atom while simultaneously accepting one or more hydrogen bonds from C-H of the ethyl group. Through comparisons with the thiazole-analogues<sup>6, 7</sup> of each complex it is evident that the presence of the ethyl group has a significant effect on the intermolecular parameters associated with the primary hydrogen bonding interaction. Within the 2-ET···(H<sub>2</sub>O)<sub>2</sub> complex, cooperativity effects within the hydrogen bonding network are evident owing to the primary hydrogen bonding interaction being stronger and the angle being closer to linearity compared to 2-ET···H<sub>2</sub>O.

The lowest-energy conformation of two isomers of ethylimidazole and the molecular geometries of several hydrate complexes were reported in Chapter 7. The experimentally observed lowest energy conformations of *N*-ethylimidazole and 2-ethylimidazole were found to differ, which was determined through the assignment of the spectrum of the parent and several <sup>13</sup>C isotopologues of each molecule. The global minimum structure of *N*-ethylimidazole has the ethyl group in a C<sub>1</sub> configuration while the lowest energy conformation of 2-ethylimidazole was observed to have C<sub>8</sub> symmetry. Water was found to preferentially bind at the pyridinic nitrogen atom of each ring, consistent with the global minimum structures of other imidazole-containing complexes.<sup>8, 9</sup> The *N*-ethylimidazole sub-unit was found to adopt a C<sub>1</sub> configuration in each of *N*-EI···H<sub>2</sub>O and *N*-EI···(H<sub>2</sub>O)<sub>2</sub> like what was observed for the isolated monomer. Whereas the lowest energy form of 2-ethylimidazole was found to change upon the formation of the monohydrate complex, with the 2-ethylimidazole sub-unit adopting a C<sub>1</sub> conformation in 2-EI···H<sub>2</sub>O. The geometrical parameters associated with *N*-EI···H<sub>2</sub>O and 2-conformation in 2-EI···H<sub>2</sub>O.

 $EI\cdots H_2O$  are consistent with other similar complexes and cooperativity effects were evident within the N- $EI\cdots (H_2O)_2$  complex.

Table 8.1 Comparison of experimentally determined structural parameters within the monohydrate complexes of five-membered heterocycles.

Complex <sup>a</sup>	$\angle$ (H <sub>b</sub> ···N3–C2)	∠(O···N3–C2)	$\angle$ (O-H <sub>b</sub> ···N3)	ref.
1	/0	/0	/0	
imidazole···H <sub>2</sub> O	99.9(41) <sup>b</sup>	97.3(25)	172.1(26)	8
N-MI····H <sub>2</sub> O	101.0(16)	100.14(18)	177(5)	9
N-EI···H <sub>2</sub> O	100.77(18)	97.40(15)	169.79(16)	Chapter 7
$5-MI\cdots H_2O$	104.53(90)	100.85(19)	168.8(25)	_c
thiazole···H <sub>2</sub> O	95.6(4)	95.62(49)	168.9(1)	6
$5-MT\cdots H_2O$	99.40(78)	94.92(13)	166.0(23)	Chapter 4 /
	` '	, ,	,	ref 1
$2-MI\cdots H_2O$	116.9(9)	112.398(78)	166.3(28)	9
$2-EI\cdots H_2O$	113.7(13)	108.021(64)	162.7(44)	Chapter 7
$2-MT\cdots H_2O$	112.6(16)	109.37(22)	170.2(50)	Chapter 4
$2-ET\cdots H_2O$	115.1(17)	109.726(91)	163.3(52)	Chapter 6 /
	` '	,	,	ref 5
$4-MI\cdots H_2O$	138.7(12)	140.74(14)	173.6(37)	_c
$4-MT\cdots H_2O$	134.7(14)	138.72(11)	167.4(44)	Chapter 4 /
	` '	, ,	,	ref 1
Complex <sup>a</sup>	$\angle$ (H <sub>b</sub> ···O1–C2)	∠(O···O1–C2)	$\angle$ (O-H <sub>b</sub> ···O1)	ref.
•	/0	/0	/0	
Furan···H <sub>2</sub> O <sup>d</sup>	105.3	98.4	154.9	Chapter 5
$2-EF\cdots H_2O$	115.30(11)	111.50(16)	167.69(16)	Chapter 5

<sup>&</sup>lt;sup>a</sup> MI = methylimidazole, EI = ethylimidazole, MT = methylthiazole, ET = ethylthiazole, EF = ethylfuran

Table 8.1 displays the intermolecular parameters of monohydrate complexes presented within this thesis<sup>1, 5</sup> and those available for other imidazole- and thiazole-containing monohydrate complexes, <sup>6, 8, 9</sup> grouped based on the values of their geometrical parameters. Results for 2-  $EF\cdots H_2O$  and  $\omega B97X$ -D calculated parameters of furan···H<sub>2</sub>O are also presented within the same table. The overall picture is that the presence of weak hydrogen bonding interactions (C– H···O) have a significant influence on the primary hydrogen bond angle, O–H···X (where X= N or O). The hydrogen bond angle is non-linear in each monohydrate complex presented in

<sup>&</sup>lt;sup>b</sup> Numbers in parentheses are one standard deviation in units of the last significant figure from primary source.

<sup>&</sup>lt;sup>c</sup> Unpublished results by E. Gougoula et al.

<sup>&</sup>lt;sup>d</sup>  $r_e$  calculated results for furan···H<sub>2</sub>O calculated at the  $\omega$ B97X-D/aug-cc-pVQZ level of theory.

Table 8.1 owing to the presence of one or more  $C-H\cdots O$  interactions. Additionally, this work has revealed that the presence of an alkyl group (CH<sub>3</sub> or C<sub>2</sub>H<sub>5</sub>) in a neighbouring position to the H<sub>2</sub>O binding site has a clear and predictable influence on the  $\angle(H_b\cdots X-C2)$  and  $\angle(O\cdots X-C2)$  geometrical parameters of the complex. When an alkyl group is positioned adjacent to H<sub>2</sub>O, each of these angles are considerably larger than observed in the un-substituted complexes or in those where the alkyl group is remote to H<sub>2</sub>O. Evidently the presence of the alkyl group has an influence on the H<sub>2</sub>O binding. Furthermore, the study of the series of complexes, 2-EF···H<sub>2</sub>O, 2-ET···H<sub>2</sub>O and 2-EI····H<sub>2</sub>O, has revealed that when an ethyl group is situated adjacent to the H<sub>2</sub>O binding site, the group was found to adopt a C<sub>1</sub> configuration in each case to maximise the number of hydrogen bonding interactions present within the complex. For each of 2-ethylfuran and 2-ethylimidazole the formation of the hydrate complex resulted in a change in the energy ordering of conformations.

Table 8.2 Comparison of experimentally determined structural parameters within dihydrate complexes of five-membered heterocycles.

	r(O1⋯O2) / Å	∠(O1···N3–C2) /°	ref.
$(H_2O)_2$	2.976(10) <sup>a</sup>	-	10
thiazole $\cdots$ (H <sub>2</sub> O) <sub>2</sub>	2.826(33)	106.5(49)	7
$2-ET\cdots(H_2O)_2$	2.894(21)	120.55(15)	Chapter 6 / ref 5
N-EI···(H <sub>2</sub> O) <sub>2</sub>	2.90(11)	106.1(48)	Chapter 7

<sup>&</sup>lt;sup>a</sup> Numbers in parentheses are one standard deviation in units of the last significant figure from primary source.

The number of studies within the current literature on complexes formed between a heteroaromatic ring and multiple water molecules is limited. The work presented within this thesis has extended the number of studies on dihydrate complexes formed with five-membered heteroaromatic rings and to the best of the authors knowledge is the first time that dihydrate complexes of substituted rings have been reported. Within this thesis the dihydrate complexes of 2-ethylthiazole<sup>5</sup> and *N*-ethylimidazole were reported in Chapters 6 and 7 respectively. The separation between the two O atoms of the (H<sub>2</sub>O)<sub>2</sub> sub-unit within each of 2-ET···(H<sub>2</sub>O)<sub>2</sub> and *N*-EI···(H<sub>2</sub>O)<sub>2</sub> was determined to be shorter than the same distance within the isolated water dimer, <sup>10</sup> like what was observed previously in the study of thiazole···(H<sub>2</sub>O)<sub>2</sub>. A shortening of this distance implies that the hydrogen bond between the two H<sub>2</sub>O molecules within the sub-unit is also shorter as a result of cooperativity effects. Additionally, the results of quantum chemical calculations and natural bond orbital (NBO) analysis performed also implied

cooperativity effects within the hydrogen bonding network of each dihydrate complex owing to the primary hydrogen bond being calculated to be shorter, stronger and the angle being closer to linearity in each case compared to the respective monohydrate complex. Comparing the experimentally determined  $\angle$ (O1···N3–C2) angle of thiazole···(H<sub>2</sub>O)<sub>2</sub> and 2-ET···(H<sub>2</sub>O)<sub>2</sub> it is evident that the presence of the ethyl group influences the binding of (H<sub>2</sub>O)<sub>2</sub> since this angle is  $\sim$ 15° greater in the latter. No study is available for imidazole···(H<sub>2</sub>O)<sub>2</sub>, however, the value of  $\angle$ (O1···N3–C2) determined for *N*-EI···(H<sub>2</sub>O)<sub>2</sub> compares with the value observed for thiazole···(H<sub>2</sub>O)<sub>2</sub>, consistent with the ethyl group being remote and not influencing the (H<sub>2</sub>O)<sub>2</sub> binding. It is expected that a similar value would be observed in the  $r_0$  geometry of imidazole···(H<sub>2</sub>O)<sub>2</sub>.

The work presented within this thesis has expanded the number of studies on ethyl-substituted aromatic rings and increased the number of studies on hydrate complexes formed with substituted five-membered heteroaromatic rings. Further studies on other ethylated aromatic rings and their weakly-bound complexes with one or more water molecules are currently in progress within the group. This work has set the foundations for future studies on other aromatic and heteroaromatic derivatives and their weakly-bound complexes. For example, alkylsubstituted heteroaromatic rings with more than two carbon atoms within the chain could be investigated. Molecules such as 1-butylimidazole and 2-propylfuran would have a greater number of possible conformations owing to the flexibility within the side chain. Studies on complexes formed between five-membered heteroaromatic rings and their derivatives with a greater number of water molecules could be performed. It would be interesting to know what is the highest microsolvated cluster which could be observed with these heteroaromatic rings and the influence that a greater number of water molecules has on the internal dynamics and conformations of heteroaromatic ring derivatives. Finally, it would be worth investigating weakly-bound complexes formed between heteroaromatic rings and their derivatives with other small molecules such as H<sub>2</sub>S, NH<sub>3</sub>, CH<sub>3</sub>OH and C<sub>2</sub>H<sub>5</sub>OH to investigate whether the binding site preference changes.

## **8.1 References**

- 1. C. N. Cummings, I. Kleiner and N. R. Walker, *The Journal of Physical Chemistry A*, 2023, **127**, 8133-8145.
- 2. W. Jäger and H. Mäder, Zeitschrift für Naturforschung A, 1987, 42, 1405-1409.
- 3. W. Jäger and H. Mäder, Journal of Molecular Structure, 1988, 190, 295-305.
- 4. H. V. L. Nguyen, *Journal of Molecular Structure*, 2020, **1208**, 127909.
- 5. C. N. Cummings and N. R. Walker, *ChemPhysChem*, 2024, **25**, e202400011.
- 6. W. Li, J. Chen, Y. Xu, T. Lu, Q. Gou and G. Feng, *Spectrochimica Acta Part A: Molecular and Biomolecular Spectroscopy*, 2020, **242**, 118720.
- 7. E. Gougoula, C. N. Cummings, Y. Xu, T. Lu, G. Feng and N. R. Walker, *The Journal of Chemical Physics*, 2023, **158**, 114307.
- 8. E. Gougoula, D. J. Cole and N. R. Walker, *The Journal of Physical Chemistry A*, 2020, **124**, 2649-2659.
- 9. E. Gougoula, C. N. Cummings, C. Medcraft, J. Heitkämper and N. R. Walker, *Physical Chemistry Chemical Physics*, 2022, **24**, 12354-12362.
- 10. J. A. Odutola and T. R. Dyke, *The Journal of Chemical Physics*, 1980, **72**, 5062-5070.

# Appendix

A1 (Chapter 4) Atomic coordinates of the optimised geometry of 2-MT $\cdots$ H<sub>2</sub>O calculated at the  $\omega$ B97X-D/aug-cc-pVQZ level of theory.

ωB97X-D/aug-cc-pVQZ				
	a /Å	b/Å	c/Å	
S(1)	1.718082	-0.526042	0.016587	
C(2)	-0.008733	-0.588557	0.001988	
N(3)	-0.565821	0.583841	-0.013528	
C(4)	0.364896	1.587780	-0.018757	
H(4)	0.034684	2.614701	-0.034168	
C(5)	1.655982	1.185672	-0.004176	
H(5)	2.546684	1.788813	-0.002125	
C(6)	-0.760814	-1.876473	-0.016109	
H(6)	-0.657330	-2.365344	-0.984880	
H(6)	-0.392457	-2.561752	0.745818	
H(6)	-1.815528	-1.676488	0.158154	
$H_b$	-2.514151	0.576602	-0.022834	
O	-3.460322	0.361286	-0.031191	
$H_{nb}$	-3.825895	0.793245	0.738024	

A2 (Chapter 4) Atomic coordinates of the optimised geometry of 2-MT $\cdots$ H<sub>2</sub>O calculated at the B3LYP(D3BJ)/aug-cc-pVTZ level of theory.

	B3LYP(D3BJ)/aug-cc-pVTZ				
	a /Å	b/Å	c/Å		
S(1)	1.717626	-0.548992	-0.007214		
C(2)	-0.031428	-0.583127	0.013406		
N(3)	-0.565243	0.603913	0.019563		
C(4)	0.381883	1.598419	0.006017		
H(4)	0.064324	2.629596	0.006704		
C(5)	1.671888	1.178818	-0.008756		
H(5)	2.570656	1.770595	-0.020146		
C(6)	-0.801953	-1.862331	0.013144		
H(6)	-0.620070	-2.424780	-0.903832		
H(6)	-0.512318	-2.495094	0.852885		
H(6)	-1.864673	-1.640396	0.083126		
$H_b$	-2.487109	0.611156	-0.006374		
O	-3.430163	0.361207	-0.059433		
$ H_{nb}$	-3.878583	0.891026	0.604414		

A3 (Chapter 4) Atomic coordinates of the optimised geometry of 2-MT $\cdots$ H<sub>2</sub>O calculated at the MP2/aug-cc-pVDZ level of theory.

MP2/aug-cc-pVDZ				
	a /Å	b/Å	c/Å	
S(1)	1.702495	-0.592357	0.022417	
C(2)	-0.045559	-0.564899	-0.008284	
N(3)	-0.555304	0.662438	-0.029851	
C(4)	0.434776	1.620913	-0.023665	
H(4)	0.165830	2.677880	-0.036859	
C(5)	1.732285	1.134843	0.003647	
H(5)	2.668930	1.691122	0.017815	
C(6)	-0.865061	-1.823838	-0.030250	
H(6)	-0.754309	-2.345028	-0.994244	
H(6)	-0.554129	-2.511445	0.770938	
H(6)	-1.922709	-1.560877	0.109322	
$H_b$	-2.500265	0.658189	-0.000240	
O	-3.427496	0.344073	0.029644	
$H_{nb}$	-3.960812	1.147143	0.063598	

A4 (Chapter 4) Atomic coordinates of the optimised geometry of 4-MT $\cdots$ H<sub>2</sub>O calculated at the  $\omega$ B97X-D/aug-cc-pVQZ level of theory.

ωB97X-D/aug-cc-pVQZ				
	a /Å	b/Å	c/Å	
S(1)	2.022138	-0.463750	-0.053039	
C(2)	0.510681	-1.248050	0.110898	
H(2)	0.435180	-2.322442	0.177219	
N(3)	-0.510960	-0.454331	0.142843	
C(4)	-0.129991	0.861572	0.034237	
C(5)	1.210948	1.043290	-0.081379	
H(5)	1.745598	1.971735	-0.180835	
C(6)	-1.174024	1.926922	0.056372	
H(6)	-1.689065	1.932148	1.016878	
H(6)	-0.734364	2.907808	-0.108679	
H(6)	-1.925286	1.737917	-0.709307	
$H_b$	-2.426683	-0.825440	-0.006987	
O	-3.381957	-0.878949	-0.162564	
$H_{nb}$	-3.754232	-1.191681	0.659280	

A5 (Chapter 4) Atomic coordinates of the optimised geometry of 4-MT $\cdots$ H<sub>2</sub>O calculated at the B3LYP(D3BJ)/aug-cc-pVTZ level of theory.

B3LYP(D3BJ)/aug-cc-pVTZ				
	a /Å	b/Å	c/Å	
S(1)	2.048543	-0.434163	-0.015810	
C(2)	0.531089	-1.261319	0.025755	
H(2)	0.480429	-2.338631	0.037296	
N(3)	-0.508232	-0.484435	0.038429	
C(4)	-0.154065	0.849721	0.013730	
C(5)	1.191200	1.064564	-0.016577	
H(5)	1.713605	2.004575	-0.040494	
C(6)	-1.223099	1.891378	0.018329	
H(6)	-1.846435	1.795576	0.907643	
H(6)	-0.794020	2.890831	-0.005945	
H(6)	-1.880317	1.767554	-0.842726	
$H_b$	-2.405256	-0.850513	0.001525	
O	-3.378706	-0.851451	-0.069344	
$H_{nb}$	-3.680910	-1.547101	0.519833	

A6 (Chapter 4) Atomic coordinates of the optimised geometry of 4-MT···H<sub>2</sub>O calculated at the MP2/aug-cc-pVDZ level of theory.

MP2/aug-cc-pVDZ				
	a /Å	b/Å	c/Å	
S(1)	2.098264	-0.330444	-0.000175	
C(2)	0.648656	-1.280138	0.000266	
H(2)	0.688944	-2.369866	0.000440	
N(3)	-0.476447	-0.577919	0.000418	
C(4)	-0.219749	0.780812	0.000180	
C(5)	1.133427	1.101161	-0.000191	
H(5)	1.592007	2.089457	-0.000491	
C(6)	-1.363501	1.756591	0.000186	
H(6)	-1.998345	1.603714	0.886192	
H(6)	-0.986843	2.789683	0.000997	
H(6)	-1.997432	1.604830	-0.886677	
$H_b$	-2.399050	-0.918171	0.000113	
O	-3.370177	-0.798476	-0.000465	
$H_{nb}$	-3.724637	-1.695848	0.001302	

A7 (Chapter 4) Atomic coordinates of the optimised geometry of 5-MT $\cdots$ H<sub>2</sub>O calculated at the  $\omega$ B97X-D/aug-cc-pVQZ level of theory.

ωB97X-D/aug-cc-pVQZ				
	a /Å	b/Å	c/Å	
S(1)	-1.094843	-1.169022	0.016412	
C(2)	0.606365	-0.960226	-0.049631	
H(2)	1.284566	-1.799800	-0.058986	
N(3)	0.994839	0.272890	-0.081158	
C(4)	-0.078202	1.121547	-0.053273	
H(4)	0.090801	2.187781	-0.072187	
C(5)	-1.303401	0.541368	0.000442	
C(6)	-2.640493	1.201188	0.051162	
H(6)	-3.281370	0.877418	-0.768448	
H(6)	-3.157671	0.986094	0.986003	
H(6)	-2.515386	2.279697	-0.024839	
$H_b$	2.944962	0.431497	0.028953	
O	3.903074	0.315986	0.115239	
$\underline{\hspace{1cm}}$	4.269998	0.647495	-0.701634	

A8 (Chapter 4) Atomic coordinates of the optimised geometry of  $5\text{-MT}\cdots H_2O$  calculated at the B3LYP(D3BJ)/aug-cc-pVTZ level of theory.

	B3LYP(D3BJ)/aug-cc-pVTZ				
	a /Å	b/Å	c/Å		
S(1)	-1.178570	-1.151347	0.016925		
C(2)	0.551390	-1.056128	-0.038781		
H(2)	1.165199	-1.942983	-0.044489		
N(3)	1.020029	0.152767	-0.066915		
C(4)	0.006543	1.079362	-0.044084		
H(4)	0.251809	2.130448	-0.059217		
C(5)	-1.261452	0.585962	0.000843		
C(6)	-2.552383	1.332282	0.035127		
H(6)	-3.180244	1.091810	-0.823820		
H(6)	-3.124297	1.107134	0.936229		
H(6)	-2.355975	2.403311	0.019719		
$H_b$	2.937721	0.360068	0.011373		
O	3.909011	0.348758	0.105097		
$H_{nb}$	4.250549	0.600845	-0.756559		

A9 (Chapter 4) Atomic coordinates of the optimised geometry of 5-MT $\cdots$ H<sub>2</sub>O calculated at the MP2/aug-cc-pVDZ level of theory.

MP2/aug-cc-pVDZ				
	a /Å	b/Å	c/Å	
S(1)	-0.953136	-1.211028	0.003870	
C(2)	0.729757	-0.789703	-0.040356	
H(2)	1.512100	-1.549810	-0.051566	
N(3)	0.973697	0.515140	-0.053705	
C(4)	-0.206124	1.223618	-0.027824	
H(4)	-0.181334	2.315012	-0.032760	
C(5)	-1.376631	0.474574	0.004669	
C(6)	-2.798341	0.961845	0.038872	
H(6)	-3.367963	0.607240	-0.834229	
H(6)	-3.318454	0.625077	0.949147	
H(6)	-2.802345	2.062247	0.028039	
$H_b$	2.934277	0.568506	0.017325	
O	3.849344	0.233857	0.093368	
$H_{nb}$	4.315977	0.651425	-0.640987	

A10 (Chapter 4) Nuclear quadrupole coupling constants in the principle nuclear axis framework determined using QDIAG.

	$2-MT\cdots H_2O^a$	2-Methylthiazole <sup>b</sup>	Thiazole <sup>c</sup>
$\chi_{xx}$ (N3) (MHz)	1.663(56)	1.7883(63)	1.83(18)
$\chi_{yy}$ (N3) (MHz)	2.061(23)	2.3876(14)	2.585(11)
$\chi_{zz}$ (N3) (MHz)	-3.724(33)	-4.1759(65)	-4.41(18)
	$4-MT\cdots H_2O^a$	4-Methylthiazole <sup>b</sup>	Thiazole <sup>c</sup>
$\chi_{xx}$ (N3) (MHz)	1.55(47)	1.79(60)	1.83(18)
$\chi_{yy}$ (N3) (MHz)	2.27(23)	2.5385(66)	2.585(11)
$\chi_{zz}$ (N3) (MHz)	-3.82(13)	-4.33(60)	-4.41(18)
	$5-MT\cdots H_2O^a$	5-Methylthiazole <sup>b</sup>	Thiazole <sup>c</sup>
$\chi_{xx}$ (N3) (MHz)	1.56(52)	1.75(43)	1.83(18)
$\chi_{yy}$ (N3) (MHz)	2.05(20)	2.711(14)	2.585(11)
$\chi_{zz}$ (N3) (MHz)	-3.62(37)	-4.46(43)	-4.41(18)

<sup>&</sup>lt;sup>a</sup> Calculated from experimentally determined values of nuclear quadrupole coupling constants,  $\chi_{aa}$ ,  $\chi_{bb}$  and  $\chi_{cc}$  (displayed in Tables 4.2, 4.3 and 4.4) and the off-diagonal term  $\chi_{ab}$  calculated at the  $\omega$ B97X-D/aug-cc-pVQZ level of theory.

<sup>&</sup>lt;sup>b</sup> Calculated from results provided in references 5 – 7 and the off-diagonal term  $\chi_{ab}$  calculated at the  $\omega$ B97X-D/aug-cc-pVQZ level of theory.

<sup>&</sup>lt;sup>c</sup> Results for thiazole provided in reference 2.

A11 (Chapter 4) Molecular parameters of 4-MT···H<sub>2</sub><sup>16</sup>O and 5-MT···H<sub>2</sub><sup>16</sup>O in the rho axis system (RAM) obtained using the BELGI-C<sub>s</sub>-hyperfine code.

D	T.T., 34	4 MT II O	5 MT II O	0
Parameter. <sup>a</sup>	Unit	4-MT···H <sub>2</sub> O	$5-MT\cdots H_2O$	Operator
A	MHz	3590.(17)	4838.4(12)	$P_a^2$
B	MHz	1537.(17)	1105.3(12)	${ m Pb}^2$
C	MHz	958.37546 (84)	892.5059(11)	$P_c^2$
$D_{ab}$	MHz	798.(22)	-270.9(80)	$\{P_a,P_b\}$
extstyle  ext	kHz	0.1101 (97)	0.1479(41)	$-P^4$
$\Delta_{JK}$	kHz	2.579(58)	12.137(23)	$-P^2P_a^2$
$2\chi_{aa}$	MHz	-7.640(71)	-5.96(11)	
$2\chi_{bb}$	MHz	3.23(21)	1.82(31)	
$2\chi_{ab}$	MHz	0.	0.	
$V_3$	cm <sup>-1</sup>	329.(5)	329.(4)	$(1/2)(1-\cos 3\alpha)$
ho	unitless	0.0161(11)	0.0304(16)	$P_aP_{lpha}$
$\overset{\cdot}{F}$	cm <sup>-1</sup>	5.3983 <sup>b</sup>	$5.4909^{b}$	$P_{\alpha}^{2}$
$N_A / N_E / N_q^c$		82/54/136	68/53/121	
$ m rms^d$	kHz	20.5	17.7	

<sup>&</sup>lt;sup>a</sup> All parameters refer to the rho axis system and cannot be directly compared to those referred to the principal axis system.  $P_a$ ,  $P_b$ , and  $P_c$  are the components of the overall rotation angular momentum, P is the angular momentum of the internal rotor rotating about the internal rotor axis by an angle  $\alpha$ . {u,v} is the anti-commutator uv + vu. The product of the parameter and operator from a given row yields the term actually used in the vibration-rotation-torsion Hamiltonian, except for F, and A, which occur in the Hamiltonian in the form  $F(P-P_a)^2 + AP_a^2$ , where  $F = h^2/8\pi^2 cr I_\alpha$  (cm<sup>-1</sup>). Statistical uncertainties are shown as one standard uncertainty in the last digit.

<sup>&</sup>lt;sup>b</sup> Fixed to the value from the XIAM *A/E* fit.

<sup>&</sup>lt;sup>c</sup> Number of *A*- and *E*- species transitions as well as hyperfine components.

<sup>&</sup>lt;sup>d</sup> Root-mean-square deviation of the fit.

A12 (Chapter 4) Inertial defect and planar moments of 2-MT···H<sub>2</sub>O, 4-MT···H<sub>2</sub>O and 5-MT···H<sub>2</sub>O calculated using rotational constants determined from global (XIAM) fits.

	$2-MT\cdots H_2O^a$								
Parameter	$H_2^{16}O$	$H_2^{18}O$	DOH	HOD	$D_2O$				
$\Delta_0$	-1.6408(10)	-1.6451(9)	-1.6696(11)	-1.7569(14)	-1.8122(15)				
$P_{aa}$	367.8193(5)	391.4143(4)	373.8073(5)	383.2605(7)	389.1330(8)				
$P_{bb}$	135.3714(5)	135.5903(4)	135.8092(5)	136.2299(7)	136.6269(8)				
$P_{cc}$	0.8204(5)	0.8225(4)	0.8348(5)	0.8784(7)	0.9061(8)				
		4-M7	$\Gamma$ ···H <sub>2</sub> O						
Parameter	$H_2^{16}O$	$H_2^{18}O$	DOH	HOD	$D_2O$				
$\Delta_0$	-3.6540(23)	-3.6493(27)	-3.6453(32)	-3.859(4)	-3.861(4)				
$P_{aa}$	398.3404(12)	421.4885(13)	403.7909(16)	412.7571(22)	418.1207(20)				
$P_{bb}$	128.9856(12)	130.1384(13)	129.8368(16)	130.7168(22)	131.5055(20)				
$P_{cc}$	1.8270(12)	1.8247(13)	1.8227(16)	1.9293(22)	1.9305(20)				
		5-M7	$\Gamma$ ···H <sub>2</sub> O						
Parameter	$H_2^{16}O$	$H_2^{18}O$	DOH	HOD	$D_2O$				
$\Delta_0$	-3.2681(22)	-3.2541(26)	-3.2719(22)	-3.668(6)	-3.677(4)				
$P_{aa}$	463.8443(11)	493.0632(13)	472.2396(11)	482.7168(31)	490.9310(21)				
$P_{bb}$	102.3986(11)	102.4574(13)	102.9455(11)	102.8196(31)	103.3429(21)				
$P_{cc}$	1.6340(11)	1.6270(13)	1.6360(11)	1.8339(31)	1.8387(21)				

<sup>&</sup>lt;sup>a</sup> Planar moments and inertial defect for 2-MT···H<sub>2</sub>O calculated using results of effective (*A*-species only fits).

A13 (Chapter 4) Atomic coordinates of 2-MT $\cdots$ H<sub>2</sub>O and 5-MT $\cdots$ H<sub>2</sub>O determined by the  $r_0$  method.

	2-MT···H₂O						
	a /Å	b/Å	c/Å				
S(1)	-1.71506(203)	-0.54218(453)	0.00767(1)				
C(2)	0.01255(217)	-0.57866(237)	0.00518(2)				
N(3)	0.55200(257)	0.60202(452)	-0.00120(2)				
C(4)	-0.39367(651)	1.59187(75)	-0.00870(1)				
H(4)	-0.07888(1063)	2.62368(200)	-0.01723(1)				
C(5)	-1.67859(484)	1.17034(438)	-0.00513(2)				
H(5)	-2.57827(719)	1.76002(797)	-0.00682(5)				
C(6)	0.78404(725)	-1.85500(545)	-0.01318(5)				
H(6)	1.83440(640)	-1.63996(964)	0.16952(6)				
H(6)	0.69481(917)	-2.34103(510)	-0.98484(5)				
H(6)	0.42063(1003)	-2.54918(399)	0.74311(5)				
$H_b$	2.53917(724)	0.53304(5398)	0.00412(34)				
O	3.47761(473)	0.33650(176)	0.00770(3)				
$H_{nb}$	3.90287(4622)	1.19582(2652)	0.00313(29)				
	5-MT·						
	a /Å	b/Å	c/Å				
S(1)	-0.94979(239)	-1.19794(30)	0.00116(0)				
C(2)	0.71300(153)	-0.77719(311)	-0.00328(0)				
H(2)	1.49104(306)	-1.52518(470)	-0.01035(0)				
N(3)	0.94458(109)	0.49510(358)	-0.00282(0)				
C(4)	-0.22679(254)	1.20250(118)	0.00137(0)				
H(4)	-0.19233(475)	2.28165(126)	0.00009(1)				
C(5)	-1.37066(105)	0.47299(116)	0.00383(0)				
C(6)	-2.78094(204)	0.95966(405)	-0.00191(0)				
H(6)	-3.34457(125)	0.57274(520)	0.84652(0)				
H(6)	-3.30211(144)	0.66540(511)	-0.91266(0)				
H(6)	-2.78936(426)	2.04651(406)	0.05551(1)				
$H_b$	2.94797(465)	0.46306(2502)	0.00003(1)				
O	3.87466(222)	0.21701(124)	0.00133(0)				
$H_{nb}$	4.34490(2079)	1.05258(1338)	0.00208(3)				

A14 (Chapter 4) Atomic coordinates of 4-MT $\cdots$ H<sub>2</sub>O determined by the  $r_0$  method. Fit 1 assumes  $\angle$ (O-H<sub>b</sub> $\cdots$ N3-C2) = 0° and  $\angle$ (H<sub>nb</sub>-O-H<sub>b</sub> $\cdots$ N3) = 180°. Fit 2 assumes  $\angle$ (O-H<sub>b</sub> $\cdots$ N3-C2) = 180° and  $\angle$ (H<sub>nb</sub>-O-H<sub>b</sub> $\cdots$ N3) = 180°.

_	4-MT…F	I <sub>2</sub> O (Fit 1)	
	a /Å	<i>b</i> /Å	c/Å
S(1)	-2.05372(128)	0.42194(309)	0.00165(0)
C(2)	-0.56138(314)	1.25824(31)	-0.00102(1)
H(2)	-0.51720(557)	2.33643(41)	-0.00484(2)
N(3)	0.48579(144)	0.49790(267)	-0.00261(1)
C(4)	0.14210(169)	-0.83262(189)	-0.00242(0)
C(5)	-1.19686(220)	-1.05983(115)	-0.00094(1)
H(5)	-1.70604(433)	-2.00773(230)	-0.00256(1)
C(6)	1.21999(400)	-1.86393(434)	0.00060(0)
H(6)	1.80731(384)	-1.79481(567)	0.91612(0)
H(6)	0.80220(627)	-2.86544(339)	0.07067(1)
H(6)	1.90331(364)	-1.70104(590)	-0.83180(1)
$H_b$	2.50497(1568)	0.66944(7688)	-0.00020(24)
O	3.42860(681)	0.92674(247)	-0.00150(1)
$H_{nb}$	3.90896(6464)	0.09695(4341)	-0.00084(21)
	4-MT···H	I <sub>2</sub> O (Fit 2)	
	a /Å	b/Å	c/Å
S(1)	-2.05744(73)	0.41347(184)	0.00164(0)
C(2)	-0.57105(184)	1.26031(19)	-0.00099(1)
H(2)	-0.53449(329)	2.33879(24)	-0.00479(1)
N(3)	0.48148(85)	0.50740(160)	-0.00257(1)
C(4)	0.14721(104)	-0.82552(115)	-0.00242(0)
C(5)	-1.19011(135)	-1.06220(67)	-0.00095(0)
H(5)	-1.69257(262)	-2.01368(135)	-0.00260(1)
C(6)	1.23237(240)	-1.84918(261)	0.00061(0)
H(6)	1.81917(230)	-1.77593(340)	0.91614(0)
H(6)	0.82167(375)	-2.85362(206)	-0.07068(0)
H(6)	1.91454(217)	-1.68144(353)	-0.83178(0)
$H_b$	2.48184(181)	0.85039(4841)	0.00038(16)
O	3.43945(400)	0.80270(169)	0.00108(1)
$H_{nb}$	3.72539(4398)	1.71787(1650)	0.00442(1)

A15 (Chapter 4) Results of a new fit of structural parameters of thiazole...H<sub>2</sub>O (ref 24) using STRFIT.

The original fit of geometrical parameters of ref 24 was performed to 3 experimentally-determined moments of inertia for each of 7 isotopologues of thiazole···H<sub>2</sub>O (where isotopic substitutions were available at each of S1, C2, N3, C4, C5 of thiazole; and O of H<sub>2</sub>O).

A new fit of the data from ref 24 to determine revised geometrical parameters for thiazole···H<sub>2</sub>O is presented. The initial assumptions about the molecular geometry (the values of geometrical parameters used within the z-matrix) and the number of parameters determined by the fit are unchanged from ref 24. The new fit is performed to the 3 experimentally-determined moments of inertia for each of the 7 isotopologues listed above and also the 3 experimentally-determined moments of inertia for each of D<sub>2</sub>O, HOD and DOH (amounting to a total of 30 experimentally-determined moments of inertia). The experimentally-determined results used are those which were originally presented in ref 24. The parameters and coordinates determined by the new  $r_0$  fit are consistent with the  $r_s$  and  $r_e$  geometries presented in ref 24.

The inclusion of the results for the deuterium-containing isotopologues in the new fit yields more reliable and accurate  $r_0$  values for the  $r(H_b \cdots N3)$ ,  $\angle(H_b \cdots N3-C2)$  and  $\angle(O-H_b \cdots N3)$  parameters than was achieved previously. The results of the new fit are included in Table 4.10 and referred to within the discussion of the present work.

## Input data

11	<del></del>	
1 0 0 0 0.000000	0.000000  0.000000	31.9720700
2 1 0 0 1.723108	0.000000  0.000000	12.0000000
2 1 0 0 1.723108 3 2 1 0 1.301222	114.515541 0.000000	14.0030744
4 3 2 1 1.370566	111.142830 0.000000	12.0000000
5 4 3 2 1.361370	115.214000 0.000000	12.0000000
6 5 4 3 1.076695	128.557000 180.000000	1.0078252
7 4 3 2 1.079538	119.486717 180.000000	1.0078252
8 2 1 5 1.079922	122.046783 180.000000	1.0078252
9 3 2 5 2.897063	96.586000 180.000000	15.9949150
10 9 3 1 0.974476	13.614087 180.000000	1.0078250
11 9 10 3 0.961762	105.303000 180.000000	1.0078250
NO OF PARAMETERS T	ГО BE FITTED: 11	
atom no., parameter no.	FIX 2 1 0	C2-S1
atom no., parameter no.	FIX 3 1 0	N3-C2
atom no., parameter no.	FIX 4 1 0	C4-N3
atom no., parameter no.	FIX 5 1 0	C5-S1
atom no., parameter no.	9 1 0	O9-N3
atom no., parameter no.	FIX 3 2 0	N3-C2-S1
atom no., parameter no.	FIX 4 2 0	C4-N3-C2
atom no., parameter no.	FIX 5 2 0	C5-S1-C2
atom no., parameter no.	9 2 0	O9-N3-C2
atom no., parameter no.	10 2 0	H10-O9-N3
atom no., parameter no.	FIX11 3 0	H11-O9-H10-N3
!		
! parameters		
!		
NO OF CONSTANTS TO		
constant, species, value	1 1 6435.2234	parent
constant, species, value	2 1 1513.00819	
constant, species, value	3 1 1225.07882	
constant, species, value	1 2 6327.748	34S1 atom numbering from paper
constant, species, value	2 2 1493.7502	
constant, species, value	3 2 1208.5412	
constant, species, value	1 3 6399.573	13C2
constant, species, value	2 3 1512.96825	

constant, species, value	3 3 1223.76061	
constant, species, value	1 4 6408.43	15N3
constant, species, value	2 4 1511.17055	
constant, species, value	3 4 1222.92237	
constant, species, value	1 5 6268.854	13C4
constant, species, value	2 5 1512.36278	
constant, species, value	3 5 1218.46091	
constant, species, value	1 6 6374.863	13C5
constant, species, value	2 6 1500.96105	
constant, species, value	3 6 1214.98332	
constant, species, value	1 7 6422.4245	18O10
constant, species, value	2 7 1414.51745	
constant, species, value	3 7 1159.25831	
constant, species, value	1 8 6412.9180	D2O
constant, species, value	2 8 1414.74304	
constant, species, value	3 8 1160.01027	
constant, species, value	1 9 6441.4602	DOH
constant, species, value	2 9 1481.23741	
constant, species, value	3 9 1204.41989	
constant, species, value	110 6407.3711	HOD
constant, species, value	210 1443.01445	
constant, species, value	310 1178.65137	

Final cycle of fit (includes results for atomic coordinates) of structural parameters of thi···(H<sub>2</sub>O).

after: 6 iterations, ALAMDA= 0.10E-08

# FINAL RESULTS OF LEAST SQUARES FIT:

```
R(2, 1) = [1.723108]
                                 FIXED
                                            C2-S1
   R(3,2) = \begin{bmatrix} 1.301222 \end{bmatrix}
R(4,3) = \begin{bmatrix} 1.370566 \end{bmatrix}
R(5,4) = \begin{bmatrix} 1.361370 \end{bmatrix}
                                 FIXED
                                            N3-C2
                                            C4-N3
                                 FIXED
                                 FIXED
                                            C5-S1
    R(9,3) =
                  2.939587 + 0.002099
                                            O9-N3
 A(3, 2, 1) = [114.515541]
                                  FIXED
                                              N3-C2-S1
 A(4, 3, 2) = [111.142830]
                                   FIXED
                                              C4-N3-C2
 A(5, 4, 3) = [115.214000]
                                  FIXED
                                              C5-S1-C2
 A(9, 3, 2) = 
                  91.980010 +- 0.137139 O9-N3-C2
  A(10, 9, 3) = 7.408358 + 1.074698 H10-O9-N3
D(11, 9, 10, 3) = [180.000000] FIXED
                                                H11-O9-H10-N3
```

Chi-squared = 1.2055359648 Deviation of fit = 0.211304

Ni Axi	s Iobs	Icalc	Io-c	Bobs	Bcalc	Во-с
1 a 1 b			89 0.01936 382 0.0288		_	6436.8099 -1.5865 1513.1388 -0.1306
1 c	412.52775	412.50	771 0.0200	4 122	25.0788	1225.1383 -0.0595
2 a	79.86712	79.846	74 0.02038	6327	7.7480	6329.3634 -1.6154
2 b	338.32900	338.33	477 -0.0057	7 149	93.7502	1493.7247 0.0255
2 c	418.17276	418.18	151 -0.0087	5 120	08.5412	1208.5159 0.0253
3 a	78.97074	78.9463	35 0.02439	6399	9.5730	6401.5500 -1.9770
3 b	334.03147	334.04	617 -0.0147	0 15	12.9682	1512.9017 0.0666
3 c	412.97212	412.992	252 -0.0204	0 122	23.7606	1223.7001 0.0605
4 a	78.86159	78.837	75 0.02384	6408	3.4300	6410.3681 -1.9381

```
4 b
                334.41061 0.01823
                                       1511.1706 1511.2529 -0.0824
     334.42884
                                       1222.9224 1222.9426 -0.0202
4
     413.25518
                413.24836 0.00682
  c
5
      80.61745
                80.60669 0.01075
                                      6268.8540 6269.6903
  a
                                                           -0.8363
5
  b
     334.16520
                334.15650 0.00870
                                       1512.3628
                                                  1512.4021
                                                             -0.0394
5
     414.76834
                414.76320 0.00514
                                       1218.4609 1218.4760 -0.0151
  c
6
      79.27684
                79.27413 0.00271
                                      6374.8630 6375.0810 -0.2180
  a
     336.70361
6
  b
                336.66826 0.03536
                                       1500.9610 1501.1187
                                                             -0.1576
6
  c
     415.95551
                415.94239 0.01312
                                       1214.9833 1215.0217
                                                            -0.0383
7
      78.68975
                78.65228 0.03747
                                      6422.4245 6425.4844 -3.0599
  a
7
     357.28015
  b
                357.57467 -0.29452
                                       1414.5175 1413.3524
7
     435.95030
                436.22695 -0.27665
                                       1159.2583 1158.5231
                                                             0.7352
  c
8
      78.80640
                78.72580 0.08060
                                      6412.9180 6419.4837 -6.5657
  a
8
  b
     357.22318
                356.95302 0.27017
                                       1414.7430 1415.8138
                                                             -1.0708
8
     435.66770
                435.67882 -0.01112
                                       1160.0103
                                                 1159.9807
                                                             0.0296
  c
9
                                                            5.8404
      78.45721
                78.52841 -0.07120
                                      6441.4602 6435.6198
  a
9
     341.18704
                                       1481.2374 1483.8146
  b
                340.59444 0.59260
                                                             -2.5772
9
                                       1204.4199 1205.8016 -1.3817
  c
     419.60367
                419.12286 0.48082
10 a
                                      6407.3711 6420.2804 -12.9093
      78.87463
                 78.71603 0.15859
10 b
      350.22450
                350.54874 -0.32424
                                        1443.0144 1441.6797
                                                              1.3347
      428.77735 429.26477 -0.48742
                                        1178.6514 1177.3130
10
  c
                                                              1.3383
```

#### Correlation coefficients:

1 2 3

1: R(9,3) 1.000

2:  $A(\hat{9}, \hat{3}, \hat{2}) -0.706 \ 1.000$ 

3: A(10, 9, 3) -0.565 -0.157 1.000

# Final principal coordinates of parent:

ATOM	NO.	A	В	C	MASS
1	-1.485	134	-0.832064	0.000000	31.9720700
2	0.229	338	-0.659772	0.000000	12.0000000
3	0.648	182	0.572198	0.000000	14.0030744
4	-0.402	964	1.451710	0.000000	12.0000000
5	-1.638	125	0.879253	0.000000	12.0000000
6	-2.601	051	1.360963	0.000000	1.0078252
7	-0.207	474	2.513400	0.000000	1.0078252
8	0.891	012	-1.513247	0.000000	1.0078252
9	3.462	351	-0.277287	0.000000	15.9949150
10	2.573	3549	0.122255	0.000000	1.0078250
11	4.074	1215	0.464743	0.000000	1.0078250

#### Principal coordinates and estimated uncertainties:

ATOM NO.	A	dA	В	dB	C	dC	
1 -1.485 2 0.2293 3 0.648 4 -0.4025 5 -1.638 6 -2.6016	34 0.0 18 0.0 96 0.0 12 0.0 05 0.0	0119 0095 0247 0148 0232		0.00164 0.00237 0.00055 0.00160 0.00326	0.0 0.0 0.0 0.0 0.0	0000 0000 0000 0000 0000	0.00000 0.00000 0.00000 0.00000 0.00000 0.00000
7 -0.207 8 0.891			2.51340 -1.51325				0.00000 $0.00000$

```
    9
    3.46235
    0.00142
    -0.27729
    0.00019
    0.00000
    0.00000

    10
    2.57355
    0.00623
    0.12226
    0.01673
    0.00000
    0.00000

    11
    4.07421
    0.01274
    0.46474
    0.01179
    0.00000
    0.00000
```

NOTES: 1/ only the uncertainties for those coordinates which are completely defined by the fitted internals should be trusted 2/ the uncertainties are somewhat limited by the linear approximation coord=(d coord/d parameter)\*parameter used for evaluation 3/ only the effect of the internals R, A, and D is propagated

Selected internal coordinates were determined from the a, b, c coordinates (as given above) using the EVAL program available from the ProSpe website as shown below.

\_\_\_\_\_

```
EVAL - Internals and their errors from Cartesians
```

version 22.X.2012

Zbigniew KISIEL

#### WARNING:

The EVAL uncertainties are evaluated by assuming that the correlation matrix is a unit matrix.

The EVAL uncertainties may thus differ significantly (but typically by not more than 30% either way) from uncertainties in explicitly fitted internals corresponding to the input Cartesians.

! Thiazole\_H2O test

#### **INPUT CARTESIANS:**

1S	-1.48513 0.00149	-0.83206 0.00133	$0.00000 \ 0.00000$
2C	0.22934 0.00119	-0.65977 0.00164	$0.00000 \ 0.00000$
3N	0.64818 0.00095	0.57220 0.00237	$0.00000 \ 0.00000$
4C	-0.40296 0.00247	1.45171 0.00055	$0.00000 \ 0.00000$
5C	-1.63812 0.00148	0.87925 0.00160	$0.00000 \ 0.00000$
6H	-2.60105 0.00232	1.36096 0.00326	$0.00000 \ 0.00000$
7H	-0.20747 0.00431	2.51340 0.00088	$0.00000 \ 0.00000$
8H	0.89101 0.00267	-1.51325 0.00279	$0.00000 \ 0.00000$
9O	3.46235 0.00142	-0.27729 0.00019	$0.00000 \ 0.00000$
10H	2.57355 0.00623	0.12226 0.01673	$0.00000 \ 0.00000$
11H	4.07421 0.01274	0.46474 0.01179	$0.00000 \ 0.00000$

### **CALCULATED INTERNALS:**

```
! Bond lengths
!

3N 9O = 2.93959 +- 0.00177
3N 10H = 1.97724 +- 0.00724
8H 9O = 2.85296 +- 0.00298
!
! Bond angles
!

9O 10H 3N = 168.94765 +- 1.38434
10H 3N 2C = 95.62338 +- 0.48867
11H 9O 3N = 112.71112 +- 0.73971
9O 3N 2C = 91.97974 +- 0.10150
3N 9O 10H = 7.40871 +- 0.91081
9O 3N 1S = 129.84787 +- 0.09450
```

A16 (Chapter 4) NBO stabilisation energy contributions ( $\geq 0.21~kJ~mol^{-1}$ ) of 2-MT···H<sub>2</sub>O, 4-MT···H<sub>2</sub>O and 5-MT···H<sub>2</sub>O calculated at the B3LYP(D3BJ)/aug-cc-pVTZ level of theory.

-	$2\text{-MT}\cdots \text{H}_2\text{O}$							
Donor NBO	Acceptor NBO	$E^{(2)}$ (kcal mol <sup>-1</sup> )	E <sup>(2)</sup> (kJ mol <sup>-1</sup> )					
σ(S1–C2)	$\sigma^*(H_b-O)$	0.15	0.63					
σ(C4–C5)	$\sigma^*(H_b-O)$	0.09	0.38					
<b>LP(1) N3</b>	$\sigma^*(H_b-O)$	9.43	39.46					
$\sigma(H_b-O)$	$\sigma^*(C4-N3)$	0.15	0.63					
$\sigma(H_b-O)$	σ*(C6-H6)	0.05	0.21					
LP(1) O	$\sigma^*(C2-N3)$	0.05	0.21					
<b>LP(2) O</b>	σ*(C6-H6)	0.71	2.97					
	4-MT	···H <sub>2</sub> O						
Donor NBO	Acceptor NBO	$E^{(2)}$ (kcal mol <sup>-1</sup> )	$E^{(2)}$ (kJ mol <sup>-1</sup> )					
$\sigma(S1-C2)$	$\sigma^*(H_b-O)$	0.13	0.54					
σ(C4–C5)	$\sigma^*(H_b-O)$	0.09	0.38					
LP(1) N3	$\sigma^*(H_b-O)$	9.02	37.74					
$\sigma(H_b-O)$	$\sigma^*(C2-N3)$	0.10	0.42					
<b>LP(2) O</b>	σ*(C6-H6)	0.10	0.42					
	5-MT	···H <sub>2</sub> O						
Donor NBO	Acceptor NBO	$E^{(2)}$ (kcal mol <sup>-1</sup> )	$E^{(2)}$ (kJ mol <sup>-1</sup> )					
$\sigma(S1-C2)$	$\sigma^*(H_b-O)$	0.09	0.38					
σ(C4–C5)	$\sigma^*(H_b-O)$	0.09	0.38					
<b>LP(1) N3</b>	$\sigma^*(H_b-O)$	8.58	35.90					
$\sigma(H_b-O)$	$\sigma^*(N3-C4)$	0.17	0.71					
LP(2) O	σ*(S1–C2)	0.06	0.25					

A17 (Chapter 5) Atomic coordinates of the optimised geometry of 2-EF···H<sub>2</sub>O (C<sub>1</sub> conformer) calculated at the  $\omega$ B97X-D/aug-cc-pVQZ level of theory.

	ωB97X-D/aug-cc-pVQZ				
	a /Å	b/Å	c /Å		
O(1)	-0.202337	0.696740	-0.213717		
C(2)	-0.396520	-0.562417	0.266850		
C(3)	-1.722678	-0.796063	0.382752		
H(3)	-1.429460	2.263243	-0.784533		
C(4)	-2.391869	0.392121	-0.051901		
H(4)	-3.451721	0.569479	-0.099772		
C(5)	-1.422730	1.259698	-0.400218		
H(5)	-2.172797	-1.706615	0.737385		
C(6)	0.818399	-1.376204	0.528373		
H(6)	1.477109	-0.829388	1.206141		
H(6)	0.502239	-2.281329	1.046159		
C(7)	1.589364	-1.734765	-0.742991		
H(7)	1.931493	-0.837135	-1.255200		
H(7)	2.466749	-2.331993	-0.499089		
H(7)	0.962811	-2.305380	-1.427955		
$H_b$	1.637693	1.472884	0.050482		
$\mathrm{O}_{\mathrm{W}}$	2.564858	1.648473	0.233421		
$ H_{nb}$	2.564845	2.315022	0.917698		

A18 (Chapter 5) Atomic coordinates of the optimised geometry of 2-EF $\cdots$ H<sub>2</sub>O (C<sub>1</sub> conformer) calculated at the B3LYP(D3BJ)/aug-cc-pVTZ level of theory.

B3LYP(D3BJ)/aug-cc-pVTZ			
	a /Å	b/Å	c/Å
O(1)	-0.195267	0.717998	-0.123455
C(2)	-0.409855	-0.583572	0.266068
C(3)	-1.745331	-0.819374	0.293998
H(3)	-1.407727	2.321305	-0.652704
C(4)	-2.398782	0.396044	-0.096849
H(4)	-3.456854	0.569828	-0.184426
C(5)	-1.418546	1.294239	-0.338541
H(5)	-2.212826	-1.751058	0.560765
C(6)	0.791576	-1.414825	0.530831
H(6)	1.418510	-0.918764	1.275672
H(6)	0.449749	-2.351001	0.973266
C(7)	1.628138	-1.696196	-0.724272
H(7)	2.008862	-0.770779	-1.152631
H(7)	2.483218	-2.324756	-0.476154
H(7)	1.032152	-2.207842	-1.480246
$H_b$	1.619917	1.484939	0.091150
${ m O}_{ m W}$	2.571163	1.622233	0.196075
$H_{nb}$	2.660380	2.428093	0.711543

A19 (Chapter 5) Atomic coordinates of the optimised geometry of 2-EF $\cdots$ H<sub>2</sub>O (C<sub>1</sub> conformer) calculated at the B3LYP(D3BJ)/Def2-TZVP of theory.

	B3LYP(D3BJ)/Def2-TZVP				
	a /Å	b/Å	c/Å		
O(1)	0.200334	0.697577	0.212461		
C(2)	0.389886	-0.576079	-0.268183		
C(3)	1.721705	-0.810493	-0.378364		
H(3)	2.172789	-1.724671	-0.725518		
C(4)	2.398026	0.378165	0.053591		
H(4)	3.460771	0.545205	0.098458		
C(5)	1.433885	1.259598	0.400311		
H(5)	1.441696	2.265812	0.778784		
C(6)	-0.826797	-1.388059	-0.524603		
H(6)	-1.476873	-0.857254	-1.226033		
H(6)	-0.507532	-2.308395	-1.016796		
C(7)	-1.623038	-1.712728	0.745211		
H(7)	-1.984859	-0.800471	1.218467		
H(7)	-2.490252	-2.328222	0.502351		
H(7)	-1.005492	-2.254121	1.463719		
$H_b$	-1.611225	1.490818	-0.025913		
$\mathrm{O}_{\mathrm{W}}$	-2.536881	1.678719	-0.234494		
$H_{nb}$	-2.514820	2.187429	-1.050785		

A20 (Chapter 5) Atomic coordinates of the optimised geometry of 2-EF $\cdots$ H<sub>2</sub>O (C<sub>1</sub> conformer) calculated at the MP2/aug-cc-pVDZ of theory.

MP2/aug-cc-pVDZ			
	a /Å	b/Å	c/Å
O(1)	-0.228585	0.715221	-0.243003
C(2)	-0.368712	-0.561812	0.274354
C(3)	-1.712943	-0.845416	0.416030
H(3)	-1.540435	2.240705	-0.826624
C(4)	-2.439291	0.313792	-0.030748
H(4)	-3.517872	0.455825	-0.064550
C(5)	-1.491362	1.233869	-0.420115
H(5)	-2.122601	-1.778657	0.798341
C(6)	0.890370	-1.329083	0.516251
H(6)	1.540903	-0.768807	1.208564
H(6)	0.604311	-2.268689	1.015926
C(7)	1.655591	-1.623767	-0.786409
H(7)	1.969145	-0.686695	-1.269563
H(7)	2.559907	-2.215549	-0.576321
H(7)	1.021750	-2.187893	-1.488604
$H_b$	1.581227	1.533723	0.102100
$\mathbf{O}_{\mathrm{W}}$	2.529420	1.594169	0.299425
$H_{nb}$	2.660937	2.511326	0.570066

A21 (Chapter 5) Atomic coordinates of the optimised geometry of 2-EF···H<sub>2</sub>O ( $C_s$  conformer) calculated at the  $\omega B97X$ -D/aug-cc-pVQZ level of theory.

	ωB97X-D/aug-cc-pVQZ				
	a /Å	b/Å	c /Å		
O(1)	0.362762	0.835485	0.175611		
C(2)	-0.440181	-0.256448	0.057435		
C(3)	-1.718808	0.144057	-0.118855		
H(3)	-2.572975	-0.497371	-0.243400		
C(4)	-1.706112	1.576108	-0.110720		
H(4)	-2.545812	2.238457	-0.225142		
C(5)	-0.422239	1.938069	0.069168		
H(5)	0.080124	2.885506	0.137521		
C(6)	0.226202	-1.582260	0.142633		
H(6)	1.027083	-1.622672	-0.598871		
H(6)	0.716889	-1.668859	1.115237		
C(7)	-0.738680	-2.741769	-0.058775		
H(7)	-1.215507	-2.689697	-1.037250		
H(7)	-0.208522	-3.689840	0.008227		
H(7)	-1.521924	-2.740646	0.699306		
$H_b$	2.343960	0.566464	-0.042446		
$\mathbf{O}_{\mathbf{W}}$	3.252111	0.288964	-0.191218		
$H_{nb}$	3.676617	0.353835	0.662091		

A22 (Chapter 5) Atomic coordinates of the optimised geometry of 2-EF $\cdots$ H<sub>2</sub>O (C<sub>s</sub> conformer) calculated at the B3LYP(D3BJ)/aug-cc-pVTZ level of theory.

	B3LYP(D3BJ)/aug-cc-pVTZ				
	a /Å	b/Å	c/Å		
O(1)	0.526481	0.727421	0.266411		
C(2)	-0.486888	-0.182229	0.078229		
C(3)	-1.637166	0.486037	-0.186269		
H(3)	-2.597195	0.041054	-0.377164		
C(4)	-1.325493	1.886689	-0.163589		
H(4)	-2.000247	2.707222	-0.333279		
C(5)	-0.006681	1.980041	0.112424		
H(5)	0.676951	2.800466	0.226615		
C(6)	-0.121613	-1.617595	0.198869		
H(6)	0.703693	-1.832847	-0.484682		
H(6)	0.272152	-1.800882	1.203036		
C(7)	-1.295255	-2.552523	-0.078192		
H(7)	-1.680861	-2.410684	-1.087925		
H(7)	-0.983206	-3.591208	0.019405		
H(7)	-2.112693	-2.379975	0.622403		
$H_b$	2.398227	0.123433	-0.013604		
$\mathrm{O}_{\mathrm{W}}$	3.226310	-0.312483	-0.256177		
$H_{nb}$	3.786793	-0.246944	0.521523		

A23 (Chapter 5) Atomic coordinates of the optimised geometry of 2-EF $\cdots$ H<sub>2</sub>O (C<sub>s</sub> conformer) calculated at the B3LYP(D3BJ)/Def2-TZVP of theory.

B3LYP(D3BJ)/Def2-TZVP			
	a /Å	b/Å	c/Å
O(1)	-0.278721	-0.866109	0.335161
C(2)	0.411286	0.298308	0.098757
C(3)	1.690334	-0.005434	-0.236000
H(3)	2.466921	0.699666	-0.476349
C(4)	1.803941	-1.435651	-0.208830
H(4)	2.679916	-2.023860	-0.423266
C(5)	0.587789	-1.908685	0.140292
H(5)	0.181446	-2.893255	0.285546
C(6)	-0.351499	1.564251	0.255957
H(6)	-1.251410	1.514183	-0.364285
H(6)	-0.706062	1.638614	1.289956
C(7)	0.469226	2.800094	-0.099646
H(7)	0.803399	2.764424	-1.137670
H(7)	-0.128306	3.702371	0.030237
H(7)	1.351532	2.886984	0.536708
$\hat{H_b}$	-2.238405	-0.794909	-0.101929
$\mathbf{O}_{\mathrm{W}}$	-3.154717	-0.565523	-0.309510
$ H_{nb}$	-3.571173	-0.405453	0.542989

A24 (Chapter 5) Atomic coordinates of the optimised geometry of 2-EF $\cdots$ H<sub>2</sub>O (C<sub>s</sub> conformer) calculated at the MP2/aug-cc-pVDZ of theory.

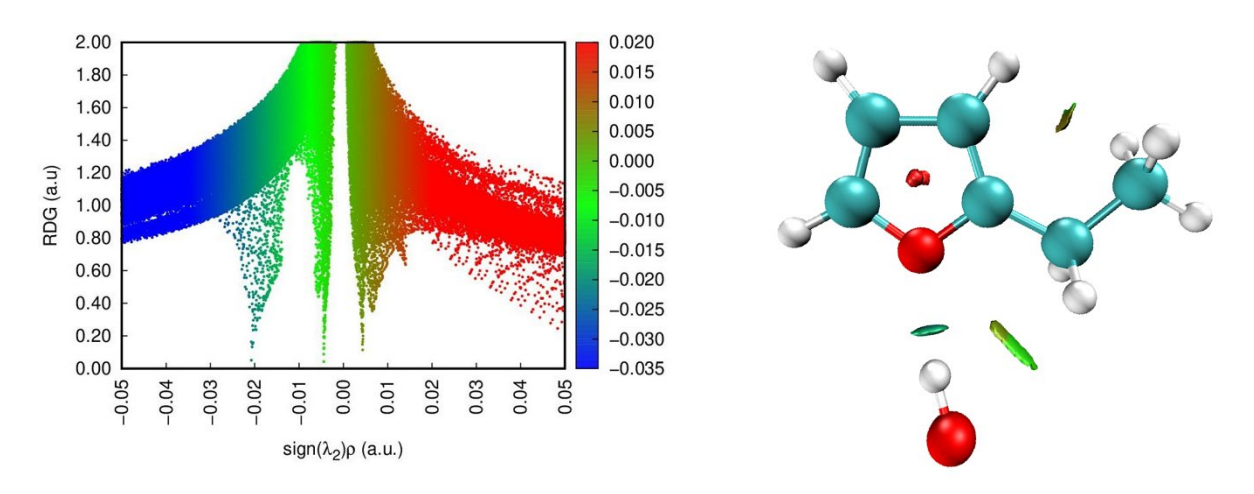
	MP2/aug-cc-pVDZ			
	a /Å	b/Å	c/Å	
O(1)	-0.307628	-0.883336	-0.490782	
C(2)	-0.154620	0.444062	-0.127455	
C(3)	-1.352490	0.918843	0.370246	
H(3)	-1.881097	-2.266341	-0.453931	
C(4)	-2.292248	-0.170448	0.314470	
H(4)	-3.336665	-0.168032	0.620942	
C(5)	-1.608440	-1.241828	-0.214374	
H(5)	-1.535279	1.928585	0.731468	
C(6)	1.197266	1.046987	-0.342614	
H(6)	1.948171	0.464886	0.217263	
H(6)	1.463205	0.958728	-1.410340	
C(7)	1.231963	2.517681	0.089909	
H(7)	0.994789	2.617169	1.160696	
H(7)	2.233177	2.940948	-0.078004	
H(7)	0.506555	3.116376	-0.483051	
$H_b$	1.377880	-1.906939	0.049968	
$O_{ m W}$	2.282794	-2.048955	0.369569	
$H_{nb}$	2.347267	-3.003827	0.494934	

A25 (Chapter 5) Atomic coordinates of 2-EF···H<sub>2</sub>O determined by the  $r_0$  method.

	a /Å	b/Å	c/Å
O(1)	0.20583(177)	-0.69954(64)	-0.22058(86)
C(2)	0.41671(123)	0.55398(60)	0.26774(6)
C(3)	1.74567(167)	0.76649(231)	0.39225(97)
H(3)	2.20780(358)	1.66815(308)	0.75421(177)
C(4)	2.39891(118)	-0.42964(373)	-0.04497(75)
H(4)	3.45620(154)	-0.62312(583)	-0.08789(135)
C(5)	1.41846(296)	-1.28033(193)	-0.40327(37)
H(5)	1.41187(512)	-2.28180(206)	-0.79284(92)
C(6)	-0.78698(292)	1.38508(288)	0.52681(39)
H(6)	-1.45785(217)	0.84500(449)	1.19799(112)
H(6)	-0.45983(494)	2.28247(251)	1.05111(34)
C(7)	-1.54514(314)	1.76214(380)	-0.74692(68)
H(7)	-1.89817(152)	0.87263(429)	-1.26575(140)
H(7)	-2.41455(440)	2.37157(562)	-0.50475(93)
H(7)	-0.90598(396)	2.32659(227)	-1.42539(11)
$H_b$	-1.73002(410)	-1.45273(98)	0.05196(26)
$\mathrm{O}_{\mathrm{W}}$	-2.66160(426)	-1.60481(210)	0.23348(71)
$H_{nb}$	-2.66627(496)	-2.27289(213)	0.91625(86)

A26 (Chapter 5) NBO stabilisation energy contributions ( $\geq 0.21~kJ~mol^{-1}$ ) of 2-EF···H<sub>2</sub>O (C<sub>1</sub> conformer) calculated at the B3LYP(D3BJ)/aug-cc-pVTZ level of theory.

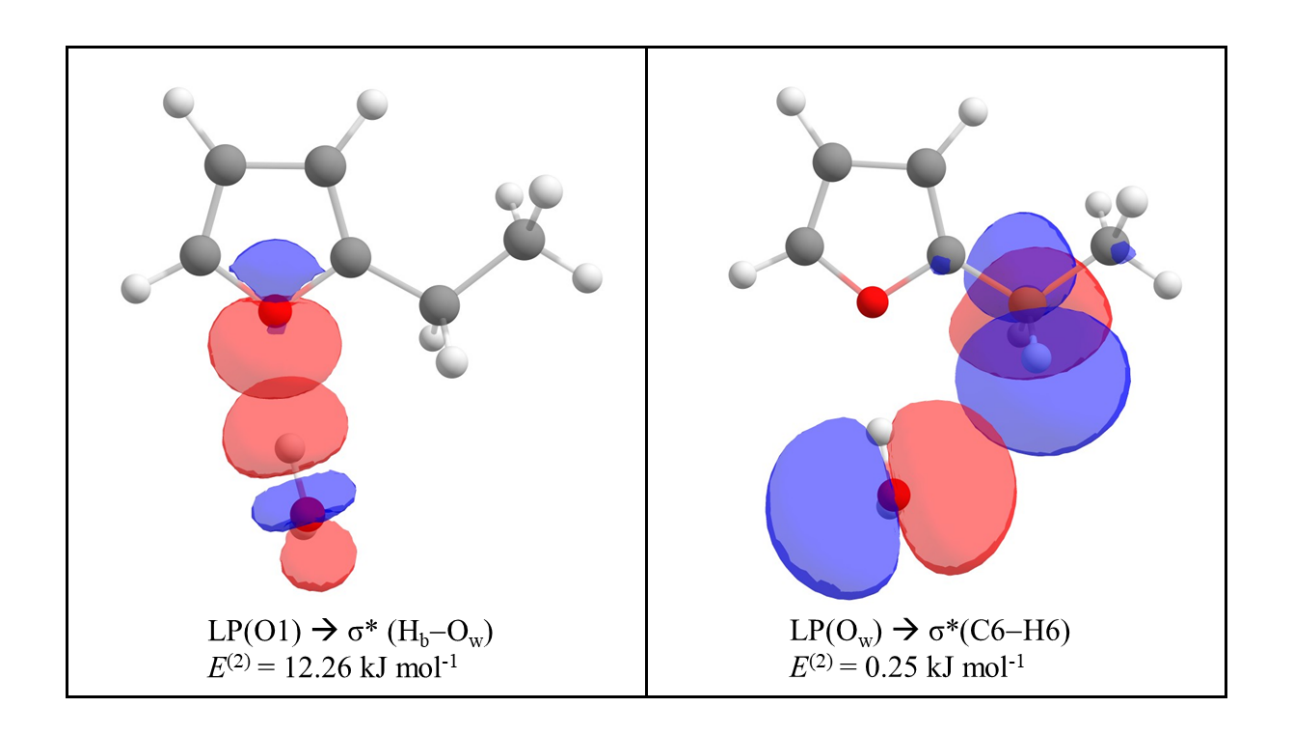
Donor NBO	Acceptor NBO	$E^{(2)}$ (kcal mol <sup>-1</sup> )	$E^{(2)}$ (kJ mol <sup>-1</sup> )
σ(C4-C5)	$\sigma^*(H_b-O_w)$	0.05	0.21
σ(C2-C3)	$\sigma^*(H_b-O_w)$	0.06	0.25
σ(C7-H7)	$\sigma^*(O_w$ - $H_{nb})$	0.05	0.21
LP(1) O1	$\sigma^*(H_b-O_w)$	2.85	11.92
LP(2) O1	$\sigma^*(H_b-O_w)$	0.23	0.96
$\sigma(H_b\text{-}O_w)$	σ*(O1-C5)	0.08	0.33
$LP(1) O_W$	σ*(O1-C5)	0.05	0.21
$LP(2) O_w$	σ*(C6-H6)	0.21	0.88
<b>LP(2)</b> O <sub>w</sub>	σ*(C6-H6)	0.08	0.33



A27 (Chapter 5) NCI isosurfaces and plots of the RDG (a.u.) vs  $sign(\lambda_2)\rho$  of the  $C_s$  conformation of 2-EF···H<sub>2</sub>O. Positive and negative values of  $sign(\lambda_2)\rho$  respectively denote repulsive (red) and attractive (blue) interactions. The isosurface s value is 0.5 au.

A28 (Chapter 5) NBO stabilisation energy contributions ( $\geq 0.21~kJ~mol^{-1}$ ) of 2-EF···H<sub>2</sub>O (C<sub>s</sub> conformer) calculated at the B3LYP(D3BJ)/aug-cc-pVTZ level of theory.

Donor NBO	Acceptor NBO	$E^{(2)}$ (kcal mol <sup>-1</sup> )	$E^{(2)}$ (kJ mol <sup>-1</sup> )
σ(C4-C5)	$\sigma^*(H_b-O_w)$	0.05	0.21
σ(C2-C3)	$\sigma^*(H_b-O_w)$	0.06	0.25
LP(1) O1	$\sigma^*(H_b-O_w)$	2.93	12.26
LP(2) O1	$\sigma^*(H_b-O_w)$	0.16	0.67
$\sigma(H_b\text{-}O_w)$	σ*(O1-C5)	0.08	0.33
$LP(1) O_W$	σ*(O1-C5)	0.05	0.21
$LP(2) O_w$	σ*(C6-H6)	0.06	0.25
$LP(2) O_{w}$	$\sigma^*(C6-C7)$	0.10	0.42



A29 (Chapter 6) Atomic coordinates of the optimised geometry of 2-ethylthiazole calculated at the  $\omega$ B97X-D/aug-cc-pVQZ level of theory.

	ωB97X-D/aug-cc-pVQZ			
	a /Å	b/Å	c/Å	
S(1)	-0.8060	-1.1343	0.0315	
C(2)	0.3888	0.0771	-0.2790	
N(3)	-0.0694	1.2874	-0.2254	
C(4)	-1.4040	1.3011	0.0677	
H(4)	-1.9183	2.2470	0.1419	
C(5)	-1.9837	0.0889	0.2434	
H(5)	-3.0107	-0.1354	0.4716	
C(6)	1.8216	-0.2626	-0.5475	
H(6)	1.9194	-1.3322	-0.7329	
H(6)	2.1186	0.2514	-1.4622	
C(7)	2.7344	0.1609	0.6025	
H(7)	2.4739	-0.3655	1.5206	
H(7)	3.7750	-0.0582	0.3673	
H(7)	2.6377	1.2293	0.7854	

A30 (Chapter 6) Atomic coordinates of the optimised geometry of 2-ethylthiazole calculated at the B3LYP(D3BJ)/aug-cc-pVTZ level of theory.

B3LYP(D3BJ)/aug-cc-pVTZ			
	a /Å	b/Å	c/Å
S(1)	-0.6947	-1.1639	-0.0315
C(2)	0.3848	0.1884	-0.3093
N(3)	-0.1900	1.3453	-0.1804
C(4)	-1.5173	1.2213	0.1450
H(4)	-2.1145	2.1106	0.2757
C(5)	-1.9789	-0.0506	0.2723
H(5)	-2.9730	-0.3850	0.5110
C(6)	1.8375	-0.0105	-0.5994
H(6)	1.9846	-0.9629	-1.1102
H(6)	2.1452	0.7795	-1.2846
C(7)	2.6943	0.0396	0.6717
H(7)	2.4080	-0.7508	1.3656
H(7)	3.7492	-0.0859	0.4273
H(7)	2.5682	0.9963	1.1766

A31 (Chapter 6) Atomic coordinates of the optimised geometry of 2-ethylthiazole calculated at the B3LYP(D3BJ)/Def2-TZVP level of theory.

	B3LYP(D3B)	J)/Def2-TZVP	
	a /Å	b/Å	c/Å
S(1)	-0.7279	-1.1554	-0.0108
C(2)	0.3861	0.1528	-0.3062
N(3)	-0.1547	1.3300	-0.1996
C(4)	-1.4842	1.2481	0.1222
H(4)	-2.0586	2.1558	0.2363
C(5)	-1.9798	-0.0109	0.2688
H(5)	-2.9847	-0.3140	0.5095
C(6)	1.8342	-0.0895	-0.5910
H(6)	1.9658	-1.0908	-1.0060
H(6)	2.1442	0.6240	-1.3567
C(7)	2.7055	0.0795	0.6589
H(7)	2.4215	-0.6370	1.4313
H(7)	3.7579	-0.0772	0.4172
H(7)	2.5901	1.0832	1.0682

A32 (Chapter 6) Atomic coordinates of the optimised geometry of 2-ethylthiazole calculated at the MP2/aug-cc-pVDZ level of theory.

MP2/aug-cc-pVDZ			
	a /Å	b/Å	c /Å
S(1)	-0.7424	-1.1641	-0.0042
C(2)	0.3918	0.1325	-0.3188
N(3)	-0.1343	1.3468	-0.2161
C(4)	-1.4691	1.2792	0.1138
H(4)	-2.0458	2.1986	0.2266
C(5)	-1.9866	0.0004	0.2748
H(5)	-3.0047	-0.2974	0.5237
C(6)	1.8464	-0.1299	-0.5912
H(6)	1.9760	-1.1608	-0.9592
H(6)	2.1669	0.5553	-1.3926
C(7)	2.6964	0.0990	0.6707
H(7)	2.3887	-0.5885	1.4745
H(7)	3.7640	-0.0690	0.4583
H(7)	2.5665	1.1311	1.0295

A33 (Chapter 6) Atomic coordinates of the optimised geometry of 2-ET···H<sub>2</sub>O calculated at the  $\omega$ B97X-D/aug-cc-pVQZ level of theory.

ωB97X-D/aug-cc-pVQZ			
	a /Å	b/Å	c/Å
S(1)	-1.7583	-0.6769	-0.1292
C(2)	-0.0750	-0.3200	-0.2500
N(3)	0.2037	0.9287	-0.0258
C(4)	-0.9199	1.6556	0.2547
H(4)	-0.8293	2.7113	0.4584
C(5)	-2.0818	0.9612	0.2463
H(5)	-3.0789	1.3204	0.4297
C(6)	0.9498	-1.3716	-0.5327
H(6)	0.4697	-2.2312	-1.0005
H(6)	1.6608	-0.9588	-1.2485
C(7)	1.6960	-1.8027	0.7309
H(7)	1.0071	-2.2072	1.4726
H(7)	2.4286	-2.5707	0.4884
H(7)	2.2226	-0.9563	1.1669
$H_b$	2.1025	1.3232	-0.0912
O	3.0719	1.2902	-0.1281
$H_{nb}$	3.3434	2.1122	-0.5309

A34 (Chapter 6) Atomic coordinates of the optimised geometry of  $2\text{-}ET\cdots H_2O$  calculated at the B3LYP(D3BJ)/aug-cc-pVTZ level of theory.

	B3LYP(D3BJ)/aug-cc-pVTZ				
	a /Å	b/Å	c /Å		
S(1)	-1.7512	-0.6956	-0.1178		
C(2)	-0.0562	-0.3088	-0.2654		
N(3)	0.2017	0.9498	-0.0505		
C(4)	-0.9302	1.6683	0.2417		
H(4)	-0.8500	2.7261	0.4375		
C(5)	-2.0867	0.9568	0.2543		
H(5)	-3.0866	1.3023	0.4479		
C(6)	0.9761	-1.3514	-0.5489		
H(6)	0.5096	-2.1947	-1.0588		
H(6)	1.7109	-0.9169	-1.2268		
C(7)	1.6826	-1.8280	0.7271		
H(7)	0.9691	-2.2533	1.4336		
H(7)	2.4205	-2.5919	0.4832		
H(7)	2.1985	-0.9982	1.2061		
$H_b$	2.0730	1.3511	-0.0890		
O	3.0488	1.2965	-0.1030		
$H_{nb}$	3.3548	2.1481	-0.4244		

A35 (Chapter 6) Atomic coordinates of the optimised geometry of 2-ET $\cdots$ H<sub>2</sub>O calculated at the B3LYP(D3BJ)/Def2-TZVP level of theory.

B3LYP(D3BJ)/Def2-TZVP			
	a /Å	b/Å	c/Å
S(1)	1.7395	-0.7047	0.1298
C(2)	0.0549	-0.3020	0.2618
N(3)	-0.1890	0.9589	0.0352
C(4)	0.9520	1.6609	-0.2546
H(4)	0.8863	2.7189	-0.4603
C(5)	2.1000	0.9327	-0.2521
H(5)	3.1063	1.2654	-0.4414
C(6)	-0.9925	-1.3306	0.5442
H(6)	-0.5404	-2.1747	1.0683
H(6)	-1.7314	-0.8798	1.2084
C(7)	-1.6912	-1.8116	-0.7337
H(7)	-0.9745	-2.2466	-1.4326
H(7)	-2.4372	-2.5692	-0.4906
H(7)	-2.1990	-0.9807	-1.2216
$H_b$	-3.0444	1.3018	0.0998
O	-3.3210	2.0143	0.6833
$H_{nb}$	-2.0687	1.3536	0.0640

A36 (Chapter 6) Atomic coordinates of the optimised geometry of  $2\text{-ET}\cdots H_2O$  calculated at the MP2/aug-cc-pVDZ level of theory.

	MP2/aug-cc-pVDZ				
	a /Å	b/Å	c/Å		
S(1)	-1.7379	-0.7272	-0.1447		
C(2)	-0.0510	-0.2926	-0.2691		
N(3)	0.1848	0.9934	-0.0238		
C(4)	-0.9764	1.6720	0.2682		
H(4)	-0.9413	2.7404	0.4857		
C(5)	-2.1330	0.9056	0.2535		
H(5)	-3.1596	1.2181	0.4412		
C(6)	1.0214	-1.3104	-0.5387		
H(6)	0.5823	-2.1733	-1.0653		
H(6)	1.7696	-0.8480	-1.2018		
C(7)	1.6982	-1.7635	0.7678		
H(7)	0.9614	-2.2132	1.4526		
H(7)	2.4790	-2.5101	0.5551		
H(7)	2.1693	-0.9025	1.2639		
$H_b$	2.0825	1.3647	-0.0955		
O	3.0546	1.2510	-0.1445		
$H_{nb}$	3.3926	2.1297	-0.3559		

A37 (Chapter 6) Atomic coordinates of the optimised geometry of 2-ET···(H<sub>2</sub>O)<sub>2</sub> calculated at the  $\omega$ B97X-D/aug-cc-pVQZ level of theory.

-	ωB97X-D/aug-cc-pVQZ			
	a /Å	b/Å	c/Å	
S(1)	-2.1946	-0.7637	-0.2631	
C(2)	-0.5246	-0.3631	-0.1223	
N(3)	-0.3177	0.9048	0.0806	
C(4)	-1.4890	1.6091	0.1321	
H(4)	-1.4587	-1.4587	0.2943	
C(5)	-2.6161	0.8790	-0.0331	
H(5)	-3.6376	1.2155	-0.0365	
C(6)	0.5548	-1.3950	-0.1824	
H(6)	0.1446	-2.3243	-0.5777	
H(6)	1.3247	-1.0563	-0.8762	
C(7)	1.1917	-1.6365	1.1859	
H(7)	0.4546	-1.9880	1.9082	
H(7)	1.9787	-2.3832	1.1003	
H(7)	1.6372	-0.7193	1.5668	
$\mathrm{H}_{1\mathrm{b}}$	1.4058	1.5567	0.2635	
O1	2.3485	1.8052	0.3491	
$H_{1nb}$	2.4563	2.6041	-0.1635	
$H_{2b}$	3.3104	0.4173	-0.3822	
O2	3.7193	-0.3531	-0.8087	
$H_{2nb}$	4.4508	-0.5940	-0.2443	

A38 (Chapter 6) Atomic coordinates of the optimised geometry of 2-ET $\cdots$ (H<sub>2</sub>O)<sub>2</sub> calculated at the B3LYP(D3BJ)/aug-cc-pVTZ level of theory.

B3LYP(D3BJ)/aug-cc-pVTZ			
	a /Å	b/Å	c/Å
S(1)	2.1994	-0.7336	0.2867
C(2)	0.5037	-0.3657	0.1246
N(3)	0.2768	0.9000	-0.0948
C(4)	1.4348	1.6356	-0.1437
H(4)	1.3795	2.6988	-0.3181
C(5)	2.5809	0.9319	0.0401
H(5)	3.5949	1.2902	0.0507
C(6)	-0.5470	-1.4258	0.1770
H(6)	-0.1295	-2.3247	0.6312
H(6)	-1.3620	-1.0832	0.8147
C(7)	-1.1070	-1.7481	-1.2140
H(7)	-0.3264	-2.1235	-1.8765
H(7)	-1.8876	-2.5030	-1.1329
H(7)	-1.5428	-0.8580	-1.6641
$\mathrm{H}_{\mathrm{1b}}$	-1.4215	1.5422	-0.3038
O1	-2.3702	1.7912	-0.4104
$H_{1nb}$	-2.4784	2.6264	0.0522
$H_{2b}$	-3.3031	0.4430	0.3915
O2	-3.6640	-0.3310	0.8668
$H_{2nb}$	-4.4934	-0.5384	0.4294

A39 (Chapter 6) Atomic coordinates of the optimised geometry of 2-ET $\cdots$ (H<sub>2</sub>O)<sub>2</sub> calculated at the B3LYP(D3BJ)/Def2-TZVP level of theory.

	B3LYP(D3BJ)/Def2-TZVP			
	a /Å	b/Å	c/Å	
S(1)	-2.1836	-0.7477	-0.2900	
C(2)	-0.5016	-0.3713	-0.0954	
N(3)	-0.2853	0.9000	0.1110	
C(4)	-1.4474	1.6278	0.1217	
H(4)	-1.4043	2.6949	0.2818	
C(5)	-2.5843	0.9108	-0.0791	
H(5)	-3.6010	1.2626	-0.1185	
C(6)	0.5585	-1.4239	-0.1186	
H(6)	0.1327	-2.3534	-0.5009	
H(6)	1.3488	-1.1154	-0.8065	
C(7)	1.1738	-1.6546	1.2666	
H(7)	0.4213	-1.9879	1.9836	
H(7)	1.9525	-2.4152	1.2042	
H(7)	1.6246	-0.7367	1.6423	
$\mathrm{H}_{1\mathrm{b}}$	1.4159	1.5271	0.3381	
O1	2.3712	1.7528	0.4470	
$H_{1nb}$	2.4874	2.6254	0.0588	
$H_{2b}$	3.2511	0.4471	-0.4778	
O2	3.5948	-0.3148	-0.9863	
H <sub>2nb</sub>	4.2726	-0.7063	-0.4276	

A40 (Chapter 6) Atomic coordinates of the optimised geometry of 2-ET $\cdots$ (H<sub>2</sub>O)<sub>2</sub> calculated at the MP2/aug-cc-pVDZ level of theory.

	MP2/aug-cc-pVDZ		
	a /Å	b/Å	c/Å
S(1)	-2.1836	-0.7477	-0.2900
C(2)	-0.5016	-0.3713	-0.0954
N(3)	-0.2853	0.9000	0.1110
C(4)	-1.4474	1.6278	0.1217
H(4)	-1.4043	2.6949	0.2818
C(5)	-2.5843	0.9108	-0.0791
H(5)	-3.6010	1.2626	-0.1185
C(6)	0.5585	-1.4239	-0.1186
H(6)	0.1327	-2.3534	-0.5009
H(6)	1.3488	-1.1154	-0.8065
C(7)	1.1738	-1.6546	1.2666
H(7)	0.4213	-1.9879	1.9836
H(7)	1.9525	-2.4152	1.2042
H(7)	1.6246	-0.7367	1.6423
$H_{1b}$	1.4159	1.5271	0.3381
O1	2.3712	1.7528	0.4470
$H_{1nb}$	2.4874	2.6254	0.0588
$H_{2b}$	3.2511	0.4471	-0.4778
O2	3.5948	-0.3148	-0.9863
$H_{2nb}$	4.2726	-0.7063	-0.4276

A41 (Chapter 6) Experimental geometrical parameters of 2-ethylthiazole derived using EVAL.

	Bond lengths / Å	
	Method	Value
S1-C2	r <sub>e</sub> (calc.) <sup>a</sup>	1.730
	$r_{\rm s}$ (exp.)	1.693(11)
C4–C5	$r_{\rm e}$ (calc.)	1.355
	$r_{\rm s}$ (exp.)	1.3674(29)
C5–S1	r <sub>e</sub> (calc.)	1.711
	$r_{\rm s}$ (exp.)	1.7173(20)
C2-C6	r <sub>e</sub> (calc.)	1.497
	$r_{\rm s}$ (exp.)	1.5177(52)
C6-C7	r <sub>e</sub> (calc.)	1.528
	$r_{\rm s}$ (exp.)	1.5346(40)
	Bond angles / °	
	Method	Value
C4-C5-S1	r <sub>e</sub> (calc.)	109.2
	$r_{\rm s}$ (exp.)	109.13(20)
C5-S1-C2	r <sub>e</sub> (calc.)	89.8
	$r_{\rm s}$ (exp.)	89.57(33)
C2-C6-C7	r <sub>e</sub> (calc.)	112.0
	$r_{\rm s}$ (exp.)	112.45(36)
	Dihedral angles / °	
	Method	Value
C7-C6-C2-S1	r <sub>e</sub> (calc.)	-110.28395
	$r_{\rm s}$ (exp.)	-98.6(10)
C4-C5-S1-C2	r <sub>e</sub> (calc.)	0.03
	$r_{\rm s}$ (exp.)	1.08(85)
C7-C6-C2-C4	r <sub>e</sub> (calc.)	65.6
	$r_{\rm s}$ (exp.)	75.7(17)
C7-C6-C2-C5	r <sub>e</sub> (calc.)	-105.5
	$r_{\rm s}$ (exp.)	-87.8(26)

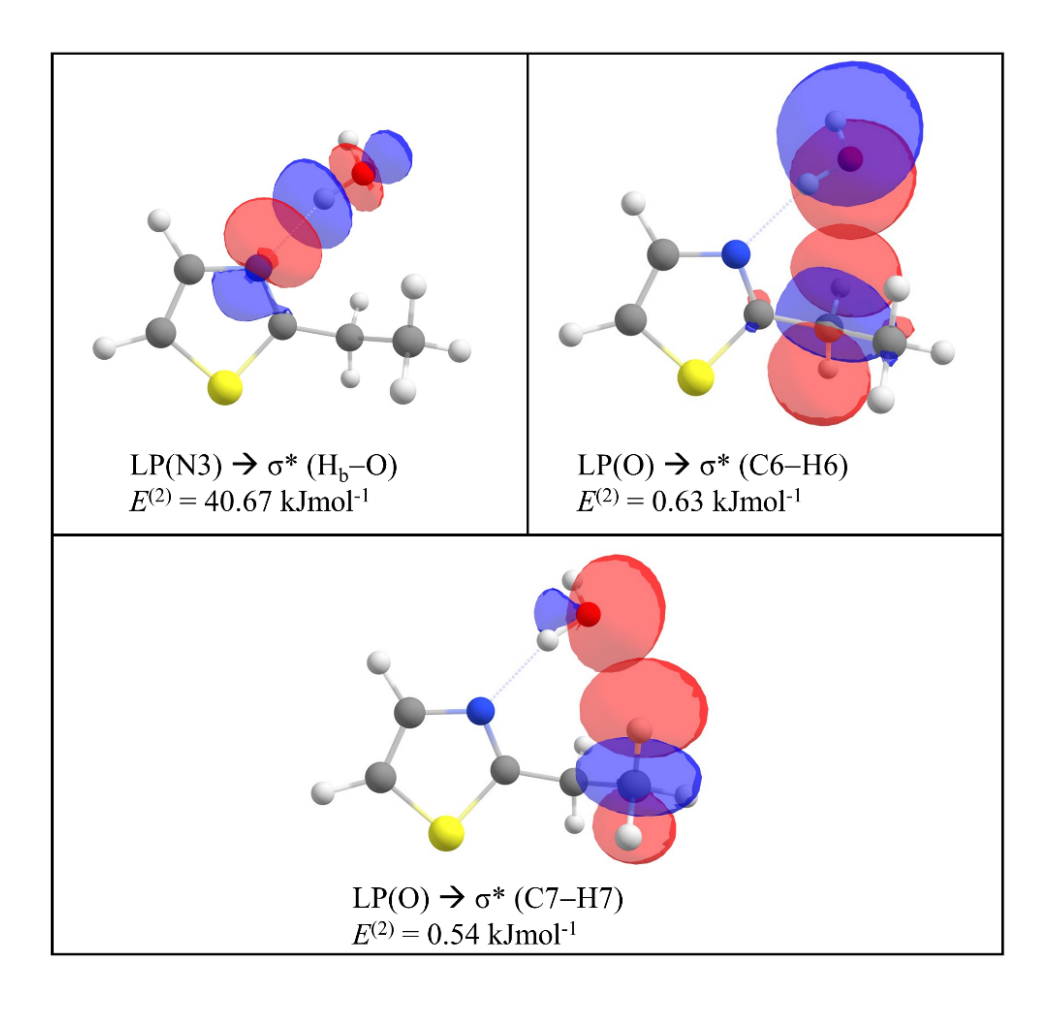
 $r_s$  (cap.) -8/.8(26) a  $r_e$  geometry calculated at the  $\omega$ B97X-D/aug-cc-pVQZ level of theory.

A42 (Chapter 6) Atomic coordinates of 2-ET···H<sub>2</sub>O and 2-ET···(H<sub>2</sub>O)<sub>2</sub> determined by the  $r_0$  method.

	2-ET···H₂O				
	a /Å $b$ /Å $c$				
S(1)	-1.76755(38)	-0.65883(74)	-0.15209(11)		
C(2)	-0.07846(20)	-0.31989(30) $-0.23985(6)$			
N(3)	0.21080(63)	0.92232(47) 0.00641(14			
C(4)	-0.90903(110)	1.65835(24)	0.27849(6)		
H(4)	-0.80985(175)	2.70993(18)	0.49844(11)		
C(5)	-2.07848(68)	0.97775(94)	0.24103(7)		
H(5)	-3.07436(92)	1.34601(156)	0.41285(15)		
C(6)	0.93891(84)	-1.37941(93)	-0.52023(12)		
H(6)	0.45699(140)	-2.22678(65)	-1.00791(4)		
H(6)	1.66651(65)	-0.96500(139)	-1.21822(20)		
C(7)	1.65880(102)	-1.83659(132)	0.74957(17)		
H(7)	0.95298(120)	-2.24319(87)	1.47400(9)		
H(7)	2.38654(150)	-2.60961(177)	0.50853(21)		
H(7)	2.18773(49)	-1.00241(163)	1.20602(25)		
$H_b$	2.14782(94)	1.31168(18)	-0.09409(9)		
O	3.11279(95)	1.27914(42)	-0.19413(19)		
$H_{nb}$	3.40222(101)	2.17721(50)	-0.02382(26)		
	2-ET	·(H <sub>2</sub> O) <sub>2</sub>			
	a /Å	b/Å	c /Å		
S(1)	-2.21319(407)	-0.74692(705)	0.26953(37)		
C(2)	-0.53687(218)	-0.37547(119)	0.12417(131)		
N(3)	-0.30841(407)	0.88860(252)	-0.07996(55)		
C(4)	-1.46744(750)	1.61319(291)	-0.12862(324)		
H(4)	-1.41908(1267)	2.67874(242)	-0.29134(499)		
C(5)	-2.60664(399)	0.90281(849)	0.03998(348)		
H(5)	-3.62215(563)	1.25707(1324)	0.04592(537)		
C(6)	0.52475(712)	-1.42607(594)	0.18183(444)		
H(6)	0.09950(1191)	-2.34786(322)	0.57855(547)		
H(6)	1.30219(647)	-1.10048(841)	0.87346(487)		
C(7)	1.15366(660)	-1.67905(1118)	-1.18813(566)		
H(7)	0.40866(730)	-2.01799(892)	-1.90835(530)		
H(7)	1.92779(1025)	-2.43936(1466)	-1.10437(793)		
H(7)	1.61403(189)	-0.76989(1398) -1.57059(470			
$H_{1b}$	1.39716(1263)	1.57365(575)	-0.27571(74)		
01	2.33394(1361)	1.84091(894)	-0.36874(90)		
$H_{1nb}$	2.43012(1571)	2.64106(844)	0.14431(152)		
$H_{2b}$	3.37343(266)	0.40502(475)	0.38800(492)		
O2	3.80112(562)	-0.35788(420)	0.80985(324)		
$H_{2nb}$	4.53246(574)	-0.58338(215)	0.23900(214)		

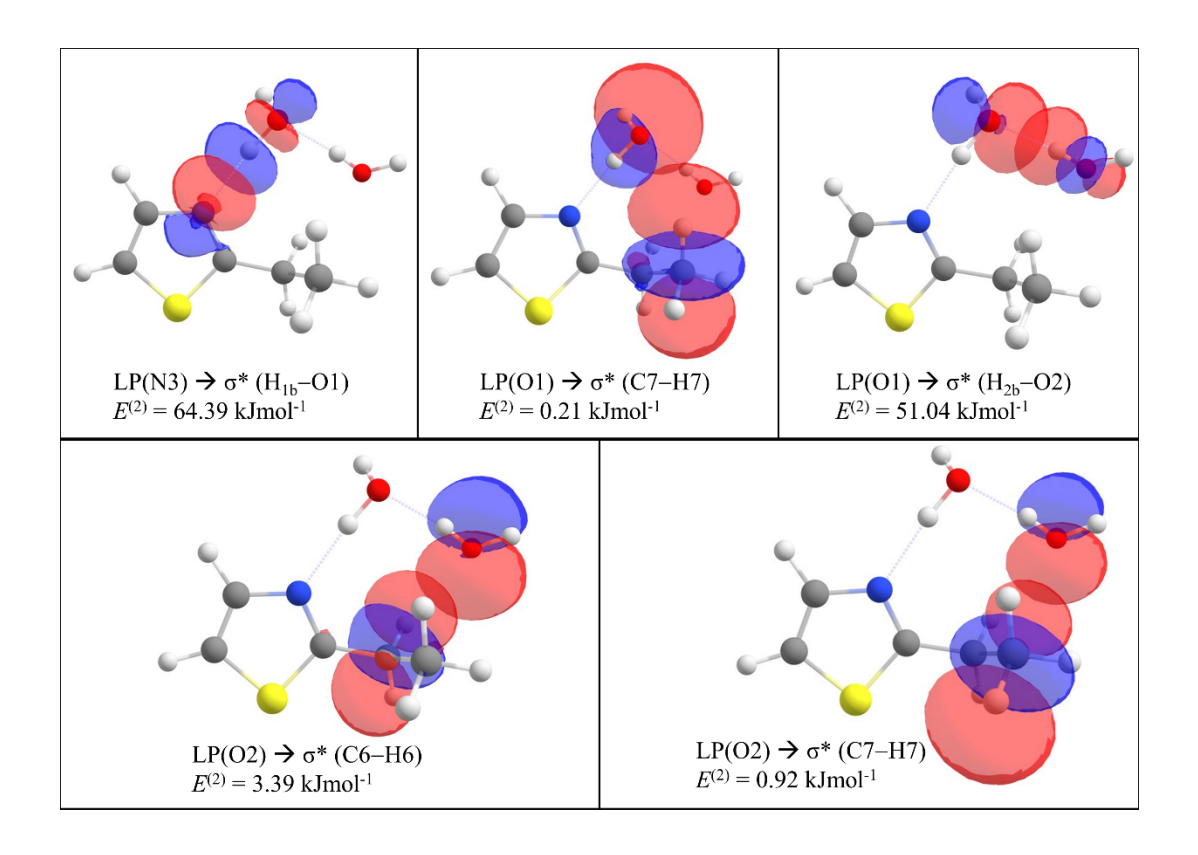
A43 (Chapter 6) NBO stabilisation energy contributions ( $\geq 0.21~kJ~mol^{-1}$ ) of 2-ET···H<sub>2</sub>O calculated at the B3LYP(D3BJ)/aug-cc-pVTZ level of theory.

Donor NBO	Acceptor NBO	E <sup>(2)</sup> (kcal mol <sup>-1</sup> )	E <sup>(2)</sup> (kJ mol <sup>-1</sup> )
σ(S1-C2)	σ*(H <sub>b</sub> -O)	0.17	0.71
σ(C4-C5)	$\sigma^*(H_b-O)$	0.10	0.42
σ(C7-H7)	$\sigma^*(O-H_{nb})$	0.09	0.38
<b>LP(1) N3</b>	$\sigma^*(H_b-O)$	9.72	40.67
$\sigma(H_b-O)$	$\sigma^*(C2-N3)$	0.17	0.71
LP(1) O	$\sigma^*(C2-N3)$	0.05	0.21
<b>LP(1) O</b>	σ*(C7-H7)	0.13	0.54
LP(2) O	$\sigma^*(C6-H6)$	0.06	0.25
LP(2) O	σ*(C6-H6)	0.15	0.63



A44 (Chapter 6) NBO stabilisation energy contributions ( $\geq 0.21~kJ~mol^{-1}$ ) of 2-ET···(H<sub>2</sub>O)<sub>2</sub> calculated at the B3LYP(D3BJ)/aug-cc-pVTZ level of theory.

Acceptor NBO	$E^{(2)}$ (kcal mol <sup>-1</sup> )	$E^{(2)}$ (kJ mol <sup>-1</sup> )
$\sigma^*(H_{1b}\text{-O1})$	0.21	0.88
$\sigma^*(H_{1b}\text{-O1})$	0.09	0.38
$\sigma^*(H_{1b}\text{-O1})$	0.11	0.46
$\sigma^*(O1-H_{1nb})$	0.07	0.29
σ*(H <sub>1b</sub> -O1)	15.39	64.39
$\sigma^*(O2-H_{2nb})$	0.09	0.38
σ*(N3-C4)	0.06	0.25
σ*(C2-N3)	0.14	0.59
σ*(C7-H7)	0.05	0.21
σ*(C2-N3)	0.07	0.29
$\sigma^*(H_{2b}-O2)$	0.17	0.71
$\sigma^*(H_{2b}-O_2)$	12.20	51.04
σ*(C6-H6)	0.06	0.25
σ*(C6-H6)	0.18	0.75
σ*(C6-H6)	0.81	3.39
σ*(C7-H7)	0.22	0.92
	$\sigma^*(H_{1b}-O1)$ $\sigma^*(H_{1b}-O1)$ $\sigma^*(H_{1b}-O1)$ $\sigma^*(O1-H_{1nb})$ $\sigma^*(O2-H_{2nb})$	$\begin{array}{cccccccccccccccccccccccccccccccccccc$



A45 (Chapter 7) Atomic coordinates of the optimised geometry of N-ethylimidazole and 2-ethylimidazole calculated at the  $\omega$ B97X-D/aug-cc-pVQZ level of theory.

N-ethylimidazole					
	a / Å	b / Å	<i>c</i> / Å		
N(1)	0.208448	-0.036124	0.308404		
C(2)	-0.632951	-1.065336	0.046759		
H(2)	-0.303772	-2.091387	0.089961		
N(3)	-1.840429	-0.659718	-0.245652		
C(4)	-1.782774	0.705331	-0.177564		
H(4)	-2.647680	1.317642	-0.367342		
C(5)	-0.525327	1.111515	0.159240		
H(5)	-0.094952	2.085368	0.311901		
C(6)	1.627272	-0.128097	0.588246		
H(6)	1.813404	-1.112332	1.016725		
H(6)	1.870379	0.605947	1.355934		
C(7)	2.484229	0.085821	-0.650019		
H(7)	2.301098	1.068391	-1.082949		
H(7)	3.540658	0.015352	-0.393387		
H(7)	2.259836	-0.665436	-1.405805		
		$C7-C6-C2-N3) = 0^{\circ}$	1.403003		
	$\frac{2 \text{ cmynnndazore } \angle \{0\}}{a / A}$	b/A	c / Å		
N(1)	0.871886	-1.074531	0.016440		
H(1)	0.818326	-2.075092	0.035303		
C(2)	-0.183353	-0.217395	-0.021086		
N(3)	0.227512	1.023327	-0.033454		
C(4)	1.598606	0.968228	-0.002819		
H(4)	2.197236	1.862781	-0.002819 $-0.003081$		
C(5)	2.021142	-0.323101	0.028304		
H(5)	2.998934	-0.767320	0.028304		
C(6)	-1.600526	-0.691448	-0.049510		
H(6)	-1.769304	-0.091448 $-1.253526$	-0.972075		
H(6)	-1.752836	-1.23320 $-1.398868$	0.769957		
H(6)	-1.732636 $-2.607686$	0.444102	0.769937		
C(7)	-2.466241	1.004325	0.033922		
H(7)			-0.771989		
	H(7) -2.489178 1.142284				
H(7)	$\frac{-3.622455}{2\text{-ethylimidazole}\angle(C)}$	$\frac{0.049043}{7 - C6 - C2 - N3} = 180^{\circ}$	0.035480		
	$\frac{2\text{-enrymindazoie} \angle(C)}{a / A}$	b/A	<i>c</i> / Å		
N(1)	0.276417	0.969012	0.000299		
H(1)	-0.301054	1.787992	0.000299		
C(2)	-0.301034 -0.159689	-0.317902	0.000823		
V(2)	0.849515	-0.317902 -1.150796	-0.000175 $-0.000040$		
N(3)		-0.374582			
C(4)	1.978536	-0.374382 -0.812066	-0.000502		
H(4)	2.962129		-0.000983 $0.000143$		
C(5)	1.649357 2.239658	0.945137 1.842956	0.000143		
H(5)		-0.707825			
C(6)	-1.603339		0.000525		
H(6)	-1.780966	-1.340760	-0.869785		
H(6)	-1.781063	-1.339115	0.872019		
C(7)	-2.576627 2.602214	0.463986	-0.000608		
H(7)	-3.603314 2.452427	0.102978	-0.000375		
H(7)	-2.452437 2.452200	1.090212	0.884334		
H(7)	-2.452209	1.088607	-0.886643		

A46 (Chapter 7) Atomic coordinates of the optimised geometry of N-ethylimdazole and 2-ethylimidazole calculated at the B3LYP(D3BJ)/aug-cc-pVTZ level of theory.

N-ethylimidazole					
	a / Å	b / Å	<i>c</i> / Å		
N(1)	0.209777	-0.074945	0.292704		
C(2)	-0.667436	-1.077474	0.003983		
H(2)	-0.369662	-2.113207	0.010148		
N(3)	-1.869591	-0.620821	-0.260414		
C(4)	-1.773545	0.744791	-0.143928		
H(4)	-2.623129	1.386191	-0.303097		
C(5)	-0.496234	1.103532	0.194406		
H(5)	-0.036402	2.058282	0.375423		
C(6)	1.630892	-0.215742	0.568203		
H(6)	1.800841	-1.251786	0.858826		
H(6)	1.876773	0.404478	1.430859		
C(7)	2.502532	0.154055	-0.626254		
H(7)	2.349254	1.193533	-0.020234 $-0.914226$		
	3.556122	0.020101	-0.379621		
H(7) H(7)	2.265178	-0.474238	-0.379021 -1.484211		
П(/)			-1.464211		
	$\frac{2\text{-etnylimidazole}}{a / \text{A}}$	$\frac{\text{C7-C6-C2-N3}) = 0^{\circ}}{b \mid \text{Å}}$	<i>c</i> / Å		
N/1)	0.878421	$\frac{b / A}{-1.078989}$	$\frac{c / A}{-0.001759}$		
N(1)		-1.078989 -2.082456			
H(1)	0.832632		-0.003151		
C(2)	-0.188378	-0.223107	0.001712		
N(3)	0.224902	1.023670	0.002915		
C(4)	1.602072	0.975355	0.000282		
H(4)	2.196761	1.872170	0.000414		
C(5)	2.030873	-0.319963	-0.002282		
H(5)	3.009933	-0.762790	-0.004902		
C(6)	-1.606254	-0.696372	0.004594		
H(6)	-1.769152	-1.341899	-0.864233		
H(6)	-1.770232	-1.328097	0.883356		
C(7)	-2.613816	0.448419	-0.004806		
H(7)	-3.630672	0.056661	-0.001857		
H(7)	-2.482856	1.087141	0.866718 -0.886467		
H(7)		-2.482597 1.073087			
	2-ethylimidazole∠(C		. 0		
	a / Å	<i>b</i> / Å	c / Å		
N(1)	-0.277674	0.972316	-0.000054		
H(1)	0.297751	1.794949	-0.000806		
C(2)	0.165071	-0.320350	-0.000110		
N(3)	-0.852025	-1.153652	0.000256		
C(4)	-1.987416	-0.377057	0.000013		
H(4)	-2.970168	-0.815805	0.000217		
C(5)	-1.656932	0.948154	-0.000042		
H(5)	-2.246238	1.846548	0.000076		
C(6)	1.609169 -0.709041		-0.000358		
H(6)	1.789431	-1.343296	0.869912		
H(6)	1.789420	-1.342284	-0.871380		
C(7)	2.584468	0.465677	0.000313		
H(7)	3.612550	0.106792	0.000160		
H(7)	2.459033	1.092786	-0.884331		
H(7)	2.458905	1.091937	0.885529		
(-,		·	<del></del>		

A47 (Chapter 7) Atomic coordinates of the optimised geometry of N-ethylimidazole and 2-ethylimdazole calculated at the B3LYP(D3BJ)/Def2-TZVP level of theory.

N-ethylimidazole					
	a / Å	<i>b</i> / Å	<i>c</i> / Å		
N(1)	0.209735	-0.074094	0.292517		
C(2)	-0.667215	-1.076972	0.004467		
H(2)	-0.368898	-2.113676	0.011365		
N(3)	-1.869281	-0.621397	-0.259802		
C(4)	-1.773545	0.743853	-0.144448		
H(4)	-2.624361	1.385295	-0.303962		
C(5)	-0.496436	1.103932	0.193554		
H(5)	-0.036706	2.059902	0.374454		
C(6)	1.630316	-0.214526	0.568417		
H(6)	1.800287	-1.251154	0.860925		
H(6)	1.876824	0.407540	1.430924		
C(7)	2.502726	0.152710	-0.626150		
H(7)	2.350624	1.192892	-0.020130 $-0.915918$		
11(7) 11(7)	3.557063	0.017822	-0.378761		
H(7) H(7)	2.264745	-0.477123	-0.378701 $-1.484051$		
П(/)	$\frac{2.204/43}{2\text{-ethylimidazole } \angle(0)}$		-1.484031		
	$\frac{2-\text{ethyllimidazole } \angle (0)}{a \mid A}$	b / Å	<i>c</i> / Å		
N(1)	0.878664	$\frac{67 \text{ A}}{-1.078721}$	$\frac{c / A}{-0.001911}$		
H(1)	0.833487	-2.083040	-0.003575		
C(2)	-0.187974	-0.223411	0.003373		
	0.224597	1.023311	0.001738		
N(3)					
C(4)	1.601001	0.975617	0.000145		
H(4)	2.195843	1.873624	0.000208		
C(5)	2.030514	-0.319793	-0.002126		
H(5)	3.010758	-0.762499	-0.004608		
C(6)	-1.606170	-0.696684	0.004700		
H(6)	-1.770096	-1.342771	-0.864971		
H(6)	-1.771160	-1.328665	0.884525		
C(7)	-2.612965	0.448608	-0.004878		
H(7)	-3.631034	0.056912	-0.001733		
H(7)			0.867269		
H(7)	-2.480994	1.073473	-0.887515		
	2-ethylimidazole∠(C'		, ¥		
37(1)	a / A	<i>b</i> / Å	c/A		
N(1)	0.277824	0.972339	0.000239		
H(1)	-0.297834	1.795785	0.000957		
C(2)	-0.164361	-0.320288	0.000118		
N(3)	0.852063	-1.153887	0.000025		
C(4)	1.986604	-0.377136	-0.000403		
H(4)	2.970295	-0.816322	-0.000805		
C(5)	1.656496	0.948394	0.000088		
H(5)	2.246438	1.847576	0.000049		
C(6)	-1.608816	-0.708933	0.000368		
H(6)	-1.789476	-1.343622	-0.870785		
H(6)	-1.789570	-1.342422	0.872383		
C(7)	-2.584464	0.465514	-0.000463		
H(7)	-3.613422	0.106245	-0.000342		
H(7)	-2.458900	1.093214	0.884990		
H(7)	-2.458660	1.092121	-0.886645		

A48 (Chapter 7) Atomic coordinates of the optimised geometry of N-ethylimidazole and 2-ethylimidazole calculated at the MP2/aug-cc-pVDZ level of theory.

N-ethylimidazole					
	a / Å	b / Å	c / Å		
N(1)	0.215752	-0.070863	0.312337		
C(2)	-0.659863	-1.085478	0.014847		
H(2)	-0.355165	-2.130543	0.029541		
N(3)	-1.885061	-0.626651	-0.268010		
C(4)	-1.782625	0.745491	-0.153058		
H(4)	-2.637592	1.397596	-0.321125		
C(5)	-0.484840	1.113458	0.201922		
H(5)	-0.019362	2.078941	0.389289		
C(6)	1.647267	-0.210252	0.575428		
H(6)	1.817900	-1.254377	0.878834		
H(6)	1.902761	0.433176	1.431843		
C(7)	2.488249	0.147145	-0.651658		
H(7)	2.318381	1.193141	-0.947969		
H(7)	3.558788	0.017487	-0.427861		
H(7)	2.222560	-0.502106	-1.499382		
		$C7-C6-C2-N3) = 0^{\circ}$	1.177302		
	a / Å	b/Å	c / Å		
N(1)	0.888916	-1.086742	-0.001866		
H(1)	0.845617	-2.099373	-0.003640		
C(2)	-0.193072	-0.235219	0.001834		
N(3)	0.214354	1.038935	0.003279		
C(4)	1.598365	0.991884	0.000499		
H(4)	2.199807	1.898497	0.000741		
C(5)	2.043325	-0.325278	-0.002734		
H(5)	3.035975	-0.768520	-0.005821		
C(6)	-1.618009	-0.712900	0.005263		
H(6)	-1.788922	-1.358541	-0.874832		
H(6)	-1.790101	-1.342869	0.896436		
C(7)	-2.608983	0.456280	-0.005516		
H(7)	-3.642582	0.077542	-0.002396		
H(7)	-2.460707	1.096230	0.876015		
H(7)	0.888916	-1.086742	-0.001866		
$\frac{11(7) \qquad 0.366510 \qquad 1.060742 \qquad 0.001600}{2-\text{ethylimidazole}\angle(\text{C7-C6-C2-N3}) = 180^{\circ}}$					
_	a / Å	<i>b</i> / Å	c / Å		
N(1)	0.269555	0.977274	0.000176		
H(1)	-0.319301	1.801768	0.000463		
C(2)	-0.170156	-0.327677	0.000118		
N(3)	0.868280	-1.171599	-0.000387		
C(4)	1.999637	-0.376591	0.000180		
H(4)	2.999233	-0.806516	0.000256		
C(5)	1.651782	0.970700	-0.000144		
H(5)	2.239841	1.884849	-0.000288		
C(6)	-1.620887	-0.722058	0.000331		
H(6)	-1.806377	-1.356150	-0.882086		
H(6)	-1.806459	-1.355295	0.883355		
C(7)	-2.582842	0.472798	-0.000274		
H(7)	-3.626699	0.126012	-0.000271		
H(7)	-2.443852	1.100791	0.895334		
H(7)	-2.443573	1.100081	-0.896332		
	4.1133/3	1.100001	V.U.J.U.J.U.		

A49 (Chapter 7) Spectroscopic parameters of N-EI···H<sub>2</sub>O and 2-EI···H<sub>2</sub>O calculated at different levels of theory.

$N$ -EI $\cdots$ H <sub>2</sub> O					
	ωB97X-D/aug-cc-pVQZ		B3LYP(D3BJ)/aug-cc-pVTZ		
$A_e$ (MHz)	4161.765	+ 17 % <sup>a</sup>	4111.755	+ 15 %	
$B_{e}\left(\mathrm{MHz}\right)$	934.169	− 7.2 %	933.223	<i>−</i> 7.2 %	
$C_e({ m MHz})$	811.329	-2.9 %	813.158	-2.6 %	
$\chi_{aa}$ (N1) (MHz)	1.2219	+1.6 %	1.2978	+8%	
$[\chi_{bb}(N1) - \chi_{cc}(N1)]$ (MHz)	3.2699	+ 0.4 %	3.3022	+ 1.4 %	
$\chi_{aa}$ (N3) (MHz)	-3.8667	+ 7.6 %	-3.7878	+ 5.4 %	
$[\chi_{bb}(N3) - \chi_{cc}(N3)]$ (MHz)	-0.4071	_	-0.2558	_	
$ \mu_{\rm a} ,  \mu_{\rm b} ,  \mu_{\rm c}  ({\rm D})^{\rm b}$	5.8, 0.	7, 1.7	5.9, 0.9, 1.6		
	B3LYP(D3BJ)	)/Def2-TZVP	MP2/aug-	MP2/aug-cc-pVDZ	
$A_e$ (MHz)	3688.719	+ 3.3 %	3452.744	- 3.3 %	
$B_{e}\left(\mathrm{MHz}\right)$	992.242	<b>- 1.4 %</b>	1017.054	+ 1.0 %	
$C_e(\mathrm{MHz})$	835.050	- 0.0 %	841.891	+ 0.8 %	
$\chi_{aa}$ (N1) (MHz)	1.2271	+ 2.1 %	0.9625	− 20 %	
$[\chi_{bb}(N1) - \chi_{cc}(N1)]$ (MHz)	3.3287	+ 2.2 %	2.6013	<b>-20 %</b>	
χ <sub>aa</sub> (N3) (MHz)	-3.8734	+ 7.7 %	-3.1616	<b>−12</b> %	
$[\chi_{bb}(N3) - \chi_{cc}(N3)] (MHz)$	-0.2133	_	0.0978	_	
$[\mu_{\rm a}], [\mu_{\rm b}], [\mu_{\rm c}] ({ m D})^{ m b}$	5.5, 0.8, 1.8		5.3, 0.7, 1.5		
		$\cdots$ H <sub>2</sub> O			
	ωB97X-D/au	ıg-cc-pVQZ	B3LYP(D3BJ)/aug-cc-pVTZ		
$A_e$ (MHz)	2615.498	+ 1 %	2606.851	+ 0.6 %	
$B_e$ (MHz)	1510.970	+ 1.2 %	1511.088	+ 1.2 %	
$C_e(\mathrm{MHz})$	1030.975	+ 1 %	1029.358	+ 0.8 %	
$\chi_{aa}$ (N1) (MHz)	1.0411	<b>-3.1 %</b>	1.1122	+ 3.6 %	
$[\chi_{bb}(N1) - \chi_{cc}(N1)] (MHz)$	3.7503	+ 6.9 %	3.801	+ 8.4 %	
$\chi_{aa}$ (N3) (MHz)	-1.8763	+ 14 %	-1.7833	+ 8.7 %	
$[\chi_{bb}(N3) - \chi_{cc}(N3)] (MHz)$	-1.991	+ 25 %	-1.789	+ 13 %	
$ \mu_{\rm a} ,  \mu_{\rm b} ,  \mu_{\rm c}   ({\rm D})$	3.6, 2.4, 0.8		3.6, 2.3, 0.7		
	B3LYP(D3BJ)/Def2-TZVP		MP2/aug-cc-pVDZ		
$A_e$ (MHz)	2639.933	+ 1.9 %	2673.740	+ 3.2 %	
$B_e$ (MHz)	1506.200	+ 0.9 %	1483.062	- 0.7 %	
$C_e(\mathrm{MHz})$	1034.186	+ 1.3 %	1031.249	+ 1 %	
$\chi_{aa}$ (N1) (MHz)	1.0771	+ 0.3 %	0.8387	− 22 %	
$[\chi_{bb}(N1) - \chi_{cc}(N1)] (MHz)$	3.8885	+ 11 %	3.2035	− 8.7 %	
$\chi_{aa}$ (N3) (MHz)	-1.6811	+ 2.5 %	-1.3845	<b>- 16 %</b>	
$[\chi_{bb}(N3) - \chi_{cc}(N3)] (MHz)$	-1.9723	+ 24 %	-1.5755	- 0.85 %	
$ \mu_{\rm a} ,  \mu_{\rm b} ,  \mu_{\rm c}  ({ m D})^{ m b}$	3.6, 2.4	4, 1.1	3.5, 2	.2, 0.4	

<sup>&</sup>lt;sup>a</sup> Calculated by  $[(A_e - A_0)/A_0] \times 100$  % where  $A_e$  are the results of computational calculations presented above and  $A_0$  are the experimental rotational constants.

<sup>&</sup>lt;sup>b</sup> Electric dipole moment components along the principal inertial axes.

A50 (Chapter 7) Spectroscopic parameters of  $N\text{-EI}\cdots(H_2O)_2$  calculated at different levels of theory.

	<i>N</i> -EI · · ·	$\cdot (H_2O)_2$		
	$\omega$ B97X-D/aug	g-cc-pVQZ	B3LYP(D3BJ)	/aug-cc-pVTZ
$A_e$ (MHz)	2004.752	+3.3%	1998.784	+3.0%
$B_e$ (MHz)	805.031	-0.2%	804.215	-0.3%
$C_e(\mathrm{MHz})$	601.334	-0.4%	602.523	+0.6%
$\chi_{aa}$ (N1) (MHz)	0.963	<b>−7%</b>	1.055	+2%
$[\chi_{bb}(N1) - \chi_{cc}(N1)]$ (MHz)	3.568	-0.2%	3.677	+2.8%
$\chi_{aa}$ (N3) (MHz)	-3.4473	+7.1%	-3.427	+6.4%
$[\chi_{bb}(N3) - \chi_{cc}(N3)] (MHz)$	-0.278	_	-0.023	_
$ \mu_{\rm a} ,  \mu_{\rm b} ,  \mu_{\rm c}  ({\rm D})^{\rm b}$	4.0, 0.3	, 0.5	4.0, 0.	2, 0.5
	B3LYP(D3BJ)/	Def2-TZVP	MP2/aug-	cc-pVDZ
$A_e$ (MHz)	1979.114	+2.0%	1928.088	-0.6%
$B_e$ (MHz)	816.004	+1.2%	816.139	+1.2%
$C_e(\mathrm{MHz})$	606.776	+1.4%	603.927	+0.9%
$\chi_{aa}$ (N1) (MHz)	1.024	-0.9%	0.764	-26%
$[\chi_{bb}(N1) - \chi_{cc}(N1)]$ (MHz)	3.596	+0.6%	2.878	-19%
$\chi_{aa}$ (N3) (MHz)	-3.4156	+6.2%	-2.820	-12%
$[\chi_{bb}(N3) - \chi_{cc}(N3)]$ (MHz)	-0.106	_	0.107	_
$ \mu_{\rm a} ,  \mu_{\rm b} ,  \mu_{\rm c}   ({\rm D})^{\rm b}$	4.0, 0.0	, 0.4	4.0, 0.	4, 0.6

<sup>&</sup>lt;sup>a</sup> Calculated by  $[(A_e - A_0)/A_0] \times 100$  % where  $A_e$  are the results of computational calculations presented above and  $A_0$  are the experimental rotational constants.

<sup>&</sup>lt;sup>b</sup> Electric dipole moment components along the principal inertial axes.

A51 (Chapter 7) Atomic coordinates of the optimised geometry of N-EI···H<sub>2</sub>O and 2-EI···H<sub>2</sub>O calculated at the  $\omega$ B97X-D/aug-cc-pVQZ level of theory.

	1 V 1./1	$\cdot \cdot H_2O$	
	a / Å	b / Å	c / Å
N(1)	0.903032	0.036977	0.307891
C(2)	-0.324162	-0.524568	0.255676
H(2)	-0.486348	-1.575569	0.432067
N(3)	-1.253444	0.352954	-0.025643
C(4)	-0.598970	1.545004	-0.168294
H(4)	-1.125110	2.453973	-0.402470
C(5)	0.737249	1.369821	0.032820
H(5)	1.565673	2.054810	0.008242
C(6)	2.156352	-0.653152	0.549139
H(6)	1.906871	-1.629205	0.962383
H(6)	2.706474	-0.110067	1.317531
C(7)	2.994355	-0.805078	-0.709805
H(7)	3.277886	0.166580	-1.111771
H(7)	3.905221	-1.359391	-0.487282
H(7)	2.440800	-1.342794	-1.478047
$H_b$	-3.025512	-0.376278	-0.163477
O	-3.846021	-0.896675	-0.192122
$H_{nb}$	-4.373364	-0.566500	0.532094
	2-EI··		
	a / Å	b / Å	c / Å
N(1)	1.585572	-0.821219	0.151532
H(1)	1.910878	-1.760201	0.282966
C(2)	0.301563	-0.406125	0.276205
N(3)	0.215799	0.881196	0.042312
C(4)	1.486598	1.309035	-0.242703
H(4)	1.697530	2.339224	-0.470168
C(5)	2.355724	0.266831	-0.179333
H(5)	3.417213	0.197048	-0.328131
C(6)	-0.839031	-1.316349	0.582356
H(6)	-0.465218	-2.200428	1.102329
H(6)	-1.508971	-0.793867	1.263680
C(7)	-1.614419	-1.724011	-0.671718
H(7)	-2.430000	-2.396689	-0.409935
H(7)	-2.040102	-0.844581	-1.150639
H(7)	-0.968640	-2.233478	-1.387601
$H_b$	-1.578811	1.506871	0.035844
O	-2.549264	1.586824	0.046556
$H_{nb}$	-2.731822	2.441843	0.429817

A52 (Chapter 7) Atomic coordinates of the optimised geometry of N-EI $\cdots$ H<sub>2</sub>O and 2-EI $\cdots$ H<sub>2</sub>O calculated at the B3LYP(D3BJ)/aug-cc-pVTZ level of theory.

	N-EI·	··H <sub>2</sub> O	
	a / Å	b/Å	c / Å
N(1)	0.916319	0.062316	0.324626
C(2)	-0.306935	-0.528483	0.323956
H(2)	-0.447649	-1.571666	0.552198
N(3)	-1.258444	0.326393	0.019251
C(4)	-0.627928	1.527959	-0.193896
H(4)	-1.175782	2.414944	-0.459357
C(5)	0.719958	1.384099	-0.011748
H(5)	1.536048	2.079827	-0.082675
C(6)	2.196520	-0.593917	0.552294
H(6)	1.989408	-1.530391	1.068167
H(6)	2.781424	0.026283	1.231889
C(7)	2.961996	-0.850022	-0.740050
H(7)	3.179856	0.084126	-1.256565
H(7)	3.906988	-1.348497	-0.523747
H(7)	2.382899	-1.482897	-1.411636
$H_b$	-3.003783	-0.388447	-0.139957
O	-3.833808	-0.902717	-0.213797
$H_{nb}$	-4.413211	-0.545451	0.463695
	2-EI·		
	a / Å	<i>b</i> / Å	c / Å
N(1)	1.581412	-0.838364	0.142928
H(1)	1.903073	-1.781934	0.266571
C(2)	0.293189	-0.415265	0.279129
N(3)	0.221569	0.881008	0.052487
C(4)	1.498680	1.304870	-0.237260
H(4)	1.715653	2.334696	-0.459823
C(5)	2.362720	0.250524	-0.185923
H(5)	3.423005	0.172924	-0.339276
C(6)	-0.851552	-1.321211	0.581371
H(6)	-0.476999	-2.218604	1.079058
H(6)	-1.509908	-0.810513	1.283313
C(7)	-1.651255	-1.702255	-0.671636
H(7)	-1.019236	-2.203005	-1.406341
H(7)	-2.468032	-2.374649	-0.409382
H(7)	-2.077943	-0.811593	-1.128451
$H_b$	-1.540323	1.526451	0.048337
0	-2.517929	1.607036	0.048831
$ H_{nb}$	-2.706671	2.493465	0.365844

A53 (Chapter 7) Atomic coordinates of the optimised geometry of N-EI···H<sub>2</sub>O and 2-EI···H<sub>2</sub>O calculated at the B3LYP(D3BJ)/Def2-TZVP level of theory.

	N-EI·	··H <sub>2</sub> O	
	a / Å	b / Å	c / Å
N(1)	0.875771	0.065779	0.321711
C(2)	-0.383605	-0.440642	0.273072
H(2)	-0.605029	-1.477245	0.470333
N(3)	-1.266008	0.483264	-0.037615
C(4)	-0.550938	1.643192	-0.205049
H(4)	-1.030188	2.572178	-0.463556
C(5)	0.778618	1.404760	0.011457
H(5)	1.641936	2.045809	-0.019622
C(6)	2.101165	-0.680361	0.568159
H(6)	1.817014	-1.612061	1.057608
H(6)	2.708653	-0.115382	1.277275
C(7)	2.883555	-0.962070	-0.708500
H(7)	3.181977	-0.034120	-1.197382
H(7)	3.785305	-1.531612	-0.478247
H(7)	2.280311	-1.538133	-1.410920
$H_b$	-2.965762	-0.376132	-0.210323
O	-3.696706	-1.025711	-0.178700
$H_{nb}$	-4.218347	-0.771770	0.588271
-	2-EI··		
	a / Å	<i>b</i> / Å	c / Å
N(1)	1.562661	-0.851038	0.158564
H(1)	1.864628	-1.800159	0.295199
C(2)	0.283277	-0.399883	0.283278
N(3)	0.240000	0.894767	0.040598
C(4)	1.526189	1.288248	-0.248029
H(4)	1.765666	2.311464	-0.482372
C(5)	2.367986	0.216602	-0.179554
H(5)	3.428213	0.115320	-0.326123
C(6)	-0.882320	-1.279341	0.584999
H(6)	-0.535000	-2.162546	1.128354
H(6)	-1.555487	-0.731135	1.244364
C(7)	-1.649488	-1.697330	-0.675975
H(7)	-1.001883	-2.229079	-1.376217
H(7)	-2.480854	-2.353381	-0.413972
H(7)	-2.055664	-0.818052	-1.174120
$H_b$	-1.531875	1.531752	0.013721
O	-2.510158	1.602826	0.034808
$H_{nb}$	-2.700910	2.376290	0.572957

A54 (Chapter 7) Atomic coordinates of the optimised geometry of N-EI $\cdots$ H<sub>2</sub>O and 2-EI $\cdots$ H<sub>2</sub>O calculated at the MP2/aug-cc-pVDZ level of theory.

	N-EI·	··H <sub>2</sub> O	
	a / Å	b / Å	c / Å
N(1)	0.875023	0.082687	0.339922
C(2)	-0.404548	-0.402320	0.294313
H(2)	-0.650652	-1.439554	0.514344
N(3)	-1.282794	0.551908	-0.043025
C(4)	-0.528621	1.692153	-0.227836
H(4)	-0.981969	2.641159	-0.506018
C(5)	0.819014	1.419942	0.001576
H(5)	1.709299	2.043945	-0.036114
C(6)	2.087535	-0.701409	0.579746
H(6)	1.778684	-1.614879	1.109660
H(6)	2.737533	-0.124207	1.255339
C(7)	2.808522	-1.040899	-0.725855
H(7)	3.118224	-0.123857	-1.249194
H(7)	3.706416	-1.642560	-0.515413
H(7)	2.145827	-1.615019	-1.390523
$H_b$	-2.962431	-0.370183	-0.165576
O	-3.627522	-1.090276	-0.167969
-	-4.301098	-0.788132	0.453491
		··H <sub>2</sub> O	
	a / Å	<i>b</i> / Å	c / Å
N(1)	1.562183	-0.861335	0.171816
H(1)	1.850627	-1.821312	0.323360
C(2)	0.278238	-0.389159	0.299257
N(3)	0.247430	0.925071	0.037759
C(4)	1.547108	1.293009	-0.257731
H(4)	1.811606	2.318828	-0.504495
C(5)	2.388799	0.189233	-0.178674
H(5)	3.458707	0.069288	-0.326573
C(6)	-0.907341	-1.258763	0.588708
H(6)	-0.575271	-2.150483	1.148319
H(6)	-1.596544	-0.694017	1.234635
C(7)	-1.636851	-1.672817	-0.702681
H(7)	-2.496608	-2.320333	-0.469663
H(7)	-2.008095	-0.777576	-1.222053
H(7)	-0.960873	-2.222139	-1.378118
$H_b$	-1.550388	1.538905	0.041577
0	-2.532840	1.549273	0.064686
$\underline{\hspace{1cm}}$	-2.762402	2.475832	0.204543

A55 (Chapter 7) Atomic coordinates of the optimised geometry of N-EI $\cdots$ (H<sub>2</sub>O)<sub>2</sub> calculated at the  $\omega$ B97X-D/aug-cc-pVQZ level of theory.

-	ωB97X-D/aug-cc-pVQZ			
	a /Å	b/Å	c/Å	
N(1)	-1.243915	0.072311	-0.292958	
C(2)	0.089857	-0.058425	-0.140858	
H(2)	0.603593	-1.007859	-0.198947	
N(3)	0.665945	1.099291	0.082828	
C(4)	-0.343179	2.023073	0.078723	
H(4)	-0.153781	3.070533	0.236690	
C(5)	-1.534672	1.405073	-0.150964	
H(5)	-2.539058	1.781031	-0.227123	
C(6)	-2.189698	-1.006709	-0.509236	
H(6)	-1.610221	-1.880334	-0.802144	
H(6)	-2.826625	-0.743057	-1.353606	
C(7)	-3.025685	-1.307764	0.723960	
H(7)	-3.628694	-0.446804	1.009449	
H(7)	-3.696794	-2.142367	0.525454	
H(7)	-2.386801	-1.570260	1.565777	
$\mathrm{H}_{1\mathrm{b}}$	2.476607	0.921856	0.238335	
O1	3.392785	0.569975	0.266090	
$H_{1nb}$	3.847246	0.976996	-0.468930	
$H_{2b}$	2.996922	-1.197437	0.000159	
O2	2.612637	-2.079657	-0.147959	
H <sub>2nb</sub>	3.025737	-2.645858	0.500342	

A56 (Chapter 7) Atomic coordinates of the optimised geometry of N-EI···(H<sub>2</sub>O)<sub>2</sub> calculated at the B3LYP(D3BJ)/aug-cc-pVTZ level of theory.

	B3LYP(D3BJ)/aug-cc-pVTZ			
	a /Å	b/Å	c/Å	
N(1)	-1.258675	0.083777	-0.308651	
C(2)	0.081353	-0.077203	-0.174300	
H(2)	0.578147	-1.032383	-0.249879	
N(3)	0.679231	1.074791	0.058958	
C(4)	-0.315821	2.022503	0.081266	
H(4)	-0.104483	3.063738	0.250174	
C(5)	-1.525356	1.426182	-0.142247	
H(5)	-2.523222	1.820517	-0.202799	
C(6)	-2.236081	-0.977188	-0.511167	
H(6)	-1.692847	-1.843523	-0.884736	
H(6)	-2.924257	-0.661678	-1.295763	
C(7)	-2.993214	-1.325882	0.764231	
H(7)	-3.544523	-0.464522	1.140124	
H(7)	-3.705241	-2.128166	0.570114	
H(7)	-2.304595	-1.655533	1.541408	
$H_{1b}$	2.458193	0.906576	0.240213	
O1	3.383855	0.559631	0.305309	
$H_{1nb}$	3.876609	0.990906	-0.397715	
$H_{2b}$	3.002870	-1.189281	0.006690	
O2	2.607470	-2.068526	-0.171237	
$H_{2nb}$	3.065927	-2.678336	0.411930	

A57 (Chapter 7) Atomic coordinates of the optimised geometry of  $N\text{-EI}\cdots(H_2O)_2$  calculated at the B3LYP(D3BJ)/Def2-TZVP level of theory.

	B3LYP(D3BJ)/Def2-TZVP			
	a /Å	b/Å	c/Å	
N(1)	-1.249626	0.094849	-0.308693	
C(2)	0.091782	-0.058829	-0.180064	
H(2)	0.598105	-1.009970	-0.269285	
N(3)	0.681241	1.094346	0.068163	
C(4)	-0.319864	2.034143	0.106823	
H(4)	-0.115445	3.075361	0.290065	
C(5)	-1.525897	1.432473	-0.122485	
H(5)	-2.527597	1.820810	-0.175407	
C(6)	-2.218683	-0.969913	-0.525352	
H(6)	-1.670312	-1.824908	-0.920108	
H(6)	-2.916022	-0.645153	-1.299580	
C(7)	-2.964233	-1.351393	0.747311	
H(7)	-3.522780	-0.502894	1.144172	
H(7)	-3.669696	-2.157964	0.541512	
H(7)	-2.266780	-1.689514	1.514363	
$\mathrm{H}_{1\mathrm{b}}$	2.464282	0.901901	0.242401	
O1	3.386797	0.540063	0.269454	
$H_{1nb}$	3.855053	0.961419	-0.457658	
$H_{2b}$	2.973361	-1.207023	-0.012211	
O2	2.560548	-2.086371	-0.151284	
$H_{2nb}$	2.902908	-2.640641	0.555951	

A58 (Chapter 7) Atomic coordinates of the optimised geometry of N-EI···(H<sub>2</sub>O)<sub>2</sub> calculated at the MP2/aug-cc-pVDZ level of theory.

MP2/aug-cc-pVDZ			
	a /Å	b/Å	c/Å
N(1)	-1.258538	0.087513	-0.324560
C(2)	0.094075	-0.045655	-0.171077
H(2)	0.614118	-1.001213	-0.244361
N(3)	0.672843	1.139885	0.077565
C(4)	-0.355277	2.060461	0.088464
H(4)	-0.177745	3.119600	0.262173
C(5)	-1.569240	1.421747	-0.155903
H(5)	-2.589024	1.792748	-0.231095
C(6)	-2.208077	-1.009719	-0.517265
H(6)	-1.634496	-1.859976	-0.914944
H(6)	-2.933515	-0.701073	-1.285780
C(7)	-2.910426	-1.383853	0.788959
H(7)	-3.482245	-0.530097	1.182845
H(7)	-3.606019	-2.219940	0.616822
H(7)	-2.171584	-1.688701	1.545061
$\mathrm{H}_{1\mathrm{b}}$	2.476484	0.927862	0.254778
O1	3.389822	0.548173	0.305868
$H_{1nb}$	3.867426	0.975384	-0.416433
$H_{2b}$	2.978108	-1.214632	0.010276
O2	2.562162	-2.082838	-0.184573
$H_{2nb}$	3.073917	-2.716217	0.332407

A59 Experimental geometrical parameters of *N*-ethylimidazole derived using EVAL.

	Bond lengths / Å	
	Method	Value
C4-C5	r <sub>e</sub> (calc.) <sup>a</sup>	1.364
	$r_{\rm s}$ (exp.)	1.3703(54)
C6-C7	r <sub>e</sub> (calc.)	1.521
	$r_{\rm s}$ (exp.)	1.4768(39)
	Bond angles / °	
	Method	Value
C2-C6-C7	r <sub>e</sub> (calc.)	112.6
	$r_{\rm s}$ (exp.)	108.99(38)
C5-C6-C7	r <sub>e</sub> (calc.)	105.9
	$r_{\rm s}$ (exp.)	113.53(40)
	Dihedral angles / °	
	Method	Value
C7-C6-C2-C4	r <sub>e</sub> (calc.)	-91.6
	$r_{\rm s}$ (exp.)	-106.59(86)
C7-C6-C2-C5	r <sub>e</sub> (calc.)	-92.7
	$r_{\rm s}$ (exp.)	-105.44(69)
C7-C6-C5-C4	r <sub>e</sub> (calc.)	104.3
	$r_{\rm s}$ (exp.)	99.1(18)

<sup>&</sup>lt;sup>a</sup>  $r_e$  geometry calculated at the  $\omega$ B97X-D/aug-cc-pVQZ level of theory.

A60 Experimental geometrical parameters of 2-ethylimidazole derived using EVAL.

	Bond lengths / Å	_
	Method	Value
CX-CY	r <sub>e</sub> (calc.) <sup>a</sup>	1.359
	$r_{\rm e}$ (calc.) <sup>b</sup>	1.360
	$r_{\rm s}$ (exp.)	1.3663(47)
C2-C6	r <sub>e</sub> (calc.)	1.495
	r <sub>e</sub> (calc.)	1.495
	$r_{\rm s}$ (exp.)	1.541(10)
C6-C7	r <sub>e</sub> (calc.)	1.521
	re (calc.)	1.523
	$r_{\rm s}$ (exp.)	1.5262(44)
	Bond angles / °	
	Method	Value
C2-C6-C7	r <sub>e</sub> (calc.)	112.9
	r <sub>e</sub> (calc.)	114.6
	$r_{\rm s}$ (exp.)	112.82(20)
	Dihedral angles / °	
	Method	Value
C7-C6-C2-CX	r <sub>e</sub> (calc.)	-6.9
	r <sub>e</sub> (calc.)	-179.9
	$r_{\rm s}$ (exp.)	14.3(87)
C7-C6-C2-CY	r <sub>e</sub> (calc.)	174.6
	r <sub>e</sub> (calc.)	0.1
	$r_{\rm s}$ (exp.)	-173.3(65)

<sup>&</sup>lt;sup>a</sup>  $r_e$  geometry of 2-ethylimidazole conformation,  $\angle$ (C7–C6–C2–N3) = 0°, calculated at the  $\omega$ B97X-D/aug-cc-pVQZ level of theory.

<sup>&</sup>lt;sup>b</sup>  $r_e$  geometry of 2-ethylimidazole conformation,  $\angle$ (C7–C6–C2–N3) = 180°, calculated at the  $\omega$ B97X-D/aug-cc-pVQZ level of theory.

A61 Atomic coordinates of N-EI···H<sub>2</sub>O and 2-EI···H<sub>2</sub>O determined by the  $r_0$  method.

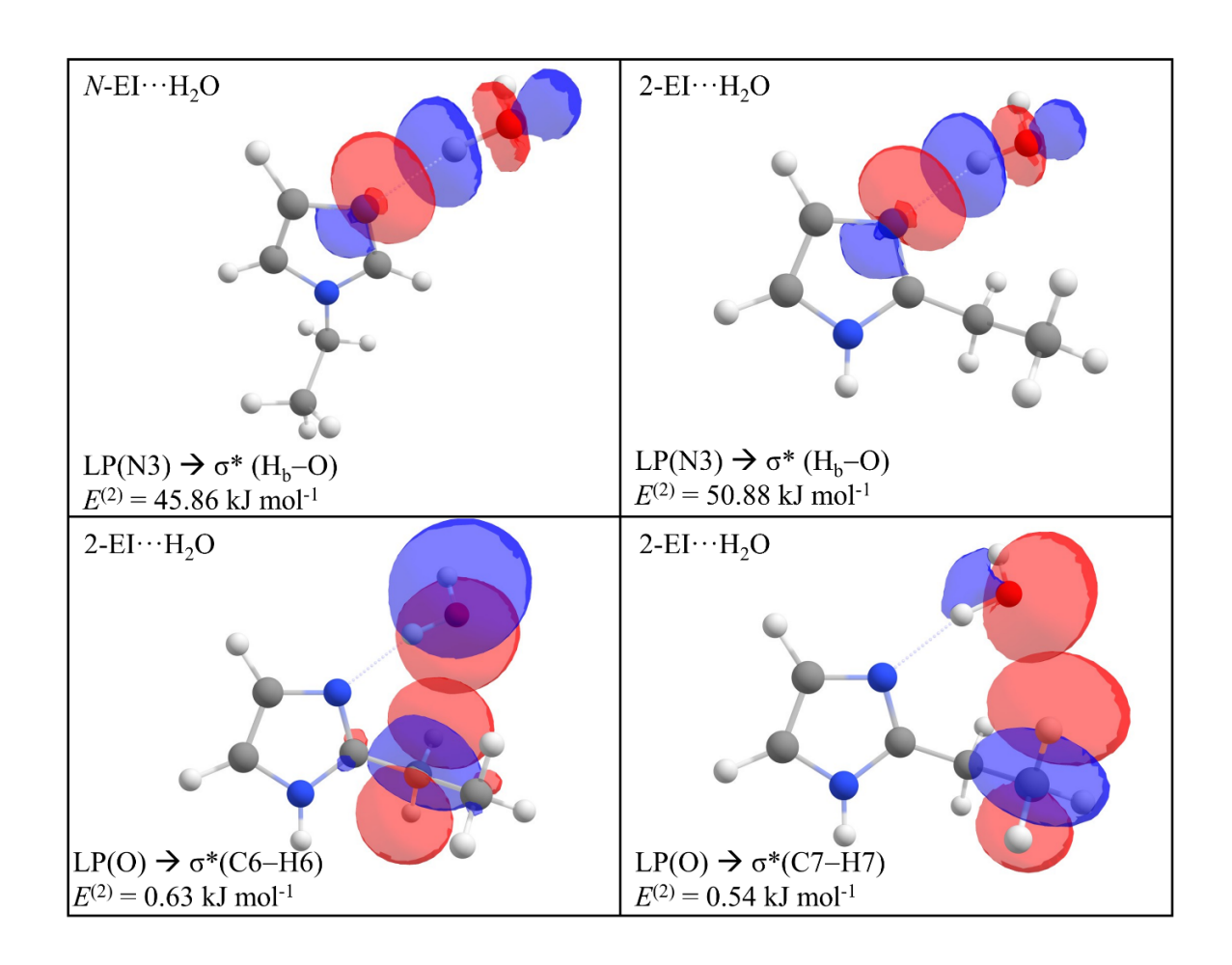
$N$ -EI $\cdots$ H $_2$ O			
	a / Å	b / Å	c / Å
N(1)	-0.85591936)	0.04730(7)	0.30471(4)
C(2)	0.41703(85)	-0.39590(188)	0.21959(40)
H(2)	0.68088(236)	-1.42875(225)	0.37966(59)
N(3)	1.25349(75)	0.56786(314)	-0.07067(48)
C(4)	0.48718(238)	1.69453(203)	-0.18483(17)
H(4)	0.92047(382)	2.65125(269)	-0.41902(16)
C(5)	-0.82193(189)	1.39255(12)	0.04247(12)
H(5)	-1.71124(277)	1.99689(121)	0.04386(40)
C(6)	-2.03336(144)	-0.75994(174)	0.56409(14)
H(6)	-2.61468(96)	-0.27878(267)	1.35056(33)
H(6)	-1.68436(291)	-1.71238(127)	0.95999(8)
C(7)	-2.88129(146)	-0.97713(284)	-0.67853(31)
H(7)	-3.26352(24)	-0.03237(336)	-1.06250(52)
H(7)	-3.73102(244)	-1.61680(411)	-0.44349(43)
H(7)	-2.29705(196)	-1.45262(190)	-1.46486(12)
$H_b$	2.94721(182)	-0.42964(75)	-0.15981(5)
O	3.68750(176)	-1.05958(162)	-0.16122(37)
$H_{nb}$	4.24412(170)	-0.78827(210)	0.56552(42)
		··H <sub>2</sub> O	
	a / Å	b / Å	c / Å
N(1)	-1.60407(79)	-0.80069(99)	0.15154(17)
H(1)	-1.94351(154)	-1.73469(126)	0.28280(27)
C(2)	-0.31394(51)	-0.40502(26)	0.27639(3)
N(3)	-0.20876(75)	0.88089(29)	0.04270(14)
C(4)	-1.47290(112)	1.32787(91)	-0.24236(11)
H(4)	-1.66826(198)	2.36117(108)	-0.46970(17)
C(5)	-2.35763(38)	0.29890(162)	-0.17923(21)
H(5)	-3.42000(37)	0.24519(251)	-0.32814(34)
C(6)	0.81274(125)	-1.33236(109)	0.58251(11)
H(6)	1.58199(146)	-1.75147(163)	-0.67152(18)
H(6)	0.42557(202)	-2.21081(82)	1.10234(8)
C(7)	1.49039(91)	-0.82015(169)	1.26394(22)
H(7)	2.38729(204)	-2.43638(231)	-0.40977(25)
H(7)	2.02093(73)	-0.87849(196)	-1.15027(28)
H(7)	0.92870(179)	-2.25101(105)	-1.38751(10)
$H_b$	1.63294(611)	1.52816(5073)	0.03343(289)
O	2.60597(428)	1.56489(166)	0.04538(11)
$H_{nb}$	2.80926(4066)	2.41810(1265)	0.43270(129)

A62 (Chapter 7) Atomic coordinates of N-EI···(H<sub>2</sub>O)<sub>2</sub> determined by the  $r_0$  method.

	N-EI···(H <sub>2</sub> O) <sub>2</sub>					
	a /Å	b/Å	c/Å			
N(1)	-1.24089(208)	0.07247(42)	0.29270(226)			
C(2)	0.09370(571)	-0.04768(4775)	0.13900(720)			
H(2)	0.61464(4003)	-0.99340(6664)	0.19344(816)			
N(3)	0.66082(3723)	1.11510(6801)	-0.08129(1062)			
C(4)	-0.35525(7030)	2.03121(3130)	-0.07319(778)			
H(4)	-0.17391(1088)	3.08060(3769)	-0.22780(963)			
C(5)	-1.54183(4675)	1.40346(1134)	0.15544(260)			
H(5)	-2.54896(5975)	1.77156(4765)	0.23374(109)			
C(6)	-2.17831(4198)	-1.01439(3396)	0.50616(251)			
H(6)	-2.81645(3594)	-0.75840(5610)	1.35196(464)			
H(6)	-1.59199(7452)	-1.88459(1246)	0.79562(137)			
C(7)	-3.01310(4825)	-1.31761(6546)	-0.72732(600)			
H(7)	-3.62285(1620)	-0.46027(8780)	-1.00938(737)			
H(7)	-3.67771(7936)	-2.15792(8927)	-0.53104(945)			
H(7)	-2.37300(5425)	-1.57244(4325)	-1.57056(386)			
$\mathrm{H}_{1\mathrm{b}}$	2.46772(8093)	0.96030(3849)	-0.23970(358)			
O1	3.38788(6562)	0.61919(8067)	-0.27010(672)			
$H_{1nb}$	3.83868(7848)	1.02872(9468)	0.46579(664)			
$H_{2b}$	2.98525(799)	-1.25217(4485)	0.00475(428)			
O2	2.61146(3424)	-2.13934(6312)	0.15011(918)			
$H_{2nb}$	3.03014(5455)	-2.69827(3834)	-0.50091(1744)			

A63 (Chapter 7) NBO stabilisation energy contributions ( $\geq 0.21 \text{ kJ mol}^{-1}$ ) of N-EI···H<sub>2</sub>O and 2-EI···H<sub>2</sub>O calculated at the B3LYP(D3BJ)/aug-cc-pVTZ level of theory.

	M EL					
N-EI···H <sub>2</sub> O						
Donor NBO	Acceptor NBO	$E^{(2)}$ (kcal mol <sup>-1</sup> )	$E^{(2)}$ (kJ mol <sup>-1</sup> )			
$\sigma(C4-C5)$	$\sigma^*(H_b-O)$	0.14	0.59			
<b>LP(1) N3</b>	$\sigma^*(H_b-O)$	10.96	45.86			
$\sigma(H_b-O)$	$\sigma^*(C4-C5)$	0.24	1.00			
$2\text{-EI}\cdots\text{H}_2 ext{O}$						
Donor NBO	Acceptor NBO	$E^{(2)}$ (kcal mol <sup>-1</sup> )	$E^{(2)}$ (kJ mol <sup>-1</sup> )			
σ(N1–C2)	$\sigma^*(H_b-O)$	0.10	0.42			
σ(C4–C5)	$\sigma^*(H_b-O)$	0.14	0.59			
σ(C7–H7)	$\sigma^*(O-H_{nb})$	0.09	0.38			
LP(1) N3	$\sigma^*(H_b-O)$	12.16	50.88			
$\sigma(H_b-O)$	$\sigma^*(N3-C4)$	0.27	1.13			
<b>LP(1) O</b>	σ*(C7–H7)	0.13	0.54			
LP(2) O	σ*(C6–H6)	0.07	0.29			
<b>LP(2) O</b>	σ*(C6-H6)	0.15	0.63			



A64 (Chapter 7) NBO stabilisation energy contributions ( $\geq 0.21~kJ~mol^{-1}$ ) of N-EI···(H<sub>2</sub>O)<sub>2</sub> calculated at the B3LYP(D3BJ)/aug-cc-pVTZ level of theory.

N-EI···(H <sub>2</sub> O) <sub>2</sub>						
Donor NBO	Acceptor NBO	$E^{(2)}$ (kcal mol <sup>-1</sup> )	E <sup>(2)</sup> (kJ mol <sup>-1</sup> )			
σ(C4–C5)	$\sigma^*(H_{1b}-O1)$	0.19	0.79			
σ(N1–C2)	$\sigma^*(H_{1b}-O1)$	0.06	0.25			
$\sigma(C2-N3)$	$\sigma^*(H_{1b}-O1)$	0.13	0.54			
LP(1) N3	$\sigma^*(H_{1b}-O1)$	17.29	72.34			
$\sigma(H_{1b}-O1)$	$\sigma^*(C2-N3)$	0.39	1.63			
LP(1) O1	$\sigma^*(C2-N3)$	0.08	0.33			
$\sigma(O1-H_{1nb})$	$\sigma^*(H_{2b}-O2)$	0.13	0.54			
LP(1) O1	$\sigma^*(H_{2b}-O2)$	0.20	0.84			
LP(2) O1	$\sigma^*(H_{2b}-O2)$	12.92	54.06			
$\sigma(H_{2b}-O2)$	σ*(C2–H2)	0.13	0.54			
LP(1) O2	σ*(C2–H2)	0.18	0.75			
LP(2) O2	σ*(N1–C2)	0.11	0.46			
LP(2) O2	σ*(C2–H2)	2.89	12.09			

